Lecture Notes in Civil Engineering

Stéphane Bonelli
Cristina Jommi
Donatella Sterpi *Editors*

Internal Erosion in Earthdams, Dikes and Levees

Proceedings of EWG-IE 26th Annual Meeting 2018

Springer

Lecture Notes in Civil Engineering

Volume 17

Lecture Notes in Civil Engineering (LNCE) publishes the latest developments in Civil Engineering - quickly, informally and in top quality. Though original research reported in proceedings and post-proceedings represents the core of LNCE, edited volumes of exceptionally high quality and interest may also be considered for publication. Volumes published in LNCE embrace all aspects and subfields of, as well as new challenges in, Civil Engineering. Topics in the series include:

- Construction and Structural Mechanics
- Building Materials
- Concrete, Steel and Timber Structures
- Geotechnical Engineering
- Earthquake Engineering
- Coastal Engineering
- Hydraulics, Hydrology and Water Resources Engineering
- Environmental Engineering and Sustainability
- Structural Health and Monitoring
- Surveying and Geographical Information Systems
- Heating, Ventilation and Air Conditioning (HVAC)
- Transportation and Traffic
- Risk Analysis
- Safety and Security

To submit a proposal or request further information, please contact the appropriate Springer Editor:

- Mr. Pierpaolo Riva at pierpaolo.riva@springer.com (Europe and Americas);
- Ms. Swati Meherishi at swati.meherishi@springer.com (India);
- Ms. Li Shen at li.shen@springer.com (China);
- Dr. Loyola D'Silva at loyola.dsilva@springer.com (Southeast Asia and Australia/NZ).

More information about this series at http://www.springer.com/series/15087

Stéphane Bonelli · Cristina Jommi
Donatella Sterpi
Editors

Internal Erosion in Earthdams, Dikes and Levees

Proceedings of EWG-IE 26th Annual Meeting 2018

Springer

Editors
Stéphane Bonelli
IRSTEA, National Research Institute
of Science and Technology for
Environment and Agriculture
Aix en Provence, France

Cristina Jommi
Department of Civil
and Environmental Engineering
Politecnico di Milano
Milan, Italy

Donatella Sterpi
Department of Civil and Environmental
Engineering
Politecnico di Milano
Milan, Italy

ISSN 2366-2557 ISSN 2366-2565 (electronic)
Lecture Notes in Civil Engineering
ISBN 978-3-319-99422-2 ISBN 978-3-319-99423-9 (eBook)
https://doi.org/10.1007/978-3-319-99423-9

Library of Congress Control Number: 2018953641

This Springer imprint is published by the registered company Springer Nature Switzerland AG
The registered company address is: Gewerbestrasse 11, 6330 Cham, Switzerland

Preface

The volume contains the contributions to the 26th Annual Meeting of the European Working Group on Internal Erosion in Embankment Dams, Levees and Dikes, and their Foundations (EWG-IE), held at Politecnico di Milano, in Milano, Italy, from September 10 to 13, 2018.

The European Working Group was set up in 1993 to focus on the vulnerability of dams to internal erosion. After an inaugural workshop on definitions and needs, the Group has regularly organized Annual Meetings to share knowledge and address emerging issues on soil internal erosion in water retaining structures. Over the years, the Meetings have seen the participation of university researchers, scientists and engineers from agencies, industries, and public bodies, from Europe and overseas.

Following the last successful event in Delft in September 2017, the objective of the meeting in Milano was to serve as a fertile discussion platform, strengthening sound knowledge as well as introducing novel ideas, in the thematic areas in line with the traditional aims of EWG-IE.

More than 100 authors, coming from academic institutions, private and public bodies, in European and overseas countries, contributed to the peer-reviewed papers included in the volume. These are grouped into four sections, namely

- Laboratory techniques and findings;
- From modeling to design criteria;
- Prevention measures and field assessment;
- Open issues for discussion and contribution.

We gratefully acknowledge the careful reviewing work by the members of the Scientific Committee, the technical and administrative support by Federica Aggio and Silvia Spada of the Department of Civil and Environmental Engineering, the skills, patience and care of Marco Caruso who took charge of the editing process, and the support of Politecnico di Milano in providing the facilities for the organization of the meeting.

Finally, we are very glad to have hosted the contributors in Milano, a city that was able to evolve and expand its horizons, from the Celtic origin to the twenty-first century, to become a center where dynamism and creativity still coexist with the quietness of old hidden corners.

Cristina Jommi
Donatella Sterpi
Chairpersons of 26th Annual Meeting

Organization

Committees

Conference Chairs

Cristina Jommi (Chairperson of 26th Annual Meeting)	Politecnico di Milano, Italy
Donatella Sterpi (Chairperson of 26th Annual Meeting)	Politecnico di Milano, Italy
Stéphane Bonelli (Chairman of the European Working Group on Internal Erosion)	IRSTEA, France

Organizing Committee at Politecnico di Milano

Marco Caruso
Cristina Jommi
Donatella Sterpi

Scientific Committee

Vera van Beek	Deltares, Delft, Netherlands
Stéphane Bonelli	IRSTEA, France
Rodney Bridle	Dam Safety Ltd, UK
Carlo Callari	Università del Molise, Italy
Jonathan Fannin	University of British Columbia, Canada
Cristina Jommi	Politecnico di Milano, Italy
André Koelewijn	Deltares, Delft, Netherlands

Didier Marot	Université de Nantes, France
Jaromír Říha	Brno University of Technology, Czech Republic
Bryant Robbins	US Army Corps of Engineers, USA
Alexander Scheuermann	University of Queensland, Australia
Donatella Sterpi	Politecnico di Milano, Italy
Akihiro Takahashi	Tokyo Institute of Technology, Japan

Organized by

POLITECNICO
MILANO 1863

Under the Auspice of

Gruppo_Nazionale
INGEGNERIA
GEOTECNICA

AGI
Associazione
Geotecnica
Italiana

With the Support of

Sistemi elettronici ed elettromeccanici (Electronic and electromechanical systems)

Contents

Prevention Measures and Field Assessment

Open Issues for Discussion and Contribution

Laboratory Techniques and Findings

Effects of Suffusion on the Soil's Mechanical Behavior: Experimental Investigations

Rodaina Aboul Hosn[1(✉)], Nadia Benahmed[1], Cong Doan Nguyen[1], Luc Sibille[2], Pierre Philippe[1], and Bruno Chareyre[2]

[1] IRSTEA, Research Unit Recover, 13182 Aix-en-Provence Cedex 5, France
rodaina.aboul-hosn@irstea.fr
[2] Université Grenoble Alpes, CNRS, Grenoble INP, 3SR, 38000 Grenoble, France

Abstract. This study presents an experimental approach to investigate the impact of suffusion on the soil's mechanical properties. A newly developed suffusion permeameter is used allowing separate erosion and mechanical tests. The effect of the initial density of the soil on the erosion process is examined. Thereafter, the influence of suffusion on the mechanical properties of the soil is investigated through drained and undrained monotonic triaxial compression tests. The results suggest that the shear strength of eroded soils may either decrease or increase or even may not be affected depending, among others, on the soil's initial density. In addition, in all cases, slightly more dilative volumetric deformations seem to occur during shearing after erosion. Understanding the mechanical behavior of eroded soils depends on the combined effect of the global void ratio, the inter-granular void ratio and the final fines content after suffusion. Taking into account such a combined effect, an approach to estimate the shear strength of eroded soils is proposed.

Keywords: Suffusion · Erosion device · Triaxial test · Shear strength

1 Introduction

Suffusion is a particular case of internal erosion which is characterized by the detachment and the migration of fine grains by interstitial flow leaving behind the granular skeleton. During such a strongly coupled fluid-solid interaction process, the coarse matrix first remains intact while fine particles in the pore spaces are mobilized and transported by the flow if smaller than the pore constriction sizes. By modifying the microstructure of the soil through the evacuation or the displacement of fines, suffusion can induce local rearrangement of the coarse particles and variations in the local density of the soil. Consequently, under a constant external mechanical load, the soil may present some changes in behavior compared to an intact specimen. Thus suffusion may lead, on one hand, to the modification of the pore spaces, thus resulting in obvious changes in the porosity and the hydraulic conductivity. On the other hand, it may lead to the loss of the mechanical resistance of the soil specimen and may eventually lead to its collapse.

S. Bonelli et al. (Eds.): EWG-IE 2018, LNCE 17, pp. 3–15, 2019.
https://doi.org/10.1007/978-3-319-99423-9_1

Experimental and numerical studies have been conducted to analyze the modifications in the shear strength of eroded soils. Either an increase (Ke and Takahashi 2014; Xiao and Shwiyhat 2012) or a decrease (Chang and Zhang 2011; Scholtès et al. 2010; Ke and Takahashi 2012) in the shear strength was noticed. Therefore, the conclusions in the literature concerning the effect of suffusion on the mechanical behavior of the soil are still controversial. Hence, the main objective of this paper is to address this issue.

2 Experimental Procedure

2.1 Tested Soil

Experiments are done using mixtures of coarse and fine silica Hostun sands, HN 1/2.5 and HN34, respectively. The siliceous sand used here is mainly composed of quartz, categorized as an angular to sub-angular material with a specific gravity, $\rho = 2.65$ g/cm^3. Soil samples with a fines content of 25% are considered in this study with minimum and maximum void ratios of 0.38 and 0.63, respectively. Figure 1 presents the particle size distributions of the used sand (with a uniformity coefficient $C_u = 8.1$, and an effective diameter, $D_{50} = 1.55$ mm).

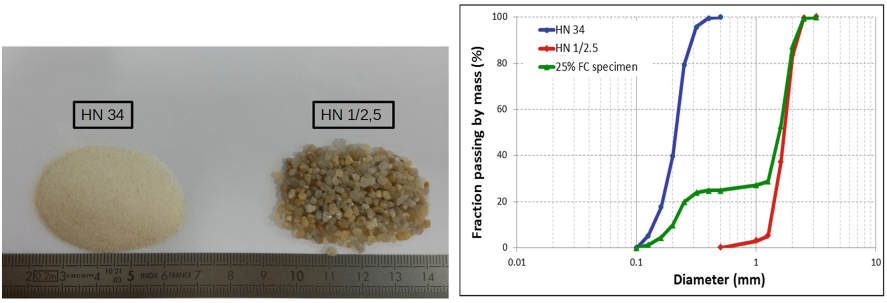

(a) (b)

Fig. 1. (a) Photograph of the two fractions of Hostun sand used in this study and (b) The particle size distributions.

2.2 Experimental Setup and Procedure

Suffusion tests were carried out using a newly developed suffusion permeameter made up of a cylindrical Plexiglas cell, 140 mm in height and 70 mm in internal diameter, in order for the soil sample to fit also the pedestal triaxial cell which is of the same diameter. The general configuration of the permeameter is illustrated in Fig. 2. The suffusion cell is connected to a water supply system and a fines collector. The soil samples were reconstituted by moist tamping. Then, they were saturated by flushing CO_2 first, followed by de-aired water in an upward direction with a very low flow rate to prevent the heave phenomenon. Thereafter, samples were subjected to the erosion test by flushing water in a downward direction.

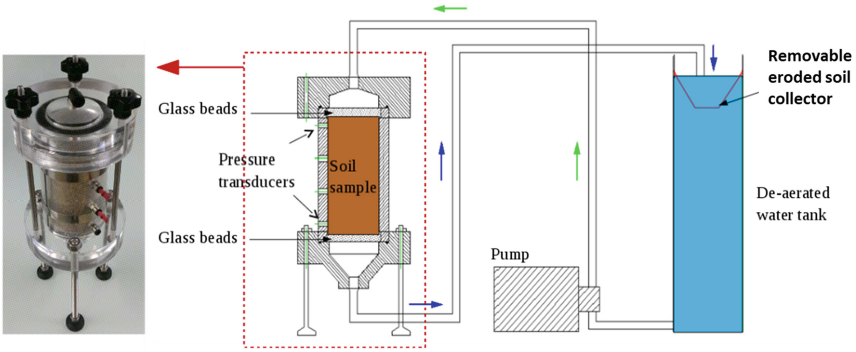

Fig. 2. Sketch of the seepage test assembly

Hydraulic soil properties, settlement-by visualization and measurement- and the eroded mass during suffusion are characterized using this apparatus. In addition, the development of preferential path near the cell wall can also be observed.

In this apparatus, the seepage test is performed by a constant-flow-rate method. The control unit is composed of a rotary pump for pumping water through the specimen and a low capacity differential pressure transducer (LCDPT) for measuring the pressure drop from the top to the bottom of the tested specimens. Note that the flow rate is increased by steps to take into account the effect of the hydraulic loading history on the suffusion development (Sibille et al. 2015). Thus, the flow rate is increased to a fixed value large enough to trigger the erosion of fine particles for each step, and then is kept constant until no more eroded fine particles are observed (Aboul Hosn et al. 2017). The test is then stopped when reaching the maximum laminar flow velocity of 0.74 cm/s.

Once the internal erosion process is done, the soil samples are recovered and frozen to preserve the soil's microstructure (Fig. 3a). Afterwards, they are installed in the triaxial cell, first confined at 50 kPa to prevent their collapse once thawed.

After about 4 h (the time needed for the soil to thaw), soil samples are confined at 100 kPa, and then sheared under drained/undrained conditions at a constant strain rate of 1% per minute to investigate the stress-strain behavior of eroded soil samples (Fig. 3b). To make sure that the freezing/thawing process has no influence on the soil's microstructure and thus on its mechanical behavior, results from drained triaxial compression tests done on soil samples frozen/thawed and those without freezing have been compared. Results showed that such a process do not have an impact on the soil's mechanical behavior. These results will be presented in a forthcoming paper.

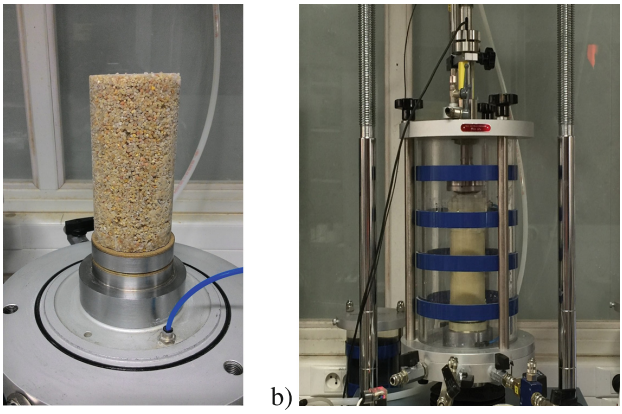

Fig. 3. (a) Frozen eroded specimen prepared for triaxial compression test, (b) Picture of the triaxial apparatus

3 Investigation of the Erosion Mechanism

Suffusion tests were conducted on soil samples prepared at three different initial densities, Id_0 = 0.2, 0.4, 0.6 (referred as samples ES-0.2, ES-0.4 and ES-0.6 respectively), to investigate the effect of the initial density on the suffusion process. Table 1 gives a summary of the suffusion test results.

Table 1. Summary of the suffusion test results.

Soil sample	$^{*}M_e$ (%)	$^{+}FC_f$ (%)	$^{\S}Id_f$	$^{¤}\varepsilon_v$ (%)	$^{\times}\Delta e_g$
ES-0.2-CD	33.42	18.16	0.15	6.57	−0.13
ES-0.2-CU	52.05	13.87	0.02	8.86	−0.19
ES-0.4-CD	40.65	16.52	0.20	5.71	−0.11
ES-0.4-CD-R	38.83	16.94	0.07	3.57	−0.08
ES-0.4-CU	47.70	14.85	≈0	4.64	−0.09
ES-0.6-CD	37.21	17.31	0.15	1.21	−0.02
ES-0.6-CU	40.42	16.57	0.15	1.86	−0.03

$^{*}M_e$: the total eroded mass; $^{+}FC_f$: the final fines content; $^{\S}Id_f$: the final density index; $^{¤}\varepsilon_v$: the volumetric deformation; $^{\times}\Delta e_g$: the variation of the inter-granular void ratio (e_g is the void ratio calculated in considering all fine particles as void); samples' label ending by: CD corresponds to drained conditions; CU corresponds to undrained conditions in the triaxial tests; R corresponds to repeatability test.

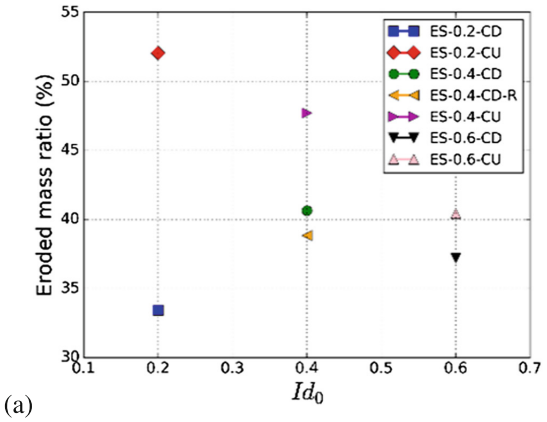

(a)

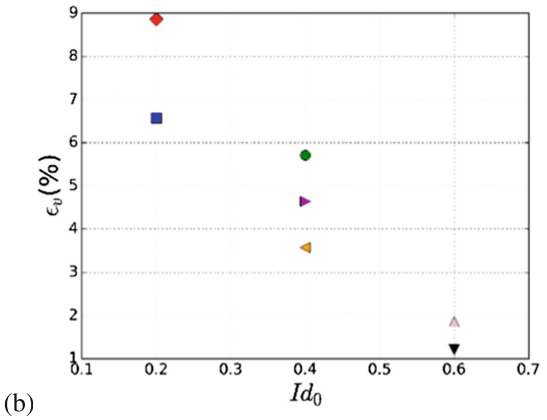

(b)

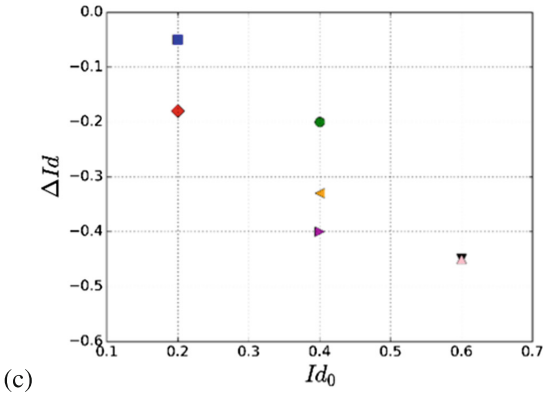

(c)

Fig. 4. The variation of (a) the final eroded mass ratio, M_e, (b) the volumetric deformation, ε_v, and (c) the variation in the sample's density, ΔId, with the initial density index, Id_0

Figure 4a shows the relation between the eroded mass at the end of the test and the samples initial density. One would notice that the looser soil specimens, ES-0.2-CD and ES-0.2-CU, may lose more fine particles than denser specimens since in a loose soil, fine particles may find larger voids to occupy without participating greatly in the stress transfer and larger pores to circulate through. So, fine particles may be more prone to erosion at looser states. However, at a loose initial density, the erosion may differ from one sample to another. This may be attributed to the effect of heterogeneities induced by erosion. Such heterogeneities are due to the inherent anisotropies linked to the initial soil deposition.

In addition to that, Fig. 4b shows the relation between the volumetric deformation after erosion and the initial density of the soil. As the initial density increases, the soil settlement decreases. In fact, the ability of the soil skeleton to resist compaction due to suffusion is higher at higher initial densities. Results show that the variation in the intergranular void ratio, Δe_g, in ES-0.6-CD and ES-0.6-CU is negligible ($\Delta e_g = -0.02$ and -0.03, respectively). This means that for the same fines content, denser samples deform less significantly compared to the other soil specimens, however, their global density change is more important than that of initially looser samples as shown in Fig. 4c.

4 Mechanical Behavior of Eroded and Non-eroded Soils

Once the erosion tests are done, the mechanical behavior of the soil is examined through drained and undrained triaxial compression tests.

4.1 Drained Response of Eroded and Non-eroded Soils

Figure 5 shows the response of eroded and non-eroded soil samples to drained triaxial compression. It can be observed that the eroded soil samples exhibit a similar tendency of stress-strain behavior as the non-eroded soil. However, quantitatively, the shear strength and the volumetric strains are different for a given initial density.

The initially loose soil sample (Fig. 5a), which had deformed significantly during suffusion, reached the same peak deviator stress as the non-eroded one.

However, in the case of initially denser soil samples (Fig. 5b and c), which had shown less deformations during suffusion resulting in a looser soil skeleton, the soil's shear strength decreases. The peak friction angle decreases from 31.4° to 28.1° for ES-0.4-CD and from 31.9° to 29.9° for ES-0.6-CD. Regarding the volumetric strains, the eroded soils seem less contracting. This may be attributed to the denser coarse fraction in the eroded soil. Note that in the case of $Id_0 = 0.4$ (Fig. 5b) the volumetric deformations of both eroded and non-eroded specimens, can be considered similar. The denser coarse skeleton and the global loose state of the material may have led to such a coincidence of volumetric deformations of eroded soil samples with different gradation and microstructure. In fact, ES-0.4-CD shows similar contractant behavior as that of the non-eroded soil. The dilatancy angle changed slightly from 1.90° for NS-0.4-CD to 2.34° for ES-0.4-CD.

Therefore, it can be concluded that in case of eroded samples, generally, the mechanical characteristics change with the erosion process. The higher is the soil's

initial density, the higher is the soil's shear strength reduction after suffusion. Moreover, volumetric deformations indicate that the soil becomes slightly more dilatant, which may be attributed to the decrease in the inter-granular void ratio and to the less compressible material due to the loss of fine particles. Thus, to understand the effect of suffusion on the shear strength, one should consider a combined role of the global and inter-granular void ratios as well as the fines content after erosion.

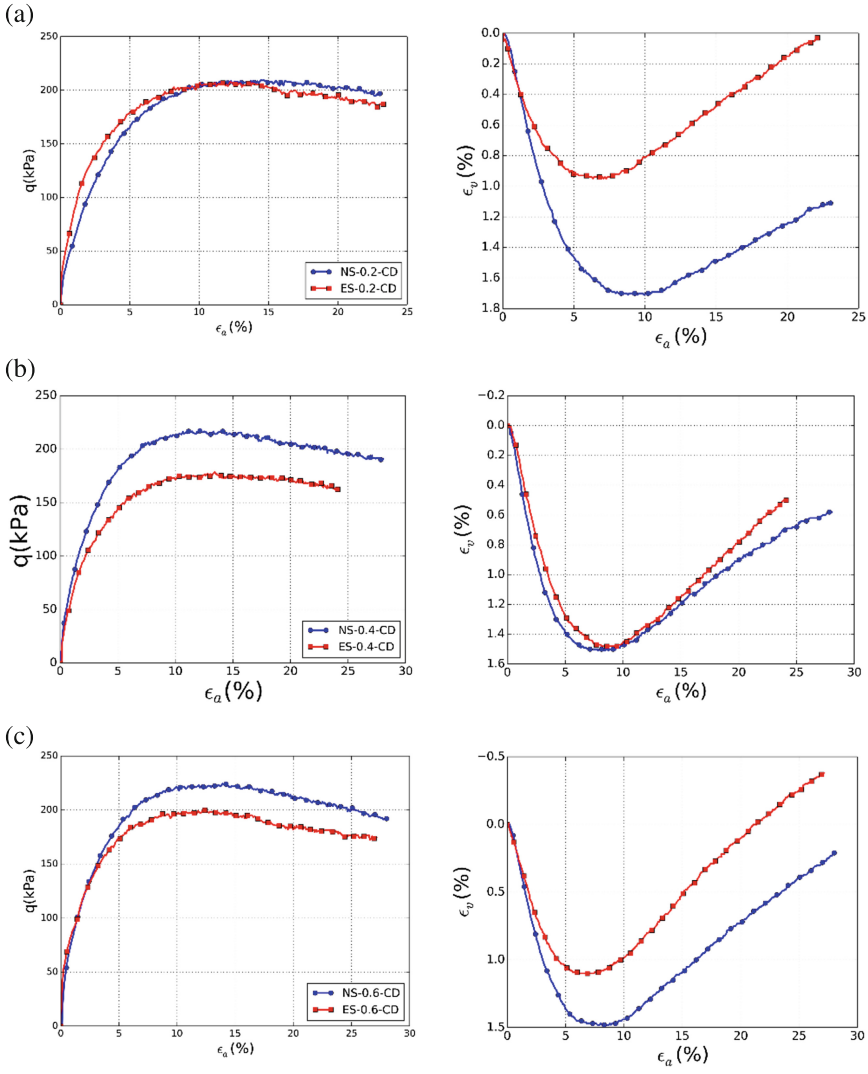

Fig. 5. Comparison of the responses to drained triaxial compression tests of the non-eroded (NS) and eroded (ES) samples at different initial densities

4.2 Undrained Response of Eroded and Non-eroded Soils

Figures 6, 7 and 8 show the response of eroded and non-eroded soil samples to undrained triaxial compressions. Results indicate that eroded soil samples have a similar stress-strain response as the non-eroded ones, i.e. contractant-dilatant behavior.

Although the inter-granular void ratio becomes smaller giving a denser coarse skeleton after erosion, the eroded samples have lower shear strength at small and medium strains (up to an axial strain of 5%). This is due to the significant loss of fine particles, which was not compensated by a decrease in the inter-granular void ratio.

Beyond an axial strain of about 5%, eroded soil samples exhibit higher shear strength with a rapid decrease in the excess pore water pressure. This is attributed tothe dilatancy development, represented here by the development of interstitial over-pressures, which is more important in the case of eroded soils. One should note the analogy between the evolution of the excess pore water pressure under undrained conditions and the volumetric strains under drained ones.

Note that, although in drained conditions the soil at higher initial densities show a lower shear strength, under undrained conditions the soil did not suffer from liquefaction instability.

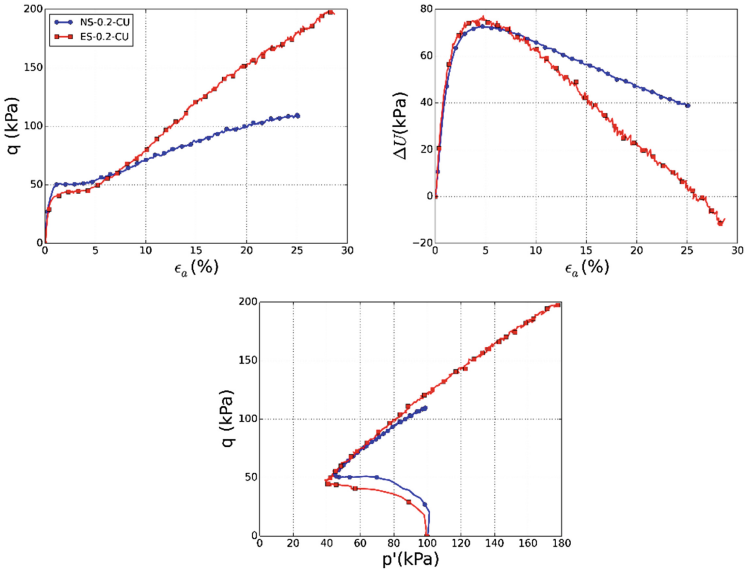

Fig. 6. Comparison of the responses to undrained triaxial compression tests of the non-eroded (NS-0.2-CU) and eroded (ES-0.2-CU) samples at an initial density $Id_0 = 0.2$

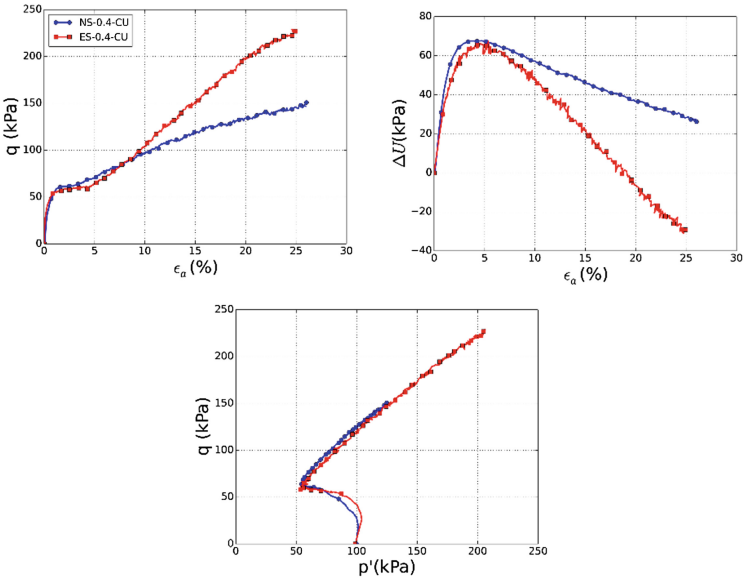

Fig. 7. Comparison of the responses to undrained triaxial compression tests of the non-eroded (NS-0.4-CU) and eroded (ES-0.4-CU) samples at an initial density $Id_0 = 0.4$

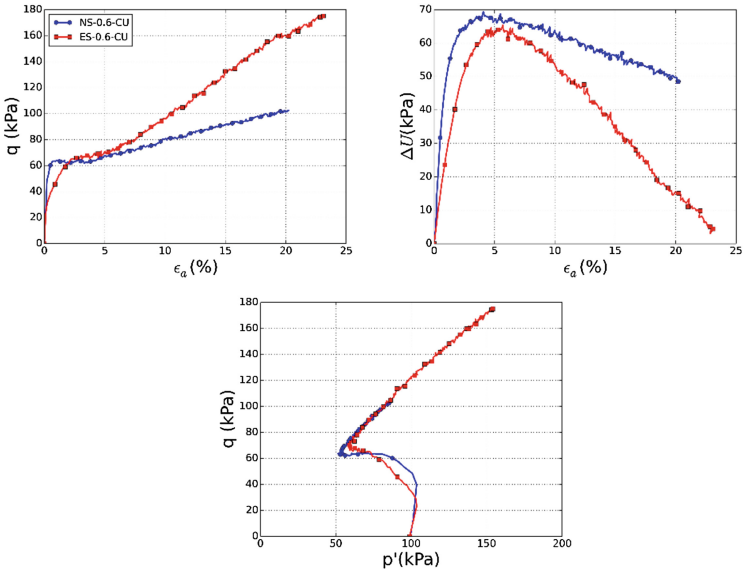

Fig. 8. Comparison of the responses to undrained triaxial compression tests of the non-eroded (NS-0.6-CU) and eroded (ES-0.6-CU) samples at an initial density $Id_0 = 0.6$

5 Synthesis on the Effect of Suffusion on the Soil's Shear Strength

From all the data presented above a synthesis on the effect of suffusion on the soil's shear strength is given in this section.

In the previous section, the results show that the soil may either lose or gain or even maintain its shear strength. To understand this behavior, Fig. 9 shows the variation of the peak friction angle before and after erosion in the case of drained (Fig. 9a) and undrained (Fig. 9b) triaxial compression tests. As can be noticed, the loosest soil ($Id_0 = 0.2$) did not lose its peak shear strength in both drained and undrained tests. Even though the soil in this case is looser after erosion (smaller Id values) as well as it lost fine particles that participate in the soil's shear strength but, as shown previously, the soil skeleton was significantly deformed which might have led to maintaining or gaining shear strength.

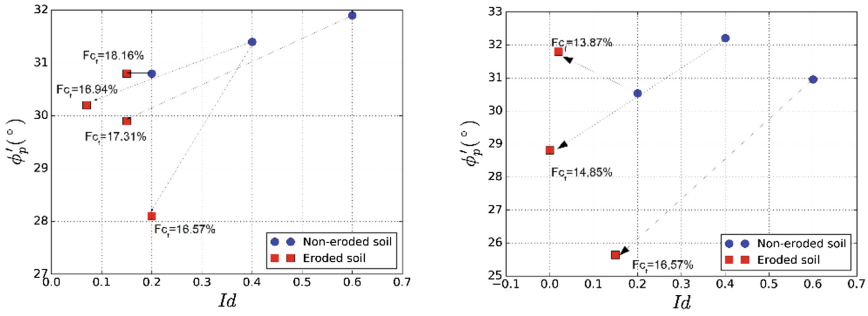

Fig. 9. The peak friction angle before and after erosion for (a) drained and (b) undrained triaxial compression tests

On the other hand, initially denser soil samples ($Id_0 = 0.4$ and 0.6) tend to lose shear strength after suffusion. Although similarly to the looser soil, the soil samples in this case become looser after erosion with a lower fines content, however, the soil skeleton did not compact significantly after erosion. Thus, the looser soil skeleton in this case results in lower peak friction angles.

Therefore, one can conclude that there is a combined effect of the global density of the soil, the densification of the soil skeleton as well as the final fines content on the peak shear strength of the soil.

Concerning the critical state, Fig. 10 shows the critical state (or failure) lines in the drained (Fig. 10a) and undrained (Fig. 10b) cases. Notice that, the critical state lines after erosion are slightly below those of the non-eroded soils. Hence, eroded soil samples seem to fail at a friction angle slightly lower than that of the non-eroded soil.

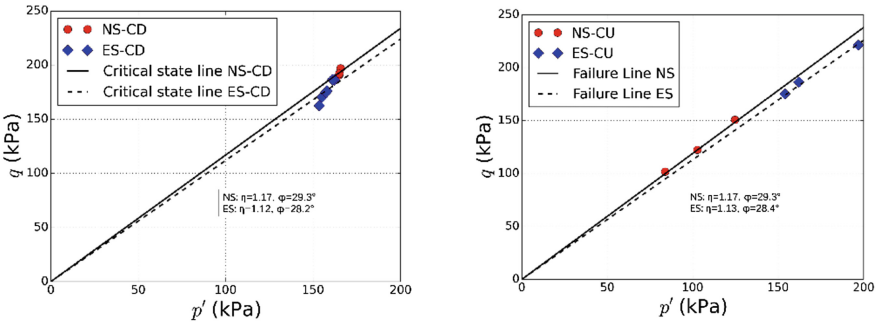

Fig. 10. The critical state lines (or failure lines) for (a) drained and (b) undrained triaxial compression tests

6 An Approach to Estimate the Soil's Shear Strength After Suffusion

From the previous experimental data and the analysis of the mechanical behavior of non-eroded and eroded soils subjected to drained triaxial compression tests, an approach to estimate the mechanical response of eroded soils is proposed hereafter.

A parameter, δ, is defined as the ratio of the variation of the volume of voids between the eroded and non-eroded states to the volume of the coarse sand fraction. δ is given by:

$$\delta = \frac{V_{vES} - V_{vNS}}{V_g} \tag{1}$$

where V_{vES} and V_{vNS} are the volumes of the voids of eroded and non-eroded samples respectively and V_g is the volume of coarse grains.

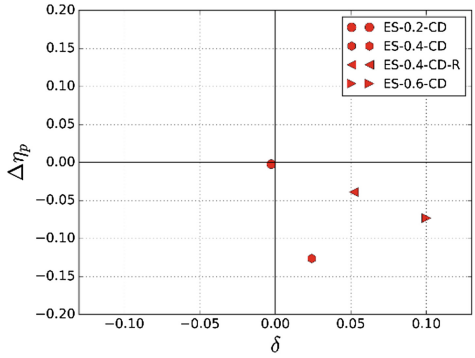

Fig. 11. Change after erosion in the shear strength, $\Delta\eta_p$, versus the parameter δ defined in Eq. 1.

The evolution of $\Delta\eta_p$ (the difference between the stress ratio at the peak, $\eta_p = \frac{q_p}{p'_p}$ where q_p and p'_p are respectively the peak stress deviator and the corresponding mean effective pressure) versus δ, is plotted in Fig. 11.

Results show that when δ is greater than 0, the stress ratio at the peak is smaller for the non-eroded sample. This means that the effect of the erosion process is dominant leading to an increase in porosity induced by the departure of fines, which is not compensated by the settlement.

When δ is close to or smaller than 0, the settlement due to erosion predominates and induces a compensation in the density of the soil skeleton, or even an increase of the later. In this case, the shear strength of the eroded samples is almost preserved and the soil behaves like the non-eroded one.

It is worth to note that the undrained tests are not presented in Fig. 10. Indeed, it was difficult to conclude in this case as the results were contradictory. This might be due to the uncertainty in determining the stress ratio at the peak strength as practically none of the undrained samples exhibit a real or distinguishable peak. This point needs more investigations and experimental data. However, it is interesting to note that in undrained conditions, erosion appears to have less effect on shear strength in small and medium deformations. Up to 5% of axial strain, there is no large difference observed between eroded and non-eroded mechanical behavior.

7 Conclusion

A newly developed suffusion apparatus has been used to investigate the seepage-induced internal instability in cohesionless soils. A novel feature of this apparatus is the freezing procedure followed to preserve the microstructure of the eroded soil which allows separate erosion and triaxial tests.

The most important contributions of this research are summarized as follows:

- As the initial density increases, less fine particles are eroded and the soil shows less volumetric deformations compared to looser eroded soil samples. Thus, the soil compaction during suffusion is more pronounced for the loosest samples; this is explained by the fact that the loose soil has a more metastable microstructure;
- Responses to drained triaxial compression tests showed that initially dense soil samples tend to have a higher reduction in its shear strength after erosion compared to initially looser soil samples;
- Even if soil samples might lose shear strength, under undrained compression, the eroded soil did not suffer from liquefaction instability;
- The shear strength after erosion depends on a combined effect of the global density of the soil, the final fines content and the densification of the soil skeleton;

- An approach to estimate the mechanical response of eroded soils was proposed based on a parameter, δ, representing the variation of the volume of voids with respect to the volume of the coarse sand fraction. This parameter helps to predict whether the eroded soil will be more resistant or not compared to the non-eroded soil. When δ is greater than 0, the shear strength of the eroded soils would be lower than that of the non-eroded soil. When δ is close to or slightly smaller than 0, the soil would behave like the non-eroded one. However, more data would be necessary to validate this tendency;
- Eroded soil samples would fail at a friction angle lower than that of the non-eroded soil.

References

Aboul Hosn R, Nguyen CD, Sibille L, Benahmed N, Chareyre B (2017) Microscale analysis of the effect of suffusion on soil mechanical properties. In: Proceedings of the 11th international workshop on bifurcation and degradation in geomaterials, Limassol, Cyprus

Chang D, Zhang L (2011) A stress-controlled erosion apparatus for studying internal erosion in soils. Geotech Test J 34:1–11

Ke L, Takahashi A (2012) Strength reduction of cohesionless soil due to internal erosion induced by one-dimensional upward seepage flow. Soils Found 52:698–711

Ke L, Takahashi A (2014) Triaxial erosion test for evaluation of mechanical consequences of internal erosion. Geotech Test J 37:1–18

Scholtès L, Hicher P, Sibille L (2010) Multiscale approaches to describe mechanical responses induced by particle removal in granular materials. C R Méc 338:627–638

Sibille L, Marot D, Sail Y (2015) A description of internal erosion by suffusion and induced settlements on cohesionless granular matter. Acta Geotech 10(6):735–748

Xiao M, Shwiyhat N (2012) Experimental investigation of the effects of suffusion on physical and geomechanic characteristics of sandy soils. Geotech Test J 35:1–11

Experimental Tests of Soil Reinforcement Against Erosion and Liquefaction by Microbially Induced Carbonate Precipitation

R. Béguin[1(✉)], L. Oxarango[2], L. Sapin[3], A. Garandet[4], A. Viglino[5], E. François[2], H. Mora[2], F. Martins[2], L. Duchesne[4], D. Albrecht[5], A. Esnault-Filet[3], I. Gutjahr[3], and L. Lépine[3]

[1] geophyConsult, 159 Quai des Allobroges, 73000 Chambéry, France
remi.beguin@geophyconsult.com
[2] IGE, Univ. Grenoble Alpes, CNRS, IRD, G-INP, 38000 Grenoble, France
[3] Soletanche-Bachy, 280 Av. Bonaparte, 92500 Rueil Malmaison, France
[4] CACOH, CNR, 69007 Lyon, France
[5] EDF-CIH, 73370 Le Bourget du Lac, France

Abstract. An innovative soil reinforcement method developed since 2004 is currently being adapted for hydraulic structures in the frame of the BOREAL project. The objective is to prevent mechanical failure of the soil due to internal erosion or liquefaction. The method is based on microbially induced urea-based carbonate precipitation. Four different erosion test apparatus have been used to assess the methodology: Contact Erosion Tests, Hole Erosion Test, Jet Erosion Test and suffusion tests. All the tests results indicate a strong increase of resistance already with a small percentage of formed calcite (~2–4%). In parallel, tests were performed in a CNR laboratory at a larger scale (8 × 4 × 2.25 m). The first experiment was performed on a homogeneous Fontainebleau Sand. The second and third tests were performed on sandy gravels, which are highly representative of the soil layers that could be treated with this method. These tests validated the effectiveness of the treatment on soils with open porosity, under natural Darcy velocity up to 10^{-3} m/s. Finally, the fourth test dealt with the treatment of an interface between a coarse and a fine soil layer, underlying the interest of the method for remediation in the case of contact erosion problems.

Keywords: Laboratory testing and physical modelling · Remediation
Biocalcification

1 Introduction

An innovative soil reinforcement method has been developed by Soletanche-Bachy since 2004 and is currently being adapted for hydraulic structures in the frame of the BOREAL project of the 16th French FUI research program (Esnault Filet et al. 2017). BOREAL started in 2014 and will end in 2018. It is led by Solétanche-Bachy and involves the two French leading hydropower producers (EDF and CNR), as well as

S. Bonelli et al. (Eds.): EWG-IE 2018, LNCE 17, pp. 16–24, 2019.
https://doi.org/10.1007/978-3-319-99423-9_2

laboratories from the universities of Grenoble (IGE and 3SR) and Angers (Microbiogeology Department), plus two SMEs (geophyConsult and Enoveo) dedicated to the mechanical and environmental characterisation of the structures to be treated. It is certified by Axelera (Chemistry and Environment competitive cluster) as well as by the SAFE cluster (focused on the management of risks). It is supported by the French FUI (French Inter-Ministry Fund).

The objective of the investigation is to prevent mechanical failure of the soil due to internal erosion or liquefaction. The method is based on microbially induced urea-based carbonate precipitation. This process consists of the injection of a suspension of specific bacteria in the soil to be treated followed by injection and reaction of a reactive solution. This leads to the binding of soil grains by carbonate crystals.

The process has been validated through numerous experiments for its application in soil reinforcement. However, optimization is requested for this process to be implemented on large hydraulic structures such as dykes or dams, where permanent hydraulic flow is present. The project is divided up into two phases including laboratory tests, where all parameters can be controlled and used to build well constrained physical models of all involved processes, and then real-site experiments, which are representative of the most common situations encountered in practice.

This article focuses on the erosion mitigation obtained with the treatment. First, results obtained at sample scale on different erosion apparatus, comparing resistance of untreated and treated soils, are detailed. Then, physical model tests and the main outcome obtained on the applicability of the treatment for different soils and configurations are described.

2 Erosion Tests on Soil Samples

A set of different erosion tests has been carried out on soil samples treated at various percentage of formed calcite in order to evaluate the interest of the treatment for erosion mitigation. The soil samples were either treated in the erosion cell (CET tests), in laboratory columns test used to characterize the efficiency of the process (Dumay et al. 2016) (JET tests) or collected during the dismantling of physical model tests (see Sect. 3, HET, JET and suffusion tests). The latter option is particularly interesting as it replicates the process which would be carried out on site.

Contact Erosion Tests (CET), suited to address erosion at soils interfaces, have been performed (CET, Oxarango et al. 2017). Fontainebleau sand treated directly in the apparatus cell to obtain calcite content ranging between 0% and 7% was tested in contact with a gravelly layer. The untreated material presents high sensitivity to contact erosion with a critical velocity around 10^{-2} m/s. For intermediate and high calcite contents (between 2% and 7%), no erosion was observed at the apparatus maximum flow rate (corresponding to a velocity of 7×10^{-2} m/s, Fig. 1). The increase of the critical velocity is thus higher than 700% (Fig. 1). At low calcite contents (between 1% and 2%), a small increase of the critical velocity could be observed (up to +50%) but the heterogeneous distribution of grain binding crystals is responsible of large discrepancy on the results.

Hole Erosion Tests, suited to assess the resistance against piping erosion of soil (Wan and Fell 2004; Bonelli et al. 2006), were performed on Fontainebleau sand samples collected during physical model tests dismantling (see Sect. 3). Calcite contents between 2 to 6% were measured on the tested samples. Hole Erosion Test could not be performed on the untreated material as the initial hole immediately collapsed. From 4.5% of formed calcite, the obtained resistance corresponds to what is usually mesured for the most resistant natural soils (usually clay): shear stress superior to 1000 Pa, Erosion Index superior to 3 (Figs. 1 and 2).

Jet Erosion Tests (Hanson and Cook 2004) have also been performed on the Fontainebleau sand with different calcite contents (between 2% to 10%). The treated material is "Resistant" in the classification proposed by Hanson in comparison with a "Very erodible" classification for the untreated material. Critical shear stress increases from values lower than 1 Pa for untreated soil to values higher than 80 Pa with $\sim$4% of formed calcite (Figs. 1 and 3).

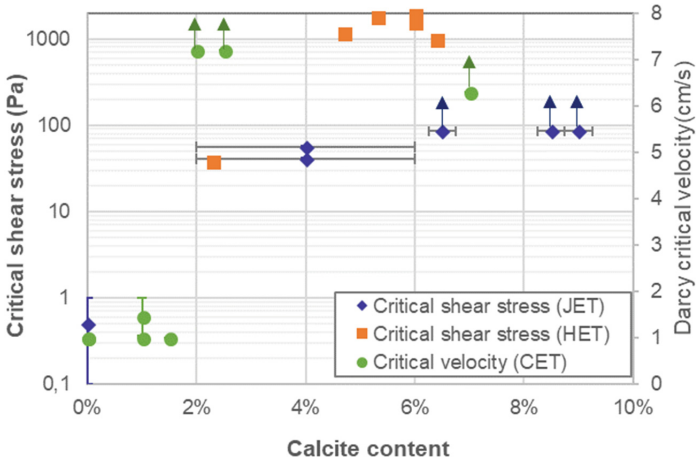

Fig. 1. Erosion resistance of Fontainebleau Sand for different calcite content formed by the treatment.

Erosion tests at the sample scale are being performed also on a sandy gravel similar to soils encountered in Rhone and Rhine dykes. This gap graded soil samples are tested before and after the treatment with JET and suffusion tests. JET tests confirmed the results obtained on Fontainebleau sand: a strong increase in the erosion resistance of the material (from $\times$5 up to $\times$100) already from few percent of calcite formed. Suffusion tests are ongoing, and the results are not yet available to date.

Before test

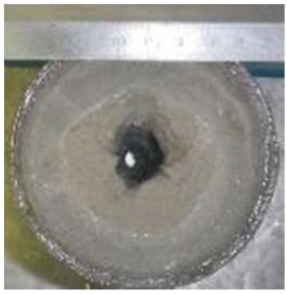

After test

Fig. 2. Fontainebleau sand sample, treated at ~6% of formed calcite, before and after Hole Erosion Test.

Untreated soil after test quasi complete erosion (15 cm)

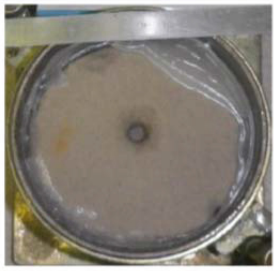

Treated soil after test at maximum apparatus capacity : 2 cm hole

Fig. 3. Fontainebleau sand sample after Jet Erosion Test: untreated (on the left) and treated at ~4% of formed calcite (on the right).

In synthesis, while the untreated material is considered very erodible for all the erosion types, from ~4% of formed calcite the treated soil resisted to the maximum eroding capacity of each apparatus used for testing (i.e. very small erosion observed at the maximum attainable hydraulic load). Depending on the soil and erosion types, the minimum formed calcite percentage needed to significantly improve the resistance seems to be in the range 2 to 4%. Significant increase in compression resistance Rc was observed from 5% of formed calcite in a Fontainebleau sand (Dadda 2017; Dadda et al. 2017).

3 Physical Model Tests

The BOREAL project includes physical models using an experimental device existing in the CACOH (Centre d'Analyse Comportementale des Ouvrages Hydrauliques) laboratory at CNR. Designed as part of the ERINOH project (for internal erosion of hydraulic structure), this system consists of a reinforced concrete structure 8 m long,

4 m wide and 2.2 m high, which can be closed at its downstream end by metal cofferdams (Beguin et al. 2012). This device allows imposing a constant hydraulic load difference (up to 3 m) to the volume of soil tested.

Two typologies of tests were selected. In "Type A" tests, the model is filled with a single homogenous soil. This type of test was dedicated to the validation of numerical models and to the assessment of injection feasibility for soils having different characteristics and permeabilities (Fig. 4). In "Type B" tests, a more permeable foundation layer is associated with a less permeable soil which has to be treated. This configuration aims at testing the efficiency of the treatment in the vicinity of interface zones, often encountered in fluvial dykes and at the origin of internal erosion pathologies. The conducted tests consisted in determining the obtained treated volume and the mechanical, hydraulic and chemical characteristics of the calcified material, after treating the soil mass under continuous gradient. From these data, homogeneity of the treatment could be evaluated and treated samples were collected for characterisation at the element scale.

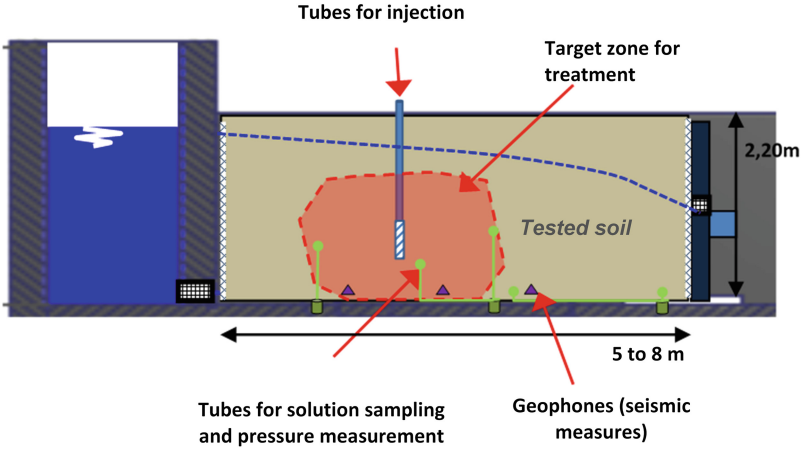

Fig. 4. Sketch of "Type A" tests

The grouting parameters, i.e. concentration of bacteria and calcifying solutions, and injection flow rates of both solutions, were modelled using Comsol Multiphysics, using a specific set of parameters able to combine the hydraulic conditions and the biochemical reactions based on laboratory experiments. Each cycle of injection consisted of one phase of bacteria injection, immediately followed by one phase of calcifying solution injection. A single and a double cycle were applied in each test, on distinct boreholes, to check the influence of the concentration on the calcification level. During all the injection tests, samples of fluid were taken inside the physical model and at the outlet, to track specific biocalcification parameters such as optical density (OD_{600}), specific urease activity and hydrolyse rates. Samples of exhaust fluid were also regularly taken with an automatic sampler in order to carry out environmental impact assessment during the injection process and the percolation through the calcified mass.

In May 2018, three Type A grouting trials have already been performed with two different types of materials: Fontainebleau sand, a fine grained sand and Chavanay sandy gravel. One Type B has been carried out with a gravel 12/20 mm as foundation layer and a 0/4 mm sand as core material (Table 1).

The four tests performed under different hydraulic conditions yielded the successful calcification of a volume of about 10 m^3 each.

Table 1. Synthesis of the physical models and main outcomes

Test name	Soils	Main outcomes
A1	Fontainebleau sand	– Validation of the numerical model on a homogeneous sandy soil – Collection of samples for characterization – Typical values of mechanical, hydraulic and chemical parameters of treated soil
A3	Chavanay sandy gravel	– Validation of the possibility to treat gap graded heterogeneous soil
A3bis	Chavanay sandy gravel	– Evaluation of the treatment with high velocities
B1	0/4 mm sand above 10/20 mm clean gravel	– Treatment of a sandy soil above a gravelly foundation
B2	Bourg-Lès-Valence silt above 0/22.4 mm sandy gravel	– *Test ongoing (May 2018)*

Injection in the fine grained sand allowed for the validation of the design model built under Comsol to predict calcification results according to injection parameters. The experimental results fitted well with predicted results regarding the shape of the obtained calcified bulbs (Fig. 5) and the calcite contents. A good correlation was found between penetrometer test results and calcite content but, at this stage, it can only be considered a qualitative information showing an increase in strength after treatment (from $\sim$2 MPa before to >50 MPa after the treatment). Seismic measurements before and after treatment also showed a significant increase in Vs (shear velocity) from 250–300 m/s before to 500–1400 m/s after the treatment (Fig. 6), and confirmed that the technology can be employed in a controlled way, which is of particular importance for anti-liquefaction applications.

Test A3 and A3bis with a sandy gravel validated the possibility to treat this heterogeneous gap graded soil even with natural velocities up to 10^{-3} m/s. Direct comparison between numerical predictions and experiments was difficult. Due to the high natural calcite content in this material, the amount of calcite content added by the treatment is difficult to measure precisely. However, from observations during dismantling, penetrometric and seismic measurements, the treated zone could be delimited and characterized. With the ongoing suffusion tests, the experiments on this sandy gravel will illustrate the performance after the treatment of a typical embankment subjected to erosion (suffusion) and potentially prone to liquefaction.

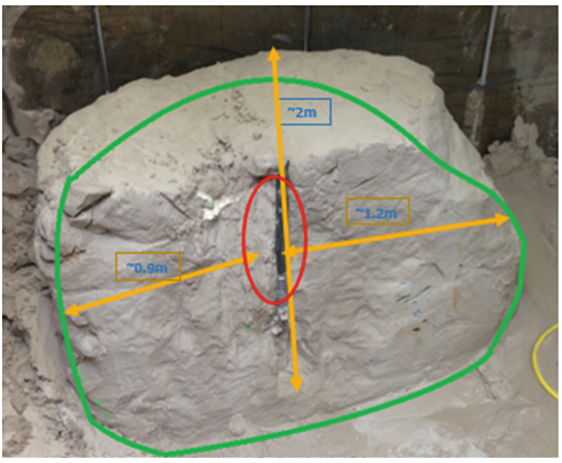

Fig. 5. Calcified block after excavation in Fontainebleau sand (test A1).

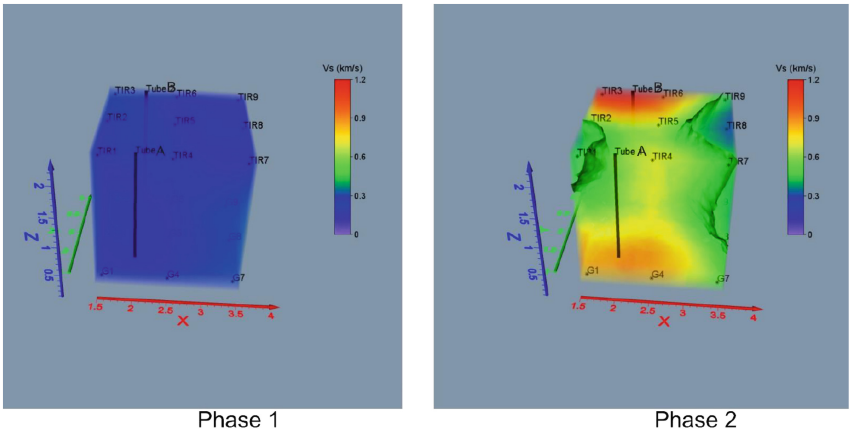

Fig. 6. Shear velocities Vs (km/s) obtained before (on the left) and after (on the right) treatment, in the center of the physical model.

Test B1 showed that the treatment could be applied to calcify a sandy core just above a gravelly foundation, with natural velocities in the foundation up to $\sim 10^{-3}$ m/s (Figs. 7 and 8). In this configuration where contact erosion might be expected, treatment of the fine soil provides a promising reinforcement solution. New Contact Erosion Tests are ongoing on samples collected during dismantling, in order to evaluate the gain in terms of critical velocity.

Fig. 7. Calcified block after excavation in 0/4 mm sand, above the gravelly foundation (test B1)

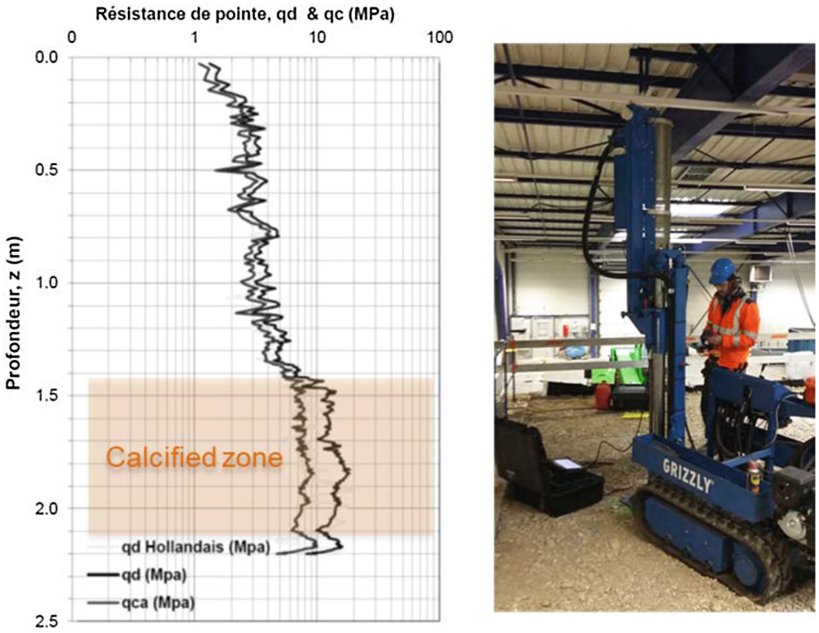

Fig. 8. Results of a dynamic penetrometer test (test B1)

4 Conclusion

Sample tests were performed to assess the resistance of soils treated by biocalcification against different types of erosion. Very high resistance was obtained, reaching the maximum erosion capacity of the apparatuses used, starting from 2% to 5% of formed calcite. Sandy and gravelly soils initially classified as very erodible become resistant to erosion after the treatment.

The physical model experiments, at decametric scale, were performed to validate and optimize the industrial process. They illustrated the possibilities of the method on different configurations and provided typical values of mechanical and hydraulic parameters that can be obtained on treated soils. Limits of the method were challenged by testing very heterogeneous gap graded soil and high flow velocity (10^{-3} m/s). The treated zones obtained for these severe conditions were less homogenous than in the homogeneous fine sand but still satisfactory. These experiments also underline that conventional investigation means such as static & dynamic penetrometer, as well as seismic measurements can be used to control the quality of the treatment on site.

References

Beguin R, Fry J-J, Picault C, Courivaud J-R, Faure Y-H (2012) Control of the risk of dyke failure caused by contact erosion. In: Proceedings of ICSE6 - Paris, 27–31 August 2012, pp 223–230

Bonelli S, Brivois O, Borghi N, Benahmed N (2006) On the modelling of piping erosion. C R Méc 334(8–9):555–559

Dadda A, Geindreau C, Emeriault F, Rolland du Roscoat SR, Garandet A, Sapin L, Filet AE (2017) Characterization of microstructural and physical properties changes in biocemented sand using 3D X-ray microtomography. Acta Geotech 12(5):955–970

Dadda A (2017) Relation between microstructural properties and strength parameters of biocemented sands. In: 6th international young geotechnical engineers' conference, September 16–17, 2017, Séoul, South Korea

Dumay A, Oxarango L, Martins JMF (2016) Evaluation of bacterial cells transport in soil using laboratory column experiments. In: Oral presentation. 8th INTERPORE international conference. Cincinnati USA, 9–12th May 2016

Esnault Filet, Gutjahr I, Sapin L, Lepine L (2017) Biocalcis, le renforcement des sols par cimentation biologique, Travaux no 933

Hanson GJ, Cook KR (2004) Apparatus, test procedures, and analytical methods to measure soil erodibility in-situ. Appl Eng Agric 20(4):455–462

Oxarango L, François-Lopez E, Mora H, Béguin R, Esnault-Filet A (2017) Improvement of erodibility of a sand (sandy soils) treated by microbially induced urea-based carbonate precipitation. In: 25th meeting European working group on internal erosion in embankment dams & their foundations, Delft, September 4–7

Wan CF, Fell R (2004) Investigation of rate of erosion of soils in embankment dams. J Geotech Geoenviron Eng 130(4):373–380

Development of a New Apparatus for the Jet Erosion Test (JET)

Maxime Boucher[1], Rémi Béguin[1(✉)], and Jean-Robert Courivaud[2]

[1] geophyConsult, 159 quai des allobroges, 73000 Chambéry, France
remi.beguin@geophyconsult.com
[2] EDF-CIH, 73370 Le Bourget du Lac, France

Abstract. The Jet Erosion Test consists of impacting a soil sample with a water jet and analyzing the evolution of the scour depth in order. It was originally designed to assess the resistance of fine soils against overflowing erosion by modelling the headcut migration. To extend this research to the overflowing erosion of mixed coarse – fine soils, EDF and geophyConsult have developed a larger JET apparatus, relying on the hypothesis, which needs to be confirmed, that some mixtures of fine and coarse soils may also have a headcut migration-type overflowing erosion process. A first test campaign has confirmed that JET tests carried out on the same soil with the original Hanson bench and the new apparatus provide comparable results. A second test campaign studied the influence of the nozzle diameter, testing the same soil successively with 6.35, 12 and 20 mm nozzle diameter. The first results confirmed that the results are not significantly influenced by this parameter. A third series of tests were related to soils that contain particles above 4.75 mm. Parallel to this experimental research, the interpretation of the test has been re-analysed, trying to understand the reason for the discrepancies observed between results obtained on French soil tests database and Hanson classification.

Keywords: Jet erosion test · Bench-testing · Automating · Overtopping Classification

1 Introduction

To characterize the erodibility of soils in relation to different erosion mechanisms, devices such as the Jet Erosion Test (JET, Hanson and Cook 2004), Hole Erosion Test (HET, Wan and Fell 2004; Bonelli 2013) or Contact Erosion Test (CET, Guidoux et al. 2010) have been developed worldwide during the last decades. The JET consists in impacting a soil sample with a water jet and analyzing the evolution of the scour depth. It is derived from the American standard ASTM D5852 by Greg Hanson (ARS-HERU). The JET was originally designed to assess the resistance of fine soils against overflowing erosion. The physical process represented by the JET is the headcut migration, usually observed for embankments constituted of fine cohesive soils. In coherence with the physical processes it is intended to model, the maximum allowable particle size of the JET is 4.75 mm. In order to extend this research to the overflowing erosion of embankments constituted of mixed coarse – fine soils, EDF and

S. Bonelli et al. (Eds.): EWG-IE 2018, LNCE 17, pp. 25–33, 2019.
https://doi.org/10.1007/978-3-319-99423-9_3

geophyConsult have launched the development of new larger JET apparatus. This development relies on the hypothesis, which needs to be confirmed by experiments, that some mixtures of fine and coarse soils may also have a headcut migration-type overflowing erosion process (Corcoran et al. 2016; Ellithy et al. 2017). First, the new bench developed to test coarser soil is presented and its validation by comparison with classical JET is described. Second the experimental studies performed on the influence of the nozzle diameter and the methodology for coarse soil testing are detailed. Finally, interpretation methods and classifications are discussed.

2 Large Jet Erosion Test: Development of a Versatile Bench-Testing

A new JET apparatus (Fig. 1) connected to a pressurized reservoir, provided with interchangeable nozzles and performing larger eroding jets has been developed. The size of the bottom reservoir has been increased so that larger samples can be tested (up to about 25 cm in diameter). In order to overcome the uncertainties associated with the operator, and carry out quicker tests, the whole bench is being automated by a system of valves and acoustic measurement devices. Flow, pressure and scour depth are recorded during the test by the data acquisition system. Mass monitoring of erosion is also planned.

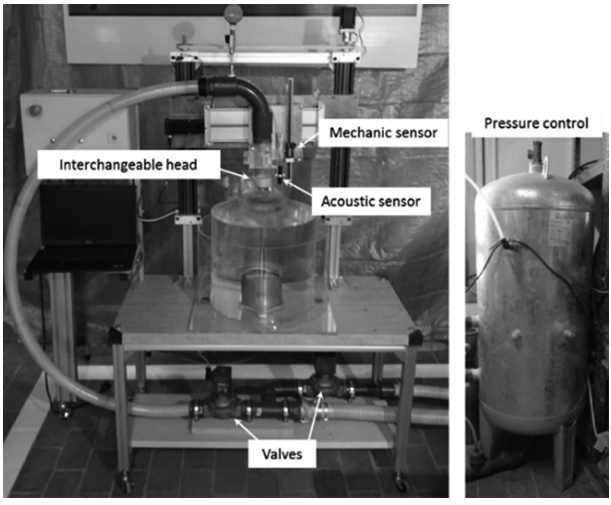

Fig. 1. Large Jet Erosion Test-bench

With its large capacity tank, interchangeable nozzles and regulation system this new test-bench makes it possible to:

– test soil samples very resistant, like treated soil with the possibility to apply hydraulic load up to ~0.8 bar (corresponding to a hydraulic shear stress of ~700 Pa);
– to use different nozzle size (6.35, 12 or 20 mm available put other size possible), especially larger nozzle size, in order to test soil containing coarse particles size without needing to sieve the soil at 4.75 mm as recommended for classical JET test (with 6.35 mm nozzle).

3 Correspondence Between JET USDA and LJET

– A first test campaign, conducted on an artificial reference soil (soli n°1, composed of 50% reference sand and 50% kaolinite, Fig. 2), classified in the middle of Hanson classification (Hanson and Cook 2004), has confirmed that JET tests carried out with the original bench and the new apparatus provide comparable results (Fig. 3). Comparisons between benches have also been conducted on two other types of artificial soils (Fig. 3): a very erodible soils (soil n°2, composed of 100% reference sand, Fig. 2) at low pressure and a very resistant soil (soil n°3, composed of 94% reference sand and 6% lime, Fig. 2) at higher hydraulic head.

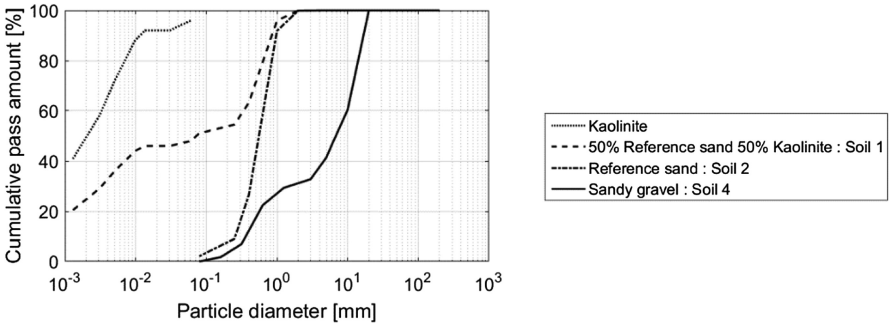

Fig. 2. Granulometric curves

– The tests have been analysed assuming a linear erosion law: $\varepsilon = k_d(\tau - \tau_c)$ with ε (m/s) the rate of erosion, k_d (m^3/N/s) the erodibility coefficient, τ (Pa) the hydraulic shear stress applied on the soil and τ_c (Pa) the critical shear stress (Hanson and Cook 2004).
– These tests confirmed the consistence of the results with the new bench. On soil 3, quite high incertitude on k_d has been obtained because a block of soil was initially detached.

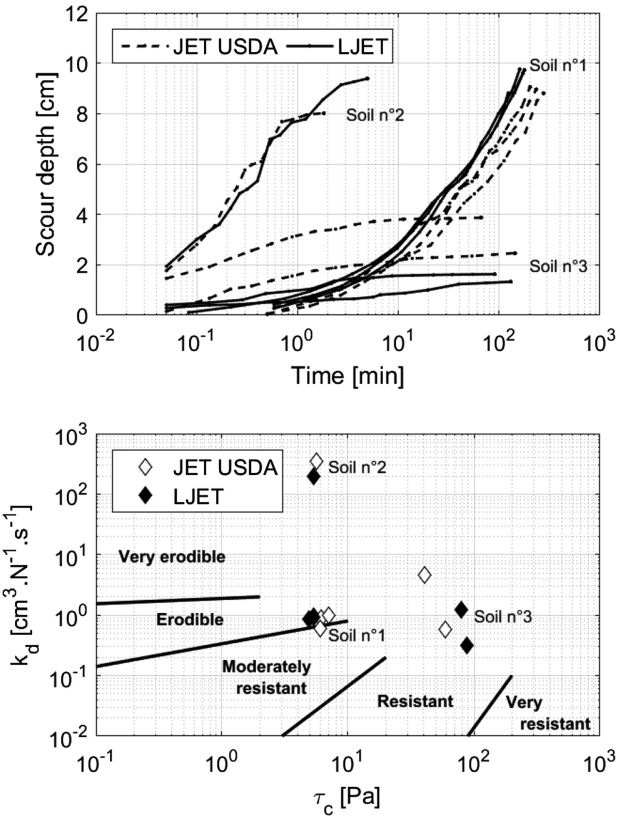

Fig. 3. Results of JET tests conducted for metrological connection between JET USDA and LJET: scour depth curve (top) and results in Hanson classification (bottom)

4 Influence of Nozzle Diameter and Coarse Soil Testing

A second test campaign studied the influence of the nozzle diameter. Three tests were conducted on the same soil (reference soil n°1) with three different jet diameters: 6.35, 12 and 20 mm (Fig. 4). The first results confirmed that the results are not significantly influenced by this parameter although a slight dispersion in the Hanson classification is noted, but usual for this kind of tests. More tests, on other soils, are planned in order to confirm this first result.

In the literature, comparisons have been made between classical JET (with 6.35 mm nozzle) and "Mini-JET" (with 3.18 mm nozzle) that concluded that there seems to be a systematic bias on the parameters obtained with both devices (Al-Madhhachi et al. 2013). However, the devices differ in nozzle size but also in sample size and in confinement of the flow. The latter may also influence strongly the results of the test (Ghaneeizad et al. 2015). Therefore it is hazardous to directly put in parallel this JET/Mini-JET comparison with the presented study of the nozzle diameter influence.

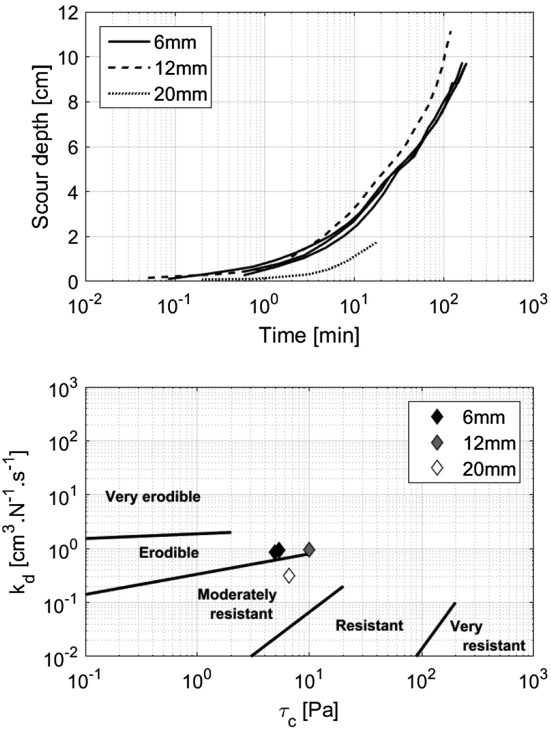

Fig. 4. Results of test campaign on the influence of the nozzle size: scour depth curve (top) and results in Hanson classification (bottom)

A third test campaign related to coarse soil testing was conducted. A sandy gravel (soil n°4 in Fig. 2), containing particles up to 20 mm, has been tested with the JET using the 20 mm nozzle. The objective of this preliminary test was to evaluate what was the issues linked with coarse soil testing. One major problem which arose was the non-ejection by the jet of the coarser particles: these particles stay in place and create an armoured layer on the surface (Fig. 5). This phenomenon could be considered as a normal behaviour if armouring is also expected on site. However, this implies that the JET test characterises a process which is a combination of detachment and transportation of soil particles. If parameters linked only with the detachment want to be measured, it is necessary to facilitate the evacuation of the particles after detachment.

One option is to use a horizontal jet impacting the sample. Nevertheless this is possible only if the soil is sufficiently cohesive and this brings (will generate some experimental issues) experimental issues (Wahl 2014). The option selected in this study was to remove manually detached particles either throughout the test (sample 1 in Fig. 6) or when scour depth stabilized (sample 2 in Fig. 6). Whatever the protocol, final results and soil classification were very closed. This solution of manually removing the detached particles that settle seems promising.

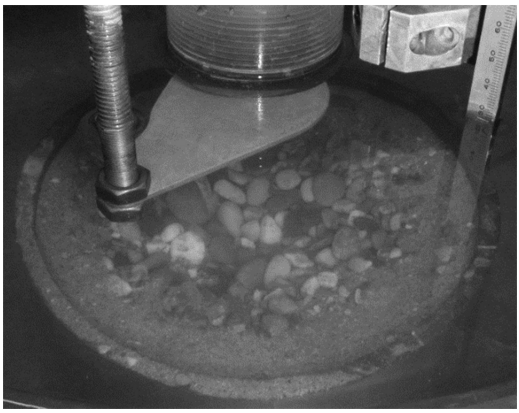

Fig. 5. Test in progress on a sandy gravel (soil n°4)

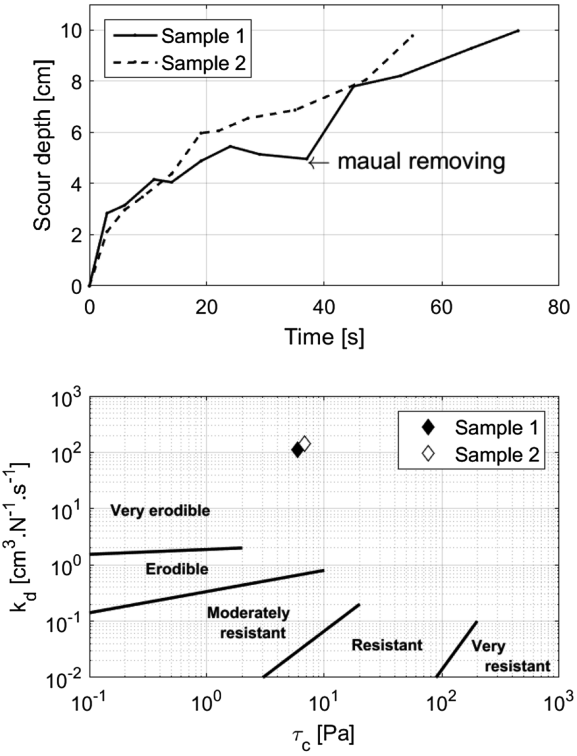

Fig. 6. Tests on sandy gravel (soil n°4) with and without manual removing of detached particles scour depth curve (top) and results in Hanson classification (bottom)

5 Soil Classification

Hanson classification (Hanson and Simon 2001) is the most used classification when analyzing results of a JET test. When plotting all the results from the commercial and research tests made by geophy*Consult* (Fig. 7), a discrepancy is observed between this database and Hanson categories: points are mainly above the classification limits proposed by Hanson.

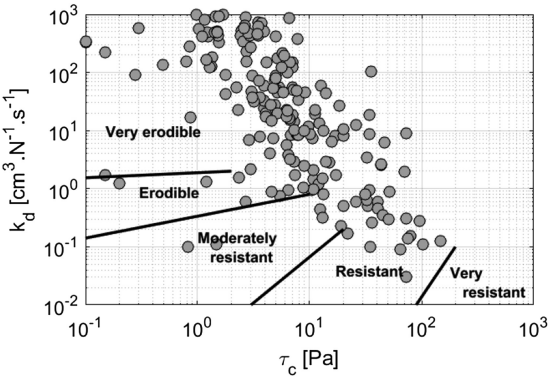

Fig. 7. Data base (295 tests)

Two explanations are proposed. First, soils in geophy*Consult* database are mainly soils from hydraulic structures in France and soils used by Hanson for the classification are from US streambeds. This could explain the differences observed and underline the interest of a more global international classification. Second, the method of interpretation of the test could influence the values obtained for the parameters, as observed by Daly et al. (2013). Actually, geophy*Consult* method for interpretation of the tests is a direct inversion of the scour depth curve, with a Monte-Carlo scheme, while Hanson data have been analysed by the so-called "Blaisdell method" (Hanson and Cook 2004). To investigate this second hypothesis, geophy*Consult* database is currently being reanalysed in order to determine the influence of the inversion method used and identify if systematic bias could be identified. In parallel of this task, the interpretation method is being completed in order to provide with the results of a test a range of uncertainty on the erosion parameters obtained. Indeed, depending on how the test progressed, the obtained parameters are constrained by an incertitude which varies strongly from one test to another (Fig. 8).

6 Concluding Remarks

A new apparatus has been developed to extend the range of application of the original Hanson bench. Comparison tests on reference soils confirmed that comparable results are obtained with both apparatus. The influence of the nozzle diameter has been

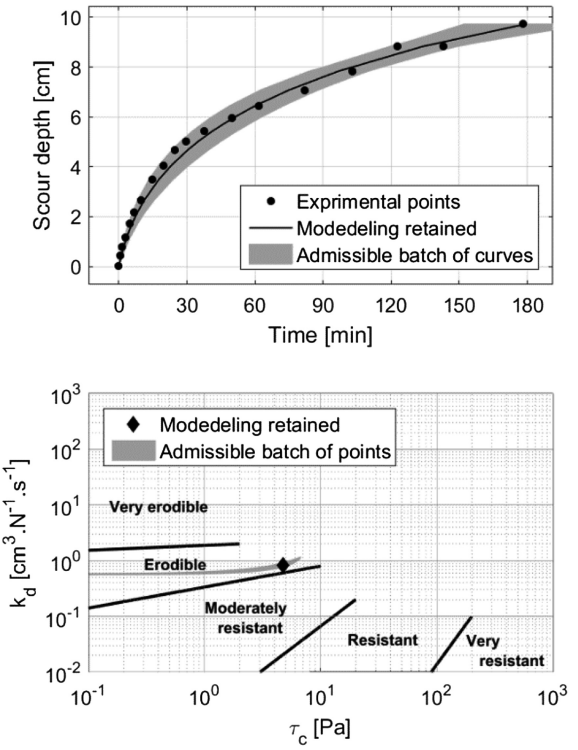

Fig. 8. Error range on the final result. Example of a LJET test on soil n°1, Fig. 3)

investigated between 6.35 and 20 mm and first tests confirmed that the results are not significantly influenced by this parameter. For testing soils that contain particles above 4.75 mm, a specific protocol (manually removing the detached particles that settle) has been tested and seems promising. Parallel to this experimental research, the interpretation of the test has been investigated, trying to understand the reason for the discrepancies observed between results obtained on French soil tests database and Hanson classification. A first step is presented which consists in calculating a range of uncertainty on the erosion parameters obtained, based on the incertitude on the fit of the experimental data points.

References

Al-Madhhachi AT, Hanson GJ, Fox GA, Tyagi AK, Bulut R (2013) Measuring erodibility of cohesive soils using a laboratory "mini" JET. Trans ASABE 56(3):901–910

ASTM Standard "D5852" Standard test method for erodibility determination of soil in the field or in the laboratory by the jet index method (1995). https://doi.org/10.1520/d5852-00r07, www.astm.org

Bonelli S (2013) Guide ERINOH: les essais de laboratoire. Digues maritimes et fluviales de protection contre les submersions 2ème Colloque national, Aix-en-Provence, 12–14 juin 2013

Corcoran MK, Sharp MK, Wibowo JL, Ellithy G (2016) Evaluating the mechanisms of erosion for coarse-grained materials. In: E3S web conference, vol 7, p 03008. https://doi.org/10.1051/e3sconf/20160703008

Daly ER, Fox GA, Al-Madhhachi AT, Miller RB (2013) A scour depth approach for deriving erodibility parameters from jet erosion tests. Trans ASABE 56:1343–1351. https://doi.org/10.13031/trans.56.10350

Ellithy GS, Savant G, Wibowo JL (2017). Effect of soil mix on overtopping erosion. In: World environmental and water resources congress 2017: hydraulics and waterways and water distribution systems analysis

Ghaneeizad, SM, Atkinson, JF, Bennett, SJ (2015). Effect of flow confinement on the hydrodynamics of circular impinging jets: implications for erosion assessment. Environ Fluid Mech 15(1): 1–25

Guidoux C, Faure Y-H, Beguin R, Ho C-C (2010) Contact erosion at the interface between granular coarse-soils and various base-soils under tangential flow condition. J Geotech Geoenv Eng 136(5):741–750

Hanson GJ, Cook KR (2004) Apparatus, test procedures and analytical methods to measure soil erodibility in situ. Eng Agric 20(4):455–462

Hanson GJ, Simon A (2001) Erodibility of cohesive streambeds in the loess area of the Midwestern, USA. Hydrol Process 15:23–38

Wahl T (2014) Measuring erodibility of gravelly fine-grained soils. Hydraulic Laboratory Report HL-2014-05, U.S. Dept. of the Interior, Bureau of Reclamation, Denver, Colorado, September 2014

Wan CF, Fell R (2004) Laboratory tests on the rate of piping erosion of soils in embankment dams. Geotech Test J 27(3):295–303

Erosion of Zoned Earthfill Dams by Internal Instability: Laboratory Testing for Model Development

Jonathan Fannin[1(✉)], Paul Slangen[2], Sara Ataii[1], Vincent McClelland[1], and Des Hartford[3]

[1] University of British Columbia, Vancouver, Canada
jonathan.fannin@ubc.ca
[2] Geosyntec Consultants Inc., Columbia, USA
[3] BC Hydro, Burnaby, Canada

Abstract. The WAC Bennett Dam is one of the largest embankment dams in North America, and one of the most instrumented and studied dams in the world. Following the 1996 sinkhole incident, considerable effort has been made to characterise the zoned materials of the dam with reference to susceptibility to internal erosion. Informed by the findings of this experience, we reflect upon the state-of-practice in dam engineering, and discuss some of its inherent limitations with reference to internal erosion, dam safety, and the management of aging embankment dams. We then describe the state-of-the-art for erosion of zoned earthfill by internal instability, a phenomenon whereby seepage flow removes a finer fraction of the soil gradation. Our paper addresses laboratory testing for materials characterization at the University of British Columbia. In collaboration with our industry research partner BC Hydro, we are seeking to advance the state-of-the-art with reference to a mechanics-based understanding of the phenomenon. We report insights gained from (i) a recent study using a flexible-wall permeameter, and (ii) the status of a new investigation using an advanced triaxial permeameter.

Keywords: Embankment dam · Internal erosion · Laboratory testing

1 Introduction

Dams play a central role in the stewardship of Canada's hugely valuable water resources, for which storage, flood control and hydropower generation are the key national interests. There are more than 10,000 dams across the country, mostly owned by the federal and provincial governments, electric utilities, industrial and mining companies, irrigation districts, and municipalities. Canada is now the world's biggest producer of hydroelectric power, generating 350 TWh/year, or approximately 13% of global output. Thus, it is not surprising to realise that British Columbia, like the provinces of Quebec, Manitoba, Newfoundland and Labrador, and the territory of Yukon, generates almost 90% of its energy from hydropower sources.

Upon completion in 1967, the Bennett Dam in British Columbia was the largest embankment dam in the world (see Fig. 1a). Mica Dam, completed in 1973, also ranks

S. Bonelli et al. (Eds.): EWG-IE 2018, LNCE 17, pp. 34–49, 2019.
https://doi.org/10.1007/978-3-319-99423-9_4

as one of the highest dams in the world. Indeed, just three embankment dams - Bennett Dam, Mica Dam, and Revelstoke Dam - generate more than half of British Columbia's electricity. They represent an enormous investment by Canadian society at-large and, as is the case for much of our public infrastructure, these northern-climate embankment dams are ageing. An effect of the ageing process, at susceptible locations, is for water seeping from the reservoir to erode, with time, fractions of soil in the embankment dam. Such internal erosion is probably the greatest, and least understood, risk of failure in embankment dams worldwide.

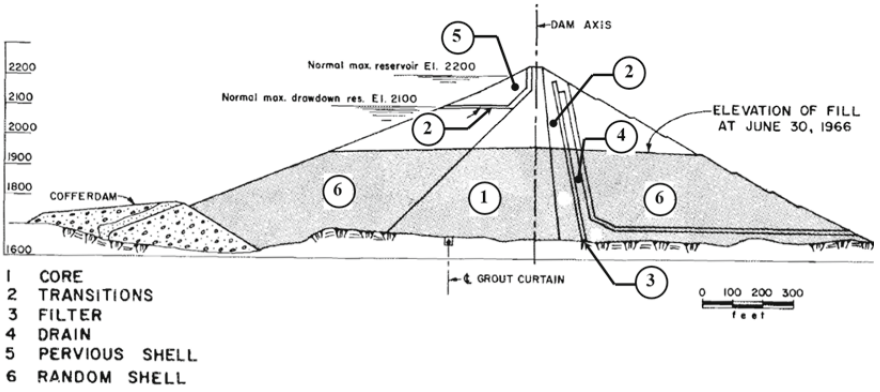

(a)

(b)

Fig. 1. a: Bennett Dam cross section (after Low and Lyell 1967). b: 1996 Bennett Dam sinkhole incident (BC Hydro)

1.1 The 1996 Sinkhole Incident

Internal erosion constitutes an uncertainty in dam safety that was poorly-understood at the time of design and construction of the Bennett Dam, and the phenomenon may well explain the June 1996 sinkhole incident. During the drill-investigation of a small pothole on the crest of the 183 m high Bennett Dam, a localised collapse of the dam crest opened a sinkhole that was 2.5 m in diameter and 6.4 m deep. The immediate response to the sinkhole occurrence included the establishment of a surveillance program, the initiation of communications with the public and news media, the mobilisation of specialist grouting contractor, and an emergency spill of the dam. Over a period of 7 weeks, a flow of 3000 m^3/s was released over the spillway (see Fig. 1b), and 2000 m^3/s through the turbines (Stewart and Watts 2000). Given the reservoir was rising to full pool, in response to inflow from the melting winter-snowpack in the catchment watershed, the controlled release resulted in a lowering of the reservoir elevation by only 2 m.

During the period of the emergency spill, a plan was made to investigate, characterise, and remediate both this sinkhole (No. 1), and a second less extensive sinkhole (No. 2) that was subsequently discovered on the crest of the dam (see Fig. 1b: 1996 Bennett Dam). Investigation of sinkhole No. 1 established an approximately 2.5 m wide column of highly disturbed core, within a 6 to 8 m annulus of moderately disturbed core, extending to a depth of 80 to 100 m. Layers and seams of fines-deficient core were found that were relatively soft and wet. These and other findings led to the working hypothesis that the sinkhole activity was a consequence of "some form of internal erosion" (Watts et al. 2000).

Dam safety incidents such as this can be expensive. The estimated cost of the Bennett Dam sinkhole remediation was $45 million. The estimated cost of foregone energy generation from the emergency spill of the reservoir was $90 million (Stewart and Watts 2000). The incident identified a need for research on seepage-induced fines migration in zoned core and filter materials of earthfill dams (Stewart and Garner 2000).

1.2 Characterisation of Zoned Earthfill Materials at the WAC Bennett Dam

The drainage system for the Bennett Dam (see Fig. 1a), located immediately downstream of the core, comprises a fine filter, a coarse filter, and a drain. A general soil description of each zone in the dam follows:

- the average gradation of the Core material (Zone 1), is a well-graded gravelly sand and silt, comprising approximately 15% gravel, 55% sand and 30% fines that exhibit little or no plasticity (Morgan and Harris 1967) and are termed non-plastic;
- the average gradation of the Transition material (Zone 2), is a gap-graded sand and gravel with a trace of fines, comprising approximately 50% gravel, 45% sand and 5% non-plastic fines, with a gap apparent in the percentage coarse sand and fine gravel;
- the average gradation of the Filter material (Zone 3), is a well-graded clean sandy-gravel, comprising 70% gravel, 30% sand and as much as 2% fines; and,
- the average gradation of the Drain material (Zone 4), is a uniformly-graded clean gravel with a trace of sand, comprising approximately 95% gravel and 5% sand.

2 Susceptibility to Internal Erosion: The State-of-Practice

Six candidate methods have been used in an assessment of all of the gradation curves for all of the zones of the Bennett Dam, where appropriate and consistent with the empirical origin of each method. The methods are clustered in three groups, based on similarity of the underlying concepts: (i) Kezdi (1979) and Sherard (1979); (ii) Kenney and Lau (1985, 1986) and Li and Fannin (2008); and (iii) Burenkova (1993) and Wan and Fell (2008). The Kenney and Lau (CDA 2007) and Sherard (USBR 2011) methods may be reasonably considered as the state-of-practice for assessment of the potential for seepage-induced internal instability in sand-gravel mixtures; the other four methods may be considered the state-of-art, although some are becoming accepted in the evolving state-of-practice (ICOLD 2017).

2.1 Empirical Screening Tools

The method of Sherard (1979) was proposed to evaluate the potential for instability in glacial tills that are commonly used as Core material in a zoned embankment dam. It does not appear to have been developed from the findings of laboratory testing of soil. Rather, the approach entails splitting the gradation into two fractions, at any delimiting grain size value 'exceeding about 0.1 or 0.2 mm' (no maximum value was given), and evaluating the grain size distribution of the coarser and finer fractions, with respect to the Terzaghi (1939) empirical criterion for soil retention by a filter, expressed as $((D'_{15}/d'_{85})_{max} \leq 4$ to 5.

The method of Kezdi (1979) similarly invokes a split-gradation analysis, with a more conservative limiting criterion of $(D'_{15}/d'_{85})_{max} \leq 4$. In contrast to the Sherard method, no recommendation was made on the value of delimiting grain size. Neither was an explicit recommendation provided on the soil types to which the method should be applied, although it may be inferred from example applications that it is suitable for sands and clayey silts.

The method of Kenney and Lau (1985) was proposed to evaluate the potential for instability in coarse-grained soil. It was conceived from interpretation of laboratory permeameter tests on gravel and sand. The method requires calculation of a stability index H/F along a prescribed length of the gradation curve. For each grain size D, and corresponding percentage of mass passing F, a value H is defined as the percentage of mass passing between D and 4D, which establishes the H/F ratio. The method is applied along the finer end of the gradation curve to maximum value of F = 20% for soil with a coarse fraction that is widely-graded (WG), and F = 30% for soil with a coarse fraction that is narrowly graded (NG). Kenney and Lau (1986) suggest a limit value to stability of $(H/F)_{min} \geq 1$.

The method of Li and Fannin (2008) was proposed in order to address some of the apparent conservatism of the Kenney and Lau method, by combining the limit value of Kenney and Lau with that of Kezdi to yield a hybrid threshold to material susceptibility. It was developed with reference to a database of laboratory permeameter tests on gravel and sand. A gradation with $(H/F)_{min} < 1$ for $F \leq 15\%$, or $H < 15\%$ for $15 \leq F \leq 30\%$, is designated potentially unstable.

The method of Burenkova (1993) was proposed to evaluate the potential for instability in soil, from interpretation of laboratory permeameter tests on gravel and sand with unreported fines content. The method requires calculation of two shape parameters, d_{90}/d_{15} and d_{90}/d_{60}, which are compared to an upper and lower boundary that enclose a region within which internally stable gradations are found to plot. The lower boundary is defined by $d_{90}/d_{60} = 0.76 \log (d_{90}/d_{15}) + 1$; the upper boundary is defined by $d_{90}/d_{60} = 1.86 \log (d_{90}/d_{15}) + 1$.

The method of Wan and Fell (2008) was proposed from interpretation of laboratory permeameter tests on gravel-sand-silt-clay mixtures, with a fines content of up to 45% that exhibited zero to low plasticity. It is explicitly declared that the method "is not able to identify the internal instability of gap graded soils." The method similarly requires calculation of two shape parameters, d_{20}/d_5 and d_{90}/d_{60}, which are compared to boundaries that enclose regions within which stable, unstable and "transition" gradations are found to plot.

Four of the six empirical methods are believed appropriate for assessing the Core material of the dam, the exceptions being Kenney-Lau and Li-Fannin that were developed for gravel and sand mixtures only. Applying them to the construction records for as-placed gradations of Core material established it to be internally stable. All six empirical methods are appropriate to assess the Transition, Filter and Drain materials of the dam. Applying them to the as-placed gradations of Drain material established it to be internally stable, whereas in contrast, a significant proportion of the Transition and Filter gradations are assessed potentially unstable. As Kenney and Lau (1985) observed "*Filter materials that exhibit unstable gradings… show their potential for instability, but whether or not they would behave as unstable materials in practice would depend on the conditions of particle transport to which they were subjected*".

All of the empirical screening tools invoke a shape analysis of the gradation curve, yielding an index value that is compared to a database of soils categorised as 'stable' or 'potentially unstable'. Major shortcoming in the state-of-practice is the inability of all empirical methods to determine where, and when, the action of seepage flow triggers internal instability in a potentially-unstable soil.

2.2 Empirical Screening Tools: Dam Case-Studies

Field observations, in the form of elevated water levels in the downstream filter, increased seepage flow, muddy discharge, and sinkhole activity, are strong indicators that internal erosion has progressed to a continuation phase. The high incidence of sinkhole activity in Swedish dams which, like those in Canada, are northern-climate embankment dams of glacial soil, was first brought to the general attention of the dam safety community nearly 20 years ago (Nilsson et al. 1999). A subsequent compilation of numerous dam safety incidents by Rönnqvist (2015), expanded upon that insight to include: the Juklavatn secondary dam in which piping progressed to an open hole through the glacial till core; similar openings in Juktan dam; cavities in the Grundsjön dam (see also Rönnqvist et al. 2015); soft zones in the core of the Lövön dam and Stenkullafors dam; turbid seepage water at Hyttejuvet dam; likely evidence of erosion in the core of the Lövön dam; a clearly defined hole through the till core in the Wreck Cove dam; and, open cavities in the Brodhead dam. Compilation (Rönnqvist et al. 2014)

of a database of 80 dams that includes 23 dams with some form of internal erosion, has demonstrated that empirical screening-tools can be used, with a reasonable degree of success, to distinguish between dams with probable occurrence of erosion and dams with no indication to-date of internal erosion.

2.3 Shortcomings of Empirical Screening Tools

There is undoubtedly a role for screening-tools in engineering practice. However, the undeniable shortcoming of such empirical tools relates to the scientific issues of spatial location and temporal rate of seepage-induced erosion in embankment dams, which defines one key aspect of current research on internal erosion. Put simply, and given the concern for internal erosion in northern-climate embankment dams, there is a compelling need to progress beyond the use of empirical screening-tools alone in dam safety risk management. Progress requires the formulation of a new mechanics-based theoretical model for decision-support. Model development, calibration, validation, and verification require advanced laboratory test data. The research effort involved represents the state-of-art.

3 Susceptibility to Internal Instability: The State-of-Art

The susceptibility of soil to seepage-induced internal instability was first tested in simple rigid wall permeameters with limited control of seepage. The susceptibility was determined based on mass loss and forensic analysis of the particle size distribution at the end of the test, without any consideration whatsoever for measurement of flux, pore water pressures or axial deformations (Kenney and Lau 1985; Åberg 1993; USACE 1953). A second-generation of rigid wall permeameters included improved seepage control systems and monitoring of the pore water pressure distribution by standpipes and measurement of the flow rate, to allow for the determination of hydraulic conductivity (Ke and Takahashi 2012; Skempton and Brogan 1994), often combined with measurement of mass loss and forensic analysis of the particle size distribution at the end of the test (Cividini et al. 2009; Lafleur et al. 1989; Sterpi 2003; Wan and Fell 2004; Wittmann 1977). Most of these studies did not apply any vertical stress, although some applied a nominal top load (Kenney and Lau 1985; Åberg 1993; Honjo et al. 1996).

The current third-generation of rigid-wall permeameters now incorporates an axial loading system with measurement of load at the top only (Chapuis et al. 1996; Li 2008), else top and base of the specimen (Moffat and Fannin 2006; Sail et al. 2011). In a companion path of investigation, flexible wall permeameters have been used to examine seepage-induced internal instability (Molenkamp et al. 1979; Sanchez et al. 1983; Sun 1989) in an attempt to eliminate any preferential seepage flow paths along the soil-wall interface of a rigid-wall permeameter, and thus more confidently establish the susceptibility of materials. The ability to control the stress on the test specimen has appealed to more recent investigators (Bendahmane et al. 2008; Chang and Zhang 2011; Ke and Takahashi 2014a, b; Luo et al. 2012; Sibille et al. 2015; Chen et al. 2016;

Slangen and Fannin 2016), all of whom have sought to investigate the conditions at the onset of instability. For this purpose, the hydraulic gradient, flow rate and eroded mass are monitored, typically in combination with deformation of the test specimen, either by means of monitoring axial or volumetric deformations.

3.1 Seepage-Induced Instability: The UBC Flexible-Wall Permeameter

The test procedure involves isotropic consolidation of the reconstituted specimen, which is then subject to multistage upward seepage flow. The double-walled cell accommodates a cylindrical test specimen with diameter of 100 mm, which is reconstituted to a length of approximately 100 mm. It is enclosed by a rubber membrane, and sealed to the base pedestal and top cap, respectively, using O-rings. The test specimen is reconstituted by a method modified slurry deposition on a series of two basal (inflow) wire meshes, of 0.033 mm opening size that is in direct contact with the specimen, and 0.6 mm opening size below it, which mount on a perforated plate in the base pedestal.

The top (outflow) boundary comprises a wire mesh that rests directly on the specimen, the opening size of which is selected based on the grain size distribution of the test material, and a second wire mesh of relatively large opening size, typically 2.8 mm, both of which mount within the top cap. A schematic section of the double-walled cell (see Fig. 2) depicts the inner and outer acrylic tube mounted between the base frame and top plate. They create an inner chamber in which the specimen is located, and an outer chamber, between the two tubes. Both chambers are pressurised equally, yielding a negligible differential pressure across the inner acrylic tube that eliminates any creep deformation. Thus, change in volume of the inner chamber is a consequence of (i) any air within the inner chamber, (ii) absorption of water by the inner acrylic tube, (iii) vertical displacement of the loading ram, and (iv) volume change of the specimen. Volume change of the specimen is then determined by monitoring the volume change of the inner chamber, and correcting for the other three factors.

The seepage control system is a closed water-circuit, in which a difference in total hydraulic head between an inflow constant-head device (I-CHD) and an outflow constant-head device (O-CHD) induces flow through the specimen. The I-CHD and the O-CHD are both open to atmospheric pressure, and thus the system cannot be back-pressured. During multi-stage seepage flow, a peristaltic pump transfers water from a storage reservoir to the I-CHD, which connects to an inlet port on the base of the specimen. An outlet port on the top cap connects to the O-CHD, from which water returns to the storage reservoir. Unidirectional upward seepage flow occurs under increasing increments of hydraulic gradient. Additional details of the flexible-wall permeameter are reported in Slangen (2015) and Slangen and Fannin (2016).

In order to characterise the mode of any seepage-induced instability, instrumentation monitors the following:

- differential pore water pressure across the specimen;
- flow rate;
- axial deformation; and,
- volumetric deformation.

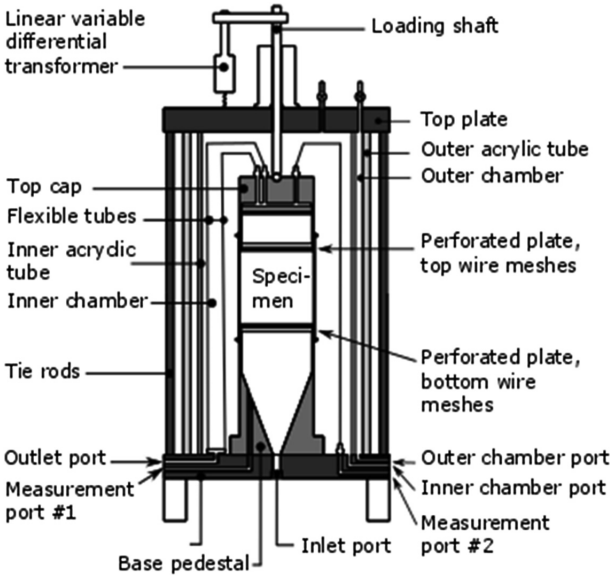

Fig. 2. UBC flexible-wall permeameter (with double-wall triaxial cell)

A total of seven tests (see Table 1) are reported on four gradations of spherical glass beads (see Fig. 3). Test No. 1 on gradation U-GB (see Fig. 4) serves as a benchmark for comparative analysis - a constant hydraulic conductivity of 1.4×10^{-2} cm/s, in the absence of any axial or volumetric deformation, defines an internally stable material. Test No. 2 on gradation 5.4GB20 exhibits a gradual increase in hydraulic conductivity at $0.5 < i < 1.8$, with no deformation, which is indicative of the instability phenomenon of suffusion. The apparent decrease of hydraulic conductivity at $i > 1.8$ is attributed to the influence of semi-turbulent flow (Slangen and Fannin 2016). Test No. 3 reveals a similar response, believed indicative of good reproducibility in the test results (see Fig. 4).

Test No. 4 on gradation 6.2GB25, and its reproducibility test No. 5, also yielded nearly identical responses. The onset of instability occurred at $i = 1.6$ and 1.9 in each test, respectively (see Fig. 4). Instability is defined by a change in hydraulic conductivity that is accompanied by contractive deformation of the specimen, which together characterise the instability phenomenon of suffosion. A suffosive response was also evident in tests No. 6 and No. 7, on gradation 7.5GB35. Visual observations reveal the seepage-induced instability to be a spatially variable phenomenon (see Fig. 5).

A unique feature of the UBC flexible-wall permeameter is the ability to measure global volumetric deformation, by means of the double-walled cell. Similar magnitudes of axial strain are found associated with different magnitudes of volumetric strain, thus measurement of global volumetric deformation during seepage flow appears important to avoid any misinterpretation of instability phenomena. This special feature of the UBC flexible-wall permeameter has been retained in the configuration of a newly-designed UBC triaxial permeameter.

Table 1. Commissioning tests

Test no.	Material	Cell pressure (kPa)	Void ratio at the end of consolidation (e_c)	B-value (−)	Hydraulic gradient at the onset of instability (i_o)
1	U-GB	102.1	0.645	0.98	NA
2	5.0GB20	54.2	0.483	0.96	0.5
3	5.0GB20	53.1	0.445	0.95	0.6
4	6.2GB35	102.0	0.359	0.95	1.6
5	6.2GB35	102.1	0.359	0.96	1.
6	7.5GB35	54.5	0.302	0.96	1.2–1.5
7	7.5GB35	101.3	0.303	0.95	1.5

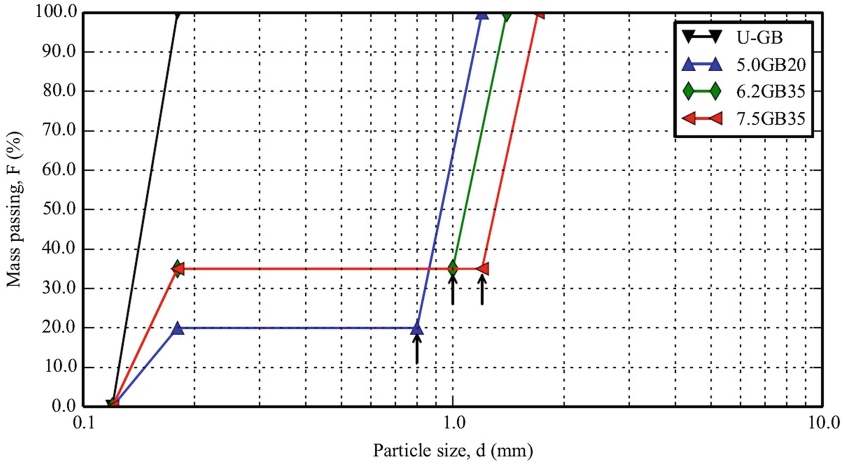

Fig. 3. Materials. Arrows indicate opening size of the outflow wire mesh used for the gap-graded materials.

3.2 Mechanical Consequences of Instability: The UBC Triaxial Permeameter

The newly-designed UBC triaxial permeameter test procedure involves isotropic consolidation of the reconstituted specimen, which is then subject to multistage downward seepage flow, prior to axial compression to cause shear failure in the specimen. The double-wall cell is identical to that described previously (see Fig. 6), and accommodates a test specimen with diameter of 75 mm that is reconstituted to a length of approximately 150 mm.

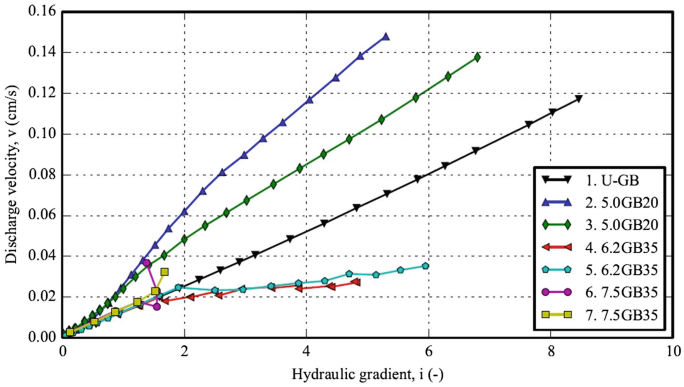

(a)

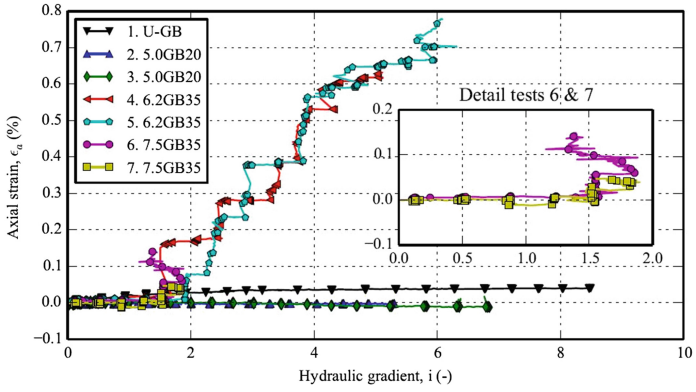

(b)

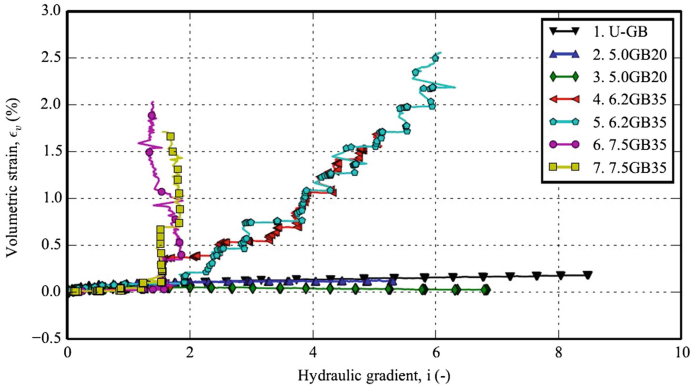

(c)

Fig. 4. Select test results

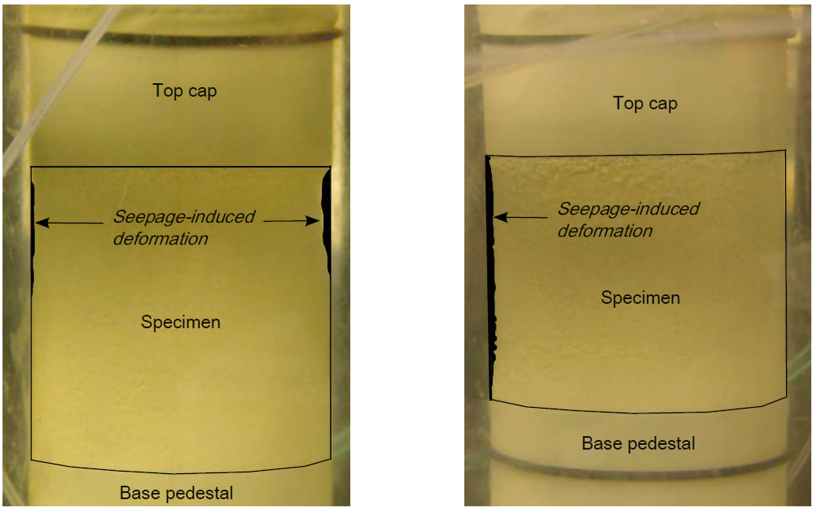

Fig. 5. Localized deformation in Test No. 5 (left) and Test No. 7 (right)

Seepage control occurs in a pressurised system, in which a difference in total hydraulic head is imposed between a pressurised inflow reservoir and a pressurised outflow reservoir (see Fig. 6). The seepage control system allows for imposition of a back-pressure on the test specimen - this feature is believed important to achieving full saturation of specimens reconstituted by the technique of moist-tamping. During multi-stage seepage flow, water flows from the inflow reservoir, through the specimen, to the outflow reservoir. Unidirectional downward seepage flow occurs under increasing increments of hydraulic gradient. There is no capacity for recirculation of the outflow water in the configuration of the seepage control system.

Any mass loss from the specimen is collected and measured using a unit (see Fig. 6) that is very similar in design to that of Ke and Takahashi (2014b), and it operates on the same principle. We note the same design concept for mass loss measurement has also been used in the triaxial permeameter device of Mehdizadeh (2018).

4 Concluding Remarks

Dam safety involves the management of uncertainty, and one of the greatest sources of uncertainty in embankment dam engineering is that of internal erosion. The cost of remediating a sinkhole incident can be measured in millions of dollars and, yet more significantly, the cost of foregone hydro-power can be measured in tens of millions of dollars.

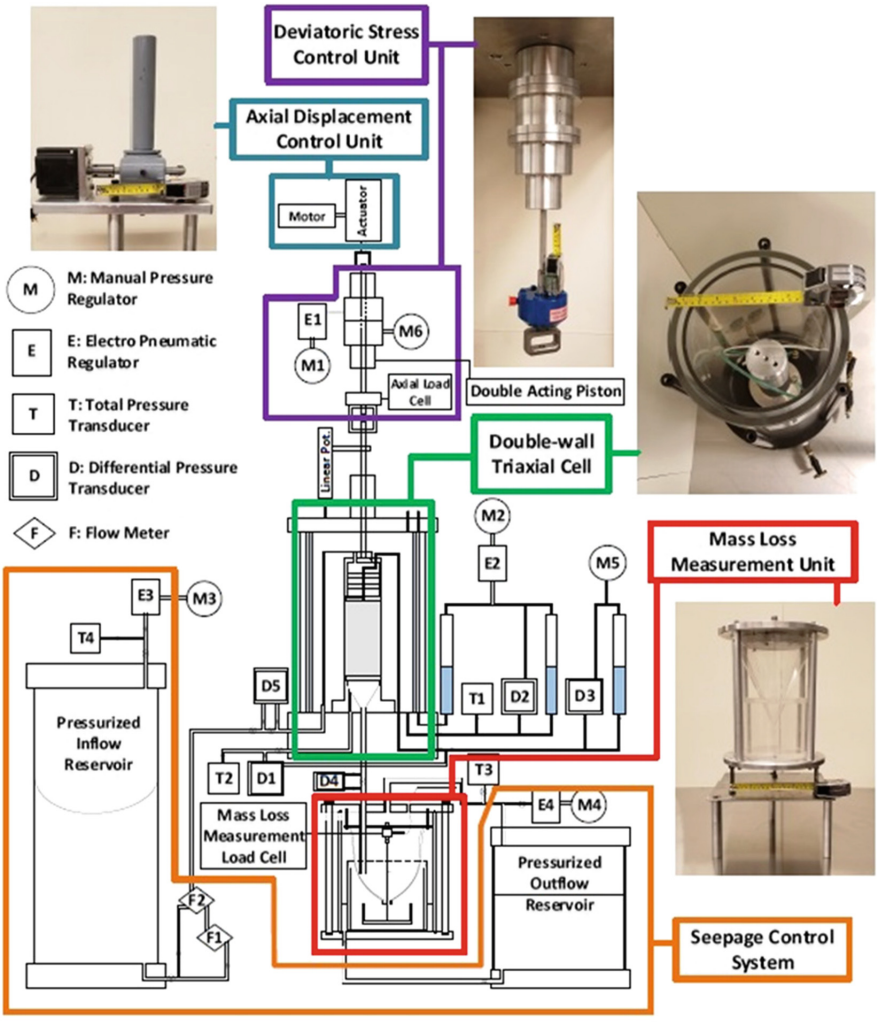

Fig. 6. UBC triaxial permeameter

Research is needed to improve our knowledge of where internal erosion initiates in an embankment dam, and the time-rate at which it progresses, which has important consequences, including:

- if a mechanics-based analysis demonstrates that seepage flow is not expected to yield internal erosion of zones within a dam, then expensive remedial works may be avoided;
- if a mechanics-based analysis shows internal erosion will initiate, an understanding of rate effects will inform the anticipated severity of erosion over the service-life of the dam; and,

– informed by the likely severity of any erosion, remedial works can be designed and implemented such that they best address the requirements for dam safety.

It has been observed (Hartford and Hicher 2015) that "*internal erosion is a poorly understood mechanism; and, that the ability to characterise the vulnerabilities involved in internal erosion will not improve until the understanding of the physics of the process improves*". The scenario of an erosion-induced change in zoned embankment materials, over the service life of a dam, offers a compelling illustration of such change.

In our most recent laboratory testing, we gave explicit recognition to gradation changes from erosion of the finer fraction of soil test specimens. We identified a change in hydraulic conductivity, with no change in the specific volume of the soil, and termed it suffusion (Fannin and Slangen 2014). The phenomenon is distinct from that in which mass loss yields a change in hydraulic conductivity and contractive volume change or collapse of the soil, which we termed suffosion (Fannin and Slangen 2014). Conceptually, it follows that suffusion occurs in a soil when seepage flow moves 'free' fines, namely those unstressed by the force chain network, from their initial location without any consequent rearrangement of the soil fabric. In contrast, suffosion is the process by which 'structural' fines that form a part of the force chain network, are moved by seepage flow, and readjustment of the soil fabric results in a volume change. The distinction has been adopted in USBR-USACE dam safety guidance (USBR-USACE 2015) and it should inform the novel contributions of advanced laboratory testing to the development of theoretical models.

The critical absence of "*well-documented experimental tests studying the impact of internal erosion on the mechanical behaviour of soil*" has been identified (Hicher 2013). Advanced laboratory testing in a triaxial permeameter is required to capture the impact of internal erosion on the mechanical behaviour of soil. Ideally, the design of the triaxial permeameter should accommodate measurement of volumetric deformation, for reasons outlined above, and mass loss from the specimen, in order to advance efforts in theoretical modelling. Few such state-of-the-art permeameters exist, and the important features of one that we have recently designed and manufactured at UBC are reported herein.

Acknowledgements. Research on internal erosion at the University of British Columbia (UBC) is supported by multi-year funding (2017–2022), provided by BC Hydro (BCH) and with matching support from the Natural Sciences and Engineering Research Council of Canada (NSERC), through its Collaborative Research Development (CRD) program. The design, fabrication and commissioning of the advanced triaxial permeameter test device has been completed in the UBC Civil Engineering workshop, for which the technical support of Harald Schrempp, Scott Jackson, and Bill Liu is specifically acknowledged with gratitude.

References

Åberg B (1993) Washout of grains from filtered sand and gravel materials. J Geotech Eng ASCE 119(1):36–53

Bendahmane F, Marot D, Alexis A (2008) Experimental parametric study of suffusion and backward erosion. J Geotech Geoenviron Eng 134(1):57–67

Burenkova VV (1993). Assessment of suffosion in non-cohesive and graded soils. In: Brauns, Schüler (eds) Filters in geotechnical and hydraulic engineering, Karlsruhe, 1992. Balkema, pp 357–360

CDA (2007). Dam Safety Guidelines (2013 edn.) Canadian Dam Association. http://www.cda.ca

Chang DS, Zhang LM (2011) A stress-controlled erosion apparatus for studying internal erosion in soils. Geotech Test J 34(6):579–589

Chapuis RP, Contant A, Baass KA (1996) Migration of fines in 0–20 mm crushed base during placement, compaction, and seepage under laboratory conditions. Can Geotech J 33(1):168–176

Chen C, Zhang LM, Chang DS (2016) Stress-strain behavior of granular soils subjected to internal erosion. J Geotech Geoenviron Eng 142(12):6016014

Cividini A, Bonomi S, Vignati GC, Gioda G (2009) Seepage-induced erosion in granular soil and consequent settlements. Int J Geomech 9(4):187–194

Fannin RJ, Slangen P (2014) On the distinct phenomena of suffusion and suffosion. Geotech Lett 4(4):289–294

Hartford DND, Hicher P-Y (2015). A case and a proposal for a soil mechanics solution to the problem of internal erosion in dams. Vingt-cinquième Congrès des Grands Barrages, pp 305–326

Hicher P-Y (2013) Modelling the impact of particle removal on granular material behaviour. Géotechnique 63(2):118–128

Honjo Y, Haque MA, Tsai KA (1996) Self-filtration behaviour of broadly and gap graded cohesionless soils. In: Lafleur J, Rollin A (eds) Proceedings Geofilters 1996, Montreal, May 29–31 1996. Bitech Publishers Ltd., Richmond, pp 227–236

ICOLD (2017) Internal erosion of existing dams, levees and dikes, and their foundations, Volume 1: Internal erosion processes and engineering assessment. International Commission on Large Dams, Paris. http://www.icold-cigb.org

Ke L, Takahashi A (2012) Strength reduction of cohesionless soil due to internal erosion induced by one-dimensional upward seepage flow. Soils Found 52(4):698–711

Ke L, Takahashi A (2014a) Experimental investigations on suffusion characteristics and its mechanical consequences on saturated cohesionless soil. Soils Found 54(4):713–730

Ke L, Takahashi A (2014b) Triaxial erosion test for evaluation of mechanical consequences of internal erosion. Geotech Test J 37(2):1–18

Kenney TC, Lau D (1985) Internal stability of granular filters. Can Geotech J 22(2):215–225

Kenney TC, Lau D (1986) Internal stability of granular filters - Reply. Can Geotech J 23(4):420–423

Kezdi A (1979) Soil physics. Elsevier, Amsterdam

Lafleur J, Mlynarek J, Rollin AL (1989) Filtration of broadly graded cohesionless soils. J Geotech Eng ASCE 115(12):1747–1768

Li M (2008) Seepage induced instability in widely graded soils (Doctoral dissertation). The University of British Columbia

Li M, Fannin RJ (2008) Comparison of two criteria for internal stability of granular soil. Can Geotech J 45(9):1303–1309. https://doi.org/10.1139/t08-046

Low WI, Lyell AP (1967) Portage Mountain Dam III. Development of construction control. Can Geotech J 4(2):184–217
Luo Y, Qiao L, Liu X, Zhan M, Sheng J (2012) Hydro-mechanical experiments on suffusion under long-term large hydraulic heads. Nat Hazards 65(3):1361–1377
Mehdizadeh A (2018) Multi scale investigation of post-erosion mechanical behaviour of granular material (Doctoral dissertation). Swinburne University of Technology
Moffat RA, Fannin RJ (2006) A large permeameter for study of internal stability in cohesionless soils. Geotech Test J 29(4):273–279
Molenkamp F, Calle EO, Heusdens JJ, Koenders MA (1979) Cyclic filter tests in a triaxial cell. In: Proceedings, 7th European conference on soil mechanics and foundation engineering, Brighton, pp 97–101
Morgan GC, Harris MC (1967) Portage Mountain Dam: II. Materials. Can Geotech J 4(2):142–166
Nilsson Å, Ekström I, Söder C (1999) Sinkholes in Swedish embankment dams. Stockholm, Sweden: Elforsk, Report 99:34
Rönnqvist H (2015) On the assessment of internal erosion of dam cores of glacial till (Doctoral dissertation). Luleå University of Technology
Rönnqvist H, Fannin J, Viklander P (2014) On the use of empirical methods for assessment of filters in embankment dams. Geotech Lett 4(4):272–282
Rönnqvist H, Fannin J, Viklander P (2015) The unified plot approach for assessing internal erosion: a case study of the Grundsjön dam sinkhole event. In: ICOLD congress 2015: international commission on large Dams, 2015
Sail Y, Marot D, Sibille L, Alexis A (2011) Suffusion tests on cohesionless granular matter Experimental study. Eur J Environ Civ Eng 15(5):799–817
Sanchez RL, Strutynsky AI, Silver ML (1983) Evaluation of the erosion potential of embankment core materials using the laboratory triaxial erosion test procedure (Report No. GL-83-4). US Army Corps of Engineers
Sherard JL (1979) Sinkholes in dams of coarse, broadly graded soils. In: Proceedings of the 13th ICOLD Congress, New Delhi, 1979, vol 2. ICOLD, Paris, pp 25–35
Sibille L, Marot D, Sail Y (2015) A description of internal erosion by suffusion and induced settlements on cohesionless granular matter. Acta Geotech 10(6):735–748
Skempton AW, Brogan JM (1994) Experiments on piping in sandy gravels. Geotechnique 44 (3):449–460
Slangen P (2015) On the influence of effective stress and micro-structure on suffusion and suffusion (Doctoral Dissertation). The University of British Columbia
Slangen P, Fannin RJ (2016) A flexible wall permeameter for investigating suffusion and suffosion. Geotech Test J 40(1):1–14
Sterpi D (2003) Effects of the erosion and transport of fine particles due to seepage flow. Int J Geomech 3(1):111–122
Stewart RA, Garner SJ (2000) Performance and safety of W.A.C. Bennett Dam a seven year update. In: LeBouf D (ed) Proceedings of the 53rd Canadian geotechnical conference, Montréal, 15–18 October 2000, vol 1. Bitech Publishers Ltd., Richmond, pp 97–105
Stewart RA, Watts BD (2000) The WAC Bennett Dam Sinkhole Incident. In: LeBouf D (ed) Proceedings of the 53rd Canadian geotechnical conference, Montréal, 15–18 October 2000, vol 1. Bitech Publishers Ltd., Richmond, pp 39–45
Sun B-B (1989) Internal stability of clayey to silty sands (Doctoral dissertation). University of Michigan
Terzaghi K (1939) Soil mechanics: a new chapter in engineering science. J Inst Civ Eng 12 (7):106–141

USACE (1953) Filter experiments and design criteria (Report No. AEWES-TM-3-360). Army Engineer Waterways Experiment Station, Vicksburg, Missisippi

USBR (2011) Design standards no. 13 Embankment dams - Chapter 5 Protective Filters. Denver, CO

USBR-USACE (2015) Best practices in dam and levee safety risk analysis. A joint publication of the US Bureau of Reclamation and the US Army Corps of Engineers. Version 4.0, July 2015. https://www.usbr.gov/ssle/damsafety/risk/methodology.html

Wan CF, Fell R (2004) Experimental investigation of internal instability of soils in embankment dams and their foundations (Report No. 429). University of New South Wales, Sydney, Australia

Wan CF, Fell R (2008) Assessing the potential of internal instability and suffusion in embankment dams and their foundations. J Geotech Geoenv Eng 134(3):401–407

Watts BD, Gaffran PC, Stewart RA, Sobkowicz JC, Kupper AG (2000) WAC Bennett Dam - characterization of sinkhole no. 1. In: LeBouf D (ed) Proceedings of the 53rd Canadian geotechnical conference, Montréal, 15–18 October 2000, vol 1. Bitech Publishers Ltd., Richmond, pp 67–75

Wittmann L (1977) Some aspects of transport processes in porous media. In: Proceedings of 6th Australasian hydraulics and fluid mechanics conference, Adelaide, 5–9 December 1977, pp 121–124

The Role of Seepage Flow Rate and Deviatoric Stress on the Onset and Progression of Internal Stability in a Gap-Graded Soil

Fahed Gaber(✉) and Elisabeth T. Bowman

University of Sheffield, Sheffield, UK
fgaberl@sheffield.ac.uk

Abstract. The potential for seepage induced internal erosion in a soil depends on a combination of both geometric and hydromechanical criteria, with the complex stress states that the soil is subject to being one of the determinant factors. This preliminary study investigates under small-scale laboratory conditions, the influence of seepage flow under complex stress states on the behaviour of a gap-graded soil including change in volume, permeability, stress-strain response and particle size distribution. The study uses a stress path triaxial permeameter capable of assessing gap-graded soils under complex triaxial stress states undergoing internal erosion via downward seepage. The results obtained from the preliminary analysis of seepage flow testing under constant stress condition indicate that erosion of fines reduces the permeability of gap-graded samples and may also reduce its shear strength. Limitations of this research and future plans are also discussed.

Keywords: Soil erosion · Gap graded · Seepage flow · Laboratory testing

1 Introduction

Seepage induced internal erosion of fines through the coarser matrix in an unstable soil is the biggest challenge to existing embankment dams, such that nearly 50% of embankment dam stability problems are due to internal instability. According to Moffat (2005), constraints on the internal erosion of dams can be separated into two different categories: geometric and hydro-mechanical. The former constraints include the composition, porosity and particle size distribution of the soil, whereas the latter encompass effects due to hydraulic gradient and velocity of seepage flow, as well as effective stress level in the content of fines (Kenney and Lau 1985; Moffat and Fannin 2011). In general, the geometric constraints will determine whether finer particles can move within the soil matrix which is, at least theoretically, influenced by whether the pores of the primary matrix are sufficiently large for the fine particles to move through, while hydro-mechanical constraints will determine the flow velocity at a certain stress level required to initiate erosion of fine particles. This paper will concentrate on the hydro-mechanical aspect of internal erosion.

Preliminary testing of seepage induced instability has been conducted to investigate, under small-scale laboratory conditions, the influence of seepage flow under

S. Bonelli et al. (Eds.): EWG-IE 2018, LNCE 17, pp. 50–59, 2019.
https://doi.org/10.1007/978-3-319-99423-9_5

complex stress states on the behaviour/properties of a gap-graded soil including the final particle size distribution, permeability and stress-strain response.

2 Material and Experimental Procedure

2.1 Material Properties

The soil used in this research is a cohesionless gap-graded soil with a particle size distribution as shown in Fig. 1, maximum and minimum void ratios e_{max} = 0.618, e_{min} = 0.416, and specific gravity Gs = 2.67. The soil gradation is a replication of G4-C which has been used by Moffat and Fannin (2006) and was originally tested by Honjo et al. (1996). The sample is unstable according to Kenney and Lau (1986), Kezdi (1979) and Burenkova (1993) methods.

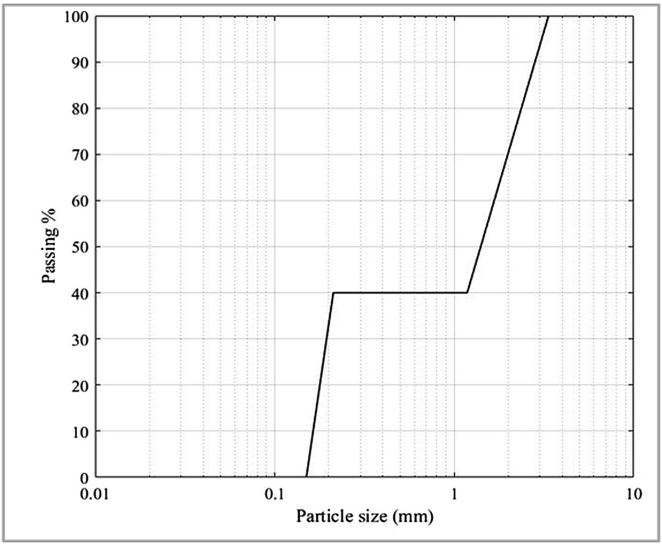

Fig. 1. Particle size distribution.

2.2 Testing Apparatus

A triaxial permeameter has been developed to study the effect of seepage flow through a gap-graded soil under controlled stress conditions. The triaxial permeameter (Fig. 2) enables the influence of seepage on volume change, permeability and stress-strain response to be examined, as well as the quantity of eroded soil over a chosen duration throughout the erosion process. A Bishop and Wesley stress path cell has been adapted

to create the permeameter. A high flow water pump with water regulator allows a high flow rate to be achieved through a section of soil. Typical porous stones at the bottom and top of the sample have been replaced with a Perspex perforated plate and mesh at the bottom to support the body while allowing the eroded fine particles to pass through to the soil collection point and a mesh finer than the fine particles at the top of the sample.

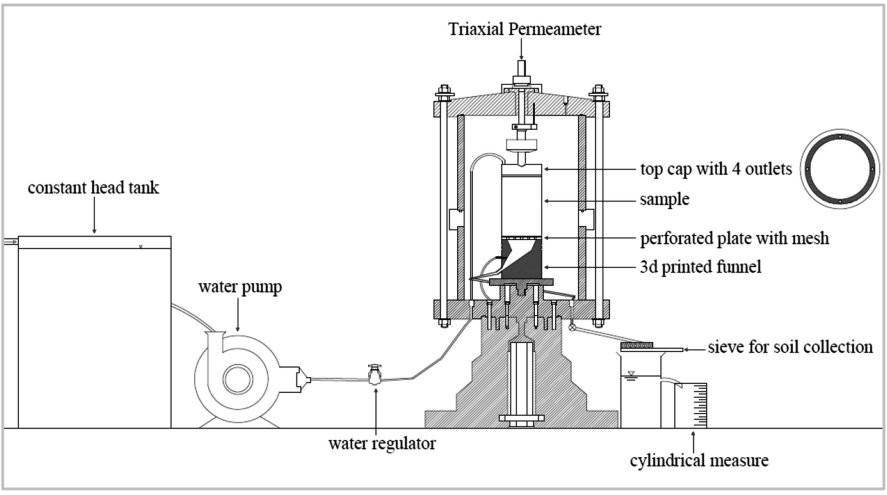

Fig. 2. Schematic of erosion triaxial permeameter.

A funnel and wide transparent tube guide the eroded soil through from the base of the sample to exit externally from the pressurised permeameter to a sieve, so the quantity of the eroded fine particles can be determined for a chosen duration of time. Furthermore, the flow rate is determined periodically via a measuring cylinder to study the change in permeability throughout the internal erosion process.

2.3 Testing Procedure

For the preliminary tests presented, 100 mm diameter samples, 100 mm in height have been prepared with 0.537 intended initial void ratio and 40% relative density. Short samples have been used to ensure reaching a sufficient hydraulic gradient to start the erosion process without reducing the effective radial stress to zero as a result of pore pressure generated by the seepage flow. The samples were prepared using the moist tamping under-compaction method proposed by Ladd (1978). The method prevents soil segregation during preparation.

Four tests have been conducted to examine the role of erosion. The first test was a conventional consolidated drained test as benchmark named I-50-B, other three erosion tests were tested under three different stress state conditions with the same effective stress value $p' = 50$ kPa and then exposed to erosion prior to shearing the samples. The three erosion tests named I-50-S, C-50-S and E-50-S (Table 1) where the first letter corresponds to the stress state condition: either I = isotropic, C = compression or E = extension stress state during the erosion test, the number corresponds to the mean effective stress, $p' = 50$ kPa and S or B for seepage (with erosion stage) or benchmark (no erosion stage), respectively.

Table 1. Testing program

Test	η^*	$q_{intended}$	$p'_{intended}$	q	p′	e_0
	–	kPa	kPa	kPa	kPa	–
I-50-S	0	0	50	0	50	0.527
C-50-S	0.75	37.5	50	39.8	50.8	0.490
E-50-S	0.60	−30	50	−31.8	49.4	0.513

*$\eta = q/p'$

Local strain transducers mounted directly on the sample were used to record the axial and radial displacement and hence axial and radial strain throughout the test. Each erosion test was conducted in five steps.

1. Saturation: Samples were confined at a radial stress of 20 kPa during the saturation process. To ensure that the sample was efficiently saturated it was first evacuated of air by injecting carbon dioxide (CO_2) gas through the sample. The CO_2 was injected at the base of the specimen and allowed to permeate through the specimen to replace air for approximately 15 min.
2. Stress state application: after saturation by water the stress state was changed from a deviatoric stress of $q = 0$ kPa and $p' = 20$ kPa to $q = 0$ kPa and $p' = 50$ kPa over 15 min, this was the end of this stage for test I-50-S; in C-50-S and E-50-S a further move in q and p′ space was made to the chosen stress state shown in Table 1.
3. Erosion test: the sample was exposed to erosion by applying seepage flow. The pressure from the water regulator was increased 10 kPa every 10 min until visible erosion was seen, the sample then was observed for 4 h.
4. Shearing: the sample was sheared in compression or extension at a rate of 0.05 mm/min to a maximum axial strain of 20%.
5. PSD analyses: after shearing step, the sample was divided into three layers to analyse the effect of erosion on PSD.

3 Experimental Results

3.1 Permeability

The discharge was recorded at every increment in seepage flow to study the velocity and permeability responses (Fig. 3). What is interesting in this data is that there is a clear trend of decreasing permeability in all tests, which was unexpected, based on results of research using rigid walled permeameters. That is, it was expected to see an increase in permeability due to a loss of fine particles from the sample matrix.

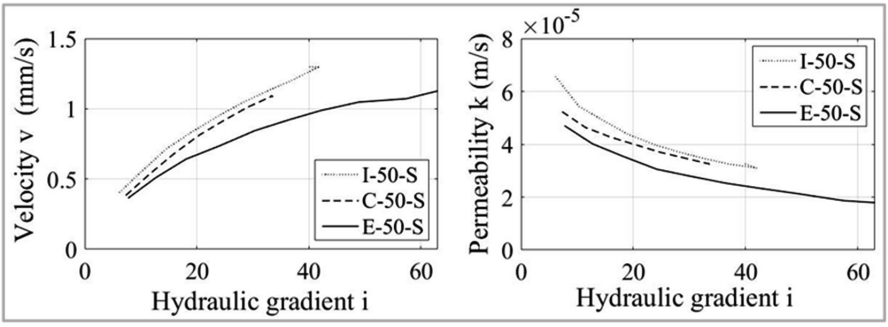

Fig. 3. Velocity and permeability vs hydraulic gradient during erosion step.

The change in permeability experienced in these three tests may occur due to a combination of three factors. Firstly, an increase in permeability may occur due to a loss of fine particles. Secondly, erosion may result in the clogging of soil filters or drainage paths and lead to a decrease in the permeability of the soil. Thirdly, a decrease in permeability may occur due to a decrease in sample volume, via a reduction in void ratio. It appears that the combination of the second and third items have a greater impact than the change due to fine particle loss, hence there is a reduction seen in the permeability in all tests. The estimated impact of the change in void ratio and loss of fine particles will be inspected in detail in future research.

3.2 Deformation

Local strain transducers mounted directly on the sample were used to record the axial and radial displacement. It can be seen from Fig. 4 that during the erosion test, the most obvious increase in the volumetric strain was recorded in the E-50-S extension test. This ties in with the quantity of the eroded fine particles as this test recorded greater fine particle loss than I-50-S and C-50-S.

3.3 Stress-Strain Response to Failure

The strain-stress behaviour of I-50-B and I-50-S were compared during shearing in order to understand the effect of erosion on the shear strength of the gap-graded soil used in this research. Figure 5 compares the stress-strain results obtained from the preliminary tests. It can be seen that test I-50-S displayed a significant loss of shear strength (by 26%) after exposing to erosion comparing to the benchmark test I-50-B.

Table 2 compares the peak angle of internal shearing resistance ϕ'_{peak} for the different tests. There was a relative reduction in ϕ'_{peak} in both I-50-S (32.9°) and C-50-S (35.8°) compared to I-50-B (37.8°), while the value for E-50-S was recorded as higher at 47.7° (the stress-strain result is not shown here). The apparently high value for ϕ'_{peak} in E-50-S is believed to be due to the influence of the rubber membrane which stretched during extension loading adding apparent strength to the sample. According to Wu and Kolymbas (1991) the rubber membrane effect has significant influence on the determined shear strength in extension. This influence depends on the confining pressure applied during shearing and is greater at lower stresses. The influence of the rubber membrane in extension tests will be examined in depth in future research.

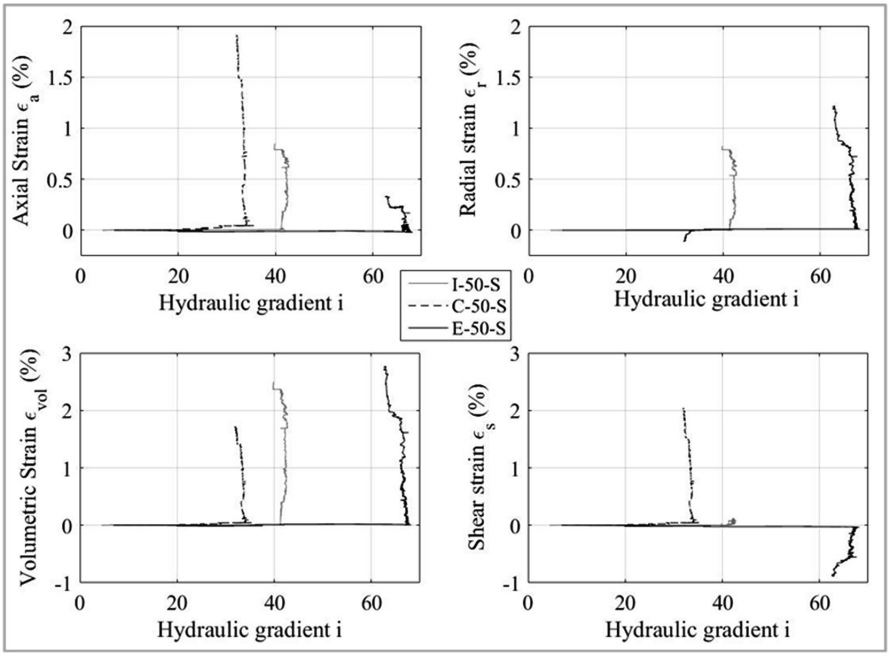

Fig. 4. Strain responses vs hydraulic gradient during the erosion step.

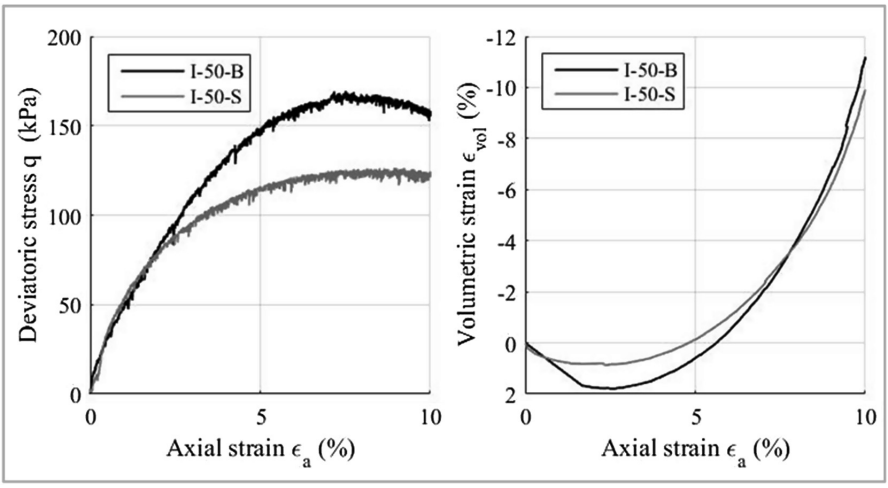

Fig. 5. Strain responses vs hydraulic gradient during the erosion step.

Table 2. Peak angle of internal shearing resistance in 4 tests, the quantity of erosion and volumetric strain after 4 h of erosion

Test	ϕ'_{peak}	Eroded fines	ε_{vol} after 4 h
	(°)	(g)	(%)
I-50-B	37.8	–	–
I-50-S	32.9	62.8	2.49
C-50-S	35.8	37.3	1.71
E-50-S	47.7[a]	109.9	2.77

[a]Without rubber membrane correction.

3.4 PSD Analysis

After shearing the samples in I-50-S, C-50-S and E-50-S, the sample was divided into three layers to analyse the effect of erosion on PSD, Fig. 6. All the tests show greatest loss of fine particles in the bottom layer with least loss of fines in the top. This may be because the fine particles in the bottom layer have to travel less distance through the soil matrix and hence it is much easier to erode, while the fine particles in the top layer are most impeded by the matrix.

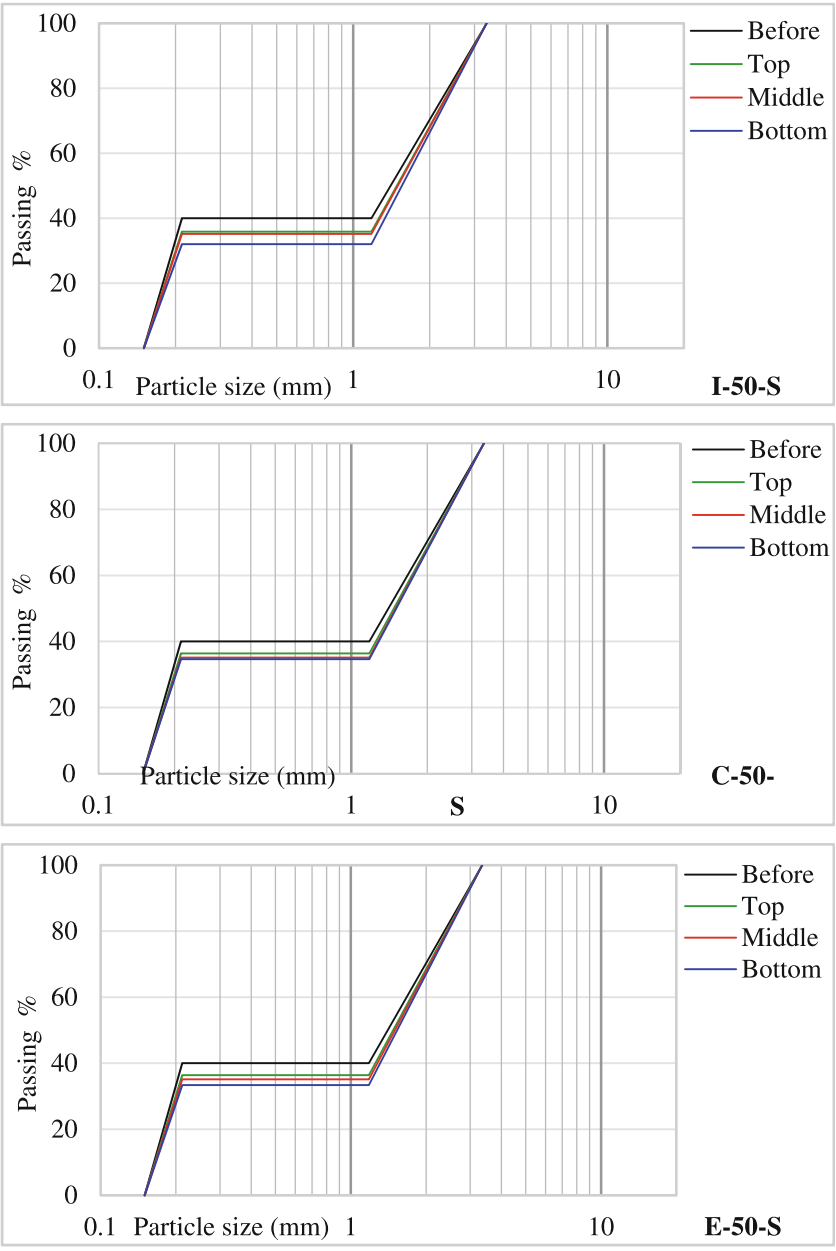

Fig. 6. PSD before and after erosion test in I-50-S, C-50-S, E-50-S respectively.

4 Conclusions

Returning to the main question of this study, what is the effect of seepage flow on the behaviour of a gap-graded sample under triaxial permeameter conditions, it is possible to state the following:

There was a reduction in permeability in all three downward erosion tests with a similar trend.

1. A change in volumetric strain in all three tests has been reported due to erosion. This may also be due to soil rearrangement (volumetric creep).
2. There was a reduction in the internal peak angle of shearing resistance in all tests apart from E-50-S; this believed to be due to the rubber membrane effect.
3. All samples show greatest loss of fine particles in the bottom layer and least in the top layer.

Recommendations for continued research:

1. The possible impact of the change in void ratio during creep and the impact of fine particles lost on permeability will be explored in detail in future research.
2. The influence of the rubber membrane in extension tests will be inspected in depth in future research. It may be preferable to shear in compression from the extension state to avoid this.
3. The hydraulic gradient needs to be maintained as the same for the erosion period in all tests to enable a more consistent comparison rather than the current method, where the sample erosion hydraulic gradient was selected based on when the first fine particle loss was observed.
4. Local radial deformation at the sample centre can be exaggerated compared to the mean in extension due to necking. Correction for, or at least consideration of, this effect needs to be made in future work.

References

Burenkova VV (1993) Assessment of suffusion in non-cohesive and graded soils. Filters in geotechnical and hydraulic engineering. Balkema, Rotterdam, pp 357–360

Honjo Y, Haque MA, Tsai KA (1996) Self-filtration behavior of broadly and gap-graded cohesionless soils. In: Lafleur J, Rollin A., (eds) Geofilters'96. Bitech Publications, Montreal

Kenney TC, Lau D (1985) Internal stability of granular filters. Can Geotech J Issue 22:215–225

Kenney TC, Lau D (1986) Internal stability of granular filters: reply. C. Geotech J 23:420–423

Kezdi A (1979) Soil physics - selected topics. Elsevier, Amsterdam

Ladd RS (1978) Preparing test specimens using undercompaction. Geotech Test J 1(1):16–23

Moffat R (2005) Experiments on the internal stability of widely graded cohesionless soils. Thesis

Moffat RA, Fannin RJ (2006) A large permeameter for study of internal stability in cohesionless soils. Geotech Test J 29(4):277

Moffat R, Fannin RJ (2011) A hydromechanical relationship governing internal stability of cohesionless soil. Can Geotech I(48):413–424

Wu W, Kolymbas D (1991) On some issues in triaxial extension tests. ASTM Geotech Test J 14:276–287

Assessment of Internal Stability of Granular Soils by Means of Theoretical and Laboratory Methods

Maria Clorinda Mandaglio(✉), Nicola Moraci, and Erika Polimeni

Department DICEAM, Reggio Calabria, Italy
linda.mandaglio@unirc.it

Abstract. The assessment of the internal stability of a base soil is a fundamental aspect in the design of the filtering transitions. It can be evaluated by means of semi-empirical, theoretical and experimental methods; the assessment of internal stability of a soil using the available semi-empirical criteria can provide different results. In the paper, in order to verify and validate two methods recently proposed by the authors (Moraci et al. 2012a, b; Moraci et al. 2015), the internal stability of granular soils using different methods is evaluated. The internal stability of test soils has been firstly obtained by Kezdi, Sherard and Kenney and Lau criteria (semi-empirical methods), then it has been assessed theoretically by the method "SimulFiltr" and finally it has been verified by long term filtration tests performed in a rigid wall permeameter. The obtained results allowed us to better define the zones that constitute the new graphical method "Butterfly Wings Chart", recently proposed by the authors.

Keywords: Internal stability · Evaluation methods · Granular soils

1 Introduction

The design of the filtering transitions is a process where a large number of parameters that influence the filtering behaviour is involved. In particular, the design is very complex especially in the case of internally unstable granular base soils. The geotechnical characterization of the base soil represents a relevant aspect. In these circumstances, recent theoretical and experimental studies have shown that the current sizing criteria are not always reliable (Moraci 2010; Moraci et al. 2012a, b, c; Moraci et al. 2014, 2015, 2016).

In an internally stable granular soil, all the particles constitute the soil skeleton. Vice versa, in an internally unstable soil, a portion of particles exists, inside the pores of the soil skeleton, which are free to move into the bordering pores. Particularly, if the constrictions (the narrow throat that connects two pores) in the net of the pores of the principal skeleton are greater than fine particles, the latter can be transported by a hydraulic flow. Such constrictions vary in dimension and in number, depending on the soil grain-size distribution, the relative density and the shape of grains which constitute the solid-skeleton. The internal stability of a granular soil mainly depends on soil

S. Bonelli et al. (Eds.): EWG-IE 2018, LNCE 17, pp. 60–68, 2019.
https://doi.org/10.1007/978-3-319-99423-9_6

grain-size distribution and relative density, as well as on the applied hydraulic gradient (which generates the drag force acting on the soil particles).

To assess the internal stability of granular soils, many methods exist in literature; among these, semi-empirical methods (Kezdi, Sherard and Kenney and Lau criteria) are those much used. The application of these methods to the same soil can provide different determinations in terms of stability. Recently, Moraci et al. (2012a, 2015) proposed new methods to evaluate internal stability, i.e. "Simulfiltr" and "Butterfly wings". The first method is a theoretical method to evaluate the internal stability of granular soils, validated by the experimental results of long-term filtration tests. In the method, the soil grain-size distribution is divided into two parts, for each diameter, beginning from the lowest and ending with the largest diameter. In this way, the soil grain-size distribution is divided as many times as the diameters. The first part represents the larger particles that form the solid skeleton (soil 1); the second part represents the finer particles (soil 2) that constitute the particles potentially free to move through the solid skeleton constrictions. For each of the considered division diameters, the soil numerical percentage constriction size distribution is obtained from the soil 1 grain-size distribution by means of proba-bilistic geometric method, taking into account the relative density. When the soil numerical percentage constriction-size distribution and the soil fine particles cumulative grain-size distribution are obtained, the schematization of the soil in layers is carried out. Each soil layer is formed by alternate constrictions and fine particles. The next step is the simulation of the filtration process of the fine particles, which constitute soil 2, through the soil 1 constrictions inside the number of layers, n, that represent the soil. To simulate this process, a generic particle inside the first layer is chosen and is compared with the relative constrictions inside the next layer. If the considered particle size is lower than that of the compared constrictions size, the particle can move to the next layer. The procedure is repeated for all the layers, that represent the soil, and the cumulative grain-size distribution of the passing soil is obtained. Finally, the largest diameter of the passing soil and the ratio between the moved mass and the average mass of the layers are determined. For the considered diameter, a set of possible simulations (Monte Carlo method) is carried out, changing randomly the constrictions and the fine particle sizes in each layer. A set of large diameters of passing soil is obtained. These values, as a result of the weak law of large numbers, converge with the increase of the simulation number to a single value taken as the final value.

The second method, "Butterfly wings", is a graphical method based on a chart to be used to verify the internal stability of a soil evaluating in which zone the representative point of soil, expressed in terms of average value of finer percentage F and of minimum slope of the grain-size distribution and Smin, falls. Two zones exist in the chart (Fig. 1), one where the soils are definitely unstable and another one where the soils are definitely stable. The remaining zones (A and B) of the chart are areas where the granular soils are stable according to some empirical criteria and unstable for others (Fig. 1).

The article deals with the results of part of a study on soil stability carried out using both these methods and long-term filtration tests, in order to better define the zones that constitute the new proposed graphical method "Butterfly Wings".

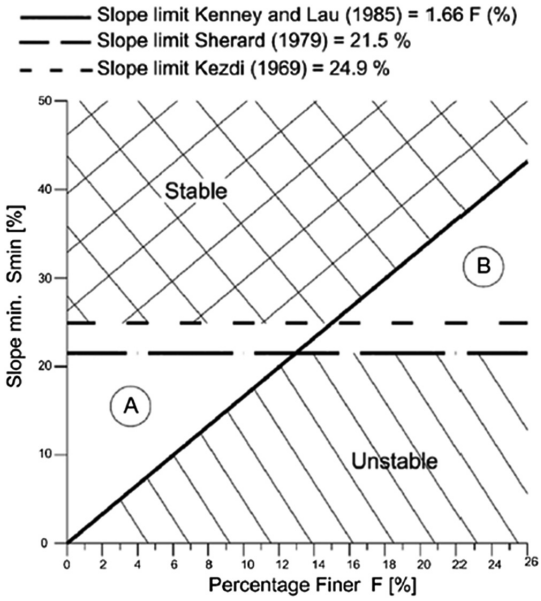

Fig. 1. "Butterfly Wings Chart" (Moraci et al. 2015)

2 Analysis of Internal Stability of Soils

In order to evaluate the internal stability of some soils that fall in zones A and B of the Butterfly Wings and of other soils that, although they fall into the unstable area of the chart (circled dots in Fig. 2), resulted stable for some authors, in-depth semi-empirical (by Kezdi (1969), Sherard (1979) and Kenney and Lau criteria), theoretical (by Simulfiltr) and experimental (by long-term filtration tests) analyses were carried out. The soils have been all collected from the literature dataset.

The soil grain size distributions are shown in Fig. 3. The percentage of fine, the coefficient of uniformity, *Cu*, and the specific weight of the soils, *Gs*, are summarized in Table 1. In particular, the determination of the G_S was carried out in the laboratory through ASTM D854 and ASTM C 127 tests.

The internal stability of the soils has been analysed by means of the semi-empirical methods of Kezdi (1969), Sherard (1979) and Kenney and Lau (1985).

The results obtained are reported in Table 2.

Subsequently, the theoretical method SimulFiltr (Moraci et al. 2012a, b) was applied to these soils and the internal stability has been evaluated theoretically (Table 3). It should be noticed that the criteria are in agreement each other except for the soils DS/KL and D/SB, which have a percentage of fine equal to 0%.

Long-term filtration tests have been performed with constant hydraulic head using two thin and thick nonwoven geotextile filters (O_{95} = 0.035 mm and O_{95} = 0.22 mm). To evaluate the internal stability of the tested granular soils, the water heads along the specimen and at the soil–geotextile filter interface have been measured using six

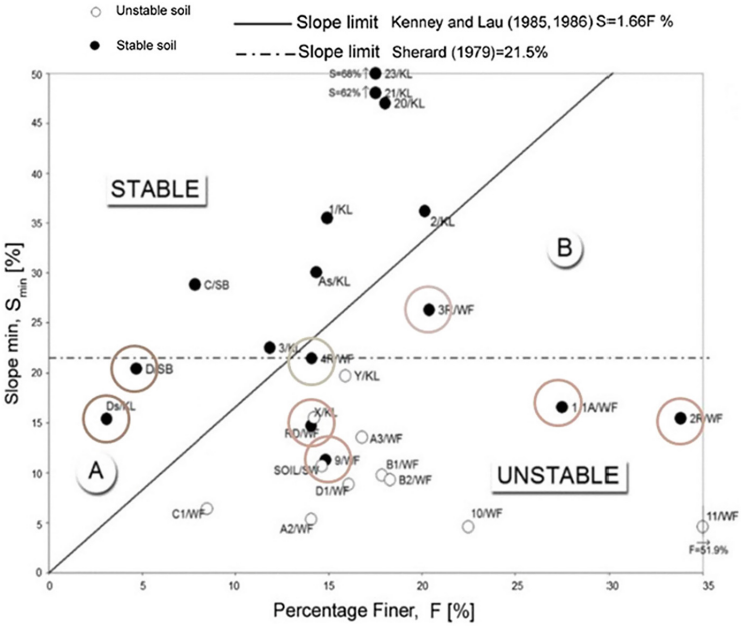

Fig. 2. "Butterfly Wings Chart" showing analysed soils (circled dots)

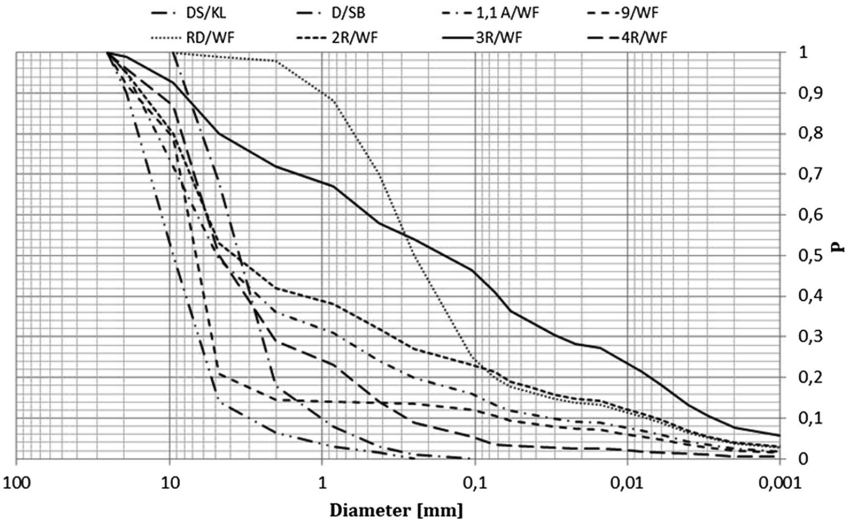

Fig. 3. Grain size distributions of tested soils

piezometers, the measured water heads have allowed the evaluation of the blinding factor (*BF*). The blinding factor (Moraci 1992) was defined as the ratio between the

Table 1. Percentage of fine, Cu, and Gs

Soils	Fine percentage	Cu	Gs
	%	–	–
DS/KL	0	3.7	2.64
D/SB	0	4.2	2.7
1,1 A/WF	16	212.5	2.67
9/WF	12	116.9	2.64
RD/WF	25	45.7	2.71
2R/WF	23	876.9	2.67
3R/WF	46.5	177.8	2.69
4R/WF	5.5	20.7	2.68

Table 2. Semi-empirical results

Soils	Kezdi	Sherard	Kenney and Lau
DS/KL	Unstable	Unstable	Stable
D/SB	Unstable	Unstable	Stable
1,1 A/WF	Unstable	Unstable	Unstable
9/WF	Unstable	Unstable	Unstable
RD/WF	Unstable	Unstable	Unstable
2R/WF	Unstable	Unstable	Unstable
3R/WF	Unstable	Unstable	Unstable
4R/WF	Unstable	Unstable	Unstable

Table 3. SimulFiltr results

Soils	Stability
DS/KL	Stable
D/SB	Stable
1,1 A/WF	Unstable
9/WF	Unstable
RD/WF	Unstable
2R/WF	Unstable
3R/WF	Unstable
4R/WF	Unstable

hydraulic gradient at the soil–filter interface and the hydraulic gradient in the adjacent soil:

$$BF = i_{cz}/i_s \tag{1}$$

$$i_{cz} = \frac{(h_5 - h_6)}{L_s''' \left[\left(\frac{L_g}{L_s'''} \cdot \frac{K_s}{K_g'} \right) + \left(\frac{L_{gR}}{L_s'''} \cdot \frac{K_s}{K_{gR}'} \right) + 1 \right]} \tag{2}$$

$$i_s = \frac{h_4 - h_5}{L_{4,5}} \tag{3}$$

where

i_{cz} = hydraulic gradient in the filter-soil contact zone,
i_s = hydraulic gradient inside the soil,
h_i = hydraulic head in piezometer i,
L_s = distance between the piezometer along the soil and the interface soil/geotextile,
L_g = thickness geotextile,
L_{gR} = thickness drain (gravel),
$L_{4,5}$ = distance between piezometers 4 and 5 along the soil,
K_s = permeability soil,
K_g' = permeability geotextile at the end test,
K_{gR}' = permeability drain (gravel) at the end test.

The soil is considered unstable when this factor is greater than 3. This value was established on the base of a large experimental campaign of long-term filtration tests that showed that when this value was reached excessive pore water pressures related to the decrease of permeability developed and a low permeability zone (filter cake) near the soil geotextile interface was created. The ratio does not include the amount of the filter clogging but only that of blinding, as demonstrated by Moraci (1992).

The soil specimens have been prepared by mixing monogranular pulverizing marble of various colours and reconstituting the specimen in the rigid-wall permeameter in a series of layers by means of dry deposition.

The filtration tests were carried out in conditions of vertical flow directed from top to bottom with constant hydraulic load and were extended for the period of time necessary to achieve the regime conditions and in any case for a duration of more than 94 h, excluding 24 h of saturation (Polimeni 2018).

The test results are shown in Table 4 in terms of blinding factor, BF.

Predictably, soils with a high percentage of fine almost immediately reached the conditions of instability, showing immediately very high BF values (Polimeni 2018).

Table 4. Experimental results

Soils	Geotextile	BF	Stability
DS/KL	Thick	<3	Stable
D/SB	Thin	<3	Stable
1,1 A/WF	Thick	<3	Stable
9/WF	Thin	<3	Stable
RD/WF	Thin	>3	Unstable
2R/WF	Thin	>3	Unstable
3R/WF	Thin	>3	Unstable
4R/WF	Thin	>3	Unstable

3 Discussion of Results

Table 5 shows the comparison of obtained results and the zone of Butterfly wings chart where they fall. While Fig. 4 shows where the tested soils fall in the Butterfly wings chart. From the experimental results obtained and from the analysis of the results reported in the tables, it is possible to observe that, among the semi empirical methods, the Kenney and Lau criterion (1985) is the most reliable since the forecasts were equal to the results obtained experimentally.

Table 5. Comparison of results

Soils	Simulfiltr	Experimental result	Butterfly wings
DS/KL	Stable	Stable	Zone A
D/SB	Stable	Stable	Zone A
1,1 A/WF	Unstable	Unstable	Zone unstable
9/WF	Unstable	Unstable	Zone unstable
RD/WF	Unstable	Unstable	Zone unstable
2R/WF	Unstable	Unstable	Zone unstable
3R/WF	Unstable	Unstable	Zone B
4R/WF	Unstable	Unstable	Bordering zone

Furthermore, the results obtained with SimulFiltr are in good agreement with the experimental results and they confirm, once again, the reliability of the SimulFiltr theoretical method. In this paper, the method has also been used to evaluate the internal stability of soils with a well graded grain size distribution.

Moreover, zone A of the Butterfly Wings Chart, seems also to be representative of stable soils while the B zone of unstable soils.

The verification of the internal stability of soils, necessary above all in the case where the different methods of analysis provided contrasting results, has been performed by means of long-term filtration tests, based on the analysis of the local gradients at the interface and in the soil. It allowed us to confirm the goodness of the

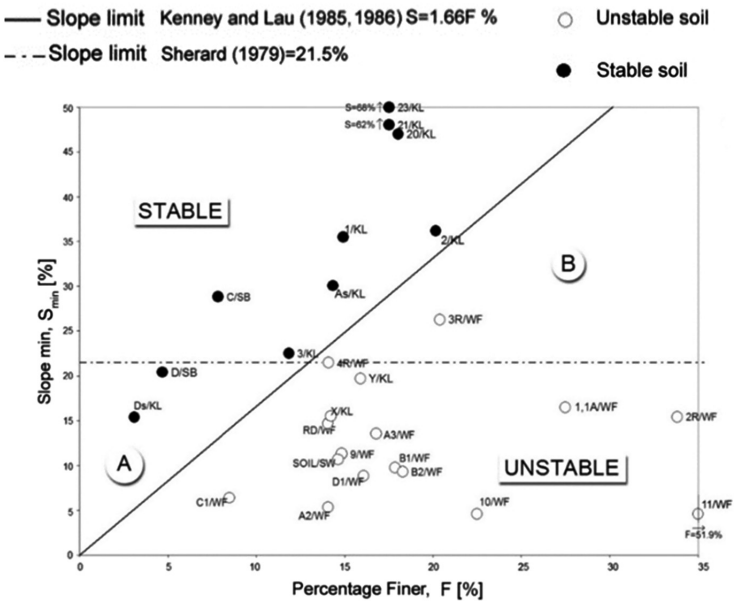

Fig. 4. "Butterfly Wings Chart" including tested soils

theoretical method of SimulFiltr and the greater reliability of the semi-empirical method of Kenney and Lau than other semi-empirical criteria.

It has also been possible to confirm the validity of the Butterfly Wings Chart and to provide a further contribution to the better definition of the A and B zones although the authors believe that more investigations are necessary above all regards the areas bordering the slopes limit.

References

Kenney TC, Lau D (1985) Internal stability of granular filters. Can Geotech J 22:215–225

Kézdi A (1969) Increase of protective capacity of flood control dikes (in Hungarian). Department of Geotechnique, Technical University, Budapest, Report No. 1

Moraci N (1992) L'azione filtrante dei geotessili a contatto con terreni granulari: caratterizzazione, interazione e modellazione. Tesi di dottorato in Ingegneria Geotecnica. Università di Padova, Italia

Moraci N (2010) Geotextile filter: design, characterization, factors affecting clogging, and blinding limit states. Theme Lecture, Discussion Session 9th International Conference on Geosynthetics, Guaruja Brazil, vol 1, pp 413–435

Moraci N, Mandaglio MC, Ielo D (2012a) A new theoretical method to evaluate the internal stability of granular soils. Can Geotech J 49(1):45–58. https://doi.org/10.1139/t11-083

Moraci N, Mandaglio MC, Ielo D (2012b) Reply to the discussion by Dallo and Wang on "A new theoretical method to evaluate the internal stability of granular soils". Can Geotech J 49 (7):866–868

Moraci N, Ielo D, Mandaglio MC (2012c) A new theoretical method to evaluate the upper limit of the retention ratio for the design of geotextile filters in contact with broadly granular soils. Geotext Geomembr 35:50–60. ISSN: 02661144

Moraci N, Mandaglio MC, Ielo D (2014) Analysis of the internal stability of granular soils using different methods. Can Geotech J 51(9):1063–1072. ISSN: 00083674. https://doi.org/10.1139/cgj-2014-0006

Moraci N, Mandaglio MC, Ielo D (2015) Reply to the discussion by Ni et al. on "Analysis of the internal stability of granular soils using different methods". Can Geotech J 52:1–7. https://doi.org/10.1139/cgj-2014-0495

Moraci N, Ielo D, Mandaglio MC (2016) Valutazione della stabilità interna dei terreni granulari (Assessment of internal stability of granular soils). Riv Ital Geotec 27–43. ISSN: 05571405

Polimeni E (2018) Theoretical and experimental study of the internal stability of granular soils (in italian). Ph.D. thesis. Università Mediterranea di Reggio Calabria, Italy

Sherard JL (1979) Sinkholes in dams of coarse, broadly graded soils. In: Transactions, 13th international congress on large dams, New Delhi, India, vol 2, pp 25–35

New Apparatus for Assessing Soil Suffusion Susceptibility Under Two Flow Directions

Didier Marot[1(✉)], Fateh Bendahmane[1], and Van Thao Le[1,2]

[1] Institut de Recherche en Génie Civil et Mécanique (UMR CNRS 6183), Université de Nantes, 58 rue Michel Ange, Saint-Nazaire, France
didier.marot@univ-nantes.fr

[2] The University of Danang -University of Science and Technology, 54, Nguyen Luong Bang, Da Nang, Vietnam

Abstract. Suffusion is the process of selective erosion of fine particles within the matrix of coarse soil particles under the effect of seepage flow. Suffusion can induce important modifications in the hydraulic and mechanical characteristics of the soil in different flow directions. Thus, to ensure the safety assessment of hydraulic earth structures, the experimental models need to match the reality of the body of dikes or dams with horizontal flow. In this paper, a new multi-directional flow apparatus is described for characterizing soil sensibility for the suffusion process and to study the effect of flow direction. A series of suffusion tests was performed using this new device with vertical flow or horizontal flow on both gap graded soils and widely graded soils. All tested specimens were subjected to a multi-stage hydraulic gradient. The comparison of the results of the new device with results obtained from another device in vertical flow was realized. The specimens have the same initial hydraulic conductivity and suffusion susceptibility classification with both devices. Furthermore, for specimens characterized by limited soil anisotropy, the suffusion susceptibilities of these soils are quite identical under vertical flow and horizontal flow. These results permit to validate the new device and the experimental method.

Keywords: Internal erosion · Erosion resistance index
Suffusion susceptibility

1 Introduction

Internal erosion processes can induce modifications of soils that can be the catalyst of instabilities for hydraulic earth structures (Fry et al. 2012). Thus, to ensure the safety assessment of these structures, soil susceptibility to internal erosion processes must be characterized. According to Fell and Fry (2013), there are four processes of internal erosion: concentrated leak erosion, backward erosion, contact erosion and suffusion. This paper focuses on suffusion which is the process of selective erosion of fine particles under the effect of seepage flow within the matrix of coarser particles. It is recognized that suffusion may cause changes in porosity and can also lead to important modifications in the hydraulic and mechanical characteristics of the soil (Marot et al. 2009; Chang and Zhang 2011; Ke and Takahashi 2014; among others).

S. Bonelli et al. (Eds.): EWG-IE 2018, LNCE 17, pp. 69–80, 2019.
https://doi.org/10.1007/978-3-319-99423-9_7

For characterizing the initiation and development of this complex internal erosion process, experimental devices comprise a rigid wall permeameter (Kenney and Lau 1985; Skempton and Brogan 1994; Moffat and Fannin 2006; Wan and Fell 2008; Sail et al. 2011) or a modified triaxial cell designed to force fluid to percolate throughout the sample (Bendahmane et al. 2008; Chang and Zhang 2011; Ke and Takahashi 2014; Slangen and Fannin 2017). These laboratory devices permit to apply a vertical flow in upward or downward direction. However, the suffusion process is induced by seepage flow and the hydraulic conductivity of compacted soil depends on the soil fabric (Smith and Konrad 2011) and on the flow direction, which can be in site in other direction than vertical. In this context, the main objective of this research is to develop a multidirectional flow apparatus which can be used to study soil suffusion susceptibility under vertical or horizontal flows. A series of suffusion tests was performed by the new device with vertical flow or horizontal flow on both gap graded soils and widely graded soils. Specimens were produced by using a static compaction technique to limit the soil anisotropy until the target value of the density was reached. All tested specimens were subjected to a multi-stage hydraulic gradient and the suffusion susceptibility of each specimen was evaluated based on the erosion resistance index I_α to suffusion (Marot et al. 2016). The test results under vertical flow are compared with results obtained from another rigid wall cylinder erodimeter.

2 Testing Apparatuses

The general configuration of the new testing apparatus is shown in Fig. 1. With the objective to avoid applying any disturbance on the core sample, the suffusion can be performed directly on the acrylic cylinder cell of the sample. The device is also composed of three systems for: applying axial strength, injecting water and collecting eroded particles. It has got a data acquisition system as well as instrumentation.

2.1 Cylinder Cell

The soil sample is contained in an acrylic cylinder used for the core sampling (80 mm in inner diameter and 500 mm in height). The height of specimens can vary from 300 mm to 400 mm. The cell is fixed by two vertical beams with two clamps to avoid any disturbance and to provide support for the inlet and outlet ports used in the case of a horizontal flow. The cell top end is closed by a cap equipped with an inlet port, an opening for the crossing of the axial load ram and a vent. The horizontal outlet and the base pedestal are specially designed to catch the detached particles and to place a downstream filter. The specimen is positioned on a 10 mm opening size grid and a mesh with a selected pore opening size can be placed in-between. The same type of mesh can be introduced in the horizontal outlet. The vertical funnel-shaped draining system and the horizontal outlet are both connected to an effluent tank by a pipe having a glass portion for a possible use of an optical sensor (Marot et al. 2011a). The horizontal inlet and outlet and the vertical funnel-shaped draining system are all equipped by a pressure port. The loading system is used to apply axial strength on specimen through a pneumatic piston which can move up or down. This piston contains

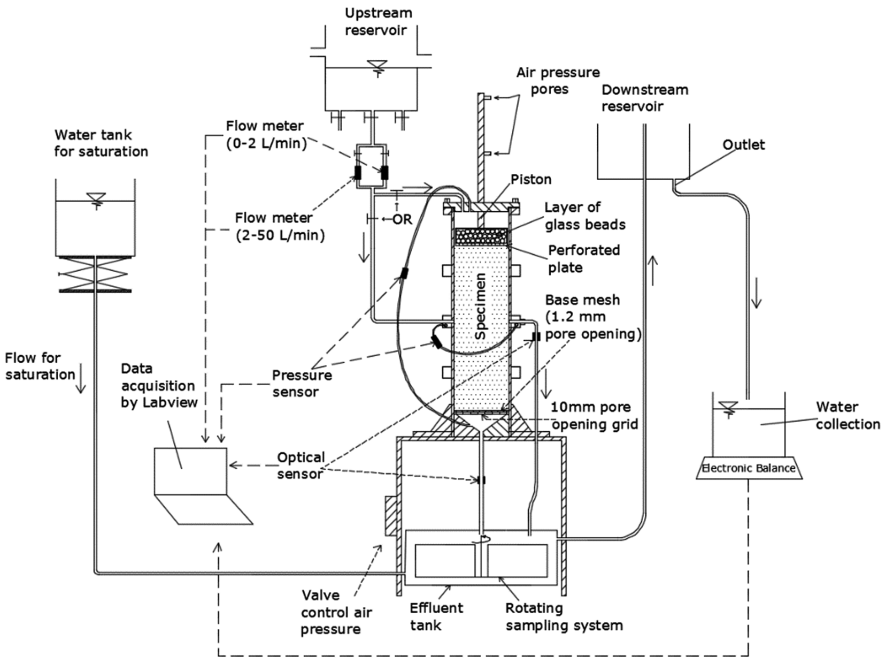

Fig. 1. Schematic diagram of the new apparatus.

a 15 mm thick layer of glass beads to diffuse the fluid uniformly on the specimen top surface. A pressure port is placed on the top cap for the pressure measurement of injected flow.

2.2 Soil Collection and Water Supply Systems

The effluent tank is equipped with three inlet valves and an overflow outlet to control the downstream hydraulic head. Two inlets permit to collect the effluent for both horizontal and vertical flows. The third inlet is connected to the upstream reservoir in order to saturate the specimen by an upward flow. Within the effluent tank, a rotating system contains 8 baskets with linen bags for the sampling of eroded particles carried with the effluent.

As suffusion is the result of the combination of three processes: detachment, transport, and filtration, which in particular depend on the history of hydraulic loading, Rochim et al. (2017) recommend to perform suffusion tests under a multistage hydraulic gradient. For this purpose, the water supply system includes upstream and downstream reservoirs both equipped with an overflow and their relative elevation can be manually modified.

2.3 Instrumentations and Data Acquisition System

The injected seepage flow is measured with two electromagnetic flowmeters of different capacities and located between the upstream reservoir and injection inlets. Depending on the hydraulic conductivity of soils, a set of gates permits to select the appropriate flow meter. In case of very low hydraulic conductivity, the water collection is placed on an electronic mass balance, in order to measure continuously the effluent mass. The same differential pressure transducer is used for horizontal or vertical flows. For horizontal flow, the differential pressure transducer is connected to the pressure ports of horizontal inlet and outlet. For vertical flow, it is connected to the pressure ports of the piston and the funnel-shaped drainage.

The data acquisition is provided by a software which was written by the authors with LABVIEW (Laboratory Virtual Instrument Engineering Workbench). This code also draws automatically the time evolution of hydraulic conductivity, hydraulic gradient, effluent mass, gradient of pressure and flow rate throughout performing the tests.

2.4 Second Device for Comparative Study

A second device, named oedopermeameter was also used. It consists essentially of a cylinder cell and specimen sizes are 280 mm in inner diameter and up to 600 mm in height. A detailed description of this device was reported by Sail et al. (2011), however, a brief summary is provided hereafter. The principle of this device is the same as the new device, in order to diffuse the fluid uniformly on the specimen top layer (the top cap contains a layer of gravel) and to catch the eroded particles (the pedestal base has a vertical funnel-shaped draining system connected to a collecting system with eight beakers). In both devices the applied hydraulic gradient is determined thanks to a differential pressure transducer connected to the pressure ports of the piston and the funnel-shaped outlet.

3 Test Specimens

3.1 Soil Gradations and Potential Susceptibility to Suffusion

Four non plastic or low plasticity soils were selected with different grain size distributions and different grain shapes to investigate suffusion susceptibility. A laser diffraction particle-size analyser was used to measure with demineralized water and without deflocculation agent, the grain size distribution of tested soils (see Fig. 2).

Three gap graded soils were created by mixing different materials. Soil (1) is composed by the mixture of sand S1 (23%) and gravel G3 (77%) (marketed by Sablière Palvadeau, France). Soil (2) is a clayey sand composed by 25% of Proclay Kaolinite and 75% of Fontainebleau sand. Soil (4) is created by the mixture of Fontainebleau sand (16.5%) and gravel G3 (83.5%). Finally, soil (3) is widely graded and comes from a French dike and was sieved with a maximum diameter of 5 mm.

According to grain size based criteria proposed by Kenney and Lau (1985) all cohesionless soils (i.e. soils 1, 3, and 4) are indeed internally unstable. As the percentage of fine P is higher than 20% for soil 2 and as the gap ratio, Gr is smaller than 3

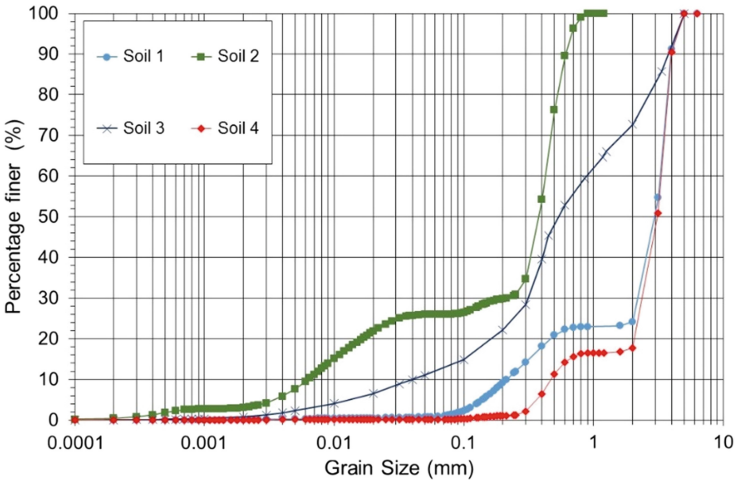

Fig. 2. Grain size distribution of tested soils.

for soil 4, Chang and Zhang's (2013) method assessed these two soils as internally stable. According to Wan and Fell (2008), the method that they proposed seems not to be applicable for gap-graded soils and soils with a mass of fine fraction lower than 15%. Then this method is only relevant for soil (3) which is classified as internally stable. Finally, soil (1) appears potentially unstable, soil 2 is classified potentially stable and no clear classification can be drawn for soils (3) and (4) when applying the four used criteria. Therefore, the erodibility characterization needs suffusion tests.

3.2 Specimen Preparation

Eight multilayer specimens were prepared by moist tamping to prevent soil segregation and per layers of 50 mm in height in order to limit the heterogeneity and to reach a specimen height of 350 mm. Specimens were produced by using a static compaction technique to limit the soil anisotropy until the target value of density was reached. The same procedure was used to prepare two specimens for testing with oedopermeameter.

All specimens were subjected to an axial stress of 60 kPa through the piston and the pore opening size of the downstream mesh was 1.2 mm in order to allow the erosion of all fine particles.

The saturation step began with injection of carbon dioxide (from the bottom) for a duration of ten minutes to improve dissolution of gases into water and afterwards the specimen was saturated with tap water in upward direction by gradually increasing the level of the upstream tank (see Fig. 1). The water level was increased until it reached the top of specimen. The inflow rate was sufficiently small to prevent soil segregation in specimen and to achieve a high degree of saturation. The whole saturation phase required approximately 24 h. With this preparation technique (Rochim et al. 2017), the final saturation ratio was determined by measuring density and water content, and it reached 95%.

4 Test Procedure and Interpretative Methods

4.1 Suffusion Test Procedure

Specimens were subjected to a seepage flow in downward direction or horizontal direction under a multistage hydraulic gradient. For the purpose of improving readability, the name of each test starts by the soil number (see Fig. 2). The first letter V or H details the vertical or horizontal flow direction. Tests performed with the oedopermeameter are identified by the last letter O. Table 1 indicates the characteristics of all performed tests. Despite precautions, it can be noted that the samples in the larger device (i.e. oedopermeameter) have a higher initial dry density compared to the samples in the new apparatus.

Table 1. Properties of tested specimens

Tested specimens	Flow direction[a]	Initial dry unit weight	Applied hydraulic gradient	Seepage length
		kN/m^3	(–)	cm
1-H	H	16.4	0.10–2.00	8.1
2-V	V	16.0	0.28–1.63	35.0
2-H	H	16.0	2.00–11.00	8.1
2-V-O	V	17.5	0.92–22.33	24.0
3-V	V	17.0	0.43–2.70	35.0
3-H	H	17.0	0.43–2.70	8.1
3-V-O	V	17.8	0.56–15.81	24.0
4-V	V	16.1	0.09–0.58	35.0
4-H	H	16.1	0.09–0.58	8.1

[a]V: vertical downward flow; H: horizontal flow.

A basket with linen bag in the rotating sampling system is selected for the duration of each stage of hydraulic gradient. At the end of each test, the eroded fine particles caught by the linen bag are dried in an oven for 24 h and their mass is determined.

4.2 Computation of Hydraulic Conductivity and Erosion Rate

The computation of hydraulic conductivity is based on the Darcy' formula.

$$k = \frac{Q}{iS} \tag{1}$$

where Q is the flow rate; i is the hydraulic gradient and S is the cross-sectional area of flow.

The erosion rate is computed by:

$$\dot{m} = \frac{m_{eroded}(t)}{St} \tag{2}$$

where m_{eroded} (Δt) is the mass of eroded particles during the duration Δt.

In the case of vertical flow, the cross-sectional area of flow corresponds to the cross section of the specimen. Whereas in the case of horizontal flow, the cross-sectional area of flow is expressed by:

$$S = \frac{S_{min} + S_{max}}{2} \tag{3}$$

where S_{min} is the flow section at the horizontal inlet with the 10 mm diameter of pipe and S_{max} is the biggest rectangular flow area: $S_{max} = D\ h_{flow\text{-}max}$, where D is the specimen diameter and $h_{flow\text{-}max}$ is the height of flow. Simulations with Plaxis software permit to compute the height: $h_{flow\text{-}max}$ = 10.80 cm (Le 2017).

4.3 Energy Based Method

Further to results on interface erosion tests, Marot et al. (2011b) proposed a new analysis based on the total flow power which is the summation of the power transferred from the fluid to the solid particles and the power dissipated by the viscous stresses in the bulk. Since the transfer appears negligible in the case of suffusion (Sibille et al. 2015), the authors suggest characterizing the fluid loading from the total flow power which is expressed by:

$$P_{flow} = (\gamma_w \Delta z + \Delta P)Q \tag{4}$$

where γ_w is the specific weight of water, $\Delta P = P_A – P_B$ is the pressure drop between the sections A and B respectively and Q is the volumetric water flow rate. $\Delta z > 0$ if the flow is in downward direction, $\Delta z < 0$ if the flow is upward and the erosion power is equal to $Q\Delta P$ if the flow is horizontal.

The expended energy E_{flow} is the time integration of the instantaneous power dissipated by the water seepage and it is computed until reaching the steady state (i.e. hydraulic conductivity tends to stabilize and the erosion rate tends to decrease). For the same duration the cumulative eroded dry mass is determined and the erosion resistance index is expressed by:

$$I_\alpha = -Log\left(\frac{m_{eroded}}{E_{flow}}\right) \tag{5}$$

Depending on the values of I_α index, Marot et al. (2016) proposed six categories of suffusion susceptibility from highly erodible to highly resistant (corresponding susceptibility categories: highly erodible for $I_\alpha < 2$; erodible for $2 \leq I_\alpha < 3$; moderately erodible for $3 \leq I_\alpha < 4$; moderately resistant for $4 \leq I_\alpha < 5$; resistant for $5 \leq I_\alpha < 6$; and highly resistant for $I_\alpha \geq 6$).

5 Test Results and Discussion

5.1 Comparison of New Apparatus Results with Results of Oedopermeameter

A series of tests under vertical downward flow on soils (2) and (3) was performed by either new device or oedopermeameter. For the purpose of this comparative study, specimens were prepared at the same order of magnitude of initial dry density (see Table 1). Tests 2-V and 3-V were performed with the new device, whereas the oedopermeameter was used to perform tests 2-V-O and 3-V-O. The hydraulic conductivity and the erosion rate are computed for these four tests by Eqs. (1) and (2), respectively. Figures 3 and 4 show the time evolution of hydraulic conductivity and erosion rate, respectively.

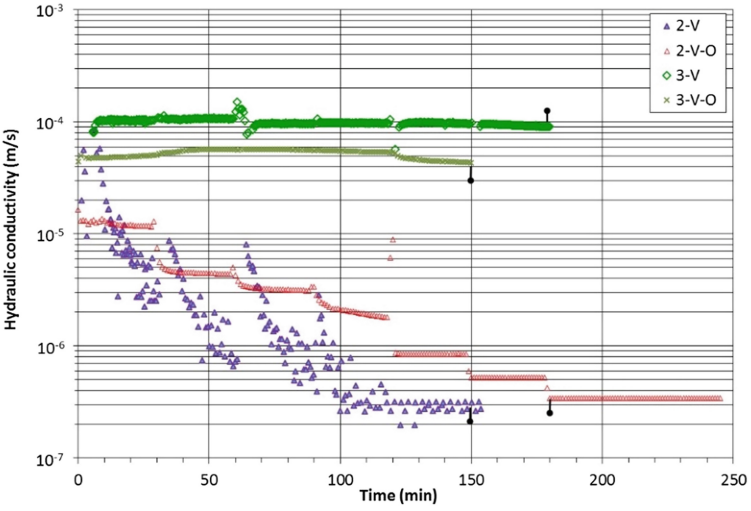

Fig. 3. Time evolution of hydraulic conductivity, soil specimens (2) and (3).

The results show that with both devices, the initial hydraulic conductivity is 2 10^{-5} m/s and between 5 10^{-5} m/s and 8 10^{-5} m/s for specimens of soil (2) and soil (3), respectively. For the clayey soil (2), the hydraulic conductivity first decreases. However, at each increase of the applied hydraulic gradient (at t = 30, 60, 90 and 120 min), the hydraulic conductivity sharply increased. This increase was immediately followed by a decrease of both hydraulic conductivity and erosion rate, which suggests that some detached particles can be filtered within the soil itself. It is worth noting that a rough increase of the erosion rate occurs simultaneously with the stabilisation of the hydraulic conductivity. These evolutions confirm that a clogging initially restricting the water flow can be blown away by a sudden increase of the hydraulic loading. Thus, under multistaged hydraulic gradient conditions, the predominant process during this second phase seems to be the detachment and transport of solid particles and the

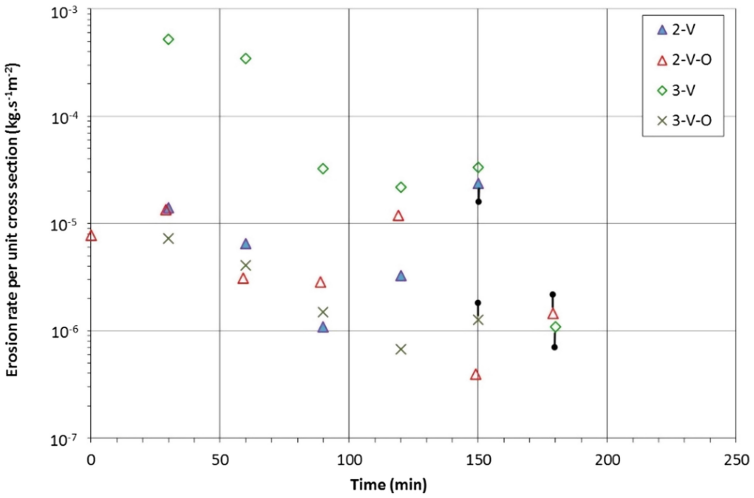

Fig. 4. Time evolution of erosion rate per unit cross section, soil specimens (2) and (3).

stabilisation of hydraulic conductivity could be explained by the presence of preferential flows created by the erosion process.

The cumulative eroded mass and the expended energy are expressed per unit specimen's volume in order to compare easily the results obtained with both devices. Figure 5 shows the cumulative eroded mass per unit volume versus the cumulative expended energy per unit volume.

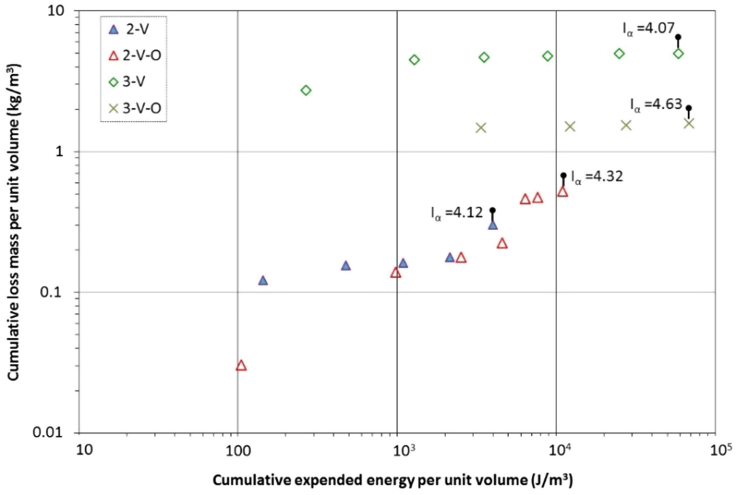

Fig. 5. Cumulative loss mass per unit volume versus cumulative expended energy per unit volume, soil specimens (2) and (3).

At the steady state, shown by black spots in Figs. 3, 4 and 5, the erosion resistance index is computed by Eq. 5. For a given soil, the highest value is obtained with the oedopermemater test. This deviation in the values of I_α can be attributed to the higher density of the corresponding specimens. However it can be noted that with both devices, the values of erosion resistance index are between 4.07 and 4.63. Accordingly, the suffusion susceptibility is moderately resistant for these two soils. This agreement of results permits to validate the new device and the experimental method.

5.2 Flow Direction Influence

For each soil, two specimens were performed under vertical flow (tests 1-V to 4-V) and horizontal flow (tests 1-H to 4-H). The first step of this comparative study consists in verifying that the initial hydraulic conductivity is approximately the same under both flow directions (see Table 2).

Table 2. Test results

Tested specimens	Initial hydraulic conductivity mass	Loss energy	Expended	I_α
	m/s	kg	J	(–)
1-V	$6.1 \cdot 10^{-3}$	0.0136	97.1	3.85
1-H	$17.0 \cdot 10^{-3}$	0.0264	177.2	3.83
2-V	$2.0 \cdot 10^{-5}$	0.0005	7.2	4.12
2-H	$0.9 \cdot 10^{-5}$	0.0013	16.0	4.09
3-V	$8.0 \cdot 10^{-5}$	0.0089	105.3	4.07
3-H	$6.9 \cdot 10^{-5}$	0.0007	8.9	4.12
4-V	$6.0 \cdot 10^{-3}$	0.0277	161.5	3.77
4-H	$2.6 \cdot 10^{-3}$	0.0077	80.6	4.02

By comparing the results for a given soil under both flow directions, it is worth noting that the cumulative loss dry mass can be higher under vertical flow (see Table 2). However in this case, the expended energy is also higher under vertical flow and finally at the steady state, the erosion resistance index is quite identical under both flow directions.

Figure 6 represents the classification of suffusion susceptibility of all tested specimens 1-V to 4-H. For specimens of soils (1) to (3), their suffusion classifications are identical for both flow directions. Soil (1) is classified moderately erodible, whereas soils (2) and (3) are moderately resistant. In the case of soil (4) a slight difference of suffusion classification appears, moderately erodible under vertical flow and between moderately erodible and moderately resistant under horizontal flow. Further studies will be performed to explain why different results are obtained for this soil.

Accordingly, for a given soil with a same initial hydraulic conductivity, the suffusion susceptibility is quite the same under both flow directions.

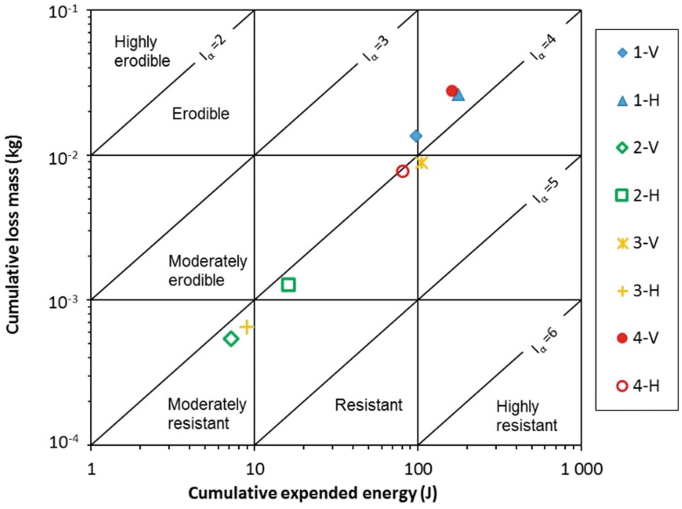

Fig. 6. Cumulative loss mass vs cumulative expended energy for all tested specimens under both flow directions.

6 Conclusion

A new device and associated data acquisition code were developed in order to investigate the suffusion susceptibility of cylindrical specimens under vertical or horizontal flows and to study the influence of the seepage flow direction.

The results of the new device are compared with the results obtained from oedopermeameter. The results show that the initial hydraulic conductivity of a given soil is approximately the same with both devices and specimens have the same suffusion susceptibility classification. These results permit to validate the new device and the experimental method.

A series of tests was carried out under vertical direction or horizontal direction. As specimens were prepared by static compaction to limit the soil anisotropy, the initial hydraulic conductivity is approximately the same under both flow directions. Consequently the suffusion susceptibility classification of these soils is quite identical under vertical flow and horizontal flow. Thus these results permit to validate the interpretative method.

Acknowledgements. The authors thank the company IMSRN, the Ministry of Education and Training of Vietnam, the University of Danang, Vietnam, for providing financial support for this work.

References

Bendahmane F, Marot D, Alexis A (2008) Experimental parametric study of suffusion and backward erosion. J Geotech Geoenviron Eng ASCE 134(1):57–67

Chang DS, Zhang LM (2011) A stress-controlled erosion apparatus for studying internal erosion in soils. Geotech Test J 34(6):579–589

Chang DS, Zhang LM (2013) Extended internal stability criteria for soils under seepage. Soils Found 53(4):569–583

Fell R, Fry JJ (2013) Erosion in geomechanics applied to dams and levees. In: Bonelli S (ed) Wiley, pp 1–99

Fry JJ, Vogel A, Royet P, Courivaud JR (2012) Dam failures by erosion: lessons from ERINOH data bases. In: Proceedings of the 6th international conference on scour and erosion, Paris, pp 273–280

Ke L, Takahashi A (2014) Experimental investigations on suffusion characteristics and its mechanical consequences on saturated cohesionless soil. Soils Found 54(4):713–730

Kenney T, Lau D (1985) Internal stability of granular filters. Can Geotech J 22(2):215–225

Le VT (2017) Development of a new device and statistical analysis for characterizing soil sensibility face suffusion process. Ph.D. thesis, Université de Nantes, France

Marot D, Bendahmane F, Rosquoët F, Alexis A (2009) Internal flow effects on isotropic confined sand-clay mixtures. Soil Sediment Contam Int J 18(3):294–306

Marot D, Bendahmane F, Konrad J-M (2011a) Multichannel optical sensor to quantify particle stability under seepage flow. Can Geotech J 48:1772–1787

Marot D, Regazzoni PL, Wahl T (2011b) Energy based method for providing soil surface erodibility rankings. J Geotech Geoenviron Eng (ASCE) 48:1772–1787

Marot D, Rochim A, Nguyen HH, Bendahmane F, Sibille L (2016) Assessing the susceptibility of gap graded soils to internal erosion characterization: proposition of a new experimental methodology. Nat Hazards 29:1–24

Moffat R, Fannin J (2006) A large permeameter for study of internal stability in cohesionless soils. Geotech Test J 23(1):116–122

Rochim A, Marot D, Sibille L, Le VT (2017) Effect of hydraulic loading history on suffusion susceptibility of cohesionless soils. J Geotech Geoenviron Eng (ASCE) 04017025:1–10

Sail Y, Marot D, Sibille L, Alexis A (2011) Suffusion tests on cohesionless granular matter. Eur J Environ Civ Eng 15(5):799–817

Sibille L, Lominé F, Poullain P, Sail Y, Marot D (2015) Internal erosion in granular media: direct numerical simulations and energy interpretation. Hydrol Process 29(9):2149–2163

Skempton AW, Brogan JM (1994) Experiments on piping in sandy gravels. Géotechnique 44 (3):440–460

Slangen P, Fannin RJ (2017) The role of particle type on suffusion and suffosion. Géotech Lett 7:1–5

Smith M, Konrad JM (2011) Assessing hydraulic conductivities of a compacted dam core using geostatistical analysis of construction control data. Can Geotech J 48:1314–1327

Wan CF, Fell R (2008) Assessing the potential of internal instability and suffusion in embankment dams and their foundations. J Geotech Geoenviron Eng ASCE 134(3):401–407

Uncertainty in Determining the Critical Hydraulic Gradient of Uniform Glass Beads

Lubomir Petrula(✉), Mario Hala, and Jaromír Říha

Brno University of Technology, Brno, Czech Republic
petrula.l@fce.vutbr.cz

Abstract. One of the local defects in soils due to seepage is heave. This may occur at the downstream toe of hydraulic structures in the case of upward external seepage where particles of uniform soils are subject to uplift and also upward seepage forces. The phenomena starts with gradual liquefaction of soil grains accompanied by gradual loss of shear strength followed by boiling, heave and possible backward erosion and overall collapse of the structure. The problem of heave has been addressed by numerous authors who have published relationships based on the balance of forces and also on results of laboratory experiments. In this paper the results of extensive systematic experimental research carried on glass beads subjected to upward seepage in the vertical Darcy apparatus are presented. Three glass beads' diameters 0.2 mm, 0.5 mm and 1.0 mm with uniformity coefficient C_U from 1.1 to 1.3 and different porosity n from 0.36 to 0.44 were tested. To enable statistical evaluation of the uncertainty in critical hydraulic gradient 177 individual tests have been performed. The results of measurements were analysed and compared with relationships proposed by various authors. The best agreement was provided by the well-known Terzaghi formula relating the critical gradient to the specific mass of grains and soil porosity. Based on the experimental data the uncertainty in the use of Terzaghi formula was expressed via reliability coefficients recommended for use in technical practice.

Keywords: Critical hydraulic gradient · Heave · Non-cohesive soil
Uniform soil · Terzaghi

1 Introduction

Breach by heave is defined in the literature as external fluidization (Vuković and Pusić 1992). This issue was dealt with by a number of authors who defined relations for the condition based on the equilibrium of forces (Terzaghi 1922), or by laboratory experiments, on various types of soil (Istomina 1957; Alhasan et al. 2015).

Probably the first equilibrium condition for heave derived Pavlovskij (Istomina 1957) for the selected grain size, later on the relationship coming from the equilibrium of forces acting on homogeneous isotropic grain material was derived by Knorre (1925). Later, this formula was adopted by Zamarin (1931) and Terzaghi (1922) and, through experimental and theoretical analysis the correlation with soil porosity was improved.

S. Bonelli et al. (Eds.): EWG-IE 2018, LNCE 17, pp. 81–90, 2019.
https://doi.org/10.1007/978-3-319-99423-9_8

Goldstein (Istomina 1957), using experimental analysis, reported the relation-ship that used the porosity number being analogical to Terzaghi (1922) formula. Gershevanov (1948) defined a relation for the determination of the critical hydraulic gradient on the basis of the transition from the laminar to the turbulent flow.

Istomina (1957) conducted experiments for more than 20 natural materials and proposed the dependence between the critical hydraulic gradient and the coefficient of uniformity based on lower envelope of observed hydraulic gradients. Unlike previous relationships, this method does not take into account unit weight and porosity.

In this study the uncertainty in determining critical hydraulic gradient at uniform glass beads was derived using experimental results by comparing with physically based Terzaghi formula.

2 Theoretical Background

2.1 Limit State Condition for Homogeneous Uniform Soil

Taking into account forces acting on the soil specimen (Fig. 1), the limit state condition may be expressed as follows (friction along smooth glass cylinder walls is neglected):

$$F_{G,d} \geq F_{w,d}, \tag{1}$$

where $F_{G,d}$ is the design value of the total soil weight and $F_{w,d}$ is the design value of the force induced by water pressure gradient (uplift and groundwater flow). To obtain these design values a characteristic values need to be specified along with appropriate reliability coefficients (EN B. 1997 2004):

$$F_{G,k}\gamma_{M,J} \geq F_{w,k}\gamma_J\gamma_1, \tag{2}$$

where $F_{G,k}$ is the characteristic value of the total soil weight and $F_{w,k}$ is the characteristic value of the force induced by pressure gradient, $\gamma_{M,J}$ is the reliability coefficient in the determination of soil weight, γ_J is the coefficient of uncertainty in de-termination of the force due to water pressure gradient, γ_1 is importance factor. Characteristic values of forces in Eq. (2) related to soil specimen are as follow:

$$F_{G,k} = \gamma_s(1-n)LA + \gamma_w nLA, \tag{3}$$

$$F_{w,k} = \gamma_w LAJ + \gamma_w LA, \tag{4}$$

where γ_s is the specific weight of soil grains, n is porosity, L is the height of the soil specimen, A is the cross section of the Darcy cylinder (permeameter), γ_w is the specific weight of the water and J is the hydraulic gradient acting on the specimen. Substituting forces from Eqs. (3) and (4) to Eq. (1) one obtains:

$$[\gamma_s(1-n)LA + \gamma_w nLA]_d \geq [\gamma_w LAJ + \gamma_w LA]_d, \tag{5}$$

where the subscript "*d*" formally indicates the design values. By separating the hydraulic gradient in the right hand side of the Eq. (5) and by adding the reliability coefficients, the final limit state condition reads:

$$\frac{(\gamma_s - \gamma_w)(1-n)}{\gamma_w}\gamma_{M,J} \geq J\gamma_J\gamma_1. \tag{6}$$

The main aim of this study is to quantify values of reliability coefficients $\gamma_{M,J}$ for different exceedance probabilities based on experimentally measured critical hydraulic gradients, the other coefficients are not subject of this study.

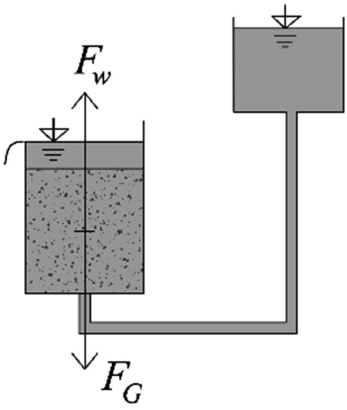

Fig. 1. Scheme of general forces acting on the soil sample

2.2 Available Formulae

Knorre's formula is based on the equilibrium of forces acting on homogeneous isotropic uniform material (Knorre 1925). Knorre (1925) recommends assessing the stability of heave using a critical hydraulic gradient as follows:

$$J_c = \frac{\gamma_s - \gamma_w}{\gamma_w}. \tag{7}$$

Later on, this formula was adopted by Zamarin (1931) and Terzaghi (1922) and through experimental and theoretical analysis modified by including the influence of porosity. Zamarin (1931) proposed the following formula:

$$J_c = \frac{(\gamma_s - \gamma_w)(1-n)}{\gamma_w} + 0.5n. \tag{8}$$

Terzaghi (1922) studying a filter stability derived formula based on Eqs. (3), (4) and (6):

$$J_c = \frac{(\gamma_s - \gamma_w)(1-n)}{\gamma_w}. \tag{9}$$

Goldstein (1953) adopted the Terzaghi's (1922) formula and modified it by substituting the porosity number e:

$$J_c = \frac{\frac{\gamma_s}{\gamma_w} - 1}{1+e}, \tag{10}$$

$$e = \frac{n}{1-n}. \tag{11}$$

Istomina (1957) expressed the critical hydraulic gradient J_c and introduced permissible hydraulic gradient J_p (design value) recommended for technical applications (Fig. 2) as a function of the coefficient of uniformity C_U. The dependence was derived for the following materials used at experimental research:

- coefficient of uniformity $C_U \in$ <2.3; 39.3>,
- grain diameter $d_{50} \in$ <0.1; 8 > mm,
- grain diameter $d_{10} \in$ <0.057; 0.28 > mm.

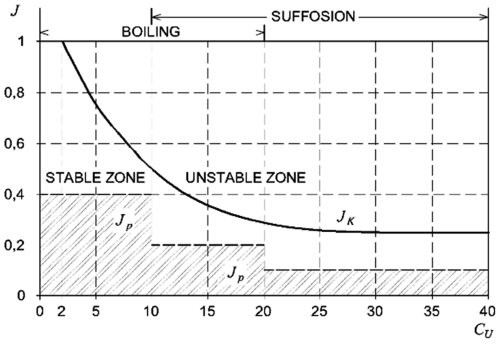

Fig. 2. Critical hydraulic gradient by Istomina (1957)

3 Experimental Laboratory Research

3.1 Device

Experiments were performed using the permeameter (plastic cylinder) with upward vertical flow. The device consists of a permeameter with sieve or geotextile at the bottom. The cylinder with the sample is fixed to the frame, the bottom is connected to the water supply and the upper part is the outflow pipe. Piezometers are attached under and above the soil sample. The water flow is governed by a vertically movable tank with a spillway. The water flow to the tank provides a pump that draws water from the storage tank. The flow of water into the sample is controlled by the valve. The scheme of the measuring device is shown in Fig. 3.

3.2 Preliminary Measurements

The experiments were conducted with three glass bead diameters with the grain size distribution according Fig. 4 and coefficient of uniformity and glass density shown in Table 1.

3.3 Experimental Procedure and Results

In order to obtain samples with different porosity, filling the beads into the permeameter involved free filling and also compacting by vibration with variable duration. The porosity was determined by weighing the sample and measuring its volume in the cylinder. Hydraulic gradient was governed by gradual raising of the movable tank (Fig. 3). The discharge was measured at each raise of the tank. In total 177 laboratory experiments were performed on the materials according to Table 1. The number of experiments, ranges of porosity and critical hydraulic gradient are summarized in Table 2. Expected measurement accuracy for individual variables is summarized in Table 3.

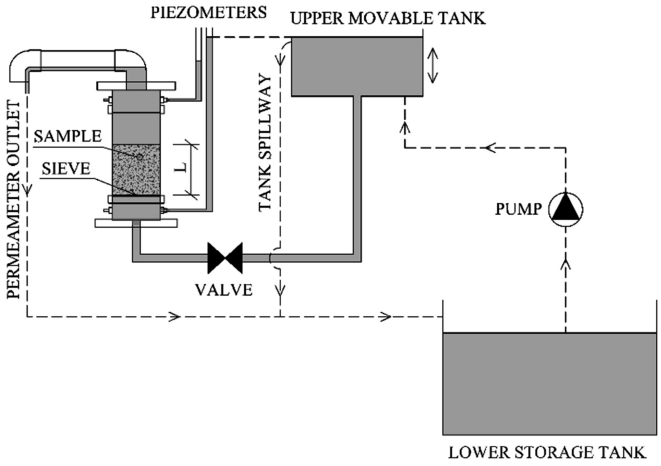

Fig. 3. Measuring device

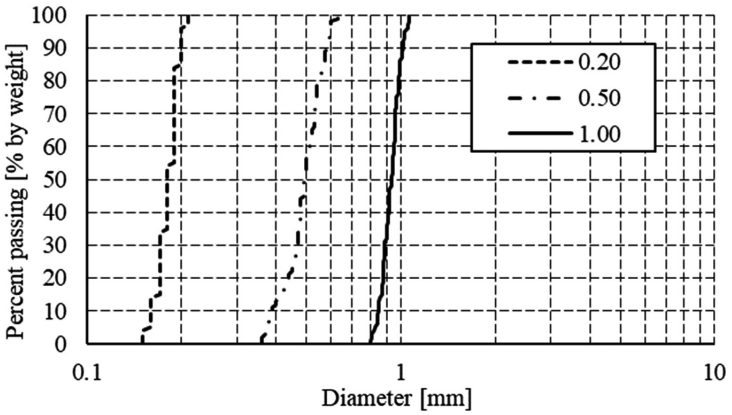

Fig. 4. Grain size distribution curves

Table 1. Properties of the tested materials

	Diameter of glass beads [mm]		
	0.20	0.50	1.00
Coefficient of uniformity C_U	1.19	1.33	1.14
Glass beads density ρ_s [kg/m^3]	2484	2480	2493

At the beginning supplementary data were collected like the permeameter diameter and its weight, glass bead density, sieve and geotextile thickness and permeability, water temperature, etc.).

The sample of the height L from 0.11 to 0.13 m was placed into the permeameter and vibrated to achieve random porosity. The surface of the sample was flattened and the permeameter with sample was weighted to identify the weight of the sample.

At the beginning of each test the soil sample was slowly saturated. From measured height of the sample porosity was calculated using the weight of the sample, its volume and density of glass beads.

Table 2. Experiment plan with properties of glass beads

Nominal bead diameter	Number of tests	Porosity		Critical hydraulic gradient	
		Minimal	Maximal	Minimal	Maximal
	[–]	[–]	[–]	[–]	[–]
0.20	52	0.377	0.446	0.7898	0.9532
0.50	53	0.368	0.437	0.8239	0.9537
1.00	72	0.353	0.416	0.8475	1.0263

Table 3. Measurement tolerances

Variable	Tolerance
Weight	0.0001 kg
Permeameter diameter	0.25 mm
Height of the sample	0.25 mm
Piezometric heights	0.25 mm
Temperature	0.25 °C

For each elevation of water tank, a difference between piezometric heads upstream and downstream of sample was measured and instantaneous hydraulic gradient was identified. This process was repeated for increasing elevations of the water tank until the limit state when the process of boiling (heave) occurred at hydraulic gradient $J_{c\text{-}measured}$.

4 Comparison of Experimental Results with Available Formulae

For available formulae mentioned above a comparison with experimental results was carried out. For each test corresponding values of critical hydraulic gradient according to Knorre (1925), Zamarin (1931) and Terzaghi (1922) were calculated and plotted against measured values (Fig. 5).

It can be seen that the best agreement is achieved by physically based Terzaghi (1922) formula (9). Therefore, the values of critical hydraulic gradient obtained from Eq. (9) are considered as characteristic values, the uncertainty was expressed by relating measured values of critical hydraulic gradient to results obtained from this formula (Fig. 6).

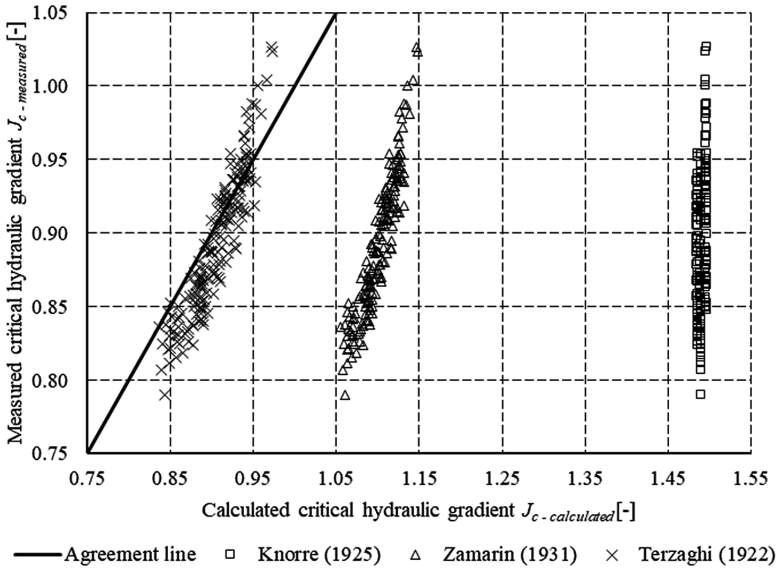

Fig. 5. Comparison of experimental results of critical hydraulic gradient with available formulae

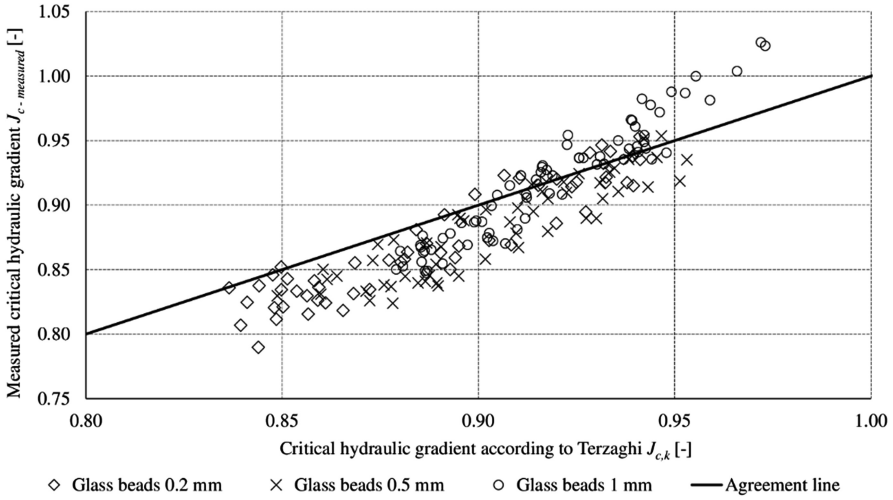

Fig. 6. Agreement of measured critical hydraulic gradient with Terzaghi formula

5 Reliability Coefficients

Both hydraulic gradient in the soil as the load and critical hydraulic gradient as the resistance are subject to uncertainty. To take this into account for heave, the reliability coefficients were applied in terms of EN B. 1997 (2004). The general form of the limit state condition (Eq. (6)) contains the Terzaghi (1922) expression for $J_{c,k}$ at its left side.

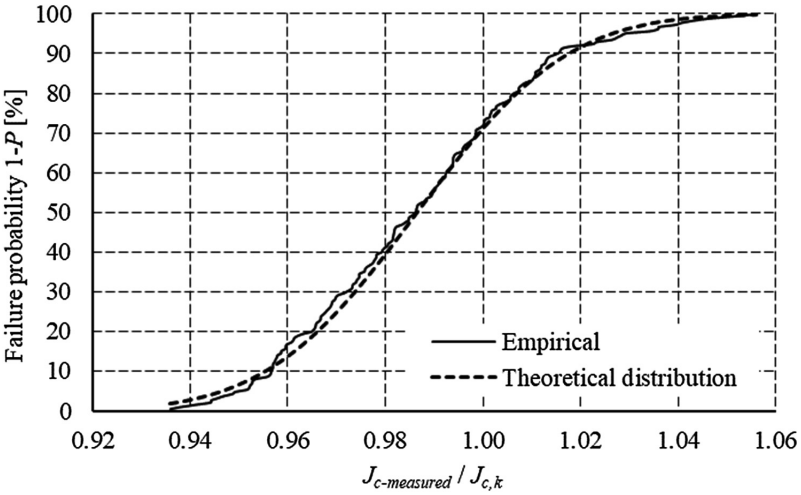

Fig. 7. Distribution function of ratios of measured data from Terzaghi (1922)

Table 4. Reliability coefficients of critical hydraulic gradient

Structure reliability P	Reliability coefficient $\gamma_{M,J\%}$
[%]	[–]
95	0.947
99	0.930
99.9	0.912

For all performed measurements ratios $J_{c\text{-}measured}/J_{c,k}$ were calculated and statistically processed using theoretical normal probability distribution function providing the best fit (Fig. 7). In Fig. 7 the ratio $J_{c\text{-}measured}/J_{c,k}$ expresses the reliability coefficient $\gamma_{M,J}$. Further on, the values of critical hydraulic gradients with a probability of exceedance P = (95%, 99%, 99.9%), which corresponds to structure reliability, were searched to determine the reliability coefficients $\gamma_{M,J\%}$ (Table 4).

6 Conclusion

In the study, the uncertainty in the critical hydraulic gradient determination by Terzaghi (1922) formula was determined for three diameters (0.2, 0.5 and 1.0 mm) of uniform glass beads. The measured data consist of 177 results of laboratory tests on glass beads with uniformity coefficient C_U = 1.1–1.3 and porosity n = 0.36–0.44.

Reliability coefficients for the probability exceedance P (95%, 99% and 99.9%) for heave were determined. The obtained reliability coefficients may be considered as the lowest envelope of the coefficients applicable to homogeneous and completely uniform soils. Further research on materials with higher uniformity coefficient is needed to determine reliability coefficients for more natural soils.

Acknowledgements. This paper has been prepared under projects: No. FAST-J-18-5328 – Problematics of external suffusion/heave; FAST-J-18-5104 – Research on conditions of initiation and progression of privileged seepage paths.

References

Alhasan Z, Hala M, Julínek T, Říha J (2015) Discussion on the critical hydraulic gradient for uniform homogenous glass beads. In: Eksploatacja budowli pietrzacych – diagnostika i zapobieganie zagroženiom. Instytut Meteorologii i Gospodarki Wodnej, Panstwowy Instytut Badawczy, Warszawa, pp 165–172

EN B. 1997. 1 (2004) Eurocode 7: geotechnical design-part 1: general rules. British Standards, London

Gershevanov NM, Polshin DE (1948) Theoretical fundamentals of soil mechanics and their practical applications. Gostroiizdat, Moscow (in Russian)

Goldstein MN (1953) Sudden fluidization of sands. In: Geotechnical tasks, Proceedings no. 1. Karanovich Institute of Transport in Dnepropetrovsk

Istomina VS (1957) Filtracionnaja ustojčivost gruntov (Soil stability to seepage). VODGEO, Gosstrojizdat (in Russian)

Knorre ME (1925) Function of sandy levees and evaluation of erosion processes. In: Methodology of hydraulic calculation applied in design of Zaporozska hydropower central on the Dnepr river

Terzaghi KV (1922) Der grundbruch an stauwerken und seine verhütung. Wasserkraft 17 (24):445–449 (in German)

Vuković M, Pusić M (1992) Soil Stability and deformation due to seepage. Water Research Publication, Colorado

Zamarin EA (1931) Ground water flow under hydrotechnical structures. Tashkent (in Russian)

Viewing Fluid Flow Inside a Granular Medium

Nicoletta Sanvitale(✉), Elisabeth T. Bowman, and Jonathan A. Black

University of Sheffield, Sheffield, UK
n.sanvitale@sheffield.ac.uk

Abstract. This paper describes preliminary tests from a 'transparent soil permeameter' that has been developed to study the mechanisms that occur during internal erosion in filter materials for embankment dams. The laboratory-based experiments utilise an optical approach where glass particles are used in place of soil, and optically matched oil is used in place of water. The refractive index matching of the fluid and solid enables a two-dimensional "slice" or plane of particles and fluid to be viewed inside the permeameter, away from its walls via a laser sheet and captured by digital camera. The developed set up has already been tested and showed that optically matched glass and oil can behave similarly to soil and water materials as used in previous laboratory testing. In this study we present a flow characterization within a refractive index matched medium made of glass beads. To this end a small amount of fluid tracers is seeded inside the fluid and the velocity field inside the porous media is obtained using PIV measurements.

Keywords: Internal erosion · Pore velocity · Laboratory tests
Seepage

1 Introduction

Seepage flow of groundwater in soil can affect the stability and the performance of large-scale civil engineering structures such as dikes and embankments dams, cut-off walls, levees. Suffusion is an instability phenomenon where fines material can be detached and eroded away within a porous media due to the hydrodynamic forces applied by the seeping water. Although suffusion is a process characterised as seepage-induced mass loss without change in volume, it can induce local regions of high permeability and high seepage velocity that can lead to the settlement and collapse of the structures once it develops in the process known as soffusion (Richard and Reddy 2007; Fannin and Slangen 2014).

The hydraulic conditions at the onset of suffusion have been widely investigated to improve the physical understanding of the process and to propose criteria to assess the instability potential for soils (Skempton and Brogan 1994; Kezdi 1979; Kenny and Lau 1985, 1986; Moffat and Fannin 2006; Li and Fannin 2008). A few experimental studies have been conducted to examine visually the movements of the fine particles during suffusion (Rosenbrand and Dijkstra 2012; Ouyang and Takahashi 2015; Hunter and Bowman 2017). Quantitative visualisation of the process allows both the structure of the soil sample and migration of the fines to be simultaneously observed and the

S. Bonelli et al. (Eds.): EWG-IE 2018, LNCE 17, pp. 91–97, 2019.
https://doi.org/10.1007/978-3-319-99423-9_9

relationship between the localised processes and the global behaviour of the specimen to be considered.

This paper describes preliminary tests performed within a rigid walled permeameter for measuring the flow field velocity occurring in granular media under upward flow, using an optical technique involving transparent media and image analysis of movements of fluid tracers diluted in the fluid.

2 Experimental Set Up and Optical Technique

The experimental set up uses a rigid wall permeameter already been tested in a previous research to study visually the processes during seepage-induced internal erosion in granular media (Hunter and Bowman 2017). The permeameter is a rectangular seepage cell (100 mm by 100 mm in plan area and 265 mm high). Five manometer ports are located at the back of the permeameter for local head measurements. A header tank above the apparatus is used to generate a flow upward through the sample (Fig. 1). The sample is arranged inside the box at the top of an underlying diffusing filter of coarse particles (4–5 cm thick) that ensure a uniform flow across the area of the sample. The specific sample to be tested is placed using a "slurry" placement method using a teaspoon (Hunter and Bowman 2017). To achieve optical access to the interior of the sample, the experiments use borosilicate glass particles in place of soil and a refractive-index-matched fluid (hydrocarbon oil) whose characteristics are described in Table 1. The resulting mixture of solid particles and fluid is completely transparent. Sanvitale and Bowman (2012) used fluid–particle scaling to determine that, for these materials, the particles need to be scaled up in size by $\sqrt{20}$ or approximately 4·4 times to counter the decrease in permeability due the oil viscosity being higher than that of the water.

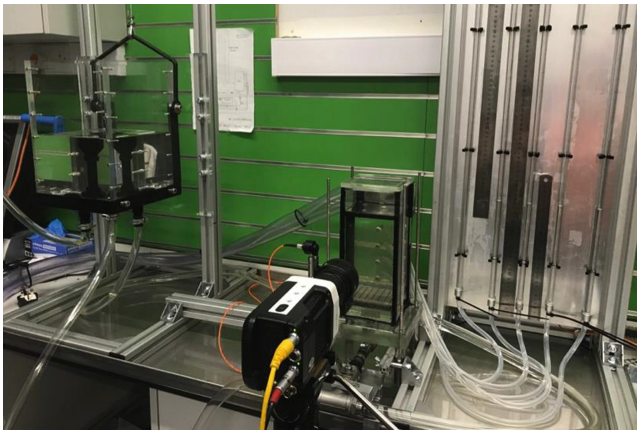

Fig. 1. Experimental set up

Table 1. Solid and fluid properties

	Refractive index	Kinematic viscosity (mm^2/s)	Density (g/cm^3)
Hydrocarbon oil	1.4715 (at 25 °C)	16 (at 25 °C)	0.846
Borosilicate glass	1.4718 (at 21 °C)		2.23

The original methodology of this experiment involved the use of a small quantity of fluorescing dye dissolved in the fluid to enable a technique known as Planar Laser Induced Fluorescence, (PLIF) to be applied. A 532 nm laser sheet illuminated a two-dimensional "slice" or plane to be viewed inside the permeameter, away from the side walls – whereupon particles appeared as black against the fluorescing fluid plane. Images were taken using a high speed-camera upon each increment in head being applied. These images allowed both the movements of the fine particles and the fabric rearrangement of the sample during the test to be analyzed by image analysis (Hunter and Bowman 2017).

In the current set up fluid tracers in place of fluorescent dye are diluted inside the fluid to enable local fluid velocities to be measured in the voids using particle image velocimetry (PIV). Those seeding particles are silver metal coated hollow glass microspheres with 5 μm–30 μm diameter and density of 0.75 g/cm^3, which is close to that of the oil. Seeding density is maintained at 5.5 mgl/1. The thickness of the laser plane for measurement is about 1.5 mm. For the preliminary experiments the tested sample is made of a random packing of borosilicate glass spheres with a diameter of 7.5 mm (Fig. 2). A Nikon AF Nikkor lens 85 mm is used with a 30 mm extension tube placed between the lens and the camera sensor to increase the lens magnification and to zoom over an area 38 mm × 24 mm upon which is possible to obtain detailed images of the pore throats. A high-speed camera, Phantom Miro 310, records images with spatial resolution of 1280 × 800 pixels at 200 frames/s.

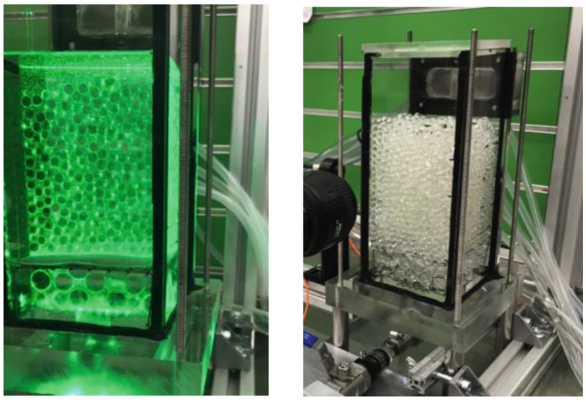

Fig. 2. Porous media before the tests on the right, illuminated 2D plane within the granular assembly on the left

3 Results

The experimental apparatus described in the previous section was used to measure the velocity field under two different hydraulic gradients, 0.16 and 0.11, respectively. The investigated granular system contains no fines and is not susceptible to any internal instability. However the test was performed in order to assess preliminarily the feasibility and the effectiveness of the proposed methodology to determine local fluid velocities in the voids.

The flow condition is investigated over an area just above the middle of the permeameter at a location between the third and fourth manometers ports, at a distance of 50 mm from the front sidewall. Figure 3 shows a raw image obtained with the high speed camera during tests. Velocity fields are obtained by image processing using the open source software PIVLab (Thielicke and Stamhuis 2014). First, an image mask is added to all images identifying the dark areas with beads and a high pass filter is applied to remove low-frequency background variations and enhance the image contrast of the tracers.

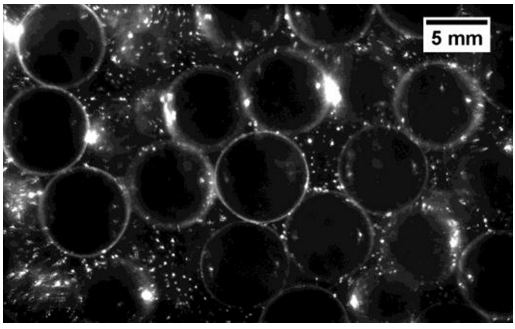

Fig. 3. Original image

Then the PIV analysis is carried out using a multi-pass approach to deform the interrogation areas in the second pass, based on the estimate obtained in the previous one. The image deformation technique implemented in the PIV analysis reduces the error associated with the correlation estimate by deforming the interrogation windows according to the local velocity gradient. The iterative process starts from interrogation areas of 64 pixels^2 with 50% overlap to the final size of 32 pixels^2.

Figure 4 shows the mean velocity field calculated over 60 frames for both the hydraulic gradient used during the test. As expected, increasing the hydraulic gradient increases the flow velocity through the pores. The flow intensity is not homogenous through the medium but becomes higher where the pores are interconnected through the existing space between grains in contact (see for instance the bottom left of the flow field in Fig. 3) and slows down in other areas, probably due to the presence of constrictions through the pore spaces.

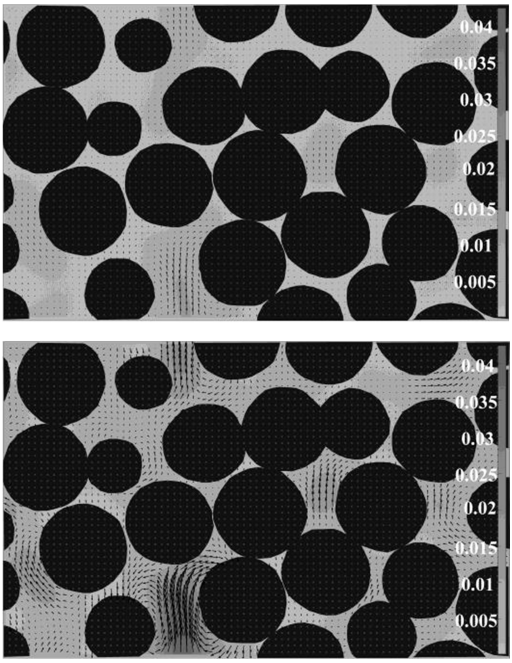

Fig. 4. Vector velocity field (arrows) and contour plot for the velocity magnitude (gray level scale map in m/s) for the flow under the hydraulic gradient of 0.11 on the top and 0.16 on the bottom.

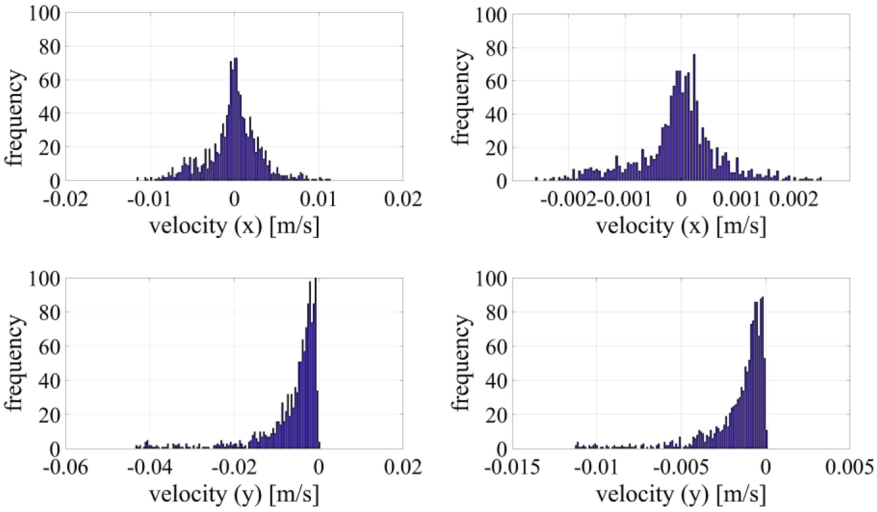

Fig. 5. Histograms of the x and y component of the velocities for hydraulic gradient equal to 0.16 on the left and 0.11 on the right.

Figure 5 shows the histogram of the velocities in horizontal and vertical directions throughout the whole field for both values of the hydraulic gradient. Both the x and y components of the velocity show increasing values with increasing the hydraulic gradient. The x component of the velocity is smaller than the y component and its distribution is mostly symmetric around 0 suggesting that the flux is globally upward. The vertical component shows a peak at small values but with a tail that spreads towards larger values confirming that greater vertical local velocity can occur inside the pore throats of the sample.

4 Conclusions

This work introduces the first experiments carried out using a rigid-walled permeameter for measuring fluid velocities field occurring in granular media under upward flows. Tests conducted with this apparatus use borosilicate glass particles and a refractive-index-matched fluid (hydrocarbon oil) to create a transparent mixture. The transparency of the medium enables a two-dimensional "slice" or plane of particles and fluid to be viewed inside the permeameter via a laser light sheet. This experimental apparatus has been already used in a previous research to study the particle movements and the rearrangement of particles during internal erosion tests in gap graded particulate systems. In the previous arrangement, a fluorescent dye was dissolved inside the oil in order to create a bright background where particles appear as black spots, allowing the movements of the fine material within the sample to be detected. In the presented study fluid tracers, instead of a dye, are diluted in the oil and illuminated by the laser. Using this set up the motion of the illuminated tracers within a sample section can be recorded by a high speed camera. PIV analysis of these images provides measurements of the internal local fluid velocities.

Preliminary tests conducted on a stable sample made of uniform beads confirm the feasibility of the apparatus and the materials for measuring the fluid flow field at the pore scale. From these results further work is going on towards the application of the same methodology using polydisperse granular specimens susceptible to suffusion.

References

Fannin RJ, Slangen P (2014) On the distinct phenomena of suffusion and suffosion. Géotech Lett 4(4):289–294. https://doi.org/10.1680/geolett.14.00051

Hunter RP, Bowman ET (2017) Visualisation of seepage-induced suffusion and suffosion within internally erodible granular media. Géotechnique. https://doi.org/10.1680/jgeot.17.P.161

Kenney TC, Lau D (1985) Internal stability of granular filters. Can Geotech J 22(2):215–225. https://doi.org/10.1139/t85-029

Kenney TC, Lau D (1986) Internal stability of granular filters: reply. Can Geotech J 23(3):420–423. https://doi.org/10.1139/t86-068

Kezdi A (1979) Soil physics. Elsevier, Amsterdam

Li M, Fannin RJ (2008) Comparison of two criteria for internal stability of granular soil. Can Geotech J 45(9):1303–1309. https://doi.org/10.1139/T08-046

Moffat R, Fannin R (2006) A large permeameter for study of internal stability in cohesionless soils. Geotech Test J 29(4):273–279. https://doi.org/10.1520/GTJ100021

Ouyang M, Takahashi A (2015) Optical quantification of suffosion in plane strain physical models. Géotech Lett 5(3):118–122. https://doi.org/10.1680/jgele.15.00038

Richards KS, Reddy KR (2007) Critical appraisal of piping phenomena in earth dams. Bull Eng Geol Environ 66(4):381–402. https://doi.org/10.1007/s10064-007-0095-0

Rosenbrand E, Dijkstra J (2012) Application of image subtraction data to quantify suffusion. Geotech Lett 2:37–41. https://doi.org/10.1680/geolett.12.00006

Sanvitale N, Bowman ET (2012) Internal imaging of saturated free surface flows. Int J Phys Model Geotech 12(4):129–142

Skempton AW, Brogan JM (1994) Experiments on piping in sandy gravels. Geotechnique 44 (3):449–460. https://doi.org/10.1680/geot

Thielicke W, Stamhuis EJ (2014) PIVlab – towards user-friendly, affordable and accurate digital particle image velocimetry in MATLAB. J Open Res Softw 2(1):e30. https://doi.org/10.5334/jors.bl

Effects of Void Ratio and Hydraulic Gradient on Permeability and Suffusion of Glacial Till Cores

Ingrid Silva[1(✉)], Peter Viklander[1,2], and Jan Laue[1]

[1] Luleå University of Technology, Luleå, Sweden
ingrid.silva@ltu.se
[2] Vattenfall Vattenkraft, Luleå, Sweden

Abstract. Dams with core of broadly graded glacial moraines (tills) exhibit signs of internal erosion by suffusion to a larger extent than dams constructed with other types of materials, as reported by Sherard (1979). Garner and Fannin (2010) indicated that internal erosion initiates when an unfavorable combination of soil material, stress conditions and hydraulic load occur. A laboratory program, carried out at Luleå University of Technology (LTU), aims to study the effects of void ratio and hydraulic gradient on the initiation of suffusion of glacial till. It consists of suffusion tests conducted in permeameters with an inner diameter 101.6 mm and a height of 115 mm. Results show, as expected, that the hydraulic conductivity is lower with lower void ratio. Nevertheless, as the hydraulic gradient increases, the hydraulic conductivity reaches steady values. Changes in the hydraulic conductivity suggest variation in the initial void ratio due to detachment of the finer particles from the soil matrix. These fine particles start clogging the lower layers, therefore the rate of water flow decreases and so does the hydraulic conductivity. The hydraulic gradient for which the hydraulic conductivity reaches steady values is considered as the upper limit without suffusion evolved.

Keywords: Internal erosion · Suffusion · Glacial till · Void ratio
Hydraulic gradient

1 Introduction

Suffusion, also called internal instability, is an internal erosion mechanism that occurs when fine-grained particles are transported through the soil matrix by seepage. Garner and Fannin (2010) indicated that internal erosion initiates when an unfavorable combination of soil material, stress conditions and hydraulic load occur; whilst continuation of internal erosion depends on the capability of the filter to retain the eroded fine graded particles. Sherard (1979) reported that dams with a core of broadly graded glacial moraines (glacial tills) exhibit signs of suffusion to a larger extent than dams constructed with other types of core materials.

Several researches on suffusion have analysed the influence of the grain size distribution on the initiation of internal erosion by suffusion, including Wan and Fell (2008), Moffat et al. (2011), Hunter et al. (2012), Correia dos Santos and Caldeira

S. Bonelli et al. (Eds.): EWG-IE 2018, LNCE 17, pp. 98–109, 2019.
https://doi.org/10.1007/978-3-319-99423-9_10

(2017), and Rönnqvist et al. (2017). Nevertheless, there is limited information regarding the effect of compaction degree on suffusion. Watabe et al. (2000) highlighted for tills that pore-size distribution and hydraulic conductivity are significantly influenced by compaction. In agreement with this, Leroueil et al. (2002) pointed out that in tills the hydraulic conductivity must not be considered as a soil characteristic but as a parameter that varies depending on the compaction conditions. However, Wan (2006) found that the 90% versus 95% compaction degree had little effect on suffusion to develop.

This paper presents an experimental study on the effects of void ratio and hydraulic gradient on the initiation of suffusion of glacial till material. The test apparatus is an adaptation of the cylinder used for Proctor compaction test, which is smaller than the one typically used by the researchers mentioned above.

2 Material and Method

2.1 Soil Sample and Test Program

The soil tested in this study is silt-sand gravel (glacial till) from northern Sweden herein named "DB_S" (material from Dam B, with stable gradation). The grain size distribution is shown in Fig. 1. The till is well graded, with coefficient of uniformity Cu = 50, clay content (less than 2 μm) 2.5% and maximum grain size 16 mm. The tested soil has a plasticity index Ip = 1, specific gravity Gs = 2.67, and maximum dry unit weight γ_d = 20.6 kN/m^3 for an optimum water content ω_{opt} = 6.5% according to modified Proctor test D-1557-91 (ASTM 1998). The soil is classified as internally stable according to the method proposed by Kenney and Lau (1985, 1986) and adapted by Li and Fannin (2008).

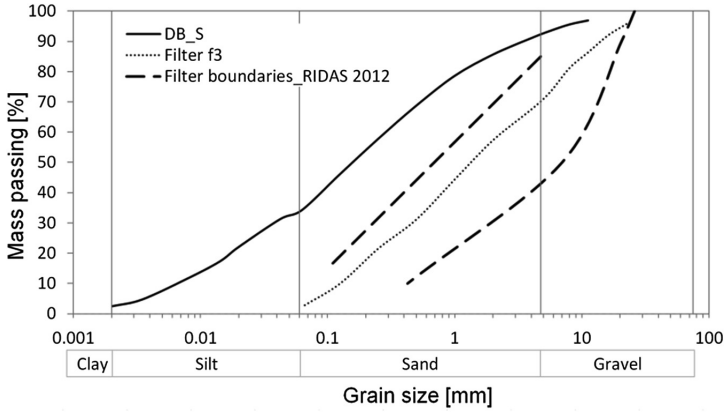

Fig. 1. Grain size distribution of the tested glacial till and filter material (f3)

The test program consists of two experimental series. The first series of tests aims to understand the potential effect of the filter on the measurement of the rate of water flow at different hydraulic gradients. The samples of this group were prepared with similar material and compaction conditions but different type of downstream filter. The types of filter used were: (i) polypropylene porous sheet (f1) 3.2 mm thick with maximum and minimum pore diameter of 75 μm and 17 μm, respectively; (ii) steel wire mesh (f2) with maximum and minimum aperture of 3 × 3 mm and 1.3 × 1.3 mm, respectively; and (iii) soil filter (f3), with gradation curve defined according to the filter criteria proposed by Svensk Energy (2012), D_{15F} = 0.18 mm and prepared with the same glacial till used for preparing the samples. D_{15F} is the particle size in filter for which 15% by weight of particles are smaller.

The second series of tests aims to evaluate the influence of void ratio on the initiation of suffusion at different hydraulic gradients. For the three type of filter considered (f1, f2 and f3), samples were prepared at three degree of compaction: 95% (e = 0.27), 90% (e = 0.28) and 85% (e = 0.29) of the maximum dry unit weight obtained with the modified Proctor test.

2.2 Testing System and Test Procedure

The test apparatus is an adaptation of the conventional cylinder used for Proctor compaction test, with inner diameter ϕ = 101.6 mm and height l = 115 mm, made of PMMA (polymethyl methacrylate, also known as acrylic glass). At the top and bottom cover transparent plastic pipes ϕ5 mm are connected as inlet/outlet. The inlet is connected to an upstream fixed reservoir, which is supplied with unfiltered municipal tap water. The outlet pipe is connected to a small container. The flow rate is estimated by the weight of water collected in the outlet container on a time increment.

The hydraulic gradient is changed by adjusting the vertical position of the permeameter. According to Wan and Fell (2008), the maximum hydraulic gradient expected in the core of a dam is around 8. In this study, hydraulic gradient varies between 2 and 20.

The tested samples were prepared at the optimum water content and compacted at the required dry density directly in the cylinder. The maximum grain size was limited to 10 mm, considering a minimum ratio of sample diameter and maximum particle size, D/Dmax, of 10.The samples are compacted in five layers of 23 mm thickness to the height 115 mm. For the samples f3, having a natural soil filter of 23 mm thickness, the height was 92 mm.

Upward incorporation of CO_2 (carbon dioxide) replaces the air content in the gaseous phase and contributes to a quicker saturation of the samples. The samples were saturated upward until a constant seepage rate measured at the top of the sample was reached. Once the samples get saturated, the suffusion tests with a downward flow started. The hydraulic gradient was increased stepwise. The initiation of suffusion is estimated based on: (i) visual observation of turbidity; and (ii) a significant and constant increment of flow rate through the sample.

Based on Darcy's law (Eq. 1), samples with a matrix of soil defined by its particle size distribution and void ratio, have a single hydraulic conductivity; therefore, it is expected that an increment of hydraulic gradient results in a proportional increment of

flow rate. However, when grains of the finer fraction migrate through interstices of the matrix formed by the coarser fraction, the increment of flow rate is significantly higher than the increment of hydraulic gradient, consequently increasing the hydraulic conductivity.

$$k = \frac{Q}{A \cdot i} \tag{1}$$

Where:
k = hydraulic conductivity [m/s]
Q = flow rate [ml/h]
A = area of cross section of the sample [m^2]
i = hydraulic gradient [−].

Changes in water pressure through the sample were not possible to measure. After the test was finished, the sample was examined layer by layer by gradation analysis. The fine-grained eroded particles retained in the container during the test were weighted. In most cases, the amount of eroded particles was very small or inexistent.

3 Results

3.1 Influence of the Type of Filter

Figure 2 shows the results of suffusion tests performed in samples prepared at the optimum water content and maximum dry density of the modified Proctor compaction test (ω_{opt} = 6.5% and γ_{dmax} = 20.6 kN/m^3, respectively). Results indicate that the hydraulic conductivity of the tested soil is in the order of 10^{-7} m/s for the filters studied. Filter f1 shows a constant decrease of hydraulic conductivity when increasing the hydraulic gradient. Filters f2 and f3 show an initial increase in hydraulic conductivity, but after additional higher hydraulic gradients the hydraulic conductivity starts decreasing.

Figures 3 and 4 show results for samples with filter f1 and f2, respectively, the changes in the flow rate, Q, with time due to increment of the hydraulic gradient, i. In both cases the behavior of the graph is irregular; however, it is possible to observe that the flow rate ranges around 60 ml/h for filter f1 and 100 ml/h for filter f2. Irregularities in the measurement may be due to air trapped in the system, affecting the flow rate; or mistakes in the collection of flow in the container. The peaks in the graphs may be due to a momentary increment of the seepage stress due to the increment of hydraulic gradient. The result of the sample with filter f3 is not presented in this paper, but is similar to filter f2 and has an average flow rate of 75 ml/h. Considering filter f1 as reference, the flow rate of filters f2 and f3 are 67 and 25% higher, respectively.

It is important to highlight that, in samples with filter f2 and f3, the flow rate initially increases when increasing the hydraulic gradient, but starts to decrease after the second increment of hydraulic gradient. Such behaviour suggests that, both filters f2 and f3, get clogged by the small particles washed out from the core until the seepage

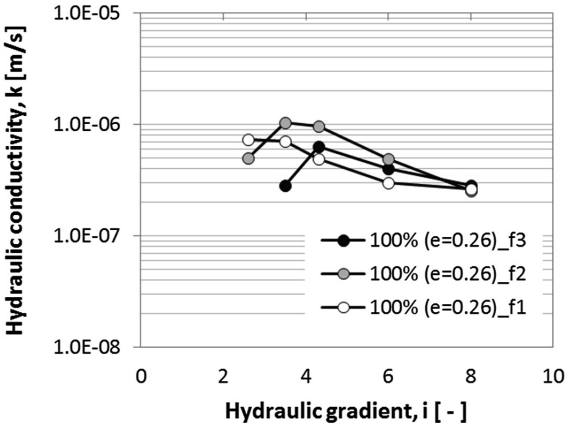

Fig. 2. Hydraulic conductivity versus hydraulic gradient for filters f1, f2 and f3 in samples at maximum dry unit weight (100% compaction (e = 0.26))

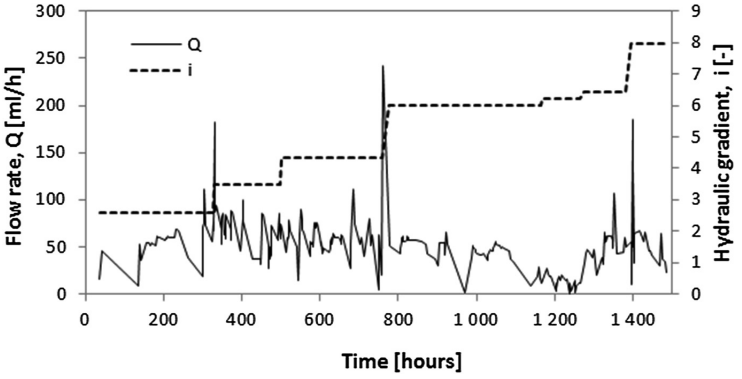

Fig. 3. Flow rate vs. hydraulic gradient by time for sample "100% (e = 0.26)_f1"

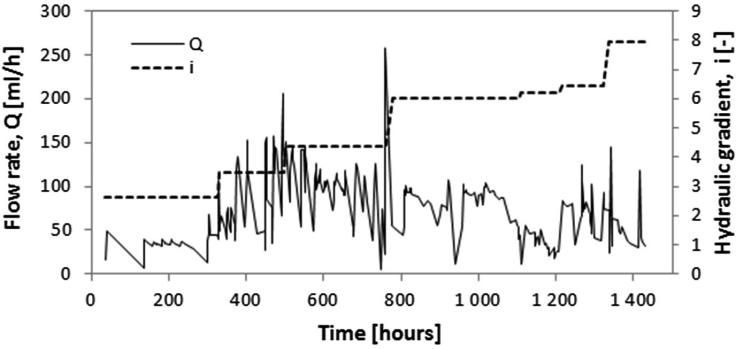

Fig. 4. Flow rate vs. hydraulic gradient by time for sample "100% (e = 0.26)_f2"

stresses reach equilibrium with the matrix of soil. In case of the sample with filter f3 "100% (e = 0.26)_f3", small amount of eroded particles of soil were observed in the outlet pipe which, based on its size, might proceed from the filter. Considering Darcy's law (Eq. 1), the initial increment of flow rate in the samples with filter f2 and f3 when raising the hydraulic gradient explains the initial increment of hydraulic conductivity showed in Fig. 2.

3.2 Influence of Void Ratio

In order to study the influence of the void ratio on the hydraulic conductivity, a second group of tests were performed for each type of filter. In case of filter f3, the set-up was improved by placing a sheet of filter f1 below the layer of filter f3; this in order to avoid segregation of the soil of filter f3 through the outlet, as happen to the sample "100% (e = 0.26)_f3" described in the previous section.

Figures 5 and 6 show for filters f1 and f2, respectively, the changes in the hydraulic conductivity with the increment of the hydraulic gradient in samples prepared at three different degree of compaction (95%, 90% and 85%). For both filters the hydraulic conductivity ranges between 1×10^{-7} and 1×10^{-6} m/s, which is in agreement with what is expected for glacial tills.

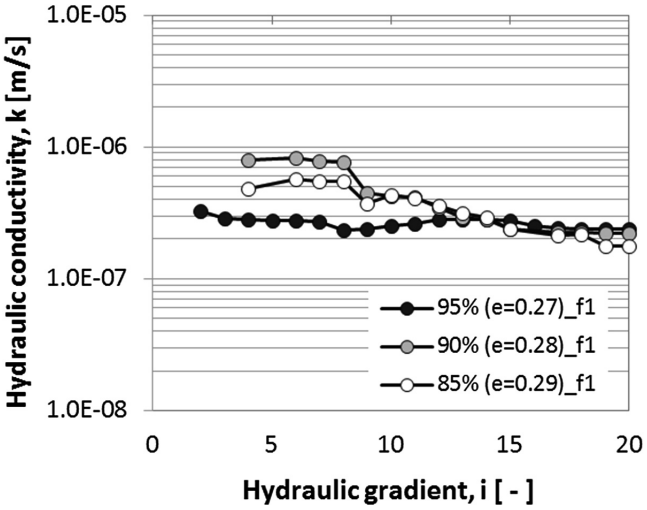

Fig. 5. Hydraulic conductivity vs. hydraulic gradient for different compaction degrees in samples with filter f1 (porous sheet)

In addition, for both type of filters the samples prepared at 95% of compaction show an approximately steady hydraulic conductivity even with hydraulic gradients up to 15 and 20, suggesting no or little suffusion. In case of the filter f1 the hydraulic conductivity decreases from 3×10^{-7} to 2×10^{-7} m/s; whilst for the filter f2 decrease from 6×10^{-7} to 4×10^{-7} m/s. This result is expected considering that the samples

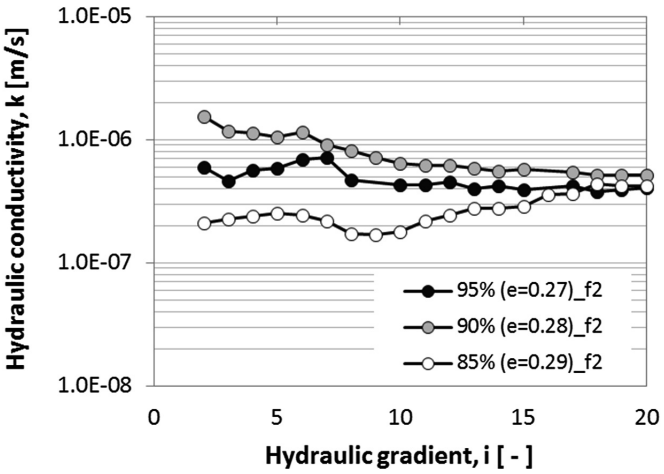

Fig. 6. Hydraulic conductivity vs. hydraulic gradient for different compaction degrees. Samples with filter f2 (wire mesh)

have a high degree of compaction and the soil is classified as internally stable, thus it is supposed to not experience significant changes in hydraulic conductivity. Comparing the results of filter f1 and f2, it is possible to say that the hydraulic conductivity measured with filter f1 is approximately half of the measured with filter f2.

It is also noted that, for both filter f1 and f2, the hydraulic conductivity of samples at 90% of compaction decreases when increasing the hydraulic gradient. With filter f1 the change is from 8×10^{-7} to 3×10^{-7} m/s, whilst for filter f2 from 1.5×10^{-6} to 5×10^{-7} m/s. For both type of filter, the rate of decrease of hydraulic conductivity is higher in samples at 90% compared to 95% of compaction. Nevertheless, for hydraulic gradient higher than 12, the hydraulic conductivity is approximately steady.

In case of samples prepared at 85% of compaction, the hydraulic conductivity also stay in order of 1×10^{-7} m/s. For the sample with filter f1, changes of the hydraulic conductivity are similar to the sample compacted at 90%. The sample tested with filter f2 presented different behavior in comparison to the others sample, in this case, the hydraulic conductivity tends to increase when increasing the hydraulic gradient above approximately 10. This behaviour suggests that the increment of flow rate is higher than the increment of hydraulic gradient, therefore the hydraulic conductivity increases according to Darcy's law (Eq. 1). Figure 7 shows that the increment of the flow rate in the sample "85% (e = 0.29)_f2" is higher when the hydraulic gradient is above 8. In addition, this sample presented a visible migration of fine particles through the outlet pipe, which is an indication of suffusion.

Regarding the samples tested with filter f3, Fig. 8 shows that the sample compacted at 95% has the lower average hydraulic conductivity of 6×10^{-8} m/s. The samples compacted at 90% and 85% have a hydraulic conductivity in the order of 2×10^{-7} m/s. All samples showed an approximately steady behaviour for hydraulic gradients above 8.

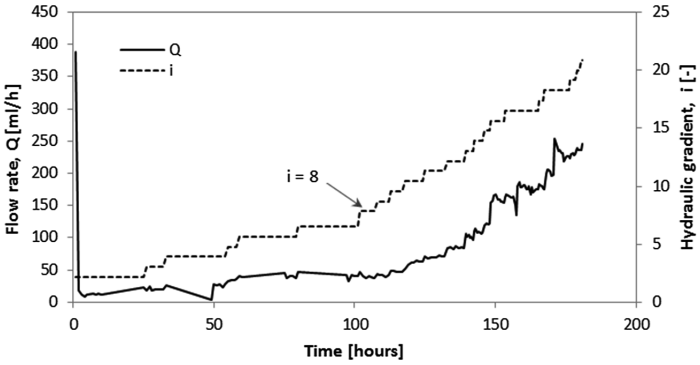

Fig. 7. Flow rate vs. hydraulic gradient in time for sample "85% (e = 0.29)_f2"

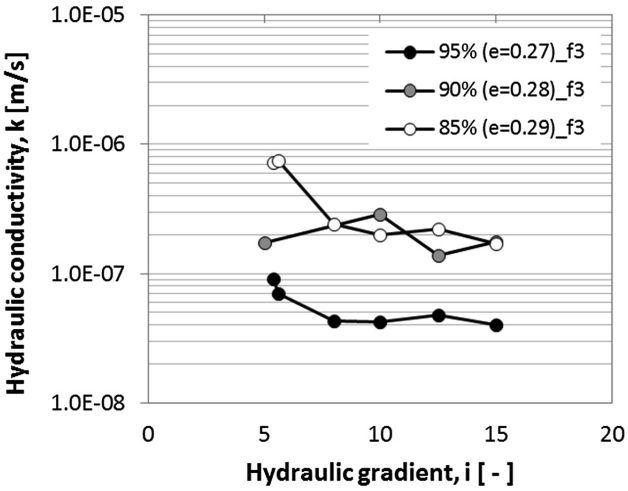

Fig. 8. Hydraulic conductivity vs. hydraulic gradient for different compaction degree in samples with filter f3 (soil filter)

Figure 9 summarizes the results obtained in this study. The hydraulic conductivity ranges between 5×10^{-8} and 1×10^{-6} m/s, with an average of 4×10^{-7} m/s. The hydraulic conductivity for each void ratio evaluated in each filter was calculated as the average of the hydraulic conductivity determined at different hydraulic gradient. In general, the measured hydraulic conductivity is higher for filter f2 (wire mesh), followed by filter f1 (porous sheet) and lastly by filter 3 (soil filter).

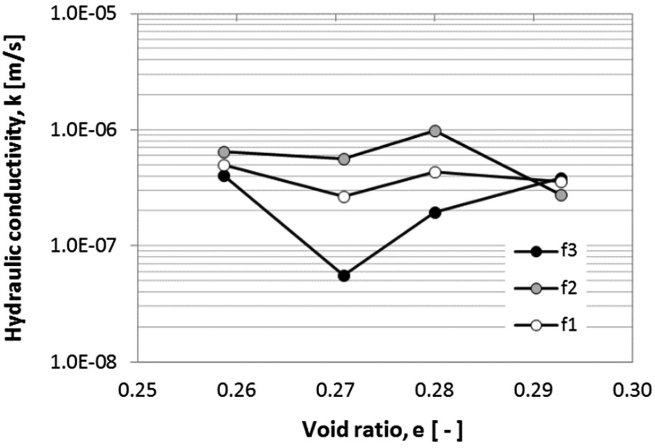

Fig. 9. Hydraulic conductivity vs. void ratio for filters f1, f2 and f3

4 Analysis of Results

Considering all the conditions tested: different compaction degree (85%, 90%, 95% and 100%), three type of filter (polypropylene membrane "f1", wire mesh "f2", and soil filter "f3"), and different hydraulic gradient (from 2 up to 20 in some tests), it was found that, for the grain size distribution of the tested soil, the hydraulic conductivity ranges between 4×10^{-8} and 1×10^{-6} m/s, with an average of 4×10^{-7} m/s (Fig. 9). These values are within the expected range for this type of soils according to literature, including Leroueil et al. (2002) who pointed out that hydraulic conductivity of tills may vary from 2×10^{-10} to 5×10^{-6} m/s.

Comparing the results obtained with different filters, samples with filter f1 shows more steady results when changing both the hydraulic gradient (Fig. 2) and the void ratio (Fig. 8), which suggests that filter f1 has less influence on the measurement. This result could be explained considering that clogging of filter f1 is less likely since the particles of soils smaller than its maximum pore diameter (0.075 mm) use to have high force of attraction, thus tend to attach together forming conglomerates bigger than the minimum pore diameter of the filter.

Comparing filter f2 and f3 to filter f1, Fig. 9 shows that the maximum difference in hydraulic conductivity is 24%; this excluding the outlier sample at 95% of compaction (e = 0.27) of filter f3, which has an average hydraulic conductivity of 5.6×10^{-8} m/s. The low hydraulic conductivity of the outlier sample could be due air trapped in the testing system.

Considering that results of the samples with filter f3 may be affected by the opening size of the bottom outlet, which is not sufficiently small to prevent movement of particles from the soil filter (f3), it is recommended to protect the sample from segregation by placing a porous sheet (f1) below the layer of soil of filter f3.

In most cases, the hydraulic conductivity has a tendency to decrease whilst increasing the hydraulic gradient. Based on Darcy's law (Eq. 1), such tendency

indicates that the rate of hydraulic gradient, Δi, is higher than the rate of flow, ΔQ. An exception is the sample tested with filter f2 at 85% of compaction degree. These results can be explained as follow:

(a) The velocity of flow through the soil matrix was high enough to move the loose fine soil particles through the constrictions between the larger soil particles.
(b) Since the tested soil is classified as internally stable, the movement of fine soil particles may be a consequence of the process where seepage stresses reach equilibrium with the matrix of soil. Thus, the amount of moved fine particles represents a small fraction of the fine content. This is consistent with what was visually observed during the tests.
(c) In case of samples with filters f1 and f3, part of the fine soil particles moving out from the core were retained by the filter. This clogging reduced the outlet flow rate and thus the hydraulic conductivity.
(d) Filter f2 has a bigger minimum opening size than filter f1 (1.3 mm versus 0.017 mm) and is not capable of self-healing as filter f3. Hence, the increment of the hydraulic gradient may contributes to the initiation and continuation of internal erosion by suffusion, increasing the flow rate thus the hydraulic conductivity. An example of this condition is the sample "85% (e = 0.26)_f2" (Figs. 6 and 7), which experienced a high increment of the flow rate for hydraulic gradient above 8. In this case, the poorly compacted conditions together with the seepage stresses generated by high hydraulic gradients initiated suffusion in the core, which continued due to the incapability of the filter to retain the fine graded particles washed out from the matrix of soil.

Finally, results show that, for samples compacted above 85% of the maximum dry unit weight, the compaction degree, which is associated to an initial void ratio, is a variable that has limited influence on the hydraulic conductivity of the internally stable till studied in this paper. This finding includes hydraulic gradients above 8 and up to 20, which, based on Cedergren (1989) and Wan and Fell (2008), is higher than would normally be expected in dams.

5 Conclusions

Based on the results presented in this paper, the following conclusions were reached for well graded glacial tills classified as internally stable:

– The hydraulic conductivity is little influenced by compaction degrees higher than 85% of the maximum dry unit weight. Therefore, the effect of such variable on the initiation of internal erosion by suffusion seems to be limitated.
– The hydraulic conductivity of samples prepared at a degree of compaction above 85%, is little influenced by the hydraulic gradient. Nevertheless, hydraulic gradients above 8 seems to generate seepage stresses high enough to move the loose fine soil particles through the constrictions between the larger soil particles.

– Regarding the experiment set-up, the type of filter used has little influence on the measurement of the hydraulic conductivity. Nevertheless, samples tested with porous sheet filter and soil filter provide more steady results than samples tested with filters made of wire mesh, especially in tests at low degree of compaction. In addition, the soil filter has the capability of retain the fine particles washed out from the core, what facilitates to quantify the amount of mass loss. This advantage makes the set-up with a layer of soil filter the optimum for suffusion test.

Acknowledgements. This study was supported by the Swedish Hydropower Centre – SVC, which is highly appreciated. Acknowledgment is also expressed to Luleå University of Technology for additional financial support and for providing the laboratory facilities for the work.

References

ASTM D1557 (1998) Laboratory compaction characteristics of soil using modified effort (56,000 ft-lbf/ft3 (2,700 kN-m/m3)). Philadelphia, USA

Correia dos Santos R, Caldeira L (2017). Erosion behaviour of gap-graded soils due to upward flow. In: Proceedings of 25th meeting of the European working group on internal erosion in embankment dams and their foundation, Delft, pp 58–68

Cedergren H (1989) Seepage, drainage and flow nets, 3rd edn. A Wiley-Interscience Publication, Hoboken, p 465

Garner SJ, Fannin RJ (2010) Understanding internal erosion: a decade of research following a sinkhole event. Int J Hydropower Dams Aqua-Media Int 17(3):93–98

Hunter G, Fell R, Topham C (2012) Backward erosion piping: what are the chances of that? In: Proceedings of Australian National Committee on Large Dams, Perth

Kenney TC, Lau D (1985) Internal instability of granular filters. Can Geotech J Natl Res Counc Can 22(2):215–225

Kenney TC, Lau D (1986) Internal instability of granular filters: reply. Can Geotech J Natl Res Counc Can 23(3):420–423

Leroueil S, Le Bihan J-P, Sebalhi S, Alicescu V (2002) Hydraulic conductivity of compacted tills from northern Quebec. Can Geotech J 39(5):1039–1049

Li M, Fannin RJ (2008) Comparison of two criteria for internal stability of granular soil. Can Geotech J 45(9):1303–1309

Moffat R, Fannin RJ, Garner S (2011) Spatial and temporal progression of internal erosion in cohesionless soil. Can Geotech J 48:399–412

Rönnqvist H, Viklander P, Knutsson S (2017) Experimental investigation of suffusion in dam core soils of glacial till. ASTM Geotechn Test J 40(3):426–439

Sherard JL (1979) Sinkholes in dams of coarse, broadly graded soils. In: Proceedings of the 13th ICOLD Congress, India, vol II, pp 25–35

Svensk Energi – Swedenergy AB (2012) Kraftföretagens riktlinjer för dammsäkerhet (RIDAS), Avsnitt 7.2 Fyllningsdammar Tillämpningsvägledning, in Swedish (Hydropower companies guidelines for dam safety, Section 7.2 Filling Dams Implementation Guidance), Stockholm, Sweden

Wan CF (2006) Experimental investigations of piping erosion and suffusion of soils in embankment dams and their foundations. Dissertation, University of New South Wales, Sydney, Australia

Wan CF, Fell R (2008) Assessing the potential of internal instability and suffusion in embankment dams and their foundations. J Geotech Environ Eng ASCE 134(3):401–407

Watabe Y, Leroueil S, Le Bihan J-P (2000) Influence of compaction conditions on pore-size distribution and saturated hydraulic conductivity of a glacial till. Can Geotech J 37(6):1184–1194

From Modelling to Design Criteria

Finite Element Analysis of Internal Erosion Effect on the Stability of Dikes

Abderrezak Bouziane[1(✉)], Ahmed Benamar[2], and Abdelkader Tahakourt[1]

[1] Université de Bejaia, Bejaia, Algeria
a.bouziane.doc@gmail.com
[2] Normandie Université, UNIHAVRE, CNRS, LOMC, 76600 Le Havre, France

Abstract. In the present study, a numerical solution is proposed in order to quantify the impact of internal erosion on dike stability. The mathematical model, consisting of erosion equations, mixture flow equations and stress equilibrium equations, is solved numerically by the finite element method using COMSOL Multiphysics. The shear strength reduction technique is used to analyze the stability of a dike taking into account the effect of internal erosion. The variation in time and space of porosity as a consequence of internal erosion is chosen as the coupling parameter. Soil stiffness and strength are made dependent on porosity, with the material becoming weaker as porosity increases. The results show that the porosity increases significantly at the dike toe, which was explained by an erosion of this zone. Erosion at the dike toe induces alterations in the mechanical response of the medium. Since the soil strength decreases at increasing porosity, the factor of safety of the downstream slope undergoes significant reduction. This study may help to better understand how internal erosion affects embankments performance, and to better prevent instability of hydraulic structures.

Keywords: Internal erosion · Slope stability · Factor of safety
Finite elements method

1 Introduction

According to Foster et al. (2000), Wan and Fell (2004) and Zhang et al. (2009), 46% of the damages observed on earthworks originate from internal erosion. Therefore, it is crucial to improve fundamental understanding of the triggering mechanisms related to the internal erosion processes. To study internal erosion of soils, various experimental studies have been proposed in the literature that rely mainly on the application of an inflow through the soil sample under a controlled hydraulic gradient and on the measurement of the amount of lost particles (Hadj-Hamou et al. 1991; Kenney and Lau 1986; Ouyang and Takahashi 2015; Sterpi 2003; Reddy and Richards 2012).

Numerical models of internal erosion are based on coupled hydromechanical analysis of the porous medium, where internal erosion of the soil skeleton and the transport of fine particles in the interstitial water are modeled by a mass exchange

S. Bonelli et al. (Eds.): EWG-IE 2018, LNCE 17, pp. 113–123, 2019.
https://doi.org/10.1007/978-3-319-99423-9_11

between the soil skeleton and interstitial water (Benamar and Seghir 2017; Chetti et al. 2016; Cividini and Gioda 2004; Govindaraju 1994).

Global instability can be tackled by the different methods reported by several researchers, namely: the limit equilibrium method (Duncan 1996), the finite element method (Matsui and San 1992) and the boundary element method (Jiang 1990). In the methods mentioned above, the stability of the slope is evaluated by the calculation of the safety factor (FOS) defined as the ratio of the resistance force to the driving force on the most critical potential sliding surface. However, in the practice slope stability is complicated by the presence of infiltration, erosion and head cutting caused by surface water. Infiltration, in particular, is often poorly represented in numerical models and its erosive power is completely neglected. It is therefore crucial to improve the models to account for accurate prediction of soil slope stability under infiltration conditions.

In this paper, we are interested in suffusion when suspended fines are diffusely transported through the solid matrix. This phenomenon is widely detected in both natural deposits and man made structures, and it is defined as the process by which fine particles in the soil gradually migrate through the voids between coarse particles, leaving behind the skeleton of the soil. In this study, we highlight the effect of internal erosion on the change in soil resistance and its effect on the global stability of a soil structure. We try to do this by relating the overall stability of the system to an internal parameter, which is porosity.

First, we present the mathematical model of the erosion kinetics, based on considerations of mass balance and particle transport. The differential equations used to model mass transfer in porous media are those proposed by Vardoulakis et al. (1996). In the Darcy's flow equations, permeability is made dependent on porosity. The processes of fluid flow and erosion coupled with mechanical damage are solved numerically by the finite element method using COMSOL Multiphysics. An analysis of the stability of a dike by the shear strength reduction method is discussed in the second part of the study in order to show the effect of suffusion on the stability of a slope.

2 Mathematical Model of Internal Erosion

2.1 Definition

The saturated porous media is modeled as a three-phase system consisting of skeletal solids (s), fluidized solids (fs) and fluid (f). Fluidized particles are suspended particles that move with the fluid. All other free particles that are trapped within the void space are considered part of the solid phase. In addition, it is assumed that fluid and fluidized particles share the same velocity at all times. Relative velocities to the soil skeleton are used. In other words, a solid particle has zero velocity when it is assigned to the solid phase, or it shares the fluid velocity when it is assigned to the mixture that fills the void space. The volume fraction of the voids is expressed by the total porosity.

2.2 Mass Balance Equations

According to Vardoulakis et al. (1996), the equilibrium equation of fluidized solid particles is expressed by

$$\frac{\partial(cn)}{\partial t} = q\nabla c + \frac{\partial n}{\partial t} \tag{1}$$

with

c = concentration of the fluidized solid.
n = porosity
q = volumetric discharge rate; with $q = n * v$, where v is the Darcy's velocity.

The evolution law for the porosity is given by

$$\frac{\partial n}{\partial t} = \lambda(1-n)cq \tag{2}$$

where λ is a coefficient related to the spatial frequency of the trigger points of erosion in the solid skeleton of the porous medium. Its dimension is the inverse of a length, $[\lambda] = L^{-1}$.

2.3 DARCY's Flow in the Porous Medium

Fluid flow can be described using the mass balance equation and Darcy's law

$$\frac{\partial n\rho_f}{\partial t} + \nabla.\rho_f u = 0 \tag{3}$$

$$u = -\frac{k}{\mu}\left(\nabla p + \rho_f g \nabla H\right) \tag{4}$$

where ρ_f is the water density (kg/m^3), t is the time (s), n is the porosity and u is the Darcy's velocity. Darcy's velocity depends on the absolute permeability $k(m^2)$, the dynamic viscosity of the fluid $\mu(Pa.s)$, the fluid pressure $p(Pa)$ and the gravity acceleration $g(m/s^2)$. The gradient of elevation $H(m)$ fixes the direction of the vertical coordinate, y.

Changes in porosity affect significantly the physical permeability k of the porous medium, e.g. according to the Carman-Kozeny:

$$k = k_0 \frac{n^3}{(1-n)^2} \tag{5}$$

3 Slope Stability Analysis

In turn, erosion causes the degradation of the porous medium by increasing the porosity and decreasing the resistance between the grains. Here, the degradation of the medium is described by a simple law of damage according to which a cohesion C is defined proportionally to the porosity (Gravanis et al. 2015).

$$C = \bar{C}\frac{1-n}{1-n_0} \tag{6}$$

Also according to Gravanis et al. (2015), we introduce a running Young modulus dependent on porosity and defined by

$$E = \bar{E}\frac{1-n}{1-n_0} \tag{7}$$

3.1 Strength Reduction Technique

The method used to evaluate the factor of safety has been referred to as the shear strength reduction technique (Matsui and San 1992). The factored shear strength parameters $\bar{C}$ and φ are divided by the factor of safety, *FOS*. Therefore, the reduced cohesion of the soil, C_r is given by

$$C_r = \frac{\bar{C}}{FOS} \tag{8}$$

and the reduced angle of internal friction φ_r is

$$\tan\varphi_r = \frac{\tan\varphi}{FOS} \tag{9}$$

here $\bar{C}$ and φ are the shear strength parameters.

4 Case Study

A dike whose geometry is shown in Fig. 1 is considered as an example of application. The soil constituting the dike is considered homogeneous.

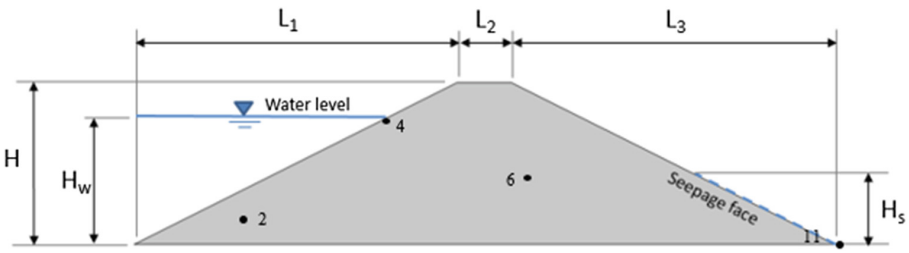

Fig. 1. Geometry of the dike

with

$$L1 = L3 = 24\,\text{m}, L2 = 5\,\text{m}, H = 12\,\text{m}, H_w = 10\,\text{m}, H_s = 4\,\text{m}.$$

Table 1. Input parameters of the calculation example

Parameter	Value
Initial porosity	$n = 0.4$
Initial concentration	$c_0 = 0$
Initial permeability (m^2)	$k_0 = 1.0228 \times 10^{-11}$
Dynamic viscosity (Pa·S)	$\mu = 0.001002$
Water density (kg/m^3)	$\rho_f = 1000$
Grains density (kg/m^3)	$\rho_s = 2700$
Initial young modulus (kN/m^2)	$\bar{E} = 10^5$
Initial cohesion (kPa)	$\bar{C} = 25$
Internal friction angle (deg)	$\varphi = 30$
Upstream pressure head (m)	$H_w = 10$

4.1 Parameters

The calculation results for the erosion and dike stability problem will be presented for the parameters listed in Table 1. Time $t = 0$ corresponds to the time at which the flow starts.

As far as global instability is concerned, the soil resistance parameters are calculated in the area of the potential sliding surface. An example of the evolution of strength along the potential sliding surface (point 6 in Fig. 1) and the corresponding factor of safety over time is presented at time intervals of 250 days is summarized in Table 2. At the end of each time interval the strength is evaluated, the stability analysis is carried out and the safety factor and the maximum displacement are determined. These results highlight that the effect of erosion on the stability of the analyzed earth structure is to reduce the factor of safety by about 16% (see Fig. 7).

Table 2. Variation of parameters over time due to internal erosion (point 6)

Time(day)	*C*(kPa)	*E*(MPa)	*FOS*	U_{max}(cm)
0	25	100	1.9	1.80
250	24.5	98	1.88	2.00
500	22	88	1.79	2.22
750	20	79.8	1.7	2.33
1000	18	75	1.6	2.5

5 Results and Discussion

In this section, we present the detailed results of the suffusion model in earthworks conducted with COMSOL Multiphysics. The soil is treated as an elasto-plastic Mohr-Coulomb solid subjected to seepage of a fluid governed by Darcy's law. The modeling was performed assuming the parameters presented in Table 1.

Takahashi (2007) argued that the type of failure essentially depends on dam permeability and material strength. In the case of very high permeability, failure is due to head cutting migrating upstream after toe erosion of the downstream face as can be seen in Fig. 2a which shows a loss of cohesion of the material, following the correspondent change in porosity (Fig. 2b). This latter mechanism is also observed by both laboratory experiments (Franca and Almeida 2002; Huang et al. 2007; Liao and Chou 2003; Wörman 1993) and field observations (Cruden et al. 1993; Leps 1973; Meyer et al. 1994; Wörman 1993). The surface flow that occurs on the dike downstream face, beneath the phreatic surface exit, is responsible for the removal of surficial layer grains and formation and migration of the head cutting erosion channel (Gregoretti et al. 2010).

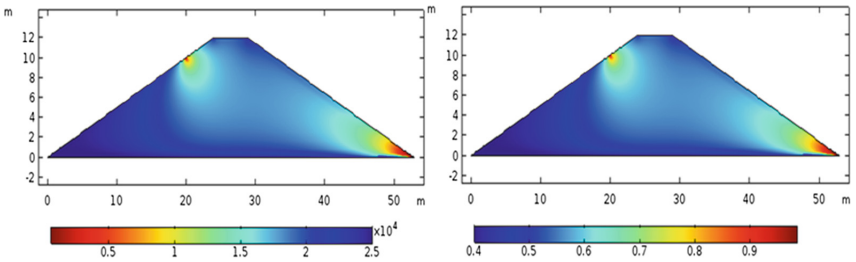

Fig. 2. (a) The spatial distribution of the cohesion at time t = 1000 d (b) The spatial distribution of the porosity at time t = 1000 d

In Fig. 3, results of porosity are plotted for the point (4) near the upstream and the point (11) near the downstream. These are the areas where the most significant increase in porosity is calculated. This increase is responsible of significant erosion, which reflects in significant loss of cohesion of the material in these areas, as shown in Fig. 4.

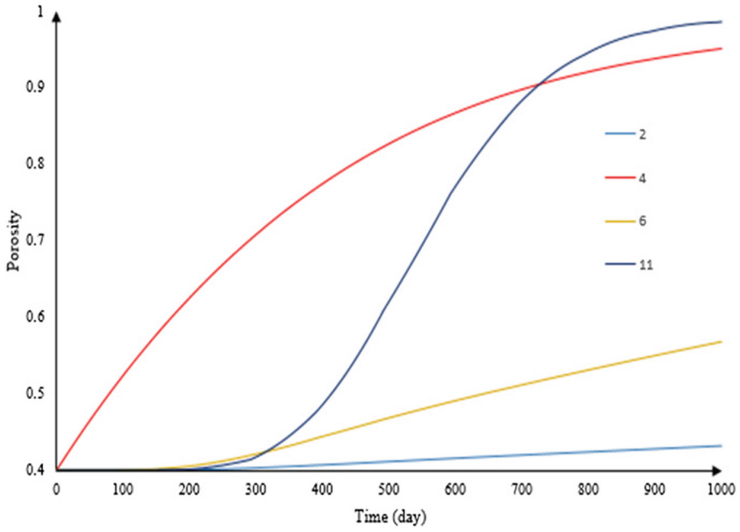

Fig. 3. Temporal variation of porosity at different locations on the dike

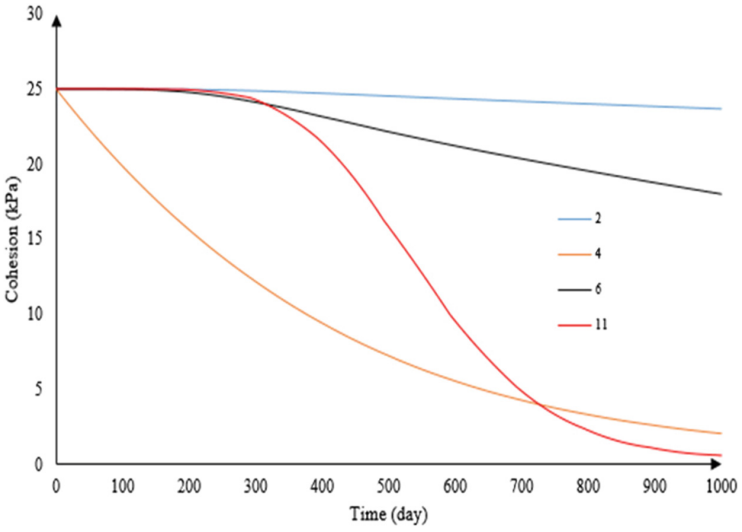

Fig. 4. Temporal variation of cohesion at different locations in the dike

The erosion of the dike toe explained by the high increase in porosity at this location as shown in Fig. 2b is in good agreement with the experience (Vandamme and Zou 2013; Stavropoulou et al. 1998; Chu-Agor et al. 2008).

Figure 5 shows the temporal variation of permeability at the dike toe and at the upstream face. It can be seen that the permeability increases significantly at the dike toe. Figure 6 shows the potential sliding surface at the final phase of the analysis, and

Fig. 7 gives the temporal variation of the safety factor, which decreases as a result of erosion.

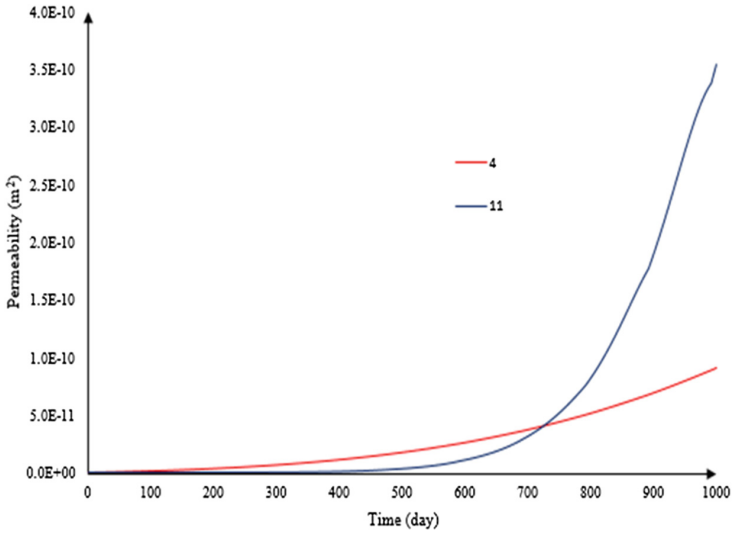

Fig. 5. Temporal variation of permeability at upstream and downstream

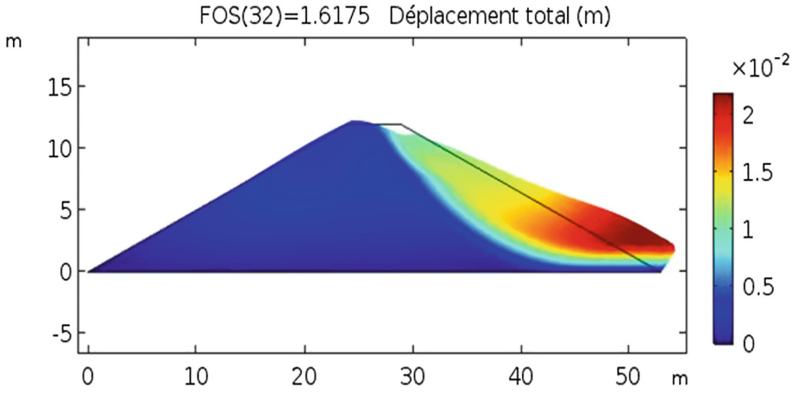

Fig. 6. Sliding surface at the final phase of erosion

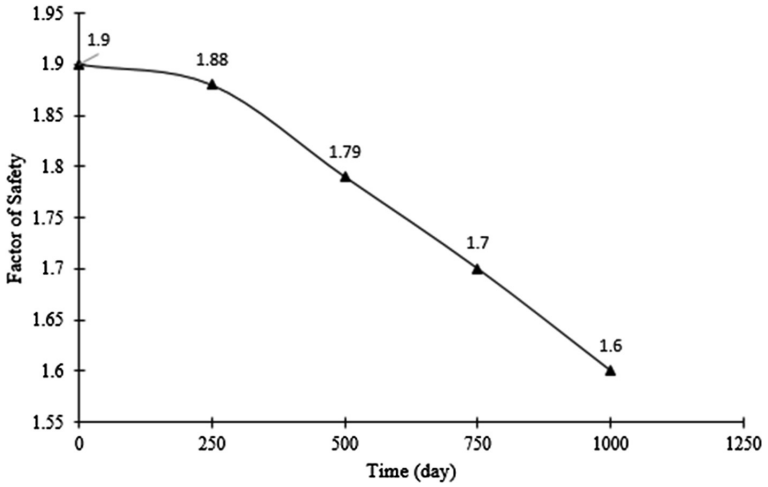

Fig. 7. Variation of the safety factor due to internal erosion

6 Conclusion

This article presents a study of the influence of internal erosion (suffusion) in a dike on its mechanical behavior. The variation in time and space of porosity, as internal erosion progresses, is chosen as the coupling parameter. We have considered that the soil stiffness and strength depend on porosity, so that the material becomes weaker as porosity increases. The mathematical model, composed of erosion equations, mixture flow equations and stress equilibrium equations is solved numerically by the finite element method. The analysis of the results made possible to draw the following conclusions:

- The erosion of the dike toe explained by the high increase in porosity at this location (water seepage zone) is in good agreement with the experience of (Vandamme and Zou 2013; Stavropoulou et al. 1998; Chu-Agor et al. 2008).
- Erosion near the free surface is accompanied by a significant increase in permeability.
- In addition, the increase in porosity results in a reduction of the cohesion between the grains and a reduction of the factor of safety.
- Erosion at the dike toe induces alterations in the mechanical behavior of the embankment. Since cohesion decreases with increasing porosity, the time at which collapse of the dike is likely to start may be identified.
- We found that erosion causes a significant reduction in slope stability and should be included in the modeling of this problem.
- Erosion at the toe of the downstream slope of the dike is captured by comparing initial and final cohesion. The total loss of cohesion leads to the loss of shear strength.

The results of the study indicate that experimental research would be needed to determine the erosion parameter (lambda), to validate the model and to better understand the different aspects of the problem, especially those related to changes in mechanical properties of soil subjected to erosion. In addition to variations in stiffness and shear strength, the influence of fines content on soil deformation and post erosion behavior could also be investigated.

References

Benamar A, Seghir A (2017) Physical and analytical modeling of internal erosion of fine particles in cohesionless soils. J Porous Media 20(3):205–216

Chetti A, Benamar A, Hazzab A (2016) Modeling of particle migration in porous media: application to soil suffusion. Transp Porous Media 113(3):591–606

Chu-Agor ML, Wilson GV, Fox GA (2008) Numerical modeling of bank instability by seepage erosion undercutting of layered streambanks. J Hydrol Eng 13(12):1133–1145

Cividini A, Gioda G (2004) Finite-element approach to the erosion and transport of fine particles in granular soils. Int J Geomech 4(September):191–198

Cruden DM, Keegan TR, Thomson S (1993) The landslide dam on the Saddle River near Rycroft, Alberta. Can Geotech J 30(25):1003–1015

Duncan JM (1996) State of the art: limit equilibrium and finite-element analysis of slopes. J Geotech Eng 122(7):577–596

Foster M, Fell R, Spannagle M (2000) The statistics of embankment dam failures and accidents. Can Geotech J 37(1992):1000–1024

Franca MJ, Almeida AB (2002) Experimental tests on rockfill dam breaching process. In: IAHR - international symposium on hydraulic and hydrological aspects of reliability and safety assessment of hydraulic structures

Govindaraju RS (1994) Non-dimensional analysis of a physically based rainfall-runoff-erosion model over steep slopes. Sed Geol 22(3–4):165–184

Gravanis E, Sarris E, Papanastasiou P (2015) Particle shape effect on macro-and micro behaviours of monodisperse ellipsoids. Int J Numer Anal Methods Geomech 32(March 2007):189–213

Gregoretti C, Maltauro A, Lanzoni S (2010) Laboratory experiments on the failure of coarse homogeneous sediment natural dams on a sloping bed. J Hydraul Eng 136(11):868–879

Hadj-Hamou T, Tavassoli MR, Sherman WC (1991) Laboratory testing of filters and slot sizes for relief wells. J Geotech Eng 116(9):1325–1346

Huang MYF, Capart H, Chen Rh, Huang AYL (2007) Experimental analysis of the seepage failure of a sand slope. In: Chen C, Major JJ (eds) Proceedings 4th International DFHM Conference. Millpress, Rotterdam

Jiang Y (1990) Slope analysis using boundary elements. Springer, New York

Kenney TC, Lau D (1986) Internal stability of granular filters. Can Geotech J 23(3):420–423

Leps, TM (1973) Flow through rockfill. In: Hirschfeld RC, Poulos SJ (eds) Embankment Dam Engineering. Wiley, New York, NY, 87–105

Liao WM, Chou HT (2003) Debris flows generated by seepage failure of landslide dams. In: Rickenmann D, Chen C (eds) Proceedings of 3rd International DFHM Conference. Millpress, Rotterdam, The Netherlands, pp 315–325

Matsui T, San KC (1992) Finite element slope stability analysis by shear strength reduction technique. Jpn Soc Soil Mech Found Eng 32(1):59–70

Meyer W, Schuster RL, Sabol MA (1994) Potential for seepage erosion of landslide dam. J Geotech Eng 120(7):1211–1229

Ouyang M, Takahashi A (2015) Influence of initial fines content on fabric of soils subjected to internal erosion. Can Geotech J 15(JANUARY):1–15

Reddy KR, Richards KS (2012) Experimental investigation of initiation of backward erosion piping in soils. Géotechnique 62(10):933–942

Stavropoulou M, Papanastasiou P, Vardoulakis I (1998) Coupled wellbore erosion and stability analysis. Int J Numer Anal Meth Geomech 22(9):749–769

Sterpi D (2003) Effects of the erosion and transport of fine particles due to seepage flow. Int J Geomech 4(September):191–198

Takahashi T (2007) A review of Japanese debris flow research. Int J Eros Control Eng 2(1):1–14

Vandamme J, Zou Q (2013) Investigation of slope instability induced by seepage and erosion by a particle method. Comput Geotech 48:9–20

Vardoulakis I, Stavropoulou M, Papanastasiou P (1996) Hydro-mechanical aspects of the sand production problem. Transp Porous Media 22(2):225–244

Wan CF, Fell R (2004) Experimental investigation of internal stability of soils in Embankment Dams and their foundation. UNICIV report; no. R-429, University of New South Wales, Sydney, Australia

Wörman A (1993) Seepage-induced mass wasting in coarse soil slope. J Hydraul Eng 119 (10):1155–1168

Zhang JY, Li Y, Xuan G X, et al (2009) Overtopping breaching of cohesive homogeneous earth dam with different cohesive strength. Sci China Ser E-Tech Sci 52(10):3024–3029. https://doi.org/10.1007/s11431-009-0275-1

A Numerical Procedure to Simulate Particle Migration at the Contact Between Different Materials in Earthfill Dams

Francesco Federico(✉) and Chiara Cesali

Department of Civil Engineering and Information Engineering,
University of Rome Tor Vergata, Rome, Italy
fdrfnc@gmail.com

Abstract. The control of the granulometric stability of a fine-grained material (*B*) requires a correctly designed protective granular material (*T*) whose voids, related to the grain size distribution (GSD) and porosity, must be small enough to stop the migrating particles of *B* within short distances (formation of "natural filter"), and simultaneously allow a safe drainage of *B* to prevent the occurrence of limit states (e.g. piping, clogging, blinding), inducing in turn uncontrolled increases of interstitial pressure. The available (empirical and analytical) methods to analyze particle migration phenomena at the contact between different materials generally don't considerer the coupled effects of the involved geometrical and hydraulic variables (e.g. GSD, porosity, volume voids distribution, permeability, piezometric gradients, seepage velocity), as well as their progressive space-time evolution. Thus, a numerical procedure allowing to simulate coupled 1D seepage and particle migration processes, by taking into account both geometrical and hydraulic governing variables, as well as their mutual dependency, has been developed and applied to carry out a detailed analysis and review of some experimental data.

Keywords: Internal erosion processes · Seepage · Numerical procedure
Review of experimental data

1 Introduction

The problems of granulometric stability related to particles migration (i) at the *contact* between materials characterized by different grain size curves (e.g. between core and downstream material, from embankment to foundation, Fig. 1a), (ii) within widely or gap graded soils (*suffusion*, Fig. 1b) are well recognized, as also shown by historical dams incidents (ICOLD 2013). For a complete simulation of these phenomena and their evolution towards possible granulometric limit conditions (*clogging*, *blinding, complete erosion*), the (space and time) variability of granulometric properties, voids volume, porosity (*n*), permeability (*k*), flow velocity, local piezometric gradients, flow direction, as well as the particles erodibility should be taken into account (Federico and Montanaro 2011). The variability of these variables, expecially of the voids volume distribution (*VVD*) and the related constriction size distribution (*CSD*), cannot be appropriately described through "*continuum*" equations (Federico 2017). Thus, a

S. Bonelli et al. (Eds.): EWG-IE 2018, LNCE 17, pp. 124–136, 2019.
https://doi.org/10.1007/978-3-319-99423-9_12

numerical procedure to simulate 1D coupled particle migration and seepage processes by considering the grain size curve, CSD, porosity of materials, rate of the suspension, piezometric gradients, drag forces associated with the seepage flow the friction triggered by normal contact forces induced by confining pressure related to the effective stress state, as well as their mutual dependency, has been developed. Validations of the proposed procedure according to laboratory measurements were carried out.

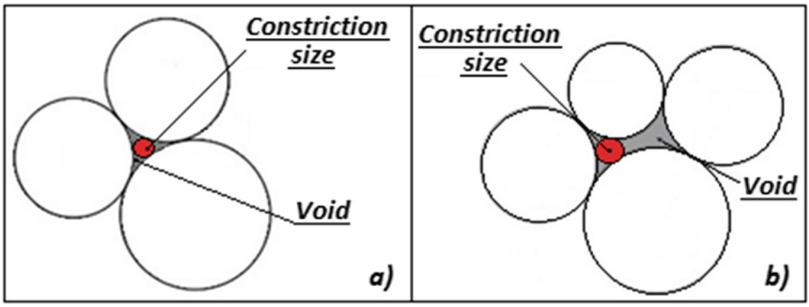

Fig. 1. Constriction size for pores formed by (a) three and (b) four particles.

2 Proposed Numerical Procedure

To model the particle migration processes and evaluate the safety of earth structures against serviceability or ultimate limit states, an advanced geometrical and hydraulic characterization of the granular material must be worked out.

Geometrical Characterization. To determine the distribution of the volume of voids (*VVD*) within porous media, several method are available in technical literature (Silveira 1965; Scheuermann et al. 2012). In the proposed procedure, the *'geometric-probabilistic'* model by Musso and Federico (1983) has been applied. Based on the concept that "*the most reliable distribution of the volume of voids within porous media corresponds to a situation of maximum "disorder" of the granular material (grains and voids)*", by maximizing the configurational entropy (E) associated with the distribution of the pore volumes V (Federico 2017):

$$E = \kappa' \int_{V_{min}}^{V_{max}} f(V) \cdot \ln[f(V)] dV \tag{1}$$

with $\kappa' = \kappa \cdot N_{vtot}$ (κ is a constant, N_{vtot} is the total number of pores equal to the total number of particles N_{ptot}), and V_{min}, V_{max} the minimum and maximum pore volumes, respectively, corresponding to the smallest (d_{min}) and largest (d_{max}) spherical particle diameters ($V_{min} = 0.16855 \cdot d_{min}^3$; $V_{max} = 0.16855 \cdot d_{max}^3$, if the pore of maximum volume is composed by three particles; $V_{max} = 0.476 \cdot d_{max}^3$, if the pore of maximum volume is composed by four particles), and applying the Lagrange's multipliers method, the following probability density function $f(V)$ of pore volumes is obtained:

$$f(V) = \frac{e^{-\beta V}}{\int_{V_{min}}^{V_{max}} e^{-\beta V} dV} \tag{2}$$

By introducing Eq. (2) in the "*compatibility*" equation: $\int_{V_{min}}^{V_{max}} V \cdot f(V) dV = \bar{V}$. The following relationship to determine the coefficient β is obtained:

$$[\beta \cdot (V_{min} - \bar{V}) + 1] \cdot e^{-\beta\, V_{min}} - [\beta \cdot (V_{max} - \bar{V}) + 1] \cdot e^{-\beta\, V_{max}} = 0 \tag{3}$$

Thus, β depends on the porosity n through the expected value $\bar{V}$ of the pores volume: $\bar{V} = \frac{n}{1-n} \cdot \sum_i \left(\Delta P_i / \sum_i \frac{6 \Delta P_i}{\pi \bar{d}_i^3} \right)$ (ΔP_i is the granulometric passing percentage associated with $\bar{d}_i = (d_{i+1} + d_i)/2$, with d_i the *i-th* granulometric fraction).

Through Eq. (2) it is possible to obtain the *cumulative probability function F(V)* ($= \int_{V_{min}}^{V} f(V) dV$) of the dimensions of voids (Musso and Federico 1983):

$$F(V) = \frac{e^{-\beta V} - e^{-\beta V_{min}}}{e^{-\beta V_{max}} - e^{-\beta V_{min}}} \tag{4}$$

For an assigned volume V of a pore, the volume of the largest particle (V_{cs}), able to move through the porous material, satisfies the relation $V_{cs} < V$. By assuming spherical particles (D, diameter), on the basis of geometric observations (Federico 2017), it is possible to determine the diameters of the smallest ($D_{cs,min}$) and largest ($D_{cs,max}$) particles passing through the smallest ($V_{cs,min}$) and largest ($V_{cs,max}$) pores; in other words, the mimimum and maximum constriction sizes (Fig. 1):

– for pores formed by *three spherical particles*

$$D_{cs,min} = 2 \cdot \left(3^{0.5}/3 - 1/2\right) \cdot D \rightarrow V_{cs,min} = 1.94 \cdot 10^{-3} \cdot D^3 \tag{5}$$

– for pores formed by *four spherical particles*

$$D_{cs,max} = \left(2^{0.5} - 1\right) \cdot D \rightarrow V_{cs,max} = 3.72 \cdot 10^{-2} \cdot D^3 \tag{6}$$

By defining the coefficient $\eta = V_{cs}/V$, it is obtained:

$$\eta_{min} = \frac{V_{cs,min}}{V_{min}} = 1.15 \cdot 10^{-2}; \tag{7}$$

$$\eta_{max} = \frac{V_{cs,max}}{V_{max}} = 7.81 \cdot 10^{-2} \tag{8}$$

Thus, the volume of constriction sizes (V_{cs}) and the corresponding diameter (D_{cs}) can be generally evaluated as:

$$V_{cs} = \eta(V) \cdot V \tag{9}$$

$$D_{cs} = \sqrt[3]{\frac{\eta(V) \cdot V \cdot 6}{\pi}} \tag{10}$$

The corresponding passing percentage P_{cs} is assumed equal to the passing percentage P_v (= $F(V)$) associated with related void (Fig. 2).

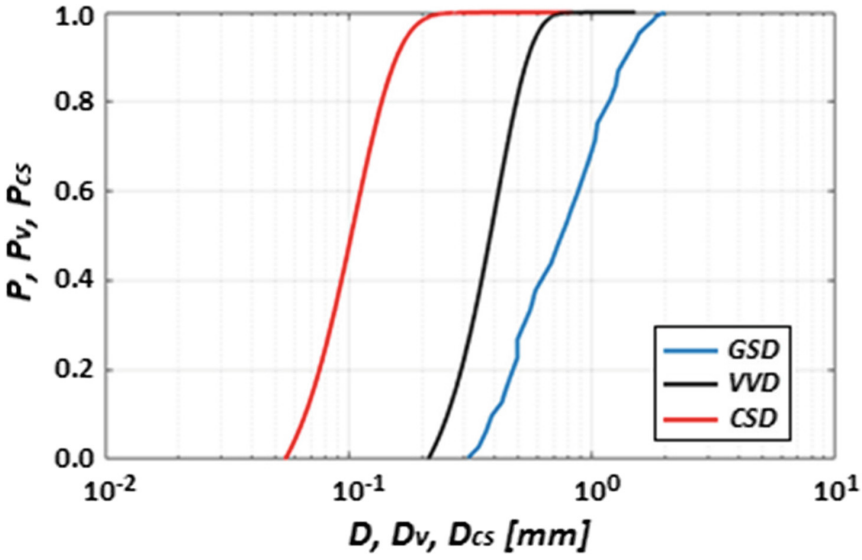

Fig. 2. Example of Volume void VVD (P_v; D_v) and Constriction size CSD (P_{cs}, D_{cs}) distributions, computed through the *'geometric-probabilistic'* method, for an assigned Grain size distribution GSD (P; D)

If a linear change of η with volume V is simply assumed, it is obtained:

$$\eta(V) = \frac{1}{V_{max} - V_{min}} \cdot [(\eta_{max} - \eta_{min}) \cdot V + (\eta_{min} V_{max} - \eta_{max} V_{min})] \tag{11}$$

Hydraulic Characterization. The permeability coefficient (k) represents the fundamental parameter on which the seepage velocity through a porous medium mainly depends. k can be evaluated through the Kozeny-Carman relationship (Kovács 1981), according to grain size properties and porosity, which may vary along space and time due to particles migration:

$$k = \chi \cdot \frac{\gamma_w}{\mu_w} \cdot \frac{n^3}{(1-n)^2} \cdot D_h^2 \tag{12}$$

D_h is the equivalent diameter of grains: $D_h = 1/\sum_i \frac{\Delta P_i}{d_i}$; χ is a numerical coefficient (Kozeny 1981); μ_w is the water viscosity. The soil particles can be scoured if subjected to a seepage velocity greater than a critical value (v_{cr}); the analysis of the actions on a movable particle and the dynamic equilibrium along the flow direction (Federico 2017) allow to estimate $v_{cr.}$ Particularly, two types of kinematics of particles can be distinguished (Fig. 3): *a)* frictional and rolling (unconfined particles, $D \leq D_{v,0}$); *b)* purely frictional (confined particles, $D \cong D_{v,0}$).

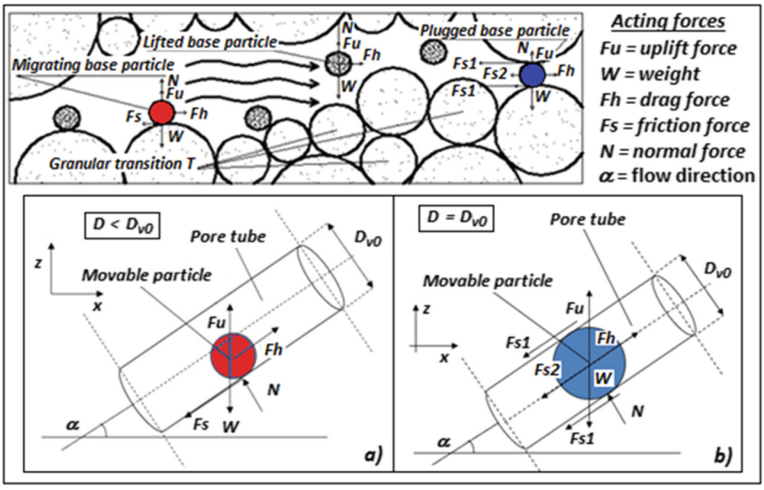

Fig. 3. Kinematics of movable particles: (a) frictional and rolling; (b) purely frictional

If the drag force F_h (Stokes law) overcomes the maximum local shear force related to the effective weight of the particle and the acting confining stresses (F_s) (Fig. 3), the particle can be eroded. By imposing $F_h = \sum_i F_{s,i}$, for a horizontal flow path under laminar flow conditions, the following general expression for v_{cr} is obtained:

$$v_{cr} = \frac{n}{3\mu_w} \cdot \left[(\gamma_s - \gamma_w) \frac{D^2}{6} + \frac{\lambda D}{2} (\sigma'_z + \sigma'_y) \right] \tan \varphi \tag{13}$$

λ is a coefficient allowing to consider the density of the granular matrix ($0 < \lambda \leq 4/\pi$); $\lambda = 4/\pi$ for granular matrix composed by spherical particles arranged in hexagonal configuration, most dense state (Silveira 1965, Kozeny 1981); γ_s is the volume unit weight of particles; γ_w is the volume unit weight of interstitial fluid; σ'_z is the effective stress along the direction z; σ'_y is the effective stress orthogonally acting to the plane x-z (Fig. 3); φ is the internal friction angle.

Problem's Setting and Governing Equations. Referring to a *B-T* system (*B* = fine grained material; *T* = transition granular material), the heterogeneous porous medium is decomposed into several elements (l_i = length of *i*th element; N = number of elements), each characterized by initial grain size curve ($D_{i,j,0}$; $P_{i,j,0}$), porosity $n_{i,0}$ and permeability $k_{i,0}$ (Fig. 4); i, j and t define the system element, materials granular fractions and the elapsed time, respectively (Federico 2017).

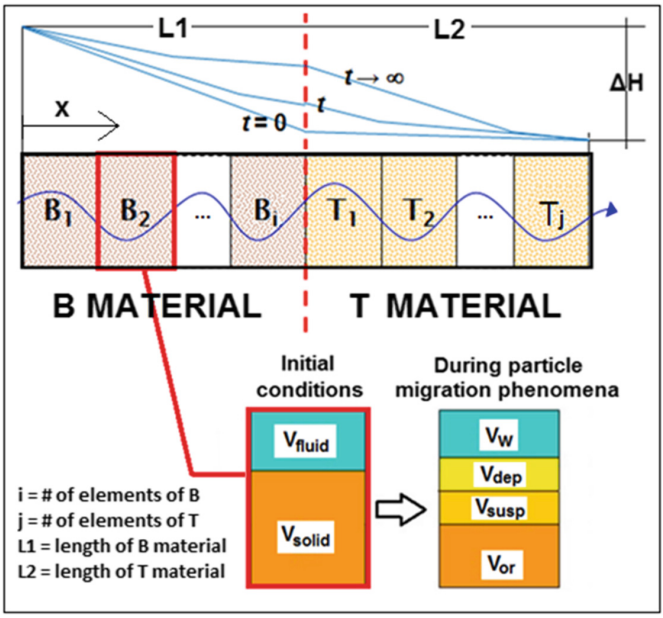

Fig. 4. Problem setting. One-dimensional unsteady seepage flow through a heterogeneous base (*B*) – transition (*T*) system; *B* and *T* are divided into elements; a constant hydraulic load ΔH is imposed.

Each element is schematically composed by original (not eroded) material ($V_{or,i,t}$), deposited/accumulated particles ($V_{dep,i,t}$) and particles in suspension ($V_{susp,i,t}$) due to migration phenomena, and water saturating the *i*th element ($V_{w,i,t}$).

The variables ($D_{i,j,t}$; $P_{i,j,t}$) and $n_{i,t}$ (and then $k_{i,t}$ according to Eq. 13) evolve because of erosion-deposition processes, associated with particle migration, causing an unsteady seepage flow.

The unsteady state is simply analyzed by considering a sequence of steady states (time interval, Δt; "successive steady states" method); for each Δt, the piezometric load for the *i*th element ($\Delta h_{i,t}$) and the corresponding seepage velocity ($v_{i,t} = k_{i,t} \cdot \Delta h_{i,t}/l_i$) are determined through the continuity equation expressed as follows:

$$\begin{bmatrix} \frac{k_{1,t}}{l_1} & -\frac{k_{2,t}}{l_2} & 0 & \cdots & \cdots & 0 \\ 0 & \frac{k_{2,t}}{l_2} & -\frac{k_{3,t}}{l_3} & 0 & \cdots & 0 \\ \vdots & \vdots & \vdots & \vdots & \vdots & \vdots \\ 0 & \cdots & \frac{k_{i,t}}{l_i} & -\frac{k_{i+1,t}}{l_{i+1}} & \cdots & 0 \\ \vdots & \vdots & \vdots & \vdots & \vdots & \vdots \\ 0 & \cdots & \cdots & 0 & \frac{k_{N-1,t}}{l_{N-1}} & -\frac{k_{N,t}}{l_N} \\ 1 & 1 & \cdots & \cdots & \cdots & 1 \end{bmatrix} \cdot \begin{pmatrix} \Delta h_{1,t} \\ \Delta h_{1,t} \\ \vdots \\ \Delta h_{2,t} \\ \vdots \\ \Delta h_{N,t} \end{pmatrix} = \begin{pmatrix} 0 \\ 0 \\ \vdots \\ 0 \\ \vdots \\ \Delta H \end{pmatrix} \tag{14}$$

being DH the hydraulic load imposed to the system. Therefore, the suspension rate Q through the elements of the section Ω, and the volume of the suspension $V_{m,t}$, composed by the scoured particles dragged by the seeping fluid, entered and washed out from each element, is the same during each Δt:

$$Q = \Omega \cdot k_{i,t} \cdot \frac{\Delta h_{i,t}}{l_i}; \quad V_{m,t} = Q \cdot \Delta t \tag{15}$$

So, the total volume of each element (V_i), generally composed of the original (not eroded) material ($V_{or,i,t}$), accumulated/deposited material ($V_{dep,i,t}$), material in suspension ($V_{susp,i,t}$) and water saturating the i^{th} element ($V_{w,i,t}$), doesn't vary during Δt ($V_i = V_{or,i,t} + V_{dep,i,t} + V_{susp,i,t} + V_{w,i,t}$ = constant).

To determine the eroded or erodible particles, the hydraulic and geometrical compatibility conditions must be verified. Particularly, the hydraulic compatibility conditions consist in comparing the previous defined critical velocity $v_{cr,i,j,t}$ of the j^{th} granulometric fraction, within the i^{th} element at the instant t, with the effective seepage velocity ($v_{i,t}/n_{i,t}$). Unconfined and confined particles are distinguished according to average diameter of voids $D_{v,0,i,t}$, defined as (Indraratna and Vafai 1997): $D_{v,0,i,t} = 2.67 \cdot n_{i,t} \cdot D_{h,i,t}/(1 - n_{i,t})$: particularly, *unconfined* if $D_{i,j,t} < D_{v,0,i,t}$; *confined* if $D_{i,j,t} \geq D_{v,0,i,t}$.

The geometrical compatibility conditions concern the comparison between the diameter of the j^{th} granulometric fraction ($D_{i,j,t}$) belonging to the i^{th} element with the constriction sizes of the $(i + 1)^{th}$ element and the evaluation of the probability of one *forward step*, $P_{F,i,j,t}$ (Locke et al. 2001). For each $D_{i,j,t}$, the percentage $P_{cs,i,j,t}$ of smaller constriction sizes of the $(i + 1)^{th}$ element is defined (Fig. 5). If $D_{i,j,t} < \min(D_{cs,i\ +\ 1,j,t}; j)$ (smaller diameter of constriction sizes of the $(i + 1)^{th}$ element), $P_{F,i,j,t} = 1$; if $D_{i,j,t} > \max(D_{cs,i\ +\ 1,j,t}; j)$ (larger diameter of constriction sizes of the $(i + 1)^{th}$ element), $P_{F,i,j,t} = 0$; if $\min(D_{cs,i\ +\ 1,j,t}; j) < D_{i,j,t} < \max(D_{cs,i\ +\ 1,j,t}, j)$, $P_{F,i,j,t}$ ($\in (0,1)$) is expressed as follows:

$$P_{F,i,j,t} = P_{cs,i,j,t} + \sum_{w=0}^{3} [1 - (1 - P_{cs,i,j,t})^4] \cdot (1 - P_{cs,i,j,t}) \cdot P_{cs,i,j,t} \cdot \left\{ \left[1 - (1 - P_{cs,i,j,t})^3 \right] \cdot (1 - P_{cs,i,j,t}) \right\}^w \tag{16}$$

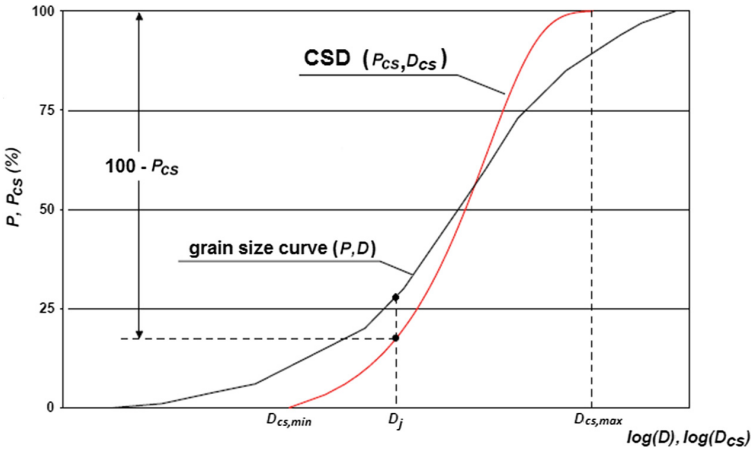

Fig. 5. Geometrical compatibility: comparison between particles (D_j) and CSD

$P_{F,i,j,t} \in (0,1)$ means that not all particles belonging to the j^{th} granulometric fraction can be eroded and then pass through the pores network up to the $(i+1)^{th}$ element; although erodible, the amount $(1 - P_{F,i,j,t})$ is trapped in the pores network and can remain in suspension or deposit (Locke et al. 2001).

Definitively, the particles with $v_{cr,i,j,t} < v_{i,t}/n_{i,t}$ (hydraulic condition) and $P_{F,i,j,t} > 0$ (geometrical condition) simultaneously, are therefore scoured.

For each eroded particle, the migration path ($L_{mig,i,,j,t}$) is determined. $L_{mig,i,,j,t}$ depends on the number ($m_{i,j,t}$) of constrictions greater than the particle ($D_{i,j,t}$), along its path, before its arrest (Musso and Federico 1983). The length of the migration path is compared to the length that the particles can cross during each step Δt; particularly, $L_{mig,i,,j,t} = \min\left(s \cdot m_{i,j,t}; v_{i,t} \cdot \Delta t\right)$, s being the unit step (average migration path for each constriction). Therefore, $V_{susp,i,t}$ is composed by particles eroded from the $(i-1)^{th}$ element ($V_{acc,in}$), particles of the i^{th} element with $P_{F,i,j,t} \in (0,1)$, V_{acc} (i.e. potentially erodible, but trapped in the pores network). All these particles can deposit; then: $V_{susp,i,t} = V_{acc,i,t} + V_{acc,in,i,t} - V_{dep,i,t-1}$. The deposited particles are determined according to the probability $P_{dep,i,j,t}$ (Reddi et al. 2000):

$$P_{dep,i,j,t} = 4\left[\left(\frac{\theta_{i,t} \cdot D_{i,j,t}}{D_{v,0,i,t}}\right)^2 - \left(\frac{\theta_{i,t} \cdot D_{i,j,t}}{D_{v,0,i,t}}\right)^3\right] + \left(\frac{\theta_{i,t} \cdot D_{i,j,t}}{D_{v,0,i,t}}\right)^4 \tag{17}$$

being $\theta_{i,t} = \theta_0 \cdot e^{-\left[\left(v_{i,t}/n_{i,t}\right)/v_{clogg}\right]}$, with θ_0 and v_{clogg} experimental coefficients.

Once re-defined $V_{or,i,t}$ (reduced by eroded particles), $V_{dep,i,t}$ and $V_{susp,i,t}$, it is possible to determined $V_{w,i,t}$ (V_i = constant); therefore, for each element the porosity $n_{i,t}$ (and then the permeability $k_{i,t}$) and the GSD ($D_{i,j,t}$; $P_{i,j,t}$) can be updated.

Thus, the main outputs provided by the proposed procedure at each time step are: grain size distributions, porosity, permeability, eroded and deposited particles volumes, discharge rate and seepage flow velocity.

3 Analyses of Experimental Results

The interpretation of some experimental results reported in technical literature (Indraratna and Vafai 1997; Ming and Shwiyhat 2012) was carried out through the proposed numerical procedure.

3.1 Indraratna and Vafai (1997)

The test aims to observe and evaluate the effects of a downward seepage flow through a *Base (B)* - *Transition (T)* system triggered from a hydraulic load $\Delta H = 1$ m. The experimental apparatus consists of a permeameter composed by two transparent vertical cylinders (15 cm diameter, 30 cm total height), equipped with instrumented points for measuring the piezometric load (Fig. 6).

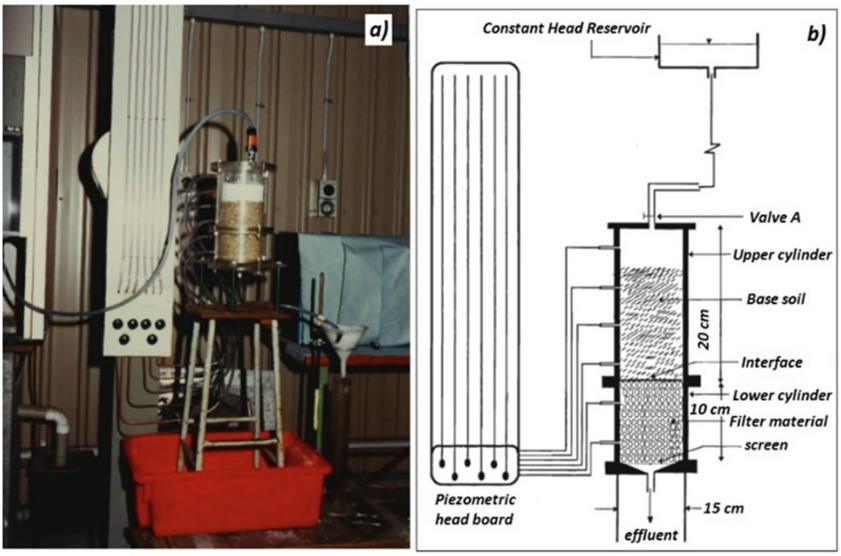

Fig. 6. (a) Test instruments; (b) Schematization of experimental apparatus

Below the lower cylinder, a screen with openings such as to reduce the washout of finer granulometric fractions is installed. The tested base (*B*) material is a silicate, without cohesion, characterized by uniformity coefficient $CU = 3.3$, porosity $n = 0.20$, permeability $k = 1.51 \cdot 10^{-6}$ m/s and thickness $L_1 = 10$ cm. The granular transition is a clean sand, consisting of rounded grains, CU = 3.1, $n = 0.28$, $k = 6 \cdot 10^{-5}$ m/s and thickness $L_2 = 10$ cm. The corresponding GSDs of the tested materials are shown in Fig. 7a. The duration of simulation is 6 h.

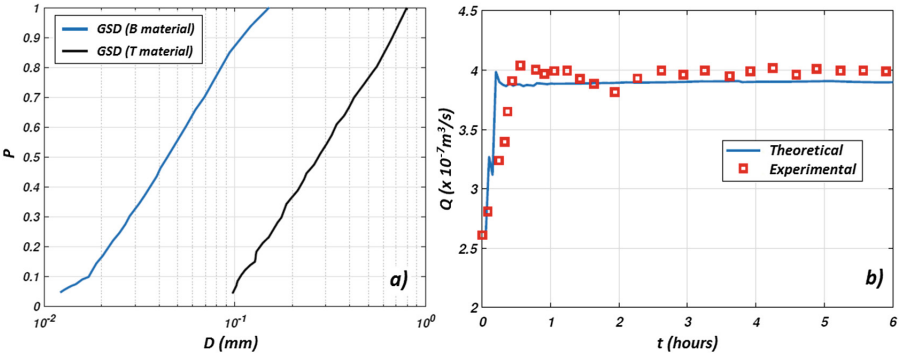

Fig. 7. (a) GSDs of the tested materials; (b) *Q vs t*: theoretical and experimental results

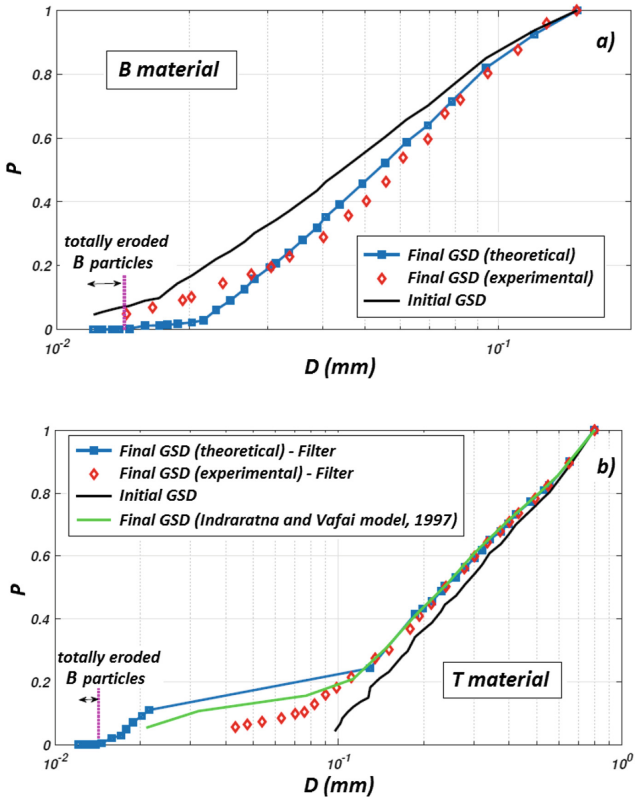

Fig. 8. Initial and final GSDs at the *B-T* interface: experimental vs theoretical results for (a) B material, (b) T material

Numerical modelling. The two materials are divided into 4 elements, each with a thickness of 25 mm. A constant hydraulic load $\Delta H = 1$ m is applied. To simulate the presence of the "screen" (of which the specifics that are not known) at the base of the apparatus, an auxiliary material affected by the same properties of the B material is placed downstream the considered B-T system (8 + 1 elements). As initial conditions, $V_{susp,i,t} = 0$; $V_{dep,i,t} = 0$, for each i-th element of the system ("clear" materials).The theoretical results in terms of discharge rate (Q) are shown in Fig. 7b.

The theoretical results agree with the experimental data; in particular, the discharge rate increases from the initial value of $2.6 \cdot 10^{-7}$ m^3/s to the value $4 \cdot 10^{-7}$ m^3/s, approximately; this increase is due to a modest erosion of B material, as the changes in GSD of the base material at the *B-T* interface show (Fig. 8a). The seepage flow reaches a steady state regime after about 1 h, indicating the reduction of the erosion phenomena and the formation of "filter" (Fig. 8b) at the *B-T* interface.

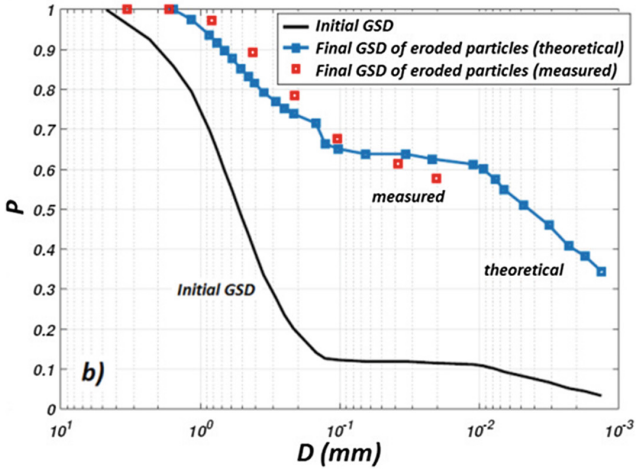

Fig. 9. (a) Lab apparatus; (b) GSDs of measured and theoretical eroded particles

The theoretical GSDs approximate the experimental ones, especially for *B* material. For *T* material, the differences between the theoretical and measured results, particularly for the finer granulometric fractions, are mainly due to the lab instruments for grain size analyses, unable to detect the finer B particles (Fig. 8b). To this purpose, the final GSD numerically obtained by Indraratna and Vafai (1997) is also shown; the agreement between the two theoretical GSDs is observed.

Numerical modelling. In this case, the system was not divided in two materials (B-T); a single material was modelled. It was divided in 3 elements (thickness of single element = 3.4 cm) and a hydraulic load of 2.07 m (deduced from the provided hydraulic gradient) was assumed. To model the presence of the basal screen, a uniform CSD with openings of 4.75 mm (reduced to 0.15 mm during the simulation to take into account the progressive clogging) at the end of system was considered. A simulation of 30 min was carried out. The theoretical results in terms of GSD of the eroded particle, collected at the base of the experimental apparatus, agree with the measured data (Fig. 9b). As previously imposed, the initial conditions $V_{susp,i,t} = 0$; $V_{dep,i,t} = 0$, for each i-th element of the system have been applied.

4 Concluding Remarks

A numerical procedure to simulate the particle migration phenomena in granular media due to seepage flows has been developed.

The procedure takes into account voids, constriction sizes and porosities of the particulate materials (geometric-probabilistic model) as well as the rate of the seeping suspension and piezometric gradients.

The progressive variations (in the space, 1D, and along time, *t*) of the physical (porosity *n*) and hydraulic (permeability *k*) properties of the granular medium, during the coupled seepage flow, deposition and scouring particles processes, are simulated. Validations of the proposed method has been carried out by simulating selected experimental tests, referred to *B (base material) – T (granular transition)* systems and materials susceptible of suffusion.

References

Federico F (2017) Particle migration phenomena related to hydromechanical effects at contact between different materials in embankment dams. GRANULAR MATERIALS, ISBN 978-953-51-5423-5, Book edited by: Michael G. Sakellariou, NTUA Greece

Federico F, Montanaro A (2011) Granulometric stability of moraine embankment dam materials. Theoretical procedure and back-analysys of cases. In: 6th international conference on dam engineering, Lisbon, Portugal

ICOLD (2013) Internal erosion of existing dams, levees and dikes, and their foundations. Bulletin n.164, Vol. 1: "Internal erosion processes and engineering assessment"

Indraratna B, Vafai F (1997) Analytical model for particle migration within base soil-filter system. J Geotech Geoenviron Eng 123:100–109

Kovács G (1981) Seepage hydraulics. Elsevier Scientific Publishing Company, New York City, p 6519. ISBN 9780080870014

Locke M, Indraratna B, Adikari G (2001) Time-dependent particle transport through granular filters. J Geotechn Geoenviron Eng 127:521–529

Xiao M, Shwiyhat N (2012) Experimental investigation of the effects of suffusion on physical and geomechanic characteristics of sandy soils. Geotech Test J **35**(6), 890–900. https://doi.org/10.1520/GTJ104594. ISSN 0149-6115

Musso A, Federico F (1983) Geometrical probabilistic approach to the design of filters. Italian Geotechn J XVII(4):173–193

Reddi LN, Ming X, Hajra MG, Lee IM (2000) Permeability reduction of soil filters due to physical clogging. J Geotech Geoenviron Eng 126:236–246

Scheuermann A, Williams DJ, To HD (2012) A new simple model for the determination of the pore constriction size distribution. In: 6th international conference on scour and erosion (ICSE-6), Société Hydrotechnique de France, pp 295–303

Silveira A (1965). An analysis of the problem of washing through in protective filters. In: 6th international conference on "soil mechanics and foundation engineering", ICSMFE, Montréal, vol 2, pp 551–555

Reliability Underseepage Assessment of Levees Incorporating Geomorphic Features

Lourdes Polanco-Boulware[1] and John Rice[2(✉)]

[1] Dewbury, Fairfax, VA, USA
[2] Utah State University, Logan, UT, USA
john.rice@usu.edu

Abstract. Levee foundations along meandering rivers are often modeled in seepage analyses with simplified models that allow for use of simplified reliability methods. Due to the complex geomorphic environment that is often encountered in the fluvial environment and curvature alignment, levee foundation geometry can range from simple to very complex. Geomorphic features in the soil layers underlying a structure often have a significant effect on the underseepage behavior and the potential for initiating internal erosion. Based on the hypothesis that levee underseepage susceptibility comes from localized subsurface geomorphic features that interrupt the characteristic profile along that levee reach, a methodology has been developed that assesses the hydraulic effect of geomorphic features in levee underseepage reliability. The methodology consists of a response surface-Monte Carlo analysis that takes into account the uncertainty in the subsurface geometry and soil properties in assessing the seepage regime associated with the feature. The method utilizes three-dimensional steady-state finite-element underseepage analyses to develop a response surface representing the relationship between soil properties and the three-dimensional levee foundation. The response surface then serves as the driving function for reliability analyses by means of Monte Carlo simulation analyses, resulting in cumulative probability functions for either hydraulic exit gradient or factor of safety against heave. These computed probability functions represent an assessment of conditional probability of initiation of internal erosion. Results can be adjusted for curvature effects when needed. The analysis of a crevasse-splay, an abandoned channel, and a meander scroll feature found in the Sacramento River (east side) levee system in California are presented as application examples.

Keywords: Internal erosion · Geomorphic features · Reliability analyses

1 Introduction

Two characteristics of levees that are relevant to this study are: (1) they are long, linear structures that extend over varied geologic terrain, and (2) a failure at any point of a levee generally has potential to flood the entire protected area (basin or polder). As a consequence, levees are subjected to a variety of failure mechanisms including underseepage and associated internal erosion. The term internal erosion has been accepted as a generic term to describe erosion of particles by water passing through a

S. Bonelli et al. (Eds.): EWG-IE 2018, LNCE 17, pp. 137–148, 2019.
https://doi.org/10.1007/978-3-319-99423-9_13

body of soil or rock (ICOLD 2015). In US levees the predominant internal erosion processes is as backward erosion piping (BEP) (ICOLD 2015).

Underseepage analysis results vary considerably based on soil parameters and geologic conditions used in the models. Nevertheless, in order to simplify the analyses, levee sections' geometry and soil profile are often simplified in a matter that the results may not represent the true state of nature of the levee itself. Since levee structures are long and subjected to variable foundation conditions, it is logical to analyze them in a reliability-based approach. However, due to the complexity of the analyses, models used in reliability-based analyses tend to be simplified even more than those in deterministic analyses.

1.1 Levee Underseepage Reliability

BEP describes the erosion that initiates when particles of soil are dislodged from the soil matrix at an unprotected seepage exit point. As BEP continues, a pathway, or pipe, is formed by progressive erosion at the upstream end of the erosion void. The "pipe" progresses against the hydraulic gradient and flow, thus the term backward erosion piping (see Fig. 1A). As described by Vrouwenvelder et al. (2010) and shown in Fig. 1A, the authors believe BEP is often preceded by the heave mechanism, where by uplift of a soil mass occurs due to underlying hydraulic pressure or seepage forces (Terzaghi and Ralph 1968). Heave usually occurs near the levee toe, lifting and cracking a low-permeability soil layer providing the unprotected exit point for BEP to occur. Both heave and BEP mechanisms can contribute to the potential for internal erosion beneath a levee; therefore, both mechanisms are included in the assessments presented herein.

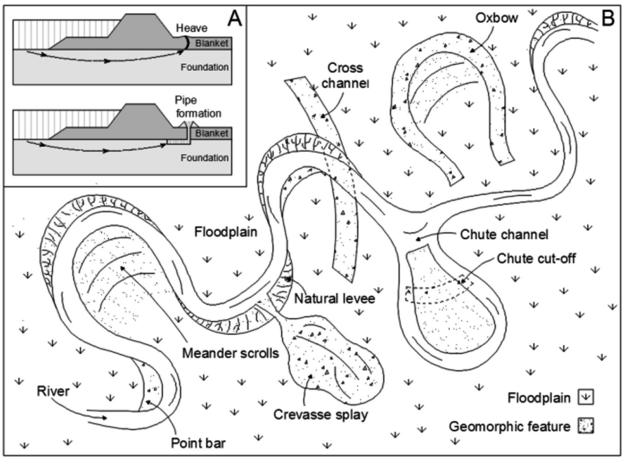

Fig. 1. Illustration of heave and backward erosion piping mechanisms (A) together with general geomorphology found in meandering river systems (B)

The most common simplified reliability approaches currently being used in the US to analyze levees against underseepage apply the first-order second-moment (FOSM) Taylor series method, using the U.S. Army Corps of Engineers (USACE) blanket theory (BT) equations as the performance functions (Wolff 1994; Wolff et al. 1996; Crum 1996; and Wolff 2008). The FOSM-BT method is commonly used in the US due to two main reasons: (1) the BT equations are an easy underseepage assessment tool and (2) the FOSM Taylor series method requires few calculations. Nevertheless, this method is limited to: (1) modeling of two-dimensional levee sections that simplify the levee subsurface geometry to the point where incorporating geomorphic features is not feasible, and (2) representing uncertainty in input parameters only through normal or lognormal probability distributions (USACE 2004, Rice and Polanco 2012, Benjasupattananan 2013, Polanco and Rice 2014, Polanco-Boulware and Rice 2017, Polanco-Boulware 2017). Therefore, based on the limitations of the FOSM-BT method, an assessment on levee underseepage by the combined effect of geomorphic features and curved alignment may not be accurately achievable.

To address the limitations discussed above, a Response Surface–Monte Carlo simulation method (RSMC) is proposed that takes into account the uncertainty in the subsurface geometry and soil properties in assessing the seepage regime associated with a geomorphic feature. Three-dimensional (3D) finite-element (FEM) seepage analyses are used to develop the response surface to take into account the inherent 3D aspects of the feature. The analysis results in a cumulative ascending distribution function (CADF) with respect to exit hydraulic gradient ($i_{blanket}$) and in a factor of safety against heave (F_{heave}).

The methodology can be adapted to any type of geomorphic feature and can be adjusted for curvature effects. As examples, the analysis of a crevasse splay and an abandoned channel intercepting the alignment of a levee section are presented. The analysis of a curved levee section intercepted by a meander scroll feature is presented with the purpose of showing the process for curvature adjustment.

2 Characteristic Geomorphology in the Levee Environment

While the methodology presented on this paper can be applied to a number of geomorphic settings, the paper is concerned with meandering river sediments upon which most of the levee structures encountered in the US are founded. Usually, the depositional environment of meandering rivers is depicted by alluvial deposits and flood (overbank) deposits (Leopold and Wolman 1957, Brierley and Fryirs 2005). Alluvial deposits are typically granular and tend to become finer in the upward direction. Overbank deposits consisting of finer grained materials deposited when flood waters exit the river channel usually overlay the alluvial deposits (Smith and Pérez-Arlucea 2008, Walling et al. 2004, Ritter et al. 2011). In the engineering community, overbank deposits are usually called the “blanket” layer whereas alluvial deposits are usually called the “foundation” layer (USACE 1956, 2000) as shown in Fig. 1A.

This stratigraphy has a significant effect on the underseepage behavior below a levee alignment and associated internal erosion mechanisms. Due to the large difference in hydraulic conductivities between the foundation and blanket layers, little total

head loss occurs in the foundation beneath the levee and large pressures develop beneath the blanket layer on the landside of the levee leading to high gradients and uplift pressures. In some cases these large pressures may result in uplift and cracking of the blanket, concentrating flow into the defect and developing high gradients that result in sand boils or in a tragic blowout (USACE 1956, Glynn and Kuszmaul 2010). Along with the general depositional stratigraphy composed of the blanket and foundation layers, geomorphic features shape the flood plain and intercept the alignment of man-made levees.

The most common geomorphic features encountered in a meandering river environment are high conductivity channels such as point bars, meander scrolls and abandoned channels; low conductivity channels such as neck cut-offs and oxbows; and crevasse splays (see Fig. 1B). Natural levees form adjacent to the river bank as a result of deposition when flood waters loose velocity when they escape the main channel. They are characterized by broad ridges that distally fade perpendicular to the river (Saucier 1994). As the river channel migrates laterally, low-velocity flow tends to deposit finer sediment (overbank deposit) on top of the existing feature, creating the blanket layer that often underlay levees (Nanson 1980, Saucier 1994). Crevasse splays and point bars both represent concentrated flow due to their granular makeup and confined reduction of the blanket layer thickness which pose a unique contribution on the internal erosion mechanism near the landside levee toe. The presence of the low hydraulic conductivity swale (scroll) may possibly block or concentrate seepage into the successive ridges, resulting in higher potential for internal erosion compared to the adjacent areas. Similar scenarios may be encountered with the presence of abandoned channels whether they are composed of granular or fine material.

3 RSMC Methodology

Due to the limitations of the FOSM-BT method and on the hypothesis that levee underseepage susceptibility comes from localized subsurface geomorphic features that interrupt the characteristic profile, Rice and Polanco (2012) and Polanco and Rice (2014) developed steady-state, 2D seepage models for assessing hydraulic conditions in geometrically complex levee profiles using what they call the Response Surface-Monte Carlo method. The RSMC method builds on the limitations of the BT-FOSM method allowing for flexibility by: defining the underseepage failure mechanism (or critical hydraulic condition), (2) allowing more complex geologic foundation arrangement and, (3) defining the probabilistic state of the key input parameters.

To improve the methodology and focus on the effect of geomorphic features encountered along levee alignments, research by Polanco-Boulware and Rice (2017) culminated in the expansion of the method by means of 3D-FEM computation and parametric analyses that help the method be less labor intensive. Geomorphic features represent a concentrated pathway or blockage of flow that affect the internal erosion mechanism of a levee. Based on this hypothesis, Polanco-Boulware and Rice (2017) and Polanco-Boulware (2017) present the RSMC methodology applied to the underseepage effect of crevasse splays and high conductivity channels (such as point bars,

meander scrolls, cross channels and chute cut-offs), respectively. The RSMC general steps that can be applied to geomorphic features are as follows:

1. Identify soil and geometric parameters with the aid of geological maps and published studies or reports,
2. Develop PDFs for all input parameters,
3. Develop a general 3D model with the key soil and geometry input parameters,
4. Simplify the general model to reduce the number of input parameters in the response surface using parametric analyses,
5. Verify the simplified model for consistency with the general model,
6. Develop response surface by means of multiple 3D-FEM analyses using the simplified model,
7. Develop a family of curves to represent the response surface and fit equations to the curves,
8. Using the @risk and Excel programs, perform a Monte Carlo analysis by randomly selecting values of key parameters from input PDFs and applying the response surface to produce CADFs taking into account curvature of levee if present and needed.

A CADF is a plot of increasing values of a key parameter versus the probability of the parameter being less than that value. It is important to mention that the resulting CADFs are a conditional (on a year flood level) probability of initiation of erosion assuming that the design flood level has been achieved. In order to compute the (total) probability of failure, similar analysis or judgement needs to be applied considering an event tree process as proposed by Foster et al. (2002) and Fell et al. (2003) of initiation, continuation and progression of erosion that leads to a failure or breach. Since the use of fragility curves, relationship of increasing flood loading versus conditional probability of occurrence (Simm et al. 2008, USACE 2010, Shannon and Wilson 2011), are useful and popular, Polanco-Boulware and Rice (2017) and Polanco-Boulware (2017) also demonstrate that fragility curves can be developed as a result of the RSMC's CADFs.

4 Internal Erosion Assessment of a Crevasse Splay Deposit

Crevasse splays form when the natural levee breaches during a flood event creating a crevase through the levee and a splay of coarse-grained soil on the landside. These deposits are often then buried with fine-grained overbank deposits. A sample map of the east side of the Sacramento River Levee system (Pearce et al. 2009; William Lettis and Associates 2008) showing mapped historical crevasse-splays is presented as Fig. 2. Geometric and soil data were collected based on geological maps and reports prepared along the east side of the Sacramento River Levee system and similar meandering systems. A 3D-FEM seepage model of the crevasse splay model geomorphic feature is presented in Fig. 3. It consists of (1) a crevasse channel directly hydraulically connected to the river and leading from the river water to the splay on the landside of the levee, (2) a splay area on the landside of the levee, and (3) a low permeably blanket on

top of the splay. As presented in Table 1, a total of 15 geometric and soil parameters comprise the crevasse splay model.

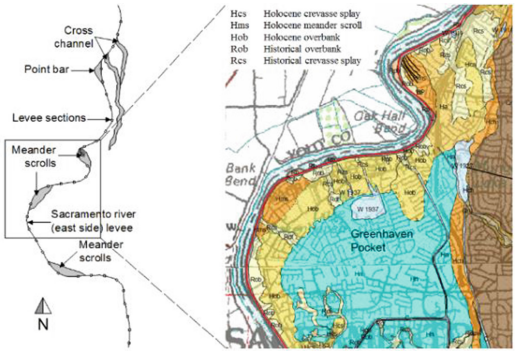

Fig. 2. Sacramento River Levee system in California showing a clip of a geological map with most common geomorphic features

The behavior of each parameter is represented by a PDF discretized by 5 or more values. Parametric analyses were performed to eliminate the parameters from the response surface that have an insignificant effect on the analysis outcome and combine the remaining significant parameters. Five parameters were eliminated: L_{ts}, K_{ds}, t_f, K_f, and γ_{blkt}. These parameters are not eliminated from the computation but are not varied during the modeling to define the response surface. To produce a response surface, a most likely value (MLV) is assigned to each respective eliminated parameter.

By eliminating parameters that have insignificant effect on the outcome, the number of parameters is decreased to 10; still too many to reasonably develop a response surface. Thus, a simplified model is developed. The simplified model combines the 10 parameters into three parameters that describe the seepage flow behavior in the crevasse splay deposit based on the theory that the total hydraulic head in the splay is controlled by the flow capacity of the three elements. The conductance of the crevasse channel, $C_{channel}$, describes the resistance to flow from the river to the splay. The transmissivity of the splay, T_{splay}, describes how easily the flow reaching the splay is distributed throughout the splay. The conductance of the blanket, $C_{blanket}$, defines the ease at which the pressures in the splay can be dissipated through the blanket. The combined parameters are calculated as presented in the following equations and schematically illustrated in Fig. 4:

$$C_{channel} = \frac{K_{ch} W_{ch} t_{ch}}{L_{ch}} \tag{1}$$

$$T_{splay} = K_s t_s \tag{2}$$

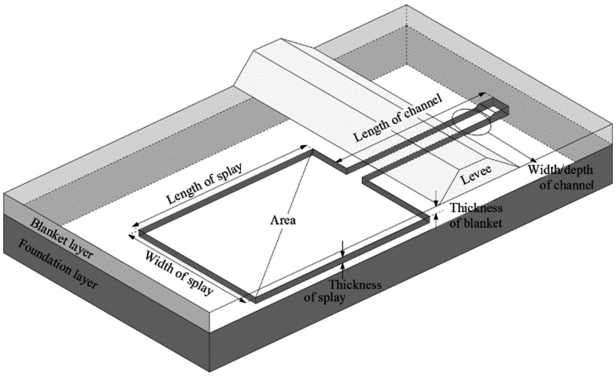

Fig. 3. Three-dimensional finite-element model of a crevasse-splay deposit

Table 1. Geometric and soil parameters for a crevasse-splay model

Parameter	Description	Significant	
		Yes	No
t_s	Thickness of the crevasse splay	✓	
t_{ch}	Thickness of the crevasse channel	✓	
t_b	Thickness of blanket above the splay	✓	
W_s	Width of the crevasse splay area	✓	
W_{ch}	Width of the crevasse channel	✓	
L_s	Length of the crevasse splay area	✓	
L_{ch}	Length of the crevasse channel	✓	
K_{ch}	Horizontal hyd. conductivity of the crevasse channel	✓	
K_{sp}	Horizontal hyd. conductivity of the crevasse splay area	✓	
K_b	Vertical hyd. conductivity of the blanket above the splay	✓	
L_{ts}	Thinning of the splay distal to the levee		✓
t_f	Thickness of the foundation		✓
K_f	Horizontal hydraulic conductivity of the foundation		✓
γ_{blkt}	Unit weight of the blanket soils		✓
K_{ds}	Decreasing hydraulic conductivity of the splay		✓

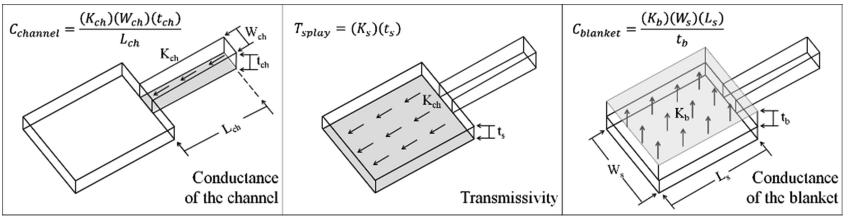

Fig. 4. Three-dimensional finite-element model of a crevasse-splay deposit

By eliminating parameters that have insignificant effect on the outcome, the

$$C_{blanket} = \frac{K_b W_s L_s}{t_b} \tag{3}$$

The simplified model presented above was validated by performing comparative parametric analyses in which individual parameters are varied independently of the remaining parameters and the results compared with those of the original model, that is, the differences between the analyses results using all the true parameter values and the results using the simplified model (combination of parameters). The maximum variation resulting from using the simplified model is less than 0.30 m (1 ft) of total head for all but three parameters. Furthermore, most of the variation that is observed occurs when using values at the ends of PDF distributions where the probability of occurrence is very low relative to the values in the center of the distribution. Refer to Polanco-Boulware and Rice (2017) for detailed data regarding these results.

Using the simplified model and the combined parameters identified above (T_{splay}, $C_{blanket}$, and $C_{channel}$), the response surface was generated for the crevasse splay geomorphic feature using multiple runs of a 3D-FEM analysis. The ranges of values for the three combined parameters represent the ranges of the possible values resulting from variation of the original parameters of the model. The results of the analyses were plotted on a family of curves that together represent a four-dimensional surface that defines the relationship between the three combined parameters and the maximum total head in the splay. The full family of curves (response surface) with its corresponding equations can be found in Polanco-Boulware and Rice (2017).

A Monte Carlo analysis was performed using a program written in an Excel spreadsheet and linked with the computer program *@Risk*. The Monte Carlo analysis is performed with *@Risk* due to the ease of use and many options available within the program. PDFs for each of the 10 original model parameters plus one additional parameter (the unit weight of the blanket, γ_{blkt}) are input into the program. For each iteration of the Monte Carlo analysis, the gradient through the blanket, $i_{blanket}$, and the factor of safety against heave, F_{heave}, are calculated using the following sequence:

1. Values of each of the 10 parameters are randomly selected based on the PDF distributions;
2. These parameter values are then combined into the three combined parameters using Eqs. 1 through 3;
3. The three combined parameters are then used with the response surface to calculate the maximum total head in the splay hmax (the zero head datum is set as the landside ground surface elevation); and
4. Using the maximum head value, the key hydraulic parameters: gradient through the blanket, $i_{blanket}$, and the factor of safety against heave, Fheave, are calculated using Eqs. 4 and 5:

$$i_{blanket} = \frac{\Delta h}{t_b} = \frac{h_{\max}}{t_b} \tag{4}$$

$$F_{heave} = \frac{t_b(\gamma_{blkt})}{u_{splay}} = \frac{t_b(\gamma_{blkt})}{(h_{max} + t_b)\gamma_w} \tag{5}$$

The sequence above was repeated for 10,000 iterations to produce CADFs representing the conditional probability of the key hydraulic parameters, $i_{blanket}$ (Fig. 5) and F_{heave}. The y-axes in Fig. 5 represent the conditional probability of $i_{blanket}$ being less than or equal to a specific cumulative frequency of a computed $i_{blanket}$. The conditional probability of exceeding an exit gradient of 1.0 is indicated in Fig. 5 and is specifically shown on the top of the figure as $P(i_{blanket} \geq 1.0) = 85.1\%$.

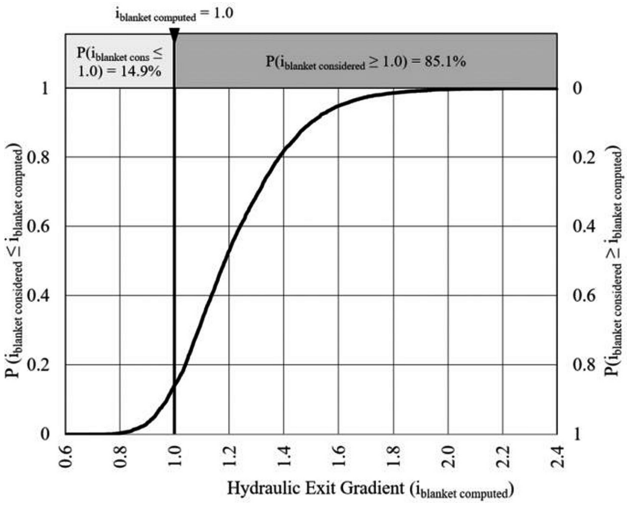

Fig. 5. CADF for hydraulic exit gradient through the blanket, $i_{blanket}$

Since this crevasse splay model is conditional on the river reaching a flood with an annual exceedance probability of 1% or the 100-year-flood level, parametric analyses were also performed with respect to other flood levels to determine a way to compute the probability of erosion initiation based on different flood stages. Results from these parametric analyses are consistent and illustrate a linear relationship of differential flood level versus head at splay. Based on these results, the crevasse splay model can compute the maximum total head at the splay with respect to various flood stages by a simple linear interpolation centered on the 100-year-flood model. Results for different flood levels are presented in Fig. 6 resulting in a fragility curve (Shannon and Wilson 2011) for the initiation of internal erosion.

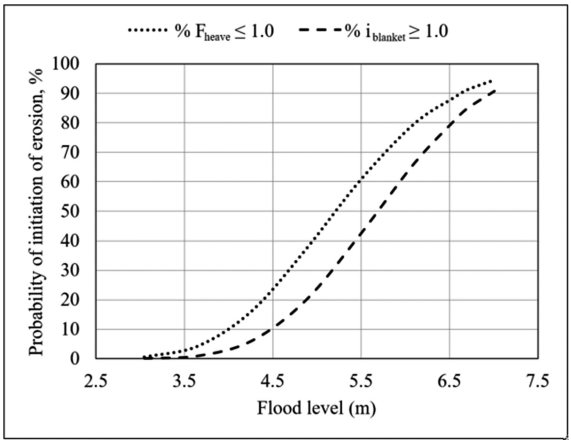

Fig. 6. Fragility curve for a crevasse splay model

5 Assessment for Additional Geomorphic Features

The analyses described above for the crevasse splay geomorphic feature has been repeated to develop response surfaces for additional geomorphic features such as: cross channels, point bars and meander scrolls, and low permeability channels such as oxbow lakes with fine-grained infill. Details of these analyses have been omitted from this paper due to space limitations. However, details of these analysis and the resulting response surfaces are provided in Polanco (2017).

6 Conclusions

This paper presents the effect that geomorphic features have on the backward erosion piping mechanism due to underseepage. An innovative method, the response-surface Monte Carlo (RSMC) simulation method, is flexible enough to account for variations in geometric and soil properties parameters as well as flood stages and curvature effects. Soil and geometric levee parameters are used to produce probability density functions and generate a three-dimensional finite-element model to perform parametric underseepage analyses with the purpose of simplifying the general model. A family of curves (response surface) are developed that represent a relationship between key soil and geometric parameters and the hydraulic design criteria. By means of the program @Risk, the developed probability density functions are used as random input parameters on the family of curves resulting in cumulative ascending density functions that represent the conditional probability of initiation of erosion.

The method is demonstrated through an example of the assessment of a crevasse splay feature where the most significant parameters are combined into three parameters. The theory being that the total hydraulic head in the splay is controlled by the flow capacity of the three elements. The conductance of the crevasse channel, $C_{channel}$, describes the resistance to flow from the river to the splay. The transmissivity of the splay, T_{splay}, describes how easily the flow reaching the splay is distributed throughout the splay. The conductance of the blanket, $C_{blanket}$, defines the ease at which the pressures in the splay can be dissipated through the blanket.

References

Benjasupattananan S (2013) Deterministic and probabilistic approaches for modelling levee underseepage. Ph.D. dissertation, University of Delaware, Newark, US

Brierley GJ, Fryirs KA (2005) Geomorphology and river management: applications of the river styles framework. Blackwell Publishing, Oxford

Crum DA (1996) Reliability applied to levee seepage analysis. In: Probabilistic mechanics and structural reliability: ASCE proceedings 7th specialty conference, pp 946–949

Fell R, Wan CF, Cyganiewicz J, Foster M (2003) Time for development of internal erosion and piping in embankment dams. J Geotech Geoenviron Eng 129(4):307–314

Foster MA, Fell R, Davidson R, Wan CF (2002) Estimation of the probability of failure of embankment dams by internal erosion and piping using event tree methods. ANCOLD Bulletin, p 121

Glynn ME, Kuszmaul J (2010) Prediction of piping erosion along middle Mississippi river levees-an empirical model. Technical Report ERDC/GSL TR-04-12

International Commission on Large Dams (ICOLD) (2015) Internal erosion of existing dams, levees, and dikes, and their foundations. In: Internal erosion processes and engineering assessment, vol 1, Paris, France

Leopold LB, Wolman MG (1957) River channel patterns: braided, meandering and straight. U.S. Geological Survey, Washington, D.C., pp 39–84

Nanson GC (1980) Point bar and floodplain formation of the meandering Beatton River, northeastern British Columbia, Canada. Sedimentology 27(1):3–29

Pearce JT, Marlow D, Avila C, Selvamohan S (2009) Use of geomorphic and airborne geophysical data for analysis of levees and floodplain processes for levee evaluations in California. In: ASFPM annual conference

Polanco L, Rice JD (2014) A reliability-based evaluation of the effects of geometry on levee underseepage potential. In: Geotechnical and Geological Engineering

Polanco-Boulware L, Rice JD (2017) Reliability-based three-dimensional assessment of internal erosion potential due to crevasse splays. J Geotech Geoenviron Eng 143(4):0401611

Polanco-Boulware L (2017) Reliability underseepage assessment of levees incorporating geomorphic features and length effects. Ph.D. dissertation, Utah State University, Logan, US

Rice JD, Polanco L (2012) Reliability-based underseepage analysis in levees using a response surface–Monte Carlo simulation method. J Geotech Geoenviron Eng 138(7):821–830

Ritter DF, Kochel RC, Miller JR (2011) Process geomorphology, 5th edn. Waveland Press, Zurich

Saucier RT (1994) Geomorphology and quaternary geologic history of the lower Mississippi Valley. U.S. Army Engineer Waterways Experiment Station, Vicksburg

Shannon & Wilson, Inc. (2011) Skagit river levee general investigation - levee risk and reliability analysis. USACE, Washington

Simm J, Gouldby B, Sayers P, Flikweert JJ, Wersching S, Bramley M (2008) Representing fragility of flood and coastal defences: getting into the detail. In: Proceedings of FLOODrisk 2008 conference

Smith ND, Pérez-Arlucea M (2008) Natural levee deposition during the 2005 flood of the Saskatchewan River. Geomorphology 101(4):583–594

Terzaghi K, Ralph P (1968) Soil mechanics in engineering practice, 2nd edn. Wiley, New York

U.S. Army Corps of Engineers (USACE) (1956) Investigation of underseepage and its control. Technical Memorandum No. 3-424. U.S. Army Engineer Waterways Experiment Station, Vicksburg, MS

U.S. Army Corps of Engineers (USACE) (2000) Design and construction of levees. Engineering Manual EM 1110-2-1913. Washington, D.C.

U.S. Army Corps of Engineers (USACE) (2010) Beyond the factor of safety: developing fragility curves to characterize system reliability. Report ERDC SR-10-1, Washington, D.C.

Vrouwenvelder ACWM, Van Mierlo MCLM, Calle EOF, Markus AA, Schweckendiek T, Courage WMG (2010) Risk analysis for flood protection systems. Deltares, main report. The Netherlands

Walling DE, Fang D, Nicholas AP, Sweet RJ (2004) The grain size characteristics of overbank deposits on the floodplains of British lowland rivers. In: Proceedings of the international symposium in sediment transfer through fluvial system, International Association of Hydrological Sciences

William Lettis & Associates, Inc. (2008) Surficial geologic map and initial geomorphic assessment, Sacramento River (east side), Sacramento County. Unpublished consultant report prepared for URS Corporation, California

Wolff D (2008) Reliability of levee systems. In: Phoon K-K (ed) Reliability-based design in geotechnical engineering. Taylor and Francis Group, New York, pp 448–496

Wolff TF (1994) Evaluating the reliability of existing levees. Army Engineer Waterways Experiment Station, Michigan State University, East Lansing

Wolff TF, Demsky EC, Schauer J, Perry E (1996) Reliability assessment of dike and levee embankments. Uncertainty in the geologic environment: from theory to practice. ASCE, Reston

Modelling of Backward Erosion Piping in Two- and Three- Dimensional Domains

Bryant A. Robbins[1(✉)] and D. V. Griffiths[2]

[1] U.S. Army Engineer Research and Development Centre, Vicksburg, MS, USA
bryant.a.robbins@usace.army.mil
[2] Colorado School of Mines, Golden, CO, USA

Abstract. Backward erosion piping is a highly three-dimensional process responsible for the failure of many embankment dams and levees. Unfortunately, the majority of numerical models developed for predicting piping are two-dimensional. This study presents finite element models for backward erosion piping computations in both two- and three-dimensional domains. Analyses results indicate that the degree of concentration of flow in three-dimensional models is much more severe than in two dimensions, resulting in higher estimates of the hydraulic gradient near the upstream end of the erosion channel.

Keywords: Backward erosion piping · Finite element model · Dams
Levees

1 Introduction

Backward erosion piping (BEP) is an internal erosion mechanism by which foundation soil is gradually removed from beneath a water retaining structure such as a dam or levee as shown in Fig. 1. Erosion typically initiates near the downstream embankment toe due to the vertical hydraulic gradient being highest at this location and progresses in the upstream direction along the interface between the sand and a cohesive cover layer. As the erosion channel progresses, groundwater concentrates towards the pipe resulting in a highly three-dimensional flow pattern. Unfortunately, the majority of models developed for predicting BEP are two-dimensional. This paper presents results from both two- and three-dimensional finite element models to examine the impact of this restriction on modelling of erosion progression.

2 Previous Studies

Previous research on BEP (de Wit et al. 1981; Hanses 1985; Townsend and Shiau 1986; Schmertmann 2000; van Beek 2015) has provided a general understanding of the physics of the process. Referring to Fig. 1, the process includes (1) Darcian flow; (2) exit related hydraulic conditions, such as orifice flow, pipe flow, or constant head boundary conditions; (3) liquefaction or fluidization at the pipe head due to concentrated flow leading to (4) occasional bursts of high suspension solids into the pipe; (5) laminar flow conditions in the open pipe that cause (6) sediment transport along the

S. Bonelli et al. (Eds.): EWG-IE 2018, LNCE 17, pp. 149–158, 2019.
https://doi.org/10.1007/978-3-319-99423-9_14

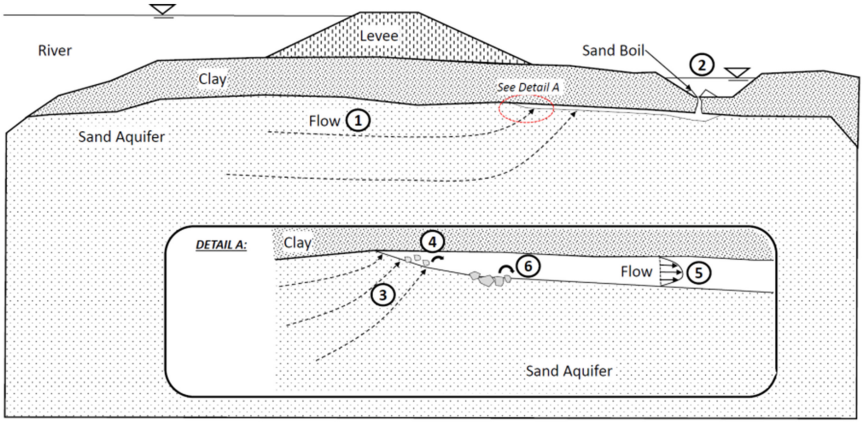

Fig. 1. Illustration of the physics of backwards erosion piping.

bottom of the pipe. The concentrated flow at the pipe tip has been shown to control pipe progression (van Beek 2015; Robbins et al. 2018). As the head loss in the pipe influences the hydraulic gradients near the pipe tip, the pipe hydraulics must be accurately accounted for. As such, models for BEP must include features to accurately and independently describe the erosion at the pipe tip, the hydraulic resistance in the pipe, and the groundwater flow.

Numerous investigators have numerically modelled BEP. Wang et al. (2014) classified these models into three broad categories in terms of how the piping process is represented, i.e., (1) models that simply increase pipe zone permeability within a routine seepage analysis (e.g., Vandenboer et al. 2013; Van Esch et al. 2013), (2) multi-phase soil models in which the erosion and transport of eroded particles are explicitly accounted for (e.g., Wang et al. 2014; Fujisawa et al. 2010; Rotunno et al. 2017), and (3) Discrete Element Method (DEM) simulations, typically coupled to a continuum description of fluid flow (e.g., Lominé et al. 2013; Zou et al. 2013; Tran et al. 2017). For analysis of BEP, it is desired to predict ultimate pipe progression limits at the structural scale (i.e. how far will the pipe progress through the foundation?). This question can be conservatively answered using Category 1 models. Given that Category 1 models are also the simplest of the three model categories, this approach was selected for investigating BEP in both two and three dimensions in the following sections.

3 Model Descriptions

Custom finite element models for simulating BEP were developed by adapting the steady state groundwater program documented in Smith and Griffiths (2004). Two dimensional models were developed for conducting BEP analysis in both plan view and elevation view (i.e., profile or cross-sectional view). Additionally, a three-dimensional program was developed. The following sections describe the model

formulations, first for elevation analysis followed by brief descriptions of the various modifications required for plan view and three-dimensional analysis.

3.1 Two-Dimensional Model: Elevation View Analysis

Consider the elevation view of a simple BEP model shown in Fig. 2. The entire domain is constructed of quadrilateral elements, with the pipe domain (Ω_p) being represented by a single row of quadrilateral "pipe" elements and the soil domain (Ω_s) consisting of remaining elements. The flow in the soil (Ω_s) is governed by the Laplace equation which can be solved by finite elements as an equivalent matrix problem given by (e.g., Smith and Griffiths 2004)

$$[K_e]\{H\} = \{Q\} \tag{1}$$

where $\{H\}$ and $\{Q\}$ are vectors of the total head and net flow at the FEM nodes, and $[K_e]$ is the assembly of element conductivity matrices given by

$$[k_e] = \int k_x \frac{\partial N_i}{\partial x}\frac{\partial N_j}{\partial x} + k_y \frac{\partial N_i}{\partial y}\frac{\partial N_j}{\partial y} d\Omega_s \tag{2}$$

with k_x and k_y denoting the hydraulic conductivity in the coordinate directions and N_i denoting the finite element shape functions. The flow in the eroded pipe is assumed to be similar to that of 1D laminar flow passing through two parallel plates. This assumption is deemed suitable due to (1) the shallow depth and large width of the erosion channels (Muller-Kirchenbauer et al. 1993) and (2) the laminar flow conditions observed in BEP pipes at the laboratory scale (Robbins et al. 2018). Restricting the model for now to only horizontal pipe progression, the flow through the pipe is related to the hydraulic gradient by

$$q_p = -\frac{a^3 \rho g}{12\mu}\frac{dH}{dx} \tag{3}$$

(Sellmeijer 1988) where a denotes the depth of the eroded pipe, g is the acceleration of gravity, and μ and ρ represent the dynamic viscosity and density of water, respectively. From continuity,

$$\frac{dq_p}{dx} + S = 0 \tag{4}$$

where S is a sink/source term due to flow along the pipe. Substitution of Eq. 3 into Eq. 4 yields the differential equation governing the pipe flow in Ω_p.

$$\frac{a^3 \rho g}{12\mu}\frac{d^2H}{dx^2} = S \tag{5}$$

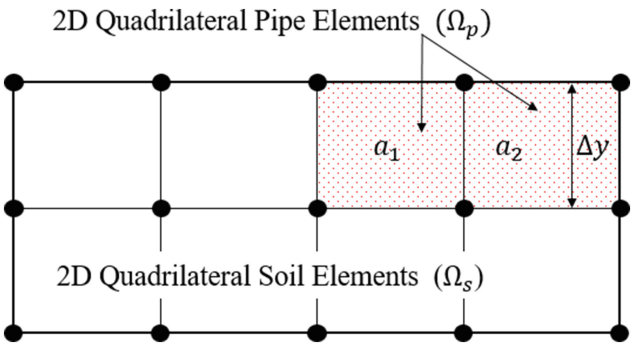

Fig. 2. Finite element discretization of BEP

Robbins and Griffiths (2018) demonstrated that Eq. 5 is satisfied in the quadrilateral pipe elements (Ω_p) by assembling the pipe elements into Eq. 1 using Eq. 2 with an equivalent hydraulic conductivity (k_{pipe}) substituted for k_x and k_y where

$$k_{pipe} = \frac{a^3 \rho g}{12 \mu \Delta y} \tag{6}$$

with Δy denoting the height of the pipe element as shown in Fig. 2 and a denoting the depth of the erosion pipe within each element. This approximation was demonstrated to provide an adequate solution provided the element size used was sufficiently small (0.25 m elements gave essentially the same solution as representing the pipe using 1D rod elements). For complete details, see Robbins and Griffiths (2018).

In addition to satisfying the pipe hydraulics given by Eq. 5, the sand grains in the bottom of the erosion pipe must be in equilibrium. If equilibrium conditions do not prevail, the pipe would deepen further resulting in a different hydraulic solution. The hydraulic shear stress at the bottom of the pipe is determined from force equilibrium to be

$$\tau = \frac{a \rho g}{2} \frac{dH}{dx} \tag{7}$$

The equilibrium condition that must be satisfied is simply given by $\tau < \tau_c$ where τ_c denotes the critical shear stress for incipient motion of the soil being eroded. The critical shear stress for cohesionless soils can readily be determined from the Shields diagram (Yalin and Karahan 1979). As the pipe depths required for equilibrium are unknown, Picard iterations over the pipe depth, a, are conducted to arrive at a satisfactory hydraulic solution satisfying grain equilibrium, pipe hydraulics, and the groundwater flow for a given erosion pipe location. In this study, the pipe depth was incremented by one half of the mean grain diameter (d) of the sand each iteration.

Once a hydraulic solution is obtained for a fixed pipe location, the potential for progression of the erosion pipe must be assessed. The pipe progresses further if

$$\frac{\partial H}{\partial x} > i_{crit} \tag{8}$$

in the element immediately upstream of the pipe where i_{crit} is the critical horizontal gradient of the soil being eroded. If Eq. 8 is satisfied in the element immediately upstream of the pipe, the element is switched to a pipe element, and the hydraulic solution must be iteratively solved once again with the new pipe geometry. This process is repeated to evaluate the potential for a pipe to progress through the domain of interest.

3.2 Two-Dimensional Model: Plan View Analysis

A plan view analysis only considers the hydraulics of the foundation sand layer. For simplicity, the model assumes a completely horizontal plane, and the pipe can readily progress in any direction in the plane, depending solely on the gradient field for a given problem. Further, it is assumed that no flow passes beneath the pipe elements (all flow in the pipe domain is in the pipe itself). With these assumptions, the equivalent hydraulic conductivity of the pipe (k_{pipe}) for plan view analyses is determined to be (following Robbins and Griffiths 2018)

$$k_{pipe} = \frac{a^3 \rho g}{12\mu} \tag{9}$$

Additionally, as the x-y plane is now in the horizontal plane, the x-y gradient must be used to assess pipe progression resulting in a progression criterion of

$$|\nabla H(x,y)| = \sqrt{\frac{\partial H^2}{\partial x} + \frac{\partial H^2}{\partial y}} > i_{crit} \tag{10}$$

for elements immediately upstream of the pipe. Except for these two changes, the plan view model is identical to the cross-sectional model.

3.3 Three-Dimensional Model

In the three-dimensional model, the element height is in the z-direction, and the pipe progression was restricted to the x-y plane for simplicity. As such, the equivalent hydraulic conductivity for the pipe elements is now given by

$$k_{pipe} = \frac{a^3 \rho g}{12\mu \Delta z} \tag{11}$$

where Δz designates the height of the element in the z-direction, and the pipe width is determined by the element width. The criterion for pipe progression is once again given by Eq. 10 as the pipe is allowed to progress horizontally in the x-y plane.

4 Analyses Results

The simple test case illustrated in Fig. 3 was used to perform an initial model comparison. The problem consists of a 10-m soil cube with constant head upstream and downstream boundary conditions. All other boundaries are no-flow boundaries. The pipe is initiated at the top-centre location on the downstream face by changing a single element to a pipe element. An element size of 0.25 m was used in the analysis. Illustrations of the corresponding finite element meshes are shown in Fig. 4 with the pipe progressed 6 m into the domain. All material properties used for the analyses are provided in Table 1. The value of i_{crit} was arbitrarily set to 0.1 (a value less than the average gradient of 0.2) to ensure that the pipe would progress completely through the domain. This was done as the focus of the investigation was on comparing the differences in the hydraulic solutions obtained from the three model formulations.

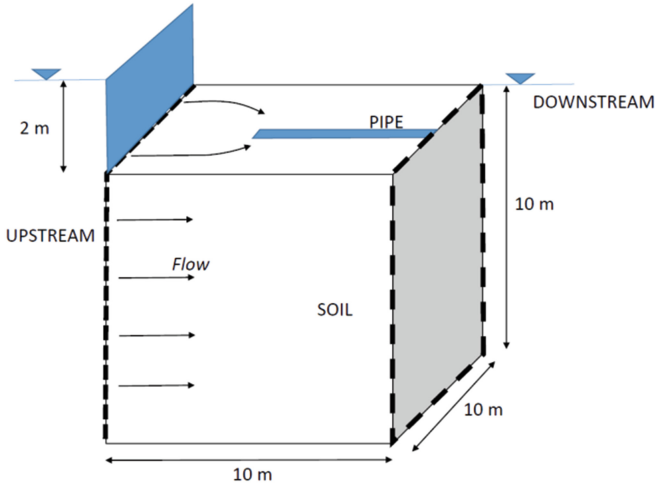

Fig. 3. Simple test problem for model comparison.

The pipe was allowed to progress through the domain entirely. For each progression step, the head profile, nodal hydraulic gradients, and calculated pipe depth profile were examined. The step at which the pipe had progressed 6 m through the domain was chosen for comparison purposes as the pipe was sufficiently developed to see differences in the pipe hydraulic computations, but enough soil remained upstream to be able to examine upstream flow patterns. The flow nets for the 2D analyses are illustrated in Fig. 5. The head profiles and pipe depth profiles along the centreline of the pipe are illustrated in Fig. 6. It is readily observed that the head profiles in the pipe are quite similar for all three models. However, the head profile upstream of the pipe is much more non-linear in the three-dimensional model. This is due to the flow concentration that is able to be captured in three dimensions, which results in higher hydraulic gradients.

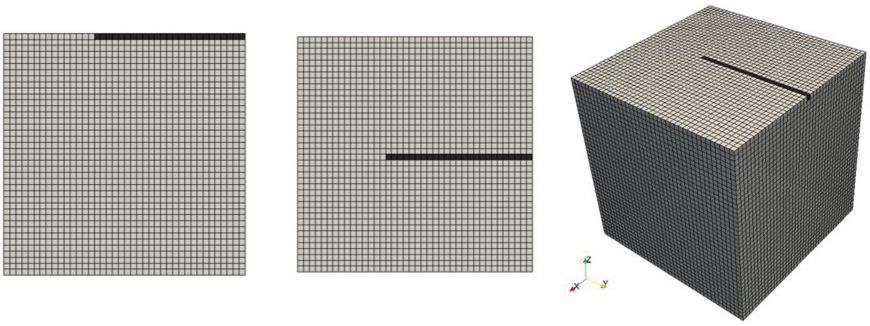

Fig. 4. Meshes with pipe progressed 6 m shown for cross-sectional analyses, plan view analyses, and three dimensional analyses (from left to right).

Table 1. Material properties and boundary condition for BEP analyses.

d (mm)	k (m/s)	τ_c (Pa)	μ (Ns/m^2)	i_{crit}	ΔH (m)
0.2	1×10^{-5}	0.33	1×10^{-3}	0.10	2

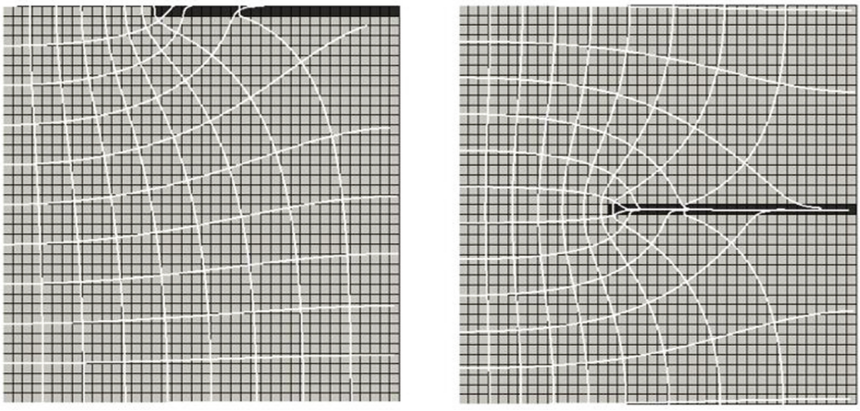

Fig. 5. Flow nets with pipe progressed 6 m for cross-sectional analyses and plan view analyses.

As the criterion for pipe progression is the horizontal gradient, a closer examination of the difference in hydraulic gradients upstream of the pipe was needed to fully understand the impacts of the model differences on analyses of pipe progression. To quantify this difference, a concentration factor was defined as

$$F_C = i_{h-3D}/i_{h-2D} \tag{12}$$

with i_{h-3D} and i_{h-2D} designating the horizontal gradient in the element immediately upstream of the pipe from the three-dimensional analyses and two dimensional analysis, respectively. A concentration factor was computed for both the cross-sectional

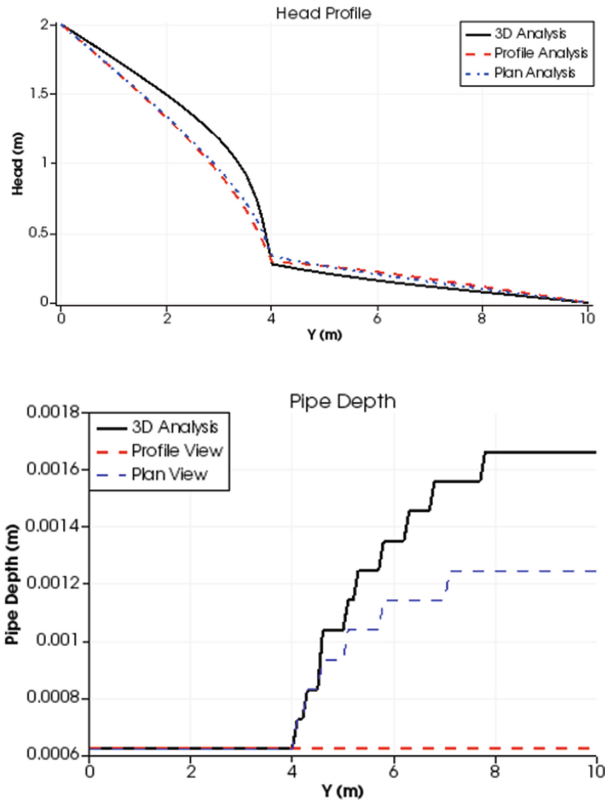

Fig. 6. Head profile and pipe depth profile for all three models with the pipe progressed 6 m.

analyses and the plan view analysis. The results are shown in Fig. 7. When the pipe location is furthest downstream, the value of F_C is 1.0 due to no flow concentration occurring into the pipe. As the pipe progresses upstream, the value of F_C increases due to the increasing amount of flow concentration. This indicates that the two-dimensional analyses are not able to fully capture the degree of concentration observed in the 3D model. This is also readily seen in Fig. 6.

5 Discussion

This study compared the results of two- and three-dimensional finite element models for piping. While the results indicate that 2D models are not able to fully capture the magnitude of hydraulic gradients upstream of the pipe, this study has been very limited in scope, and further research must be conducted into the relative merits of all three models before firm conclusions may be drawn about the utility of each model. In particular, the following points should be carefully considered.

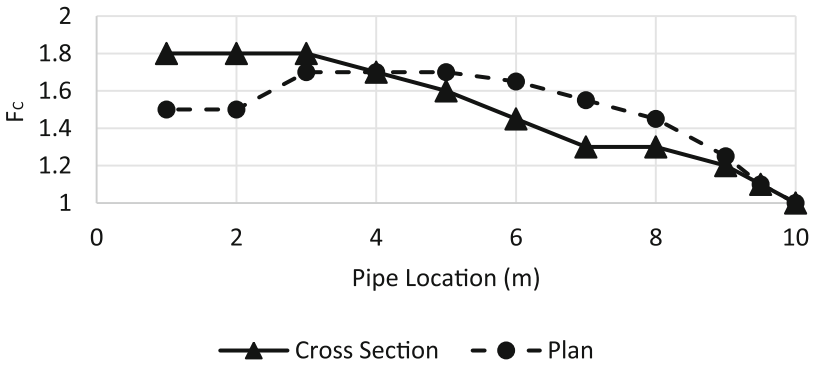

Fig. 7. Gradient concentration factors as a function of pipe location.

- The value of F_C increased as the pipe progressed. This may have in part been due to the constant head boundary conditions and small model domain.
- The F_C values presented should not be used until further research into the concentration factors is conducted for full scale levees at critical piping conditions. After further investigation, F_C values may be able to be used to correct 2D models to the equivalent 3D situation.
- Two-dimensional models calibrated to three-dimensional data may inherently include all necessary adjustments.
- The current models do not include widening of the pipe. This may also impact the concentration factors as it will allow more flow to pass through the pipe at the same gradient in both 3D and plan view analysis.
- Underprediction of the upstream gradient as observed in the 2D models may unconservatively predict BEP equilibrium.

Future research must be conducted to better understand the behaviour of the models over a broad range of conditions. Additionally, model validation is required through hindcasting of both experiments and case histories.

6 Conclusions

Finite element models for analyses of backward erosion piping were developed in both two and three dimensions. Two-dimensional modelling capabilities were developed for cross sectional analyses and plan view analyses. A simple comparison of the three types of models indicates that the hydraulic gradients upstream of the erosion pipe are much higher in the three-dimensional model than the two-dimensional models. A concentration factor was defined for correcting two-dimensional models. While the direction of this research holds much promise for better understanding of BEP, more research is required before these concepts can be applied in practice.

References

De Wit JM, Sellmeijer JB, Penning A (1981) Laboratory testing on piping. In: Soil mechanics and foundation engineering, pp 517–520. Rotterdam

Fujisawa K, Murakami A, Nishimura S-I (2010) Numerical analysis of the erosion and the transport of fine particles within soils leading to the piping phenomenon. Soils Found 50 (4):471–482

Hanses U (1985) Zur Mechanik der Entwicklung von Erosionskanälen in geschichtetem Untergrund unter Stauanlagen. Dissertation, Grundbauinstitut der Technischen Universität Berlin, Berlin, Germany (in German)

Lominé F, Scholtès L, Sibille L, Poullain P (2013) Modeling of fluid solid interaction in granular media with coupled lattice boltzmann/discrete element methods: application to piping erosion. Int J Numer Anal Methods Geomech 37(December 2011):577–596. https://doi.org/10.1002/nag

Muller-Kirchenbauer H, Rankl M, Schlotzer C (1993) Mechanism for regressive erosion beneath dams and barrages. In: Brauns H, Schuler R (eds) Filters in geotechnical and hydraulic engineering, The Netherlands

Robbins BA, Griffiths DV (2018) A simplified finite element implementation of the Sellmeijer model for backward erosion piping. In: Proceedings of the 9th European conference on numerical methods in geotechnical engineering. Puerto, Portugal, June 25–27, 2018

Robbins BA, van Beek VM, Lopez-Soto JF, Montalvo-Bartolomei AM, Murphy J (2018) A novel laboratory test for backward erosion piping. Int J Phys Model Geotech 1–14

Rotunno AF, Callari C, Froiio F (2017) Computational modeling of backward erosion piping. In: Models, simulation, and experimental issues in structural mechanics. Springer, Berlin, pp 225–234

Schmertmann JH (2000) The no-filter factor of safety against piping through sands. In: Silva F, Kavazanijian E Jr. (eds) Judgement and innovation pp 65–133. American Society of Civil Engineers

Sellmeijer JB (1988) On the mechanism of piping under impervious structures. Dissertation. Delft University of Technology

Smith IM, Griffiths DV (2004) Programming the finite element method, 4th edn. Wiley, Hoboken

Townsend FC, Shiau J-M (1986) Analytical and experimental evaluation of piping and filter design for sands. Gainesville, Florida

Tran D, Prime N, Froiio F, Callari C, Vincens E (2017) Numerical modelling of backward front propagation in piping erosion by DEM-LBM coupling. Eur J Environ Civil Eng 21(7-8):1–28

van Beek VM (2015) Backward erosion piping: initiation and progression. Dissertation. Delft University of Technology

Vandenboer K, van Beek V, Bezuijen A (2013) 3D FEM simulation of groundwater flow during backward erosion piping. In: Fifth international young geotechnical engineering conference, pp 5–8

Van Esch JM, Sellmeijer JB, Stolle D (2013) Modeling transient groundwater flow and piping under dikes and dams. In: 3rd international symposium on computational geomechanics (ComGeo III), p 9

Wang D-Y, Fu X-D, Jie Y-X, Dong W-J, Hu D (2014) Simulation of pipe progression in a levee foundation with coupled seepage and pipe flow domains. Soils Found 54(5):974–984

Yalin MS, Karahan E (1979) Inception of sediment transport. J Hydraul Div 105(11):1433–1443

Zou Y-H, Chen Q, Chen X-Q, Cui P (2013) Discrete numerical modeling of particle transport in granular filters. Comput Geotech 47:48–56. https://doi.org/10.1016/j.compgeo.2012.06.002

A Numerical Approach for the Analysis of Piping Erosion in Hydraulic Works

Andrea Francesco Rotunno[1,2,3(✉)], Carlo Callari[3], and Francesco Froiio[2]

[1] DICII, University of Rome "Tor Vergata", Rome, Italy
a.rotunno@ing.uniroma2.it
[2] LTDS, University of Lyon, École Centrale de Lyon, Ecully, France
[3] DiBT, University of Molise, Campobasso, Italy

Abstract. A method recently proposed for the computational modeling of backward erosion piping is applied for the numerical back-analysis of some pioneering experimental tests on physical models of cofferdams performed by Marsland (1953).

Keywords: Backward erosion piping · Cofferdams · Finite elements
Porous media

1 Introduction

The safety assessment of diaphragm walls in saturated sandy soils is known to require complex judgment, particularly due to the inherent mechanical instabilities being in connection with singular forms of the seepage flow. Namely, hydraulic heave but also *piping* are numbered in the European standards for civil engineering works amongst the relevant limit states (BSI 2004). Safety factors against these hydraulic failure modes are typically referred to a conveniently defined "critical hydraulic gradient" at the downstream side, i_c, or to the corresponding "critical water head", h_c. In spite of the complexity of these phenomena, extremely simple models are still used in engineering practice for the assessment of such critical values, which implies unusually high values of the safety factors.

Besides Terzaghi (1943), pioneering investigations on hydraulic failure by piping in diaphragm walls include analytical and experimental studies on cofferdams by Fox and McNamee (1948) and Marsland (1953), respectively. This failure mode is reported and discussed in a number of case studies (Bauer et al. 1980, Tanaka 1994, Duann et al. 1997), but a numerical model able to capture the triggering and time-evolution of piping failure in diaphragm walls is still missing, to the best of our knowledge.

However, interesting advances in the modelling of piping erosion at different scales can be found in recent research in the area of risk assessment of earth dams and levees.

S. Bonelli et al. (Eds.): EWG-IE 2018, LNCE 17, pp. 159–167, 2019.
https://doi.org/10.1007/978-3-319-99423-9_15

We mention in particular the analytical and numerical models for the fundamental erosion mechanisms of pipe propagation (Tran et al. 2017) and enlargement (Bonelli and Brivois 2008; Lominé et al. 2013), as well as numerical formulations incorporating one (Wang et al. 2014; Robbins 2016) or both mechanisms (Rotunno et al. 2017a,b) for the description of the piping erosion kinetics at the scale of the hydraulic work.

The latter numerical formulation is proposed herein for the safety assessment of diaphragm walls. After a brief presentation of the model in Sect. 2, in Sect. 3 we propose a back-analysis of the previously mentioned experimental tests on physical models of cofferdams (Marsland 1953). The model is assessed based on its ability to catch the "critical" water head for which the first signs of piping were detected. Summary and perspective elements for further developments are provided in the final section.

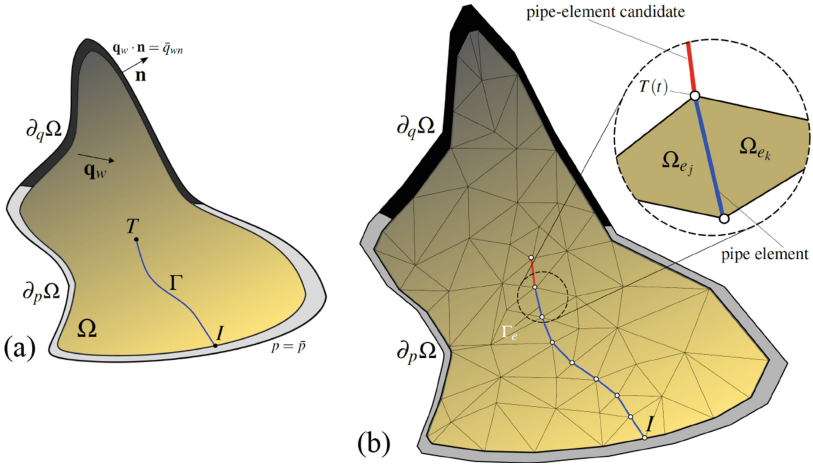

Fig. 1. In (a), two-dimensional scheme of the undeformable, saturated porous solid Ω subjected to localized erosion along a propagating line Γ, BCs in terms of pore pressure p and fluid flow $\mathbf{q}_\mathrm{w}$; in (b), FE discretization of Ω and Γ in terms of multi-dimensional elements Ω_e and one-dimensional elements Γ_e, resp. The pipe tip T propagates from the initiation point I within the porous medium. Ahead of the tip, a "pipe-element candidate" is highlighted in red.

2 Main Features of the Numerical Model

To set a minimal background for Sect. 3, we recall few selected features of the model for piping erosion proposed by Rotunno et al. (2017b). According to Fig. 1(a), we consider a saturated and undeformable porous medium Ω subjected to localized erosion along a propagating line Γ. The latter locus represents an erosion-induced one-dimensional pipe, filled with a mixture of water and fluidized solid. The flow regimes in the porous medium and in the pipe are assumed as

Darcian and turbulent, respectively. Along Γ, the two flows share the same pressures field and are subjected to common mass balance requirements. We model the turbulent flow in the erosion pipe by means of the Darcy-Weisbach law (Pope 2000), under the assumption of circular cross-section of the pipe (Regazzoni and Marot 2013).

As a criterion for backward propagation of the pipe we assume the condition

$$n_{\mathrm{T}} - n_{\mathrm{cr}} = 0 \tag{1}$$

with n_{T} the porosity ahead of the pipe tip T and n_{cr} a critical porosity value at which fluidization of the saturated porous medium occurs (Cubrinovski and Ishihara 2002). Prior to fluidization, the porosity n_{T} rises above the value n_0 assumed for the surrounding porous medium, due to localized erosion driven by the Darcy flow *normal* to the erosion front at the pipe tip T. In analogy with kinetic laws for diffused erosion (Zhang et al. 2013), for the relevant rate we assume

$$\dot{n}_{\mathrm{T}} = c_{\mathrm{n}} \langle \tau_{\mathrm{n}} - \tau_{\mathrm{cn}} \rangle \tag{2}$$

where: c_{n} is the coefficient of normal erosion; τ_{n} is a representative hydraulic shear stress, with τ_{cn} its critical value; the operator "$\langle \bullet \rangle$" returns the positive part of "$\bullet$". The shear stress τ_{n} is a pore-scale measure of the drag exerted by the Darcy flow (Ojha et al. 2003) and is computed as

$$\tau_{\mathrm{n}} = \gamma_{\mathrm{w}} \frac{D_{\mathrm{r}}}{4} \, |\nabla h|_{\mathrm{T}}, \qquad \text{with} \qquad D_{\mathrm{r}} = 4 \sqrt{\frac{2\, k_{\mathrm{T}}\, \mu_{\mathrm{w}}}{n_{\mathrm{T}}}} \tag{3}$$

in which: γ_{w} and μ_{w} are the unit weight and the dynamic viscosity of water, respectively; D_{r} is a representative diameter for the pore network; $|\nabla h|_{\mathrm{T}}$ and k_{T} are the piezometric head gradient and the permeability ahead of the pipe tip, respectively. The current value of k_{T} is computed as a function of n_{T} using the Kozeny-Carman relation (Carman 1956):

$$k_{\mathrm{T}} = \left(\frac{n_{\mathrm{T}}}{n_{\mathrm{T}_0}} \right)^3 \left(\frac{1 - n_{\mathrm{T}_0}}{1 - n_{\mathrm{T}}} \right)^2 k_{\mathrm{T}_0} \tag{4}$$

where n_{T_0} and k_{T_0} are the values of porosity and permeabilityahead of the pipe tip, prior to erosion.

When the pipe path is known beforehand, a convenient computational strategy is to combine the use of multi-dimensional *and* one-dimensional finite elements, for separate integration of the equation governing the flow in the porous medium (Abati and Callari 2014, Callari and Abati 2009) and in the pipe, respectively (see Fig. 1). The one-dimensional "pipe elements" are activated according to the progress of erosion. Namely, the porosity n_{T} is computed by time integration of (2) on the "pipe-element candidate" located upstream of the pipe tip, and the pipe formulation is then activated in the latter element upon attainment of (1).

3 Numerical Simulation of Piping in Physical Models of Cofferdams

In this section, we present the numerical simulation of some of the pioneering experimental tests performed by Marsland (1953) on physical models of cofferdams at the Building Research Station. These tests were designed to reproduce typical failures of strutted diaphragm walls in granular materials induced by seepage during dewatering. The cofferdam model was built in a seepage tank 2.75 m long, 61 cm deep and 15.25 cm wide, using a uniform Ham River sand (25–52 B.S. sieve).

Table 1. Tests on physical models of cofferdams in fairly loose uniform sand: measured critical values h_c of the piezometric head jump h in Fig. 1 (modified from Marsland (1953), lengths in cm).

Cofferdam geometry		Experimental critical head h_c	Test name in Fig. 3
$2L$ Width	D_1 Penetration		
7.6	2.5	7.75 ± 0.5	A_1
	5.1	11.6 ± 0.4	A_2
	7.6	14.5 ± 0.3	A_3
	10.2	17.0 ± 1.0	A_4
15.2	2.5	9.5 ± 0.4	B_1
	5.1	15.3 ± 0.3	B_2
	7.6	19.1 ± 1.2	B_3

Among other tests considered by Marsland (1953) to investigate the influence of cofferdam geometry on the failure onset, we focus herein on the seven experimental set-ups summarized in Table 1. These tests were performed after compacting the sand to a fairly loose state, with a measured porosity $n_0 = 0.42$, and for different combinations of the cofferdam width $2L$ and wall penetration length D_1. These quantities are defined in Fig. 2 together with the head h. The same figure reports the values of the other geometrical parameters.

During the experimental tests, the water level inside the cofferdam was slowly lowered (i.e. h was increased) until instability of downstream soil was attained. The onset of such instability, and the corresponding measurement of a "critical" value h_c for h, was identified by Marsland (1953) with the "first sign of movement", i.e. the formation of "small eruptions" or "boils" on the downstream surface, very close to the diaphragm wall. From such description it can be reasonably inferred that the condition considered as critical in the experimental tests was coincident with the onset of erosion piping at point I in Figure 1.

In view of the considerations above, the finite element method proposed by Rotunno et al. (2017b) for the modeling of erosion piping is used herein to simulate the tests in Table 1. We consider the problem domain and the boundary

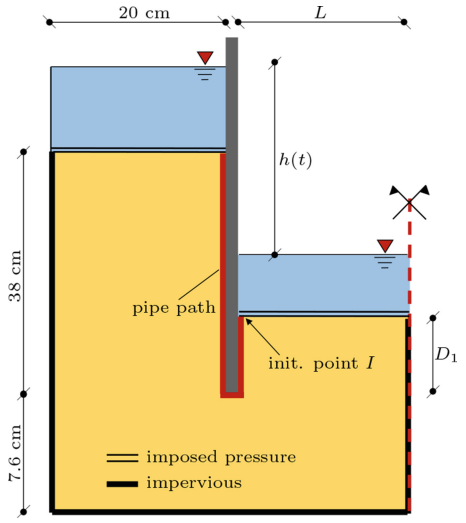

Fig. 2. Simulation of experimental tests on cofferdam physical models: problem domain and boundary conditions. The seven employed combinations of $2L$ and D_1 values are listed in Table 1. The pipe path is highlighted in red, with indication of the initiation point I at the downstream surface.

Table 2. Parameter values employed for the numerical simulation of experimental tests on cofferdam physical model

Parameter	Symbol	Units	Value
Intrinsic density, solid	ρ_s	Mg m^{-3}	2.65
Intrinsic density, water	ρ_w	Mg m^{-3}	1.0
Dynamic viscosity, water	μ_w	kN s m^{-2}	$1.35 \cdot 10^{-6}$
Initial hydr. permeability	k_0	m^2 kPa^{-1} s^{-1}	$1.1 \cdot 10^{-4}$
Initial porosity	n_0	–	0.42
Critical porosity	n_{cr}	–	0.55
Erosion coefficient	c_n	kPa^{-1} s^{-1}	$1.5 \cdot 10^{-1}$
Critical shear stress	τ_{cn}	kPa	$1.6 \cdot 10^{-2}$
Pipe radius	R	m	$5.5 \cdot 10^{-3}$

conditions illustrated in Fig. 2, where, in view of the problem symmetry, only half of the physical model is considered, by imposing the symmetry plane as impervious. We employ 3-noded triangular and 1-D linear finite elements to discretize the soil and the pipe respectively.

Uniform initial fields are assumed for both porosity ($n = n_0$) and permeability ($k = k_0$), whose changes during loading are localized at the pipe tip. The values employed for the model parameters are listed in Table 2. It can be noted

that conventional values are chosen for the intrinsic density of the fluidized-solid phase, as well as for the intrinsic density ρ_w and the dynamic viscosity μ_w of water. The initial porosity n_0 and the permeability k_0 are set consistently with the values measured and assumed, respectively, by Marsland (1953) with reference to the tests in Table 1. The remaining parameters are inferred from back analysis of the experimental tests, and the so-obtained values of the erosion coefficient c_n, pipe radius R and critical shear stress τ_{cn} fall within experimental data ranges available in the review by Knapen et al. (2007). Since measurements of the maximum porosity n_{max} for the given sand are not available in (Marsland 1953), also the value of the critical porosity n_{cr} employed in computations is inferred from back analysis. The obtained ratio n_{cr}/n_0 is consistent with those obtained for other sands for which measures of n_{max} are available (see Rotunno et al. 2017b).

In the numerical results, we consider as "critical" the value h_c of the imposed head difference h causing the onset of the erosion conduit at point I of the downstream outflow surface (see Fig. 2), i.e. the satisfaction of the propagation condition (1) in the first pipe-element candidate. In Fig. 3, measured and computed values of the critical head h_c are plotted as a function of the geometry parameter ratio D_1/L. For all the seven considered tests, a very good agreement is observed between numerical and experimental values, thus confirming that the condition considered as critical in the experimental tests was coincident with the onset of erosion piping.

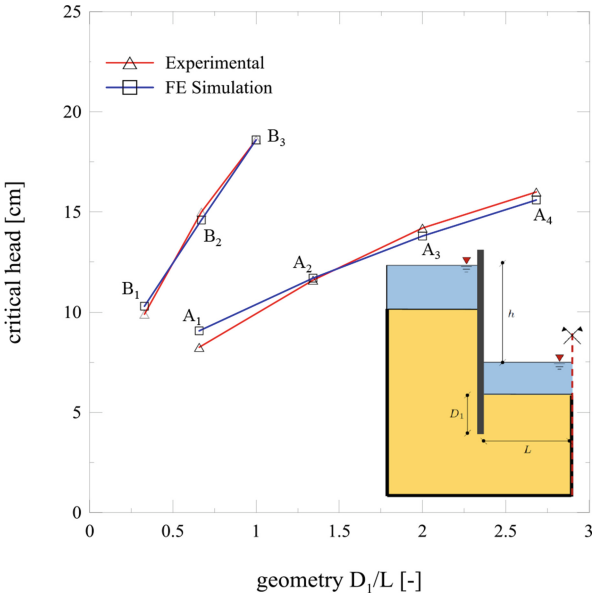

Fig. 3. Simulation of experimental tests on cofferdam physical models: Experimental (Marsland 1953) and numerical values of critical head obtained for the seven tests A_i and B_i listed in Table 3, vs. the geometry ratio D_1/L.

In all the simulated tests, the initiation of the erosion conduit was followed by its propagation up to the upstream surface. A representative example of such evolution is shown in Fig. 4, reporting a sequence of piezometric head and flow fields calculated at different time instants for the test B_1. In these plots, the moving pipe tip is pointed out by the concentration of the piezometric gradient (and thus of flow vectors). In particular, the piezometric gradient close to the pipe tip increases as the erosion front approaches the upstream surface (Fig. 4(b)–(d)). As the pipe is fully formed, the piezometric gradient redistributes along the whole seepage path (Fig. 4(e)).

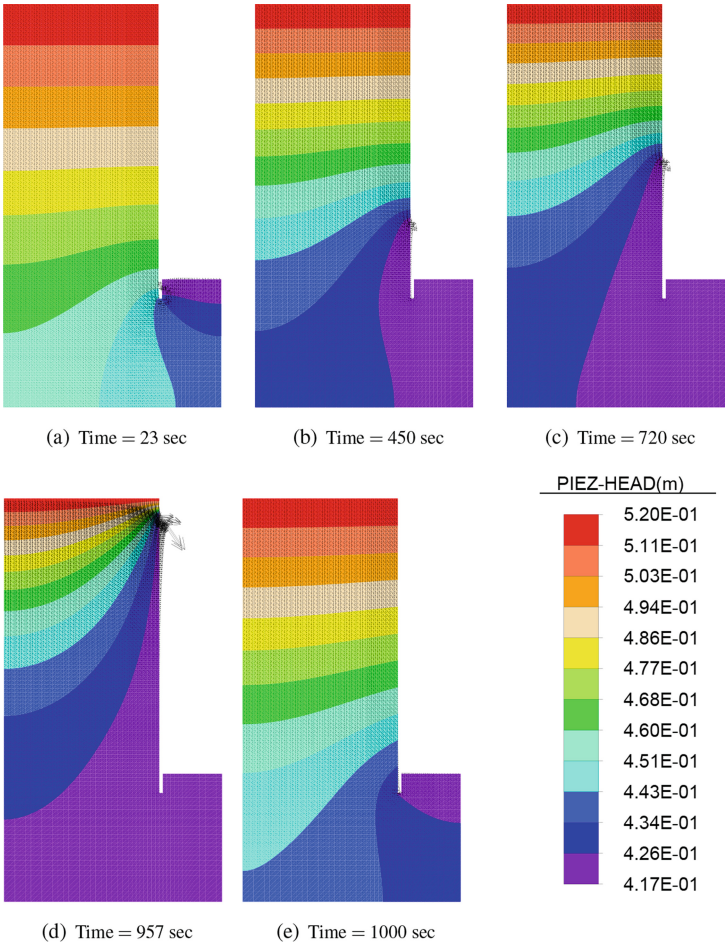

Fig. 4. Simulation of experimental test B_1 on the cofferdam physical model: fields of piezometric head and flow computed during pipe propagation (a–d) up to the full pipe formation (e).

4 Concluding Remarks and Further Developments

The numerical simulation of the experimental tests performed by Marsland (1953) on physical models of cofferdams shows the ability of the finite element method proposed by Rotunno et al. (2017b) in predicting the onset of piping erosion in diaphragm walls in saturated granular soils.

It can be also noted that Marsland (1953) observed "wedge-like" soil failure mechanisms after the aforementioned first signs of movement of the downstream surface. Obviously, the computational modeling of such collapse mechanisms requires a formulation taking into account the hydro-mechanical coupling. To this purpose, employing the formulation by Callari and Abati (2009), Abati and Callari (2014), the extension of the method by Rotunno et al. (2017b) to the coupling with solid skeleton deformation is presented in Rotunno et al. (2018). As a an application example, in the last reference we investigate the interaction between piping and typical failure mechanisms in cofferdams, similar to the case considered herein.

Acknowledgements. Research supported by GDRI GeoMech, GIS VOR 2012, LTDS 2012, PRIN 2010–2011 (2010BFXRHS_004) and DiBT "Computational modeling of erosion" projects. The first author was supported by one PhD fellowship funded by University of Rome "Tor Vergata" and by a VINCI mobility program for PhD in co-tutorship (Université Franco-Italienne). The research also benefited from several invitations of C. Callari at École Centrale de Lyon - LTDS. G. Imperatrice and S. Gargano were actively involved in the preliminary phase of the research, during the preparation of their M.Sc. thesis at the University of Rome "Tor Vergata".

References

Abati A, Callari C (2014) Finite element formulation of unilateral boundary conditions for unsaturated flow in porous continua. Water Resour. Res. 50:5114–5130. https://doi.org/10.1002/2013WR014693

Bauer GE, Scott JD, Shields DH, Wilson NE (1980) The hydraulic failure of a cofferdam. Can. Geotech. J. 17(4):574–583

Bonelli S, Brivois O (2008) The scaling law in the hole erosion test with a constant pressure drop. Int. J. Numer. Anal. Methods Geomech. 32:1573–1595. https://doi.org/10.1002/nag.683

BSI (2004) Eurocode 7: Geotechnical design - Part 1: General rules (BS EN 1997–1:2004). British standards, BSI

Callari C, Abati A (2009) Finite element methods for unsaturated porous solids and their application to dam engineering problems. Comput. Struct. 87:485–501. https://doi.org/10.1016/j.compstruc.2008.12.012

Carman PC (1956) Flow of Gases Through Porous Media, 1st edn. Butterworths, London

Cubrinovski M, Ishihara K (2002) Maximum and minimum void ratio characteristics of sands. Soils Found. 42(6):65–78

Duann SW, Wang RF, Wang CH, Liou GJ (1997) Piping failure of a cofferdam in southern Taiwan. In: Proceedings of international conference on foundation failures, pp 12–13

Fox EN, McNamee J (1948) The two-dimensional potential problem of seepage into a cofferdam. Lond. Edinb. Dublin Phil. Mag. J. Sci. 39(290):165–203
Knapen A, Poesen J, Govers G, Gyssels G, Nachtergaele J (2007) Resistance of soils to concentrated flow erosion: a review. Earth-Sci. Rev. 80(1):75–109
Lominé F, Scholtès L, Sibille L, Poullain P (2013) Modeling of fluid-solid interaction in granular media with coupled lattice Boltzmann/discrete element methods: application to piping erosion. Int. J. Numer. Anal. Methods Geomech. 37(6):577–596
Marsland A (1953) Model experiments to study the influence of seepage on the stability of a sheeted excavation in sand. Géotechnique 3(6):223–241
Ojha C, Singh V, Adrian D (2003) Determination of critical head in soil piping. J. Hydraul. Eng. 129(7):511–518
Pope SB (2000) Turbulent Flows, 1st edn. Cambridge University Press, Cambridge
Regazzoni P, Marot D (2013) A comparative analysis of interface erosion tests. Nat. Hazards 67(2):937–950
Robbins BA (2016) Numerical modeling of backward erosion piping. In: Gómez P, Detournay C, Hart R, Nelson M (eds) Applied numerical modeling in geomechanics 2016, Lima, Perú, 7–9 March 2016, pp 551–558
Rotunno AF, Callari C, Froiio F (2017a) Computational modeling of backward erosion piping. In: Models, simulation, and experimental issues in structural mechanics. Springer, pp 225–234
Rotunno AF, Callari C, Froiio F (2017b) A finite element method for localized erosion in porous media with applications to backward piping in levees, submitted for peer review to international journal
Rotunno AF, Callari C, Froiio F (2018) A computational method for piping erosion in deep excavations, to be submitted
Tanaka T (1994) A case study on piping during excavation for bridge abutments. In: Proceedings of international symposium on underground construction in soft ground, pp 159–162
Terzaghi K (1943) Theoretical Soil Mechanics. Wiley, Hoboken
Tran DK, Prime N, Froiio F, Callari C, Vincens E (2017) Numerical modelling of backward front propagation in piping erosion by DEM-LBM coupling. Eur. J. Environ. Civ. Eng. 21(7–8):960–987
Wang D, Fu X, Jie Y, Dong W, Hu D (2014) Simulation of pipe progression in a levee foundation with coupled seepage and pipe flow domains. Soils Found. 54(5):974–984
Zhang XS, Wong H, Leo CJ, Bui TA (2013) A thermodynamics-based model on the internal erosion of earth structures. Geotech. Geol. Eng. 31:479–492. https://doi.org/10.1007/s10706-012-9600-8

Constitutive Modeling of a Suffusive Soil with Porosity-Dependent Plasticity

Quentin Rousseau[1(✉)], Giulio Sciarra[1], Rachel Gelet[2], and Didier Marot[2]

[1] Institut de Recherche en Génie Civil et Mécanique (UMR CNRS 6183), Ecole Centrale de Nantes, Nantes, France
quentin.rousseau@ec-nantes.fr

[2] Institut de Recherche en Génie Civil et Mécanique (UMR CNRS 6183), Université de Nantes, Saint-Nazaire, France

Abstract. Seepage flow through a deformable porous medium may cause detachment, transport, and even deposition of fines particles which are initially parts of the granular skeleton. This volumetric erosive process is called suffusion. With the aim of modelling the mechanical consequences of suffusion, we propose a constitutive framework for a fully coupled poromechanical model of a suffusive soil. Considering kinematics, suffusion is modeled as a mass transfer from the solid phase to the fluid phase. We therefore introduce, into the classical poromechanical framework, a new state variable ϕ_{er} as the suffusion induced porosity. From thermodynamics of porous media, we deduce a possible coupling between suffusion and seepage flow. In order to capture the mechanical consequences of suffusion, ϕ_{er} is also regarded as an internal variable into a poroplastic model so that it contributes to the hardening rule. Numerical integrations of the developed model were carried out under monotonic drained loading conditions in such a way that a part of the abilities of the model are illustrated.

Keywords: Suffusion · Thermodynamics · Poromechanical model

1 Introduction

Recent experimental studies provided a new understanding of the behaviour of soils under suffusion, see e.g. (Chang and Zhang 2013), (Ke and Takahashi 2015) i.e. when fine grains are dislodged and transported through the voids, between the coarse grains, by seepage flow. Consequences of suffusion concern both the hydraulic and the mechanical properties of the soil, the modification of porosity induced by grain erosion may greatly alter both the hydraulic conductivity and the stress-strain relationship. Our main interest is to capture these two coupled effects parametrizing the problem via an additional internal variable capable of accounting for variations of porosity induced by suffusion. The most important mechanical consequences of this phenomenon are the triggering of plastic strains, possibly changing from contractant to dilatant during the erosion process (Ke and Takahashi 2014), and the strength modification (typically a reduction), which has been extensively observed in drained triaxial tests (Ke and Takahashi

S. Bonelli et al. (Eds.): EWG-IE 2018, LNCE 17, pp. 168–179, 2019.
https://doi.org/10.1007/978-3-319-99423-9_16

2014). At the same time modification of the hydraulic conductivity can alter the pore-water pressure distribution within the soil and consequently the corresponding effective stress. Discrete element analysis has been recently used, see e.g. (Muir Wood et al. 2010), (Scholtés et al. 2010) to simulate the progress of suffusion by particle removal, at different level of the deviator stress q. The simulation corroborated the experimental observation showing that suffusion may trigger the soil state to change from contractant to dilatant. Starting from these evidences some macroscopic models have been proposed. Among others, (Muir Wood et al. 2010) mainly focused their attention on the mechanical effects of erosion and developed a model, in the framework of the critical state theory, in which a volumetric deformation mechanism is added to describe compression due to loosening of the structure. A similar approach has also been developed by (Hicher 2013). (Zhang et al. 2012) treated the erosion problem within the framework of poromechanics and identified a thermodynamically consistent constitutive law for the above mentioned internal variable describing porosity variation due to erosion. Our analysis fits into this scientific framework and tries to explore a more complete way to construct a macroscopic model of suffusion. A poromechanical Lagrangian formulation of the problem is proposed, including a possible coupling between suffusion and seepage flow, which is consistent with the principles of thermodynamics. Moreover an elasto-plastic model parametrized by an internal variable describing the suffusion induced porosity variation is considered. Numerical simulation at the scale of a material point are performed in drained conditions to illustrate the abilities of the model to reproduce the occurrence of plastic deformations induced by erosion.

2 Problem's Definition

2.1 Kinematics

Consider the suffusive soil as a porous medium constituted by two phases: a solid and a fluid. We note s the solid phase, including both erodible and non-erodible grains, and f the fluid phase, constituted by both the pore liquid (noted by wf) and fluidized grains (noted by pf). In this way, the pore liquid and the fluidized grains are not phases but species included in the fluid phase f.

We note $\mathscr{D}$ the current configuration of the porous medium. Following the framework of poromechanics (Coussy 2004), we introduce η, the Eulerian porosity and ϕ the Lagrangian one so that $\phi = J\eta$ where J stands for the determinant of the deformation gradient $\boldsymbol{F}$. The intrinsic density of the solid ρ^s is assumed constant in space and time. By restricting our model to soil mechanics, we also consider the matrix incompressibility hypothesis. A new variable ϕ^{er}, defined as the Lagrangian porosity induced by the sole suffusion process, is introduced in such a way that the matrix incompressibility hypothesis is formulated as follows:

$$J - 1 = \phi - \phi_0 - \phi^{er} \tag{1}$$

where ϕ_0 is the reference Lagrangian porosity. We note ρ^{wf} the intrinsic density of the pore liquid also assumed incompressible. The density of the fluidized grains is the same as that of the solid phase: $\rho^{pf} = \rho^s$. Conversely, the density of the fluid depends on the

concentration C^f of fluidized grains: $\rho^f = \left(1 - C^f\right)\rho^{wf} + C^f\rho^s$. We note $\boldsymbol{v}^s$ the skeleton velocity and $\boldsymbol{v}^f$ that of the fluid phase. If we introduce the Lagrangian hydraulic diffusion vector $\boldsymbol{M}^f = \phi\rho^f\boldsymbol{F}^{-1}\cdot\left(\boldsymbol{v}^f - \boldsymbol{v}^s\right)$ the Lagrangian mass conservation laws of the solid and the fluid phases read as:

$$-\rho^s\frac{d^s\phi^{er}}{dt} = \hat{\Gamma}^s \qquad \text{and} \qquad \frac{d^s\left(\rho^f\left(J+\phi^{er}\right)\right)}{dt} + \nabla_X\cdot\boldsymbol{M}^f = \hat{\Gamma}^f \tag{2}$$

where $\hat{\Gamma}^s$ is the Lagrangian solid source mass and $\hat{\Gamma}^f$ the fluid one. The solid mass source represents the mass of grains leaving or entering the solid skeleton. During suffusion, grains transfer predominantly from the solid phase to the fluid one, which means that $\hat{\Gamma}^f$ is positive and consequently ϕ^{er} increases. Considering the mass balance of the overall porous medium, $\hat{\Gamma}^s$ is the opposite of $\hat{\Gamma}^f$. For convenience, we wrote from now on $\hat{\Gamma}^f = -\hat{\Gamma}^s = \hat{\Gamma}$.

2.2 External Working

Here, the classical poromechanical approach establishing the external working is extended to the case of a porous medium constituted by a superimposed mass exchanging pair of phases. Let $\mathscr{V}$ be the vector space of the velocities on $\mathscr{D}$. For each phase π the term $\boldsymbol{b}^\pi$ indicates the bulk force over $\mathscr{D}$ and $\boldsymbol{t}^\pi$ the surface forces over the boundary $\partial\mathscr{D}$ of $\mathscr{D}$. Then, the external working of the porous medium is defined as follows:

$$P_{ext}\left(\boldsymbol{v}^s, \boldsymbol{v}^f\right) = \int_{\mathscr{D}} \boldsymbol{b}^s\cdot\boldsymbol{v}^s + \boldsymbol{b}^f\cdot\boldsymbol{v}^f\,\mathrm{d}\Omega_t + \int_{\partial\mathscr{D}} \boldsymbol{t}^s\cdot\boldsymbol{v}^s + \boldsymbol{t}^f\cdot\boldsymbol{v}^f\,\mathrm{dS}\,, \quad \left\{\boldsymbol{v}^s, \boldsymbol{v}^f\right\} \in \mathscr{V} \tag{3}$$

Now, let $\boldsymbol{\sigma}^\pi$ be the stress acting on the phase π, such that considering the Cauchy stress theorem we get $\boldsymbol{\sigma}^\pi\cdot\boldsymbol{n} = \boldsymbol{t}^\pi$ for each phase π and everywhere on $\partial\mathscr{D}$. For the fluid constituent, we assume the stress to be isotropic, say $\boldsymbol{\sigma}^f = -\eta p\boldsymbol{\delta}$. Assume now that the porous medium is balanced, which means that $\boldsymbol{b} + \nabla_x\cdot\boldsymbol{\sigma} = (1-\eta)\rho^s\gamma^s + \eta\rho^f\gamma^f + \hat{\rho}\left(\boldsymbol{v}^f - \boldsymbol{v}^s\right)$ with $\boldsymbol{\sigma} = \boldsymbol{\sigma}^s + \boldsymbol{\sigma}^f$ being the total stress, $\boldsymbol{b} = \boldsymbol{b}^s + \boldsymbol{b}^f$ the overall bulk force, $(1-\eta)\rho^s\gamma^s$ and $\eta\rho^f\gamma^f$ the accelerations of the solid and the fluid phases respectively, the term $\hat{\rho}\left(\boldsymbol{v}^f - \boldsymbol{v}^s\right)$ being the contribution to the derivative of momentum due to mass exchange. Let $\boldsymbol{b}^f$ be provided by a volume force $\eta\rho^f\boldsymbol{f}$, the external working follows:

$$\begin{aligned} P_{ext}\left(\boldsymbol{v}^s, \boldsymbol{v}^f\right) = &\int_{\mathscr{D}} \boldsymbol{\sigma} : \mathrm{d}^s + \left((1-\eta)\rho^s\gamma^s + \eta\rho^f\gamma^f\right)\cdot\boldsymbol{v}^s\,\mathrm{d}\Omega_t \\ &\int_{\mathscr{D}} -\nabla_x\cdot\left(\eta p\left(\boldsymbol{v}^f - \boldsymbol{v}^s\right)\right) + \left(\eta\rho^f\boldsymbol{f} + \hat{\rho}\boldsymbol{v}^s\right)\cdot\left(\boldsymbol{v}^f - \boldsymbol{v}^s\right)\mathrm{d}\Omega_t \end{aligned} \tag{4}$$

where the tensor d^π denotes the Eulerian strain rate such that $\mathrm{d}^\pi = \left(\nabla_x\boldsymbol{v}^\pi + \nabla_x^T\boldsymbol{v}^\pi\right)/2$.

3 Thermodynamics

3.1 The First Principle: Internal Energy

The global Eulerian form of the first principle of thermodynamics for a porous medium is the following:

$$P_{ext}\left(\boldsymbol{v}^s,\boldsymbol{v}^f\right)+\mathring{\mathscr{Q}}=\frac{d^s}{dt}\int_{\mathscr{D}}(1-\eta)\rho^s\left(e^s+\frac{\boldsymbol{v}^s\cdot\boldsymbol{v}^s}{2}\right)\mathrm{d}\Omega_t +\frac{d^f}{dt}\int_{\mathscr{D}}\eta\rho^f\left(e^f+\frac{\boldsymbol{v}^f\cdot\boldsymbol{v}^f}{2}\right)\mathrm{d}\Omega_t \tag{5}$$

where $\mathring{\mathscr{Q}}$ is the heat source which could be represented in terms of a heat flux through the boundary $\partial\mathscr{D}$. After several calculations, we write the local Lagrangian form of the first principle as follows:

$$\frac{d^sE}{dt}=\boldsymbol{P}^{(2)}:\frac{d^s\Delta}{dt}-\nabla_X\cdot\left(h^f\boldsymbol{M}^f\right)+\left(\boldsymbol{f}-\gamma^f-\frac{\hat{\Gamma}}{2\left(\rho^f\phi\right)^2}\boldsymbol{F}\cdot\boldsymbol{M}^f\right)\cdot\boldsymbol{F}\cdot\boldsymbol{M}^f-\nabla_X\cdot\boldsymbol{Q} \tag{6}$$

where E, $\boldsymbol{P}^{(2)}$, Δ, h^f and $\boldsymbol{Q}$ are the total Lagrangian internal energy of the porous medium, the second Piola-Kirchhoff total stress tensor, the Green-Lagrange strain tensor, the free enthalpy of the fluid and the pull-back of the heat flux in the reference configuration of the solid, respectively.

3.2 The Second Principle and the Clausius-Duhem Inequality

We consider that the temperature of the solid and the fluid phases is the same such that $T^s=T^f=T$. Following a classical framework, the second principle of the thermodynamics introduces the entropy balance of the porous medium (in the local Lagrangian form):

$$\frac{d^sS}{dt}\geqslant-\nabla_X\cdot\left(s^f\boldsymbol{M}^f+\frac{\boldsymbol{Q}}{T}\right) \tag{7}$$

where S is the total entropy and s^f the entropy per unit mass of the fluid phase. We consider the state variable $\Psi=E-TS$ as the total Helmoltz free-energy of the porous medium such that $\Psi=\Psi^s+m^f\psi^f$. We assume the fluid state laws to be:

$$p=-\frac{\partial\psi^f}{\partial 1/\rho^f}\qquad\text{and}\qquad s^f=-\frac{\partial\psi^f}{\partial T} \tag{8}$$

Then we introduce (6) into (7) to get the Clausius-Duhem inequality. Herein, the total dissipation is denoted by Φ and the Gibbs potential of the fluid by g^f. The Clausius-Duhem inequality reads as:

$$\Phi=\boldsymbol{P}^{(2)}:\frac{d^s\Delta}{dt}+p\frac{d^s\phi}{dt}-g^f\hat{\Gamma}-S^s\frac{d^sT}{dt}-\frac{d^s\Psi^s}{dt}-\frac{\boldsymbol{Q}}{T}\cdot\nabla_XT +\left(-\frac{1}{\rho^f}\nabla_Xp+\left(\boldsymbol{f}-\gamma^f-\frac{\hat{\Gamma}}{2\left(\rho^f\phi\right)^2}\boldsymbol{F}\cdot\boldsymbol{M}\right)^T\cdot\boldsymbol{F}\right)\cdot\boldsymbol{M}\geqslant0 \tag{9}$$

In order to guarantee that this inequality is verified, several assumptions are formulated in what follows. The first assumption concerns the dependency of Ψ^s in terms of state variables: we suggest that the free energy of the solid depends on the temperature, the strain tensor and the porosity induced by suffusion such that: $\Psi^s = \Psi^s(T, \Delta, \Phi_{er})$. Next, the Clausius-Duhem inequality is split into three contributions: one for the solid skeleton Φ^s, one related to thermal effects Φ^{th} and the last one relative to the fluid Φ^f. Each contribution is assumed to be positive. Supplying (1) and (2) in (9), we get the following form of the Clausius-Duhem inequality: $\Phi = \Phi^s + \Phi^f + \Phi^{th}$. The solid disspation reads:

$$\Phi^s = \left(\boldsymbol{P}^{(2)} + pJ\boldsymbol{F}^{-1}\cdot\boldsymbol{F}^{-T} - \frac{\partial\Psi^s}{\partial\Delta}\right) : \frac{d^s\Delta}{dt} - \left(S^s + \frac{\partial\Psi^s}{\partial T}\right)\frac{d^sT}{dt} \geqslant 0 \tag{10}$$

This is the classical form already stated by (Coussy 2004), which implies that the skeleton constitutive law can be described following the soil elasto-plasticity framework. We shall discuss this aspect in the following section. The second contribution concerns the classical thermal dissipation:

$$\Phi^{th} = -\frac{\boldsymbol{Q}}{T}\cdot\nabla_X T \geqslant 0 \tag{11}$$

The novelty of the proposed thermodynamic model is in the fluid dissipation, which reads as:

$$\begin{aligned}\Phi^f = &\left(-\frac{1}{\rho^f}\nabla_X p + \left(\boldsymbol{f} - \gamma^f\right)^T\cdot\boldsymbol{F}\right)\cdot\boldsymbol{M}^f \\ &+ \left(p\left(1 - \frac{\rho^s}{\rho^f}\right) - \frac{\partial\Psi^s}{\partial\phi^{er}} - \frac{\rho^s}{2\left(\rho^f\phi\right)^2}\left(\boldsymbol{F}\cdot\boldsymbol{M}^f\right)^2\right)\frac{d^s\phi^{er}}{dt} \geqslant 0\end{aligned} \tag{12}$$

where we can identify the first term of Φ^f as the so-called "Darcy's term". The proposed form of Φ^f allows to consider the coupling between the diffusion velocity $\boldsymbol{M}^f$ and the variation of porosity induced by suffusion ϕ^{er}:

$$\begin{pmatrix}\boldsymbol{M}^f \\ \dfrac{d^s\phi^{er}}{dt}\end{pmatrix} = \begin{Bmatrix}\mathscr{K} & \mathscr{C}^{flu} \\ \mathscr{C}^{suff} & \mathscr{R}\end{Bmatrix}\cdot\begin{pmatrix}-\dfrac{1}{\rho^f}\nabla_X p + \left(\boldsymbol{f} - \gamma^f\right)^T\cdot\boldsymbol{F} \\ p\left(1 - \dfrac{\rho^s}{\rho^f}\right) - \dfrac{\partial\Psi^s}{\partial\phi^{er}} - \dfrac{\rho^s}{2\left(\rho^f\phi\right)^2}\left(\boldsymbol{F}\cdot\boldsymbol{M}^f\right)^2\end{pmatrix} \tag{13}$$

where $\mathscr{K}$ is the classical permeability tensor, $\mathscr{R}$ is a real to be identified and $\mathscr{C}^{flu}$ and $\mathscr{C}^{suff}$ are coupling terms. To ensure the positivity of the fluid dissipation, the coupling matrix is required to be symmetric and positive definite which implies $\mathscr{R}$ to be positive, $\mathscr{C}^{flu} = \mathscr{C}^{suff}$ and also the determinant of the matrix to be positive. At this stage, no assumption is made on the magnitude of the direct fluxes compared with the coupled ones. In a quasi-static context, the inertial terms $\frac{\rho^s}{2\left(\rho^f\phi\right)^2}\left(\boldsymbol{F}\cdot\boldsymbol{M}^f\right)^2$ and γ^f may reasonably be neglected.

The above coupled constitutive relationship should be a relevant starting point to study the suffusion process. If the components of the permability tensor are easily measurable, there is a real scientific challenge to measure the coupling term and $\mathscr{R}$.

4 Porosity Dependent Plasticity

We now focus on the local stress-strain behaviour of the elasto-plastic skeleton. While the above development assumed finite strains, we now consider the small strain hypothesis to hold true. Consequently, the second Piola-Kichhoff stress tensor $\boldsymbol{P}^{(2)}$ is assimilated to the Cauchy one σ, and the Green-Lagrange tensor Δ to the linearized strain tensor $\varepsilon = 1/2\left(\nabla \boldsymbol{u} + \nabla^T \boldsymbol{u}\right)$. We assume the additive strain partition such that the total strain tensor is equal to the sum of an elastic and a plastic contributions: $\varepsilon = \varepsilon^e + \varepsilon^p$. Furthermore considering (10), we introduce the effective stress concept σ' such that $\sigma' = \sigma + p\boldsymbol{\delta}$. In this way, the elasto-plastic model will be formulated in terms of effective stress; in particular an extention of Nova's Sinfonietta-Classica model (Nova 1988) is proposed. Sinfonietta Classica is based on both the Cam-Clay model (Schofield and Wroth 1968) and the Matsuoka-Nakai criterion (Matsuoka and Nakai 1982). In particular, it allows to limit the pure compressive stress state to finite values. If this model well captures the monotonic behaviour of sands, it is also able to describe the behaviour of soft rocks. In this way, our developments could be expanded and then used for the study of internal erosion of rocks, for example within oil reservoirs (Vardoulakis et al. 1996), (Papamichos and Vardoulakis 2005). The model is non-associated, the hardening variable is the preconsolidation pressure p_c which evolves following a hardening law given in terms of ε^p. To introduce the effects of suffusion on the mechanical behaviour of the skeleton, we introduce ϕ^{er} as a second internal variable governing the hardening variable evolution.

4.1 Flow Rule: Loading Surface and Plastic Potential

Our study takes place into the soil elasto-plasticity framework. We supposed the existence of a loading function f of σ' and p_c defining the elastic domain $\mathbb{S}$ and bounded by the loading surface $\partial\mathbb{S}$:

$$\mathbb{S} := \left\{\sigma' \in \mathbb{R}^3 \times \mathbb{R}^3, p_c \in \mathbb{R} \,|\, f\left(\sigma', p_c\right) < 0\right\} \tag{14a}$$

$$\partial\mathbb{S} := \left\{\sigma' \in \mathbb{R}^3 \times \mathbb{R}^3, p_c \in \mathbb{R} \,|\, f\left(\sigma', p_c\right) = 0\right\} \tag{14b}$$

The evolution of the plastic strain occurs when the stress state is on the loading surface, $f = 0$, and its evolution is such that $\dot{f} = 0$. If one of this two conditions is not fulfilled, the strain evolution remains purely elastic. Whereas the original model uses a hypoelastic law, our study favored a linear, isotropic elastic law for simplicity. Hence, we use the following incremental Hooke law: $\dot{\sigma}' = \mathbb{C} : (\dot{\varepsilon} - \dot{\varepsilon}^p)$ where $\mathbb{C}$ is the Hooke tensor. Concerning the plastic evolution of ε, we consider the flow rule for a non-associated material:

$$\dot{\varepsilon}^p = \dot{\lambda}\frac{\partial g}{\partial \sigma'} \tag{15}$$

where $\dot{\lambda}$ is the so-called plastic multiplier and g a plastic potential. We introduce p' the first invariant of σ' such that $p' = -1/3Tr(\sigma')$ and s' the deviatoric part of σ'. The second invariant of s' is $J_2 = s' : s'/2$, where : denotes the scalar product between second order tensors, and we define the deviatoric stress q as $q = \sqrt{3J_2}$. We then introduce the deviatoric ratio tensor $\xi = s'/p'$ and its second and third invariant $J_{2\xi}$ and $J_{3\xi}$

are such that $J_{2\xi} = \xi : \xi$ and $J_{3\xi} = 3\det(\xi)$ (Nova 1988). As already said we adopt the Sinfonietta-Classica plastic model so that the loading function f and the plastic potential g are:

$$f\left(\sigma', p_c\right) = 3\beta\left(\mu - 3\right)\ln\frac{p'}{p_c} + \frac{9}{4}\left(\mu - 1\right)J_{2\xi} - \mu J_{3\xi} \leqslant 0 \tag{16a}$$

$$g\left(\sigma', p_g\right) = 9\left(\mu - 3\right)\ln\frac{p'}{p_g} + \frac{9}{4}\left(\mu - 1\right)J_{2\xi} - \mu J_{3\xi} \tag{16b}$$

where μ is defined by $\mu = \left(9 - Z^2\right)/\left(3 - Z^2 + 2Z^3/9\right)$ and Z denotes the slope of the phase transition line: $Z = 6\sin\varphi/\left(3 - \sin\varphi\right)$. Here, φ physically represents the friction angle measured at the transition between a dilative and a contractive behavior. When the stress state is such that $q/p > Z$ then the soil behaviour is dilative, and inversely when $q/p < Z$ the soil is contractive. The parameter p_g should be non-zero and positive but the knowledge of its value is of no importance since only the derivative of g with respect to σ' is considered in all computations.

4.2 Hardening Law and Porosity Parametrization

We note $\varepsilon_v^p = Tr\left(\varepsilon^p\right)$ the volumetric plastic strain and ε_D^p the deviatoric plastic strain. The original Sinfonietta-Classica hardening law links the variations of the preconsolidation pressure with the plastic strain rates:

$$\dot{p_c} = \frac{p_c}{\beta_p}\left(-\dot{\varepsilon}_v^p + \varkappa\sqrt{\dot{\varepsilon}_D^p : \dot{\varepsilon}_D^p} + \varpi\sqrt[3]{\det\dot{\varepsilon}_D^p}\right) \tag{17}$$

where β_p is a non-dimensional plastic stiffness which can be regarded as an oedometric compressibility, $\varkappa$ is a non dimensional coefficient traducing the contribution of the deviatoric plastic strain to hardening and ϖ is a non-dimensional coefficient traducing the effect of the specific direction of the plastic strain evolution. In many cases, this parameter can be neglected.

Consider the case of a soil which is not subjected to any degradation inducing changes of porosity, the matrix incompressibility condition links $\dot{\varepsilon}_v^p$ with the variation of porosity and consequently allows to interpret the first term on the right hand side of (17) as the effect of porosity changes on the variations of the preconsolidation pressure. Consider now the case of a soil subjected to suffusion and assume that suffusion causes porosity changes. As explained in the previous subsection, we have introduced ϕ^{er}, an irreversible suffusion-induced porosity, as an internal hardening variable which is therefore assumed to play a role similar to that of a volumetric plastic strain. The new formulation of the matrix incompressibility conditions for a suffusive soil reads:

$$\varepsilon_v^e + \varepsilon_v^p = \phi^p + \phi^e - \phi_0 - \phi^{er} \tag{18}$$

Next we consider only the rate of irreversible terms: $\dot{\varepsilon}_v^p + \dot{\phi}^{er} = \dot{\phi}^p$ and we introduce this relationship into the hardening law assuming the first term to be given by the variation of the plastic porosity:

$$\dot{p_c} = \frac{p_c}{\beta_p}\left(-\left(\dot{\varepsilon}_v^p + \dot{\phi}^{er}\right) + \varkappa\sqrt{\dot{\varepsilon}_D^p : \dot{\varepsilon}_D^p} + \varpi\sqrt[3]{\det\dot{\varepsilon}_D^p}\right) \tag{19}$$

Equation (19) describes soil material hardening due to mechanical loading and suffusion. This hardening law allows a variation of the preconsolidation pressure solely induced by suffusion, i.e. $\dot{\phi}^{er} \neq 0$ while $\dot{\varepsilon}_v^p = 0$. If we assume that $\dot{\phi}^{er}$ is positive during suffusion, then the preconsolidation pressure tends to progressively decrease and the loading surface $\partial\mathbb{S}$ to shrink on the stress state. In particular, imagine a suffusion process without change of the stress state: $\dot{\sigma}' = 0$. If σ' is fixed and such that the soil behaviour is fully elastic $f(\sigma', p_c) < 0$, then the preconsolidation pressure may decrease until the loading surface reaches the stress state, with no plastic strains. Once the stress state reached by the loading surface, the preconsolidation pressure can no more decrease since the stress state must remain on the loading surface. Then, to balance the increase of ϕ^{er} and keep p_c constant, the plastic strain ε^p necessarily varies. Depending on the stress ratio q/p' during suffusion, the volumetric and/or deviatoric plastic strain vary preferentially. Two specific cases may be described: if $q/p' = 0$ only the volumetric plastic strain varies, inversely if $q/p' = Z$ only the deviatoric plastic strain varies.

To enable the model to reproduce the phase transition (from dilation to contraction) during suffusion, we assumed that the friction angle φ, and consequently Z may depend on ϕ^{er}. We assume that φ varies from an initial value noted φ_{max} to a minimal one φ_{min} reached when every erodible grains are detached. To construct this dependance, we consider that during suffusion, the first set of detached particles does not take parts to the force chains so that the friction angle is not affected during the early evolution of ϕ^{er}. Next, we assume that a threshold value of ϕ^{er} exists beyond which φ is strongly affected by the increase of porosity. This threshold is supposed to be proportional to the maximum of ϕ^{er} i.e. $\phi_c^{er} = A\phi_{max}^{er}$ with $0 \leqslant A \leqslant 1$. The following transition law is therefore proposed:

$$\begin{aligned}\varphi(\phi^{er}) = &\frac{1}{2}\varphi_{min}\left(1+\tanh\left(\frac{1}{l}\left(\phi^{er} - A\phi_{max}^{er}\right)\right)\right)\\ &+\frac{1}{2}\varphi_{max}\left(1+\tanh\left(\frac{1}{l}\left(A\phi_{max}^{er} - \phi^{er}\right)\right)\right)\end{aligned} \tag{20}$$

where l is a non-dimensional width factor. The higher the value of l is, the smoother the transition from φ_{max} to φ_{min} will be. If the effective stress state is fixed, the consequence of the decrease of φ is the following: when the stress state is such that $q/p' < Z(\varphi_{min})$, then the soil is contractive and will stay contractive during suffusion. When the stress state is above the intact phase transition line, i.e. $q/p' > Z(\varphi_{max})$, the soil is dilative and will stay dilative during suffusion. Finally, if the stress state leads to $Z(\varphi_{min}) < q/p' < Z(\varphi_{max})$ then the soil is first contractive and becomes dilative during suffusion. From now-on, we call this region the phase transition zone. We recall that the present phenomenon is not interpreted as an hardening process so that ϕ^{er} acts simply as a parameter of Z. To conclude, the porosity dependant hardening law enables our model to reproduce strains variations during suffusion, while the Z parametrization governs the nature of this strain variation: purely dilative, purely contractive, or dilative then contractive. This latter parametrization is most probably strongly influenced by the grain size distribution of each soil (Muir Wood et al. 2010).

4.3 Numerical Results

With the aim of illustrating the ability of the elasto-plastic model to qualitatively reproduce the mechanical behaviour of a suffusive soil, different drained triaxial loading paths are considered. In what follows, we do not consider how the suffusion porosity is induced by the seepage flow and we limit our analysis of the suffusion process to a quasi-static variation of ϕ^{er} considered as a loading parameter. The triaxial loading paths are split in three steps: the first one is a strain driven drained pre-loading, during which a stress ratio $(q/p')_i$ is reached. Next, this stress state is kept constant during the whole suffusion process. To mimic the suffusion process, increments of ϕ^{er} are carried out from the value 0 to ϕ^{er}_{max}. When the maximum value of ϕ^{er} is reached, a new strain driven drained loading is carried out until the maximum strength of the soil is reached. We perform different loading paths, related to different values of $(q/p')_i$, represented by the symbol $*$ (see Fig. 1). The tested material is a fictive one and is characterized by arbitrary but realistic parameters for a sandy soil, say $E = 15\,\text{MPa}$, $\nu = 0.33$, $\beta = 1.5$, $p_{co} = 150\,\text{kPa}$, $\beta_p = 2.5\,\text{E} - 3$, $\varkappa = 0.3$, $\varpi = 0$. Finally the set of the phase transition parameters is such $\varphi_{min} = 24$, $\varphi_{max} = 30$, $A = 0.5$, $l = 0.01$ $\phi^{er}_{max} = 0.2$.

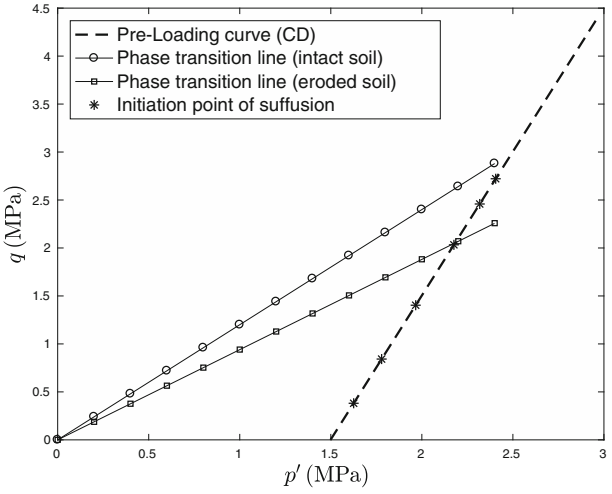

Fig. 1. Drained loading-pathes in the Cambridge plane

The volumetric plastic strain is plotted in Fig. 2 which reproduces the experimentally observed suffusion induced strain (Ke and Takahashi 2014). Furthermore, the larger the stress ratio $(q/p')_i$ before suffusion is, the larger the cumulative plastic strain (deviatoric and volumetric) will be. The transitive behaviour of a soil during suffusion (from contractive to dilative) is recovered if the stress state at the beginning of suffusion is into the phase transition zone. After suffusion, the volumetric plastic strain tends asymptotically to a given line, regardless of the value of the stress ratio at the beginning of suffusion. Also the maximum strength tends towards an asymptotic value independently of $(q/p')_i$ (see Fig. 3). Both the final value of the total strain and the variation

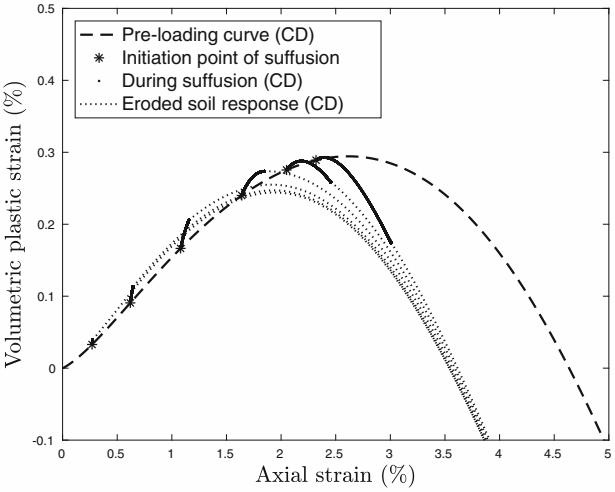

Fig. 2. Drained volumetric response of a suffusive soil

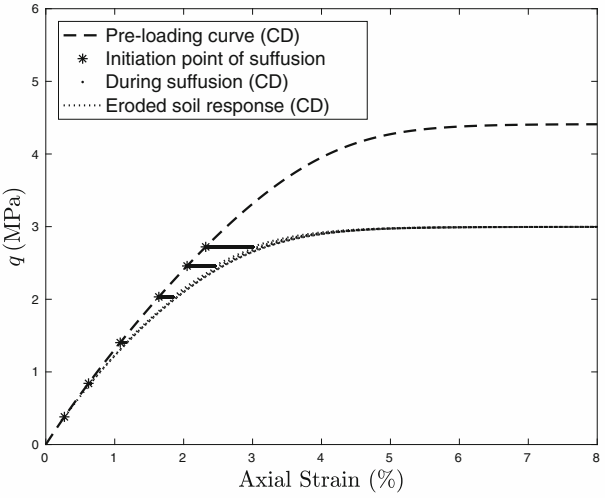

Fig. 3. Drained stress-strain response of a suffusive soil

ranges of ϕ^{er} are imposed and equal for every $(q/p')_i$, then only the reponse to suffusion depends on $(q/p')_i$, the final volumetric plastic strain being independant of $(q/p')_i$. Actually, the maximal suffusion induced porosity ϕ^{er}_{max} should depend on the mechanical configuration of the skeleton (i.e. to the stress-strain state) and the hydraulic loading. In other words, the quantity of removable particles, for all admissible hydraulic loadings, should depend on the stress state applied over the soil. Hence, the lack of relation between ϕ^{er} and $(q/p')_i$ is somewhat artificial and has been chosen only to demonstrate the abilities of the model. Regarding the tangent modulus of the suffusive soil (see Fig. 3), it appears lower than that of the intact soil even if there is no suffusive degradations of the elastic properties. This is a consequence of the changes in the phase transition line slope. By changing the values of the derivatives of f and g with respect to σ', the tangent stiffness of the suffusive soil is different from that of the intact soil.

5 Conclusion

The present study establishes a new thermodynamically consistent approach to the analysis of suffusion. We proposed that the soil response to suffusion and hydraulic loading are coupled, which is expected be the starting point of the formulation of a constitutive law governing the kinetics of suffusion. Furthermore, we established a porosity dependant elasto-plastic model as a possible way to model the mechanical effects of suffusion. Further developments will be devoted to the identification of the constitutive parameters $\mathscr{C}^{suff}$ and $\mathscr{R}$ applying double scale homogenization techniques to a properly defined micro-mechanical model of the suffusion process.

References

Chang DS, Zhang LM (2013) Critical hydraulic gradients of internal erosion under complex stress states. J. Geotech. Geoenviron. Eng. 139(9):1454–1467. https://doi.org/10.1061/(ASCE)GT.1943-5606.0000871

Coussy O (2004) Poromechanics. Wiley, Chichester

Hicher PY (2013) Modelling the impact of particle removal on granular material behaviour. Géotechnique 63(2):118–128. https://doi.org/10.1680/geot.11.P.020, https://hal.archives-ouvertes.fr/hal-01529503

Ke L, Takahashi A (2014) Experimental investigations on suffusion characteristics and its mechanical consequences on saturated cohesionless soil. Soils Found. 54(4):713–730. https://doi.org/10.1016/j.sandf.2014.06.024

Ke L, Takahashi A (2015) Drained monotonic responses of suffusional cohesionless soils. J. Geotech. Geoenviron. Eng. 141(8):04015032. https://doi.org/10.1061/(ASCE)GT.1943-5606.0001327

Mastuoka H, Nakai T (1982) A new failure condition for soils in three dimensional stresses. In: Vermeer PA, Luger HJ (eds) Proceedings of the IUTAM symposium deformation and failure of granular materials. Delft, pp 253–263

Muir Wood D, Maeda K, Nukudani E (2010) Modelling mechanical consequences of erosion. Géotechnique 60(6):447–457. https://doi.org/10.1680/geo.2010.60.6.447

Nova R (1988) "Sinfonietta Classica" : an exercice on classical soil modelling. In: Saada AS, Bianchini GF (eds) Constitutive equations for granular non-cohesive soils, Balkema, Rotterdam, pp 510–519

Papamichos E, Vardoulakis I (2005) Sand erosion with a porosity diffusion law. Comput. Geotech. 32:47–58

Schoefield AN, Wroth CP (1968) Critcal State Soil Mechanics. McGraw-Hill, New York City

Scholtès L, Hicher PY, Sibille L (2010) Multiscale approaches to describe mechanical responses induced by particle removal in granular materials. C. R. Méc. Mec. 338(10–11):627–638. https://doi.org/10.1016/j.crme.2010.10.003

Vardoulakis I, Stavropoulou M, Papanastasiou P (1996) Hydro-mechanical aspects of the sand production problem. Transp. Porous Media 22:225–244

Zhang XS, Wong H, Leo CJ, Bui TA, Wang JX, Sun WH, Huang ZQ (2012) A thermodynamics-based model on the internal erosion of earth structures. Geotech. Geol. Eng. 31(2):479–492. https://doi.org/10.1007/s10706-012-9600-8

Micro-scale Flow Conditions Leading to the Onset of Erosion

Alexander Scheuermann[1(✉)], H. M. D. Harshani[1], and S. A. Galindo-Torres[2]

[1] University of Queensland, St Lucia, QLD, Australia
a.scheuermann@uq.edu.au
[2] University of Liverpool, Liverpool, UK

Abstract. The flow conditions influencing the onset of contact erosion have been investigated physically using a novel setup based on the Particle Imaging Velocimetry (PIV) and numerically using a coupled DEM-LBM (Discrete Element Method-Lattice Boltzmann Method) approach. The flow conditions at the transition from base to filter material were experimentally quantified and computationally simulated resulting in a satisfactorily good agreement. An interesting and important outcome of these investigations is that the maximum flow velocity is not appearing in the base material, but in the constriction of the filter material in the transition zone from base to filter just above the surface of the base material. A generalised relationship between flow velocity and geometrical conditions at the transition zone was developed based on the Froude number. The characteristic evolution of the curve clearly shows the competition between hydraulic and geometric/mechanical conditions influencing the onset of contact erosion.

Keywords: Contact erosion · Particle Imaging Velocimetry (PIV) DEM-LBM

1 Introduction

Contact erosion is probably the most comprehensively investigated form of erosion. Starting with the first geometric criteria (Schwarz and Prinz 1923; Bertram 1940; Peck and Terzaghi 1948), numerous investigations have been conducted to develop criteria – either geometric or hydraulic – for more realistic situations with respect to the uniformity of the particle size distribution, the statistical variation of the particle size distribution or the direction of flow (Schuler and Brauns 1993). Although, the hydro-mechanical interconnection is well understood on the macro-scale, the processes taking place on the micro-scale influencing and supporting the onset and at a later stage progress of erosion are still not fully understood. For example, questions concerning the local conditions supporting the onset of erosion or the mixing process of fine (base) and coarse (filter) material during the progress of erosion are still open.

A novel Particle Imaging Velocimetry (PIV) system has been developed at the University of Queensland allowing the investigation of flow processes on the micro- or pore-scale. The measurement results from the PIV system were used to verify a

S. Bonelli et al. (Eds.): EWG-IE 2018, LNCE 17, pp. 180–188, 2019.
https://doi.org/10.1007/978-3-319-99423-9_17

computational model combining the Discrete Element Method with the Lattice Boltzmann Method (DEM-LBM). With this model, it was possible to consider base/filter combinations that could not be experimentally investigated. DEM-LBM models have been successfully used in the past for simulating fluid-particle interaction in 2D (Lominé et al. 2013; Tran et al. 2017). The model used in this study is considering the processes in 3D and is thus more realistic. Within this study, the simulation results formed the basis for the development of a generalized relationship for describing the onset of erosion on the pore-scale based on the Froude number. The presented contribution introduces both methods and presents the generalized relationship.

2 Experimental and Computational Methods

2.1 Particle Imaging Velocimetry (PIV)

PIV is a common method for investigating flow processes in wind tunnels or in flumes to measure the distortions of the flow field around obstacles (Raffel et al. 2007). The observation of flow processes in porous media is much more difficult as particles of a solid material is required that is refractive-index-matched with the used liquid. Usually, glass beads are used in combination with fluid mixtures made of glycerine and additives. At the same time, laser systems are used to illuminate the flow field in combination with a synchronized high speed camera. Seeding particles with neutral buoyancy in the size range of micrometres are used to highlight the flow within the flowing liquid. PIV systems have been used in the past for investigating contact erosion due to horizontal water flow parallel to the interface of a base/filter combination (Beguin et al. 2012).

The PIV system developed at the School of Civil Engineering of the University of Queensland is innovative because of two reasons. Firstly, it uses hydrogel beads as solid material that is refractive-index-matched with pure water. The advantage is that conventional methods can be used to measure the pressure conditions as well as the flow rate with commercially available and affordable devices. Secondly, the illumination system is LED based, which does not require the usual high standards in terms of safety.

Figure 1 introduces the PIV system with the main features. Figure 1(a) shows the system in operation with the green illumination field and the high-speed camera in front of the sample holder. The system is enclosed in a tent within the laboratory to provide the necessary darkness for operating the PIV system as can be seen in Fig. 1(b). The sample holder is quadratic in shape to provide even faces that are ideal for illuminating the sample and recording the pictures. A screen made of coarse glass beads in the funnel-shaped entrance into the sample holder homogenizes the flow, and a grid above the screen provides a gap that can easily be simulated computationally.

A reservoir with pump and overflow outside the tent provides the constant head boundary condition for the set-up. A valve at the outlet of the overflow controls the flowrate. The seeding particles with a size of 15 μm are mixed to the water in the reservoir before each test. Seeding particles accumulate on the surface of the hydrogel

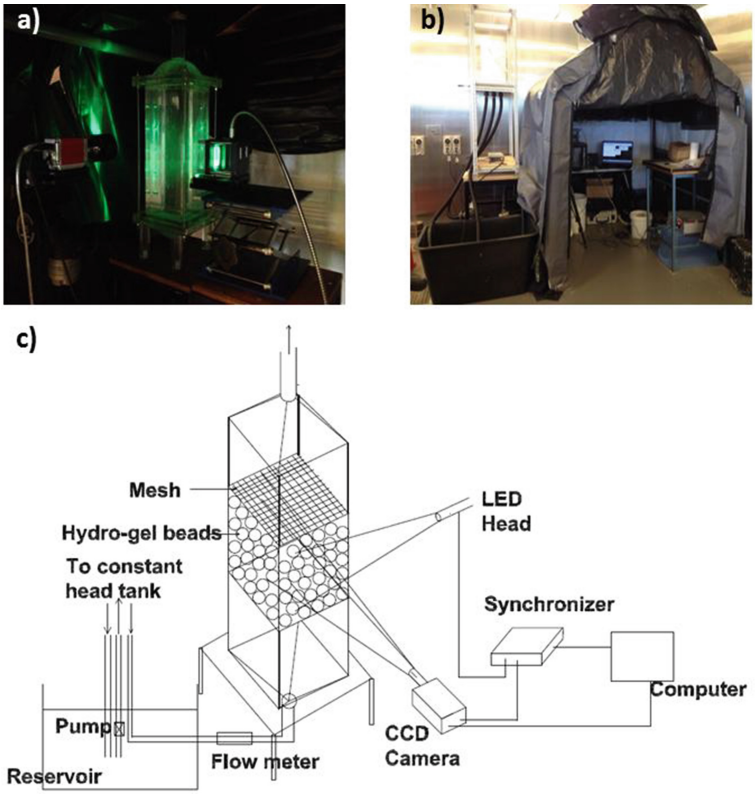

Fig. 1. PIV System at the University of Queensland. (a) Sample holder with illumination source in action and high speed camera, (b) tent with complete PIV system, (c) schematic of the PIV set-up including hydraulic system.

beads with time after several runs of tests. Flushing with clear water cleans the gel beads and allows their use for further tests.

Recordings have been conducted with a spatial resolution of 25 μm/pixel. The pulse delay time was adjusted to ensure that the displacement of the tracer particles stay between 1.5 and 4.8 pixels to allow cross-correlation for the used interrogation windows and the calculation of the most probable particle displacement within the interrogation window. For this analysis, the pictures were divided into 24 by 24 interrogation windows.

The analysis of the recordings is done with the PIVView 2c software and involves a stepwise procedure. The measured pictures with the high-speed camera are in fact composed of two pictures taken with a given time step (Fig. 2(a)). The solid particles are covered in a first step with a mask to avoid mistakes in the analysis as the particles attached to the surface of the hydrogel beads could be considered as moving particles in the flowing liquid (Fig. 2(b)). After placing the masks, the pictures are binarized in order to highlight the floating particles by applying a high-pass filter with appropriate threshold values (Fig. 2(c)). The velocity of an individual pair of pictures is calculated

based on a cross-correlation scheme with a combination of multi-grid interrogation process and a grid refinement technique. By taking a sufficient number of individual pictures and the elimination of outliners, an averaged flow field is determined that can be presented either as trajectories (Fig. 2(d)) or as a contour plot (Fig. 2(e)). A detailed introduction of the system and the analysis of the PIV measurements can be found in Harshani et al. (2016).

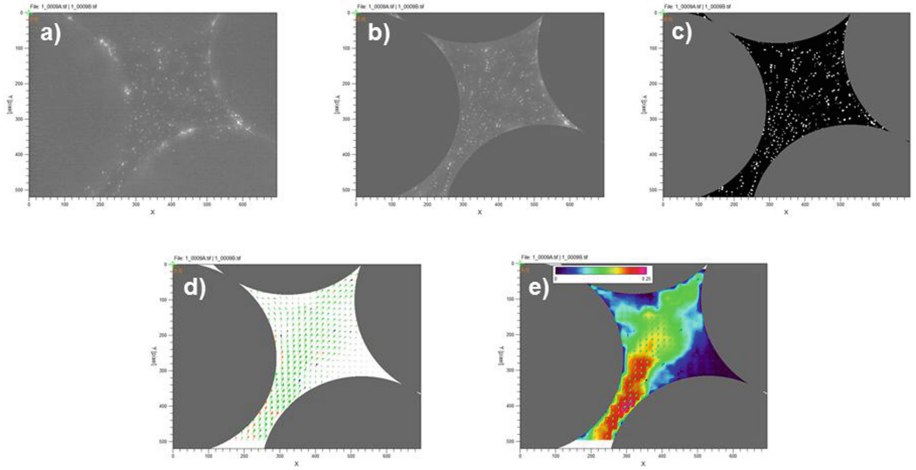

Fig. 2. Procedure for analyzing PIV measurements. (a) Recorded picture, (b) picture with masks to cover areas of particles, (c) binarized picture to highlight seeding particles, resulting flow field as (d) trajectories of flow velocity or (e) contour plot.

2.2 Coupled DEM-LBM Approach

For the presented research, a DEM-LBM method developed by Galindo-Torres was applied (Galindo-Torres et al. 2015). The particles are idealized as spheres to model filter and base material that are subjected to forces applied by neighbouring particles, by gravity and by the fluid flow. The fluid flow is simulated using the Lattice Boltzmann Method based on a regular lattice grid. The three-dimensional flow in the presented work was simulated using a D3Q15 scheme that is a common scheme for representing 3D flow conditions (Fig. 3).

The coupling between DEM and LBM to represent the interaction between fluid and solid phase (Bouzidi et al. 2001) is solved by using a method implemented and simplified by Galindo-Torres (2013). In this method, the volume fraction covered by a solid particle in a lattice cell is used to correct the forces acting on a DEM particle (Fig. 3). Galindo-Torres suggested a computationally efficient approach for calculating the volume fraction by using the intersection length between LBM lattice and DEM particle. The parameters for the DEM-LBM model can be found in Harshani et al. (2015). The coupling with the DEM is based on the Immersed Boundary Method as

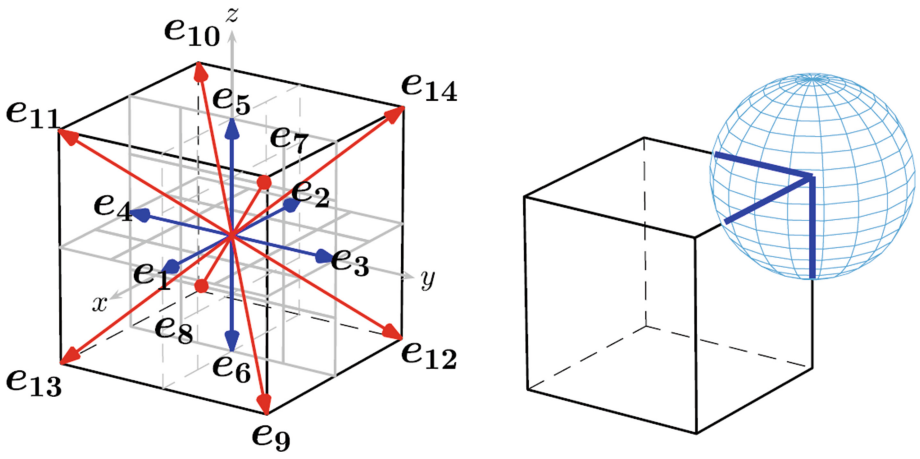

Fig. 3. Left: LBM cell for the D3Q15 scheme showing each flow direction of the 15 possible discrete velocities. Right: DEM sphere interacting with a lattice of the LBM.

explained in Galindo-Torres (2013). Pressure boundary conditions were imposed at both boundaries to control the hydraulic head conditions.

3 Results and Discussion

3.1 Flow Conditions at the Transition from Base to Filter

The conditions of the flowing liquid at the transition from the fine base material into the course filter material was experimentally investigated and computationally simulated in a one-to-one comparison with exactly the same sizes for base and filter material and the same porosities. For this comparison, the complete width of the sample was divided into small sections covered by the PIV system, and the flow velocities within the pore space at different elevations according to the chosen resolution in the simulations and the size of the interrogation windows were averaged. With the PIV system, the flow trajectories in the third – out of plane – dimension are not captured. In order to allow a direct comparison between simulations and experiment, the simulated 3D flow field was analysed in a way to match the procedure of the PIV analysis and thus to provide the same information content. Figure 4 shows the resulting comparison between experimentally measured and computationally simulated flow conditions.

The graph in Fig. 4 shows the normalized pore velocity determined based on the measured filter velocity $V_m = Q/A$. A normalized flow of one means that the pore velocity corresponds to the filter velocity of the packing. The pore velocity was calculated as a mean velocity in that elevation averaging all measured or computationally simulated velocities over the entire width of the sample, neglecting the existence of velocity profiles.

The comparison of Fig. 4 shows nicely the good agreement between experiments and simulations. All flow velocities seem to be slightly elevated near the transition with

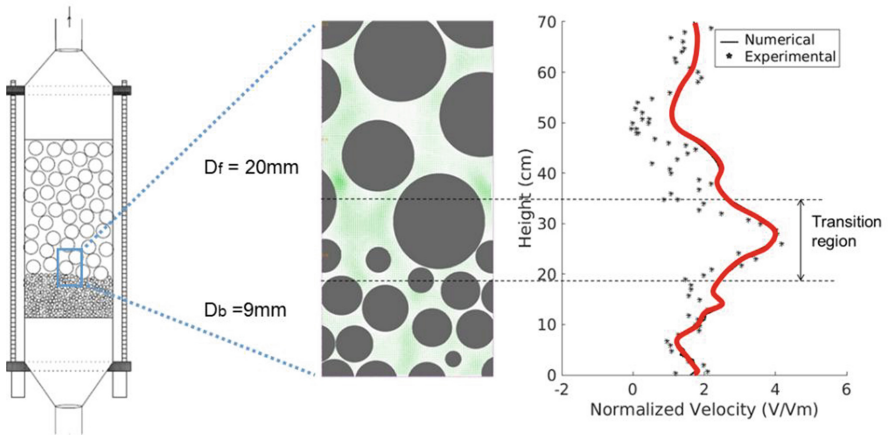

Fig. 4. Comparison of flow conditions at the transition from base to filter from experiments and simulation. Left: Model with base/filter combination (schematic), middle: simulation result, right: velocity profile simulated (in red) and measured (symbols).

the maximum of nearly four times the filter velocity occurring in the constrictions of the first layer of filter particles just above the base layer. This observation is somewhat surprising, as the highest velocity should be expected in the small mixing area where the porosity reaches locally minimum – so to say over a small elevation range – due to mass conservation. Physical experiments and computational simulations have both independently revealed this observation.

As can be seen in Fig. 5, the maximum flow velocity always occurs in the constriction of the first filter particles just above the base material regardless of the size of the constriction. The flowing water in the base material hits the much larger filter particles where the water flow is re-directed around the filter particles. When exiting the base layer the velocity reaches the maximum in the constrictions being the smallest openings formed by the filter particles. This observation needs to be further investigated in future experimental and numerical studies especially for conditions where there is a more pronounced mixing zone between base and filter.

3.2 Criterion for the Onset of Erosion

The flow velocity in the constrictions of the filter layer for the situation when erosion sets in was used to define a criterion for the onset of contact erosion. This critical velocity was determined for the situation when the first particle started to get dislodged within a constriction of the filter. Based on computational simulations with three base/filter combinations with size ratios between filter and base particle of 6, 8 and 10 (see Fig. 6) different constriction sizes have been selected and analyzed. The width of the constriction L_p was normalized using the diameter of the base material D_b. The Froude number Fr describes the ratio of inertial to gravitational forces, and is used in hydromechanics to describe different flow regimes. In the present study, Fr is

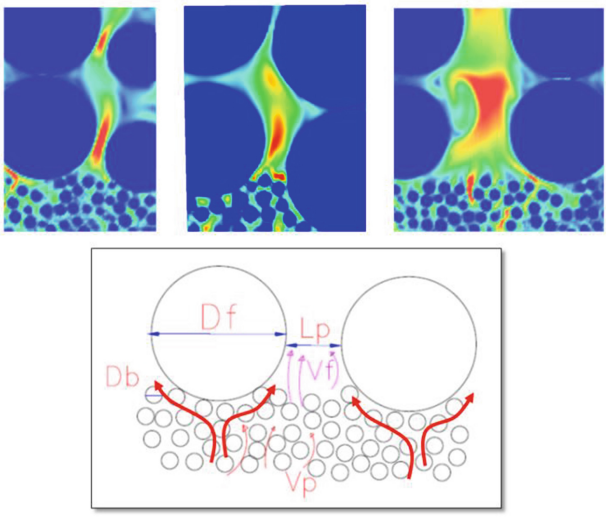

Fig. 5. Top: Flow conditions in the constrictions of filter particles for different widths L_p of constrictions. Bottom: Flow of water around filter particles (highlighted with red arrows) with length and velocity scales considered in the study.

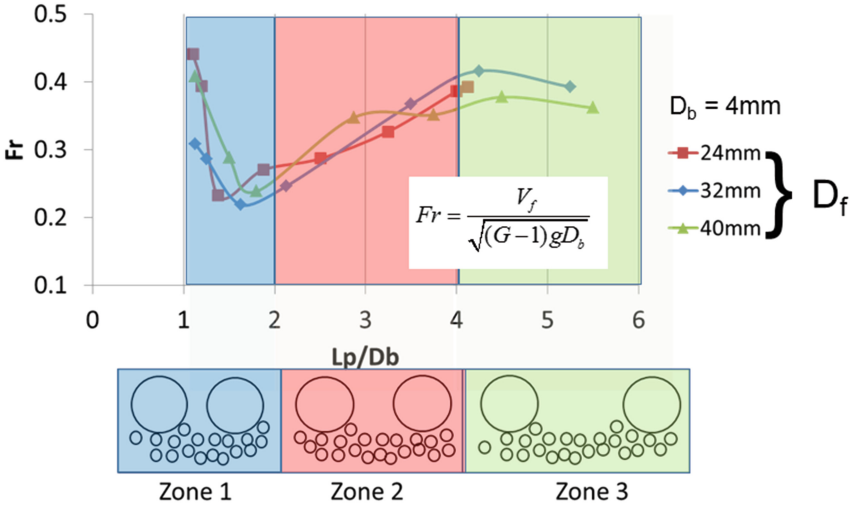

Fig. 6. Criterion for the onset of erosion based on the Froude number defined for the flow condition when erosion starts.

calculated with the flow velocity V_f in the filter constriction and the particle diameter of the base material D_b. With G being the specific gravity, Fr considers here the effective weight of the particles under buoyancy forces.

As can be seen from Fig. 6, the relationship of Fr versus the normalized constriction size of the filter shows a very characteristic evolution for all three base/filter combinations. A similar observation was made for contact erosion due to horizontal flow of water parallel to the interface (Brauns 1985). These regimes are influenced by the competition between hydraulic and geometric/mechanic conditions influencing the onset of erosion. Three distinct regimes can be identified:

1. At the beginning of the blue region, constrictions are just large enough to allow one particle to move through the constriction. The presence of other particles lead to a partly blockage that vanishes with increasing constriction sizes. The optimum size for particles to get dislodged is around 2 when the flow velocity in the filter constriction and thus Fr reaches a minimum.
2. In the red region, Fr increases with increasing normalized constriction size suggesting that the flow conditions between base and filter become more equalized and the funneling effect vanishes.
3. In the green region, a constant value seems to be reached asymptotically. The normalized constriction size is larger than four base material diameters and the situation can be compared with a fluidized bed.

The results presented here need to be confirmed and further investigated based on experimental studies and computational simulations using other size ratios. However, the result of Fig. 6 already allows the determination of the onset of erosion once the constriction size distribution of the filter material is known.

4 Conclusions

Micro-scale experimental and computational investigations have been conducted on the flow conditions at the intersection from base to filter with the aim to develop a generalised relationship describing the onset of contact erosion. The experimentally observed velocity profile in a base filter combination measured with a PIV system fits very well with the results of computational simulations using a DEM-LBM approach. A surprising and yet important observation from these investigations is that the highest velocities are observed in the constrictions of the filter material just above the base layer. Based on mass conservation, the highest flow velocities should be expected in the mixing zone of base and filter material where the porosity is the smallest. This observation needs to be verified in future investigations.

A computational parametric study with three base/filter combinations has been conducted and analyzed for the situation when erosion starts using the Froude number that was calculated using the flow velocity in the constriction of the filter layer and the particle diameter of the base material. The Froude number plotted against the normalized constriction size based on the particle diameter of the base shows a characteristic evolution with three distinct regimes that are influenced by the competition between hydraulic and geometric/mechanical processes. Further investigations with

polydisperse materials and natural granular materials need to be conducted in order to validate this observation.

References

Beguin R, Philippe P, Faure YH (2012) Pore-scale flow measurements at the interface between a sandy layer and a model porous medium: application to statistical modeling of contact erosion. J Hydraul Eng 139(1):1–11

Bertram GE (1940). An experimental investigation of protective filters. Publ 267, SOIL MECHANICS SERIES, NO 7, 21 PP, 26 FIG, 4 TAB

Bouzidi et al (2001) Momentum transfer of a Boltzmann-Lattice fluid with boundaries. Phys Fluids 13(11):3452

Brauns J (1985) Erosionsverhalten geschichteten Bodens bei horizontaler Durchströmung. Wasserwirtschaft 75:448–453

Galindo-Torres SA (2013) A coupled discrete element lattice Boltzmann method for the simulation of fluid–solid interaction with particles of general shapes. Comput Methods Appl Mech Eng 265:107–119

Galindo-Torres SA, Scheuermann A, Mühlhaus HB, Williams DJ (2015) A micro-mechanical approach for the study of contact erosion. Acta Geotech 10(3):357–368

Harshani HMD, Galindo-Torres SA, Scheuermann A, Muhlhaus HB (2015) Micro-mechanical analysis on the onset of erosion in granular materials. Philos Mag 95(28–30):3146–3166

Harshani HMD, Galindo-Torres SA, Scheuermann A, Muhlhaus HB (2016) Experimental study of porous media flow using hydro-gel beads and LED based PIV. Meas Sci Technol 28 (1):015902

Lominé F, Scholtés L, Sibille L, Poullain P (2013) Modeling of fluid–solid interaction in granular media with coupled lattice Boltzmann/discrete element methods: application to piping erosion. Int J Numer Anal Meth Geomech 37(6):577–596

Peck RB, Terzaghi K (1948) Soil mechanics in engineering practice. Wiley, New York

Raffel M, Willert CE, Kompenhans J (2007) Particle image velocimetry: a practical guide. Springer, Berlin

Schuler U, Brauns J (1993) Behaviour of coarse and well-graded filters. In: Filters in geotechnical and hydraulic engineering, pp 3–18

Schwarz T, Prinz E (1923) Handbuch der Hydrologie

Tran D, Prime N, Froiio F, Callari C, Vincens E (2017) Numerical modelling of backward front propagation in piping erosion by DEM-LBM coupling. Eur J Environ Civil Eng 21(7–8):960–987

Simplified Estimation of Some Main Characteristics of Pores and Constrictions in Granular Materials

Feda Seblany[1(✉)], Eric Vincens[1], and Christophe Picault[2]

[1] Université de Lyon, Ecole Centrale de Lyon, LTDS, Ecully, France
feda.seblany@doctorant.ec-lyon.fr
[2] CACOH, Compagnie Nationale du Rhône, Lyon, France

Abstract. The void space of granular materials can be considered as a collection of poly-sized pore bodies separated by narrow pore throats or constrictions. Pore network models have been developed to estimate the probable path length covered by fine particles flowing through a granular filter. For this calculation two pieces of information are required: the constriction size distribution and the mean void spacing between two constrictions which corresponds to the mean pore diameter. Different assumptions have been previously made in the literature to determine this void spacing. However, they all neglect the influence of the density and thus, the estimation of this quantity remains an open issue. This paper compares different definitions for the mean pore size based on statistical analyses performed on numerical samples composed of spheres by means of the Discrete Element Method. Different sphere packings with different gradings and density states were considered and a weighted Delaunay tessellation was applied to extract the main void characteristics. In a second part, a simple formula is proposed to quickly estimate the equivalent sieve opening size of the granular filter. This value is very close to the mode value of the constriction size distribution which is related to the most represented constriction size in a granular material.

Keywords: Void space · Spheres · Filter · Mean pore size

1 Introduction

It is now well established that a better insight into the problems of internal erosion in earth structures can be provided by investigating the void space within granular materials and more specifically by determining their so called constriction size distribution (Silveira 1965; Wittmann 1979; Kenney et al. 1985; Witt 1986; Soria et al. 1993).

Indeed, within a granular material, constrictions are the narrowest channels between the pores and, therefore, represent the main obstacles to overcome for a fine particle flowing under seepage through the filter.

Since constrictions govern the filtration performance of granular soils, different methods have been proposed to obtain the constriction size distribution (CSD) based on an analysis of the void space. Among these methods, we can cite: experimental

The original version of this chapter was revised: Author provided figure corrections have been incorporated. The correction to this chapter is available at https://doi.org/10.1007/978-3-319-99423-9_32

S. Bonelli et al. (Eds.): EWG-IE 2018, LNCE 17, pp. 189–199, 2019.
https://doi.org/10.1007/978-3-319-99423-9_18

techniques (Witt 1986; Soria et al. 1993), numerical approaches (Reboul et al. 2008; Homberg et al. 2012) and analytical models (Silveira et al. 1975; Locke et al. 2001; Reboul et al. 2010; O'Sullivan et al. 2015). Vincens et al. (2015) provided a detailed review of these methods.

The CSD has been at the basis of new filter criteria for earth dams (Witt 1993; Indraratna et al. 2007). Moreover, constrictions are increasingly being used in models to predict the transport of fine particles through filters (Locke et al. 2001; Sjah and Vincens 2013). It has also been involved in the study of materials prone to suffusion (Scheuermann et al. 2010; To et al. 2015).

The CSD is intimately related to pore network models which idealise the void space in porous media by a lattice of pore bodies linked by pore throats following a respective size distribution. Such models have been widely used to simulate and understand the transport of particles in soils.

For example, Silveira (1965) and Kenney et al. (1985) proposed a multi-layered constriction network where fine particles can move from one layer to another if their size are smaller than the associated constriction sizes. Following Schuler (1996), many studies considered a regular cubic model where each pore is modelled by a void cube having six exists (constrictions), one on each cube face (Locke et al. 2001; Sjah and Vincens 2013). In the case of a unidirectional movement of fine particles, the movement from one layer to another layer is directly related to the probability P of occurrence of a constriction (between two consecutive layers) smaller than the particle diameter. Therefore, the probability of passing n layers for a fine particle of a given diameter is equal to P^n. The probability P' to be captured after a path corresponding to n layers is equal to $1 - P^n$. Consequently, n is given by $\log (1 - P')/\log (P)$.

However, if one needs either to compute the CSD from the probabilistic models (experimental technique) or to estimate the maximal distance L travelled by fine particles through a filter using these models, a statement for the unit layer size s must be taken. Indeed, L is equal to $n.s$.

In the past, different estimates for this unit layer size which is generally associated to the mean pore size have been proposed but the authors did not always provide a clear justification for them or the influence of density was not taken into account. Since the characteristics of the void space including pores and constrictions are highly related to both the grading and the density of the filter, a relevant estimate for the void spacing should involve this information.

This paper compares different estimates for the mean pore size with statistical values extracted from numerical samples for different types of gradings at different density states. For this purpose, the Discrete Element Method (DEM) was used to generate packings of spheres, and a weighted Delaunay tessellation is applied to discretize the whole space into tetrahedra. On the basis of this partition, the main void characteristics including the size of constrictions located on each tetrahedron face and the inscribed void sphere between the four particles vertices of each tetrahedron are deduced (Al-Raoush et al. 2003; Reboul et al. 2008).

In a second part, a quick estimate of the equivalent sieve opening size on the base of the CSD is proposed. This property that may be used for the design of filter criteria discriminates fine particles able to travel large distances through the filter from those that will be trapped after a rather short distance.

2 Samples of Numerical Spheres

Numerical packings were prepared by means of DEM-Yade (Šmilauer et al. 2010). Samples composed of spheres are generated by deposit under gravity within a box. Periodic boundary conditions are imposed on the lateral sides of the samples. The contact between spheres is ruled by an elastic-frictional model with a normal and a tangential stiffness (K_n and K_t) and by a Coulomb friction angle (φ). The final equilibrium state is supposed to be reached when the unbalanced forces become negligible.

Table 1 summarizes the characteristics of the five samples studied herein. Different types of soils (Uniformly Graded, Widely Graded and Gap Graded) are tested. In addition to the materials studied by Reboul et al. (2010), samples with a higher coefficient of uniformity (C_u) were tested. The labels of samples indicate the material type (for example, UG for uniformly graded material).

Table 1. Characteristics of DEM samples

Sample	Number of particles	D_0–D_{100} (mm)	Coefficient of uniformity (C_u)	Maximum void ratio (e_{max})	Minimum void ratio (e_{min})
UG	2000	3–12	1.7	0.61	0.52
WG1	25000	0.7–10	3.9	0.49	0.33
GG1	25000	0.7–10	3.6	0.52	0.33
WG2	40000	0.7–14	6	0.41	0.27
GG2	40000	0.7–14	6	0.43	0.27

For each sample, two density states are evaluated (L and D denoting Loose and Dense respectively). For the loosest samples, the coefficient for inter-particles friction is set to 0.3 (0.15 for UG material) in order to reach the maximum void ratio obtained by experiments on similar actual materials (Biarez and Hicher 1994). The densest samples were obtained by setting the friction value at contact to zero.

For these numerical samples, pores and constrictions were identified using a weighted Delaunay tessellation. The void space is then partitioned into tetrahedra whose vertices are formed by the centres of spherical particles.

The pore sizes can be estimated by means of the maximum void sphere inscribed in each tetrahedron, whereas the constriction sizes are computed by considering the maximum inscribed disc that can fit between the three particles defining each face in the tetrahedral partition. This direct computation is referred to level 0 (L_0) (Reboul et al. 2008).

According to Al-Raoush et al. (2003), this partition leads to an over-segmentation of the void space and thus, a pore merging must be applied. In this study, a level 1 (L_1) of merging is adopted (Reboul et al. 2008; Seblany et al. 2018). A merging applies when the inscribed void spheres of two adjacent tetrahedra overlap.

3 Mean Pore Size

In this section, we give a brief summary of the previous estimates of the mean pore size considered in the literature, and we evaluate these assumptions by performing a statistical analysis over DEM samples.

3.1 Previous Estimates

Since actual granular soils are composed of polydisperse and mostly disordered particles and since direct measurements are difficult to carry out, estimating the mean pore size is not an easy task.

Witt (1986) deduced the mean pore size by defining the mean pore volume which is equal to the porosity divided by the mean grain volume. Silveira (1965) and Soria et al. (1993) used D_{50} by mass (D_{50M}), i.e. the diameter corresponding to 50% finer by weight. Locke et al. (2001) proposed to take the mean diameter D_{50} by number (D_{50N}). Referring to Indraratna et al. (2007), the D_{50} of the PSD by lateral surface area (D_{50SA}) is adopted. Such values can be derived from the filter particle size distribution (PSD) by mass, by number or by surface area.

According to Humes et al. (1996), the PSD by mass may overestimate the role of coarser particles in the organisation of the void space, and conversely, the PSD by number may overestimate the role of the finer particles. The use of the PSD by surface area can be considered as the best compromise between these two choices. However, all these estimates were proposed without a clear proof of their validity or have been validated only for the tested soils at their densest state.

Sjah and Vincens (2013) showed that the diameter of the mean void sphere inscribed within the four particles forming the tetrahedra in a Delaunay partition can give a good estimate of the mean pore size. However, their study was restricted to a uniformly-graded granular filter at its loosest state and could not give a general and convenient framework for the study of actual granular materials.

To provide a better estimate of the mean pore size s for an assembly of spheres at a given density, Wu et al. (2012) used a simplified equation stating that any change of the void ratio can be associated to a variation of the diameter of the mean inscribed void sphere:

$$s = \sqrt[3]{\frac{e}{e_{\max}}} s_{\max} \tag{1}$$

where e and e_{max} are the actual and maximum void ratio of the filter respectively. s_{max} is the mean pore size at the loosest state for the material and can be computed following an analytical methodology similar to the one used for the determination of the CSD (Locke et al. 2001). In this case, $s_{max} \approx 0.5 D_{50SA}$.

3.2 Statistics over DEM Samples

In order to select the best estimate for the mean pore diameter from previous proposals, a comparison has been established with statistics over DEM samples including the

mean inscribed void sphere for both loose and dense samples. They will be compared to the mean constriction spacing which may better reflect the distance crossed by a fine particle within a mean local pore. Knowing the number of constrictions in each sample, a simple estimate of the constriction spacing can be given by the mean distance between centers of adjacent pores computed from the initial statistics over the entire sample (non-directional approach) (Seblany et al. 2017).

Figure 1 shows the mean pore size computed from different approximations normalized by D_{50M} for both loose (Fig. 1a) and dense states (Fig. 1b). As C_u increases, the mean void spacing (L_0 computation is considered herein) decreases which is in agreement with results found by Reboul (2008). The influence of density is less pronounced than that of grading which was expected (Reboul 2008).

Secondly, the proposal by Sjah and Vincens (2013) to use the mean inscribed void sphere as an estimate of the mean pore spacing seems to be validated in this study since it led to the closest value to this latter. The other ones (D_{50N}, D_{50SA}, D_{50M}) overestimate the mean pore spacing. In Fig. 1, D_{50M} is systematically equal to 1 due to the chosen normalisation process. This result agrees with a recent work by Taylor et al. (2018) who estimate the constriction spacing by considering the constriction density in micro computed tomography images and DEM samples.

Finally, the formula (Eq. 1) proposed by Wu et al. (2012) which allows the density to be taken into account is in good agreement with the mean pore spacing from DEM samples for both loose and dense samples.

For lower C_u values, particularly in the case of UG, the discrepancy between the mean pore size using Eq. (1) and the mean pore spacing from DEM samples can be due to the imposed void ratio in this case. Indeed, in order to match the actual void ratio from experiments by Biarez and Hicher (1994), a lower friction value is used for generating the loosest sample (UGL) contrary to the other loosest samples. The error was found much lower if the same friction value as for the other samples is used to create the loosest state.

Seblany et al. (2017) highlighted that a consistent choice for the mean pore size must be associated to a given choice for the computation of the CSD, since when applying a merging of adjacent tetrahedra (case of L_1 merging), the number of constrictions tends to reduce. As a consequence, the value for the mean constriction spacing tends to increase. In this case, as the number of constrictions decreases by approximately 30% from L_0 to L_1 regardless of the grading and the density state of the sample, a division factor of 0.7 can be suggested (we denote this formula as Eq. 1*).

The estimate of the mean void spacing (labelled L_1) resulting from the modified formula (Eq. 1*) is shown in Fig. 2. It seems that the new estimate is close to the mean void spacing derived from DEM data considering L_1 criterion. The lesser quality of the result provided by Eq. 1* in the case of C_u smaller than 2 arises from the same reason that was previously mentioned for L_0.

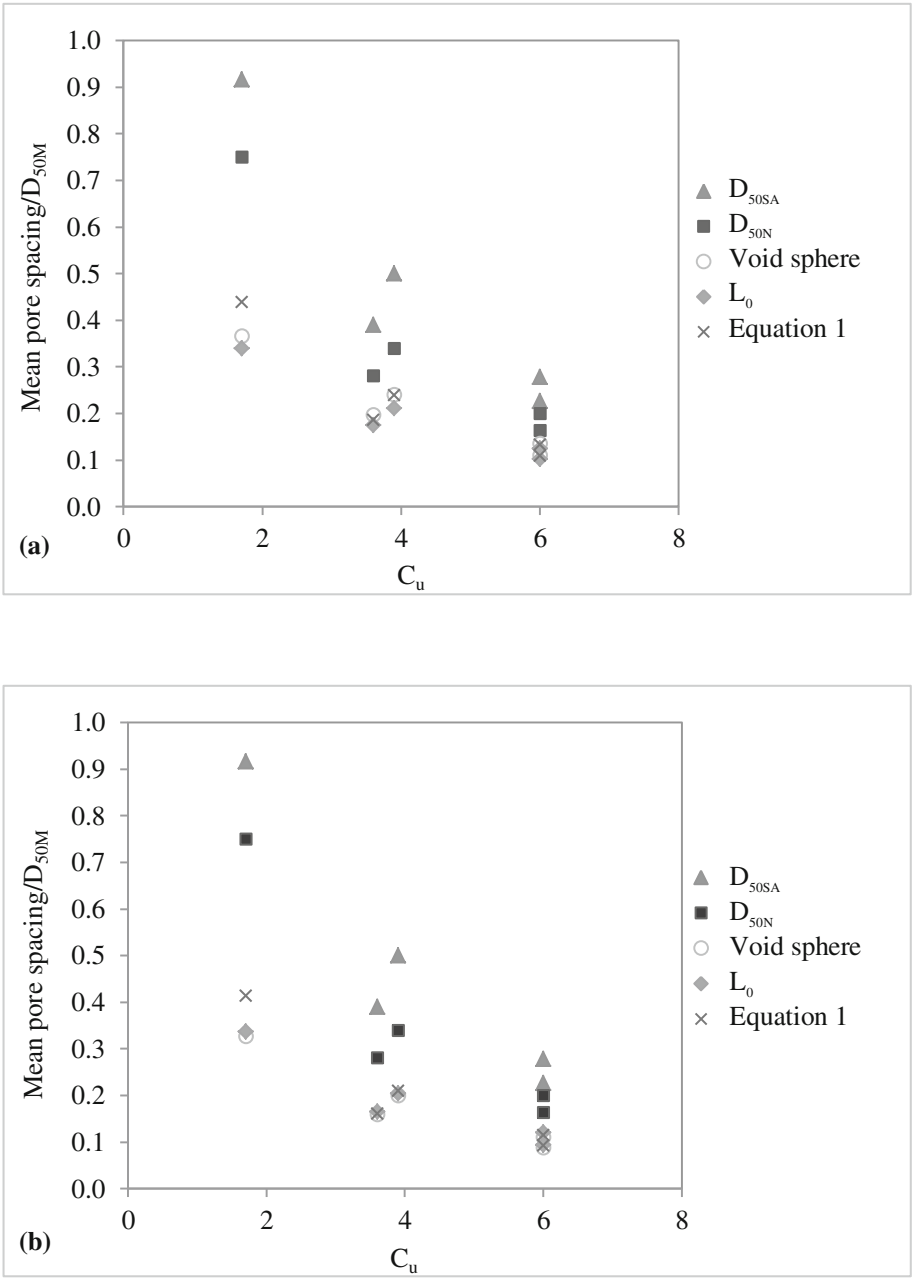

Fig. 1. Comparison of the mean pore spacing based on DEM statistics (L_0) with estimates proposed in the literature for (a): loose samples; (b): dense samples

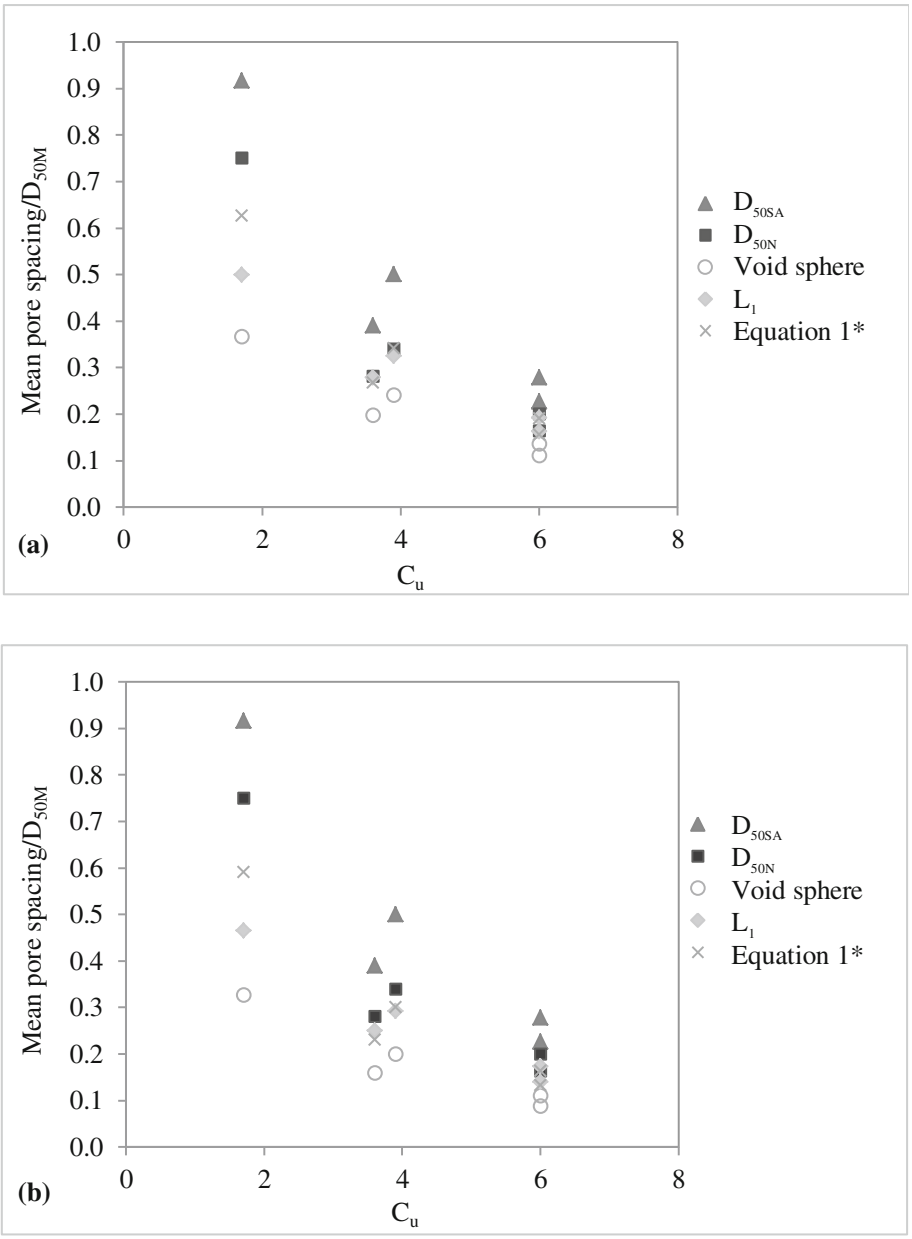

Fig. 2. Comparison of the mean pore spacing based on DEM statistics (L_1) with estimates proposed in the literature for (a): loose samples; (b): dense samples

4 Equivalent Sieve Opening Size

It is well established that the CSD is a key factor for understanding the mechanisms of filtration in granular materials. Indeed, within the framework of the probabilistic theory, a flowing fine particle having a diameter greater than the largest constriction size in the filter cannot enter the filter and conversely, if this fine particle is smaller than the smallest constriction size, it can cross the entire filter. This statement is based on the assumption of a constant hydraulic loading independent from the porous media thickness.

Kenney et al. (1985) introduced the notion of controlling constriction size to design the maximum particle size that can cross the filter. In other words, it corresponds to the smallest constriction size that can be found along a filtration path. Sari et al. (2011) performed some numerical filtration tests and find that the finer part of the CSD curve and more precisely constrictions smaller than the mode are mainly responsible for trapping particles.

In fact, the mode of the constriction size distribution can hold an important physical meaning being the most represented constriction size within the sample. Fine particles smaller than this value can easily cross the filter since the probability of finding constrictions larger than their own sizes, is significant.

Herein, the study does not focus on determining the characteristic constriction size corresponding to the mode of the distribution but rather on a value slightly larger by 5%. It implies that we limit the possible travel distance within the granular filter (herein smaller than forty confrontations with constrictions) which may be large if the flowing fine particle has a diameter equal to the mode of the CSD. Hereafter, we denote this characteristic the equivalent sieve opening size d_{OS}.

The knowledge of this value may be then useful to quickly evaluate the efficiency of a filter to retain a fine particle of a given diameter. A quick and general estimate of the equivalent sieve opening size can be given following the method that allowed building analytical models for CSD. Under this guidance, the constrictions within the sample can result from two main geometrical configurations for the solid particles generating constrictions: three mutually tangent spheres (densest state) and four tangent particles (loosest state). The size of the constriction formed by these arrangements (d_{c3} or d_{c4}) corresponds to the diameter of the circle that can fit between the three or four spherical particles of diameter D. d_{c3} and d_{c4} can be computed analytically by using Eqs. (2) and (3) respectively.

$$d_{c3} = \left(\frac{2}{\sqrt{3}} - 1\right) D \tag{2}$$

$$d_{c4} = \left(\sqrt{2} - 1\right) D \tag{3}$$

The equivalent sieve opening size, at the loosest state, $d_{OS,L}$ associated to a cumulative probability P is eventually given by a weighted contribution of the two configurations within the sample (Locke et al. 2001):

$$d_{OS,L}(P) = Pd_{c4} + (1 - P)d_{c3} \tag{4}$$

For other densities, Reboul et al. (2010) proposed a 1-parameter model validated on the results obtained by the Delaunay approach. For gap-graded materials, they used a more sophisticated model. In this work, the 1-parameter model from Reboul et al. (2010) is considered sufficient since it gave a good match with the dense DEM samples irrespective of the grading (continuous or discontinuous grading). More precisely, the mean relative error was found to be less than 7% which is reasonable.

$$d_{OS}(P, e) = \frac{e}{e_{\max}}(d_{OS,L}(P) - d_{c\min}) + d_{c\min} \tag{5}$$

where d_{cmin} is the minimum constriction size formed between the three smallest particles of the sample in mutual contact (Eq. 2).

Since the smaller particles are responsible for the formation of the finer fraction of the CSD curve, a trial and error process is applied to the lower range of the PSD by surface area to find the characteristic particle size that must be involved in these calculations which allows a direct determination of equivalent sieve opening size. It was found that D_{35SA} as a characteristic diameter for the grading can give a good estimate of the equivalent sieve opening size for all materials whatever their density state except for GG1 material which represents a special case of gap-graded soils.

In fact, the distribution of constriction sizes for GG1 material exhibits two modal values even for L_1 computation. This bimodal shape is related to a significant contribution of particles larger than the gap size to the CSD. In this special case, it would be better to find the second mode of the constriction size distribution; a larger particle diameter must be then involved in the analytical calculation. In this special case, D_{45SA} can be considered adequate for the characteristic diameter of the grading.

Table 2 gives the value of the equivalent sieve opening size derived from the numerical distribution of constriction sizes and the calculated value obtained by using Eqs. (4) and (5) for loose and dense states, respectively. One can note that the analytical values are very close to the numerically computed equivalent sieve opening sizes with a relative error of about 5%.

Table 2. Comparison of numerical and analytical values for the equivalent sieve opening size d_{OS} (in *mm*)

Sample	Numerical value (Loose)	Analytical value (Loose)	Numerical value (Dense)	Analytical value (Dense)
UG	1.14	1.15	1.03	1.04
WG1	0.27	0.26	0.22	0.21
GG1	0.34	0.32	0.28	0.26
WG2	0.27	0.27	0.22	0.21
GG2	0.27	0.26	0.22	0.21

5 Conclusion

In this work, we proposed a technique to estimate two main characteristics of the void space within a granular material involving spherical particles. The first one is the mean pore size which is used in pore network models either to compute the CSD or to predict the longest path covered by a flowing fine particle through a granular filter. The second one is the equivalent sieve opening size defined on the basis of the mode of the constriction size distribution which can be used for the design of filter criteria.

The estimates of the mean pore size and of the equivalent sieve opening size are built on main physical properties of the granular material, namely the grading and the density of the material. The results were validated by means of statistics over DEM samples involving different materials at their loosest or densest state. The proposed estimates were found of very good quality irrespective of the grading and of the density of the sample.

References

Al-Raoush R, Thompson K, Willson CS (2003) Comparison of network generation techniques for unconsolidated porous media. Soil Sci Soc Am J 67(6):1687–1700

Biarez J, Hicher PY (1994) Classification of and correlations between parameters. In: Elementary mechanics of soil behaviour. A.A. Balkema, Rotterdam, pp 81–106

Homberg U, Baum D, Prohaska S, Kalbe U, Witt KJ (2012) Automatic extraction and analysis of realistic pore structures from μCT data for pore space characterization of graded soil. In: Proceedings of the 6th international conference on scour and erosion, Paris, pp 820–830

Humes C, Lafleur J, Rollin A (1996) A new approach to compute the void size distribution curves of protective filters. In: Proceedings of Geofilters'96, pp 57–66

Indraratna B, Raut A, Khabbaz H (2007) Constriction-based retention criterion for granular filter design. J Geotech Geoenviron Eng 133(3):266–276

Kenney T, Chahal R, Chiu E, Ofoegbu G, Omange G, Ume C (1985) Controlling constriction sizes of granular filters. Can Geotech J 22:32–43

Locke M, Indraratna B, Adikari G (2001) Time-dependent particle transport through granular filters. J Geotech Eng Div 127(6):521–528

O'Sullivan C, Bluthé J, Sejpar K, Shire T, Cheung LYG (2015) Contact based void partitioning to assess filtration properties in DEM simulations. Comput Geotech 64:120–131

Reboul N (2008) Transport de particules dans les milieux granulaires - Application à l'érosion interne (in French). Ph.D. thesis, Ecole Centrale de Lyon

Reboul N, Vincens E, Cambou B (2008) Statistical analysis of void size distribution in a simulated narrowly graded packing of spheres. Granul Matter 10(6):457–468

Reboul N, Vincens E, Cambou B (2010) A computational procedure to assess the distribution of constriction sizes for an assembly of spheres. Comput Geotech 37(1): 195–206

Sari H, Chareyre B, Catalano E, Philippe P, Vincens E (2011) Investigation of internal erosion processes using a coupled DEM-fluid method. In: Oate E, Owen DRJ (eds) Proceedings of particles 2011 II international conference on particle-based methods, Barcelona, pp 1–11

Scheuermann A, Steeb H, Kiefer J (2010) Internal erosion of granular materials - identification of erodible fine particles as a basis for numerical calculations. In: 9th international congress of the Hellenic society of theoretical and applied mechanics, pp 275–282

Schuler U (1996) Scattering of the composition of soils. An aspect for the stability of granular filters. In: Proceedings of GeoFilters'96, pp 21–33

Seblany F, Homberg U, Vincens E, Winkler P, Witt KJ (2017) Merging criteria for the definition of a local pore and the CSD computation of granular materials. In: Proceedings of the 25th meeting of European working group on internal erosion, Delft, pp 150–159

Seblany F, Homberg U, Vincens E, Winkler P, Witt KJ (2018) Merging criteria for defining pores and constrictions in numerical packing of spheres. Granul Matter 20:37. https://doi.org/10.1007/s10035-018-0808-z

Silveira A (1965) An analysis of the problem of washing through in protective filters. In: Proceedings of the 6th international conference on soil mechanics and foundation engineering, Montréal, Que, pp 551–555

Silveira A, de Lorena Peixoto T, Nogueira J (1975) On void size distribution of granular materials. In: Proceedings of the 5th Pan American conference on soil mechanics and foundation engineering, Buenos Aires, pp 161–177

Sjah J, Vincens E (2013) Determination of the constriction size distribution of granular filters by filtration tests. Int J Numer Anal Meth Geomech 37(10):1231–1246

Šmilauer V, Catalano E, Chareyre B, Dorofeenko S, Duriez J, Gladky A, Kozicki J, Modenese C, Scholtès L, Sibille L, Stránský J, Thoeni K (2010) Yade Documentation

Soria M, Aramaki R, Viviani E (1993) Experimental determination of void size curves. In: Filters in geotechnical and hydraulic engineering. Balkema, Rotterdam, pp 43–48

Taylor HF, O'Sullivan C, Shire T, Moinet WW (2018) Influence of the coefficient of uniformity on the size and frequency of constrictions in sand filters. Géotechnique 1–9. https://doi.org/10.1680/jgeot.17.T.051

To HD, Scheuermann A, Galindo-Torres SA (2015) Probability of transportation of loose particles in suffusion assessment by self-filtration criteria. J Geotech Geoenviron Eng 142 (2):04015078

Vincens E, Witt KJ, Homberg U (2015) Approaches to determine the constriction size distribution for understanding filtration phenomena in granular materials. Acta Geotech 10 (3):291–303

Witt KJ (1986). Filtrationsverhalten und Bemessung von Erdstoff-Filtern (in German). Ph.D. thesis, Institut für Bodenmechanik und Felsmechanik der Universität Fridericiana in Karlsruhe

Witt K (1993) Reliability study of granular filters. In: Filters in geotechnical and hydraulic engineering. Balkema, Rotterdam, pp 35–42

Wittmann L (1979) The process of soil-filtration - its physics in engineering practice. In: Proceedings of the 7th European conference on soil mechanics and foundation engineering vol 1, pp 303–310

Wu L, Nzouapet BN, Vincens E, Bernat-Minana S (2012) Laboratory experiments and the determination of the constriction size distribution of granular filters. In: Proceedings of 6th international conference on scour and erosion

Numerical and Physical Modelling of Seepage-Induced Internal Erosion Around Holes on Permeable Sheet Pile

Akihiro Takahashi[1(✉)], Hibiki Kokaki[2], Takahiro Maruyama[3], and Kazuki Horikoshi[1]

[1] Tokyo Institute of Technology, Tokyo, Japan
takihiro@cv.titech.ac.jp
[2] Nippon Telegraph and Telephone West Corporation, Osaka, Japan
[3] East Japan Railway Company, Tokyo, Japan

Abstract. Installation of steel sheet piles at the toe of a levee has been adopted as a seismic countermeasure against liquefaction-induced lateral spreading of the levee foundation. Since installation of the sheet piles alters the seepage flow in the foundation ground, use of permeable steel sheet piles is proposed. Holes sufficient to secure the water flow in the ground on the sheet pile might induce internal erosion due to the concentrated seepage flow. In this study, development of seepage-induced internal erosion near the holes on the permeable steel sheet pile is examined by physical model test and numerical simulation. Comparison between physical model test and numerical analysis reveals that the experimental result can be captured by the numerical analysis as a whole. However, the clogging of fines in the experiment cannot be modelled, as detachment of fines from the soil skeleton and fines redeposition are not separately considered in the erosion model used.

Keywords: Internal erosion · Seepage · Permeable sheet pile

1 Introduction

Structures built on liquefiable ground have been seriously damaged in the past earthquakes. Major cause of the damage of levees built on the liquefiable ground is the lateral spreading of the liquefied foundation ground. The spreading of the foundation ground causes excessive settlement and stretching-induced cracking of the levee. To minimize the lateral spreading of the liquefied foundation ground, installation of steel sheet piles at the toe of the levee has been applied as a countermeasure. Recently installation of the sheet piles at the shoulder of the levee with tying the sheet pile heads by rods is proposed. In this configuration, since the core of the levee acts as a double-walled sheet pile cofferdam, this is also effective against overtopping-induced erosion.

H. Kokaki and T. Maruyama—Formerly, Tokyo Institute of Technology, Tokyo, Japan.

S. Bonelli et al. (Eds.): EWG-IE 2018, LNCE 17, pp. 200–207, 2019.
https://doi.org/10.1007/978-3-319-99423-9_19

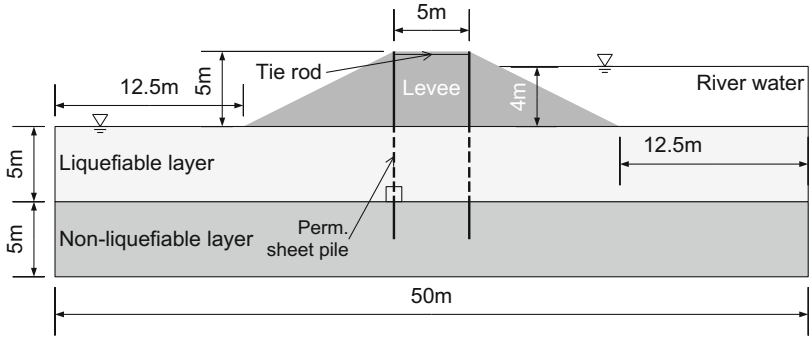

Fig. 1. Target levee with permeable sheet piles

Since installation of the sheet piles alters the seepage flow in the foundation ground, use of permeable steel sheet piles is also proposed. On the permeable sheet pile, there are holes sufficient to secure the water flow in the ground so that the existence of the sheet pile does not interrupt the seepage flow in the persistent situation, i.e., in the no-flooding time. However, onset and development of internal erosion might occur by the concentrated seepage flow due to the large hydraulic gradient around the holes.

In this study, physical model test is performed to observe onset and development of the seepage-induced internal erosion near the hole on the permeable steel sheet pile. Numerical simulation of this experiment is also conducted to examine applicability of a simple constitutive model for the internal erosion on this type of problems.

2 Outline of Physical and Numerical Modelling

Figure 1 shows the target levee with the permeable steel sheet piles installed at the shoulder of the levee. The foundation ground consists of liquefiable layer (hydraulic conductivity, $k = 1.7 \times 10^{-3}$ m/s) and non-liquefiable base layer ($k = 1.0 \times 10^{-4}$ m/s.) Embedment depth of the sheet pile in the non-liquefiable layer is 2.5 m. The permeable sheet pile has five holes (diameter = 80 mm) with 1 m spacing in the liquefiable layer section. Under the condition shown in the figure, seepage analysis is conducted to estimate the flow condition around the hole of the permeable sheet pile. According to the seepage analysis, the seepage flow is almost uniform and horizontal at a distance of 0.52 m from the hole (average hydraulic gradient = 0.30). This area around the hole of the permeable sheet pile is modelled in the physical model test and is analysed with the finite element method.

Setup of the physical model is shown in Fig. 2(a). The physical model is 1/4 scale model and the flow direction is changed to vertical for easy testing. The model ground is made of mixture of Silica No. 3 and No. 8 ($k = 1.7 \times 10^{-3}$ m/s and porosity, $n = 0.407$). Silica No. 3 ($D_{50} = 1.76$ mm) works as coarse particles, while Silica No. 8 ($D_{50} = 0.16$ mm) is the erodible fines. The percentage of Silica No. 8 in the mixture, i.e., the fines content, is 15%. This mixture is internally instable (Ke and Takahashi 2014). The sheet pile is modelled by the 5 mm-thick acrylic plates and the

gap between the plates (width of the model hole) is 20 mm. Here, actual seepage flow around the hole on the sheet pile is three dimensional, but for simplicity and for easy observation, two dimensional flow is assumed in the modelling. Upward seepage flow is imposed to the model for 18 h.

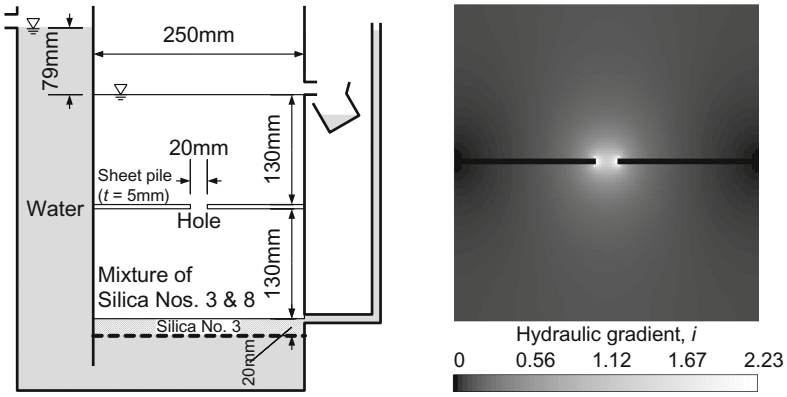

(a) Physical model setup

(b) Hydraulic gradient distribution

Fig. 2. Setup of physical model and hydraulic gradient distribution

In the numerical modelling, it is assumed that the fines eroded from the soil skeleton are transported by the water seeps through the soil skeleton. Conservation equation of the mass of fines transported by a seepage flow is solved:

$$\frac{\partial \rho_e}{\partial t} + \frac{\partial (\rho_e v_i)}{\partial x_i} - Q_e = 0 \tag{1}$$

where ρ_e = density of the eroded fines in the pore fluid, v_i = Darcy's velocity in x_i direction, and Q_e = flux of the eroded fines taken in the pore fluid (Cividini and Gioda 2004). To obtain stable calculation results, the time-spatial discretization is made by Taylor-Galerkin method (Donea 1984). Size of the finite element at the hole is 2.2 × 2.5 mm and that in the other area is 2.2 × 2.2 mm. Number of finite elements is 13,354 and Δt = 0.2 s is adopted.

To solve this advection equation, flow velocity field of the seepage is needed. In this study, two cases are considered; one is the case with use of the seepage analysis on the initial condition, i.e., it is assumed that flow velocity field does not change with erosion (uncoupled). Figure 2(b) shows distribution of the initial hydraulic gradient in the analytical domain. Even under the average hydraulic gradient of 0.30, the local maximum hydraulic gradient exceeds 2.2.

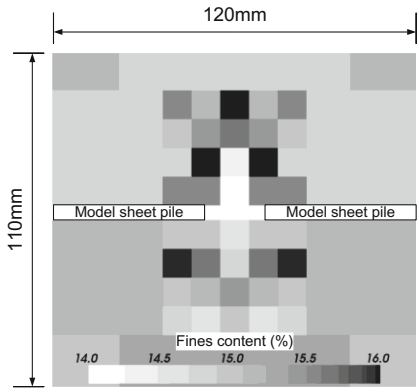

Fig. 3. Distribution of fines content around hole (18 h)

The other is the case considering the change of the flow velocity field with erosion. In this case, distribution of the hydraulic conductivity is regularly updated based on the change of the porosity due to erosion (weakly coupled). In this analysis, an empirical equation obtained from seepage tests (on samples with different fines content) is used to link k and n ($k = 0.0697n - 0.0267$ (m/s)) and the update is made every 10^4 s.

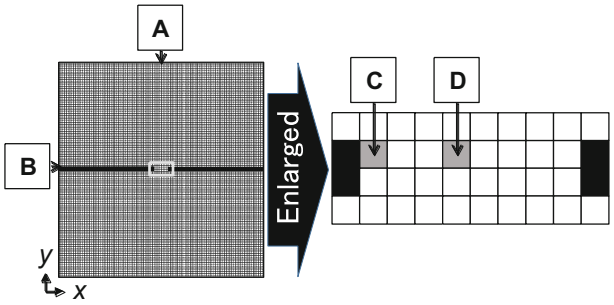

Fig. 4. Picked-up elements

The flux of the eroded fines taken in the pore fluid, or simply erosion rate of the fines, is modelled as follows with reference to Cividini et al. (2009) and Uzuoka et al. (2012).

$$Q_e = -\frac{\partial \rho_f}{\partial t} = -(1-n)\rho_s \frac{\partial f_c}{\partial t} \tag{2}$$

$$\frac{\partial f_c}{\partial t} = d_1 (f_c - f_{c\infty})\, i^{d_2} \tag{3}$$

$$f_{c\infty} = f_{c0}\left\{(1-c)\exp\left(-a\cdot i^{b}\right)+c\right\} \tag{4}$$

where ρ_f = fines density, ρ_s = soil particle density, f_c = volumetric fines content, $f_{c\infty}$ = ultimate fines content, i = hydraulic gradient, f_{c0} = initial fines content, a, b, c, d_1, & d_2 = fitting parameters. The estimated fitting parameters from the one-dimensional seepage erosion test are 1.1, 1.2, 0.67, 0.000024 (1/sec) & 0.11, respectively.

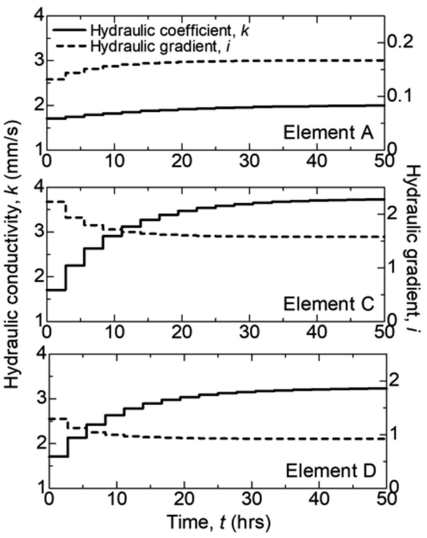

Fig. 5. Variations of hydraulic conductivity and hydraulic gradient (weakly-coupled case)

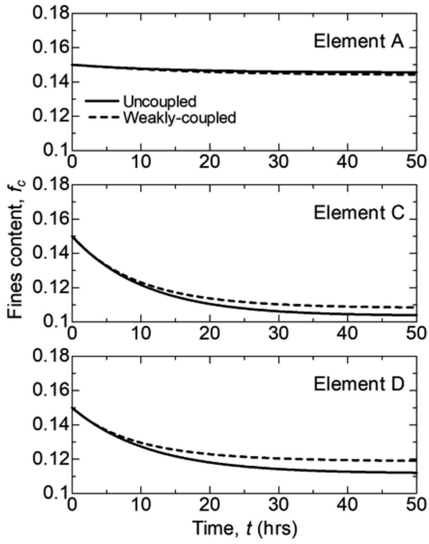

Fig. 6. Variations of fines content

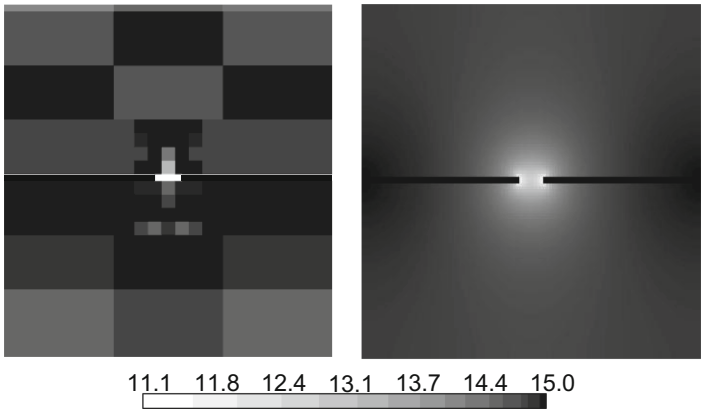

Fig. 7. Distribution of fines content (18 h, Left: Physical model test, Right: Weakly-coupled analysis)

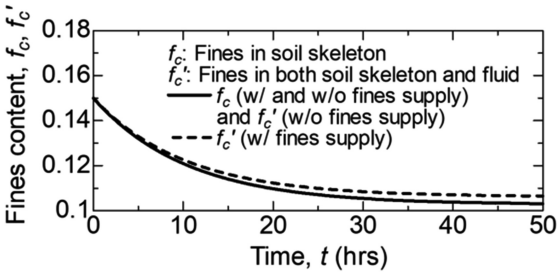

Fig. 8. Variations of fines content at edge of hole in target levee

3 Results and Discussion

Distribution of fines content around the hole on the permeable sheet pile after elapsed time of 18 h in the test is shown in Fig. 3. Since the distribution is expected to be line symmetric, only the fines contents in the left hand side are actually examined. It is also noted that to exaggerate the fines content change, the area whose fines content is less than 14% is coloured with white (the same as 14%). Relatively large change is observed around the hole (the fines content after the test is 11.2% at the hole), while the fines content is hardly changed in the distant locations. At a certain distance (30–40 mm) from the hole, clogging of the fines is observed, probably because the local hydraulic gradient (or pore fluid velocity) is not large enough to transport the fines outside that region.

In the following, responses of the soil at four elements shown in Fig. 4 are retrieved and compared. Figure 5 plots variations of the hydraulic conductivity and hydraulic gradient with time in the weakly-coupled case. At the hole (Elements C & D), the porosity and hydraulic conductivity increase with progress of the erosion and the hydraulic gradient decreases with time. On the contrary the hydraulic gradient increases slightly at Element A. Variations of the fines content with time are shown in Fig. 6. In all the element, the fines content monotonically decreases with time and reaches steady state after elapsed time of 50 h. Comparison between the uncoupled and weakly-coupled analysis reveals that the loss of fines is slightly smaller in the weakly-coupled case. This is due to the decrease in the local hydraulic gradient around the hole in association with erosion-induced increase in the hydraulic conductivity. The fines content at the hole at elapsed time of 18 h is around 11–12%, which is close to that in the physical model test (11.2%).

Figure 7 shows distributions of fines content for the physical model test and weakly-coupled analysis after elapsed time of 18 h. Comparison with physical model test reveals that the experimental result can be captured by the numerical analysis as a whole. However, the clogging of fines in the experiment cannot be modelled, as detachment of fines from the soil skeleton and redeposition are not separately considered in the erosion model used.

In the physical model test and numerical analysis shown above, there is no supply of the fines from the upstream. To examine this impact on the internal erosion around the hole of the permeable sheet pile, separate analysis on the region near the hole of the permeable sheet pile in the target levee is conducted (the box whose size = 1.61 m 1.00 m in Fig. 1). In this analysis, two conditions are considered; one is no supply of fines from upstream and the other is with supply of fines from the upstream. For the latter, periodic side boundary condition is considered, i.e., the fines eroded away from the left boundary is supplied to the right boundary when the direction of the seepage flow is leftward. In this analysis, coupling between the erosion and seepage flow is not considered. Figure 8 shows variations of the fines content at the edge of the hole in the target levee. Extent of the erosion near the hole does not change much with or without supply of the fines from upstream, as the fines content in the region far from the hole does not change much.

4 Summary

In this study, development of seepage-induced internal erosion near the holes on the permeable steel sheet pile is examined by physical model test and numerical simulation. In the numerical modelling, it is assumed that the fines eroded from the soil skeleton are transported by the water seeps through the soil skeleton. Conservation equation of the mass of fines transported by a seepage flow is solved. Erosion rate of the fines is modelled as follows with reference to Cividini et al. (2009) and Uzuoka et al. (2012).

Comparison between physical model test and numerical analysis reveals that the experimental result can be captured by the numerical analysis as a whole. However, the clogging of fines in the experiment cannot be modelled, as detachment of fines from the soil skeleton and fines redeposition are not separately considered in the erosion model used. In addition, impact of the supply of fines from upstream is examined. Within the scope of this study, extent of the erosion near the hole does not change much with or without supply of the fines from upstream, as the fines content in the region far from the hole does not change much.

References

Cividini A, Bonomi B, Vignati GC, Gioda G (2009) Seepage-induced erosion in granular soil and consequent settlements. Int J Geomech 9(4):187–194. https://doi.org/10.1061/(ASCE)1532-3641(2009)9:4(187)

Cividini A, Gioda G (2004) Finite-element approach to the erosion and transport of fine particles in granular soils. Int J Geomech 4(3):191–198. https://doi.org/10.1061/(ASCE)1532-3641(2004)4:3(191)

Donea J (1984) A Taylor–Galerkin method for convective transport problems. Int J Numer Methods Eng 20(1):101–119. https://doi.org/10.1002/nme.1620200108

Ke L, Takahashi A (2014) Experimental investigations on suffusion characteristics and its mechanical consequences on saturated cohesionless soil. Soils Found 54(4):713–730. https://doi.org/10.1016/j.sandf.2014.06.024

Uzuoka R, Ichiyama T, Mori T, Kazama M (2012) Hydro-mechanical analysis of internal erosion with mass exchange between solid and water. In: Fry JJ, Chevalier C (eds) Proceeding on 6th international conference on score and erosion, Paris, 27–31 August 2012, pp 655–662

Prevention Measures and Field Assessment

Investigating the Formation of a Filter Cake in Column Experiments, for Combinations of Filter and Fine Sand in a Coarse Sand Barrier

Sepideh Akrami[1(✉)], Adam Bezuijen[1,2], Esther Rosenbrand[2], André Koelewijn[2], Ulrich Förster[2], and Vera van Beek[2]

[1] Ghent University, Ghent, Belgium
Sepideh.akrami@ugent.be
[2] Deltares, Delft, The Netherlands

Abstract. The coarse sand barrier (CSB) is a single granular filter used to retrofit an existing structure, making it more stable against backward erosion piping. The barrier material should be chosen carefully to retain particles from the sand layer upstream of the barrier, yet provide optimal resistance against backward erosion piping. This means the particles in the barrier should be large, thus difficult to transport, and the barrier should have a high permeability in order to reduce the local hydraulic gradient inside the barrier. However, transport of the fine sand upstream of the barrier into the barrier, may result in less permeable filter cake just inside the barrier. Therefore, a column set-up was designed and experiments were conducted with various sand types, using the same materials as used in small-scale and medium-scale backward erosion piping experiments with at CSB. The aim was to compare the results of different tests and check if the criterion for the formation of a filter cake is the same as the well-known filter rules. Consequently, this paper presents the results of different column experiments. These materials were carefully selected and fulfilled the selected filter rules but one soil composition caused the filter cake formation. This indicates that to avoid filter cake formation for the conditions tested stricter rules apply than the filter rules considered here.

Keywords: Filter cake · Coarse sand barrier · Column experiments
Filter rules

1 Introduction

1.1 The Coarse Sand Barrier

The coarse sand barrier is considered as a promising measure to prevent failure of embankments as a consequence of backward erosion piping. Backward erosion piping is an internal erosion mechanism that can occur underneath levees when there is an opening in the cohesive cover layer (this can be a ditch or a shrinkage crack). With sufficient hydraulic gradient over the dike, this may cause transport of sand particles by seepage water towards the surface and forms a shallow pipe in the upstream direction

S. Bonelli et al. (Eds.): EWG-IE 2018, LNCE 17, pp. 211–220, 2019.
https://doi.org/10.1007/978-3-319-99423-9_20

below the cohesive layer that progressively grows towards the river. When this pipe reaches the river, the flux through the pipe increases dramatically, which can lead to embankment collapse (e.g. Sellmeijer 1988; Van Beek et al. 2011, 2015).

The coarse sand barrier (CSB) is a coarse grained filter, covered with cohesive material, that is placed in the path of the pipe, see Fig. 1. Due to the larger grain size of the particles in the barrier and the relatively high hydraulic conductivity contrast between the barrier and the background material, there is a much higher resistance against erosion of the barrier material, than that of the fine sand, resulting in a much higher safety level for the levee.

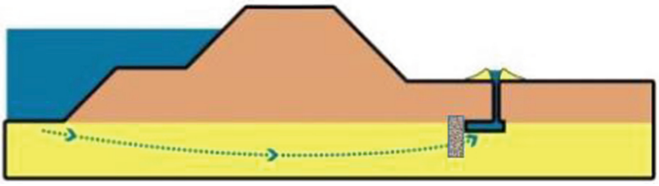

Fig. 1. Principle of the coarse sand barrier.

1.2 The Filter Cake

A filter cake could occur when background sand particles are transported into the barrier, and are captured at the interface of the barrier. When the pores of the barrier are blocked by the fine particles this forms a layer of a lower hydraulic conductivity inside the barrier, that can be referred to as a filter cake.

The consequence of such a filter cake on the effectiveness of the barrier is not directly clear, but it will have an influence on the groundwater flow below the levee and therefore it should be known.

The literature on filtration and suffusion (washout of fine particles from a gap-graded soil) provides several rules for designing a filter, such as the filter rules derived by Terzaghi as given by Lambe and Whitman (1969), and Sherard et al. (1984) that give guidance to whether particles can be transported into or through the barrier. Although these filter rules are well established, a filter cake due to migration of fines into the CSB was indicated by the measured head profile in model tests. It was realized that a possible cause was the high porosity of the CSB. In their simplest form the filter rules do not take into account the influence of porosity, but it is clear that the pores in sand with a high porosity are larger than in sand with a low porosity.

Literature on filtration and suffusion (washout of fine particles from a gap graded soil) provides several rules that give guidance to whether particles can be transported through a filter. When the combination of original sand upstream of the barrier and the barrier material fulfils the filtration and suffusion rules, failure of the barrier can only occur when the pipe forms through the barrier, provided that the barrier is deep enough and clogging of the barrier does not occur.

For the selection of the barrier material, the following requirements have been applied:

1. $d_{15,barrier}/d_{85,base\ material} < 5$
2. $d_{50,barrier}/d_{50,base\ material} < 25$
3. Kenney and Lau (1985, 1986) criterion for internal stability of the barrier material

The first and the second requirements are filter rules as derived by Terzaghi, as given by Lambe and Whitman (1969), International Committee on Large Dams (2015), USACE (2000). The third requirement is given by Kenney and Lau (1986) and implies that for the whole sieve curve, the value of the percentage of grains (by mass) with a diameter between d and $4*d$, divided by the percentage of grains with a diameter smaller than d should be larger than 1.0, provided $d_5 > 0.075$ mm (USACE 2000) (d_5 is the diameter at which 5% of the sample's mass is comprised of particles with a diameter less than this value).

The Kenny & Lau criterion is meant to determine whether finer fractions are sufficiently prevented from washing out from the coarser fraction in a wide graded soil. The fine sand used in our tests and the CSB material are stable according to this criterion. Here the criterion is used as an alternative filter requirement for the combination of the fine sand and the coarse sand of the barrier, since this requirement takes into account the influence of the porosity, which is not the case with requirements 1 and 2.

1.3 Laboratory Investigations

The possibility of the formation of a filter cake was tested in a column tests before the same combination of sands was used in medium-scale tests. The experiments performed are comparable to the "gradient ratio test" that can be used to test the possibility of sand erosion through a geotextile or blocking the pores of that geotextile (ASTM 2000).

2 Experimental Study

2.1 Experimental Set-Up

A column set-up has been used for investigation of the filter cake formation in the coarse sand barrier. A schematic illustration of the set-up is shown in Fig. 2. In these tests the hydraulic gradient is applied by using an upstream reservoir and a downstream overflow with the adjustable head difference.

The sand sample is prepared homogeneously at a high relative density in the column that has a total height of 39 cm and a diameter of 9 cm. On the acrylate wall of the column, several piezometers are installed to measure the piezometric head at each step. Seven piezometers are installed at the wall of the column with approximately 22 mm distance between them to measure the piezometric head in the barrier, the background sand and the boundary between the barrier and sand. Also, one piezometer is used to indicate the piezometric head in the water on the top of the soil sample (h8). The positions of the piezometers with respect to the bottom of the column are shown in Table 1.

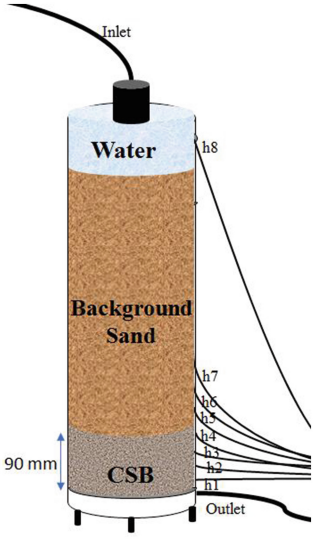

Fig. 2. Schematic presentation of the experimental setup.

Table 1. Position of piezometers

Piezometer No.	h1	h2	h3	h4	h5	h6	h7	h8
Position from bottom (mm)	13	43	65	86	106	128	150	364

For sample preparation, the column was filled with de-aired water from the bottom of the container to prevent any air bubble in the sample and piezometers. After filling the container with water, the cover on the top is removed and the first sand layer, the barrier material, is rained in (Van der Poel and Schenkeveld 1998). The sand is placed underwater in thin layers and was densified by tamping it under water in case the highest density has to be reached. Then the background sand is applied and densified also by tamping. The last sand layers have a lower density compared to the first applied layers because densification of the last layers will also densify the previously applied layers. After this procedure, the cover is mounted again and the set-up is ready for starting the test.

2.2 Test Procedure

During the experiments, a constant head difference is maintained between the inlet and outlet of the set-up. The initial hydraulic head difference of 0 cm is increased in steps of 3.5 cm every 5 min, in order to increase the gradient in steps of 0.1, every 5 min. This process is repeated until the head difference of 24.5 cm (corresponding to an overall gradient of 0.7) is achieved. In every step, the flux is measured through the outlet tube at the bottom of the column.

3 Results

In this study, two different background sands and barrier materials were used in the column tests with high relative density of the sands. Test 1 was conducted using Metselzand as a background sand and GZB2 as a coarse sand barrier.

In Test 2, a combination of Baskarp fine sand as a background sand and GZB1 as a coarse sand barrier was used. Sand characteristics can be found in Table 2, and the grain size distribution is shown in Fig. 3.

Table 2. Sand type characteristics and filter rules requirement

Test No.	Sand type	n	d15	d50	d85	$d_{15,barrier}/d_{85,base\ material}$	$d_{50,barrier}/d_{50,base\ material}$
Test 1	Metselzand	0.338	0.22	0.38	0.875	0.7	2.8
	GZB2	0.349	0.602	1.053	1.311		
Test 2	Baskarp fine	0.388	0.095	0.123	0.160	3.6	10
	GZB1	0.307	0.58	1.23	1.79		

As can be seen in the table, selected materials fulfill the filter rules requirements.

During the experiment, the piezometric head and flux values were measured for each gradient and then the required values were calculated. Some of the results are presented here. The course of the piezometric head as a function of the location of piezometers on the column is shown in Figs. 4 and 5.

In the column tests, the boundary between the barrier and the fine sand is located at the height of 90 mm from the bottom of the column. The measurement points above that boundary, at 106 and 128 mm showed a sharp increase in piezometric head, see Fig. 5. Comparing the results of these two tests indicates that the piezometric head in Test 1 followed a different trend in the barrier material compared to Test 2. This could be considered as caused by filter cake formation. However, according to the filter rules applied, no filter cake would be expected and Test 1 should follow the same trend as Test 2.

Flow could possibly transport some finer grains over a short distance into the barrier, forming a filter cake at the upstream interface between the barrier and the fine sand. Therefore, the hydraulic conductivity across this interface is presented using h5 (16 mm upstream of the interface in the fine sand) and h4 (6 mm downstream of this interface in the barrier). For comparison the hydraulic conductivity calculated in the upstream part of the barrier based on h4 and h3, inside the barrier near the interface where the filter cake could possibly appear, and the hydraulic conductivity of the fine sand upstream of the barrier (h5-h7) is also shown, see Figs. 6 and 7.

In Test 1, the hydraulic conductivity measured between h4-h3, which is inside the barrier, is less than in other locations of the barrier and is in between the fine sand permeability and the barrier permeability, indicating the formation of a filter cake. This

soil composition was also used as a material for small-scale backward erosion piping tests and consequently those tests also indicated a filter cake formation (Rosenbrand et al. 2018).

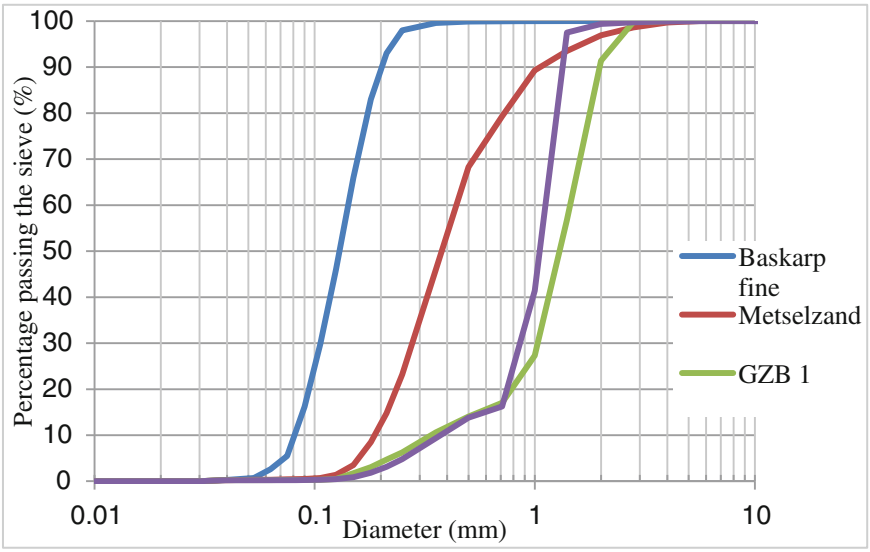

Fig. 3. Grain size distribution of the sand and the barrier material

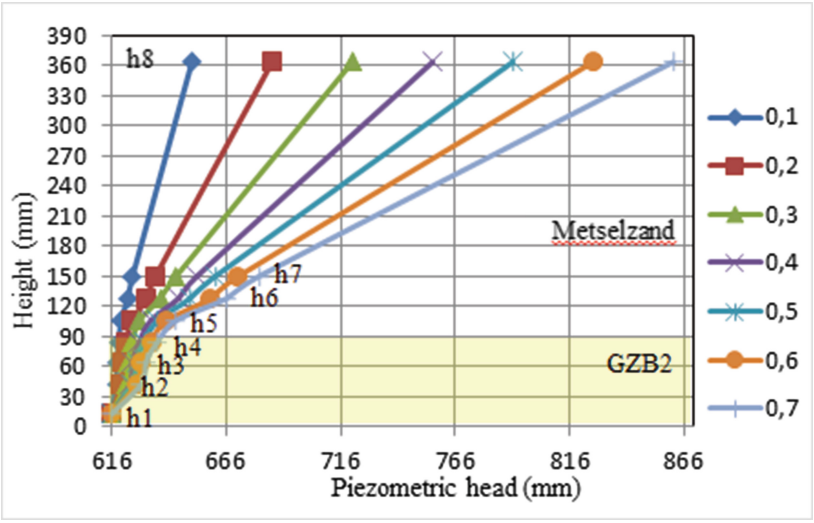

Fig. 4. Piezometric head as a function of location of piezometers on the column for different values of the average gradient, Test 1.

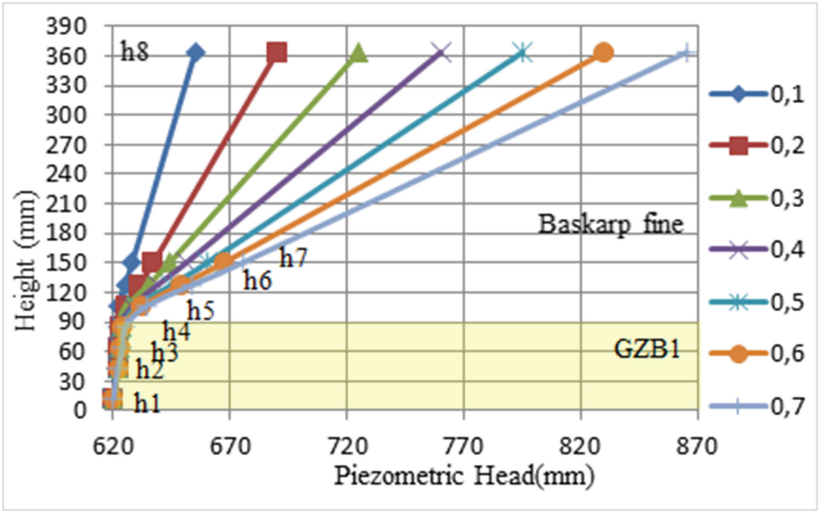

Fig. 5. Piezometric head as a function of location of piezometers on the column for different values of the average gradient, Test 2.

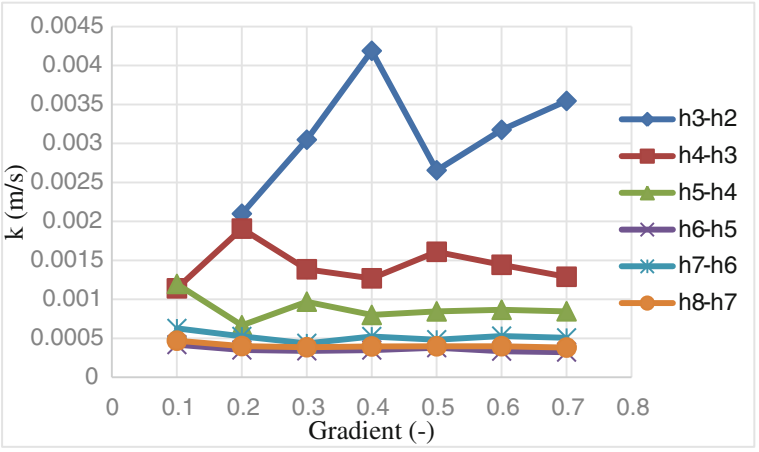

Fig. 6. Permeability as function of gradient, Test 1

In Test 2, shown in Fig. 7, the hydraulic conductivity of h4-h3 is similar to the other values in the barrier. This indicates that there was no formation of a filter cake, as a filter cake would have increased the resistance inside the barrier.

These experiments also were done as 'long-term experiments' by waiting for one hour during the test to investigate the influence of time and presence of continues erosion, but the results did not change. This can imply that in this case there is some migration, but no ongoing migration. Remarkable is that the permeability as measured between h4-h3 is already low at low gradients and remains more or less constant during

the test. This may indicate that the filter cake is already formed during the construction of the sample, probably when densifying the sand. This result is different from what was found in small-scale backward erosion piping tests, where the permeability decreased over time.

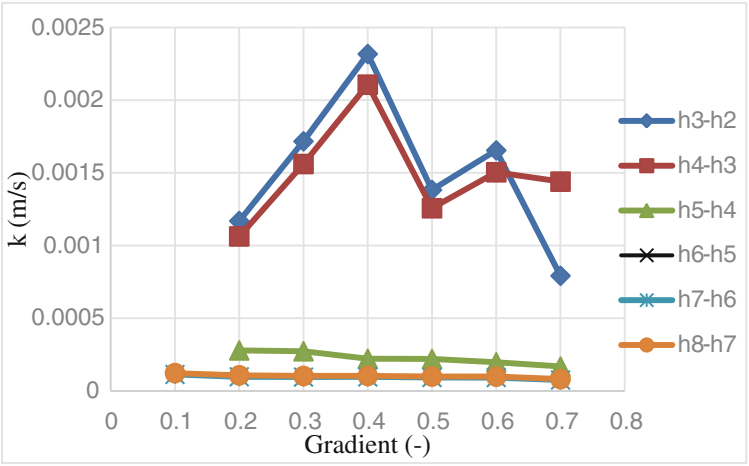

Fig. 7. Permeability as function of gradient, Test 2

4 Discussion and Conclusions

For the two column tests analysed in this paper, variations in permeability have been found with different gradients in the CSB. The permeability of the background sand was in all tests more or less constant. According to Darcy's law the permeabilities should be constant, whereas they are not for the CSB. Partly this could be inaccuracy in the measurements (1 mm inaccuracy in reading the piezometric pipes), a large permeability means a small pressure drop that is difficult to measure with sufficient accuracy, see also Figs. 4 and 5. However, the good congruence between the permeabilities measured for h4-h3 and h3-h2 indicates that not all fluctuations in the CSB permeability can be explained by inaccuracy in the measurements and that there is some real permeability fluctuation. This may be caused by migration of fines from the Metselzand upstream through the CSB. Until gradients of 0.4 fines are washed out from the CSB, for higher gradients the picture is inconsistent and needs further study.

Remarkable is that the grain size ratio is much larger in Test 2 than in Test 1. Therefore sand migration in the CSB should be expected in Test 2, but it was found in Test 1. Test 2 had only poorly graded materials while in Test 1 the metselzand is more widely graded. Furthermore, this sand had a 'dust tail'. The dust tail can only be a very limited amount of the total Metselzand, since it was not measured in the grain size distribution. However, either the dust tail or the wider grading of the Metselzand must have caused the decrease in permeability between h4 – h3 in Test 1. This will be subject to further research.

The maximum gradient of 0.7 that is used in these experiments may seem high. Yet, experiments on coarse sand barrier configurations show that even higher gradients in the fine sand can occur before failure of the CSB (Bezuijen et al. 2018a; Rosenbrand et al. 2018); therefore tests with such a high gradient are relevant.

In Test 1, the permeability is the lowest between h5 and h6 and higher between h6 and h7. This can be caused by some washing out of fines between h6 an h7 that have migrated between h3 and h4. Therefore, it is clear from the measurements that the permeabilities in Test 1 are influenced by sand migration. In this test, although the sand combinations fulfill the filter criteria mentioned above, there are still values in between the permeability of the sand and the coarse material.

Therefore, this analysis leads to consequence that the filter rules presented here are not sufficient to exclude fine sand migration, which may be very important for the CSB. Further study will be necessary to check if other filter criteria, for example those given by Burenkova (1993), give a better prediction of the occurrence of fine sand migration.

References

ASTM D5109-90 (2000) Standard Test Method for measuring the soil-geotextile system clogging potential by the gradient ratio. Annual Book of ASTM standards, ASTM Philadelphia

Bezuijen A, Rosenbrand E, van Beek VM, Vandenboer K (2018a) Experiments for a coarse sand barrier as a measure against backwards erosion piping. In: International conference physical modelling in geotechnics

Bezuijen A, Van Beek V, Rosenbrand E, Akrami S (2018b) Analytical groundwater flow calculations for understanding the flow and erosion in a coarse sand barrier. In: Proceedings of 26th meeting of the European working group on internal erosion, Milan

Burenkova VV (1993) Assessment of suffusion in non-cohesive and graded soils. In: Proceedings of the 1st international conference "geo-filters", Karlsruhe, 20–22 October 1992, pp 357–360

International Committee on Large Dams (2015) Internal erosion of existing dams, levees and dikes, and their foundations. ICOLD Bull 1(164):342

Kenney TC, Lau D (1986) Internal stability of granular filters. Can Geotech J 23:420–423. https://doi.org/10.1139/t86-068

Kenney TC, Lau D (1985) Internal stability of granular filters. Can Geotech J 22:215–225. https://doi.org/10.1139/t85-029

Lambe TW, Whitman R (1969) Soil mechanics. Wiley, New York

van der Poel JT, Schenkeveld FM (1998) A preparation technique for very homogenous sand models and CPT research. In: Kimura T, Kusakabe O (eds) Proceedings of the international conference centrifuge, vol 98. Balkema, Rotterdam, pp 149–154

Rosenbrand E, Van Beek V, Koelewijn A, Akrami S, Förster U, Bezuijen A (2018) Scale effects in coarse sand barrier experiments. In: Proceedings of 26th meeting of the European working group on internal erosion, Milan

Sherard JL, Dunnigan LP, Talbot JR (1984) Basic properties of sand and gravel filters. J Geotech Eng 110(6):684–700

Sellmeijer JB (1988) On the mechanism of piping under impervious structures. TU Delft, Delft
USACE (2000) Engineering Manual 1110-2-1913, Design and Construction of Levees. http://oai.dtic.mil/oai/oai?verb=getRecord&metadataPrefix=html&identifier=ADA402946
Van Beek VM (2015) Backward erosion piping initiation and progression. TU Delft, Delft
Van Beek VM, Knoeff H, Sellmeijer H (2011) Observations on the process of backward erosion piping in small-, medium- and full-scale experiments. In: Erosion in geo-materials, pp 1115–1137. https://doi.org/10.3166/ejece.15.1115-1137

Analytical Groundwater Flow Calculations for Understanding the Flow and Erosion in a Coarse Sand Barrier

Adam Bezuijen[1,2(✉)], Vera van Beek[1], Esther Rosenbrand[1], and Sepideh Akrami[2]

[1] Deltares, Delft, The Netherlands
adam.bezuijen@deltares.nl
[2] Ghent University, Ghent, Belgium

Abstract. The coarse sand barrier (CSB) is a promising method to avoid ongoing backward erosion piping resulting in increased safety of a dike for this failure mechanism. Experiments are performed at different scales at Deltares, the Netherlands. These experiments show a significant increase in the critical head for structures with a CSB compared to structures without a CSB. The increase of critical head cannot only be ascribed to the lower erodibility of the coarser particles in the barrier, but also to the reduction of hydraulic load on these coarse particles in the barrier, resulting from the permeability contrast of barrier material and surrounding sand. To investigate the influence of a CSB on the flow pattern numerical and analytical calculations have been performed. This paper focusses on the analytical calculations. It will be shown that these can explain the increase in strength and the measured scaling effects.

Keywords: Backward erosion piping · Mitigating measures
Analytical calculations · Coarse sand barrier

1 Introduction

Backward erosion piping is seen as a major threat for the stability of cohesive dikes built on sandy soil layers. Seepage flow may loosen sand grains such that a pipe is formed underneath a dike starting at the landward side and progressing to the river side. When the pipe connects with the river a significant increase of erosion will occur, with dike failure as a likely result. This mechanism is studied by various groups, for example in Australia, Belgium (Vandenboer et al. 2017), China (Cao 1994), Italy (Gracía Martínes et al. 2017), the Netherlands, and the USA (Robbins et al. 2018).

The traditional method to reduce the risk of backward erosion piping is to increase the seepage length underneath the dike by widening the dike or install a so called piping berm. With a given head difference between the water level in the river (maximum expected level) and the water level on the landward side, an increased seepage length will reduce the average hydraulic gradient across the structure and thus reduce the risk of backward erosion piping. This can be directly concluded from the research of Bligh (1915) and Lane (1935). However, the combination of increased

S. Bonelli et al. (Eds.): EWG-IE 2018, LNCE 17, pp. 221–233, 2019.
https://doi.org/10.1007/978-3-319-99423-9_21

safety levels, climate change and land subsidence leads to larger head drops during design circumstances. Consequently the seepage length has to increase leading to uneconomical wide berms that in some cases would imply the demolition of historical buildings close to the dike. Therefore, alternative piping prevention measures have been developed (Förster et al. 2015).

One of these piping prevention methods is the 'Coarse Sand Barrier' (CSB). For this measure, a layer of coarse sand is applied just underneath a dike or a berm in the top of the sand layer (Fig. 1). Pipes that form in the fine sand at the landward side of the dike, cannot pass the coarse sand, because its resistance against erosion is higher than the resistance of the fine surrounding sand, due to the larger grain size. However, the coarse sand will not only change the strength against erosion. It will also change the flow pattern of the groundwater flow in the sand underneath the dike, due to the permeability contrast of the CSB and the surrounding sand. Although the groundwater flow can be calculated numerically, an analytical model is useful to develop a first idea about the important parameters. With an analytical model it is possible to estimate how the local loading on the barrier changes for different scales and for different configurations. It is of importance to investigate the scale effects, since the real situation, a dike on a sand layer with a thickness of, in some cases, more than 10 m, can never be tested on full scale in the laboratory. Results of the calculations will be compared with the results of measurements of small-scale and medium scale tests.

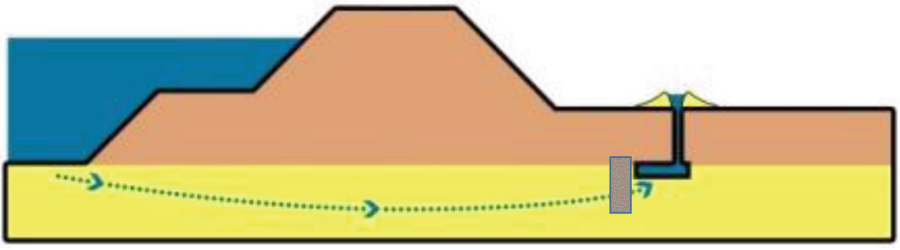

Fig. 1. Principle of the coarse sand barrier.

2 Failure Mechanism CSB

Figure 1 is used to explain the possible failure mechanism of the CSB. When the water level on the river side (left in Fig. 1) increases, backward erosion piping may occur on the landward side as shown. The CSB has hardly any influence on the head difference at which the first erosion pipe occurs. This erosion pipe will grow upstream until the CSB is reached. When the pipe is blocked by the CSB, it will grow to the sides of the CSB, perpendicular to the cross-section shown in Fig. 1. The flow through the CSB and the outward flow to the pipe will reduce the slope on the landward side (right) of the CSB. The slope crumbling is illustrated in Fig. 2, which shows a moment in a medium scale test (the width of the CSB in the middle of the picture is 0.3 m, the depth of the container is approximately 0.4 m). In these tests the hydraulic head is high on the

left hand side and low on the right hand side. The coarse sand of the barrier is clearly visible in the middle of the picture, the red lines in these figures indicate the damage to the barrier. Theoretically, when the gradient at the outflow area between the CSB and the pipe reaches a value of approximately one in the outflow area of the pipe, the sand of the CSB can be lifted and transported from the CSB into the erosion pipe and one or several pipes will form into the CSB. However, these pipes will not break through the barrier, because when they grow, the outflow area of the pipes increases and consequently the local gradient in the outflow area decreases. Due to this, a significant increase in head difference is needed to go from the first damage at the barrier until a complete breakthrough. An example of a nearly break through situation for the CSB in a medium scale test is shown in Fig. 3. At the moment shown in Fig. 2, there has already been quite some erosion in the fine sand at the right hand side of the barrier.

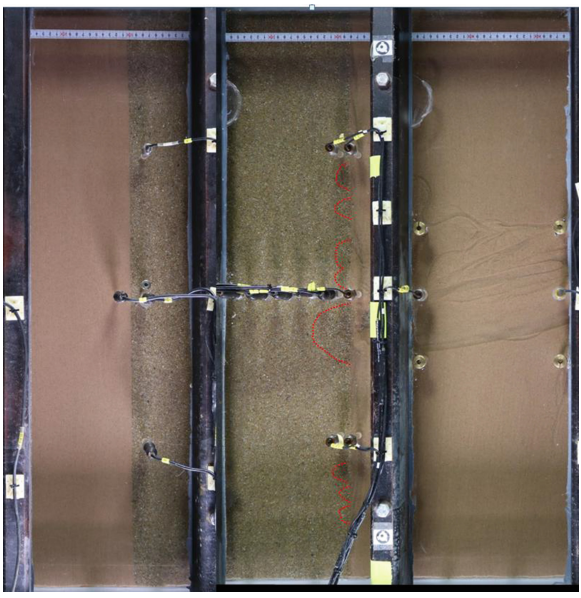

Fig. 2. Image of part of the medium scale test (plan view). Water flows towards the circular exit beyond the right side of the image. The image shows the first damage to barrier, the red lines indicate the position of the erosion front.

Here it should be noted that the head in both the pipe and the CSB is low as soon as the erosion pipe has reached the CSB. Both the CSB and the pipe have a high permeability and consequently the major part of the flow resistance is caused by the sand on the river side of the CSB. This flow resistance remains constant as the CSB is eroding and thus the amount of water that flows through the CSB is more or less constant.

The aim of the analytical calculation method to be presented is to calculate the flow distribution for the situation shown in Fig. 2. In later stages of the erosion, as an

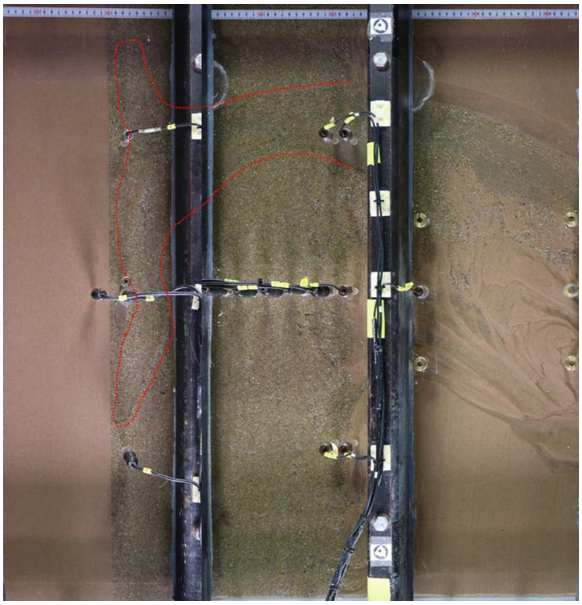

Fig. 3. Image of part of medium scale test. Pipe just prior to failure of the CSB.

example shown in Fig. 3, it is difficult to assume a fixed geometry, or 2D flow, since the erosion patterns inside the barrier will be different. Since the fine sand has eroded all along the downstream side of the barrier a 2 dimensional approximation is possible.

3 Theory

A coarse sand barrier will have a piezometric head close to the downstream level, after the pipe has reached the barrier. The barrier and the pipe to the barrier will create a permeable outflow. However, in a field situation the barrier would normally only reach to small depth compared to the thickness of the sand layer below the dike. Consequently, the geometry of the dike and the leakage length in the polder also will have an influence on the pressure distribution in the coarse sand barrier and thus the strength of such a barrier.

3.1 Assumptions

To be able to make analytical calculations, it is assumed that the barrier will fail when the gradient at the outflow area of the barrier is around 1. As mentioned before, a 2D situation is assumed. This is justified by the erosion pipe that will grow parallel to the barrier as is seen in small-scale and medium-scale tests. The geometry used, is shown in Fig. 4. Like in previous calculations (Bezuijen 2017), it is assumed that there is an impermeable dike and a semi-confined aquifer in the polder. A horizontal water flow is assumed underneath the dike and it is assumed that the flow in the semi-confined

aquifer can be described with a one-dimensional equation. In the neighbourhood of the CSB and in the CSB, there are circular equipotential lines that have the outflow point of the CSB as a centre, see also Fig. 4. It is assumed that the flow towards the CSB only comes from the upstream part of the sand.

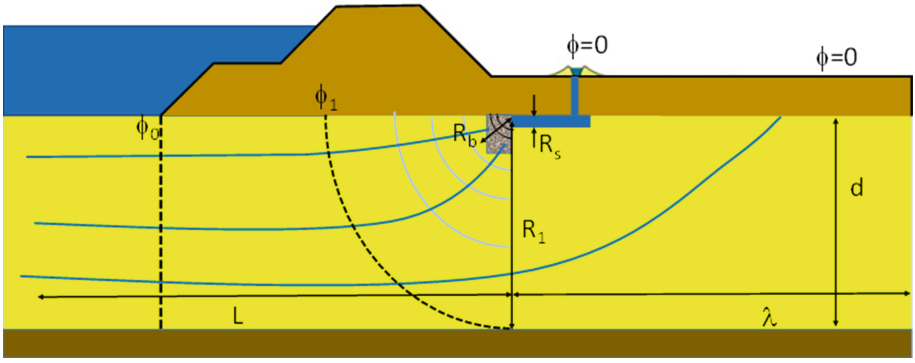

Fig. 4. Sketch flow lines and equipotential lines in CSB.

In this analysis, the moment is studied in which the groundwater flow just starts to erode some grains from the barrier. In this situation it is still allowed to assume a 2D flow pattern. Assuming circular flow in and around the barrier is only allowed in case depth and width of the CSB are much smaller than the depth of the fine sand layer in which the CSB is constructed. This is normally the case in field situations, but was not always the case in the laboratory tests.

The dimensions presented in Fig. 4 need some explanation: L is the length of the seepage flow under the dike up to the end of the barrier. In reality, the upstream part of the flow will not be a straight line, because it will bend towards the water in the river. However, this scheme is used for simplification. λ is the leakage length of the semi-confined aquifer in the polder. This can also be seen as if there would be a flow in the sand under an impermeable clay layer over a length λ. d defines the thickness of the sand layer. R_s is the distance where the CSB is in connection with the erosion pipe.

In Fig. 4, this R_s is shown as the vertical distance. However, if there is some erosion of the barrier a larger distance should be taken: the length where the CSB and the pipe are in contact, which will exceed the depth of the pipe. R_b is the average distance from the boundaries of the CSB to the pipe and R_1 the maximum radius possible in the sand, this can be equal to the thickness of the sand layer, but normally it will be less, as is explained later.

3.2 Assumed Flow Pattern Compared with 2-D FEM Calculations

The assumed flow pattern corresponds with the results of a 2-D FEM calculation that show equipotential lines underneath the dike, which is illustrated in Figs. 5 and 6, that are perpendicular to the flow lines. Calculations were run with DgFlow (Van Esch

2013, 2014). In the calculation it is assumed that the dike and the bottom of the sand (at −3 m) are impermeable, that the pipe to the CSB is very permeable and the CSB has a permeability that is 4 times larger than the permeability of the sand. The side boundaries are impermeable and a constant head of 6 m is applied on the horizontal part of the mesh at the upstream part (left from the dike) and the head is zero in the pipe. The upstream part is longer than shown here and extended until −25 m.

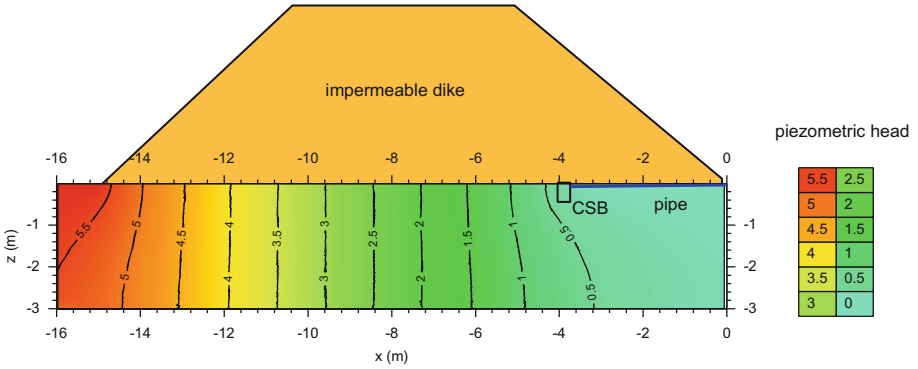

Fig. 5. Equipotential lines in sand layer underneath impermeable dike.

The equipotential lines are vertical under most of the dike and more or less circular close to the barrier, as also appeared from the detail around the CSB in Fig. 6. Assuming these flow patterns (horizontal flow in the sand underneath the dike and circular flow near and into the barrier) it is possible to derive an analytical calculation model.

3.3 Calculation Method

With the assumptions mentioned above and the parameters as explained in Fig. 4, the flow Q per meter dike length underneath the dike can be written as:

$$Q = k_s \frac{\phi_0 - \phi_1}{L} \tag{1}$$

and the outflow to the semi-confined aquifer (Q_s) downstream of the CSB as:

$$Q_s = k_s \frac{\phi_1}{\lambda} \tag{2}$$

The head drop caused by the circular flow in the sand and through the barrier then becomes (assuming only flow through the quarter circle shown in Fig. 4 and scheming the barrier also to a quarter circle):

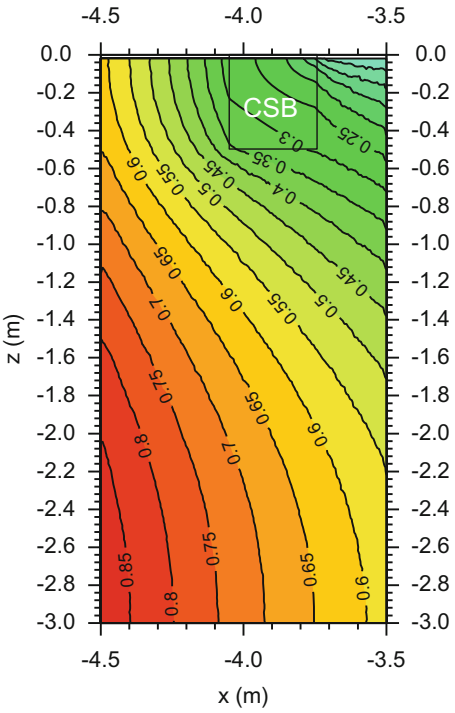

Fig. 6. Detail of Fig. 5 around the barrier.

$$\phi_1 = \frac{Q_c}{0.5\pi k_z} \ln \frac{R_1}{R_b} + \frac{Q_c}{0.5\pi k_b} \ln \frac{R_b}{R_s} \tag{3}$$

In these equations k_s is the permeability of the sand and k_b is the permeability of the barrier and λ, the leakage length, defined as: $\lambda = \sqrt{ad.k_s/k_a}$ with a the thickness of the cover of the semi-impermeable layer on top of the aquifer, d the thickness of the aquifer and k_a the permeability of the aquifer

With Eq. (3), Q_c, the outflow through the CSB, can be written as:

$$Q_c = \frac{0.5\pi\phi_1 k_s}{\ln \frac{R_1}{R_b} + \frac{k_s}{k_b} \ln \frac{R_b}{R_s}} \tag{4}$$

Since:

$$Q = Q_s + Q_c \tag{5}$$

Equations (2), (4) and (5) can be combined to write ϕ_1 as a function of ϕ_0 and the other parameters:

$$\phi_1 = \phi_0 \frac{1}{1 + \frac{L}{\lambda} + \frac{0.5\pi L/d}{\ln\frac{R_1}{R_b} + \frac{k_s}{k_b}\ln\frac{R_b}{R_s}}} \tag{6}$$

and ϕ_b, the head at the upstream side of the barrier caused by only the circular flow to the barrier, as function of ϕ_1:

$$\phi_b = \phi_1 \frac{1}{1 + \frac{k_b}{k_s} \cdot \ln\frac{R_1}{R_b} / \ln\frac{R_b}{R_s}} \tag{7}$$

The gradient in the barrier at R_s is of importance, since this gradient determines whether there will be erosion into the barrier or not.

$$i_{b,R_s} = \frac{\phi_1 - \phi_b}{\ln\frac{R_1}{R_b}} \tag{8}$$

Circular flow lines are assumed and therefore it is easy to calculate the outflow gradient where the barrier meets the pipe:

$$i_s = i_b \frac{k_s}{k_b}\frac{R_b}{R_s} \tag{9}$$

In this calculation, it is assumed that the flow in the semi-confined aquifer is not influenced by the erosion pipe in the sand in that aquifer. This is justified for field situations, but not for the simulation of small-scale model tests. In small scale model tests λ can be approximated as the distance from the barrier to the outflow point starting at half the sand layer depth.

In this calculation R_1 is not yet defined. A possibility is to take the depth of the sand layer as shown in Fig. 4, but that is not very realistic, because that would mean that in all cases, also for a very thick sand layer, there will be a water flow from the deepest part of the sand layer to the barrier. Looking at the equipotential lines in the numerical calculation this seems not to be the case. At some depth below the barrier, the flow in the sand is not influenced by the flow in the barrier. Therefore the following assumption was used. The ratio between R_1 and the depth of the sand layer (d) is the same as the ratio between the flows through the barrier (Q_c) and the total flow (Q) or in formula:

$$\frac{R_1}{d} = \frac{Q_c}{Q} \tag{10}$$

This formula means that there is no explicit expression for i_s, since R_1 depends on the calculated Qc and Q. However, in a spreadsheet there is a fast convergence, starting with the value $R_1 = d$.

4 Validation

To investigate the accuracy of the calculation method, it was validated using the results of small-scale model tests. Most small scale model tests were performed with a barrier extending from top to bottom through the sand layer. Two tests described by Bezuijen et al. (2018) are suitable due to the limited depth of the barrier: Test 192 and Test 198. The tests were performed different set-ups of the same dimensions. Test 192 was performed in a flat box (L × W × D = 483 × 300 × 101 mm) and Test 198 in a narrow higher box (L × W × D = 483 × 101 × 300 mm). Further details of the set-up can be found in Bezuijen et al. (2018). Dimensions and parameters are presented in Table 1.

For both tests is reported at what difference in piezometric head damage occurred.

The values mentioned in Table 1 are different from what is mentioned in Bezuijen et al. (2018). The reason is that after publication it was found that there is an inflow resistance at the inflow side of the set-up. The value used here is the corrected value for that resistance. Two different calculations were run for each test. In the first calculation, the measured permeability was used for both materials (the fine sand and the CSB) by means of a standard permeability test. The results with fixed permeability (fixed perm.) are shown in Table 1. In the second calculation, the measured permeabilities and also the ratio in the permeabilities were adjusted in a way that the calculated and measured discharge are in agreement (results with "adj. perm" in header of Table 1). Furthermore, it was assumed that at the start of damage, the pipe has grown 1 cm in the barrier. This is a rather arbitrary choice and it should be realized that the results depend to a large extend on that choice. Since, during the experiments, when the pipes are formed downstream of the barrier (see Sect. 2), most head drop is realized over the fine sand upstream of the barrier, changing the assumption of the damage criterion for the growth of the pipe into the barrier to, for example, 0.5 cm, implies that the gradient at the outflow point from the CSB to the erosion pipe nearly doubles. Of course this would mean that the boundary of the CSB is not stable and will erode until the pipe is 1 cm in the barrier. Consequence is that the head should double to allow a growth of 2 cm into the barrier. However, as mentioned before, as the growth of the pipe into the barrier increases, it cannot be guaranteed that there is still a 2D situation.

From Table 1, it can be concluded that at the start of damage the calculated gradient is close to 1, which was assumed as damage criterion in the calculations. If the calculations are adjusted in a way that the measured and calculated outflow fit, the calculated gradients for the assumption that the pipe has grown all over the CSB 1 cm into the barrier are equal and 1, which is, using that criterion, an almost perfect agreement.

5 Predictions

The model was used to predict the outcome of Delta Flume tests. In one of these large scale model tests a seepage length of 10 m until the barrier is created and a total seepage length of 17 m. The barrier stretches over the whole width of the flume (5 m). The thickness of the sand layer underneath the dike is 3 m and the barrier itself is 0.5 m

Table 1. Results of calculations. The calculations for T192 and T198 are performed for a fixed R_s. In the other calculations R_s is adjusted to achieve an outflow gradient of 1. The width of the container is not defined for the Boretto calculation. The number is used to calculate the discharge in litres/minute.

CSB calculations	T192	T192	T198	T198	1st test	2nd test	
	N box	N box	Tilted box	Tilted box	Delta flume	Delta flume	Boretto
	Fixed perm	Adj. perm	Fixed perm	Adj. perm	Length p.	Length p.	Length p.
ϕ_0 (m)	0.408	0.408	0.264	0.264	6	6	10
l. Upstream barrier (L) (m)	0.178	0.178	0.178	0.178	10	3.7	200
l. Downstr. barrier (λ) (m)	0.15	0.15	0.15	0.15	7	7	1400
Depth sand layer (d) (m)	0.1	0.1	0.3	0.3	3	3	30
R_b (avg. dim. barrier) (m)	0.04	0.04	0.04	0.04	0.4	0.4	0.4
R_1 (m)	7.49E−02	7.50E−02	1.17E−01	1.16E−01	2.02E+00	2.04E+00	2.83E+01
k_b/k_s	8.67	8.97	8.67	7.20	13.5	13.5	10
R_outflow (R_s) (m)	0.01	0.01	0.01	0.01	0.046	0.097	0.064
Gradient outflow point (-)	1.04	1.01	0.84	1.00	1.01	1.00	1.00
Width container (m)	0.3	0.3	0.1	0.1	5	5	10
Perm. sand (k_s) (m/s)	3.00E−04	2.90E−04	3.00E−04	3.61E−04	1.40E−04	1.40E−04	2.90E−04
Discharge (Q) (m/s)	5.68E−04	5.49E−04	2.94E−04	3.53E−04	6.84E−05	1.41E−04	1.04E−05
Flow (l/min)	1.02E+00	9.89E−01	5.29E−01	6.35E−01	6.15E+01	1.27E+02	1.86E+02
Flow through barrier (l/min)	7.66E−01	7.42E−01	2.06E−01	2.45E−01	4.14E+01	8.63E+01	1.76E+02
Flow through sand (l/min)	2.56E−01	2.47E−01	3.23E−01	3.90E−01	2.01E+01	4.08E+01	1.07E+01
Total discharge (l/min)	1.02E+00	9.89E−01	5.29E−01	6.35E−01	6.15E+01	1.27E+02	1.86E+02

deep and 0.3 m wide, which means an average dimension R_b of 0.4 m. Other parameters are presented in Table 1. It was calculated what ingrowth of the pipe could be expected at the maximum head difference of 6 m water column that can be applied in these tests. An ingrowth of 4.6 cm was calculated. This means that there will be

some damage to the barrier, but a breakthrough is very unlikely. Since a calculated ingrowth of 1/3 of the barrier width seems necessary before in tests a breakthrough was found. As mentioned before, this depends how the pipe growth develops into the barrier. A second test in the Delta Flume will be performed with a seepage length of 3.7 m to the barrier. With all other parameters the same as in the previous calculation, the model predicts an ingrowth of 9.7 cm for this situation. This means that there will be damage to the barrier, but it is still possible that no breakthrough can be realized. The test is not yet performed, thus this is a real prediction.

It is of interest to see the outcome of the model for a real field situation. Therefore, a field case is calculated. What are the consequences when a CSB would be applied along the piping prone stretch of the Po river dike near Boretto (Bezuijen 2017; Gracía Martínes et al. 2017)? The parameters for this calculation are taken from Bezuijen (2017), apart from the maximum head difference before overtopping. Bezuijen mentions 6 m head difference, but that is when the summer dike overtops. The winter dike will overtop at a head difference of 10 m and this value is used in the calculation. A permeability ratio CSB/sand of 10 is assumed. This is possible when the original sand is rather homogeneous, otherwise a filter cake may form (Akrami et al. 2018) and the solution presented here is not valid for the situation with such a filter cake. The calculations indicate that at the maximum possible head difference the pipe will growth 6.5 cm into the barrier. Remarkable is that the average gradient underneath the dike is only 0.035 in that situation. The reason is the long leakage length of the aquifer on the landward side. The flow in the aquifer to the landward side will be limited and as a consequence most of the water that flows underneath the dike has to flow through the CSB. A long leakage length of the aquifer also decreases the stability of a CSB.

6 Discussion and Conclusions

An analytical model has been presented to estimate the stability of a CSB. This model is validated with two small scale model tests. Further validation is necessary using tests at different scales. The model assumes that the first damage to a CSB is caused by the outward directed gradient (the primary erosion according to Van Beek 2015) and not by the traditional erosion assumption of grains moving in a pipe due to the flow in the pipe as assumed in the Sellmeijer model (Sellmeijer 1988), denoted by secondary erosion in Van Beek (2015).

The model assumes that an exit gradient of 1 at the outflow point is decisive for the onset of damage of the CSB regardless of the scale. As expected, the outcomes of the model show scale effects. The critical gradient for the CSB (as defined by Bligh for situations without a CSB) is much lower for larger structures. This is purely caused by the groundwater flow.

Assuming that the model is correct, within the limits that can be expected from an analytical model with some simplifications, the following conclusions are possible:

– A CSB can significantly increase the strength of the dike against backward erosion piping.

- This increase is largest when the leakage length of the aquifer at the landward side of the dike is limited.
- For comparing of the results of the model to the results of tests it is necessary to measure the permeability of the sand during the test, to avoid deviations that are caused by deviations in permeability.
- Looking at the results up to now, it is reasonable to assume that the inaccuracies in the permeabilities of the different layers will be more decisive for the results of the calculations than the inaccuracy of the model.

The model is developed to be used as a first check for the potential strength increase against backward erosion piping of CSB for a dike founded on a sandy subsoil. Numerical models as described by Rosenbrand et al. (2018) can be used for more detailed analysis. This analytical model predicts a significant influence of the leakage length of the aquifer on the stability against backward erosion piping. This has to be investigated further for field applications.

References

Akrami S, Bezuijen A, Rosenbrand E (2018) Investigating the formation of a filter cake in column experiments, for combinations of filter and finer sand in a coarse sand barrier. In: Proceedings of 26th meeting of the European working group on internal erosion, Milan

Bezuijen A, Rosenbrand E, van Beek VM, Vandenboer K (2018) Experiments for a coarse sand barrier as a measure against backwards erosion piping. In: International conference physical modelling in geotechnics, London

Bezuijen A (2017) The influence of the leakage length on the initiation of backward erosion piping. In: Proceedings of 25th meeting of the European working group on internal erosion, Delft

Bligh WG (1915) Submerged weirs founded on sand. Dams and weirs: an analytical and practical treatise on gravity dams and weirs; arch and buttress dams, submerged weirs; and barrages. Chicago, pp 151–179

Cao D (1994) Countermeasures for seepage erosion of Yangtze River main dikes. Yangtze River 25(1):25–30

Förster U, Bezuijen A, Van den Berg SG (2015) Vertically inserted geotextile used for strengthening levees against internal erosion. In: 16th European conference on soil mechanics and geotechnical engineering, Edinburgh, 1995–2000

Gracía Martínes MF, Marchi M, Tonni L, Gottardi G, Bezuijen A (2017) Numerical simulation of the groundwater flow leading to sand boil reactivation in the Po River. In: Proceedings of 25th EWG-IE, Delft

Lane EW (1935) Security from under-seepage masonry dams on earth foundations. Trans Am Soc Civ Eng 100(1):929–966

Robbins BA, van Beek VM, Lopez JF, Montalvo Bartolomei AM, Murphy J (2018) A novel laboratory test for backward erosion piping. https://doi.org/10.1680/jphmg.17.00016 (pre-print)

Rosenbrand E, Van Beek V, Koelewijn A, Akrami S, Förster U, Bezuijen A (2018) Scale effects in coarse sand barrier experiments. In: Proceedings of 26th meeting of the European working group on internal erosion, Milan

Sellmeijer JB (1988) On the mechanism of piping under impervious structures. TU Delft, Delft

Van Beek VM (2015) Backward erosion piping initiation and progression. TU Delft, Delft
Vandenboer K, Van Beek VM, Bezuijen A (2017) 3D character of backward erosion piping. Géotechnique. https://doi.org/10.1680/jgeot.16.P.091
Van Esch JM (2014) Flood defense assessment tools for piping in WTI 2017—Report 9b. Groundwater Flow Simulator DgFlow 3D Validation piping module. Deltares report 1209435-006-GEO-0001. Delft
Van Esch JM (2013) Modeling groundwater flow and piping under dikes and dams model validation and verification. Deltares report 1207809-005-GEO-0001-jvm. Delft

Multidisciplinary Analysis and Modelling of a River Embankment Affected by Piping

Giulia Bossi[1], Silvia Bersan[2], Simonetta Cola[2(✉)], Luca Schenato[1], Fabio De Polo[3], Celeste Menegazzo[2], Jacopo Boaga[4], Giorgio Cassiani[4], Fabiano Donini[4], and Paolo Simonini[2]

[1] National Research Council, Research Institute for Geo-Hydrological Protection, Rome, Italy
[2] Department of Civil, Environmental and Architectural Engineering, University of Padova, Padua, Italy
simonetta.cola@unipd.it
[3] Dam Office, Autonomous Province of Bolzano, Bolzano, Italy
[4] Department of Géosciences, University of Padova, Padua, Italy

Abstract. The paper presents a multidisciplinary analysis carried out for the characterization and monitoring of a levee in Bozen Province, North Italy. The study treats a small section of the Adige river embankments, interested in the recent past by moderate piping phenomena and subjected to some subsequent interventions for the risk mitigation. The data acquired with an Electrical Resistivity Tomography (ERT) investigation and an optical fiber distributed temperature sensing (DTS) are compared to boreholes information, laboratory tests and piezometers measurements. They provided a multi-dimensional characterization of the levee and of the close subsoil water-meadows, possible piping preferential paths. Since the presence of more permeable lenses within the silty matrix characterizing the levee foundations, the subsequent 2D seepage analysis was carried out with the Boolean Stochastic Generation (BoSG) method, which randomly generates lenses with specific rheological properties within a matrix with another set of parameters. The soil configurations that are more congruent with the monitoring data were selected within a pool of 360 simulations, providing information about the probable seepage mechanism within the levee and the reliability of the interventions.

Keywords: Embankment · Piping · Fiber optic sensor
Electrical resistivity tomography · Stochastic modelling

1 The Test Site

The study concerns a levee on the Adige River in Bozen Province (Fig. 1), North Italy (46°14′11.0″N 11°10′52.8″E). In the long history of the Adige valley, several anthropic interventions were performed in the area. Particularly, in the 19th century straight embankments were realized to confine the river that was before free to migrate along the narrow alluvial plan. Therefore, a complex sedimentological environment with point-bar structures and paleo-channels characterizes the subsoil system. In the recent past, moderate piping phenomena and flooding affected a 350 m long segment of the

S. Bonelli et al. (Eds.): EWG-IE 2018, LNCE 17, pp. 234–244, 2019.
https://doi.org/10.1007/978-3-319-99423-9_22

right levee (Fig. 1). To reinforce the protection system and avoid internal erosion the embankment was recently reinforced with a 10 m deep jet-grouting diaphragm. Nevertheless, moderate piping phenomena still persist in the area when the water level in the river is high.

In order to identify the areas more prone to internal erosion a multidisciplinary survey was carried out. It consisted of boreholes and penetrometer tests, laboratory tests and a monitoring performed with electrical piezometers installed in boreholes. The in-site investigation was completed with several Electrical Resistivity Tomographies (ERT) executed along the river and in the neighbour area and the monitoring system was integrated with a fiber optic based system installed in a shallow trench at the bank base on the landside. All the collected data were used as input for the realization of an innovative stochastic seepage model. Of course, for a lack of space, only some results of the in-situ investigation and preliminary output of the stochastic model are reported in this work.

2 The Monitoring Network

Since many years, the measurement of temperature inside levees is extensively investigated as a tool for identifying abnormal filtration flows across the dam. The basic principle at the basis of the detection by temperature sensing consists in assuming that when normal flow regime exists, temperature fluctuations are driven by heat conduction from the air and the foundation, on a seasonal basis. On the contrary, when abnormal seepage flows take place, the amplitude of temperature fluctuations increases as advection from the water upstream becomes way too significant. On these premises, only a measuring campaign performed over a long time and with sufficient spatial resolution can detect any relevant change.

In the Salorno test site, we installed both optical fiber cable and traditional sensors in order to assess the potentiality of distributed sensing with fiber optics for detecting local heterogeneity in seepage rate.

2.1 Traditional Sensor Network

As Fig. 1 depicts, two cross sections of the levee were equipped with piezometers and spot temperature sensors. One Casagrande piezometer was placed on the riverside to indirectly record the river water level. Other two piezometers were deployed on both sides of the barrier as to assess its efficacy and evaluate its influence on the seepage pattern. Lastly, a two-level piezometer is located below the landside berm.

A spot temperature sensor was deployed along Adige bank, to control the temperature of the river water. Another one is located on the deeper level of the piezometer below the berm and three were placed near the trench that would accommodate the optical fiber.

All traditional sensors work in real-time, acquiring every hour and sending data to a remote server. Data acquisition stated in June 2016. As the monitoring system is finalized to identify the presence of anomalous seepage paths and not as an early-warning system, the acquisition time step of 1 h was considered enough short to find a relation among observations in the subsoil and the water level in the river.

2.2 Distributed Temperature Sensing by Optical Fiber Sensors

Distributed fiber optic sensing (DFOS) is the only available contact sensor technology, capable of providing the measurement of temperature with sufficient spatial resolution in soil over a long length (Schenato 2017). Remarkably, the first applications of DFOS to embankment temperature monitoring are dated to the middle of the 1990s (Albalat and Garnero 1995). In particular, the DFOS exploiting Raman-based distributed temperature sensing (DTS) technique is the mostly used optical fiber sensor in this kind of application and also employed in this specific study.

According to DTS, when a fiber is probed with an input light signal, due to the molecular bonds' inhomogeneity of the fiber material two signals are generated and back propagated along the fiber. Namely, they are the Stokes signal at a higher wavelength and the anti-Stokes one at a lower wavelength. Only the intensity of the anti-Stokes signal is temperature-dependent, while the Stokes one is temperature insensitive. Therefore, the ratio between the anti-Stokes and the Stokes light intensity generated all along the fiber is quantitatively related to the local temperature. By probing the fiber with pulsed light and by measuring the roundtrip propagation time, it is straightforward to determine the position at which those back propagating signals have been generated.

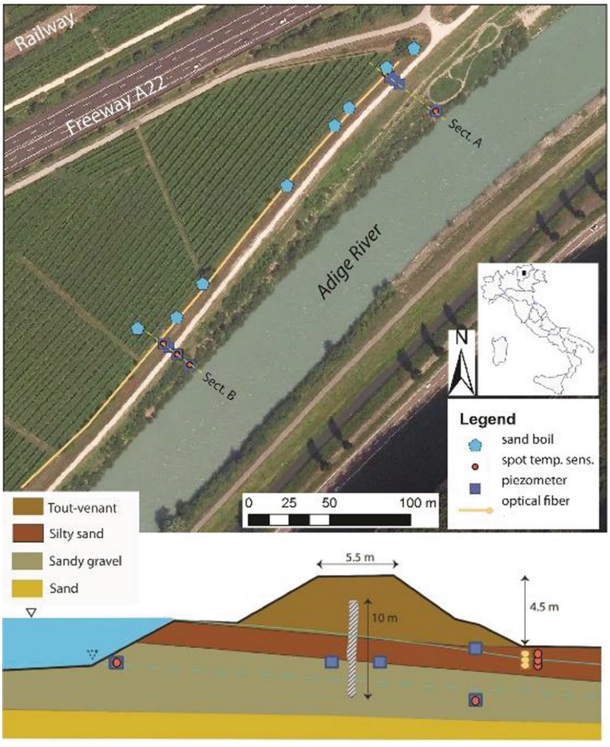

Fig. 1. Study area (*above*) and section of the levee (*below*) with the deployed sensor network.

Depending on the specific implementation, spatial resolution in the order of one meter or less can be achieved over a length of several kilometres. Temperature resolution may easily reach few tenths of a Celsius degree or even less, with a measurement time of few minutes. In our application, we used the interrogator Oryx SR DTS by Sensornet, characterized by 1 m spatial resolution and 0.1 °C temperature resolution of over 2 km, with 30 s of measurement time. The temperature accuracy is limited to 0.5 °C.

Despite the features of DTS, one of the main challenges of the thermometric approach is the identification of distinctive "signatures" of seepage (regarding time rate, amplitude, spatial gradient, etc.) from the raw temperature field data. Several factors other than those related to existing filtration flows can affect the temperature dynamics in the embankment. To address this issue, an alternative method, the so-called "heat-up" or "active" thermometric method, has been proposed. This method consists of using a hybrid cable embedding an optical fiber and one or more electrical wires, used to heat the cable via the Joule effect. The temperature dynamics during the heating and cooling phases, i.e. the time to reach a final stable temperature, are correlated to different thermal conductivity ascribable to abnormal filtration flows. This approach has been proved efficacious in those embankments with small seasonal temperature variations of the reservoir water or with very small temperature gradients between the water and the measurement point in the soil, and it has also been applied to the embankment here addressed.

Here an optical fiber cable was installed in a 350 m-long trench longitudinally excavated at the toe of the embankment. The fiber has been deployed at three levels, at depths of approximately 50, 100 and 180 cm, and it has an overall length of 1100 m. In this application, a hybrid cable, embedding an optical fiber and four copper wires, has been used to possibly enable also the active thermometric measurement of the dam.

Of course, the excavation of the trench could interfere with the undisturbed groundwater seepage paths, but we adopted every possible action to minimize the negative effects: the trench was kept as narrow as possible, also with respect to the horizontal size of the embankment; the fiber was deployed near the trench wall and the filling soil was adequately compacted to prevent vertical flows inside the trench.

Plots of Fig. 2 show two examples of the temperature field along the fiber at the three depths, taken in summer and winter respectively. Seasonal fluctuation differently affects the temperature at the three layers. In particular, the mean temperature decreases from the lower level to the upper one during winter, while it behaves oppositely in summer, when the temperature decreases with depth.

Moreover, one can observe that the temperature at the three levels in each plot shows a common trend, with localized spikes and dips at precise locations. We believe that these features are ascribable to the local characteristics of the soil (e.g. lenses with different permeability). Unfortunately, high water discharge events did not occur during the monitored period and we had not the possibility to record the soil temperature during an intense seepage phenomenon. Further investigation are currently on going, as it will be see in the section about the stochastic modelling.

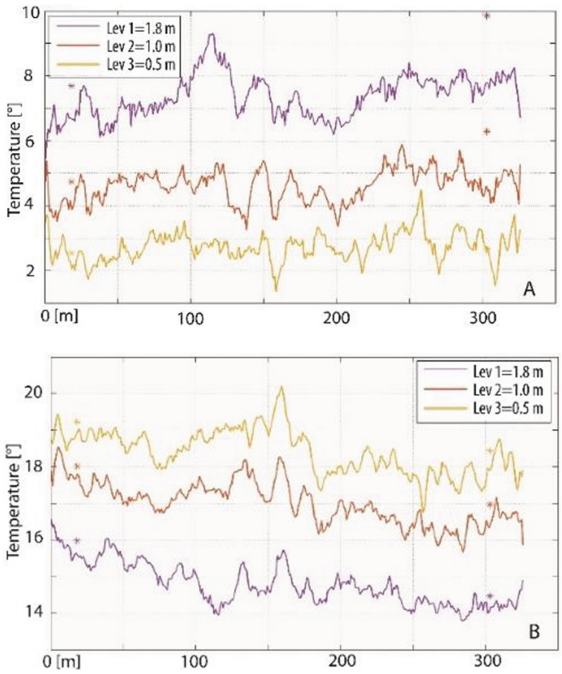

Fig. 2. Temperature along the three levels of the fiber cable in winter (A-above) and in summer (B-below).

3 Electrical Resistivity Tomography

Electrical resistivity tomography (ERT) can provide meaningful, high-resolution images of the subsoil electrical conductivity (Binley and Kemna 2005). In the context of embankment investigation this results in very detailed information concerning the levee structure (e.g. Niederleithinger et al. 2012; Perri et al. 2014; Weller et al. 2006, Busato et al. 2016), particularly when the fine-grained sediments (clay and silt), which are generally more electrically conductive than coarse materials, constitute the core of a well-built embankment. ERT is also very flexible in terms of scaling and resolution, so it is particularly suitable for this type of investigation.

At this site, several ERT surveys were applied in different configurations, in order to vary depth of investigation, resolution, and explore longitudinal and transverse sections of the embankment and the closer areas. The ERT surveys consisted of N.48 or N.72 channels, with variable electrode spacing from 0.75 m to 2 m. The ERT lines are divided in L (longitudinal) and T (transversal), as reported in Fig. 3.

We adopted the acquisition scheme dipole-dipole skip-4, which provides the best lateral resolution for our aims. Figure 4 shows as example the longitudinal ERT (L1-L3) along the levee compared to the simplified stratigraphy of boreholes S6, S5 and S7 and a transversal ERT across the levee. As it can be seen, ERT results are in very good accordance with the borehole information highlighting the presence of coarse and fine materials.

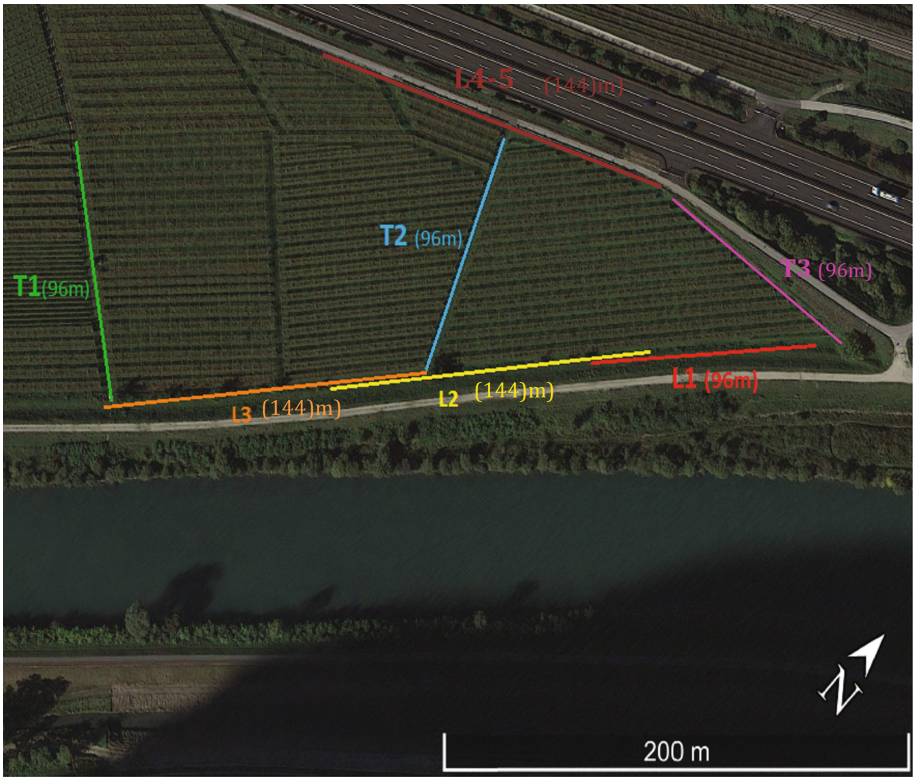

Fig. 3. Map of the ERT lines acquired in the Adige embankment.

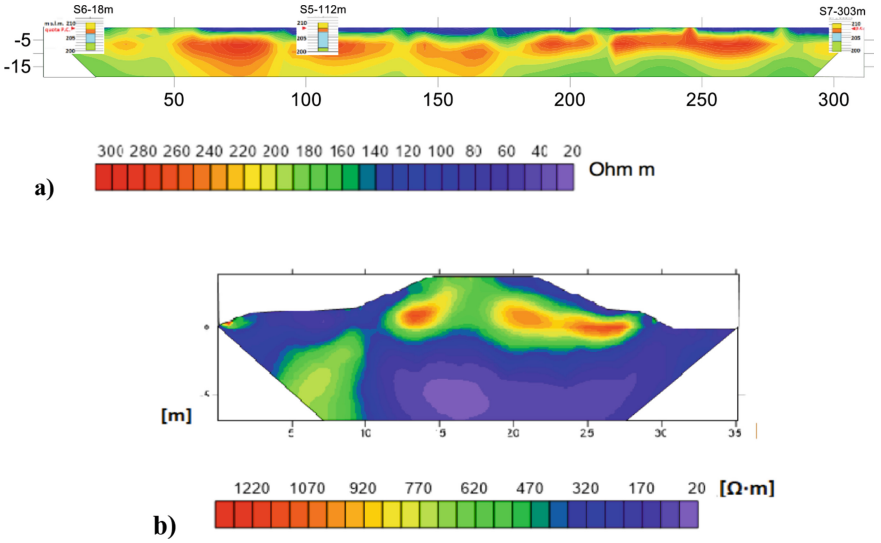

Fig. 4. Longitudinal ERT along the levee compared to boreholes information (yellow and orange: clay and silty clay; light blue gravel) (a). Transversal ERT across the levee highlights the more resistive coarser core of the embankment (b).

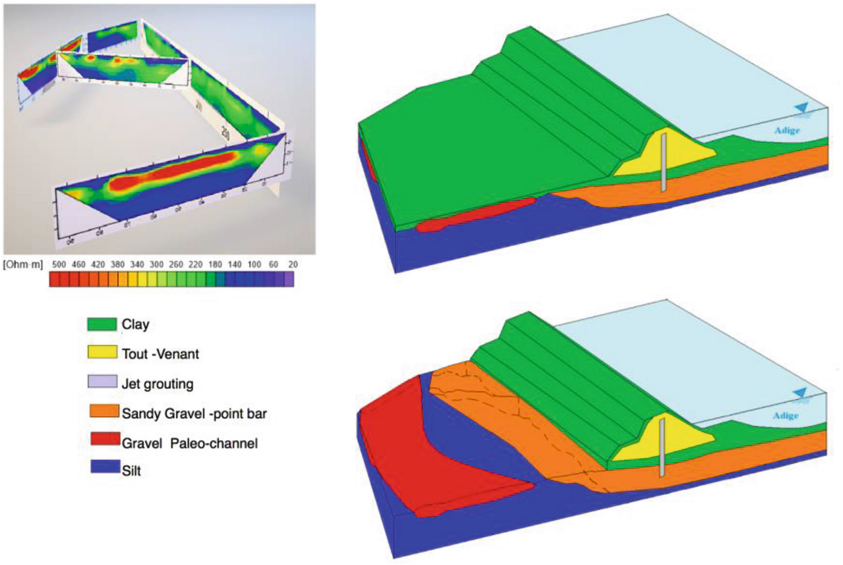

Fig. 5. The ERT results collected in the Adige areas and the 3D geological model of the paleo-channels as derived by the ERT information and the historical geomorphological map.

Figure 5 summarizes the ERT results coupling longitudinal and transversal lines in a homogenized scale. More resistive levels are clearly visible, representing the coarser sandy ad gravel levels. These resistive bodies were interpreted as the paleo-channel deposits that interest all the right side of the river, as already pointed out in some geomorphology studies (internal reports of Bolzano Province; ETSCH 2000 Proc.; Zen et al. 2016). The right panel presents a paleo-channel geological 3D model reconstructed on the base of ERT results, borehole information and the historical geomorphological maps. The ERT results, coupled with the geotechnical information, provided the input for the 2D seepage models.

4 The Stochastic Model

To investigate the seepage in the levee foundation, in light of the ERT analysis coupled with monitoring data and stratigraphic evidence, the effects of the presence of lenses with different permeability, originated from the fluvial depositional process, was analysed using the method called Boolean Stochastic Generation (BoSG) method (Bossi et al. 2016).

BoSG method randomly generates lenses with specific rheological properties within a matrix with another set of parameters. The procedure integrates scripts in Matlab® and numerical simulations with the geotechnical software FLAC (Fast Lagrangian Analysis of Continua) to generate a large number of possible dispositions of lenses. The pool of the resulting configurations is then analyzed in order to evaluate the effect of different configurations of lenses and select the configuration giving the most reliable response in comparison with the monitored data.

For the Salorno case study, 120 soil configurations in a bi-dimensional model of section A were generated: particularly, 30 configurations with 3, 6, 9 and 12 lenses respectively, were analysed. To each soil configuration, three different values of permeability, namely lens A, B and C, were associated to the lenses, bringing the grand-total of the simulations to 360. The horizontal extension of the lenses and their position are randomly assigned, while the thickness is assumed constant and equal to 20 cm. The disposition of lenses was kept horizontal to mimic the fluvial depositional process that formed them.

An example of a soil configuration with 9 lenses is shown in Fig. 6. The soil parameters for the model are indicated in Table 1. They were obtained on the base of results of laboratory tests executed on undisturbed samples during the boreholes and trench excavation.

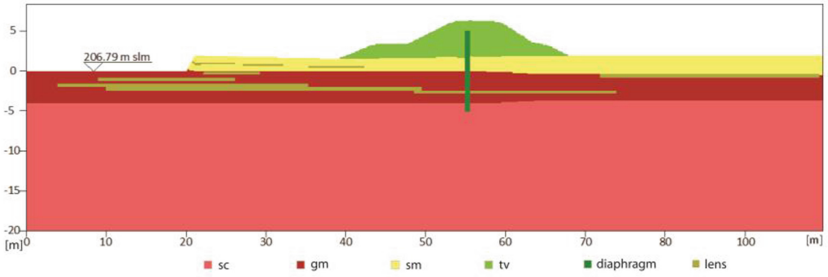

Fig. 6. Example of a modelled section with 9 randomly generated lenses (configuration #9-19).

Table 1. Soil parameters assumed for the soils and the generated lenses.

Material	ρ	Φ	*c*	*M*	υ	*k*
	[kg/m^3]	[°]	[kPa]	[MPa]		[m/s]
tv*	1936	34	0	69.7	0.30	9.70E−07
sm	1985	27	50	34.8	0.35	9.77E−06
gm	1936	33	0	83.6	0.40	2.10E−05
sc	1936	35	0	55.7	0.40	6.29E−06
lens A	1936	33	0	83.6	0.40	6.29E−05
lens B						1.25E−04
lens C						2.10E−04

(*) tv = tout-venant, well graded soil, sm = silty sand, gm = silty gravel, sc = clayey sand.

The stochastic model was tested on data from a modest flood event recorded in the 16th and 17th June 2016. The transient effect induced on pore pressure on the 360 soil configurations were confronted with data from the piezometers, checking within the pool of results those that were more congruent with the monitoring data. For instance, in Fig. 7 all the pressure head vs time curves, obtained with the numerical model for the set "lensA", are reported and compared with the data recorded at the piezometer PA03. In Fig. 8 the best and the worst fitting curves selected among the simulation obtained for set "lens C" are compared with data recorded at PA03.

The stochastic generated configurations in average better represent the seepage mechanism within the levee than the configuration without lenses. This means that there is indeed an influence of layers with higher permeability in the dynamic of the section. In particular, our first results show a greater influence of permeable layers located on the riverside.

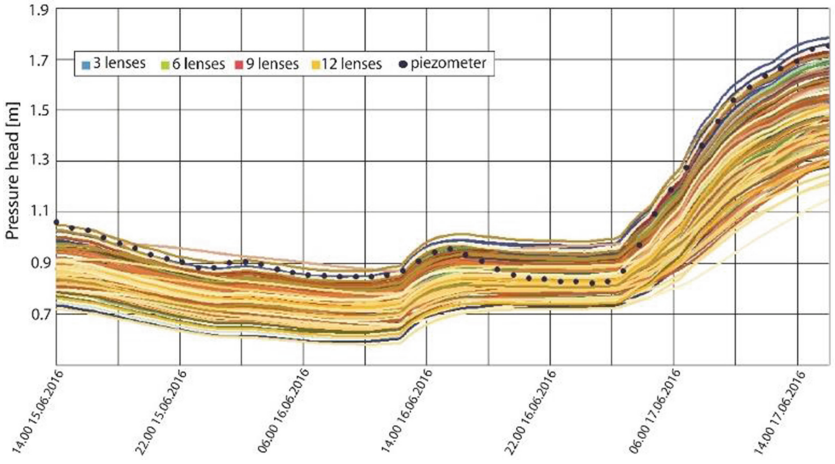

Fig. 7. Pressure head curves predicted at piezometer PA03 located near the diaphragm on the landside by all the configurations with permeability values "lens A" and compared with in-situ measures.

5 Final Remarks

The paper presents the preliminary results of a comprehensive multidisciplinary study carried out on 350 m-long portion of the right levee of the Adige River in Salorno. Different and advanced techniques (i.e. ERT and Raman-based DTS) were coupled to traditional techniques to investigate the embankment foundation and the neighbor farmland. Particularly, a very detailed ERT survey permitted to point out the subsoil structures and evidence the presence of paleo-channel sediments intercepting the levee

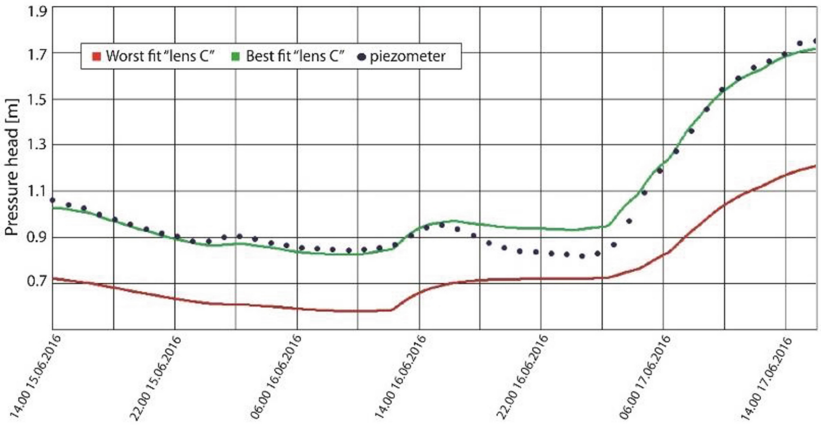

Fig. 8. Best and worst predictions for the pressure head vs time curve, among all the configurations "lens C", compared with the trend recorded at piezometer PA03.

constructed in the last 50 years, while the DFOS gave detailed information on the soil stratigraphy below the landside berm. The in-situ and laboratory data permitted the reconstruction of a seepage model on which a BoSG procedure is applied to study the influence of soil heterogeneity on the subsoil seepage and the efficiency of flooding protection.

Unfortunately, even if the monitoring system was installed in March 2016, up to now no significant flooding has occurred and DFOS could not be applied during a high seepage rate occurrence. For the same reason the stochastic seepage model was calibrated on data from a modest flood event recorded in June 2016 and the results obtained up to now cannot be considered sufficient to give final conclusion of the work. Moreover, a 3D seepage model will be constructed in the next future and different heterogeneities, i.e. heterogeneity of the waterproof barrier, will be analyzed to complete the study.

References

Albalat C, Garnero E (1995) Mesure de Fuites Sur le Canal de Jonage Avec un Capteur De Température à Fibre Optique Continûment Sensible. Technical report EDF-D4007/23/GC/95-3018; Électricité de France S.A., Paris

Binley A, Kemna A (2005) DC resistivity and induced polarization methods. In: Rubin Y, Hubbard SS (eds) Hydrogeophysics, vol 50. Water Science and Technology Library. Springer, Dordrecht, pp 129–156. https://doi.org/10.1007/1-4020-3102-5_5

Busato L, Boaga J, Peruzzo L, Himi M, Cola S, Bersan S, Cassiani G (2016) Combined geophysical surveys for the characterization of a reconstructed river embankment. Eng Geol 211:74–84. https://doi.org/10.1016/j.enggeo.2016.06.023

Bossi G, Borgatti L, Gottardi G, Marcato G (2016) The Boolean Stochastic Generation method—BoSG: a tool for the analysis of the error associated with the simplification of the stratigraphy in geotechnical models. Eng Geol 203:99–106. https://doi.org/10.1016/j.enggeo.2015.08.003

ETSCH—2000 Project, final conference proceedings June 22 2017, University of Bozen, Bozen

Niederleithinger E, Weller A, Lewis R (2012) Evaluation of geophysical techniques for dike inspection. J Environ Eng Geophys 17(4):185–195

Perri MT, Boaga J, Bersan S, Cassiani G, Cola S, Deiana R, Simonini P, Patti S (2014) River embankment characterization: the joint use of geophysical and geotechnical techniques. J Appl Geophys 110:5–22. https://doi.org/10.1016/j.jappgeo.2014.08.012

Schenato L (2017) A review of distributed fibre optic sensors for geo-hydrological applications. Appl Sci 7(9):896. https://doi.org/10.3390/app7090896

Weller A, Canh T, Breede K, Vu NT (2006) Multi-electrode measurements at Thai Binh dikes (Vietnam). NSG 4(2):135–143. https://doi.org/10.3997/1873-0604

Zen S, Bogoni M, Zolezzi G, Lanzoni S, Scorpio V (2016) Modeling the long-term planform evolution of meandering rivers in confined alluvial valleys: Etsch-Adige River, NE Italy. American Geophysical Union, Fall General Assembly 2016, abstract #EP51A-0855

Detection of Permeability Defects Within Dams and Levees Through Coupled Seepage and Heat Transport Analyses

Chiara Cesali[1(✉)] and Vincenzo Federico[2]

[1] Department of Civil Engineering and Information Engineering, University of Rome Tor Vergata, Rome, Italy
cesali@ing.uniroma2.it
[2] Rome, Italy

Abstract. Due to several triggering causes, e.g. heterogeneity of the grain size of quarried materials, inappropriate compaction, discontinuities of displacements, dynamic effects, particles migration and internal erosion processes and animal actions, permeability defects (p.d.) are practically unavoidable in earthen structures. Their detection, usually carried out through the monitoring of seepage flow and erosion phenomena, is needed to evaluate the safety evolution of these structures and prevent exceeding serviceability (change of discharge, turbid water) or ultimate (local or global instabilities, piping, structural collapses) limit states. To this purpose, distributed thermal monitoring systems, based on optical fibers sensors, are becoming more popular. The variations in measured temperature values are not however immediately linkable to the effects of p.d., due to the 'coupling' of seepage flow process and heat transport mechanism through materials and foundation soils. To better understand the mutual dependence between these coupled processes and to investigate the effects of a p.d. due to internal erosion, several numerical simulations have been run. The analysis of a large scale test on a monitored experimental dyke is finally carried out.

Keywords: Permeability defects · Internal erosion processes · Seepage
Heat transport process · Monitoring

1 Introduction

Particle migration and internal erosion phenomena represent the main causes of developing/occurring of permeability defects (p.d.) in earthen structures (Foster et al. 1998; ICOLD 2013). The detection of these dangerous, often hidden, phenomena and, in particular, of the induced p.d., is difficult (Talbot and Ralston 1985; Federico and Montanaro 2011). The need to understand how p.d. modify the seepage flow characteristics (e.g. discharge rate, interstitial pressure distribution and free surface profile) through embankment dams and levees, causing exceedance of serviceability (change of discharge, turbid water) or ultimate limit states (local or global instabilities, piping, structural collapses), is well recognized (Sjödahl and Johansson 2012). In turn, permeability defects (p.d.) may induce undesirable phenomena, such as leakages,

S. Bonelli et al. (Eds.): EWG-IE 2018, LNCE 17, pp. 245–257, 2019.
https://doi.org/10.1007/978-3-319-99423-9_23

redistribution of interstitial pressures, soil shear strength reduction, instability phenomena and local increases of the hydraulic gradients, whose related drag forces may trigger internal erosion and particles migration that might evolve up to embankment collapses (Radzicki 2014).

Appropriate monitoring of the seepage flow within earthen dams/levees may allow to detect possible internal erosion phenomena before the safety of these structures is totally compromised. In addition to "conventional" instruments (e.g. piezometers, discharge measurements), among the available methods for monitoring seepage and erosion processes, thermal sensors recently became popular (Radzicki 2014). Temperature can be used as an indirect measure of the soil saturation degree, exploiting the dependency of the thermal properties of the soil (conductivity and heat capacity) on its water content. In saturated conditions, temperature measurements can provide information on seepage flow velocities, allowing identification of the development and evolution of erosion channels (pipes) and zones of higher permeability, caused by particles migration phenomena. However, the correct interpretation of temperature measurements, coupled to piezometric heads (p.h.) readings, must considerer the mutual dependency of thermal and hydraulic properties of soils.

Thus, numerical analyses of the *coupled* seepage flow process and heat transport mechanism through (homogeneous and zoned) earth structures have been carried out to evaluate the effects of p.d. (particularly, of their geometrical sizes) due to internal erosion processes on the main hydraulic variables (e.g. piezometric heads, interstitial pressure) and temperature.

2 Coupled Seepage and Heat Transport Processes in Embankment Dams and Levees

The temperatures in the upstream water reservoir and in the environment mainly affect the temperature distribution within embankment dams and levees. The air and the water reservoir temperatures seasonally vary. Furthermore, the upstream water reservoir also seasonally changes.

Advection by seepage flow and heat conduction causes temperature variations within the earthen structure. Particularly, in absence of leakage (empty reservoir) through an earth structure, heat transfer is driven entirely by conduction process. Water flow from the reservoir through the dam (or levee) material affects the temperature field in the proximity of the flow path. The presence of flow adds advection to the heat transfer process induced by the flow. As leakages increase, the thermal field is driven increasingly by advection and heat transfer by conduction reduces and might eventually become negligible.

For small seepage flow through a pervious structure, the seasonal temperature variation in its upper part mostly depends on the air temperature variations.

The air influence decreases with depth; thus, this process must be considered when temperature measurements are carried out at shallow depths and in small dam or levees. If the seepage flow increases, the seasonally temperature variation will become more appreciable.

These coupled mechanisms (seepage and heat transport) are analytically described (2D case) through the following partial differential equation (TEMP/W manual):

$$\frac{\partial}{\partial x}\left(k_{T,x}\frac{\partial T}{\partial x}\right)+\frac{\partial}{\partial y}\left(k_{T,y}\frac{\partial T}{\partial y}\right)+\theta_w\rho_w c_{pw}\left[\frac{\partial(q_w T)}{\partial x}+\frac{\partial(q_w T)}{\partial y}\right]+Q_T = \left(\rho_s c_{ps}+L\theta_w\frac{\partial w_u}{\partial T}\right)\frac{\partial T}{\partial t} \quad (1)$$

being T the temperature; $\rho_s \cdot c_{ps}$, the volumetric heat capacity of soil; $\rho_w \cdot c_{pw}$, the volumetric heat capacity of water; q_w, the specific discharge of water (i.e. Darcy velocity); $k_{T,x}$ and $k_{T,y}$ the thermal conductivity in the x and y directions, respectively; Q_T, the applied boundary thermal flux; c, the volumetric heat capacity of the material; L, the latent heat associated with the phase change; w_u, the total unfrozen (liquid) volumetric water content, defined as: $w_u = W_u \cdot \theta_w$, with W_u unfrozen (liquid) water content ($\in [0, 1]$) and θ_w, the volumetric water content.

To solve Eq. (1), the definition of the thermal properties of soils as a function of the hydraulic variables and *viceversa* is thus required; in particular: (*i*) unfrozen water content as a function of temperature; (*ii*) thermal conductivity as a function of the volumetric water content; (*iii*) volumetric specific heat capacity versus volume water content (Fig. 1).

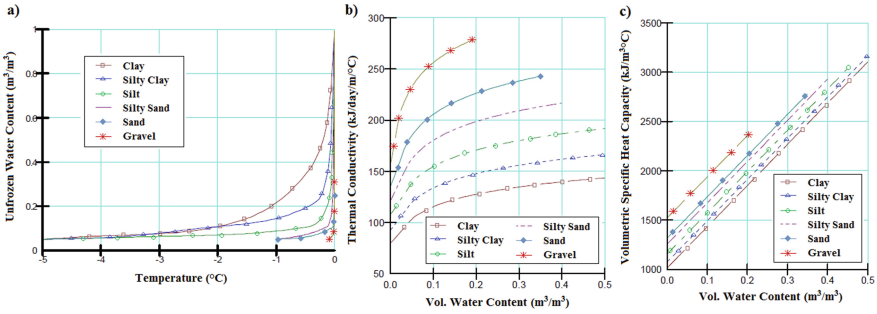

Fig. 1. (*a*) Unfrozen water content versus temperature; (*b*) thermal conductivity versus volume water content; (*c*) volumetric specific heat capacity versus volume water content. (adapted from TEMP/W manual)

3 Hydraulic and Thermal Modelling of Permeability Defects

The effects of permeability defects (p.d.) induced by *a*) backward (*piping*) erosion in foundation soils of homogeneous embankment dams or levees and *b*) concentrated leak erosion within the core of zoned embankments (Fig. 2), on the distributions of piezometric heads (p.h.) and temperature, have been investigated through coupled analyses using two commercial numerical, finite element (FE) codes, TEMP/W and SEEP/W (Cesali and Federico 2018).

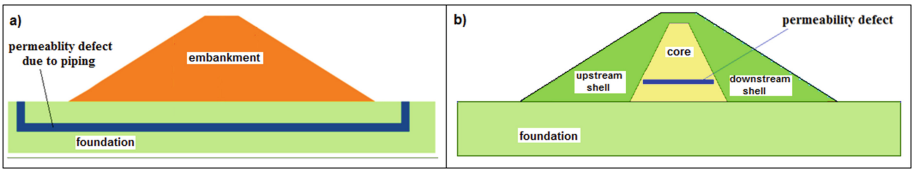

Fig. 2. Permeability defects due to (*a*) piping erosion; (*b*) concentrated leak erosion

Coupled seepage and heat transport analyses have been initially carried out for a homogeneous small dam or levee (*case A*): the height H of the structure is 10 m; the cross section is trapezoidal; the width at the top (L_{crest}) is 4 m; the thickness T_f of the foundation soil is 6 m (Fig. 3a). The considered hydraulic (permeability and volume water content) and thermal (conductivity and heat capacity) properties have been taken by TEMP/W user's manual (Fig. 1), according to typical construction materials. The assigned hydraulic (h_w = initial upstream hydraulic head, p_w = pore pressure; Q = total water flux) and thermal (T_1 = upstream temperature; T_2 = downstream temperature) boundary conditions are shown in Fig. 3b. A linear (uniform) increase of the length (L_d) of the p.d. or pipe during the simulation (up to the maximum value $L_{d,max}$, Fig. 3a) is assumed; particularly, for the examined case, the piping progression lasts 12 h, approximately.

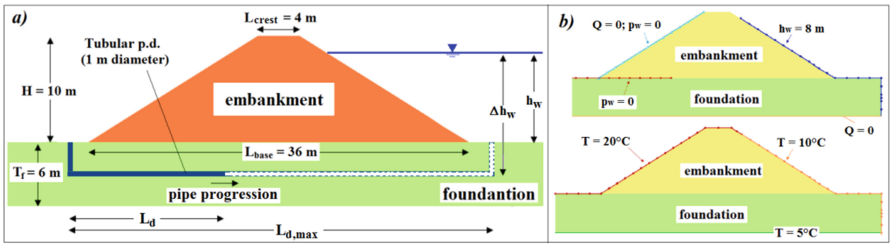

Fig. 3. *Case A* – (*a*) considered homogeneous earthen structure; (*b*) Boundary conditions

Each numerical simulation has been thus divided in 15 steps of 3000 s, for a total duration of 45,000 s. Moreover, the progression of piping has been simply modelled by increasing the length of pipe of 3 m, at each step.

Afterwards, FE analyses had run for a zoned earthen structure: height H = 10 m; height of the core H' = 9 m; width at the top (L_{crest}) = 4 m; thickness T_f of the foundation soil = 4 m (*case B*, Fig. 4).

The following hypotheses and conditions have been considered:

- *case* (*A*) steady state seepage flow with constant upstream hydraulic head (h_w = 8 m) and unsteady state heat transport process (elapsed time ≅ 12 h = t_{er}), and tubular p.d. (due to *piping* erosion, 1 m diameter, simply schematized in the proposed 2D hydrothermal model by a horizontal layer of variable length representing the erosion

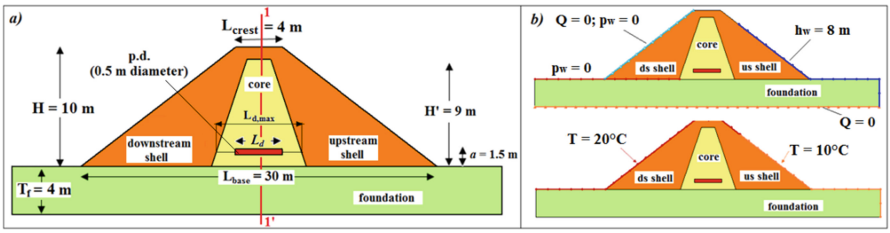

Fig. 4. *Case B* – (*a*) considered zoned earthen structure; (*b*) boundary conditions

channel/pipe) in pervious foundation soils of a homogeneous levee (permeability of the defect, $k_d = 10^{-2}$ m/s);

- *case* (*B*) steady state seepage flow with constant hydraulic head ($h_w = 8$ m), impervious foundation soils and unsteady state heat flux, and p.d. (0.5 m diameter; elevation $a = 1{,}5$ m; $k_d = 10^{-2}$ and 10^{-5} m/s) within the core (maximum width of the core corresponding to elevation of the p.d., $L_{d,max} = 7$ m) of a zoned earth structure, for $L_d/L_{d,max} = 0.60, 0.90, 0.95, 1$.

The results of numerical simulations are shown in the following figures.

Case (*A*). Measurable variations (≅0.1 °C) in temperature (*T*) distribution along a horizontal section, at the downstream toe, are observed during the progression of piping from $L_d/L_{d,max} \cong 0.60$ (Fig. 5a, c). By increasing $L_d/L_{d,max}$, the changes in *T* become more appreciable, up to ≅1 °C for $L_d/L_{d,max} = 0.90$ (Fig. 5a).

As soon as the pipe reaches the upstream side ($L_d/L_{d,max} = 1$), great variations in temperature distribution (≅6 °C) can be observed/measured (Fig. 5d). On the contrary, variations in temperature distribution along a vertical section become sensible (up to 1 °C) only for $L_d/L_{d,max} = 1$ (Fig. 5b).

Concerning the piezometric heads (p.h.) distributions along a vertical section (Fig. 6a) and at the point *P* (Fig. 6b), appreciable changes (1 m and 0.20 m, respectively) can be observed only for $L_d/L_{d,max} = 1$, as the previous case.

Thus, fiber optics or thermal sensors along a horizontal section, spaced every 0.50 m for 3 m width, at the downstream toe of earthen structures, appears more reliable to monitorate piping erosion progression, allowing to develop early emergency action plans before breaching.

Case (*B*). The effects of the dimensions of a p.d. on the evolution of temperature distribution within zoned embankments are investigated. The obtained results in terms of temperature distribution along the section 1-1′ (see Fig. 4a), for $k_d = 10^{-5}$ m/s and 10^{-2} m/s (core permeability $k_c = 5 \cdot 10^{-8}$ m/s) and $L_d/L_{d,max} = 0.60, 0.90, 0.95$ and 1.0, are shown in Figs. 7 and 8. According to the implemented hydro-thermal model, for $L_d/L_{d,max} = 1$, appreciable (≅0.5 °C if $k_d = 10^{-5}$ m/s) and great (≅3 °C if $k_d = 10^{-2}$ m/s) variations in temperature can be measured at the elevation of the p.d.

The progressive evolution of the p.d. within the core induces small, but detectable, changes in time of the temperature distribution (0.2 ÷ 0.3 °C) only for $L_d/L_{d,max} \geq 0.95$; if $L_d/L_{d,max} < 0.95$, variations in temperature distribution are difficulty recognizable.

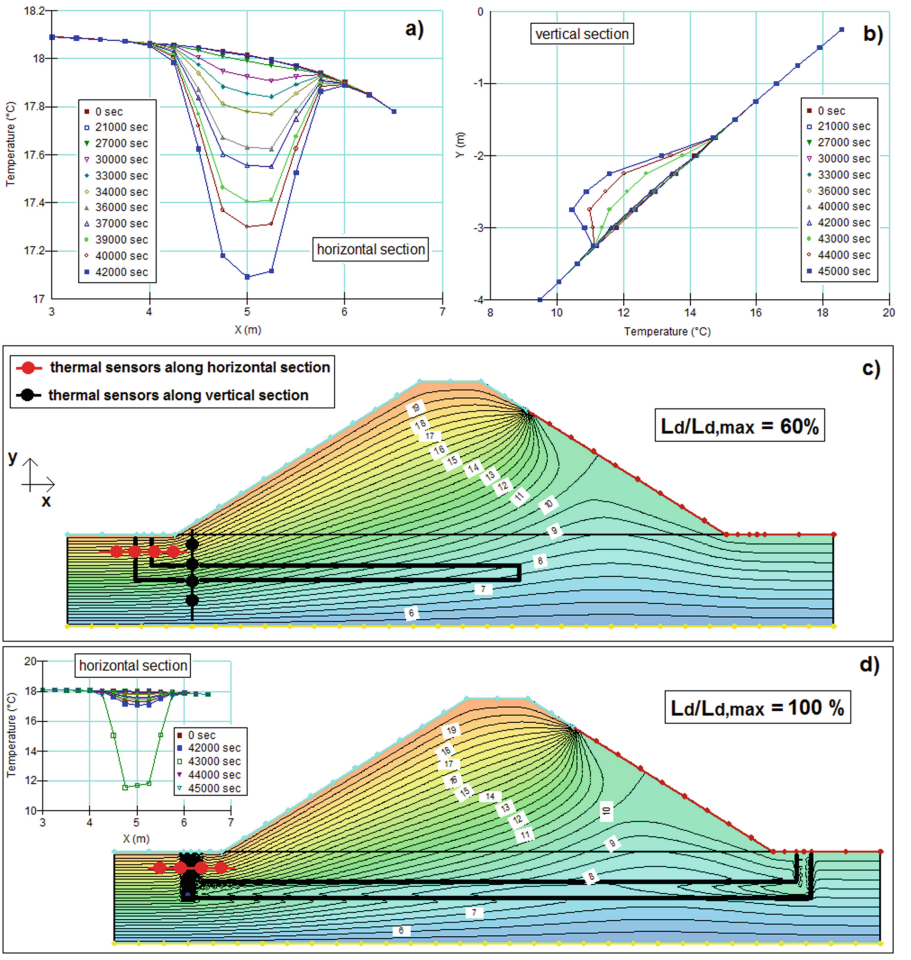

Fig. 5. Temperature distributions versus time (*a*) along a horizontal section; (*b*) along a vertical section; (c, d) within the earthen structure for $L_d/L_{d,max}$ = 0.60, 1.0, respectively

In Fig. 9, the piezometric heads (p.h.) distributions along horizontal sections at different elevation are shown. Through the search of irregular profiles of p.h., the elevation (*a*) and length (L_d) of the permeability defect can be estimated.

However, to obtain these profiles, a careful piezometric monitoring in numerous specific points, which is not always easily practicable especially for long earthen structures, is needed.

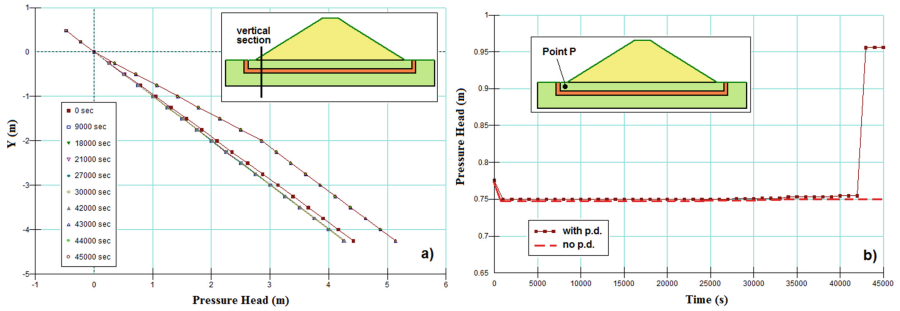

Fig. 6. Piezometric heads versus time (*a*) along a vertical section; (*b*) at the point P, at the downstream toe of the earthen structure

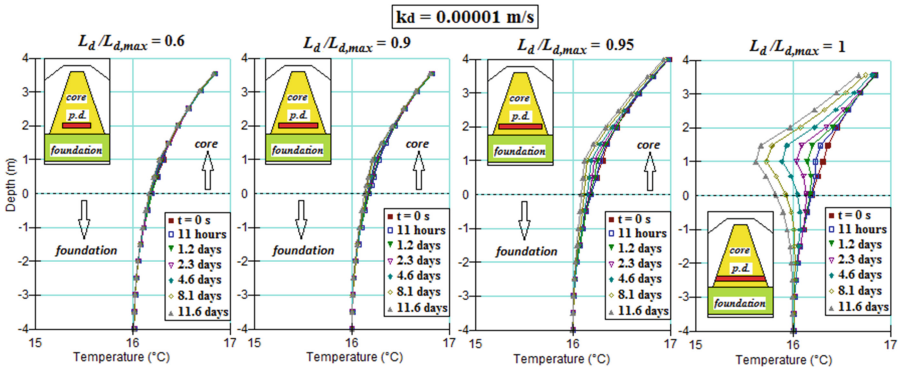

Fig. 7. Temperature distribution at section 1-1′, for $k_d = 10^{-5}$ m/s and different values of $L_d/L_{d,max}$

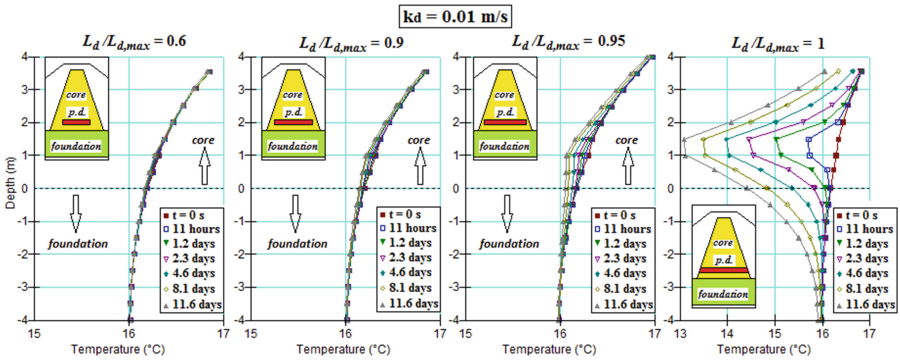

Fig. 8. Temperature distribution at section 1-1′, for $k_d = 10^{-2}$ m/s and different values of $L_d/L_{d,max}$

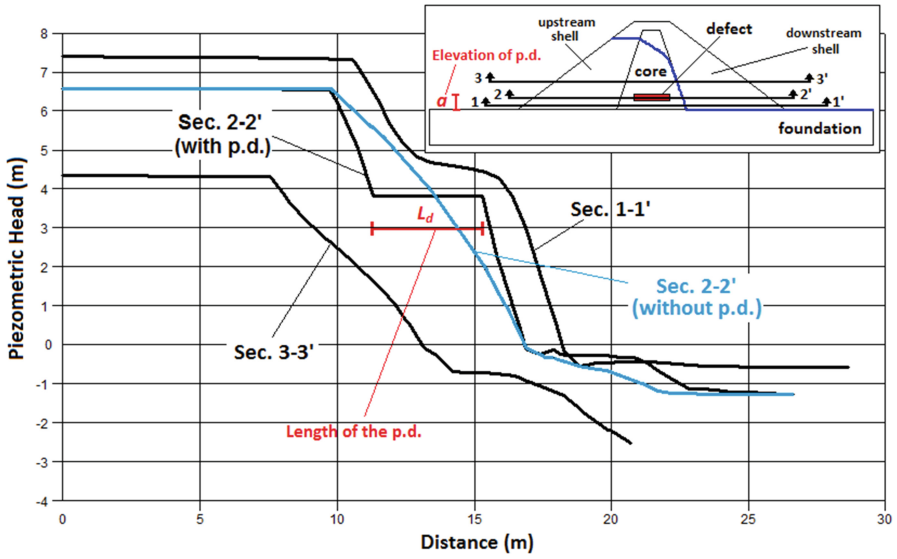

Fig. 9. Piezometric heads distributions along horizontal sections: estimate of elevation (a) and length (L_d) of a permeability defect.

4 Analysis of a Large Scale Failure Test

Very few large scale experimental tests on piping backward erosion are reported in technical literature. Among these, the IJkdijk piping test by University of Delft (Netherlands) is very significant because the seepage flow, the piping erosion phenomenon progression and the instability of the downstream shell have been carefully described and recorded (Bersan and Koelewijn 2015; Bersan et al. 2017).

Numerical simulations of the measured temperature and piezometric heads distributions, reported by Bersan and Koelewijn (2015) have been carried out in the paper.

The experimental dyke was 3.5 m high, 19 m long and 15 m wide at its base (Fig. 10a). The lower part of the dike was constituted of a 0.7 m clay layer, which separated hydraulically the foundation from the dike body.

A small clay dike (1.7 m high) was firstly built at the upstream side; a sand core (behind the small dike) and a cover of organic clay were successively put in place. The test dikes and the clay embankments delimiting the basins enclosed two reservoirs, each one with a volume of approximately 2000 m^3, to be filled during the test to apply the desired hydraulic load (Fig. 10b).

Conventional monitoring instruments (Fig. 10a), including two liquid level sensors, 4 lines of 17 pore pressure sensors in foundation, 4 lines of 3 pore pressure sensors in the sand core (above the clay layer) were installed to monitor the course of the test. In addition, distributed fiber optic sensors encased in a geotextile strip were placed within the dyke; particularly, 5 lines of fiber optic sensors in foundation soils, at the base of the dyke, and 3 lines of sensors in the downstream shell.

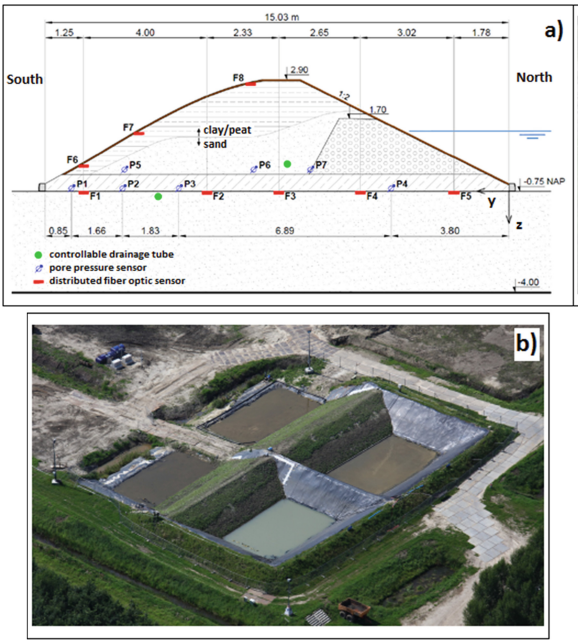

Fig. 10. (*a*) Cross section and (*b*) aerial view of the experimental dike. (adapted from Bersan and Koelewijn 2015; Bersan et al. 2017)

Test Procedure. The upstream reservoir was filled according to water level law reported in Fig. 11a. In the downstream basin, the water level was taken constant, at 10 cm above the sand layer, to ensure complete saturation of the foundation soil.

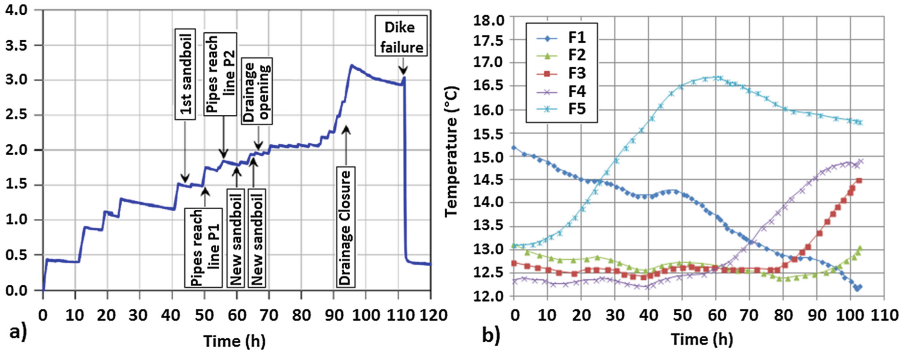

Fig. 11. (a) Applied hydraulic load; (b) temperature measurements. (adapted from Bersan and Koelewijn 2015; Bersan et al. 2017)

The permeability coefficient of the sand layer was estimated to $k = 1.5 \cdot 10^{-4}$ m/s. The first evidence of backward erosion (piping) was detected after two days of testing

(elapsed time ≅ 50 h) at the cross sections corresponding to the (longitudinal) abscissa x = 4.8 m, 8.2 m, 11.2 m; as a consequence, the transducers P1 (at 0.85 m from the downstream toe, see Fig. 10a) recorded a slight reduction in interstitial pressures. By increasing the hydraulic load, after 55–60 h of testing, reductions in interstitial pressures were also recorded in transducers P2, indicating the evolution/progression of the piping phenomenon.

Erosion stopped after opening the controllable drainage tube installed in the foundation soil, between the transducers P2 and P3 (see Fig. 10a). Since no appreciable/significant reductions in pore pressure in P3 were recorded, the pipe should have reached a length ranged between 2.5–4.3 m, i.e. the distances of the transducers P2 and P3 from the downstream toe, respectively. However, the failure of the experimental dyke was caused by the instability of the downstream slope, after 5 days of testing.

Temperature Measurements. Figure 11b shows the evolution of the measured temperature at the lines F1–F5, corresponding to the central section of the dam (x = 10 m), near the section at the (longitudinal) abscissa x = 11.2 m, in which piping phenomena was observed. A few hours after the beginning of the test, the temperature recorded in F5 started to increase, suggesting that the water in the upstream reservoir was warmer than the sand layer in the foundation. Unfortunately, the measurements of reservoir water temperature are not available due to technical problems. At the lines F4 and F3, a temperature increase was recorded after 2 and 3 days, respectively. In F2, on the contrary, the temperature started to decrease slowly immediately after the beginning of the test and continued to decrease up to 2 days before the end of the test. At the F1 line, the temperature remarkably decreased during the whole duration of the test (Fig. 11b).

Numerical Simulation. Several SEEP/W and TEMP/W models reproducing the temperature and piezometric head measurements within the experimental dyke have

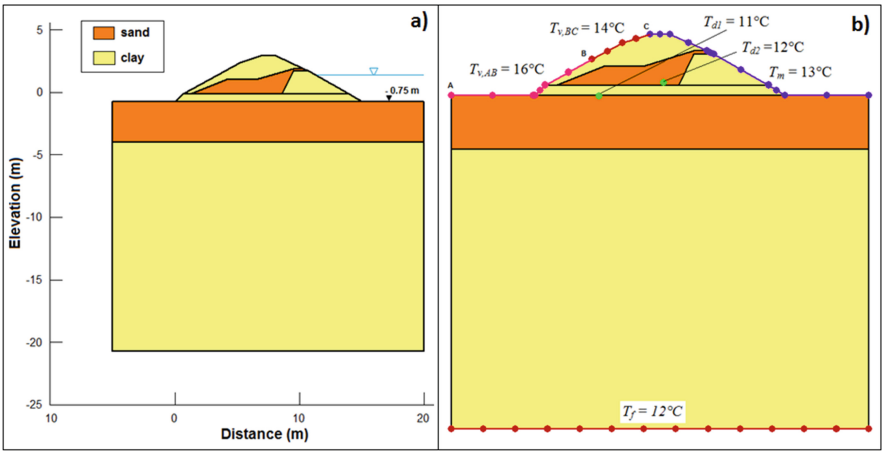

Fig. 12. (a) Cross section of the simulated dyke; (b) Initial thermal boundary conditions

been developed. The schematization of the cross section of the dam is shown in Fig. 12a.

Simulation of initial thermal and hydraulic conditions (uncoupled steady state seepage and heat transport processes) was firstly carried out. To reproduce the initial conditions of temperature (before the start of the experiment), specific *thermal* boundary conditions have been assigned (Fig. 12b).

The initial *hydraulic* boundary conditions, H_{up} (upstream load) = 0.10 m and H_{dw} (downstream load) = 0 m have been imposed. The considered hydraulic and thermal properties of the dyke materials are shown in Table 1 (Bersan and Koelewijn 2015; Bersan et al. 2017).

Table 1. Hydraulic and thermal properties of materials. (adapted from Bersan and Koelewijn 2015; Bersan et al. 2017)

Parameter	Sand	Clay	Unit
Volumetric water content	0.4	0.3	–
Permeability	$1.5 \cdot 10^{-4}$	$7.5 \cdot 10^{-6}$	m/s
Thermal Conductivity	2.77	1.39	W/(m K)
Volumetric heat capacity	$2.8 \cdot 10^{-6}$	$2.5 \cdot 10^{-6}$	J/(m^3 K)

After the beginning of the test, different boundary conditions must be applied; in particular, by referring to thermal variables defined in Fig. 12b: T_m linearly decreases between 24 and 11 °C, $T_{v,BC}$ = 20 °C, $T_{v,AB}$ = 10 °C, T_f = 9 °C, T_{d1} = 14 °C and T_{d2} = 18 °C (at the opening of drainage); in addition, H_{up} variable with time (t), according to applied hydraulic load (Fig. 11a), and H_{dw} = 0.1 m (constant).

Therefore, coupled unsteady state seepage and heat transport processes have been simulated following five phases:

(a) $t \in [0; 50]$ hours (pipe reaches P1 sensor);
(b) $t \in [50; 65]$ hours (pipe reaches P2 sensor);
(c) $t \in [65; 85]$ hours (uncompleted opening of the lower drainage tube - possible occlusion of pores is assumed - and total opening of the upper drain);
(d) $t \in [85; 94]$ hours (total opening also for the lower drainage tube);
(e) $t \in [94; 110]$ hours (closure of the both drainage tubes and evolution of hydraulic and thermal processes up to the dyke failure).

The pipe has been simply schematized by a thin layer whose length varies along time (according to experimental observations and measurements), in the foundation sandy soil, just below the basal clay layer. The pipe is affected by the same properties of the material "*sand*" except for the permeability coefficient (k_{pipe}); in particular, k_{pipe} = 0.005 m/s.

By referring to the cross section at x = 11.2 m (near the central section, x = 10 m), the obtained results in terms of temperature at the lines F1–F5 and of piezometric head at the sensor P2 are closed to the measured values (Fig. 13).

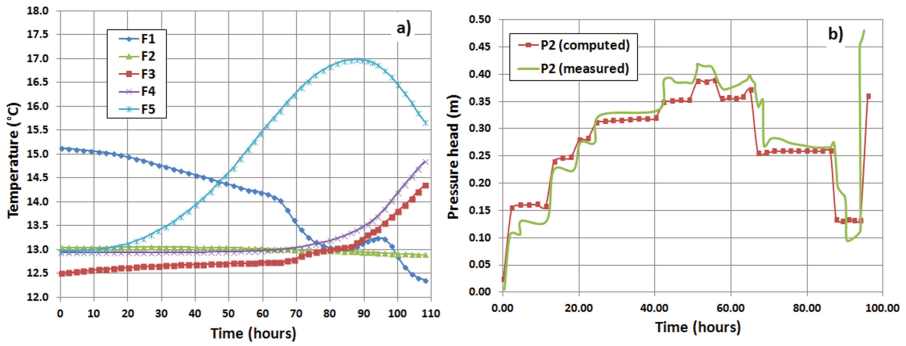

Fig. 13. Numerical results: (a) temperature at lines F1–F5; (b) piezometric head at P2

5 Concluding Remarks

Results of numerical simulations (*case A*) indicate that for a clearer detection of piping phenomena, the temperature sensors should be installed at the downstream toe of earthen structures, preferably along a short horizontal section, spaced every 0.50 m. Referring to a p.d. within the core (*case B*), the "absence of sensible variations" in time of the temperature distribution, for $L_d/L_{d,max} < 0.95$, confirms the well-known difficulties in detecting the evolution of these dangerous, hidden, phenomena. Proposed simulations are referred to 2D cases. The *real* progression of piping erosion is a 3D phenomenon. Therefore, the applicability of the obtained results is limited to cases for which the evolution of the piping may be analyzed as a 2D process, in particular when differences between the permeability of the p.d and the contiguous materials are significant, being the seepage flow mainly addressed along the longitudinal axis of the p.d. and then the flow contributions along directions orthogonal to the p.d. axis rather negligible. Finally a possible interpretation of coupled hydraulic and thermal measures as well as of piping mechanisms, which affected the large scale IJkdijk piping test, is provided.

References

Bersan S, Koelewijn AR (2015) Temperature monitoring in piping-prone hydraulic structures. In: Lollino G, et al (eds) Engineering Geology for Society and Territory, vol 2

Bersan S, Koelewijn AR, Simonini P (2017) Effectiveness of distributed temperature measurements for early detection of piping in river embankments. Hydrol Earth Syst Sci 22:1491–1508

Cesali C, Federico V (2018) Coupled thermal and piezometric heads monitoring to detect permeability defects within embankment dams and levees. In: Third international DAM WORLD conference 2018, Foz do Iguassu, Brazil, 17–21 September 2018 (in press)

Federico F, Montanaro A (2011) Permeability defects in zoned earth structures. Forecasting, F.E. modeling and analyses of effects. In: Pina C, Portela E, Gomes J (eds) 6th international conference on dam engineering. Lisbon, Portugal, 15–17 February 2011

Foster M, Spannagle M, Fell R (1998) Report on the analysis of embankment dam incidents. UNICIV report no. R374, University of New South Wales

ICOLD (2013) Internal erosion of existing dams, levees and dikes, and their foundations. Bulletin n. 164, vol 1: "Internal erosion processes and engineering assessment"

Radzicki K (2014) The important issues of levees monitoring with special attention to thermal-monitoring method application. In: South Baltic conference on new technologies and recent developments in flood protection, 5–6 June, Gdańsk, Poland, p 10

Sjödahl P, Johansson S (2012) Experiences from internal erosion detection and seepage monitoring based on temperature measurements on Swedish embankment dams. In: ICSE6 Paris, 27–31 August 2012

Talbot JR, Ralston DC (1985). Earth dam seepage control. In: Symposium on seepage and leakage from dams and impoundments. A.S.C.E., Geotechnical Engineering Division, 44(6)

TEMP/W user's manual (2012) by GEO-SLOPE International Ltd

The Role of the Hydraulic Resistance of the River Bed and the Time Dependent Response of the Foundation Layers in the Assessment of Water Defences for Macrostability and Piping

Dario Garuti[1], Cristina Jommi[1(✉)], and Richard Rijkers[2]

[1] Delft University of Technology, Delft, The Netherlands
c.jommi@tudelft.nl
[2] Movares, Utrecht, The Netherlands

Abstract. In the assessment of water defences for macrostability and backward erosion piping the design hydraulic load mostly refers to steady state conditions in equilibrium with the maximum river water level. In this contribution, we show selected results of coupled hydromechanical numerical analyses of a paradigmatic Dutch case, which demonstrate that this assumption leads to high overestimation of the true hydraulic loads at the toe of the water defence embankment. The hydraulic resistance of the bed of the river and the deformability of the foundation layers introduce a decay in the pore pressure time history, which largely reduces the action on the hydraulic protection structure. The finite element model was developed to assist in the assessment of an innovative solution based on passive wells as a measure to reduce the risk for macrostability and piping. It was calibrated on available pore pressure measurements in the foundation of critical sections of the dykes of the river Lek in the Netherlands under the daily tidal action. The model was used to determine the distribution of pore pressure expected in the subsoil of the dykes for the design maximum load. The calibration stage of the model is specifically interesting to the aim of evaluating the reduction of the input pore pressure due to the hydromechanical resistance of the geotechnical system.

Keywords: Dykes assessment · Numerical analysis · Time dependent response
Water pressures

1 Introduction

Groundwater flow and pore water pressure build-up are known to be critical factors on the stability of river embankments. Among the failure mechanisms potentially affecting such retaining structures towards the inland, uplift and piping are a main concern, besides macro-instability of the embankment slopes (U.S. Department of Homeland Security 2016).

The ground conditions most critical to the occurrence of these types of mechanisms are those characterised by the presence of a permeable layer (aquifer) underlying a

S. Bonelli et al. (Eds.): EWG-IE 2018, LNCE 17, pp. 258–271, 2019.
https://doi.org/10.1007/978-3-319-99423-9_24

more impervious unit (aquitard), on top of which the embankment is built. When the permeable layer is in direct connection with the main water body, increases in water level of the latter may cause the aquifer water pressure to rise to a point where it might impair the stability of the embankment. This is not uncommon in fluvial environment, and the effects of uplift mechanisms were recognised in a wide range of cases, including rivers of remarkable size such as the Thames (Padfield 1978) and the Danube (Grambalickova and Bednarova 2005).

Among the remedial measures to counteract the pressure build-up, relief wells have been first employed by the U.S. Army Corps of Engineers by lowering the pressures under two dams (U.S. Army Corps of Engineers 1992). These devices are meant to intercept the seepage water, relieve the pressures, and better control the flow and the discharge.

In the past, the design of relief wells has been based both on analytical and numerical approaches, and more than one method were proposed to evaluate a factor of safety for the functioning of the device (Guy et al. 2014). While analytical calculations (e.g. Barron 1982) are valuable in the case of simple geometry and isotropic soil conditions, a numerical solution is worthwhile in case of aquifer anisotropy, complex geometry and non-steady or transient analyses (e.g. U.S. Department of the Interior 2014). An instance of the employment of 2D Finite Element models to facilitate the design of relief well systems can be found in a case study analysed by Guy (2010).

In this contribution we analyse in detail the influence of hydromechanical coupling on the pore water pressure response of the subsoil of a paradigmatic river dyke, to evaluate the relevance of the hydraulic resistance of the river bed and of the compressibility of the subsoil layers on a reliable estimate of the pressure at the toe of the water defence embankment.

2 The Schoonhovenseveer-Langerak Research Project

The system of embankments under study lies on the left bank of the river Lek, in the Netherlands (Fig. 1). This river is characterised by daily tidal fluctuations, and by relevant changes in the discharge due to seasonal precipitations. The variable hydraulic loads can be particularly detrimental on this site, due to the characteristics of the local subsurface. While the first meters are composed of a relatively impervious Holocene clay layer, permeable shallow Holocene and deeper Pleistocene sand layers are found below the embankment, and these typically act as preferential paths for the water pressure fluctuations originating at the river (Simpson 2014a).

The major problem for the safety of the embankment analysed in this contribution is the macrostability of the inner slopes, which may be prone to failure along slip surfaces passing close to the dike toe (Teunissen 2014b). However, in various other sections of the water defence system nearby, backward erosion piping is the main concern in the assessment (Fig. 2).

One of the solutions developed to provide the necessary relief for water pressure is called “waterontspanner”, and consists of a system of vertical passive drain, encased in a PVC tube, equipped with a gravel filter layer (Fig. 3). The filter is installed in the permeable sand layer where most of the seepage under the embankment takes place, at

a depth of approximately 10 m. In this way, the excess water can be conveyed though the drain, collected by a conduit at the top of the tube, and then discharged to a nearby drainage ditch, which runs parallel to the embankment (Fig. 4). On the upper end of the drain, a control device allows to adjust the value of the water pressure in the aquifer above which the drain starts functioning.

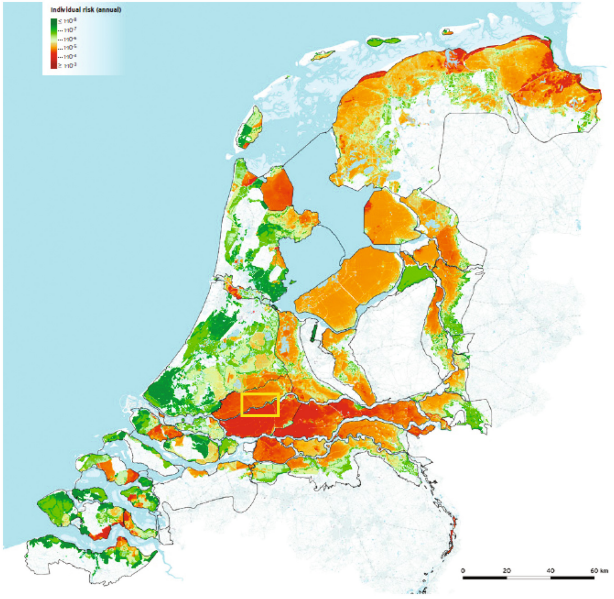

Fig. 1. Indication of the area under investigation

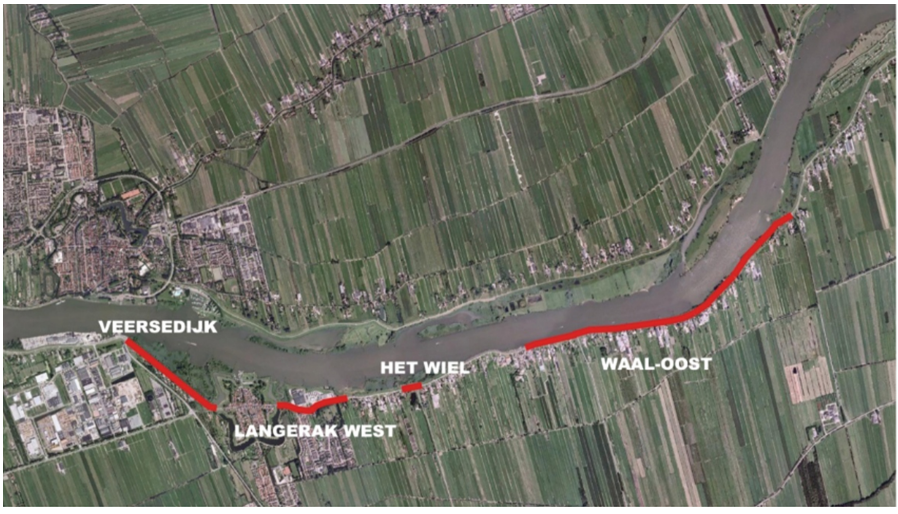

Fig. 2. Critical sections of the water defence system

The preliminary design procedure was based on the combination of pore water pressure results obtained by means of a finite-different software, MODFLOW, and stability calculations performed in 2D with D-Geo Stability, using Limit Equilibrium methods. The design high water wave was employed to simulate a high-water event with a return period of 2000 years. For each time step, the groundwater head profile was calculated by MODFLOW, and subsequently employed by D-Geo Stability to start Limit Equilibrium stability calculations.

Overlooking hydromechanical coupling neglects the stress–strain behaviour of the soil, and the influence that soil strains have on the hydraulic transmissivity. It should also be noted that a two-dimensional representation of the soil entails a great simplification of the properties of the subsurface, which is only representative of plain–strain conditions. In cases in which soil properties change considerably with respect to the longitudinal position along the embankment, the safety assessment is highly dependent on the choice of the section under study.

To gain better understanding of the dynamics behind the case under study, and provide more reliable estimates of the pore pressure history under after a high water event, a coupled hydromechanical 3D Finite Element model was developed on the PLAXIS 3D platform. The model carefully replicates local soil data and is calibrated on the available field information.

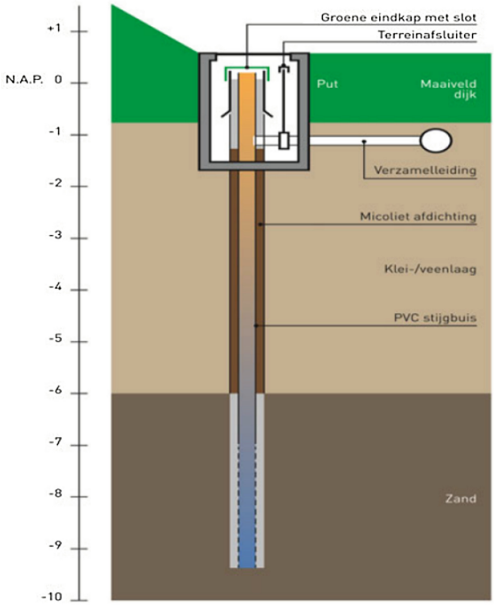

Fig. 3. Scheme of the passive well set up

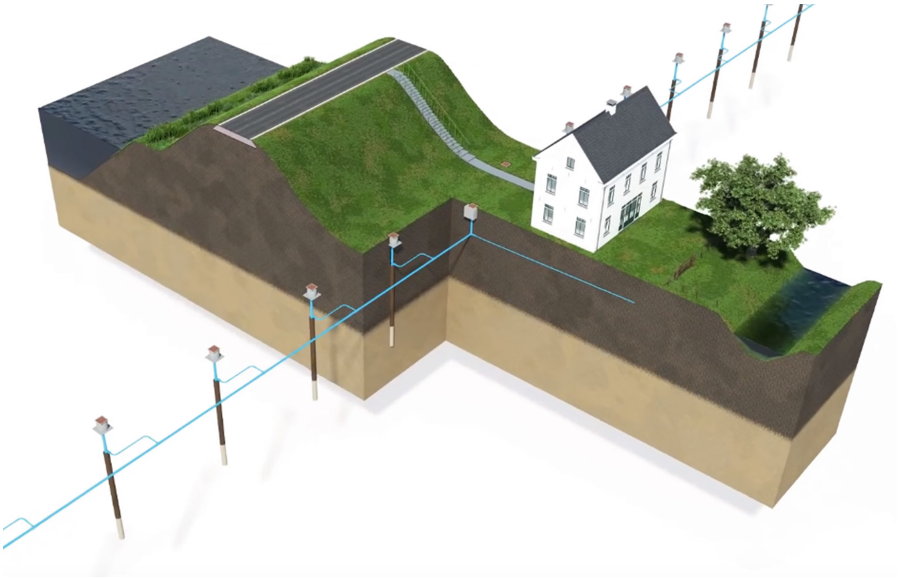

Fig. 4. Scheme of the Waterontspanner system

3 Calibration of the Model on Field Observation

The portion of the embankment chosen for the study is a 80 m × 80 m portion of the Veersedijk embankment (Fig. 5), centred around two observation wells (B99 and B100), which were employed in the calibration phase. Observation well B99 is located at the dike crest and B100 at a distance of 35 m inland. Soil data from six boreholes were employed to describe the soil profile (Fig. 6). Soil characteristics for both the Holocene and Pleistocene aquifers and the interbedded clay and peat layers were obtained from a former site investigations and boreholes taken in locations nearby the embankment under investigation.

The calibration stage is based on field observations of tidal oscillations of the groundwater head retrieved from the two observation wells. The nature of the soil of the riverbed and of the interface between the river and the two aquifers is not known. The riverside boundary is separated from the river banks by a strip of land characterised by an irregular shape and variable width. No data were available for the water table far from the dyke on the polder side.

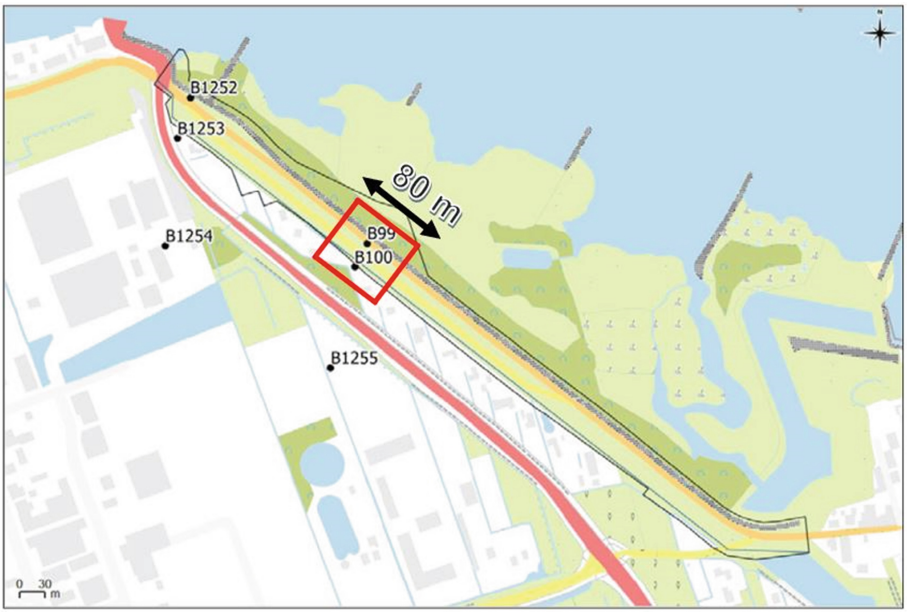

Fig. 5. Veersedijk, domain area and observation wells

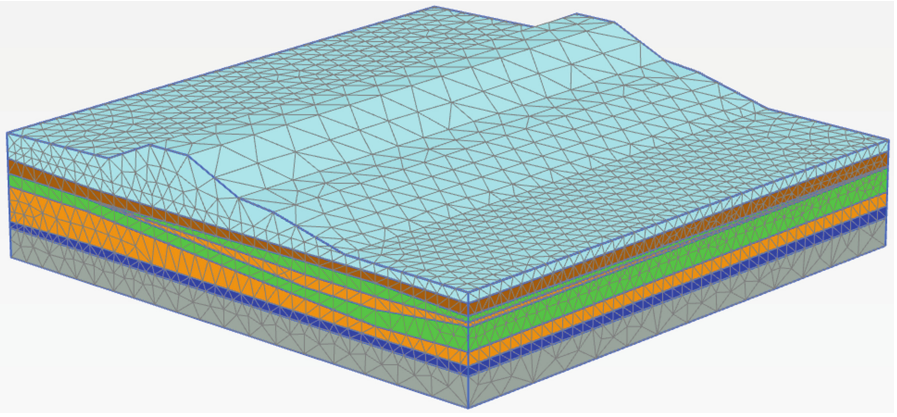

Fig. 6. 3D FE model of the Veersedijk

Groundwater head measurements for the Holocene and Pleistocene aquifers in the two observation wells B99 and B100 are shown in Fig. 7, together with the tidal fluctuations of the river level during the same time frame.

From the values of the groundwater head recorded in the two aquifers in B99, it can be observed that the amplitudes of the oscillations are reduced dramatically compared to the river level. This reduction is due to the hydraulic resistance of the river bed and the outer land. This decay observed between the river and well B99 is roughly the same in both aquifers.

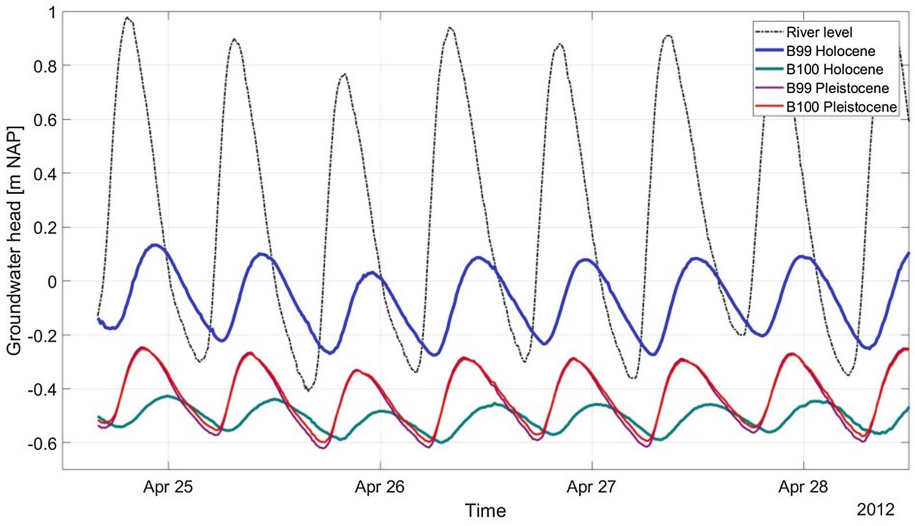

Fig. 7. Observed groundwater heads in B99 and B100

However, the comparison between the readings in B99 and B100 in each single aquifer clearly shows that the amplitude of the pressure wave in the Holocene layer is further reduced towards the inland and delayed, while in the Pleistocene aquifer the decay and the decay are barely detectable. This suggests that the hydraulic conductivity of the Pleistocene sand is considerably higher than that of the Holocene layer, and that the compressibility of the upper layer plays a role too.

Based on these consideration, and in the absence of any detailed information on the river bed and outer land, it was decided to infer the pore pressure boundary conditions for the model on a back analysis of the measurements in the boreholes, which was performed using a simplified analytical solution for cyclic consolidation. The calibration was split in two phases: a stationary phase, in which constant head boundary conditions were applied to let the model equilibrate around the average values observed in B99 and B100, and a time-dependent phase in which, both at the riverside and landside boundaries, fluctuating boundary conditions were applied.

In the time-dependent phase of the calibration, the boundary conditions applied on the riverside of the domain should include an intrinsic decay and delay with respect to the river level data. Conversely, the landside boundary condition should include a decay and delay with respect to the riverside boundary, governed by the soil characteristics assigned to the domain.

3.1 Boundary Conditions and Reduction Factor

The simplified solution for cyclic consolidation in a river bed proposed by Barends (Baudin and Barends 1988) was used to backanalyse the response and assign the hydraulic boundary conditions to the numerical model. The solution was proposed for the typical Dutch river beds. However, it has been recently validated for the silty-sandy subsoil of different river dykes, where it proved to well capture pore pressure measurements (Jommi and Muraro 2014).

For a two-layered system of an aquifer and aquitard, the decay of the peaks amplitude H can be modelled with an exponential function of the distance x from a reference river section:

$$H(x) = H_0 \cdot e^{-\left(\frac{x}{\lambda_\omega}\right)} \tag{1}$$

where λ_ω is a function of the hydraulic conductivities (k, k_0) and of the compressibilities of the aquifer and aquitard.

Similarly, for the decay of the amplitude between two points x_A and x_B

$$\frac{H(x_B)}{H(x_A)} = e^{-\left(\frac{x_B - x_A}{\lambda_\omega}\right)} \tag{2}$$

The delay between the peaks in x_A and x_B can be expressed as a linear function of the distance:

$$\Delta t_{A \to B} = \frac{a(x_B - x_A)}{\omega \lambda_\omega} \tag{3}$$

where ω is the angular frequency of the fluctuations and a is a function of the hydraulic conductivity and of compressibility of the two soil units.

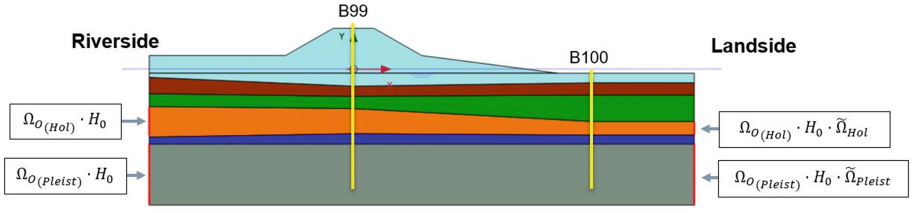

Fig. 8. Scheme of the groundwater head boundary conditions

The time-dependent phase of the calibration consists in detecting the dynamic boundary conditions on the outer and inner boundaries of the Holocene and Pleistocene sand layers. Such boundary conditions are characterised by a time dependent head fluctuation $\Delta h(t)$ around the mean value resulting from the stationary phase. The functions describing such fluctuations are indicated as $\Delta h_0(t)$ for the outer (riverside)

and $\Delta h_0(t)$ for the inner (landside) boundary (Fig. 8). In both cases, the function is chosen to be proportional to the measured river level on the Lek $\Delta h_L(t)$. It should be noted that, for both boundary conditions, a decay Ω and a delay ϕ with respect to the river must be introduced:

$$\Delta h_O(t) = \Omega_O \cdot \Delta h_L(t - \phi_O) \tag{4}$$

$$\Delta h_I(t) = \Omega_I \cdot \Delta h_L(t - \phi_I) \tag{5}$$

If we substitute $t' = t - \phi_I + \phi_O$ in the first equation, a straightforward result is that:

$$\Delta h_I(t) = \tilde{\Omega} \cdot \Delta h_O\left(t - \tilde{\phi}\right) \tag{6}$$

$$\tilde{\Omega} = \frac{\Omega_I}{\Omega_O}, \quad \tilde{\phi} = \phi_I - \phi_O \tag{7}$$

Therefore, if a reduction factor with respect to the river level is chosen for the outer boundary condition, the same factor should also be applied to the inner boundary condition.

The expected delays and decays between the two boundaries, separated by a distance of 80 m, was calculated via the analytical solution, written for the local soil properties. The results showed that an optimal value for the reduction factor Ω_O was equal to 0.5 for both aquifers. The fact that the same factor is suitable for both aquifers, shows that the river bed resistance acts in a similar way on the two layers. The result of the calibration stage are shown in Figs. 9 and 10.

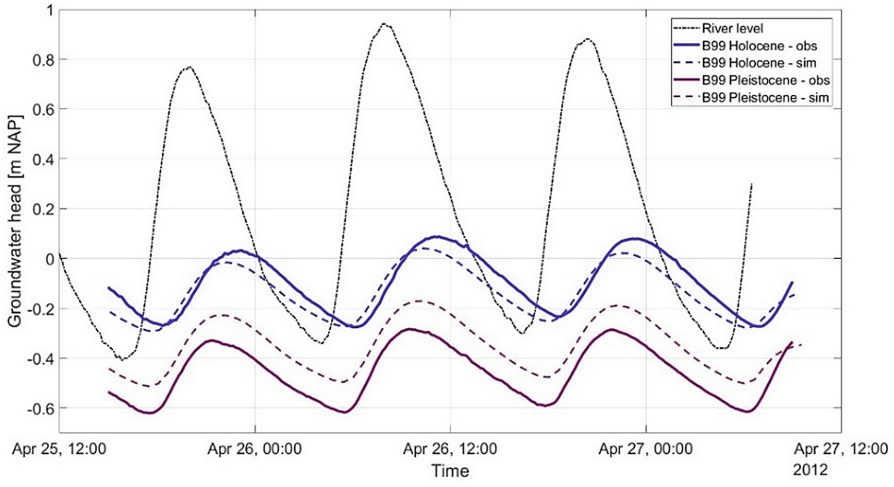

Fig. 9. Simulated and observed groundwater heads in B99

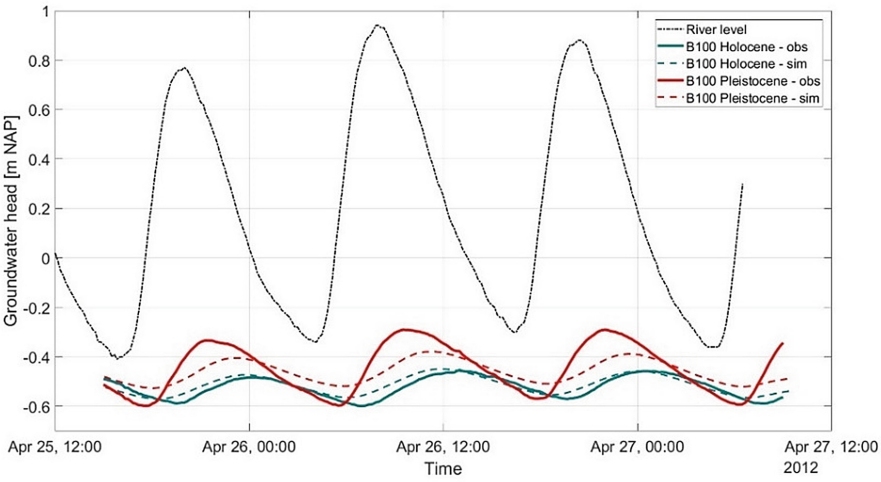

Fig. 10. Simulated and observed groundwater heads in B100

The results in Figs. 9 and 10 show that a remarkable accordance could be achieved for the Holocene aquifer. Instead, for the Pleistocene aquifer, the nearly undetectable decay between the two boreholes was far less satisfactory. However, due to the fact that the Pleistocene aquifer is far less crucial to the stability of the structure, the back analysis was not refined further.

4 Selected Numerical Results

4.1 Preliminary 2D Analyses

Numerical analyses were performed to assess the response of the system to the Design High Water wave. Preliminarily, a 2D plane strain section of the dyke was employed to address the following issues: establishing the most critical time of the high-water wave for the stability of the structure, examining the influence of the distance between the drain system and the embankment, providing a sketch of the failure mechanism. To assess the consequences of the pore pressure oscillation on this dyke section, the factor of safety (FoS) against macrostability was calculated by means of the strength reduction method (e.g. Griffiths and Marquez 2007; Vaughan et al. 2008).

The evolution over time of the FoS in Fig. 11 allows highlighting that the response of the system, even for aquifers with relatively high hydraulic conductivity, is clearly time dependent, and that the most critical conditions typically follow the peak of the high water event with a considerable delay. In the case analysed, the dip in the FoS is predicted to occur with a delay of 2 days, proving that time dependent behaviour of the soil should be considered when choosing the most critical time for the stability calculations. The shape of the associated failure surface (Fig. 12) shows the influence of underpressures at the toe, with a failure mechanisms extending beyond the toe for an overall length of roughly 30 m.

4.2 3D Pore Pressure Distribution

Some aspects of the design of a system of relief wells was studied analysing the displacements, the factor of safety against macrostability and the pore water pressure distribution. Selected results of the latter aspects are summarised in the following due to their relevance for the global response of the system, possibly including backward erosion piping staring at the toe. The number of drains in the domain was increased from three to eight, corresponding to a spacing decreasing from 27 to 10 m. The horizontal distance from the dike body was kept equal to 20 m, roughly equalling three times the height of the structure.

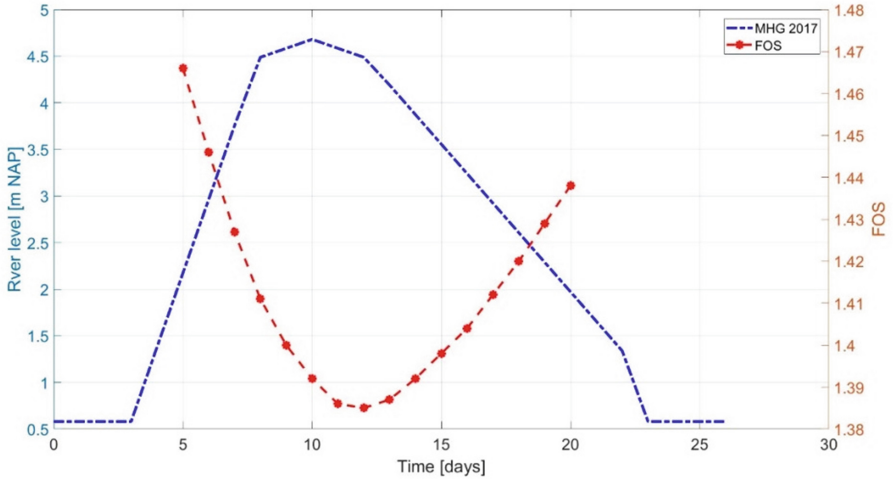

Fig. 11. Time evolution of the FoS during the simulated design high water event

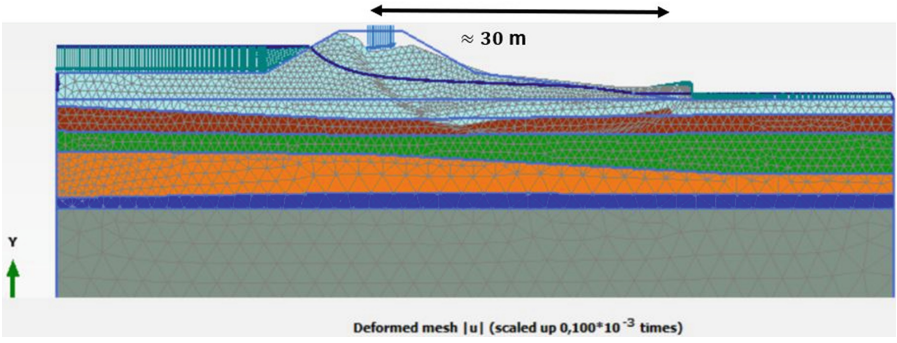

Fig. 12. Predicted failure mechanism (2D-analysis)

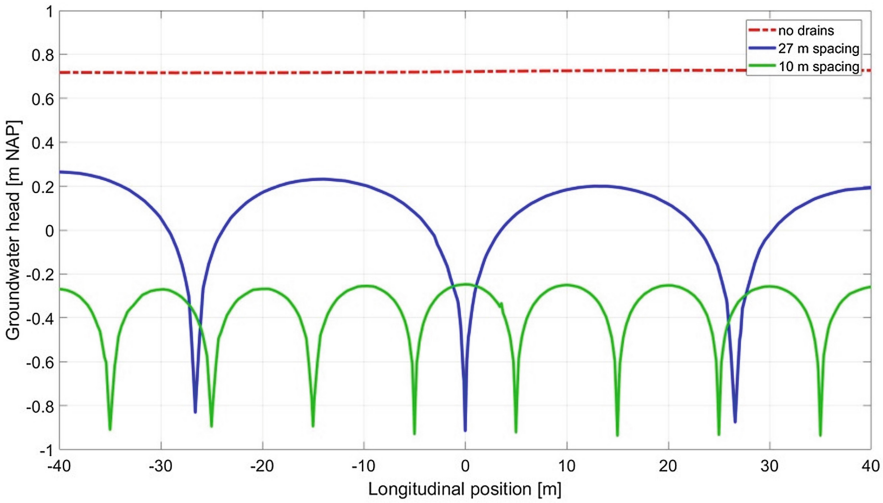

Fig. 13. Longitudinal profile of the highest ground water head following the design high water at the drains location

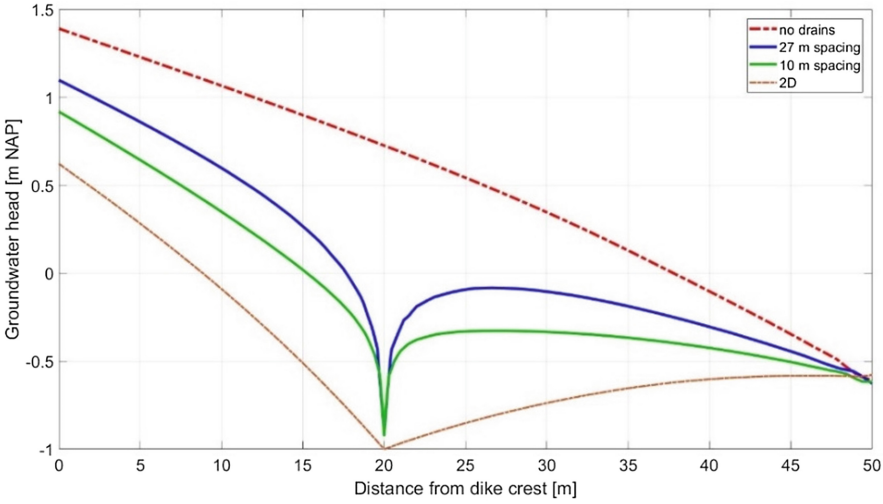

Fig. 14. Groundwater head profile at drain location - transversal section

If a longitudinal section is taken at the drains location and the drawdown plotted for the Holocene aquifers (Fig. 13), a pattern of peaks and dips is visible, whose height clearly depends on the spacing between the drains.

A useful insight on what happens in the subsoil of the embankment can be obtained by drawing two transversal sections: one corresponding to a drain location, and the other taken midway between two drains. On the transversal section including a drain (Fig. 14) the drawdown profiles always lie between the one corresponding to the pore pressure profile obtained without drains, and the limiting maximum one obtained with a 2D simulation, which obviously overestimates the efficiency of the true system.

Figure 15 shows that efficiency of the drains system is not limited to the location where the drains are installed. In the area closer to the embankment, where the effects of the drawdown are the greatest, the results show that there is no significant difference in the drawdown observed between the two sections of Figs. 14 and 15. It appears therefore that the effect of the drains, despite being longitudinally non-uniform at the location of the screens, flattens out in proximity of the dike, resulting in a mitigating effect on the excess pore water pressure that does not markedly depend on the longitudinal coordinate.

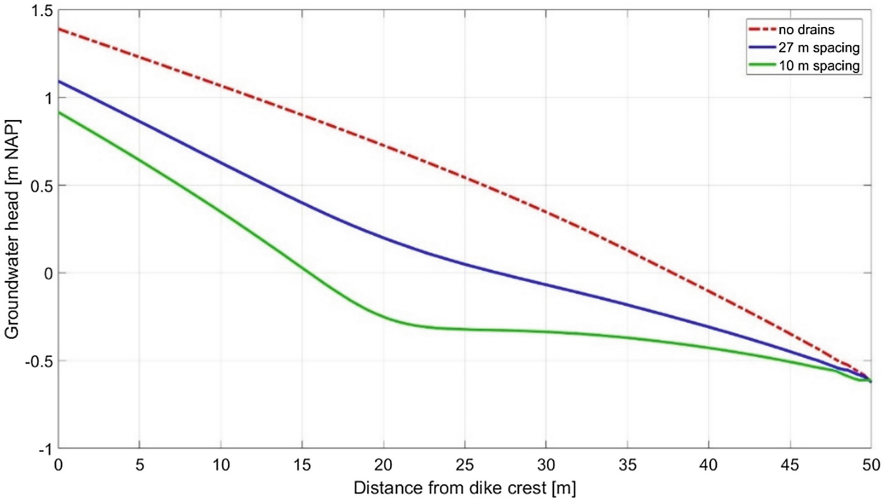

Fig. 15. Groundwater head profile between two drains - transversal section

5 Conclusions

The numerical exercise was set up to assess a possible technical solution designed to increase the factor of safety of river dykes by means of passive wells at the toe. The solution is being studied for the improvement of critical dyke sections both for macrostability and backward erosion piping.

To the aim of design and assessment, a time-dependent coupled analysis appears to be crucial to avoid overestimating the pore pressure which enter in the calculation. The river bed hydraulic resistance can be quite high reducing to a large extent the forcing hydraulic head. In the upper sandy aquifers, the compressibility plays a role too in attenuating the pressure wave affecting the subsoil.

The individual contribution of these aspects is not immediate to assess. However, a thorough backanalysis of multilevel piezometer readings will help in calibrating numerical models set up to predict the response of the water defence under high water events. Especially the river bed resistance is typically unknown, and the results of the analyses presented suggest that better characterisation of the area will help in more reliable assessment of water defences, hence better addressing reinforcement efforts.

References

Baudin CMHLG, Barends FBJ (1988) Getijde-respons in grondwater onder Nederlandse dijken. H_2O 21(1):2–5

Barron R (1982) Mathematical theory of partially penetrating relief wells. Technical Report, US Army Engineer Waterways Experiment Station, Vicksburg, Mississipi

Grambalickova D, Bednarova E (2005) Some aspects of the safety of flood embankments. Slovak J Civil Eng 1:6–13

Griffiths DV, Marquez R (2007) Three-dimensional slope stability analysis by elasto-plastic finite elements. Géotechnique 57:537–546

Guy ED (2010) Relief well system design approach: HHD case study. In: Association of State Dam Safety Officials Proceedings, Charleston, West Virginia

Guy ED, Ider HM, Darko-Kagya K (2014) Several relief wells design considerations for dams and levees. In: 45th annual Ohio river valley soils Seminar

Jommi C, Muraro S (2014). The geotechnical response of dykes and levees to hydraulic loads (in Italian). Panel contribution. In: La Geotecnica nella Difesa del Territorio e delle Infrastrutture dalle Calamità Naturali, XXV National Geotechnical Conference, Baveno, Italy

Simpson D (2014a) Achtergrondrapport Geohydrologie: Dijkverbetering Schoonhovenseveer – Langerak. Technical Report, de Vries & van de Wiel, Amsterdam NL

Teunissen P (2014b) Ontwerpnota: Dijkverbetering Schoonhovenseveer – Langerak. Technical Report, de Vries & van de Wiel, Amsterdam NL

Padfield CJ (1978) The stability of river banks and flood embankments, Ph.D. thesis, University of Cambridge

U.S. Department of Homeland Security (2016) Training aids for dam safety: evaluation of seepage conditions

U.S. Army Corps of Engineers (1992) Design, construction and maintenance of relief wells

U.S. Department of the Interior (2014) Embankment dams (Ch 21): water removal and control: dewatering and unwatering systems

Vaughan P, Griffiths DV, Marquez R (2008) Authors' reply. Géotechnique 58:683–685

Impact of the Use of 3D Modeling on Sand Boil Risk Management

M. Daniela Giliberti[1(✉)], Massimiliano Cirincione[2], and Alessandro Cavagni[3]

[1] Department of European Projects-Interregional Agency of the Po River, Parma, Italy
daniela.giliberti@gmail.com
[2] IHO Cat. A Hydrographer, Genova, Italy
[3] Officine Maccaferri Italia S.r.l., Bologna, Italy

Abstract. The study will present a further salient advance of 3-D modelling and its application in the efficient design of hydraulic barriers intended to prevent sand boil formation. The approach to hydraulic analysis was carried out using FEMWATER (Lin et al. 1997) a 3-D Finite Element model while data have been processed by the graphical interface of the Groundwater Modelling System (GMS 2017 software). The area that arose our interest due to the reoccurrence in the past 70 years of several impressive sand boils, is located along a stretch of the Po river, Italy, between the villages of Boretto (RE) and Pieve Saliceto (RE). Recorded sand boils formed after flood events in 1951, 1994 and 2000 (reactivated in 2014), each one appearing downstream from the previous one and ever closer to a freeway fly-over, without though a significant change in distance from the levee toe. In order to mitigate sand boil risk formation one of the solutions to be studied was: build a new cut-off wall along the same stretch of river embankment.

Keywords: 3-D numerical simulation · Constraint · Piping-sensitive Efficiency · Identification

1 3-D Numerical Model

A potentially dangerous phenomenon associated with flooding is seepage under levees and the formation of sand boils. It represents serious hazard due to the difficulty in forecasting where erosion initiates. In our experience, the 3-dimensional modelling can offer more reliable tools in flood risk management in comparison with a 2-dimensional modelling. The analysis has been carried out using FEMWATER a 3-D Finite Element model, which is able to solve the saturated-unsaturated flow field, both in steady and unsteady conditions. It is a package contained in the GMS software (GMS 2017) (Aquaveo company). The heterogeneity of the foundation soil was recovered on the basis of the existing investigations, consisting of several boreholes and geo-electrical tomographies. These data have been processed by the graphical interface of the Groundwater Modeling System (GMS 2017) software. To build the model, a Digital Terrain Model (DTM) based on a 1 m grid of ground levels derived from the 2005

S. Bonelli et al. (Eds.): EWG-IE 2018, LNCE 17, pp. 272–288, 2019.
https://doi.org/10.1007/978-3-319-99423-9_25

LiDAR survey, was imported to define the topographic elevation of the levee and the surrounding land.

The unsteady seepage flow in saturated and unsaturated soils may be described by the following three-dimensional differential equation (1):

$$\frac{\partial}{\partial x}\left(k(\theta_w)\frac{\partial h}{\partial x}\right)+\frac{\partial}{\partial y}\left(k(\theta_w)\frac{\partial h}{\partial y}\right)+\frac{\partial}{\partial z}\left(k(\theta_w)\frac{\partial h}{\partial z}\right)=S_0\frac{\partial h}{\partial t},\quad h=z+\frac{p_w}{\gamma_w}=z-\psi \tag{1}$$

where $\boldsymbol{h}$ [L] is the pressure head inside groundwater, $\boldsymbol{\theta_w}$ [-] the water capacity, $\boldsymbol{k}$ [$L \cdot T^{-1}$] the conductivity, depending on the water capacity, $\boldsymbol{S_0}$ [L^{-1}] the specific storativity of the soil. Richards equation (1) must be linked with functions describing the dependence between the pressure head and the water content of the soil (retention curves, i.e. $h = h(\theta_w)$) and the function relating the conductivity and the water content of the soil ($k = k(\theta w)$).

FEMWATER allows to define both the properties of the soil and those of the fluid. The input parameters of the fluid properties are related to its density, viscosity and compressibility. As for the properties of the soil must be assigned for each element of the 3D Mesh. The properties of the soil to be defined are the following: permeability, compressibility, dispersion and diffusion. In particular, since FEMWATER models both saturated and unsaturated soil, it is also necessary to identify the particular retention curve of the model and therefore the water capacity curve that is the derivative of the previous one, as well as the relative permeability function. For the filtration simulations of FEMWATER it is necessary to define the three curves that describe the behavior of the materials in unsaturated conditions and which relate the pressure with the relative permeability, with the water content and with each other. In the GMS software can be used either the Van Genuchten curves (1980) or personalized relations. The Van Genuchten curves were chosen, in which the relative permeability is a function of the actual water content θ_e. The program has an internal library of retention curves for different types of soil traced using the expression of Van Genuchten. and we chose the curves for silt and sand.

1.1 Previous Experience in 3D Simulations of Underseepage and Sand Boils

In 2017 we considered two piping – sensitive subsoil case studies in Italy, along the Po river: Sacca di Colorno (Cavagni 2017), Caselle Landi (Cremonesi 2017). In 2018 we were able to run a simulation also for a stretch of levee in the village of Boretto (Virderi 2018). All cases were analysed in unsteady conditions using the historical flood waves occurred in the Po river in 2000 and 2014. Occurrences of sand boils for these events are documented: they have been used as a constraint to improve seepage forecasting reliability and also as a check of the soil heterogeneity identification and the hydraulic parameters (Ozkan 2003). We must point out though that much sand boil information is derived from observational data based on subjective descriptions by different people, and usually does not represent observations made on a continual basis.

The occurring of sand boils can happen if certain subsoil conditions exist. In a document (Mansur et al. 1956) the top stratum landside of levees is classified into one of three categories: (1) no top stratum; (2) top stratum of insufficient thickness to resist hydrostatic pressures that can develop; and (3) top stratum of sufficient thickness to resist hydrostatic pressures that can develop during the maximum design flood. Information extracted from site investigations used to generate the 3D model of the subsoil shows that in the Sacca di Colorno and Boretto we have an upper layer of silty soil overlying a thick layer of sand aquifer, similar to condition (2), while in Caselle Landi we have a situation similar to condition (1).

In Sacca di Colorno (Fig. 1) the aerial photograph shows the main levee with a white line and the spur levee with a yellow line. The first recorded sand boils occurred during the 1994 flood event in the Po river, but it's in the 2000 that the phenomenon reached the maximum size.

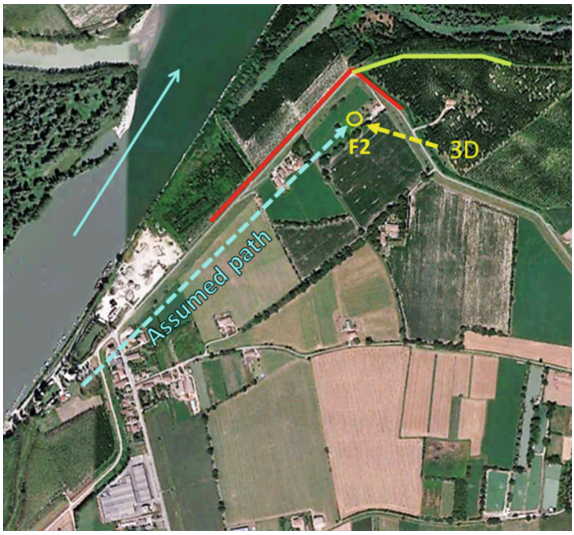

Fig. 1. Sacca di Colorno: indicated main levee, spur levee and seepage path.

The yellow circles indicate the location of the sand boils, the biggest was the one called F2 which was treated with sandbags to prevent further damage. In 2001 a concrete cut off wall was drilled down into the main levee, white line in Fig. 1, to a depth between 20 and 30 m, which is shown with the red line. Nevertheless, the F2 sand boil reoccurred during the 2002 and 2014 floods, slightly further away from the toe of the levee and smaller in size. The first assumption was that water was flowing downstream from the river channel through the subsoil covering a length of about 1 km, the arrow labelled Assumed path in Fig. 1.

Based both on the particle-size distribution and the conductivity values obtained from Lefranc tests carried out every other meter in the borehole, the geologic formations recorded in the borehole logging were grouped in four main soil types: medium

fine sand, medium fine silty sand, coarse and gravelly sand and clayey silt. Moreover in order to represent the embankment and the cut off wall in the model two more materials were added (Table 1).

Table 1. Legends and corresponding coefficients of permeability of main material zones

Material name	Conductivity [m/s]
Medium-fine sand	$2 \cdot 10^{-4}$
Medium-fine silty sand	10^{-4}
Coarse and gravelly sand	$5 \cdot 10^{-3}$
Clayey silt	$5 \cdot 10^{-6}$
Embankment	10^{-6}
Cut-off wall	10^{-8}

As stated earlier, to build the model, a 1 m grid cell Digital Terrain Model (DTM) generated from the 2005 LiDAR survey, was imported to define the topographic elevation of the levee and the surrounding land. The contour of the domain was defined following the central line of the river channel and cutting the levee normally. From here a 2D mesh was generated, with nodes closer to each other nearer to the levee where more information in detail is needed. The mesh was linked to the soil elevations to generate two TINs (Triangulated Irregular Network). One TIN with the body of the levee, and one TIN cutting out the body of the levee.

In order to prevent software failure due to absence of "cut-off wall material" values available for the mesh, fictitious layers of this material were then added at the bottom of the boreholes and the 3D Mesh was rebuilt, identical to the previous one except for a layer of cut-off wall material in the lower limit of the model. This layer, after being identified as cut-off wall material with the procedure described above, was then transformed into a layer of "levee material", which does not affect the simulations. The cut-off wall was represented with an impervious material with $k = 10^{-8}$ m/s light blue color and the levee material in grey colour in Fig. 2.

From borehole data collected in the same area, we found out that holes were cored only through the upper levee. Borehole investigations were only located on the levees. To reconstruct the spatial distribution of the sediments along the overbank, far from the levee, new core logs were created by duplicating existing lithologic logs. These additional "mock" boreholes were created and added on both sides of the levee. The duplicated boreholes on the riverside were reconstructed so to avoid the presence of clayey silt that can never be found in the Po riverbed. The software interpolates the distribution of the subsoil materials and it generates a 3D mesh (Fig. 2).

In the Sacca di Colorno the floods peaks of 1994 and 2000 are respectively 7.58 and 8.01 m on the zero level. The only thing that can be deduced is that the trigger level of the sand boils before the cut-off wall was less than 7.58 m. The two floods in which the phenomenon occurred after the construction of the diaphragm are those of 2002 and 2014, whose maximum levels were respectively 6.63 and 7.01 m above zero level. These are also the only floods after the 2000 event in which the flood plain has flooded, which could suggest that flooding of the floodplain is a necessary condition for the activation of

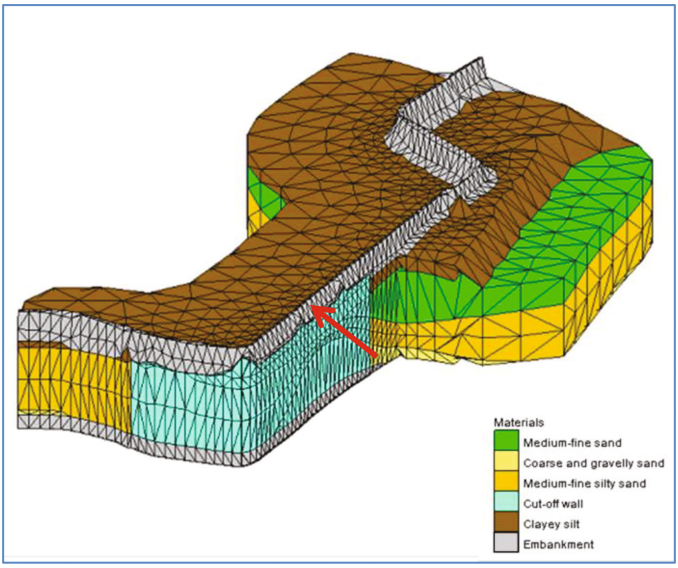

Fig. 2. 3D model with cut-off wall constructed on the river side of the levee (arrow).

the phenomenon. Regarding the 2002 event, we know that the sand boil has activated 6 h before the peak (Technical Advice AIPo 2002) at a level of 6.5 m above z.l.

The latter could therefore be a value indicative of a trigger level of the phenomenon, variable depending on the degree of saturation of the ground and water table level. Based on the analysis of piezometric heights of the area under examination with similar precipitation periods we have identified the value of 1 m as the average depth of the water table during high water discharges in a period with precipitation. Therefore, it has been decided to insert a constant load of 25 m a.s.l., which corresponds to a water table at about 1 m below the ground; on the river side the historical flood waves levels were set, using the observations at the Casalmaggiore (CR) gauge. The remaining lateral boundaries and the floodplain surface are considered impervious. Dirichlet (DB) boundary conditions have been imposed, thanks to which a load value can be assigned to the 3D Mesh nodes. The load can be constant or variable over time, and is converted in the piezometric height by the calculation code, subtracting from the total load the value of the geodesic dimension z for each node to which the Dirichlet condition has been assigned. In the unsaturated areas the piezometric height is negative.

For clarity, only positive piezometric heights are displayed, so the appearance of a colored area behind the levee coincides with the occurrence of the sand boils. It is important to note that here the sand boil is considered active when the load in the node exceeds the value of zero. The level of activation of the sand boil does not correspond to the static load present in the river that makes it activate, but is the consequence of various factors including the level of pre-existing water table.

Results of the simulations for the 2014 flood wave are shown in Fig. 3: only the positive pressure values are visualized. Positive values in the area behind the levee mean that sand boils can occur. The simulation shows the occurrence of the

phenomenon with water bypassing the cut off wall in the northern part of the model, after the overbank behind the spur levee is flooded. The positive pressure area in the southern part of the model (not completely realized during the flood event) can be justified with the missing representation of an ancient cut off wall, whose geometry and location are not completely known. Having neglected this cut off wall, it makes more influent the effects of the upstream seepage, getting a conservative result.

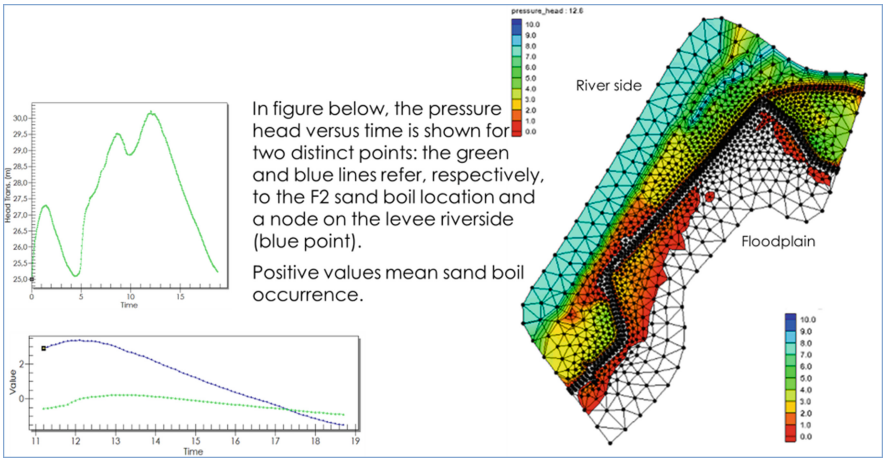

Fig. 3. Sacca di Colorno results of simulation for the 2014 flood wave with presence of cut-off wall (yellow dashed line).

In conclusion, the sand boil F2 occurs when the area between the spur levee and the main levee is saturated, and this happens only for remarkable river levels. The new plausible seepage flux path is reduced from 1 km to about 200 m as shown in Figs. 1 and 3. and is indicated with an arrow label 3D. The water depth above the land that triggers the sand boil results higher than 1.5 m depending on the degree of saturation of the soil and the water table position downstream. The delay (shift) between the peaks of the flood wave and the pressure history in the sand boil ranges between 8 and 48 h.

The other case study located near the village of Caselle Landi is an area which has been affected in the past centuries by severe flooding and levee breaches due to piping. Sand boils occurred during the October 2000 flood event. Here no cut-off walls are present. This time the geologic formations recorded in the borehole logging returned 10 soil types leading us to have twice the number of nodes and elements when creating our 3D domain. The 3D Mesh was made of 14279 nodes and 73822 elements. We have an alternation of soil types along the investigated depth, without a well identified top stratum (Fig. 4).

By setting analogous boundary conditions as in Sacca di Colorno, we show the results of the simulation for the 2000 flood wave in terms of pressure head distribution in the condition of the maximum pressures. Areas z1, z2 and z3, with positive pressure head in the floodplain, correspond to the areas historically interested with sand boils occurrence (Fig. 5).

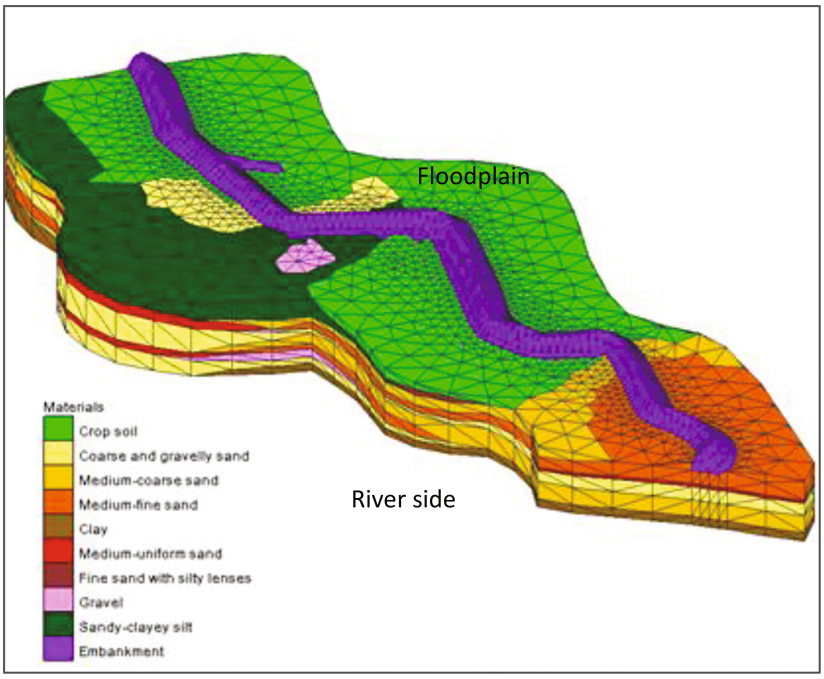

Fig. 4. Caselle Landi model creation

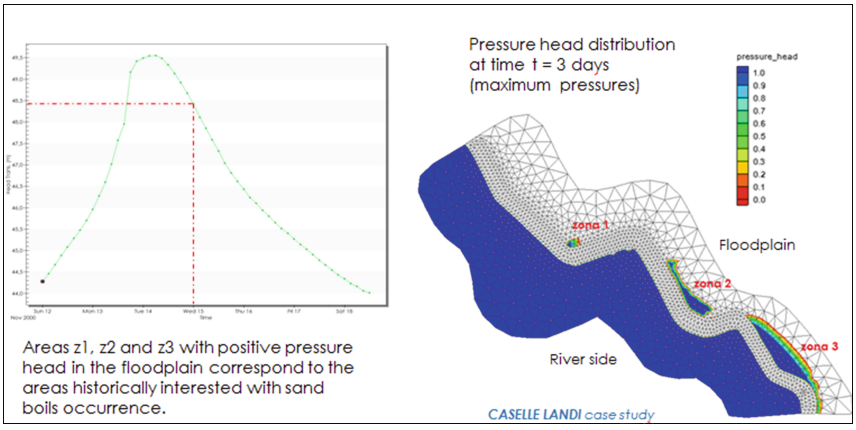

Fig. 5. Caselle Landi- results for the 2000 flood wave

With such result we placed cut off walls in the identified critical areas and checked if they were effective in bringing below zero the pressure values in the floodplain preventing the occurrence of sand boils. We tried different cut off walls geometries in the simulations reaching the configuration shown in Fig. 6, where instead of having only one long cut off wall we have three smaller ones.

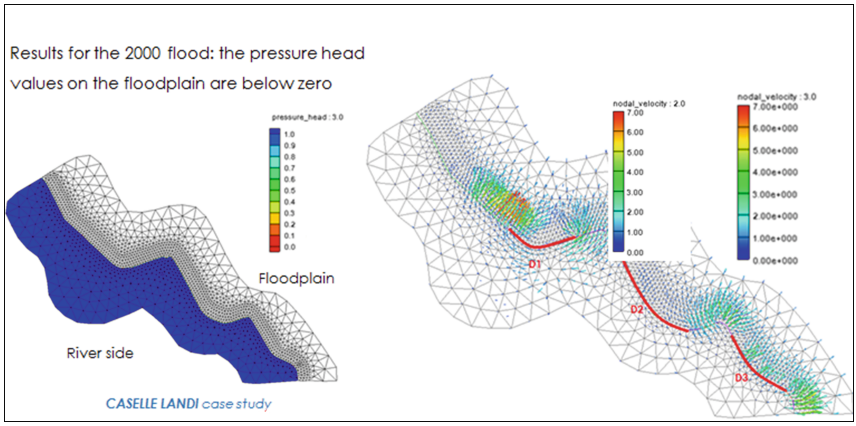

Fig. 6. Caselle Landi - Design and representation of cut-off walls

The 2-D simulations carried out in previous studies suggested the realization of a cut off wall with an extension involving the entire site while the 3-D simulation allowed a location and extent of the barrier optimized with regards to economic budget and hydraulic efficiency. The pressure head values on the floodplain are below zero. There is no longer bypass of the cut of walls by water.

1.2 Advances in 3D Simulations

We present a further salient advance of 3-D modeling and application in the efficient design of hydraulic barriers intended to prevent sand boil formation.

On a stretch of the Po river, Italy, between the towns of Boretto (RE) and Pieve Saliceto (RE) and upstream from the existing freeway fly-over connecting the Cispadana and S.S. n.62, we find the area that some time ago arose our interest due to the reoccurrence in the past 70 years, on the landside of the main earthen levee, of several impressive sand boils. Recorded sand boils formed after flood events in 1951, 1994 and 2000 (reactivated in 2014), each one appearing downstream from the previous one and closer to the fly-over, without a significant change in distance from the levee toe (Fig. 7).

Along the same stretch of river embankment, between 1995 and 2000 cut-off walls of different lengths and geometry were driven into the river embankments to reduce seepage forces. Between 1998 and 2001 the same stretch of levee was raised to meet the system's standard of protecting against the 200 year flood. In 2014 this same stretch

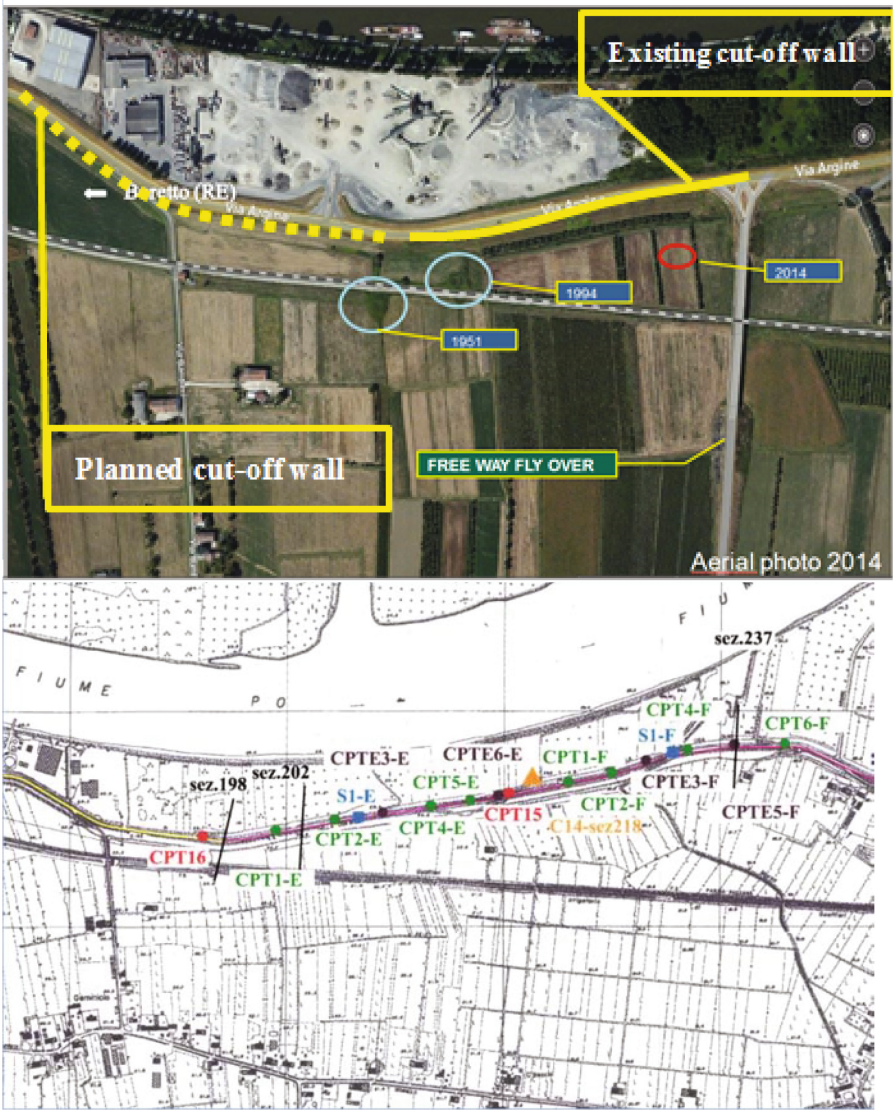

Fig. 7. Boretto: above: chronological order of the events where evidence from the 1951 and 1994 sand boil "cup" is visible; below: location map of the study area showing the borehole locations and interpreted profiles; S1-E/F = boreholes.

of levee showed to be a critical area due to sand boil formation during high water levels as shown in Fig. 8.

In order to mitigate sand boil risk formation one of the solutions to be studied was: build a new cut-off wall along this stretch of river embankment so to complete the impervious barrier already in place.

Fig. 8. Boretto: the 2014 flood induced sand boil (red double line circle) at about 70 about 320 m downstream from a previous sand boil "cups", dating to 1951 and 1994 (light blue dashed line circle).

The 2-D simulations carried out in previous studies suggested that the realization of a cut-off wall with an extension involving the entire site could not mitigate risk. The analysis of levee stability were performed using the finite element code SEEP/W part of GEOSTUDIO, GEOSLOPE 2003, which is a conventional finite element formulation of the saturated flow equation. Using SEEP/W solution as an input then the stability of levee structures was analyzed with a limit equilibrium software SLOPE/W by GEO-SLOPE International, Ltd (2003). While the minimum value of F = 1.4 imposed by Italian laws was always verified for river side slope, the land side slope was not always verified in case of rapid drawdown analysis methods. Cut off wall showed not to improve the land side slope stability (Giliberti et al. 2017). This arouse concern about the interaction between the freeway fly-over and the new planned cut off wall to be built in response to the migrating sand boils.

To verify this concern a later 3-D simulation (Virderi 2018) was run. The 3-D reconstruction technique is very similar to 3-D simulations carried out in previous studies along the Po river: Sacca di Colorno (PR) and Caselle Landi (LO), where the 3-D modeling gave new information on the plausible direction of the seepage flux that caused the formation of sand-boils, suggesting a new perspective for the remediation measures (Cavagni et al 2017). The approach to hydraulic analysis was again carried out using FEMWATER (Lin et al. 1997) a 3-D Finite Element model, and the morphology has been described by means of a 1 m grid cell DTM (Fig. 9).

The stratigraphic frame, lithology, water table and geotechnical properties of the slice of foundation soil under exam have been recovered through spatial extrapolation of the existing investigations, which were all lined up along the main levee (Fig. 7). These data have been processed by the graphical interface of the Groundwater Modeling System (GMS 2017 software) as in Fig. 10.

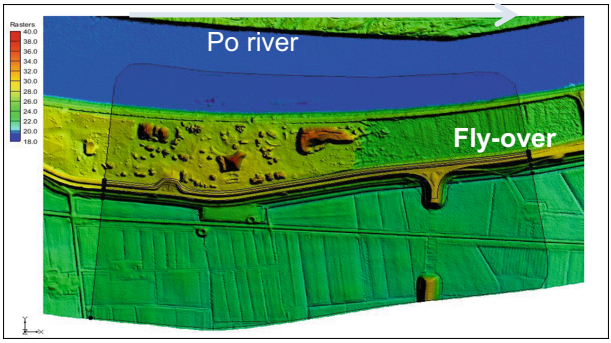

Fig. 9. Boretto: Digital Terrain Model of the area.

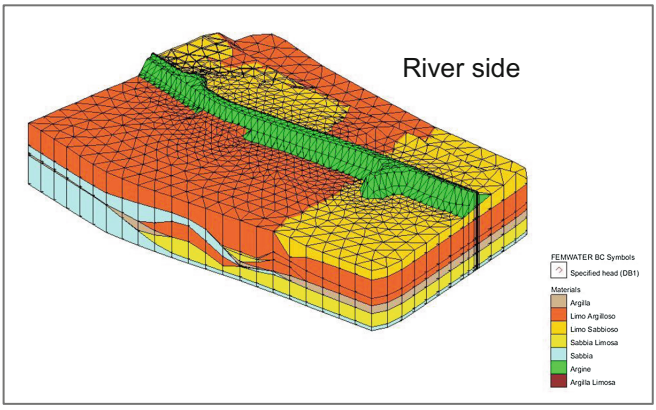

Fig. 10. Boretto: 3D model.

The geologic formations recorded in the borehole logging are represented from top to bottom by the following soil types: clayey silt (about 3–4 m thickness), clay, medium fine silty sand, medium fine sand, coarse and gravelly sand. In 2017 a new geological survey campaign started. The S4 borehole was drilled on the flood plain behind the levee and on the same location where the 2014 sand boil occurred (Fig. 11a).

During the drilling operations, from the depth of 15 m up to 30 m at each change of drilling maneuver sand began to fill the hole, rising back up in the borehole for about 1,5 m (Vicenzetto 2017). As an example in Fig. 12 a borehole log (S4) from the 2017 geological survey campaign.

In this setting the fine-grained layer (blanket) is underlain by a thicker coarse grained layer, which opens to the riverside and behaves as a confined aquifer layer that conveys water beneath the embankment. In our study the top stratum appears of insufficient thickness to resist hydrostatic pressures that can develop during the flood.

Building the model the variable boundary conditions can be of two types, depending on whether a period is simulated in the absence of precipitation or a period

a) b)

Fig. 11. Borehole S4 on the flood plain close to the fly-over.

with precipitation. We chose the latter. During rainy periods, rain infiltrates the subsoil with a velocity equal to the precipitation flow. By imposing a variable boundary condition, if the precipitation flow exceeds the infiltration capacity of the ground or the groundwater level exceeds the surface of the 3D Mesh, the piezometric height cannot exceed the "ponding depth", ie the depth of the ponds that are created on the surface of the model (value that is entered by the user).

Based on the analysis of the pluviometry and piezometric heights of the area under examination with similar precipitation periods we have identified the value of 1,5 m as the average depth of the water table during high water discharges in a period with precipitation. So, regarding the boundary conditions, the water table depth on the floodplain side has been fixed at 1.5 m below the ground surface; on the river side the historical flood waves levels have been set, using the observations at the Boretto (RE) gauge. The case has been analyzed in unsteady conditions, using the historical flood waves occurred in the Po river in 2000 and 2014. The remaining lateral boundaries and the floodplain surface are considered impervious. Moreover, occurrences of sand boils for these events are well documented and they have been used as a constraint to improve seepage forecasting reliability.

The results in terms of piezometric height are shown in Fig. 13 and it can be seen how they did not allow for an optimal location and geometry of the barrier to be built with regards to its hydraulic efficiency. The 3D results identify a much longer stretch of levee that can be affected by seepage, than the one in project as in Fig. 13.

The figure refers to the most critical moment of the flooding of the flood plain in 2014, where it is possible to see how the area in which the sand boil appeared falls within the area with positive pressure head values.

The circle (green) indicates where the sand boil appeared in 2014. The double red line indicates the location of the fly-over and the dashed yellow line the new cut-off wall in project. The 3D simulations proved to be more able to tell where sand boils occurred and where not, as the cases of the 1951 and the 1994 not reactivated sand boils, thus delivering results more adherent to the real scenario. These results suggest that the sand boils can only be activated when the flood plain on the river side of the levee experiences flooding during periods of high discharge as it happened in 2014.

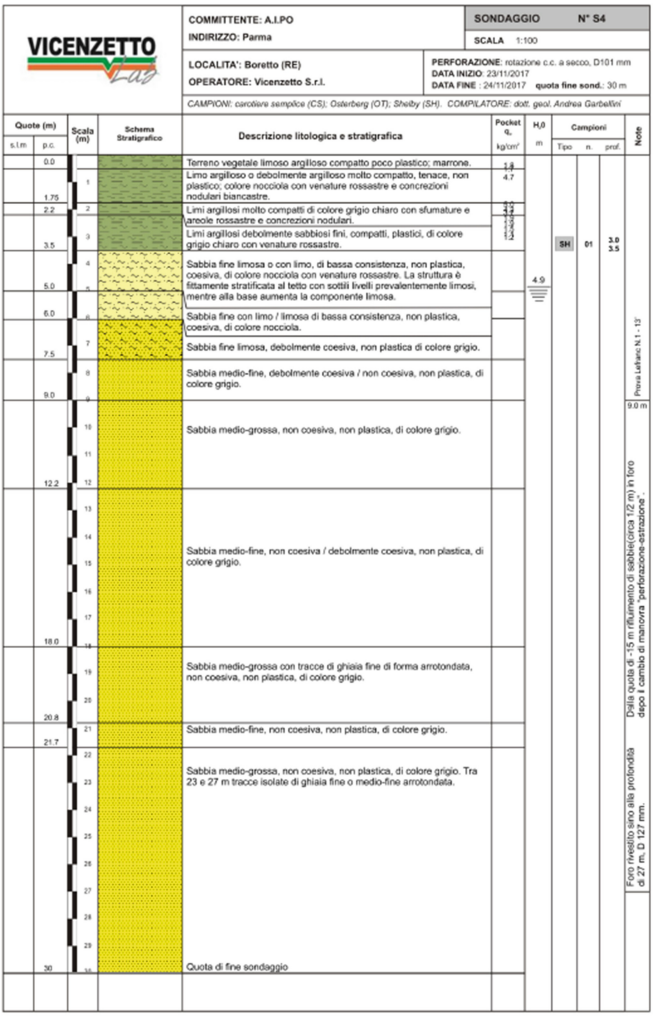

Fig. 12. Boretto interpreted profile of borehole S4.

Even in 2010 the flood plain experienced flooding but the duration of the flood was shorter and therefore could not activate the sand boils. The 3-D modeling allowed a better identification of the piping-sensitive subsoil areas and pointed out an unexpected preferential flow located downstream from the piles of the freeway fly-over.

The study pointed out also the importance of using Digital Terrain Model with cell grid equal or smaller than 1 m, which allows to take into account geological information that can be used as a guide in defining the geological structures showing a strong correlation with relief. A DTM displays the relationships between topography and geological features related to geological and geomorphological processes, taking into account the lithostatic load. The DTM, used to run the calculation, yielded an

accurate representation of the relief of the 1951 and 1994 sand boils "cups". Such representation has been processed by computer, confirming that these two sand boils never reactivated probably due to the weight of the sand bags left around them. This leading to consider as another solution the construction of a berm, instead of a cut-off wall.

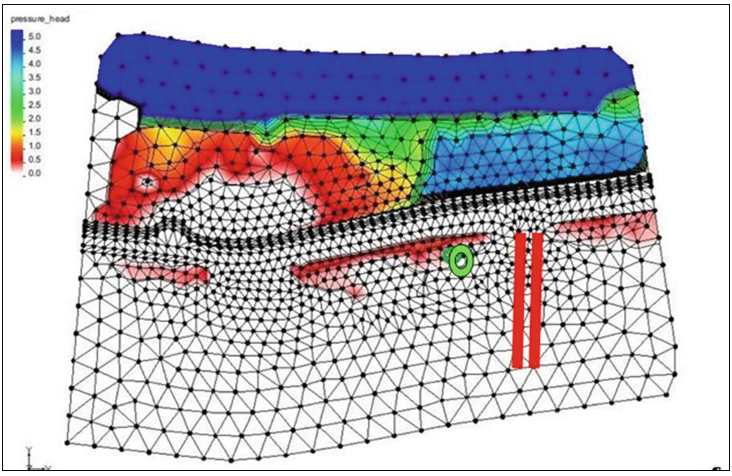

Fig. 13. Computation grids for Boretto. Piezometric head during the most critical time of the 2014 flood wave.

Observing the results obtained from the 3D simulation performed without the insertion of the existing cut-off wall illustrated by a continuous line in Fig. 7, we were struck by how these results were very similar to the reality of the filtration phenomena that took place during the flooding in 2014.

We made the assumption that therefore the existing cut-off wall might be deteriorated, if not completely absent. We decided to perform additional, non-conventional on site tests.

We carried out *Electrical resistivity tomography* (ERT), of which 150 m (Ert 14, 15 e 16) lines where placed across the levee, and a non-vertical borehole, SI-3 in Fig. 14. This is the area where the 3D resistivity survey was carried out to map the lateral and vertical extent of the buried cut-off wall. What appears is the presence of infiltration zones which, in this area, have also determined a certain degree of disturbance of the layers: in particular, sections 5 and 7 show that the flat-parallel structure of the surface layers has been partly compromised; the areas that have undergone hydraulic lifting phenomena (sand boils) are clearly visible.

The lines 14, 15 and 16, placed normally to the embankment, deserve separate mention; these ERTs were made for the purpose of determining the presence or absence of the plastic cut-off wall. These lines were then made with inter-distance between the electrodes of 1 m.

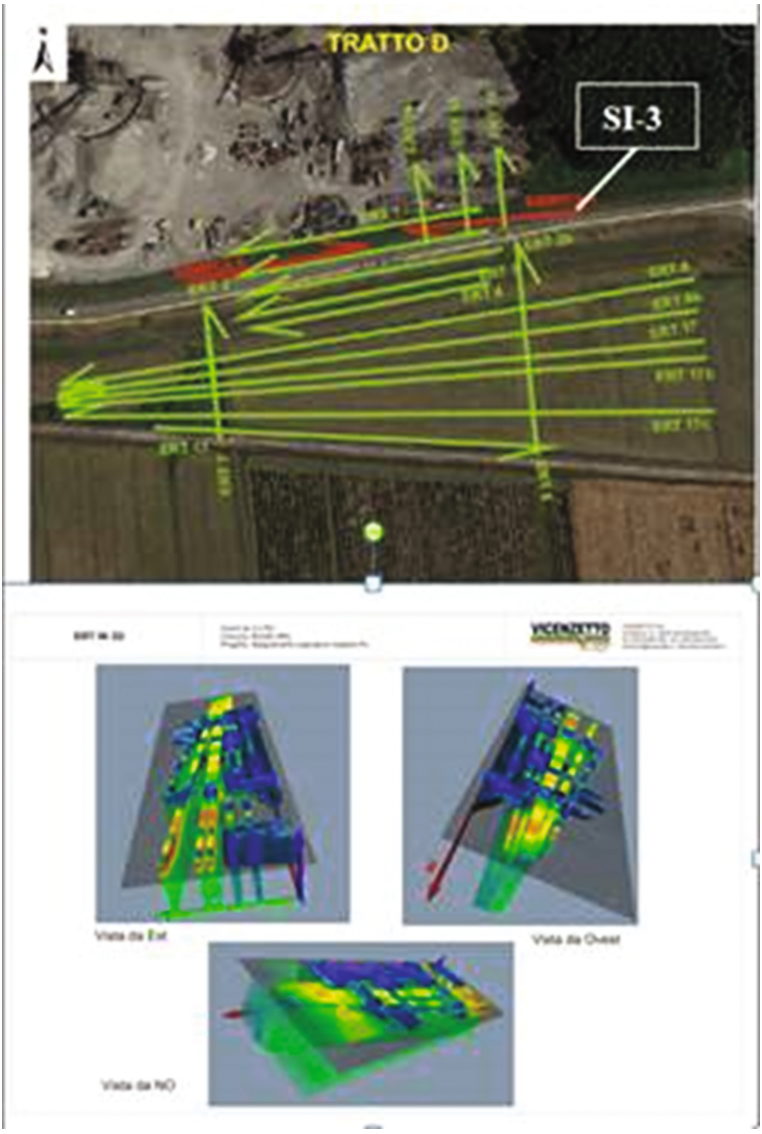

Fig. 14. Resistivity tomography lines and the non-vertical borehole SI-3.

From the results obtained, an intervention of levee lifting is evident: the resistivity of the materials laid during the intervention is higher than the material constituting the old levee body.

On the other hand, there is no evidence of the cut-off wall: probably it is too thin to be detected; it is also possible that, by increasing the lithostatic pressure with depth, it is literally closed in depth; in fact, these cut-off wall, when put in place, are fluid. The non-vertical borehole (dip from vertical 22°) SI-3 at the depth of 4.7/5.45 m has

detected material with non-natural physical characteristics. The material is gray, not plastic, flaky, with low resistance to compression and has a very low density. We assume it may be the deteriorated cut-off wall.

2 Conclusions

In our experience the 3D simulation, which takes into account the entire subsoil region, can give information free of assumed flow direction, as the one imposed with the 2D modelling. In the Sacca di Colorno study the 3D modelling allowed a better definition of the design of efficient hydraulic barriers to be realized in order to avoid the formation of sand-boils. In the Boretto case study the 3D simulations proved to be more able to tell where sand boils occurred and where not, as the cases of the 1951 and the 1994 not reactivated sand boils, thus delivering results more adherent to the real scenario. It did not though, allow for an optimal location and geometry of the barrier with regards to its hydraulic efficiency. So the new cut-off wall, though fit for localized purpose, could shift the sand boil further downstream, under the flyover. A key role of the process was played by the detailed knowledge of the ground sediment structure and by the accurate hydro-geologic conceptual model, highly dependent from the DTM cell grid. Results could still improve with information from geophysical surveys and boreholes on each side of the embankment, so not to duplicate borehole logs to have far field conditions. Piezometric head monitoring downstream will be useful to make the boundary conditions closer fitting to reality.

In our experience 3D simulations are more realistic than 2D simulations because they can capture gradients along the third direction that in 2D concept is assumed to be infinitely extended. Differences can arise due to the following aspects:

- different meshing procedure and elements used;
- different boundary conditions;
- asymmetries unable to be caught in a 2D domain.

The computational burden related to a 3D simulation is higher but for sophisticated systems, like liquid flows, it is a way to ensure more realistic results.

References

GMS (2017). http://www.aquaveo.com/software/gms-groundwater-modeling-system-introduction

Cavagni A et al (2017) Experience in 3-D modeling tricks and fitting techniques in seepage and piping prediction in levee subsoil. In: Abstract, 25th meeting of European working group on internal erosion in embankment dams & their foundations, EWG-IE, 4–7 September 2017, Delft, The Netherlands

Cremonesi S (2017) 3D modeling of the seepage and piping phenomena in a Po River embankment in the Lodi province, MSc Thesis in Environmental and Land Engineering, Parma University, Italy

Giliberti MD et al (2017) Escalation in local structural flood protection measures. Then what? In: Abstract, 25th meeting of European working group on internal erosion in embankment dams and their foundations, EWG-IE, 4–7 September 2017, Delft, The Netherlands

Lin H-CJ, Richards DR, Talbot CA, Yeh GT, Cheng JR, Cheng HP, Jones NL (1997) FEMWATER a three-dimensional finite element computer model for simulating density-dependent flow and transport in variably saturated media. U.S. Army Engineer Waterways Experiment Station, Vicksburg

Mansur CI, Kauffman RI (1956) Underseepage, Mississippi river levees. St. Louis District. In: Proceedings of the American Society of Civil Engineers GMS (2017). http://www.aquaveo.com/software/gms-groundwater-modeling-system-introduction. Paper 864

Ozkan S (2003) Analytical study on flood induced seepage under river levees. Doctoral Dissertation. Department of Civil and Environmental Engineering/Faculty of Louisiana State University

TACFD - Technical Advisory Committee on Flood Defenses (2002). Technical report on Sand Boils (Piping). The Netherlands

Vicenzetto S.r.l. (2017) Technical Report on Geognostic investigations to design works for functional adjustment of Po river main levee in the municipality of Boretto (RE) to control seepage. Villa Estense (PD) Italy

Virderi L (2018) Internship report 2017/2018—Civil Engineer. Parma University, Italy

A Statistical Framework for Incorporating Sand Boil Observations in Levee Risk Analysis

Bryant A. Robbins[1(✉)], M. Doughty[2], and D. V. Griffiths[2]

[1] U.S Army Engineer Research and Development Centre, Vicksburg, MS, USA
bryant.a.robbins@usace.army.mil
[2] Colorado School of Mines, Golden, CO, USA

Abstract. The presence of sand boils near the toe of a levee indicates that backward erosion piping, an internal erosion process, has initiated at a given location. As a primary failure mechanism for levees, backward erosion piping is commonly evaluated as part of levee risk analysis. Currently, sand boil observations are subjectively incorporated into risk analyses through expert judgement. This study presents an approach in which sand boils are statistically assessed as point pattern data. Results indicate that density estimates may provide a convenient means to compute initiation probabilities for backward erosion piping, and cluster analysis may provide a means of estimating characteristic levee segment lengths. Further research is needed to explore the generality of these concepts under various geologic conditions.

Keywords: Sand boils · Backward erosion piping · Levees · Statistics
Risk analysis

1 Introduction

Backward erosion piping (BEP) is an internal erosion process by which shallow erosion channels progress upstream through foundation sands beneath levees as shown in Fig. 1 (Bonelli 2013). As a leading risk driver for levee failure in the United States (Baker 2018), BEP is an issue of major concern. The risks associated with BEP are currently evaluated as part of levee risk analyses through application of event trees (USBR and USACE 2015) that separate the BEP process into a sequence of distinct events that must occur to reach failure. A simplified event tree for BEP is shown in Fig. 2, with corresponding event numbers shown in Fig. 1 at the associated location on the cross section. For BEP to progress to failure, erosion must (1) initiate due to seepage heaving the clay layer or exploiting existing defects, (2) progress upstream due to high hydraulic gradients, (3) have overlying soils (clay) sufficient to support the enlarging void, and (4) enlarge enough to result in collapse and breach of the overlying embankment. Assuming each event in the event tree is independent, the probability of failure is the product of all event probabilities in the tree (Fig. 2).

The presence of sand boils near the levee toe is indicative of BEP initiation. As thousands of sand boils occur along levees during floods (USACE 2012), it is critical to have an objective analysis procedure for computing initiation probabilities from past performance observations. This study investigates the application of spatial statistics,

S. Bonelli et al. (Eds.): EWG-IE 2018, LNCE 17, pp. 289–300, 2019.
https://doi.org/10.1007/978-3-319-99423-9_26

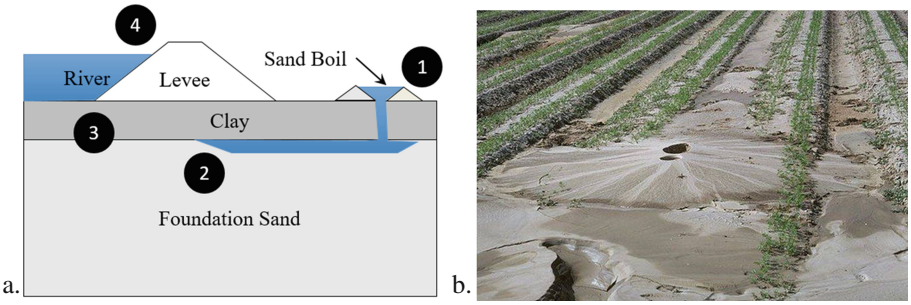

Fig. 1. (a) Schematic illustration of BEP and (b) photograph of a sand boil.

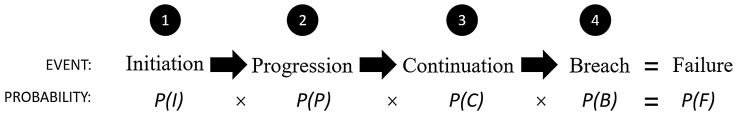

Fig. 2. Simplified event tree of BEP process leading to failure.

specifically point pattern analysis, to arrive at estimates of initiation probabilities from analyses of past sand boil observations.

2 Background

The initiation of piping was originally thought to be predicted by the vertical gradient for heave of a soil mass given by

$$i_c = (1 - n)(G_s - 1) \tag{1}$$

where n denotes the soil porosity and G_s denotes the specific gravity of the soil particles (Terzaghi 1922; Taylor 1948). Equation 1 predicts the heave of a uniform mass of soil, but it cannot be relied on to predict the initiation of piping in many cases (Terzaghi and Peck 1967). Sand boils are often caused by concentrated seepage through defects such as cracks, rodent holes, and root holes. The concentrated seepage causes sand boils to initiate at gradients significantly lower than indicated by Eq. 1.

Field measurements of vertical hydraulic gradients (over clay confining layers) in the vicinity of sand boils indicated that sand boils may initiate at vertical gradients as low as 0.2; however, most sand boils observed in the field along the Mississippi River occurred at or above vertical gradients of 0.5 (Turnbull and Mansur 1961). Recent observations along dikes in Florida during a test filling have arrived at similar conclusions (Huzjak et al. 2016). Because of these observations, a vertical hydraulic gradient of 0.5 at the levee toe was set as the empirical design guideline for levees in the United States (USACE 2000).

While using an empirical design criterion is an acceptable design approach, it does not provide a suitable means of estimating the actual probability of piping initiation for risk analysis. As such, current practice makes use of subjective probabilities elicited from expert engineers in an attempt to meld observed performance and seepage analyses into a coherent probability for BEP initiation. This approach has been used on numerous risk analyses with success; however, there is an inevitable degree of subjectivity put forward by the experts involved. The following sections explore the use of spatial statistical analyses as a means for estimating BEP initiation probabilities from sand boil observations in an objective and consistent manner.

3 Spatial Statistics: Point Process Theory

The field of spatial statistics separates spatial data into three categories, i.e., geospatial data, lattice data, and point pattern data (Cressie 1993). Point pattern data refers to data for which the random location of an event is the variable of interest. Sand boils most naturally fall into this category. Just as in classical statistics, we are interested in *first order* properties, i.e., mean or expected values, and *second order* properties, i.e., covariance structure that describes the interrelation between events. The expected number of events per unit length, referred to as the intensity (λ), is the first order property of interest and is related to the probability density function of the underlying process. The relationship in the intensity between locations is the second order property of interest and can be used to describe spatial patterns in the data. Using terminology that is more related to the goals of the sand boil analysis, we will refer to the two analyses as

1. Density estimation – analysis of event probability at each location.
2. Cluster analysis – detection of patterns in event locations (random vs. clustered vs. regularly-spaced events).

Cluster analysis may reveal information regarding the spacing of events, which is informative in selection of characteristic lengths for levee segments, and density estimation is directly related to estimating the probability of BEP initiation. The following sections provide a brief overview of each type of analysis. For further details, refer to Cressie (1993) and Waller and Gotway (2004).

3.1 Density Estimation

Density estimation refers to techniques focused on estimating the underlying probability density function (PDF) of a process. In analysis of point pattern data, density estimation techniques may also be used to assess the intensity (λ) of the events at each location. In this study, the focus will be on estimating the probability density function as it more closely relates to the desired probability of BEP initiation.

There are numerous techniques for estimating density functions (Cressie 1993). In this study, a nonparametric kernel density estimator was used. The PDF $\hat{f}(u)$ is estimated in one dimension from observations $u_1, u_2, \ldots, u_N$ as

$$\hat{f}(u) = \frac{1}{Nb}\sum_{i=1}^{N} kern\left(\frac{u-u_i}{b}\right) \tag{2}$$

where the kernel is any valid probability density function scaled by bandwidth, b. The kernel density estimator is simply an empirical PDF similar to what would be obtained from a normalized histogram, except that it is continuous and smooth due to the "stacking", or summation, of smooth, continuous PDFs at each observation as shown in Fig. 3. The choice of the kernel has been demonstrated to be relatively insignificant, whereas the bandwidth, b, has a large influence on the degree of smoothing in the final PDF (Waller and Gotway 2004). For analysis in this study, a Gaussian kernel was used.

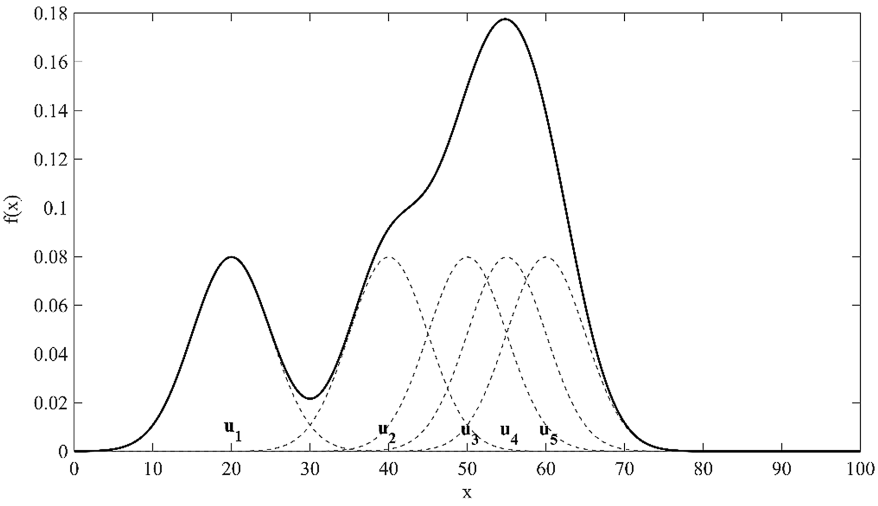

Fig. 3. Illustration of nonparametric PDF obtained from kernel summation as part of a kernel density estimate.

3.2 Cluster Analysis

While the density analysis provides an estimate of the event probability at each location, it does not provide any information regarding the spatial relationships between "hot spots" with high probability of occurrence. One method for examining the spatial trends in point pattern data is to compare the observed data to a null hypothesis of complete spatial randomness (homogenous, isotropic, stationary, Poisson process) through the use of an L-function. The L-function for one dimensional data is defined as

$$L(h) = \frac{1}{\hat{\lambda}N}\left[\sum_{i=1}^{N}\sum_{j=1,j\neq i}^{N} I(d(i,j)\leq h)\right] - 2h \tag{3}$$

where $d(i,j)$ is the distance between observed events i and j, h is the search distance, or length scale, over which the patterns in the data are being assessed, and $I()$ is an indicator function that takes a value of 1 if the input is true and a value of 0 otherwise (Waller and Gotway 2004). Assuming the null hypothesis of complete randomness is true, the intensity is estimated as

$$\hat{\lambda} = N/L \tag{4}$$

where N denotes the total number of observed events that occurred over the entire, one dimensional domain of length L. Under the null hypothesis, $L(h) = 0$. If $L(h) > 0$, the data are clustered together more than random data, whereas $L(h) < 0$ indicates that the data are more regularly spaced than random data (Waller and Gotway 2004). By reviewing the value of the L-function for a dataset over a range of values of h, distances between locations at which data tend to cluster can easily be identified. This will be demonstrated in the following sections through analysis of actual sand boil data.

4 Example Analysis of Sand Boil Data

In 2011, widespread flooding led to record river stages occurring on the Mississippi River, which exerted substantial stress on the levee systems (USACE 2012). During this flood, the locations of 1000+ sand boils were recorded through the use of smartphone applications designed for flood data collection. No breaches due to BEP were reported. These data have been consolidated into a national levee database where additional sand boil location data from prior flood events have also been entered using information from past flood reports. The resulting data set is a comprehensive database of sand boil locations for more than 2,000 observed sand boils along the Mississippi River and tributaries as shown in Fig. 4.

Four sections of the full data set were identified as being suitable for spatial analyses of sand boils due to these areas having relatively complete observations as indicated by the high data density. The discussions below present the analysis conducted on solely the eastern levee of section 2, containing 102 sand boil observations. Analyses of the remaining study areas are currently underway.

The sand boil observations along the eastern levee in section 2 are shown in Fig. 5. This subset of the data will be used for the example analyses. The sand boil locations are treated as a one-dimensional data set based on the distance along the levee. A histogram of the sand boils along the levee is shown in Fig. 6 demonstrating the spatial distribution of the data points along the levee. This one-dimensional data set of the sand boils along the eastern levee of section 2 will be used for the kernel density estimation and cluster analysis in the following sections.

4.1 Kernel Density Analysis

For an initial demonstration of the use of kernel density estimation as a means of estimating the probability of BEP initiation, it was assumed that all sand boil observations were independent and identically distributed (IID) random variables, i.e., all

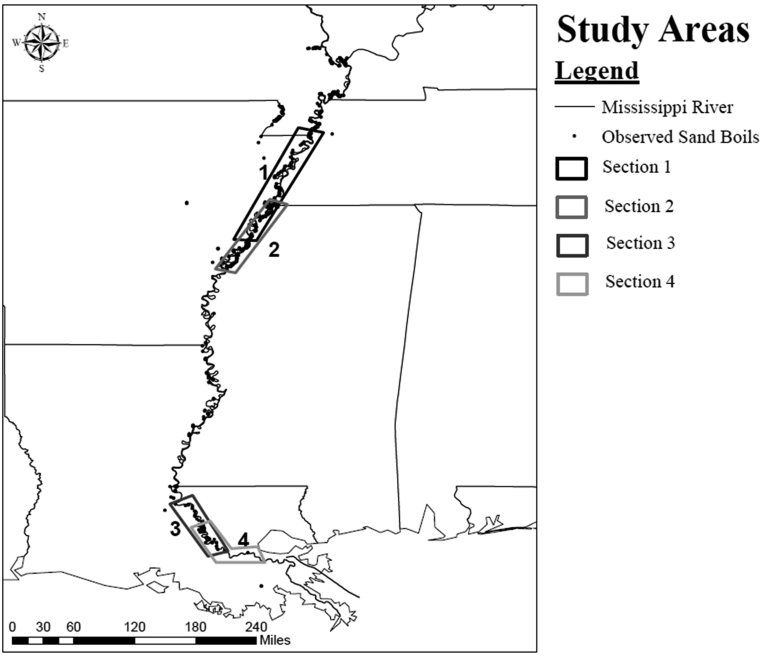

Fig. 4. Sand boil data along the Mississippi River and select study areas.

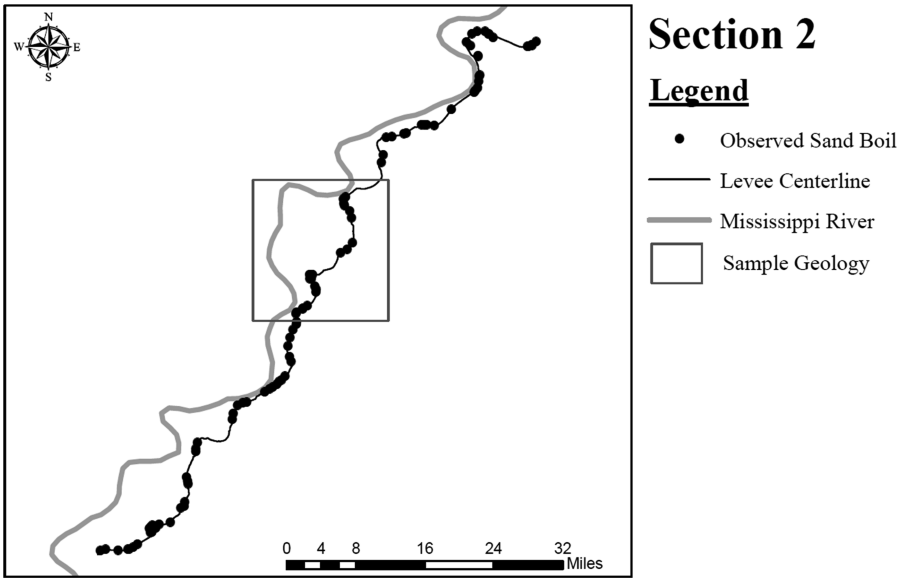

Fig. 5. Sand boils (102) along the eastern levee alignment of section 2 (Sample geology for indicated area provided in Fig. 10).

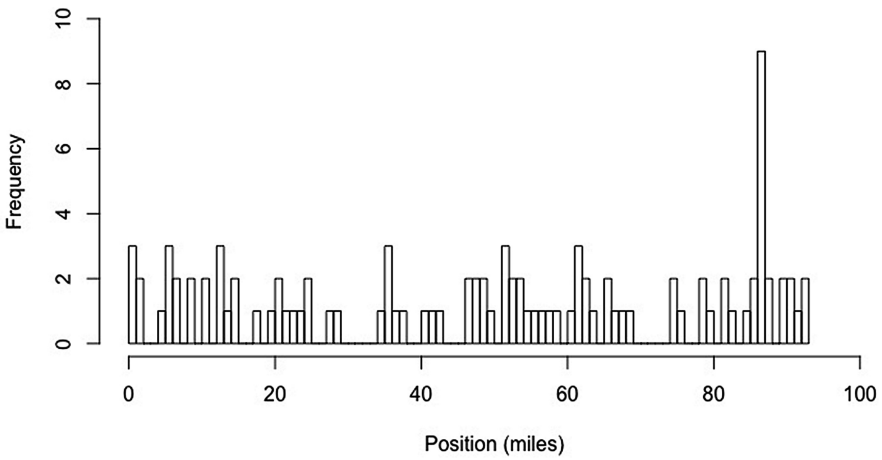

Fig. 6. Histogram of sand boils along the levee alignment.

observations are mutually independent samples drawn from the same distribution. While spatial variation of probability of initiation will be accounted for, this assumption ignores the contributions of many factors, such as hydraulic loading, confining layer thickness, and geology, which are known to affect the likelihood of sand boil initiation (Turnbull and Mansur 1961). Nevertheless, this crude assumption provides a simple demonstration of how kernel density estimates may be used to predict piping initiation.

The kernel density estimate (kde) function of the Kernel Smoothing package (Duong 2017) in the software R (R Core Team 2016) was used to estimate the kernel density function. A Gaussian kernel was used with a bandwidth (b) of 2 miles. The bandwidth was arbitrarily selected for this analysis but should be carefully considered in practice. The resulting estimate of the density function is a smooth, continuous function as shown in Fig. 7 with an underlying area equal to 1.0.

The PDF in Fig. 7 represents the probability density function of the location at which a single boil would occur. In a flood event, hundreds of sand boils may occur over a levee system. The probability of BEP initiation for a given location is the probability that one or more sand boils occur. Let n denote the number of sand boils that occurs at a given location. The probability of initiation is then given by

$$P(I) = P(n > 1) = 1 - P(n = 0). \tag{5}$$

Under the IID assumption, the number of sand boils occurring at a given location, n, is a Bernoulli random variable $n \sim B\left(M, \hat{f}(x)\right)$ with the total number of sand boils expected to occur on the system (M) being the number of trials, and the kernel density function (Eq. 2 or Fig. 7) being the probability of a success at each location. Thus, the probability of BEP initiation at each location given M sand boils occur in total is given by

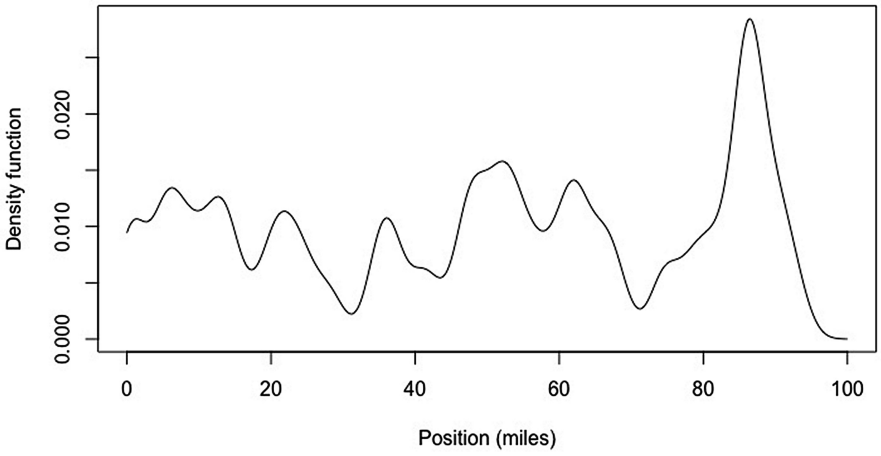

Fig. 7. Kernel density estimate of sand boil data set.

$$P(I,x|M) = 1 - B\left(0;M;\hat{f}(x)\right) = 1 - \left(1 - \hat{f}(x)\right)^{M} \tag{6}$$

with $B()$ denoting the value of the PDF of the binomial distribution with no successes in M trials and success probability $\hat{f}(x)$. To compute the probability of initiation using Eq. 6, an estimate must be made of the total number of sand boils on the system. One approach for estimating M is based on rank ordering of the sand boil observations by stage (Fig. 8). As an example, using a river stage of 56 feet for determining an initiation probability, the observations indicate that 40 sand boils were observed in the past at or below river stages of this magnitude. Assuming that half of actual sand boil events is observed and recorded, an estimate of 80 sand boils was used to calculate the probability of BEP initiation using Eq. 6. The resulting PDF is shown in Fig. 9. The resulting spatial probability distribution is a scaled version of the density function. Nevertheless, the probability values shown in Fig. 9 capture variations between levee segments spatially while also providing a seemingly reasonable probability of BEP initiation.

While the procedure described yields a continuous spatial distribution of BEP initiation (Fig. 9), much more research is needed to develop the procedure for use in practice. Conditional density functions need to be considered that take into account other variables, such as river stage. Additionally, analyses should be conducted in parallel to existing methods to further develop the process and ensure it gives intuitive probability estimates that are coherent with engineering judgment and current practice.

4.2 Cluster Analysis

A cluster analysis of the data set was also performed by computing the L-function over a range of length scales using Eq. 3. By examining the L-function, it can be determined if there are distances at which the observations tend to cluster together, or regularly

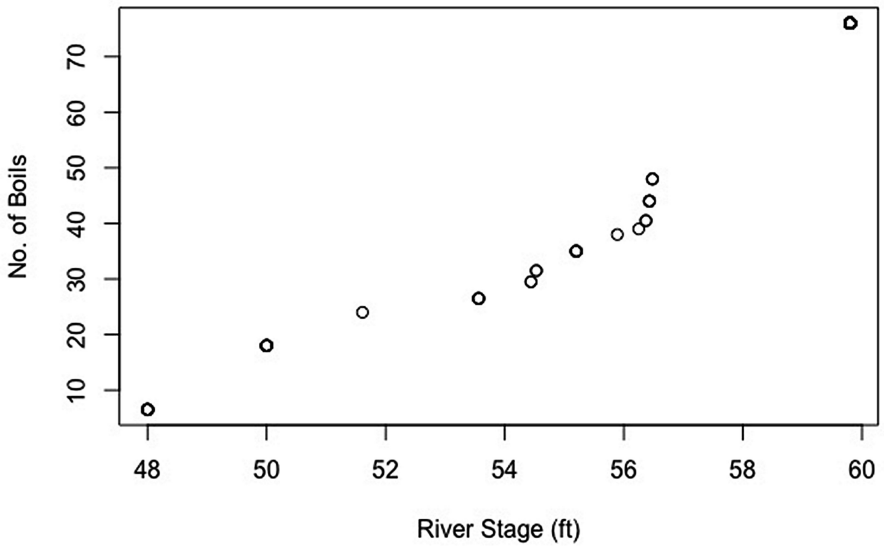

Fig. 8. Number of observed sand boils as a function of river stage.

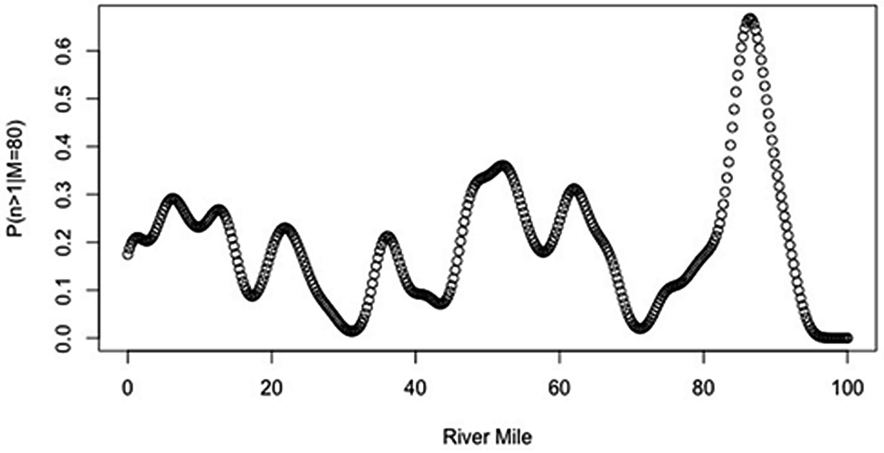

Fig. 9. BEP initiation probabilities along levee profile assuming 80 sand boils occur.

occur. Identifying these key distances may provide insight into the length scale associated with causal factors for sand boil formation.

It is known from previous studies that sand boils tend to occur in point bar deposits on the inside bends of river meanders (USACE 1956). Point bar deposits display a characteristic fining-upward sequence of sand and gravel that are capable of readily conveying water through the foundation of the levee. As such, it seems logical that sand boils would cluster at the length scale associated with the spacing of point bar

deposits along the levee alignment. To test this concept, river meanders were measured throughout the study area based on both the current and historic channel alignments. Sample measurements are illustrated in Fig. 10 for the area shown in Fig. 5.

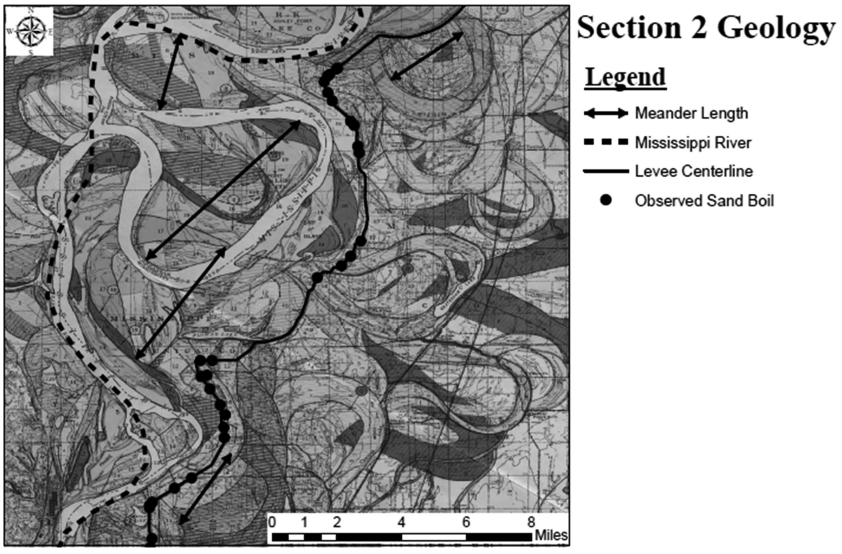

Fig. 10. Section 2 sand boil data along the eastern levee alignment.

The computed L-function and a histogram of meander measurements made throughout the study area are shown in Fig. 11. The L-function is positive indicating the sand boil data exhibit clustering at all length scales assessed. Interestingly, the L-function peaks, indicating the strongest degree of clustering, at the minimum meander length measured. While definitive conclusions cannot be drawn from this preliminary analysis, the results are promising and suggest that the L-function may provide a means of identifying the length scale associated with the causal mechanism of sand boil formation. At the very least, the L-function provides a convenient means of understanding the spatial patterns in sand boil observations for a levee system.

5 Conclusions

This study proposes a statistical approach for estimating BEP initiation probabilities through application of point pattern data analysis techniques to sand boil observations. The approach was demonstrated on an example data set yielding continuous estimates of BEP initiation along a levee. Additionally, cluster analysis of sand boil observations using L-functions indicated that sand boils tend to cluster at all length scales assessed. The maximum degree of clustering was observed at a length scale associated with the minimum river meanders, indicating that the L-function may be useful for identifying characteristic length scales associated with geologic features influencing BEP initiation.

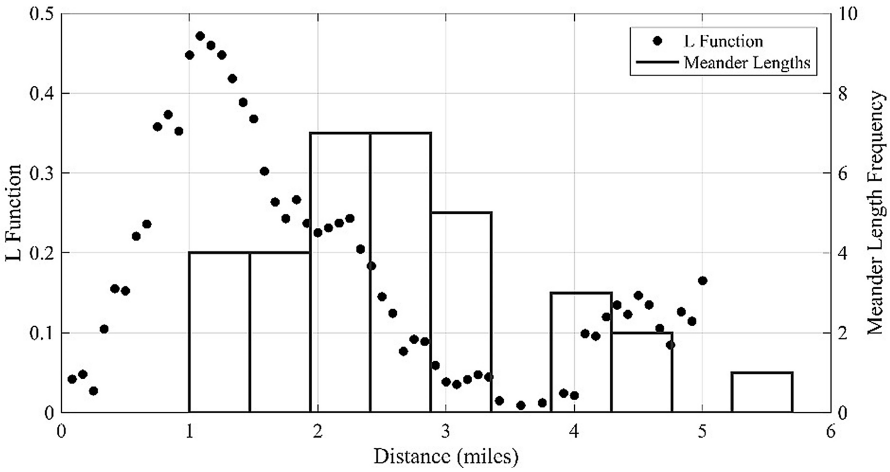

Fig. 11. L-function values at various lengths compared to meander length measurements.

While both the estimated density function and spatial information obtained from the cluster analysis can be used to inform risk analysis of BEP, it must be recognized that there are many criticisms that can be made of the proposed approach, especially for the simplified analysis presented in this paper. In particular, the approach will be inherently biased towards easily inspected areas and is entirely subject to data completeness and quality. Further, the data is not IID, but must rather be separated into populations to account for differing river stage and other influential variables (e.g., account for temporal changes due to levee modifications). Future research will focus on conditional analysis that incorporates these factors.

References

Baker C (2018) USACE conducts first analysis of risk and benefits of USACE levees. FRM Newsletter 11(1):11–13. U.S. Army Corps of Engineers, Washington, DC

Bonelli S (ed) (2013) Erosion in geomechanics applied to dams and levees. Wiley, New York

Cressie N (1993) Statistics for spatial data. Wiley, New York

Duong T (2017) ks: kernel smoothing. R package version 1.10.6. https://CRAN.R-project.orj/package=ks

Huzjak R, Olsen J, Robbins B (2016) Full scale test fill supports emerging research into exit gradients. In: Proceedings of dam safety 2016, Philadelphia, Pennsylvania, 11–14 September 2016, Association of State Dam Safety Officials

R Core Team (2016) R: a language and environment for statistical computing. R Foundation for Statistical Computing, Vienna, Austria. https://www.R-project.org/

Taylor D (1948) Fundamentals of soil mechanics. Chapman and Hall, Limited, New York

Terzaghi K (1922) Failure of dam foundations by piping and means for preventing it (in German). Die Wasserkraft, Zeitschrift fur die gesamte Wasserwirtschaft 17(24):445–449

Terzaghi K, Peck R (1967) Soil mechanics in engineering practice. Wiley, Hoboken

Turnbull WJ, Mansur CI (1961) Underseepage and its control: a symposium: investigation of underseepage - Mississippi river levees. Trans ASCE 126(1):1429–1481

USBR and USACE (2015) Best practices in dam and levee safety risk analysis. https://www.usbr.gov/ssle/damsafety/risk/methodology.html. Accessed 9 May 2018

USACE (2000) Design and construction of levees. Manual No. 1110-2-1913 dated 30 April 2000. U.S Army Corps of Engineers, Washington, DC

USACE (2012) Mississippi river and tributaries system 2011 post-flood report. Hery De-Haan, Jeffery Stamper, Bret Walters, et. al. USACE Mississippi Valley Division. December

USACE (1956). Investigation of underseepage and its control, lower Mississippi river levees, vol 1, TM 3-424, U.S. Army Engineer Waterways Experiment Station. Vicksburg, MS

Waller LA, Gotway CA (2004) Applied spatial statistics for public health data. Wiley, Hoboken

Scale Effects in Coarse Sand Barrier Experiments

Esther Rosenbrand[1(✉)], Vera van Beek[1], André Koelewijn[1], Sepideh Akrami[2], Ulrich Förster[1], Koen van Gerven[3], and Adam Bezuijen[1,2]

[1] Deltares, Delft, Netherlands
esther.rosenbrand@deltares.nl
[2] Ghent University, Ghent, Belgium
[3] Water Authority Rivierenland, Tiel, Netherlands

Abstract. The coarse sand barrier is considered as a promising measure to prevent backward erosion piping from causing failure of embankments. A pipe is allowed to progress backwards until it encounters the coarse sand barrier, which prevents it from progressing unless the head difference over the embankment is significantly increased. A three stage experimental programme supported by groundwater flow modelling is carried out to investigate the feasibility of this method. The hypothesis is that the strength of the barrier is characterised by a local gradient at the interface between the barrier and the pipe. Major questions are: can the horizontal gradient as measured in laboratory tests be used to characterise the strength of the barrier material, over which distance should a horizontal gradient be determined, and is this distance the same for models at different scales? This paper presents the background theory and demonstrates the effects using scale dependent criteria. Preliminary results of small- and medium-scale experiments are used to compare the two approaches.

Keywords: Backwards erosion piping · Coarse sand barrier
Prevention measure

1 Introduction

The coarse sand barrier (CSB) is considered as a promising method to prevent backwards erosion piping from leading to failure of water-retaining structures. Backwards erosion piping (BEP) is a failure mechanism that occurs below dikes overlying a granular aquifer that is covered by a cohesive blanket layer. When there is an interruption of the blanket layer on the landward side of the embankment, flow concentrates towards this opening. When the local hydraulic gradient is sufficient to erode sand grains, an erosion lens is formed, followed by a pipe that lengthens by erosion in the upstream direction. The cohesive cover layer forms a roof over the eroded pipe. Whilst the pipe grows upstream, it is still relatively small, but once the pipe makes contact with the outside river level, the flux in the pipe increases erosion dramatically, which can lead to embankment collapse (e.g. Sellmeijer 1988; Van Beek et al. 2011, 2015). In

S. Bonelli et al. (Eds.): EWG-IE 2018, LNCE 17, pp. 301–312, 2019.
https://doi.org/10.1007/978-3-319-99423-9_27

the Netherlands, several embankment failures that occurred in the early 20th century were attributed to piping (Vrijling et al. 2010).

The CSB is a coarse-grained filter that is placed in the path of the pipe, below the blanket layer. The resistance of the coarse sand against erosion is higher than that of the fine sand; thereby the pipe is prevented from progressing upstream until the head drop over the embankment becomes significantly higher than it would be in the case without a CSB.

The feasibility of this method is being investigated in a three stage research project. The aim of the research is to determine the strength of a barrier, and investigate how to define a strength criterion that can be used to compute the strength of an embankment with a CSB in a finite element groundwater computation.

This paper first briefly introduces the erosion mechanisms that are considered to play a role in the backwards progression of a pipe, and describes the effect of a CSB on these. Effects of scale in the case of a CSB are introduced, and subsequently a brief overview of the research project is provided. The first stage (small-scale) experiments are briefly described, as well as the derivation of a preliminary strength criterion for damage of the barrier based on the small-scale experiments. Numerical modelling is used to show the implications of using that criterion for medium-scale experiments. The preliminary results of one medium-scale experiment are used to make a first assessment of the applicability of the small-scale criterion for the medium-scale tests.

2 Background

2.1 Primary and Secondary Erosion

The critical head drop for BEP is often considered as the head drop over a structure whereby a pipe can progress all the way upstream. The critical gradient is the corresponding average gradient over the structure. The critical gradient is known to be scale dependent due to the convergence of flow towards the pipe (e.g. de Wit 1984; Van Beek 2015). Two mechanisms are considered to govern the backwards progression of a pipe, these are: primary erosion mobilising grains at the tip of the pipe, and secondary erosion causing the widening and deepening in the body of the pipe (Hanses 1985; Van Beek et al. 2015; Robbins et al. 2018).

Currently, safety assessments of embankment in the Netherlands use the modified Sellmeijer model (Sellmeijer et al. 2011). This model predicts the critical head drop based on consideration of only secondary erosion in the body of the pipe. Sellmeijer (1988) modelled the limit equilibrium state for particles on the bottom of an existing pipe, and the inherent assumption is that the pipe progresses when this limit equilibrium is exceeded. The Sellmeijer model appears to work well for a fixed geometry and soil profile for which the model was developed, as the coupling between flow in the soil and flow in the pipe results in a fixed relation between the hydraulic gradient in the pipe (restricted by the grain equilibrium criterion), and the hydraulic gradient at the tip of the pipe. A change in the geometry, such as occurs when a coarse sand barrier is placed in the path of the pipe, changes the relation between the hydraulic gradient in the barrier

and the hydraulic gradient in the pipe, will change this relation and the model will no longer predict the process.

Primary erosion is considered to be governed by the local gradient at the tip of the pipe (Hanses 1985; Robbins et al. 2018). In experiments, where the head was increased in order to cause the pipe to progress after initiation, Robbins et al. measured the same local horizontal gradient upstream of the tip of the progressing pipe, in experiments on different scales for the same material. This can be considered evidence that the critical local horizontal gradient upstream of the pipe tip that causes the pipe to progress is a material property, which is independent of scale. This would imply that laboratory tests could be used to find the parameters required for field-scale numerical models of the process of backward erosion piping (Robbins et al. 2018).

The CSB will have a relatively high resistance against primary erosion due to its high hydraulic conductivity relative to the hydraulic conductivity of the fine background sand. With a higher hydraulic conductivity contrast (ratio of conductivity of the barrier over the conductivity of the fine sand), a larger portion of the total head drop will be dissipated over the fine sand upstream of the barrier, resulting in relatively low local gradients in the barrier as shown schematically in Fig. 1. Thus, to achieve a sufficiently high local gradient inside the barrier to fail the barrier, the average gradient over the structure must be significantly higher than in a situation with no barrier.

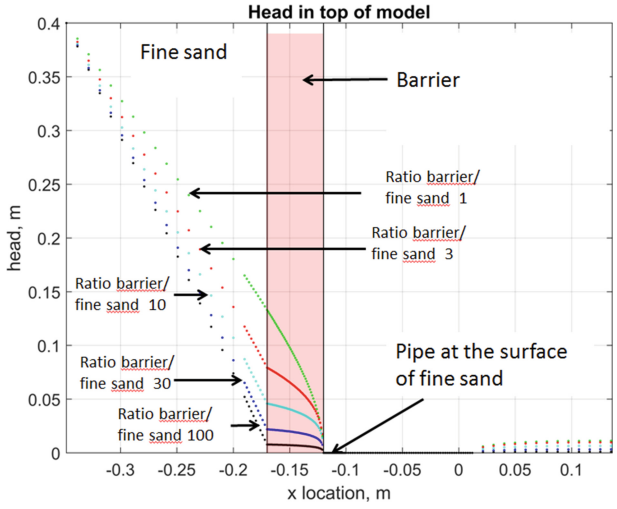

Fig. 1. Schematic illustration of head drop in a sample consisting of fine sand upstream (left side of the model), a CSB (shaded) and fine sand downstream, in which a pipe has progressed towards the barrier

The local critical gradient of the barrier material is expected to increase with relative density and uniformity coefficient.

2.2 Scale Effects

The average gradient in a uniform sand will be scale dependent when the local critical gradient is constant. This is shown by De Wit (1984) by numerical modelling of the head distribution in the top of an intact sand, bed below an impermeable cover, converging towards an outflow. As scale increases the same local gradient is achieved with lower average gradients.

In the case of a CSB, the distance over which the local gradient is measured relative to the thickness of the barrier is of high importance. As can be seen in Fig. 1, the local gradient inside the barrier is steepest in the downstream portion of the barrier. Thus, a critical local gradient that is defined over a fixed distance will encompass a different portion of the head profile in models at different scales. One question is therefore whether the strength criterion should be defined as a gradient over an absolute distance, or relative to the barrier thickness. In this paper, the effect of these two options is shown based on the numerical simulations for the small- and medium-scale CSB tests.

2.3 Coarse Sand Barrier Research Project

The feasibility of the CSB is investigated in a three stage experimental project, supported by numerical groundwater flow modelling. During the first stage, small-scale (ca. 0.35 m seepage length, 0.05 m barrier thickness) laboratory experiments are conducted in order to test the principle of the CSB and investigate the strength of different barrier materials. During the second stage, medium-scale laboratory experiments (ca 1.4 m seepage length, 0.3 m barrier thickness) are conducted in order to investigate the scale effects that play a role. During the third stage, two tests are conducted on a test embankment in the Delta Flume (ca. 15 m seepage length, 0.3 m barrier thickness).

The hypothesis is that the strength of the barrier is governed by primary erosion at the tip of the pipe, based on the findings by (Hanses 1985; Robbins et al. 2018). Therefore the local horizontal gradient in the barrier near the pipe tip would characterize the strength of a given barrier material at a given density.

As a conservative approach, the local horizontal gradient at which a pipe first damages the barrier is considered as the preliminary strength criterion for a barrier, referred to here as the ‘damage criterion’. Small- and medium-scale tests indicate that the head must be increased significantly to cause the pipe to progress through the barrier, so there is a significant amount of strength beyond the damage point.

Questions for practical implementation of the damage criterion include:

- How to model the pipe, and the interface between the barrier and the pipe at damage?
- Over which distance can the local critical horizontal gradient for damage sensibly be defined?

The convergence of flow towards the interface between the barrier and the pipe in the situation with a CSB is strongly affected by hydraulic conductivity contrast between the barrier and the fine background sand (Fig. 1). A gradient that is defined over a larger distance inside the barrier will not be a property of only the material any more,

but also of this contrast. However, a gradient computed over a very short distance will be relatively more sensitive to measurement uncertainty. There is uncertainty in the head measurements, but also regarding the exact location of the barrier and the pipe tip, and the dimension of the interface between the pipe and the barrier in the model. Furthermore, the question can be raised as to whether the continuum approach for computing the gradient just upstream of the pipe is valid directly at the tip of the pipe (Van Beek et al. 2015).

3 Small- and Medium-Scale Experiments

The small-scale experiments were used to define a preliminary damage criterion for a barrier material called GZB2 (d_{50} = 1.053 mm; d_{60}/d_{10} = 3). A detailed description of the test apparatus for the small-scale experiments is given in (Bezuijen et al. 2018a; Negrinelli et al. 2016), and here a brief overview is provided. The setup is shown in Fig. 2. The top cover is transparent so the piping process can be observed. Flow enters on the left side of the model and exits at the exit hole 0.348 m further downstream. The barrier is 0.05 m thick and placed ca 0.178 m from the inflow point, and in the majority of the tests, has the depth of the entire model. The row of transducers along the width of the model set-up (h19-h16) is in the fine sand just in front of the interface between the barrier and the fine sand downstream. When a pipe forms and progresses along the width of the barrier these transducers are inside the pipe.

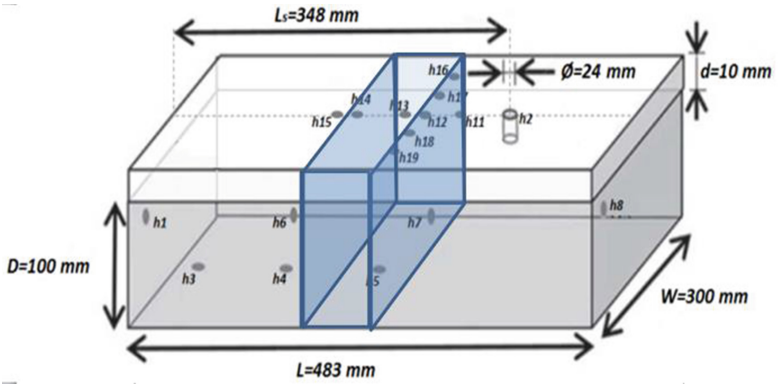

Fig. 2. Setup used for the small-scale experiments (not to scale), h1–h19 are locations of capillary tubes connected to standpipes for pore water pressure measurements. Barrier is indicated by shaded area

In the medium-scale setup the dimensions of the sand body and the area of the exit hole are approximately four times larger (seepage length 1.385 m; total length 1.753 m; width 0.881 m; depth 0.403 m, diameter of the exit hole 0.082 m). The barrier thickness is 0.30 m in order to also be able to study progression of the pipe through the barrier. In the majority of the tests, the barrier has the depth of the entire

model. Pore water pressure is measured by using pressure transducers mounted in the top and bottom of the setup with a frequency of 1 Hz.

The test procedure during small- and medium-scale tests is the same and also described in (Bezuijen et al. 2018a; Negrinelli et al. 2016; Van Beek et al. 2015). During the tests, water enters the setup through a filter in order to ensure a homogeneous flow distribution. A constant head drop is applied for 5 min, or longer if required, until grain movement at the tip of the pipe had ceased for several minutes, after which the head is increased again. Flow rate is measured for each head increment by collecting the discharge over a given time span and weighing the effluent. In the small-scale tests, head measurements were recorded for each step, using standpipes.

Different combinations of fine sand and barrier materials are tested in order to investigate the effect of the hydraulic conductivity contrast on the local gradient inside the barrier. The effect of the depth of the barrier in the model is also varied, by doing tests with a barrier that does not extend down the entire depth of the model. On the smaller scale, experiments are also performed in a model with a width of 0.10 m and a depth of 0.30 m in order to investigate scale effects, those tests are described in Bezuijen et al. (2018a).

3.1 Observations on the Piping Process

The observed process of pipe formation was similar in all small-scale tests. The pipe initiates at the exit hole. Due to the 3D flow configuration, the pipe initiates at a relatively low average gradient, and further increases in head are required for the pipe to progress upstream (Van Beek et al. 2015). When the pipe reaches the barrier, further head increases are required, and the pipe first grows perpendicular to the flow direction, along the width of the barrier. This was also observed in small-scale experiments with a CSB by Negrinelli et al. (2016).

There is minor crumbling of barrier grains into the pipe. This crumbling is not yet considered as damage of the barrier. Approximately at the centreline of the model, close to the barrier a deeper ‘pothole’ is eroded. For the establishment of the head that damages the barrier, the head was used at which a pipe shape could be observed in the barrier. After damage, further head increases were applied that caused additional pipes to form inside the barrier at the downstream interface, and that caused the pipes in the barrier to lengthen. Typically, several pipes progressed and lengthened inside the barrier during a single test.

In the medium-scale tests, the process of pipe progression was observed to be similar to the development in the small-scale tests. However, there was significantly more crumbling of the barrier, and this affected a larger zone inside the barrier than in the small-scale tests. The pothole in front of the barrier also appeared to be deeper than in the small-scale tests. Due to the crumbling, the damage point was more difficult to register. Again a significant additional head increase was required after damage before the barrier was breached. One or several pipes were observed to progress through the barrier. There were several discrete steps when the head was increased in which significant progression of the pipe or pipes was observed. In several of these experiments, a pipe was observed to progress until a few centimetres short of the upstream interface

between the barrier and the fine sand, and subsequently progress parallel to this interface inside the barrier.

4 Numerical Modelling of Damage Criterion

Numerical simulations of the experiments were made using the finite element groundwater flow code DgFlow (Van Esch 2013, 2014). A steady state flow computation was conducted where the head across the sample at the critical point before damage was modelled.

The pipe was modelled as a constant head boundary condition, assuming that there was no head loss in the pipe. Initially it was considered to model the pipe with zero depth. However, in that case the interface between the barrier and the pipe tip is a single node in a 2D model, which causes a strong convergence of flow that would not be realistic and the result strongly depends on the local mesh. When in reality a pipe with a finite depth is formed downstream of the barrier, the barrier is crumbles slightly forming a stable slope towards the pipe. This increase in the outflow area between the barrier and the pipe affects the head profile. Therefore, it was decided to model the pipe with a fixed depth for the analysis of the small-scale experiments. The pipe was given a depth by removing the elements that would be in the pipe. The interface between the pipe and the barrier was vertical (Fig. 3). The modelled pipe depth is 2 mm for the small-scale based on visual estimates of the pipe depth. The pipe ran from the outlet hole to the interface between the barrier and the fine sand. The vertical upstream boundary was a constant head boundary condition, with the head corresponding to that applied in the experiment at the critical step for damage, i.e. the last step before damage occurred. A quadrilateral mesh was used and the element size at the top inside the barrier is locally refined to 1 mm by 1 mm in both the small- and the medium-scale models (Fig. 3).

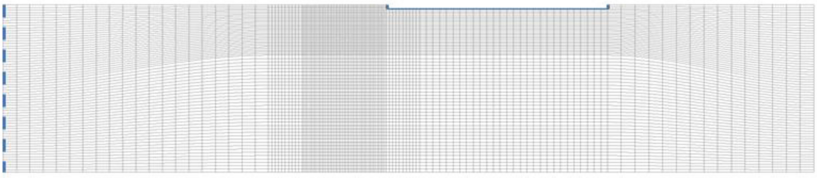

Fig. 3. Small-scale model mesh: local refinement of 1 mm elements in the top of the barrier. Boundary conditions constant head upstream (dashed thick line) and downstream (thick line)

The relative density of the fine sand upstream and downstream of the barrier is different. Furthermore, the background sand used in the small-scale tests contained a fraction of finer grains that tended to form a filter cake, a zone of a lower hydraulic conductivity than the rest of the barrier material, in the upstream portion of the barrier (this is investigated in Akrami et al. 2018). Therefore, the models consist of four zones, the fine sand upstream of the barrier, fine sand downstream of the barrier, the barrier

material, and inside the barrier a thin zone of filter cake (Fig. 4). The hydraulic conductivity of these zones was used as a fitting parameter to match the measured head distributions and fluxes at the damage point.

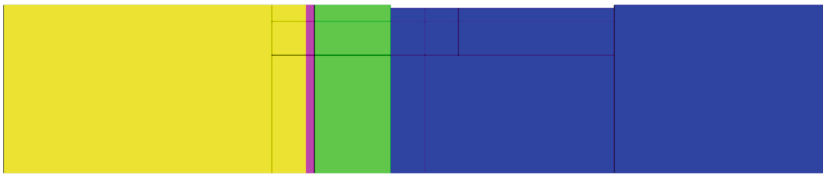

Fig. 4. Small-scale model materials, from left to right: yellow is fine sand upstream, pink is filter cake, green is barrier material, blue is fine sand downstream (separate blocks within different materials were used for local mesh refinement).

4.1 Derivation of Damage Criterion from Small-Scale Experiments

An example of a numerical simulation of a small-scale test with barrier material GZB2 is shown in Fig. 5. The hydraulic conductivity of the materials was adjusted in order to match the head profile, and the measured flux.

In order to reduce the effect of uncertainty regarding the location of the pipe tip in the barrier and the high concentration of flow at the tip of the pipe, the critical gradient for damage was analysed for the region starting 1 cm upstream of the pipe tip in the small-scale model. Due to the filter cake in the upstream portion of the barrier, the maximum distance over which the gradient could be determined was 3.5 cm, between −0.130 m and −0.165 m as shown in Fig. 4. This resulted in a gradient of 0.48 as a preliminary damage criterion. This was only preliminary as it is based on a limited number of small-scale numerical simulations (5 experiments of which only 2 were considered reliable).

4.2 Application of Damage Criterion to Medium-Scale Experiments

For the medium-scale experiments, the critical gradient for damage could be computed over the same absolute distance as in the small-scale model, i.e. over 3.5 cm starting 1 cm from the downstream interface between the barrier and the fine sand, or over the same relative distance i.e. between 6 cm upstream of the downstream interface and 21 cm upstream of this.

A numerical simulation was made for one experiment with GZB2, in order to determine the hydraulic conductivity of the four zones. Based on the head measurements no filter cake appeared to be present, therefore the entire barrier has the same hydraulic conductivity. The hydraulic conductivities in the model are: barrier 1.10e−3 m/s; fine sand upstream 7.64e−5 m/s; fine sand downstream 8.40e−5 m/s. The hydraulic conductivity contrast between the barrier and the fine sand downstream is 13. With these parameters the modelled flux is 1.31 L/min, comparable to the measured flux of 1.33 L/min.

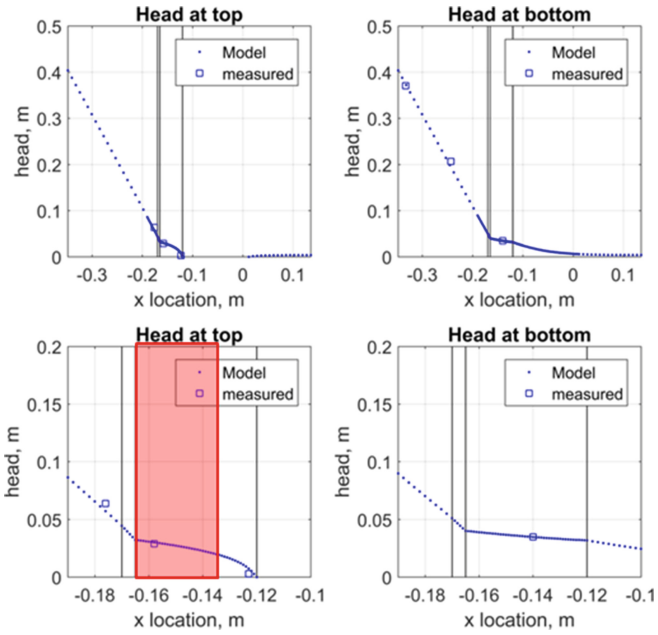

Fig. 5. Numerical simulation of test 191 with CSB material 2 (GZB 2). Dots show modelled heads at the top of the model (left column) and at the bottom of the model (right column); blue squares are measured heads. Vertical solid lines at −0.12 m and −0.17 m indicate the barrier location, filter cake is modelled between −0.17 m and −0.165 m (dotted line). The distance over which the local gradient is determined as a first approximation of the damage criterion is indicated by shaded rectangle

The pipe was modelled with a depth of 4 mm based on visual estimates of pipe depth at the point of damage. The measured upstream head at damage was 0.52 m, and this was applied as the upstream boundary condition. The head distribution is shown in Figs. 6 and 7. The local horizontal gradient over the absolute distance of the damage criterion (3.5 cm) is 0.438; over the relative distance (21 cm) the local horizontal gradient is 0.097.

Linear extrapolation of the head profile shows that the critical head drop that would be expected based on the damage criterion over the absolute distance is 0.57 m, and 2.57 m based on the criterion over the same relative distance.

5 Discussion and Conclusion

For the single medium-scale experiment that is numerically analysed, the local gradient inside the barrier over the same absolute distance inside the barrier is close to the local critical gradient for damage that was determined in the small-scale experiments.

The local gradient inside the barrier over the same relative distance inside the barrier (i.e. a significantly greater distance that is also further away from the interface

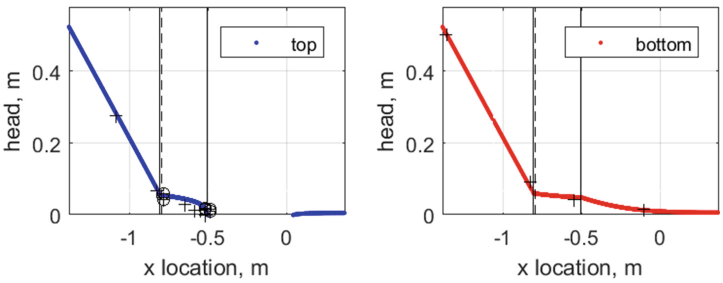

Fig. 6. Head profile computed at damage for medium-scale test MSP 22 (dots) in the top of the model (left) and the bottom of the model (right), solid black lines indicate the location of the barrier. Crosses indicate measurements in the centre line of the model, circles with a cross indicate measurements 0.2 m from the centre line of the model

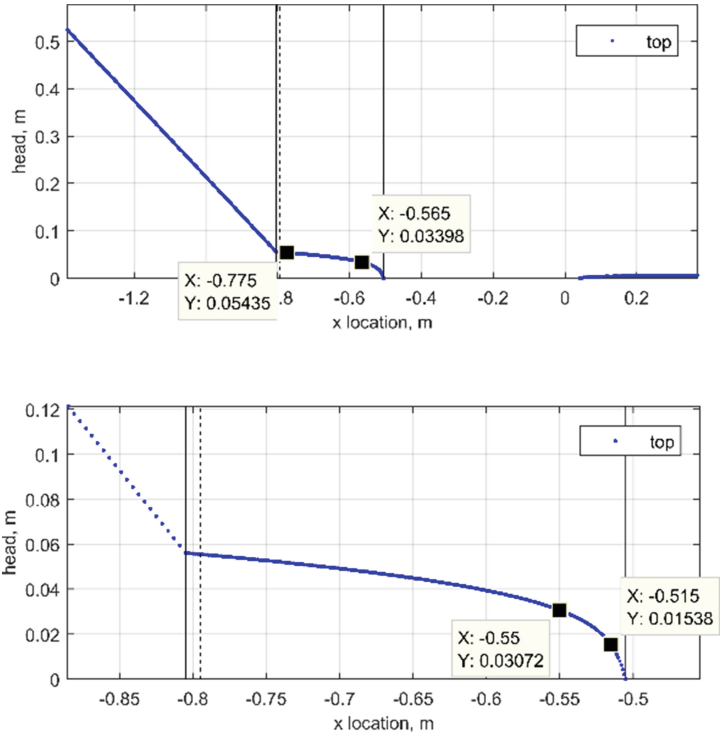

Fig. 7. Head profile computed at the point of damage for medium-scale test MSP 22 (dots) at the top of the model, data tips indicate points used to compute the critical gradient for damage. Top: the damage criterion over the same relative distance as in the small-scale experiments. Bottom: the damage criterion over the same absolute distance as in the small-scale experiments

between the barrier and the fine sand) is significantly lower. This suggests that the gradient over a fixed distance would sufficiently characterise the strength of a given

barrier material. A local critical horizontal gradient over a fixed distance is also imposed in analytical calculations in Bezuijen et al. (2018b).

However, these are only preliminary results from one medium-scale experiment; analyses of the full set will be required in order to reach a conclusion. Additionally, in the medium-scale experiments, the point of damage was extremely difficult to establish visually, as there was significant crumbling of the barrier prior to damage. In the numerical models used in the current analysis, the pipe was modelled only up to the interface between the barrier and the fine sand and assigned an estimated depth of 4 mm. Whereas this type of schematisation might have been appropriate for the small-scale experiments, in the medium-scale experiments crumbling of the barrier edge caused barrier material to be eroded a longer distance into the barrier. This crumbling would have reduced hydraulic heads in the downstream end of the barrier, and indeed those were not matched well in the current numerical simulation. Therefore, the computed local gradients were significantly higher than the measured local gradients in this zone.

This analysis leads to two major questions to be addressed:

1. Can the actual damage point in the medium-scale experiments be established visually, and is this comparable to the damage point that was identified in the small-scale tests?
2. Is it appropriate to model the pipe as growing up to the point of the interface between the barrier and the fine sand, or should the pipe already be modelled some distance inside the barrier at the damage point?

Further work is being done analysing the set of medium-scale experiments, in order to answer these questions. With regards to point 1, in addition to the point of damage the discrete growth steps of the pipe through the barrier that were observed in the medium-scale tests are modelled in order to analyse local gradients at those steps. With regards to point 2, in further medium-scale numerical simulations, the pipe is modelled a certain horizontal distance into the barrier at damage and subsequent growth steps. The horizontal interface between the pipe and the barrier provides an outflow area. This reduces modelled heads in the downstream region of the barrier, and the interface between the top of the barrier and the pipe also provides an outflow area, so that the depth of the pipe becomes less relevant as well.

Acknowledgements. The Dutch Water Authority Rivierenland and the National Flood Protection Programme HWBP are acknowledged for their financial support.

References

Akrami S, Bezuijen A, Rosenbrand E (2018) Investigating the formation of a filter cake in column experiments, for combinations of filter and finer sand in a coarse sand barrier. In: Proceedings of 26th meeting of the European working group on internal erosion, 10–13 September 2018. Politecnico di Milano, Milan

Bezuijen A, Rosenbrand E, Van Beek VM, Vandenboer K (2018a) Experiments for a coarse sand barrier as a measure against backwards erosion piping. In: International conference on physical modelling in geotechnics, 17–20 July 2018. University of London, London

Bezuijen A, Van Beek V, Rosenbrand E, Akrami S (2018b) Analytical groundwater flow calculations for understanding the flow and erosion in a coarse sand barrier. In: Proceedings of the 26th meeting of the European working group on internal erosion. Politecnico di Milano, Milan, 10–13 September 2018

De Wit JM (1984) Onderzoek zandmeevoerende wellen Rapportage Modelproeven. Grondmechanica Delft Report CO220887/10, Delft

Hanses U (1985) Zur Mechanik der Entwicklung von Erosionskanalen in geschichtetem Untergrund unter Stauanlagen. Dissertation, Grundbauinstitut der Technischen Universität Berlin

Negrinelli G, Van Beek VM, Ranzi R (2016) Experimental and numerical investigation of backward erosion piping in heterogeneous sands. In: Proceedings of the 8th international conference on scour and erosion. Oxford, 12–15 September 2016

Robbins BA, Van Beek VM, Lopez JF, Montalvo-Bartolomei AM, Murphy J (2018) A novel laboratory test for backward erosion piping. Int J Phys Model Geotechn. https://doi.org/10.1680/jphmg.17.00016

Sellmeijer H, López de la Cruz J, Van Beek VM (2011) Fine-tuning of the backward erosion piping model through small-scale, medium-scale and IJkdijk experiments. Eur J Environ Civ Eng 15(8):1139–1154

Sellmeijer JB (1988) On the mechanism of piping under impervious structures. Dissertation. TU Delft, Delft

Van Beek VM (2015) Backward erosion piping initiation and progression. Dissertation. TU Delft, Delft

Van Beek VM, Knoeff H, Sellmeijer H (2011) Observations on the process of backward erosion piping in small-, medium- and full- scale experiments. Eros Geomater 15(8):115–1137

Van Beek VM, Van Essen HM, Vandenboer K, Bezuijen A (2015) Developments in modelling of backward erosion piping. Géotechnique 65(9):740–754

Van Esch JM (2014) Flood defense assessment tools for piping in WTI 2017: report 9b. In: Groundwater flow simulator DgFlow 3D validation piping module. Deltares report 1209435-006-GEO-0001, Delft

Van Esch JM (2013). Modeling groundwater flow and piping under dikes and dams model validation and verification. In: Deltares report 1207809-005-GEO-0001-jvm. Delft

Vrijling JK, Kok M, Calle EOF, Epema WG, van der Meer MT, van den Berg P, Schweckendiek T (2010) PipingRealiteit of rekenfout? ENW report. The Netherlands

Assessing Suffusion Susceptibility of Soils by Using Construction Data: Application to a Compacted Till Dam Core

Lingran Zhang[1], Rachel Gelet[1(✉)], Didier Marot[1], Marc Smith[2], and Jean-Marie Konrad[3]

[1] Institut de Recherche en Génie Civil et Mécanique (UMR CNRS 6183), Université de Nantes, Saint-Nazaire, France
rachel.gelet@univ-nantes.fr
[2] Hydro Québec, Montréal, Canada
[3] Département Civil Engineering, Université Laval, Québec, Canada

Abstract. Suffusion is one of the main internal erosion processes in earth structures and their foundations. The assessment of this phenomenon can be difficult since in-situ geotechnical properties of soils are variable and uncertain. By means of a case study, this paper aims at presenting a general method to assess the suffusion potential of compacted impervious cores of zoned embankment dams. First, the suffusion susceptibility of the compacted layers forming the analysed dam core is estimated from four soil parameters that can be easily measured in situ or in laboratory during construction. Second, the saturated hydraulic conductivity of the compacted layers is evaluated based on the amount of fines content and on available construction data. Moreover, the power dissipated by seepage flow is inferred based on the saturated hydraulic conductivity and simplified fluid boundary conditions. Finally, the combined consideration of erosion resistance index and dissipated energy allows the identification of zones characterized by a relatively larger suffusion potential.

Keywords: Embankment dam · Internal erosion · Erosion resistance index
Suffusion susceptibility

1 Introduction

Internal erosion is one of the main causes of embankment dam incidents (Foster et al. 2000). Among the four types of internal erosion that have been identified (Fry 2012), suffusion is a volumetric erosion, i.e. within a single material fine solid particles can be detached, transported, and for some of them blocked under seepage flow. The eroded finer fraction leaves the coarse matrix which will modify the soil's hydraulic conductivity, induce greater seepage velocities, and potentially higher hydraulic gradients, possibly accelerating the rate of suffusion (ICOLD 2013). The development of suffusion gives rise to a wide range of dam incidents including piping and sinkholes.

Due to the lack of physically-based understanding, the assessment of suffusion progression is uncertain. Since the consequences of this phenomenon can be catastrophic, its initiation must be avoided. Hence, practical research mainly focus on the

S. Bonelli et al. (Eds.): EWG-IE 2018, LNCE 17, pp. 313–324, 2019.
https://doi.org/10.1007/978-3-319-99423-9_28

main initiation conditions for suffusion. Garner and Fannin (2010) identified three components: material susceptibility, critical hydraulic load, and critical stress condition.

Marot and Benamar (2012) review the numerous methods that have been proposed to characterize the initiation of suffusion by use of material susceptibility criteria and/or hydraulic criteria. On one hand, material susceptibility criteria are usually solely related to the initial grain size distribution, regardless of the material behaviour within a permeameter test. On the other hand, three approaches have been proposed to describe the hydraulic action on particles: the hydraulic gradient (Skempton and Brogan 1994; Li 2008), the hydraulic shear stress (Reddi et al. 2000) and the pore velocity (Perzlmaier et al. 2007). However, suffusion tests carried out with permeameters of different sizes indicate that scale effects exist when measuring critical hydraulic criteria (Li 2008; Marot et al. 2012). Particularly, Marot et al. (2012) pointed out that the critical hydraulic gradient concept depends on the length of the seepage path. Moreover, Rochim et al. (2017) showed the significant effect of hydraulic loading history on the value of the critical hydraulic gradient. In the same manner, the authors demonstrated that the critical hydraulic load based on the rate of erosion is influenced by the hydraulic loading history. Therefore these approaches cannot be generalized nor be used directly to evaluate the suffusion susceptibility at dam scale. Alternatively, Marot et al. (2011) focused on the improvement of the material susceptibility estimation. This estimation is not based on the sole initiation, rather the whole suffusion process is considered. The authors proposed an energy approach to evaluate the material susceptibility of soils based on suffusion experiments performed up to a "final state". This "final state" is obtained towards the end of each test when the hydraulic conductivity reaches a plateau with a concomitant decrease of the rate of erosion. The hydraulic loading is characterized by the cumulative energy dissipated by the water seepage E_{flow}. The response of the sample is related to the standard measure of the total dry eroded mass during the whole test m_{eroded}, and the erosion resistance index is expressed by:

$$I_\alpha = Log\left(\frac{m_{eroded}}{E_{flow}}\right) \tag{1}$$

Based on this index, a classification is proposed from highly resistant to highly erodible (Marot et al. 2016). For example, soils characterized by $I_\alpha > 6$ can be considered non-suffusive. Since the erosion resistance index I_α has been proven to be intrinsic, i.e. independent of the sample size (Zhong et al. 2017) and of the loading path (Rochim et al. 2017), at least at the laboratory scale, it may be applied for an actual case study.

Due to the construction phase and to the progressive extraction of the soil from the borrow pit, the material parameters of a dam core are characterized with a spatial variability that cannot be easily reduced (Smith and Konrad 2011). This spatial variability affects a number of parameters, in particular the hydraulic conductivity, the dry unit weight and the grain size distribution. This, in turn, also affects the erosion resistance index. Hence, it does not seem reasonable to characterize the suffusion susceptibility of a large dam with only a single value, based on a single laboratory test.

Rather, a contour map of the erosion resistance index would provide a valuable information for assessing the dam's condition.

The objectives of this paper are to assess the suffusion susceptibility of soils used for compacted impervious cores of zoned dams based on construction data and to locate zones characterized with a relatively larger suffusion potential. Using an actual case study, a novel approach is presented that may be applied or adapted to other dams. This approach is based on four steps: (i) estimation of the erosion resistance index values, (ii) estimation of hydraulic conductivities, (iii) estimation of power dissipated by seepage flow, since larger values of the power are related to a larger rate of erosion (Marot et al. 2012) and (iv) correlation of power with erosion resistance index to locate zones characterized by a relatively larger suffusion potential.

2 Presentation of Methodology Based on Construction Data

This section presents a general approach to estimate the erosion resistance index I_α and the saturated hydraulic conductivity K_{sat} of core layers based on construction data.

2.1 Assessment of Suffusion Susceptibility

The erosion resistance index of a soil is traditionally obtained by performing an experimental test on a dedicated erodimeter (Marot et al. 2012, 2016). Yet, soils belonging to dam cores are characterized by a spatial variability that is related to the construction phase and intrinsic properties of materials in the borrow pit. Hence, the characterization of suffusion susceptibility would require a large number of erosion tests. To circumvent these difficulties, the proposed approach is based on the principal component analysis of 32 suffusion tests and 14 physical parameters (Le et al. 2016). The erosion resistance index is then linearly related to four relevant soil parameters (for generally low-plasticity and widely-graded soils):

$$I_\alpha = -11.32 + 0.45\gamma_d + 0.20V_{BS} + 0.10\varphi + 0.06\ Finer\ KL \tag{2}$$

where γ_d is the dry unit weight, V_{BS} is the Blue Methylene value, φ is the friction angle and *Finer KL* is the percentage of finer F corresponding to the minimum value of Kenney and Lau (1985)'s ratio (H/F). The first parameter describes the compaction state, while the second accounts for the soil's activity. The friction angle is used to account for the angularity of the soil's particles (Marot et al. 2012) and the *Finer KL* parameter the grain size distribution. This approach adapts that of Wan and Fell (2004) to suffusion. Another relationship has been developed for gap graded soils (Le et al. 2016).

2.2 Assessment of Hydraulic Conductivity

The hydraulic conductivity of a dam core is in fact a heterogeneous property that reflects the variability of compaction conditions, progressive construction phases and intrinsic properties of the borrow pit. Estimation of saturated hydraulic conductivity of

till (gravelly, silty sand) can be realized using empirical methods based on fines content (passing 2 μm or passing 80 μm) and in-situ compaction conditions (Leroueil et al. 2002; Smith and Konrad 2011; Malenfant-Corriveau 2016). The latter method focused on till characterised by a low percentage of fines (<2 μm on the fraction passing 5 mm). For those particular tills having about 1% of such fines, the measured saturated hydraulic conductivity is not influenced by the soil's fabric (aggregated or homogeneous).

Considering the dam studied herein (see Sect. 3), the saturated hydraulic conductivity K_{sat} is best predicted based on the modified Kozeny-Carman equation (Malenfant-Corriveau 2016),

$$K_{sat} = 0.024622\ \alpha^{0.7825} \quad \text{for} \quad \alpha \geq 0.01\ \text{mm}^2 \tag{3}$$

$$K_{sat} = 0.1264\ \alpha^{1.1377} \quad \text{for} \quad \alpha < 0.01\ \text{mm}^2 \tag{4}$$

where, the parameter α (Chapuis 2004) is expressed as a function of the porosity n and d_{10} (effective diameter for the soil fraction passing 5 mm):

$$\alpha = (d_{10})^2 \frac{n^3}{(1-n)^2} \tag{5}$$

Note that the parameter α is expressed in mm^2 in Eqs. (3) to (5). The d_{10} value is normally obtained from sedimentation tests and the porosity n can be obtained from in-situ density measurements.

2.3 Assessment of Relative Suffusion Potential

The hydraulic loading on the grains is often described by one of these three parameters: hydraulic gradient, hydraulic shear stress and pore velocity. However, the filtration of some detached particles can induce a rearrangement and clogging process within the soil causing a localized decrease in the hydraulic conductivity (Marot et al. 2016). Therefore, knowledge of variations of both seepage velocity and hydraulic gradient (or pressure gradient) is required to evaluate the hydraulic loading conditions. Hydraulic loading can be expressed in terms of power expended by the seepage flow P_{flow}. This requires as input for each soil layer the pressure field, the elevation and the hydraulic conductivity. The pressure field can either be estimated from simplified boundary conditions, or can be precisely computed with a FEM simulation. Deriving Eq. (1) with respect to time, we obtain the rate of mass transfer:

$$\dot{m}_{eroded} = 10^{-I_\alpha} P_{flow} \tag{6}$$

As a consequence, the relative suffusion potential of the dam core may be characterized by a contour map of the erosion resistance index I_α and that of the power dissipated by seepage flow P_{flow}. The former is used to assess the suffusion susceptibility of the till core. In addition, it may indicate the variations of this parameter and point out zones characterized with a low resistance to suffusion. This approach

represents a first attempt to apply the energy approach at the dam scale. The P_{flow} contour map is used to assess the hydraulic load within the till core. The combination of these two contour maps allow the identification of zones characterized by a greater suffusion potential (higher I_α and lower P_{flow} values).

3 Application to a Particular Dam

3.1 Brief Description of the Dam

The analysed dam is located in Northern Québec, Canada. Construction was completed in 2016. It is a 92.2 m-high and 456 m-long zoned embankment founded on bedrock foundations. The central impervious core (zone 1 on Fig. 1) is made of till (gravelly, silty sand) which was compacted near optimum conditions in terms of water content and density. The dam is also comprised of a downstream filter (zone 2A), an upstream filter (zone 2B) transitions (zones 3A, 3B and 3C) as well as rockfill shoulders (zones 3D and 3E). The crest level is 368 m and the maximum reservoir level is 366.3 m.

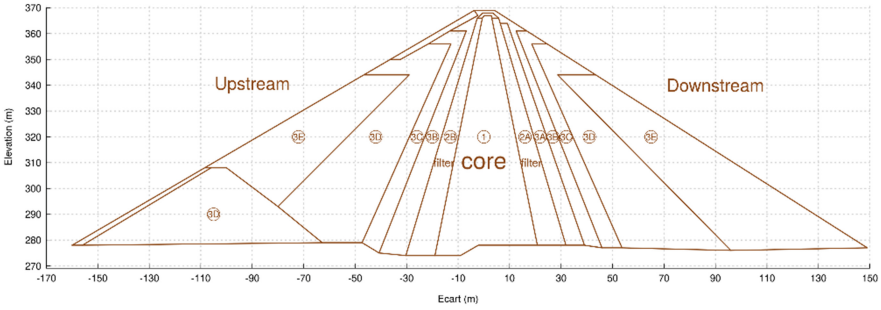

Fig. 1. Section view of the dam at *PM* 330

The location of each laboratory sample taken from the dam core for construction control is referred to by *PM*, *ecart* and *elevation* for longitudinal, transversal and vertical direction, respectively. A cross section of the dam at its highest section (*PM* 330) is shown in Fig. 1.

The till is a well-graded soil having a maximum particle size of 300 mm. The mean fines content (<2 μm on the fraction passing 5 mm) is equal to 1% (see Fig. 2).

Due to the spatial variability of the material properties and of the compaction process, the dam may be characterized by heterogeneities in terms of soil physical properties, such as porosity, hydraulic conductivity and erosion resistance index. Other construction control tests (laboratory and in-situ measurements) were conducted to obtain, partial grain size distributions based on sieve tests (0.08–80 mm), densities, water contents, degrees of compaction and degrees of saturation at numerous sampling points.

Since the placement of the till during the construction was realized by dumping and spreading the material in lifts of 0.45 m in height across the entire width of the core, the

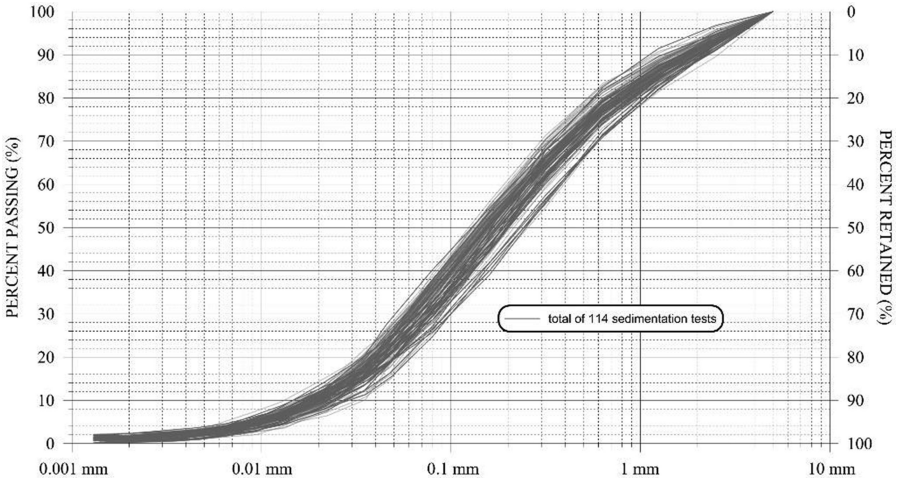

Fig. 2. 114 sedimentation tests results on the fraction passing 5 mm

dam core can be divided into layers of 0.45 m height for this analysis to account for the construction procedure. Each layer can therefore be characterised by a single set of physical parameters.

3.2 Estimation of the Erosion Resistance Index I_α

For the analysed dam, the estimation of erosion resistance index is based on Eq. (2) since all soil samples are widely-graded. The relevance of this estimation has been experimentally validated by Le (2017) on one sample taken from the analysed dam. This laboratory sample was sieved at D_{max} equals 5 mm. The internal friction angle for the sieved till was measured at 37° and the Blue Methylene value was measured at 0.7 g/100 g. The erosion resistance index obtained from the suffusion experiment equals 5.76, which is very close to the predicted value using Eq. (2) based on the statistical analysis (5.72). Therefore, this suffusion test validates the use of Eq. (2) for till samples taken from the dam.

Next, Eq. (2) is applied to investigate the suffusion susceptibility of each constructed layer. While the internal friction angle and Blue Methylene values are considered constant for the whole dam core, $\varphi = \varphi_0 = 37°$ and $V_{BS} = V_{BS0} = 0.49$ g/100 g, the spatial variability of the erosion resistance index I_α accounts for the spatial variabilities of γ_d and *Finer KL*. Figure 3 presents the contour map of the erosion resistance index which is obtained by using a smoothing technique to minimize the number of layers (Zhang et al. 2018). This technique was used with care, i.e. without affecting the results and the conclusions.

The predicted values of I_α lie within the range of 5.6–7.3 (Fig. 3). The dam core appears as fairly homogeneous with the soils mainly characterized as highly resistant to suffusion ($I_\alpha \geq 6$), except two zones near the elevations at 315.6 m and 318.3 m that

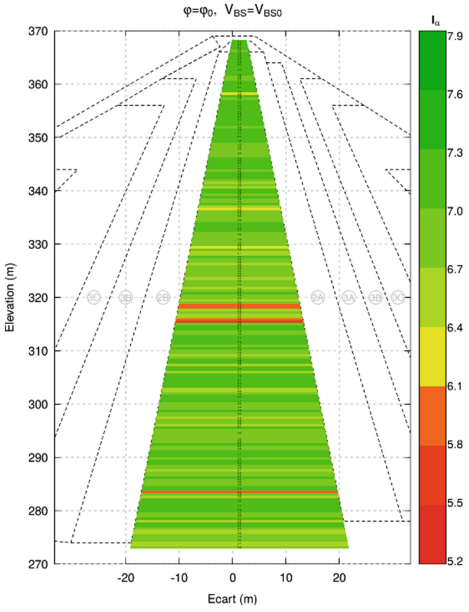

Fig. 3. Contour map of the predicted erosion resistance index I_α

are characterized as resistant to suffusion due to the relatively lower erosion resistance index values ($5.6 < I_\alpha < 6$) (Marot et al. 2016).

3.3 Estimation of Saturated Hydraulic Conductivity K_{sat}

Estimation of saturated hydraulic conductivity of the till core is realized using the approach described in Sect. 2.2 since the fines content is low (see Fig. 2). This choice is also validated by laboratory measurements (Malenfant-Corriveau 2016).

Equation (3) is applied to investigate the spatial variability of the saturated hydraulic conductivity based on the spatial variability of the effective diameter d_{10} (obtained from Fig. 2) and that of the porosity n (obtained from construction control data). Figure 4 is obtained thanks to a smoothing technique to minimize the number of layers (Zhang et al. 2018).

Overall, the hydraulic conductivity distribution is found to be reasonably homogeneous within the range of 0.6 10^{-7} m/s and 6.8 10^{-7} m/s. Slightly larger values of K_{sat} (>5.0 10^{-7} m/s) are predicted in zones near the central parts of the core within the elevations between 322 m and 342 m.

The proposed estimation of the hydraulic conductivity does not take into account the temperature of the water (5 °C) in the dam core. Dynamic viscosity of water tends to increase with decreasing temperatures. This effect lowers slightly the estimation of hydraulic conductivity which is based on laboratory results realized at 20 °C.

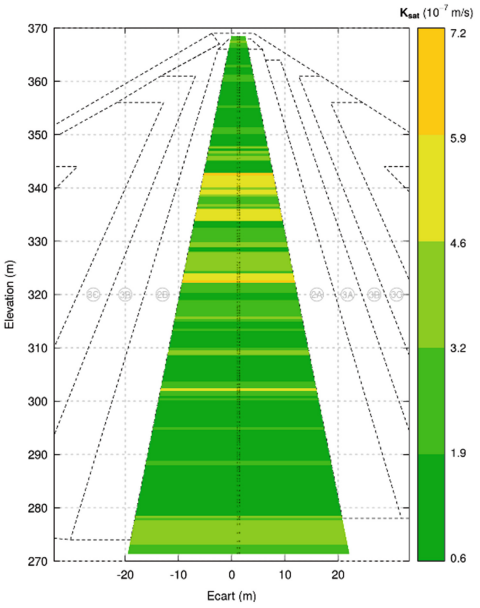

Fig. 4. Contour map of predicted saturated hydraulic conductivity K_{sat}

3.4 Estimation of the Suffusion Potential at Dam Scale

Based on the obtained contour map of hydraulic conductivity, the power dissipated by the flow P_{flow} is evaluated for each dam core layer. The method to compute P_{flow} within each layer is based on a simplified pressure field. Three assumptions are used: (1) no loss of hydraulic head is accounted for the dam materials upstream of the till core, (2) the fluid pressure is assumed equal to the atmospheric pressure all along the downstream side of the till core and (3) the flow within the core is assumed horizontal in the transversal direction. By using those three assumptions, P_{flow} within each layer is expressed by:

$$P = -\frac{K_{sar}\gamma_w h_w^2 s}{L_{AB}} \tag{7}$$

where γ_w is the unit weight of water, h_w is the water head, S is the layer section along PM, and L_{AB} the layer longitudinal length.

Following Eq. (7), the spatial distribution of P_{flow} in the dam core is presented in Fig. 5 (right), the unit of [10^{-4} W] is due to the large dispersion of the P_{flow} values (the maximum power is 1.42 W, which is 5 orders of magnitude larger than the smallest non-zero value). The spatial discretization of the core into layers for P_{flow} is the same as that of the hydraulic conductivity, so that P_{flow} share the same layer thickness and layer number as that of hydraulic conductivity.

The contour maps of the power dissipated by the flow and of the erosion resistance index are plotted next to each other for comparison purposes (Fig. 5).

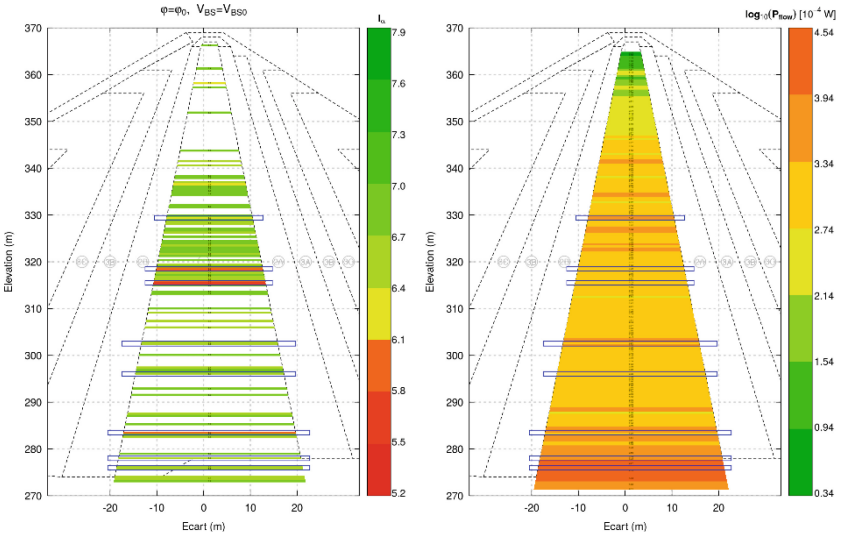

Fig. 5. Contour maps of: (left) the predicted erosion resistance index for layers characterized with values smaller than the average value of 6.95 and (right) the predicted power dissipated by the flow. Layers characterized with both relatively smaller I_α and larger P_{flow} values are highlighted in blue

Areas characterized by a lower erosion resistance index than the average value of 6.95 can be considered to be more sensitive to suffusion. Core layers near the elevations 326 m, 303 m and elevations below 288 m are characterized with power values larger than the average value of 0.14 W. The combination of these two results shows that for zones around elevations 329.4 m, 318.5 m, 315.5 m, 302.5 m, 296 m, 283.5 m, 278 m, 276 m, the power dissipated by seepage flow is relatively large and erosion resistance indices have relatively lower values. The occurrence of these two characteristics highlights zones with a relatively larger suffusion potential, compared with other zones in the dam core. Thus the combination of spatial variability of both power dissipated by seepage flow and erosion resistance index, is a novel approach to assess the spatial variability of suffusion potential of the dam core. The main advantage of this approach is that it accounts for both soil physical characteristics and construction process.

This approach helps in assisting dam owners in identifying zones that may require specific monitoring with respect to suffusion. One possible improvement of the presented approach would be to account for the increased effective stress in the dam core which could limit the suffusion potential. Also, additional work could be done to predict the kinetics of the suffusion process over the dam's lifetime.

In the case of non-plastic soils, the process of concentrated leak erosion may not appear. However if the downstream filter is poorly designed, a backward erosion process may occur. This case could be studied by using the empirical relationship between physical parameters and the erosion resistance index for interface erosion (Regazzoni and Marot 2011).

4 Conclusion

The aim of this paper is to present a method to assess the suffusion susceptibility of a dam corebased on the spatial distributions of the erosion resistance index I_α, the saturated hydraulic conductivity K_{sat} and the power dissipated by seepage flow P_{flow}. The method is applied to a large embankment dam located in Northern Québec, Canada. For this case study, the erosion resistance index values I_α were estimated using an empirical relationship obtained from a principal component analysis. This relation involves the dry unit weight, the Blue Methylene value, the friction angle and the *Finer KL* parameter (Kenney and Lau 1985). This relation has been validated against experimental tests.

The spatial variation of the dry unit weight and the *Finer KL* parameter were computed to account for the construction process which is realized in successive horizontal layers. The inferred values of the erosion resistance index lie between 5.6 and 7.3 which are indicative of soils being resistant and highly resistant to suffusion. For the analyzed dam, the hydraulic conductivities were inferred using a modified Kozeny-Carman equation. This relation involves the porosity and the effective diameter d_{10}. The spatial variation of the porosity accounts for the compaction conditions, while that of the effective diameter d_{10} reflects the progression of till placement during construction. The predicted values of hydraulic conductivities are within the order of magnitude of 10^{-7} m/s. Overall, the hydraulic conductivities appear fairly homogeneous.

Based on the estimated hydraulic conductivities and on simplified pressure boundary conditions, the power dissipated by seepage flow is inferred using the energy approach (Marot et al. 2012). This relation involves both fluid flow rate and pressure variation in each layer in order to model the entire hydraulic loading. This method, which combines construction control data and a statistical approach to infer the spatial variation of both erosion resistance index and power dissipated by seepage flow, is an efficient and practical tool to characterize global dam heterogeneities allowing the localization of zones of *relatively* larger suffusion potential. The detected zones, which are characterized by a lower erosion resistance index and a larger power than their average values, have a greater suffusion potential.

In conclusion for the analyzed dam, based on the homogeneity of the hydraulic conductivity and on the erosion resistance index values (all $I_\alpha > 5$), the overall suffusion potential appears to be fairly low.

Acknowledgements. The authors thank the Region Pays de la Loire and Hydro Québec for providing financial and practical support for this work through the RI-Adaptclim project.

References

Chapuis RP (2004) Predicting the saturated hydraulic conductivity of sand and gravel using effective diameter and void ratio. Can Geotech J 41(5):787–795

Foster M, Fell R, Spannagle M (2000) The statistics of embankment dam failures and accidents. Can Geotech J 37(5):1000–1024

Fry J-J (2012) Introduction to the process of internal erosion in hydraulic structures: embankment dams and dikes. In: Erosion of geomaterials. ISTE Ltd and John Wiley and Sons, Inc., pp 1–37

Garner S, Fannin R (2010) Understanding internal erosion: a decade of research following a sinkhole event. Int J Hydropower Dams 17(3):93–98

ICOLD (2013) Internal erosion of existing dams, levees and dykes, and their foundations. Bulletin 164, volume 1: internal erosion processes and engineering assessment

Kenney T, Lau D (1985) Internal stability of granular filters. Can Geotech J 22(2):215–225

Le VT (2017) Development of a new device and statistical analysis for characterizing soil sensibility face suffusion process. Ph.D. Thesis, Université de Nantes, France

Le VT, Marot D, Rochim A, Bendahmane F, Nguyen HH (2016) Suffusion susceptibility characterization by triaxial erodimeter and statistical analysis. In 8th International Conference on Scour and Erosion (ISCE-8), 12–15 September 2016, Oxford, UK, pp 453–460

Leroueil S, Le Bihan J-P, Sebaihi S, Alicescu V (2002) Hydraulic conductivity of compacted tills from northern quebec. Can Geotech J 39(5):1039–1049

Li M (2008) Seepage induced instability in widely graded soils. Ph.D. Thesis, University of British Columbia

Malenfant-Corriveau M (2016) Propriétés hydrauliques d'un till compacté possédant un faible pourcentage de particules argileuses. Master's Thesis, Université Laval

Marot D, Regazzoni P-L, Wahl T (2011) Energy-based method for providing soil surface erodibility rankings. J Geotech Geoenviron Eng 137(12):1290–1293

Marot D, Benamar A (2012) Suffusion, transport and filtration of fine particles in granular soil. In: Erosion of geomaterials. ISTE Ltd and John Wiley and Sons, Inc., pp 39–79

Marot D, Le VD, Garnier J, Thorel L, Audrain P (2012) Study of scale effect in an internal erosion mechanism: centrifuge model and energy analysis. Eur J Environ Civ Eng 16(1):1–19

Marot D, Rochim A, Nguyen H-H, Bendahmane F, Sibille L (2016) Assessing the susceptibility of gap-graded soils to internal erosion: proposition of a new experimental methodology. Nat Hazards 83(1):365–388

Perzlmaier S, Muckenthaler P, Koelewijn A (2007) Hydraulic criteria for internal erosion in cohesionless soil. In: Assessment of risk of internal erosion of water retaining structures: dams, dykes and levees. Intermediate Report of the European Working Group of ICOLD. Technical University of Munich, Munich, Germany, pp 30–44

Reddi LN, Lee I, Bonala MVS (2000) Comparison of internal and surface erosion using flow pump test on a sand-kaolinite mixture. Geotech Test J 23:116–122

Regazzoni P-L, Marot D (2011) Investigation of interface erosion rate by jet erosion test and statistical analysis. Eur J Environ Civ Eng 15(8):1167–1185

Rochim A, Marot D, Sibille L, Le Thao V (2017) Effects of hydraulic loading history on suffusion susceptibility of cohesionless soils. J Geotech Geoenviron Eng. https://doi.org/10.1061/(ASCE)GT.1943-5606.0001673

Skempton A, Brogan J (1994) Experiments on piping in sandy gravels. Géotechnique 44(3):449–460

Smith M, Konrad J-M (2011) Assessing hydraulic conductivities of a compacted dam core using geostatistical analysis of construction control data. Can Geotech J 48(9):1314–1327

Wan CF, Fell R (2004) Investigation of rate of erosion of soils in embankment dams. J Geotech Geoenviron Eng 130(4):373–380

Watabe Y, Leroueil S, Le Bihan J-P (2000) Influence of compaction conditions on pore-size distribution and saturated hydraulic conductivity of a glacial till. Can Geotech J 37(6): 1184–1194

Zhang L, Gelet R, Marot D, Smith M, Konrad J-M (2018) A method to assess the suffusion susceptibility of low permeability core soils in compacted dams based on construction data. Eur J Environ Civ Eng. https://doi.org/10.1080/19648189.2018.1474386

Zhong CH, Le VT, Bendahmane F, Marot D, Yin ZY (2017) Investigation of spatial scale effects on suffusion susceptibility. J Geotech Geoenviron Eng 144:04018067

Open Issues for Discussion and Contribution

Collection and Analysis of the Reactivation Data of the Historical Sand Boils in the Po River Levees

Stefano Aielli[1], Sara Pavan[1], Stefano Parodi[1], Alessandro Rosso[1(✉)], Maria Giovanna Tanda[2], Michela Marchi[3], Giovanni Vezzoli[4], Alessandro Pantano[4], Davide Losa[4], and Mirko Sirtori[4]

[1] Interregional Agency for the Po River, Parma, Italy
alessandro.rosso@agenziapo.it
[2] University of Parma, Parma, Italy
[3] University of Bologna, Bologna, Italy
[4] University of Milano Bicocca, Milan, Italy

Abstract. A recent study (Aielli et al. 2017) about sand boil reactivations in the major Po river banks (Italy) has demonstrated how a structured database of historic information can significantly contribute to better understanding of seepage phenomena and provide a practical tool for safe management of hydraulic works. The primary aim of the present work is to enhance the information collected in the database (DB), which cover the whole course the Po river, to the beginning of the delta. In particular, an improved estimation of the critical height (i.e. height of the water level in the river which causes a sand boil reactivation) for sand boil phenomena is discussed herein. The maximum height without reactivation and the minimum height with reactivation have been evaluated for each recorded sand boil. The DB information and processing of the available data allow defining how the values of the critical heights are distributed along the course of the river. The DB information, connected to the alert thresholds and to the early warning system, can provide an indication of the possible reactivations of the piping phenomena in advance, enabling efficient coordination of the emergency actions against backward erosion piping progression.

Keywords: Levees · Sand-boils · Seepage · Flood management
Data management

1 Introduction

The alluvial plain the of northern Italy (Po Basin) is one of the most intensively cultivated and populated areas in Europe, hosting ~20 million people and considerable groundwater and hydrocarbon resources (Fig. 1). The river Po (length 660 km, catchment area 71,000 km^2; Fig. 1) is the fourth longest river in Europe after the Danube, the Rhine and the Rhone. It rises at ~2000 m a.s.l. in the Western Alps (Mt. Monviso 3842 m a.s.l) and flows eastward to the mouth in the Adriatic Sea, with a

S. Bonelli et al. (Eds.): EWG-IE 2018, LNCE 17, pp. 327–335, 2019.
https://doi.org/10.1007/978-3-319-99423-9_29

mean annual discharge of 1500 m^3/s (measured from 1918 to 2003 at Pontelagoscuro gauging station).

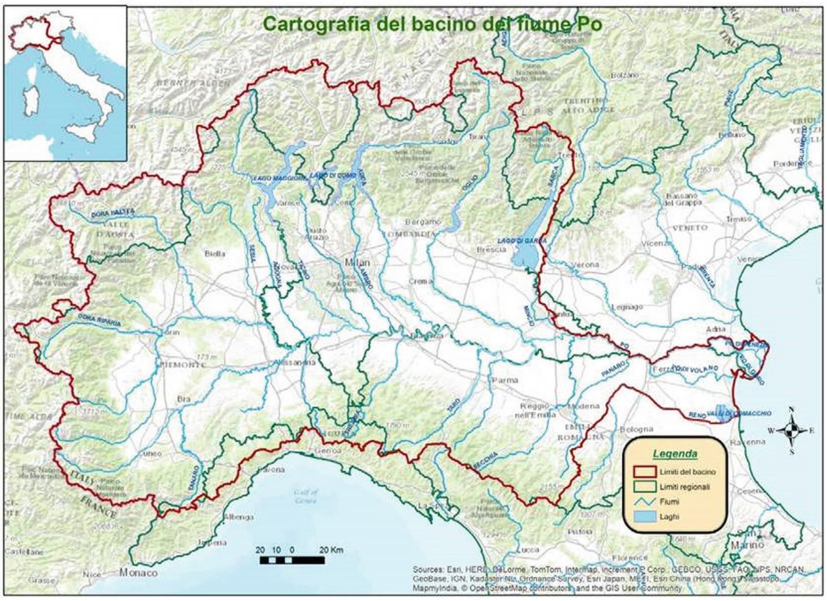

Fig. 1. The Po river basin

The Po River embankment system, which stretches for about 900 km along the main course and 150 km along the arms of its delta, was built and developed over the course of recent centuries. This embankment system is managed by a single Interregional Agency for the river Po (AIPo).

In consideration of the fact that the piping is still one of the main mechanisms threatening the embankments, AIPO has recently launched a series of activities aimed at deepening the knowledge of the piping phenomena. These activities are aimed at both defining new and more detailed levels of criticality of the embankment structures, and improving and updating the management and the design of the embankments (Fig. 2).

In particular, numerical models have been developed for the study of the triggering mechanisms (Garcia Martinez et al 2017) and for seepage and piping prediction (Cavagni et al. 2017). At the same time we worked on the construction of a database (Aielli et al. 2017) with the aim to find a relationship between the height reached by the water during the various high water events and the reactivation of sand boils ("fontanazzi").

Fig. 2. Sand boil after the 2000 high water event

2 Updating the Cadaster of the Main Embankments of the Po River

The first organized list of seepage phenomena (e.g. sand boils, underseepage) has been built in 2004 by the Basin Authority of the Po River (AdBPo in short in the following) and published in a document named "Catasto delle arginature maestre del fiume Po" ("Cadaster of the main embankments of the river Po"). This document contains information on the levees system and classifies systematically the main features of the hydraulic works (Fig. 3).

Information that can be found in this document is:

- Levees geometry (tables and sections);
- Reference high water levels (for different return periods, e.g. Tr = 200 years);
- Presence of cut-off walls (concrete or plastic);
- Seepage areas;
- Position of the #77 identified sand boils.

Sand boils are registered with a unique identification number all along Po main course until the Po di Goro inlet (start of the delta area).

Following the flood event in 2014, the need emerged for reorganizing available information in an updated an easily accessible tool. Therefore, a GIS cartographic project was created, combining the information available for the different sections of the Po river (main course and delta area), and unifying the classification criteria in the available tables.

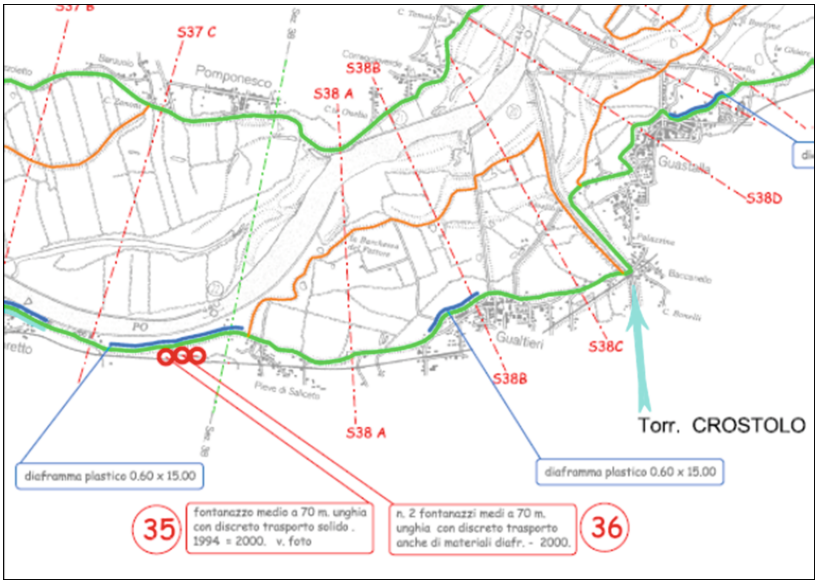

Fig. 3. Example from the "Cadaster of the main embankments of the river Po"

To easily allow for the inclusion of further data in the current data base from future high water events, a survey form has been prepared, which directly links the newly available information in the GIS attribute tables.

Information on sand boils observed in the delta area were recently added, which brought the number of observed "fontanazzi" case histories to about #130 (Fig. 4).

3 Data Processing

In order to improve the potential of the data base for management and early warning activities, some data processing and reorganization was designed. To properly compare the information from different high water events, an absolute reference height above the sea level (a.s.l.) was introduced, for the significant flood events registered in 2000, 2014 and 2016. This substitutes the previously adopted "hydrometric zero", which was an arbitrary local height defined on single independent sections.

Secondly, for each recorded sand boil the nearest upstream and downstream measurement stations are identified. A MATLAB script enables interpolating the recorded hydrographs at these two stations to associate a curve giving the hydrometric level over time to the section where the sand boil was recorded (see Fig. 5).

For each individual sand boil, this flood curve, obtained by interpolating the curves of the upstream and downstream measurement stations, represents a reliable estimate of the really transited flood curves.

The second step was the "filling" phase of the DB, inserting for each sand boil all the available information: geographic coordinates, Google Maps link for rapid

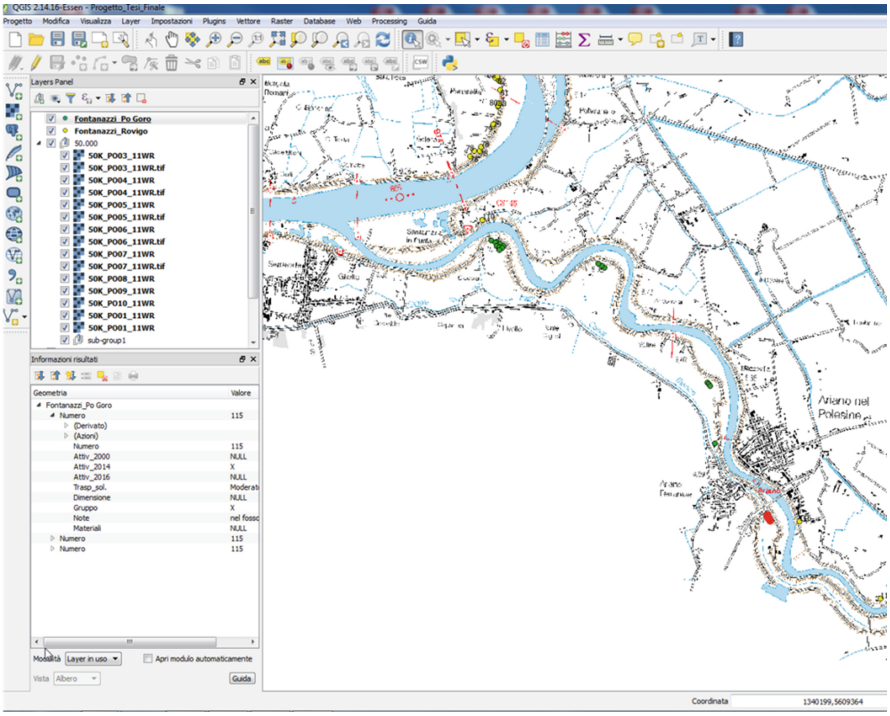

Fig. 4. An example from the the GIS database

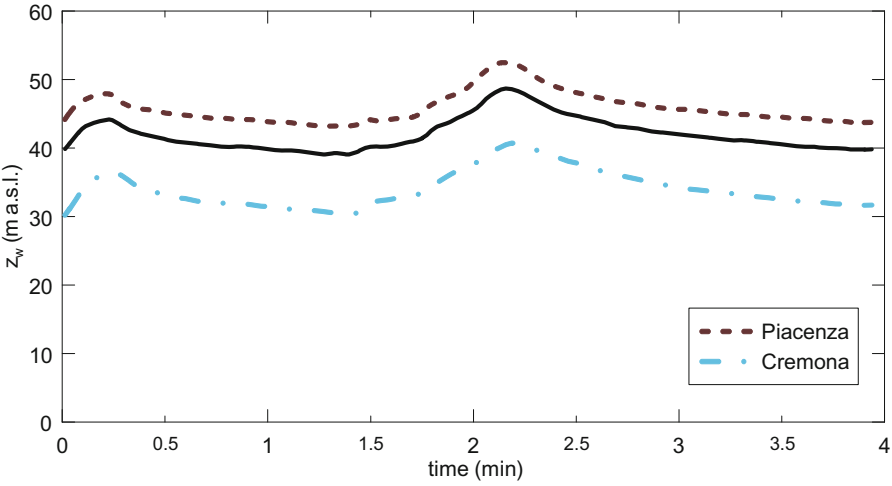

Fig. 5. The 2014 estimated flood curve for the #21 sand boil located between the section of Piacenza (above, red) and Cremona (below, light blue)

geolocation, cartography of the sand boils ADBPo Registry, estimated water levels, any associated files (granulometric analysis, images and files that are considered useful for a better description of the phenomenon), behavior of the sand boil in correspondence with the events of floods occurred, and main physical characteristics.

Having systematized the data relating to the sand boils, relating in particular their behavior with the hydrometric heights of the river, for the different events examined, allows to make a prediction on the possible activation of these phenomena. The comparison, in particular, between the maximum recorded hydrometric levels without the activation of a sand boil (Hmax) and the minimum value recorded with activation of the same (Hmin) allows to define an interval within which there is the probability that the phenomenon occurs, which it will be as great as Hmin = Hmax. The relationship between the forecasting models and the definition of these new alarm levels for each sand boil greatly increases the cognitive picture of the critical aspects along the entire river.

Comparing the different events examined, as in the case of the most significant flood, in 2000, the number of reactivations of the sand boils is much higher compared to the other floods.

In the event of October/November 2000 we have almost total reactivation of the sand boils, passing to a dozen for that of 2014, up to sporadic reactivations for that of 2016.

An exception is the delta of the Po, where the condition of pensile river creates the conditions of reactivation even with low levels of flooding (Fig. 6).

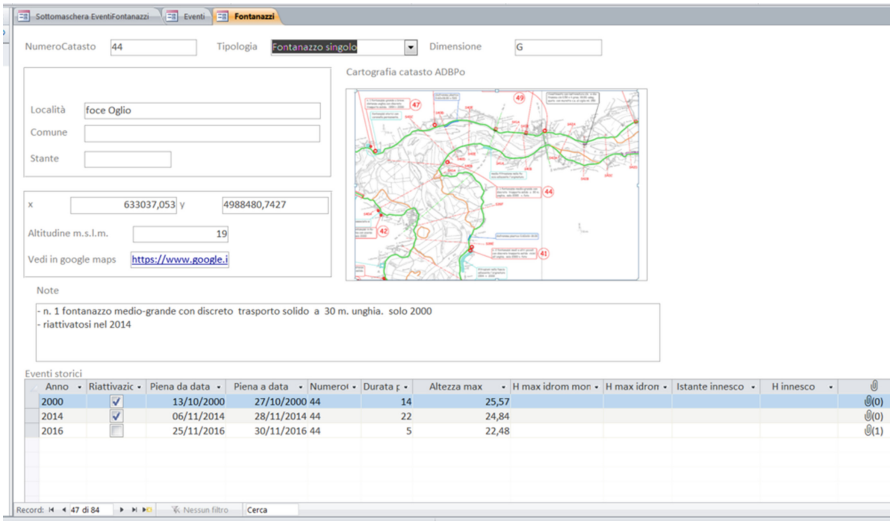

Fig. 6. Extract of data base

The following figures show the trend (up to the Po del Goro) distribution (according to the progressive kilometre) of the different Hmax (maximum reached without

activation) and Hmin (minimum value recorded with activation) of each sand boil. In particular, Fig. 7 shows the trends of the maximum and minimum height levels with reference to the left and right banks together; Figs. 8 and 9 show the same quantities with reference, respectively, to the left and right bank.

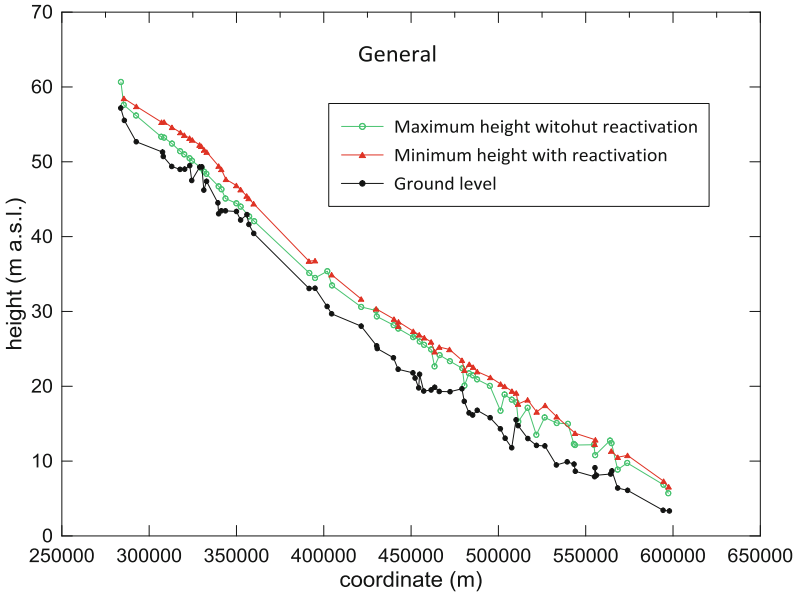

Fig. 7. General distribution of Hmax without reactivation (green) and Hmin with reactivation (red)

Although the hydraulic gradient is not directly deducible from the proposed graphs, it is significant to observe how the proposed diagrams allow to extrapolate the minimum hydraulic load difference that has generated the reactivation of each cataloged sand boil. In flood conditions, in fact, generally the side of the countryside coincides with the countryside itself. Consequently, the difference in height between the countryside and the minimum height without reactivation corresponds to the difference in hydraulic load that causes the sand boil. Finally, it is interesting to note that an accurate study of flood waves can also provide useful information on the relationship between activation of phenomena and permanence of flood waves. This last observation will be the subject of further study.

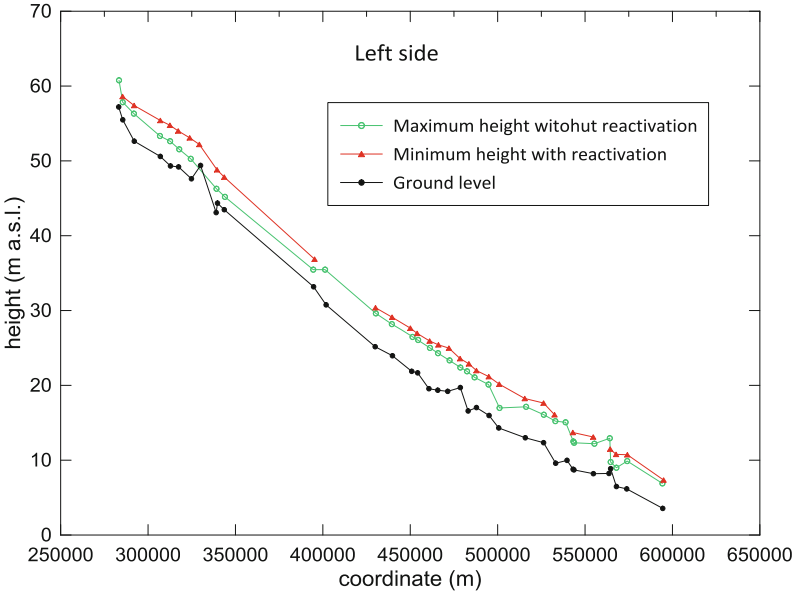

Fig. 8. Distribution for the left side of the Hmax without reactivation (green) and Hmin with reactivation (red)

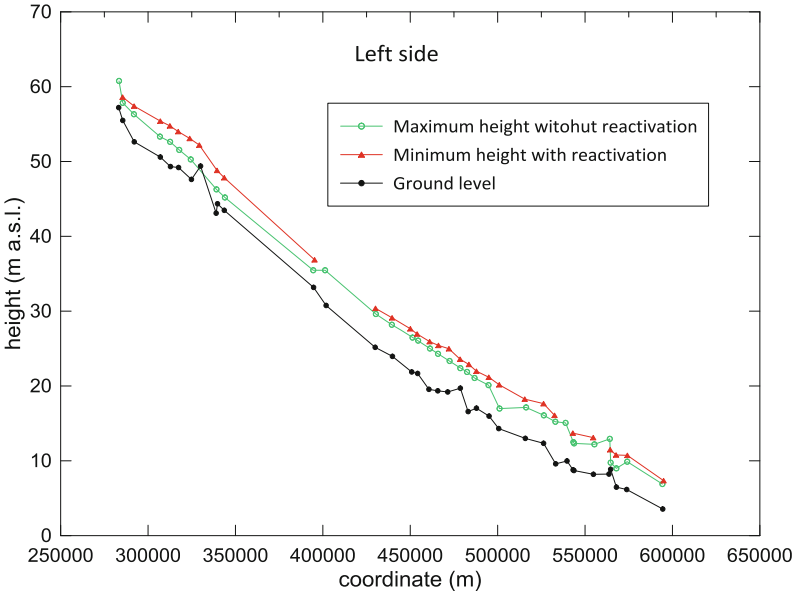

Fig. 9. Distribution for the right side of the Hmax without reactivation (green) and Hmin with reactivation (red)

4 Conclusions

The construction of a GIS and an associated Data Base has allowed to catalogue and make available all the information related to each sand boil recorded along the river Po. Although we currently have few data sets, as the information is limited to only three flood events (2000, 2014 and 2016), it is possible to make some general considerations:

- A trend of critical heights has been deduced: it therefore seems possible to hypothesize the identification of a critical flood level with the foresight to introduce adequate confidence levels that take into account the complexity of the filtration phenomena;
- The shifts from the general trend seem minimal, and probably related to local conditions (small variation in the stratigraphies and the technical characteristics of the land, which in any case determine the localization and intensity of the phenomena), which however can be variable in time;
- Slight variability in the orographic right side;

However, we can say that the analyzes carried out can help to pre-define some critical issues (piping) during flood event, in fact, the prediction of exceeding the alert thresholds is favored by a system of early warning of floods, based on hydrological and hydraulic models.

The forecasts are summarized in a risk bulletin that is shared by AI-Po to all the public bodies that may be involved in the management of the flood event. This system allows the civil protection structure to know in advance the expected water levels and the related problems.

All of this can help to get through new flood management protocols.

References

Aielli S, Parodi S, Pavan S, Rosso A (2017) Historical information and advanced tools for flood protection and structures management. In: Proceedings 25th meeting of the European working group on internal erosion, Delft, The Netherlands, pp 69–78

Garcia Martinez MF, Marchi M, Tonni L, Gottardi G, Bezuijen A, Rosso A (2017) Numerical simulation of the groundwater flow leading to the sand boil reactivation in the Po River. In: 25th Meeting of the European working group on internal erosion, Delft, The Netherlands, pp 79–87

Cavagni A, Cremonesi S, Tanda MG, Giliberti MD, La Torre L, Zanichelli G, Pavan S (2017) 25th Meeting of the European working group on internal erosion, Delft, The Netherlands

Autorità di Bacino del fiume Po (2005) Catasto arginature maestre del fiume Po, Parma, Italy

Databases for Backward Erosion Piping Laboratory Experiments and Field Observations

Vera van Beek[1(✉)], Ane Wiersma[1], Martijn van Egdom[1], and Bryant A. Robbins[2]

[1] Deltares, Delft, Netherlands
vera.vanbeek@deltares.nl
[2] U.S. Army Engineer Research and Development Center, Vicksburg, USA

Abstract. Backward erosion piping is a failure mechanism which involves the formation of shallow pipes in a sandy foundation layer and is considered to be a major risk for levees. For understanding this mechanism and the development of prediction models, laboratory experiments are essential. In addition, due to scale effects and heterogeneity in field conditions, field observations and case histories are indispensable for validation of models and delineation of piping sensitive conditions. However, both experiments and field observations are often not easily utilized for this purpose. Piping experiments have been conducted in various research programmes, countries, and in a variety of configurations making the experiments difficult to compare due to inconsistent observations and differing configurations. Case histories are often poorly documented and like experiments, described in different sources and different levels of detail, due to which their full potential is often not reached. Given the importance of experimental and field data for the prediction of backward erosion piping, a need exists for a centralized organization of data. Two different databases are presented here, for laboratory experiments and field observations respectively, each combined with a web application for viewing and exporting the data. The laboratory experiment database is populated with 332 experiments. The field observation database is currently populated with 3 failure cases and 2840 sand boils located in the Netherlands and the United States. Future work will focus on a more complete population of the databases, user-friendliness of the web viewer, and analysis of the gathered data for improvement of prediction models.

Keywords: Backward erosion piping · Database · Field observations
Sand boils · Failure cases · Laboratory experiments

1 Introduction

In both the United States (U.S.) and the Netherlands, backward erosion piping (BEP) - the formation of shallow pipes in a sandy foundation layer - is considered to be a major risk for levees. In both countries numerous sand boils are observed during high water situations, and several cases of failure from the past have been attributed to this failure mechanism. Backward erosion piping is a complex mechanism. It involves both micro-scale

S. Bonelli et al. (Eds.): EWG-IE 2018, LNCE 17, pp. 336–346, 2019.
https://doi.org/10.1007/978-3-319-99423-9_30

phenomena, like the erosion at the pipe tip and the erosion in the pipe; and macro-scale phenomena like the flow towards the pipe through the aquifer. The progression of the micro-scale pipes can lead to uncontrolled erosion and collapse of the water-retaining structure. Several models are available to predict the progression of the pipe (Schmertmann 2000; Sellmeijer et al. 2011), but questions with respect to the prediction of this phenomenon remain.

For understanding of the backward erosion piping mechanism and the development of prediction models, experiments are essential. Many prediction models are based upon, calibrated, or validated with experiments. Piping experiments are generally conducted to establish the critical head for a variety of sand types and configurations, or to analyse the process in more detail. Since the critical head and observed process both depend on the experimental configuration and sand properties, researchers have used a variety of configurations and sand types to investigate the mechanism.

Piping experiments are generally conducted with a regular cover surface and homogeneous samples. The few experiments with irregular cover surface or sand property variation in the seepage path indicate the significance of incorporating heterogeneity in calculations. In addition, scale effects are known to influence the critical gradient as well, and experiments are generally fairly small-scale. An extrapolation to field conditions is therefore always necessary. Field observations and case histories therefore are an indispensable addition to experimental data for validation of models and delineation of piping sensitive conditions.

Ideally, models rely on a decent theoretical understanding of the piping process, validated with substantial data, which was illustrated conceptually by Hartford and Hicher (2015) as shown in Fig. 1.

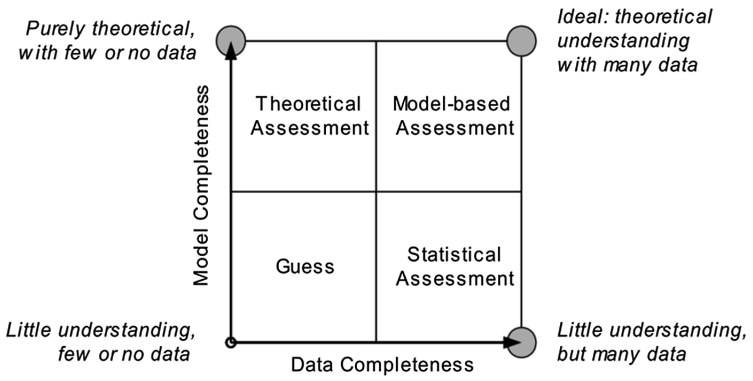

Fig. 1. Considerations of predictability (Hartford and Hicher 2015)

However, both experiments and field observations are often not easily utilized for the purpose of model validation. Piping experiments have been conducted in various research programmes, countries, and in a variety of configurations and are therefore difficult to compare. Case histories are often poorly documented and like experiments,

described in different sources and different levels of detail, due to which their full potential is often not reached.

Given the importance of experimental and field data for the prediction of backward erosion piping, a need exists for a centralized organization of data. Due to the large differences in relevant parameters for field observations and experimental data, two different databases are presented here, each combined with a web application for viewing and exporting the data.

2 General Description of Databases

The databases are developed to be open access for all users that intend to use the data for research purposes. The data is exposed through a web viewer. The website address at which both databases can be found is http://pipingdb-rws-coe.nl, representing the involvement of both Dutch and U.S. governments. The web applications are implemented using a three layered approach:

- The first layer contains the user interface and resides in the user's web browser. The user interface layer is responsible for displaying the experimental or field data and provides interaction for the user. This interface layer connects with the logic layer to request data.
- The logic layer processes data requests from the interface layer. The logic layer consists of two components: a geoserver that provides geological maps and an http rest server that provides all non-geological data.
- The third layer is a relational database which stores all of the data and retrieves data for the logic layer.

Input is provided to the database using a standard data exchange format (csv) and is currently restricted to moderators at Deltares and USACE. For purposes of quality control the addition of data is not (yet) possible for external users.

3 Laboratory Experiment Database

Many backward erosion piping experiments are available from the literature, but due to the different set up conditions and inconsistent documentation they are difficult to compare. The collection of experiments in a database will allow for a structured selection of experiments to assess influential factors or to validate models (benchmark). Additionally, the database will contribute to international sharing of data and will encourage standardization of experiments. An open database of organized experimental data could also encourage further research on this topic. The databases may therefore improve the rate at which the international community makes developments in this field, ultimately leading to practical solutions for assessing BEP in a more timely manner.

3.1 Database Structure

A backward erosion piping experiment is defined as any experiment in which a granular soil sample is subjected to a hydraulic head difference, such that a (nearly) horizontal pipe is formed in the opposite direction of flow under a roof consisting of cohesive material. Most experiments are designed to investigate the critical head, with some variables. However, the objective can also be to study the erosion process or pipe characteristics. The database focuses on the relation between critical gradient and relevant parameters.

The data to be collected can be categorized in five groups:

1. Test series information.
2. Test device configuration.
3. Soil data.
4. Test measurements.
5. Test interpretation/post-processing.

Typically test devices and soil data are used multiple times within one test series or are even used for multiple test series. The structure of the database is such that the measurements within a test series can be coupled to test devices and soil data. Figure 2 illustrates the general structure of the database. The test series information, test device information and soil data are coupled to the measurement. The measurement data

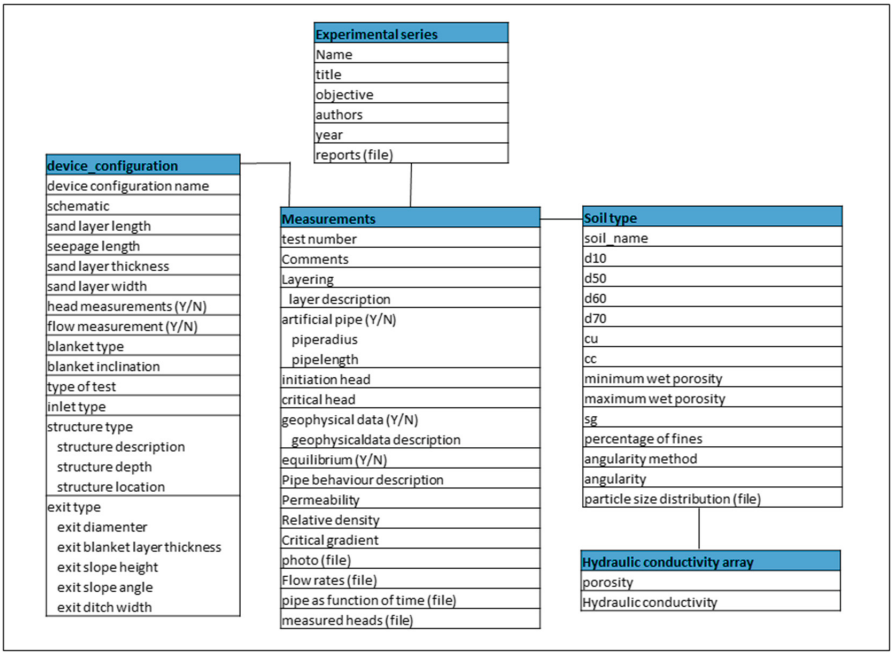

Fig. 2. Structure of the laboratory experiment database

consists of data obtained in the test directly and data obtained by interpretation of processing.

3.2 Viewer and Export Functionality

The web application allows for viewing and exporting of the data. The viewer shows a tree-structure on the left of the window showing the measurements sorted by experimental series, soil types or experimental devices (Fig. 3). After selecting one of the measurements more detailed information is provided in the categories measurement, device, soil, interpretation and test series (examples in Figs. 3 and 4). For each data field a description is provided when hovering the mouse arrow above the 'i' symbol. Photographs and images are shown per category, and files (documents) can be downloaded from this window.

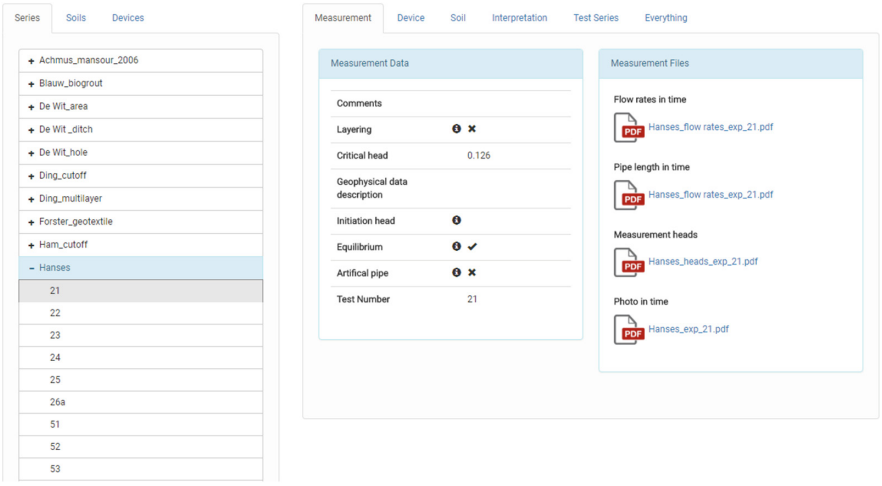

Fig. 3. Web viewer with tree structure showing a list of experimental series and experiments on the left and a window with more detailed information and attached files in 5 categories on the right

The data can be exported as .csv file or. json file. Either all data can be exported or a selection of measurements and data fields can be made based on user defined search constraints. The measurements to be exported can be selected using logical operators for all data fields within the device configuration category or soil type category. After the selection of measurements is completed, the data fields to be exported can be selected using check boxes.

3.3 Population

The experiment database is currently populated with 332 experiments in 27 series. For all experiments information on test configuration, sand properties and results (critical

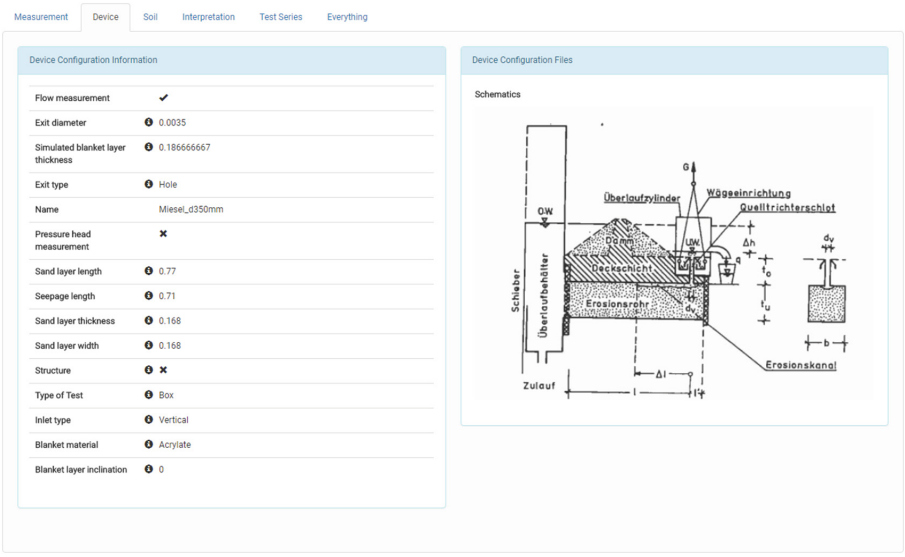

Fig. 4. Example of device data as illustrated by the web viewer

head) are provided, along with a document describing the experiments in more detail (research paper or report). The database also contains experiments with a structure, such as a cut-off wall or vertical geotextile. The database is not exhaustive and will continue to be populated in the future.

4 Field Observation Database

A potential piping failure starts with a sand boil, which can only occur when an unfiltered exit is present, requiring cracking or the presence of a defect in the blanket layer, or even the absence of a blanket layer. Due to the concentration of flow lines towards the exit, a sand boil may emerge at a hydraulic loading much lower than that at which the pipe would progress. The presence of a sand boil is therefore not necessarily an imminent sign of potential failure. Full-scale experiments have indicated that the degree of progress of the pipe cannot be judged by the sand transport rate of the sand boil (Van Beek et al. 2011). Case histories confirm the sudden transition from apparently insignificant sand boil to failure. The sand boil can therefore not be directly related to piping models. They can however be related to models predicting cracking of the blanket layer and for delineation of piping-sensitive areas. Furthermore, measurements in water boils or sand boils are valuable to validate head loss in the blanket for piping conditions.

Although relatively limited in number, case histories of failed levees are a valuable indication for the susceptibility of a location to backward erosion piping and are indispensable for a comparison with models in realistic conditions and for detecting piping-sensitive areas or geologic deposits. Only observations which are related to

backward erosion piping (not to be confused with other types of internal erosion) are included in the database.

4.1 Database Structure

Three types of relevant observations were distinguished for the field observations database: sand boil, sand boil and deformation, and failure. The relevant parameters for these observations are divided in 5 categories:

1. Location.
2. Hydraulic conditions.
3. Hydrological conditions.
4. Geological conditions.
5. Sand boil characteristics.

Since a sand boil can change in time and may even occur during different flood situations, it is possible to enter a series of observations in time. Series of observations may often occur. In particular, in the case of more severe sand boils, the site should be revisited often. It is also convenient in terms of database efficiency, since storing sand boil data as series of observations reduces redundancy. Finally, for interpretation purposes, it is useful to be able to compare observations at different times, for example to derive water levels at which sand boiling stops or to describe the effect of an emergency measure.

The geological conditions are an important part of the database, since the type of deposits (i.e. fluvial, marine, aeolian) give an extra dimension to the observed properties of the sediments. By being able to compare the geology of case histories, certain types of deposits can be identified as more or less sensitive to BEP.

Figure 5 illustrates the structure of the database. Each observation contains temporal information and is coupled to an observation series. The observation series contains general time-independent information with respect to location of the observation and is coupled to geologic information, borings, and cpts in the vicinity of the observation location. Sand descriptions may originate from borings or from the sand boil as well. In the latter case the data is coupled to an observation. For some data fields it can be questioned whether they belong to a temporal observation or to a series of observations, such as the maximum water level during the flood. The maximum water level during a flood will be the same for each observation within one flood event, but will vary in different flood events. In these cases redundancy is preferred, and the data is considered temporal.

4.2 Viewer and Export Functionality

The web viewer allows for the comparison of different maps to the spatial distribution of observations and for export of data. On the left side of the viewer an observation series can be selected from the map. Similar to the laboratory experiment database, more detailed information, categorized in 5 groups, is provided in the window next to the map (Fig. 6). The standard map is the open street map, but various background maps and data layers can be combined with the data to delineate piping sensitive areas

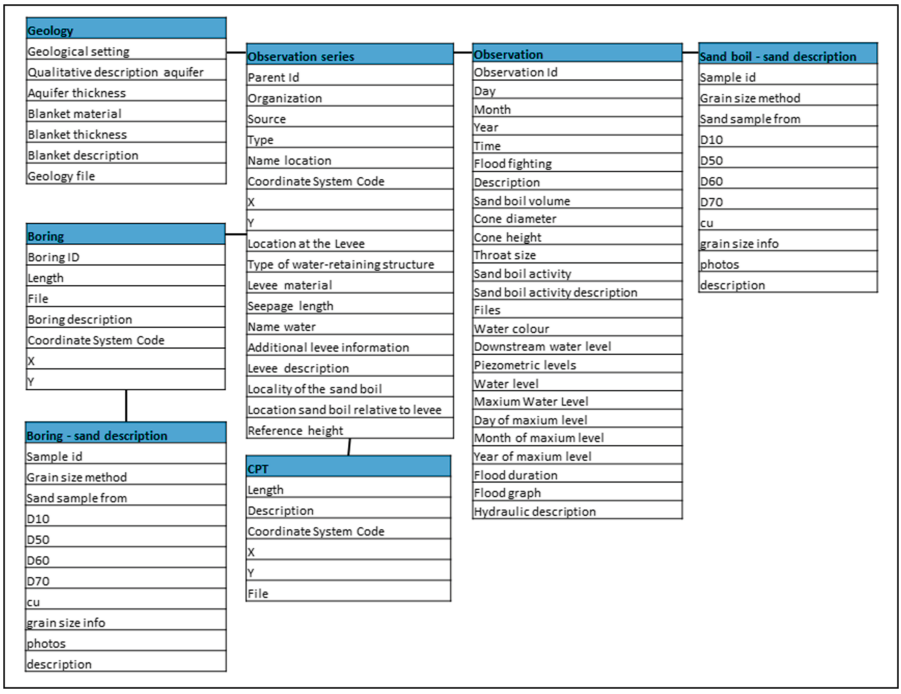

Fig. 5. Structure of the laboratory experiment database

or to explain the occurrence of sand boils. Figure 7 shows some of the different maps and data layers currently available for combination with the data from the Netherlands.

Export of data is supported in a similar way as for the laboratory experiment database: observations can be selected through logical operators on selected data fields from all categories, after which data fields to be exported can be selected using check boxes to a .csv file or .json file.

4.3 Population

The field observation database is currently populated with 3 failure cases and 2840 sand boils located in the Netherlands and the United States (Fig. 8). The field observations can be entered as series of observations in time, with information on the location, hydraulic, hydrogeological and geological conditions, and sand boil.

In the Netherlands field observation data is mainly collected by the water boards. Many water boards collect the occurrences of sand boils in a structured way. Water board Rivierenland has developed an application for structured collection of data in the field that is now being used by several other water boards as well. From a scientific point of view, parameters in addition to those currently being collected may also be relevant. Improved consistency in data collection would be beneficial to the population of the database and analysis of the occurrence of piping. Therefore the fields in the application will be compared to the database and modified when necessary in the future.

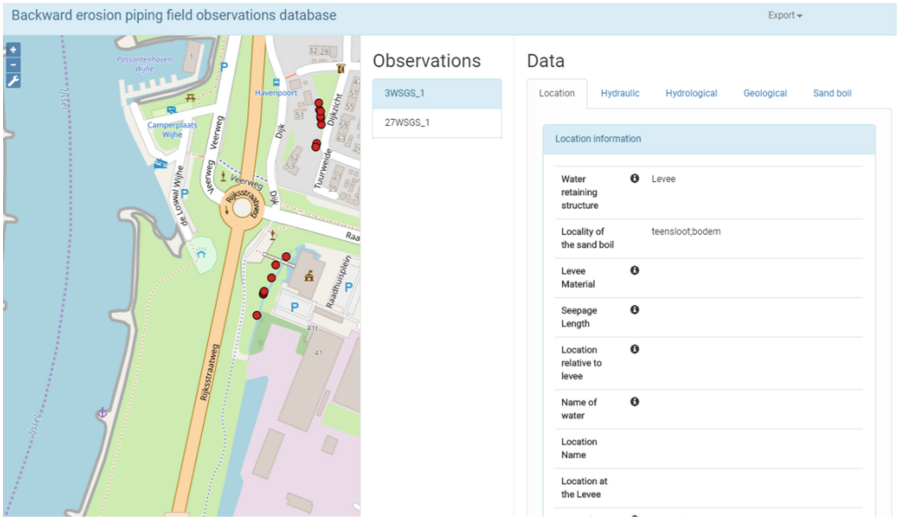

Fig. 6. Web viewer with map showing several series of observations on the left and a window with more detailed information and attached files in 5 categories on the right.

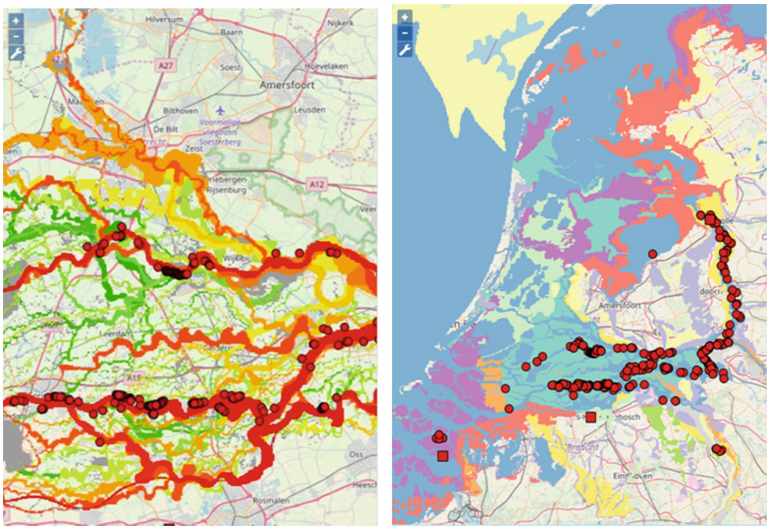

Fig. 7. Sand boil observations in the central part of the river area in the Netherlands combined with a map of sandy channel fills (left) and sand boil observations in the Netherlands combined with a geologic map (right)

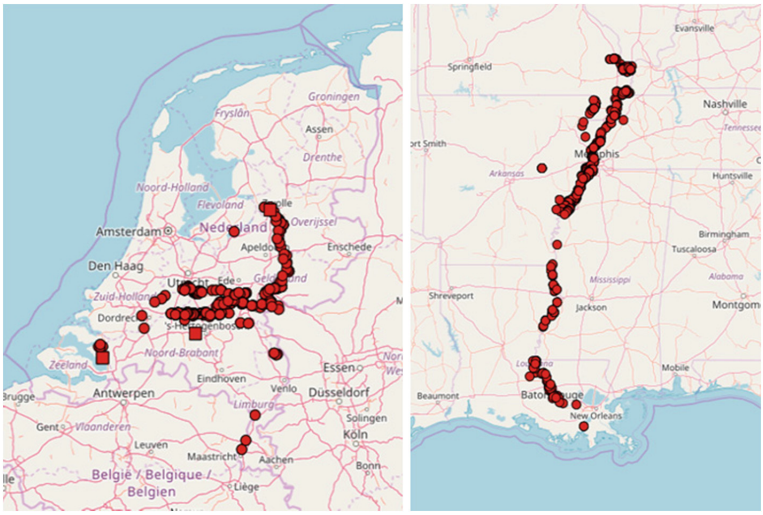

Fig. 8. Sand boils and levee failures included in the database in the Netherlands (left) and along the Mississippi in the United States (right)

In the U.S. historical field observations (pre 2011) have predominantly been entered based upon observations documented in flood reports. For more recent observations, smartphone based mobile applications have been deployed to collect photos and GPS coordinates of sand boils. The large majority of U.S. observations were collected during the 2011 Mississippi River flood using smartphone applications.

5 Conclusions and Recommendations

Two backward erosion piping databases are presented for the structured collection of laboratory experiments and field observations. Future work on the databases will focus on a more complete population and user-friendliness of the web application. In addition, the databases would benefit from a more structured and uniform data collection for both experiments and field observations, and hopefully will give rise to this more systematic collection. International standards, guidelines, and applications for the collection of data in the field will be helpful for the comparison of data and models. As such, the collected experiments and observations will be used for improvement of safety assessment and design with respect to backward erosion piping.

Acknowledgements. This paper was produced as part of an international co-operation between the U.S. Army Corps of Engineers (USACE) and Rijkswaterstaat, part of the Dutch Ministry of Infrastructure and the Environment. The authors express sincere gratitude to USACE and Rijkswaterstaat for this opportunity. The research presented is funded by the Dutch Government and the USACE. The results are intended to inform the assessment and design of flood defences.

References

Hartford DND, Hicher P-Y (2015) A case and a proposal for a soil mechanics solution to the problem of internal erosion in dams. In: Commission Internationale des Grands Barrages - Vingt-Cinquième congres des grands barrages, Stavanger, pp 305–326

Schmertmann JH (2000) The no-filter factor of safety against piping through sands. In: Silva F, Kavazanijian EJ (eds) Judgement and innovation. American Society of Civil Engineers, pp 65–133

Sellmeijer H, López de la Cruz J, van Beek VM (2011) Fine-tuning of the backward erosion piping model through small-scale, medium-scale and IJkdijk experiments. Eur J Environ Civ Eng 15:1139–1154. https://doi.org/10.3166/EJECE.15.1139-1154

Van Beek VM, Knoeff H, Sellmeijer H (2011) Observations on the process of backward erosion piping in small-, medium- and full-scale experiments. In: Erosion in geomaterials, pp 1115–1137. https://doi.org/10.3166/ejece.15.1115-1137

Harmonisation of Terminology and Definitions on Soil Deformation Due to Seepage

Jaromír Říha[1(✉)], Zakaraya Alhasan[1], Lubomir Petrula[1], Paweł Popielski[2], Agnieszka Dąbska[2], Jean Jacques Fry[3], Stanislav Viktorovich Solski[4], Natalia Andreevna Perevoshchikova[4], and Florian Landstorfer[5]

[1] Brno University of Technology, Brno, Czech Republic
riha.j@fce.vutbr.cz
[2] Warsaw University of Technology, Warsaw, Poland
[3] EDF, CIH, 73 373 Le Bourget du Lac Cedex, France
[4] Vedeneev VNIIG JSC, Saint Peterburg, Russia
[5] VERBUND Hydro Power, Vienna, Austria

Abstract. When comparing different literature sources, differences in the terminology concerning soil deformation due to seepage may be found. The distinctions are caused by language barrier (Slavic and Germanic language groups), by the view on the mechanisms and by the way of understanding individual soil deformation processes. These differences in terminology are related to the naming of the phenomenon itself or to translation issues. Clear terminology is important when comparing stability criteria applied in different countries. Here "western" and "eastern" schools may be distinguished. This study provides an overview on terminology for soil deformation due to seepage in English, French, German, Russian, Polish and Czech languages, some suggestions are presented with discussion. The paper is an initial phase for further comparison of criteria for individual soil deformation modes.

Keywords: Suffosion · Suffusion · Erosion · Piping · Clogging
Soil instability

1 Introduction

Certain differences are found in the terminology applied by "eastern" and "western" schools. These two schools have developed relatively independently for many decades and each of them appears to use its own terminology based on the original language. The western school originates in English (the English terminology was summarised in Bulletin 164 (2015)) and also in German, the eastern has origin in Russian and other Slavic languages. However, German terminology, due to past political configuration, adapted some eastern nomenclature (Busch and Luckner 1973) and may be a bridge between both schools similarly as former Yugoslavian publications in English (Vukovic and Pusic 1992). The aim of the paper is to provoke a discussion leading to harmonisation of used terms. In this text phenomena caused only by water are considered (not by the wind or chemical or biological processes).

S. Bonelli et al. (Eds.): EWG-IE 2018, LNCE 17, pp. 347–366, 2019.
https://doi.org/10.1007/978-3-319-99423-9_31

2 Terminology

Numerous mechanisms describing the seepage-induced soil deformation are defined in the literature. The clarity of each term is important for selecting appropriate criteria when designing or assessing safety of hydraulic structures as misunderstandings can lead to serious exploitation problems, failures or even disasters. Therefore, an overview of terminology used to describe different phenomena of deformation due to seepage flow is provided in this section. Types of defects due to seepage (based on the available literature) are shown in Fig. 1 and dictionary is presented in Tables 1 and 2 at the end of this paper. Furthermore, only mechanical processes which cause soil deformation, are presented, the processes like chemical or biological clogging are not discussed. Also soil freezing and effects of water chemistry are not discussed here.

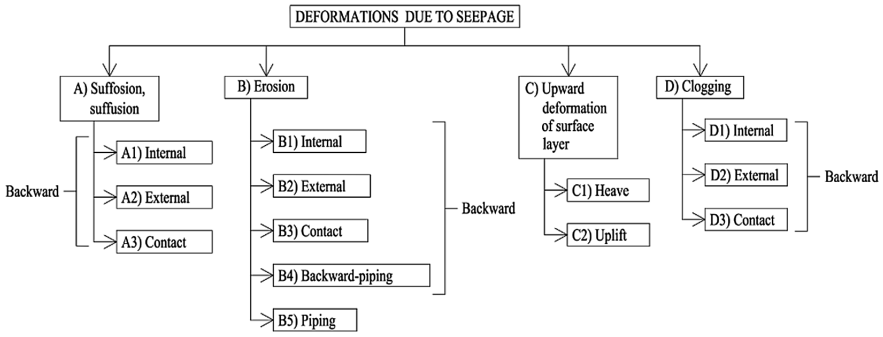

Fig. 1. Types of deformations due to seepage

2.1 Deformation Due to Seepage

Deformation due to seepage refers to any kind of change of the soil subjected to seepage. This concerns either changes of the soil surface or changes within the soil body. According to VNIIG (1989) the filtration deformation of the soil is a deformation resulting from an exceeding the strength of the soil when subject to seepage (as a result of mechanical suffusion, clogging, heave or contact erosion).

The term seepage needs a brief discussion. Only subjective boundary exists between seepage, piping or concentrated leak e.g. based on the pore/pipe size.

2.2 Suffosion, Suffusion

Suffosion is defined as transport of fine particles in non-uniform soils which leads to the volume change of original soil (Busch et al. 1993; BAW MMB 2013 and others). In case of suffusion, the soil volume does not change. Also as a result of particle loss changes of mechanical properties will occur for suffosive soils (see discussion below).

2.2.1 General Definitions on Suffosion and Suffusion

Busch et al. (1993): If suffusion occurs fine particles of a non-cohesive non-uniform soil, that fill the voids of the skeleton, are detached and migrate through the pores of the skeleton. The structure of the skeleton is not changed. Suffosion increases porosity and hydraulic conductivity while reducing the density. Vulnerable to suffusion are widely-graded soils and gap-graded soils.

BAW MMB (2013): Suffosion means detachment and migration of fine fraction of a soil in the voids of the skeleton of the coarse fraction. The skeleton carrying the load is not affected and the structure of the soil is not destroyed. Suffusion increases porosity and hydraulic conductivity, while density decreases. Continuing suffusion enables erosion processes, if the stability of skeleton is affected by loss of fines. There is no sharp edge between erosion and suffusion. Suffosion occurs mainly in non-cohesive soils.

2.2.2 Suffosion Definitions

BAW MMB (2013): Migration of particles followed by a deformation of a skeleton.

Kenney and Lau (1985): Suffosion describes the transport of small particles from a soil.

VNIIG (1991): The change of grain size distribution and structure of the soil caused by the transport of fine particles due to seepage inside the soil body or by particle washout resulting in potential affection of soil strength and stability.

Vukovic and Pusic (1992): Suffosion is a form of failure caused by removal of fine grains from the soil due to seepage. It typically occurs in a porous medium of non-uniform grain-size composition when hydraulic gradient exceeds certain critical value. Coarse grains form the skeleton of the porous medium and remain in place during suffosion.

Fannin and Moffat (2006): Internal instability describes the migration of a portion of the finer faction of a soil through its coarser fraction. Redistribution of the finer fraction, termed suffusion, may yield a loss of grain.

Richards and Reddy (2007): The erosion of fine grains that would yield a reduction in total volume and a consequent potential for collapse of the soil matrix.

Bonelli and Marot (2011): Suffosion (or suffusion) is an internal erosion process by which finer soil particles are detached/separated from the solid matrix and transported through pore constrictions by seepage flow.

Moffat et al. (2011): In the geological context of landform processes, suffosion has been used to describe "bursting/exploding out on the surface, in little eruptions, of highly mobile or water saturated material".

2.2.3 Suffusion Definitions

BAW MMB (2013): Migration of particles without deformation of the skeleton.

Wan and Fell (2002): Suffusion, also known as internal instability, involves selective erosion of fine particles from a soil whose particle size distribution does not satisfy self-filtering conditions. The finer soil particles are fine enough to be removed through the constrictions between the larger particles by flow leaving behind an intact soil skeleton formed by the coarse soil particles.

Fell and Fry (2005): Suffusion involves the washing out of fines from internally unstable soils. Soils which are gap-graded, or which have only a small quantity of fine soil in a mainly coarse sand or gravel are susceptible to suffusion. The inability of the coarser fraction of a soil to prevent migration of its finer fraction as the result of seepage flow is defined as internal instability.

Bonelli (2012): Suffusion affects cohesionless soils where a fraction of the fine particles can move between coarse particles because it does not receive the effective stress forces transmitted by the hydraulic structure. The outflow erodes the small grains through the pores of the coarser grains.

Kovacs (1981): Redistribution of fine grains within the layer, when the solid volume of the layer is not changed only the local permeability is altered.

Fannin and Moffat (2006): Internal instability describes the migration of a portion of finer fraction of a soil through its coarser fraction. Redistribution of the finer fraction may yield a loss of grain and instigate a process of undermining (suffusion).

Richards and Reddy (2007): The phenomenon that the finer fraction of an internally unstable soil moves within the coarser fraction without any loss of matrix integrity or change in total volume.

Ke and Takahashi (2014): The phenomenon that fine soil grains are eroded through the voids between the coarse grains by seepage flow, usually accompanied by seepage flow over the years.

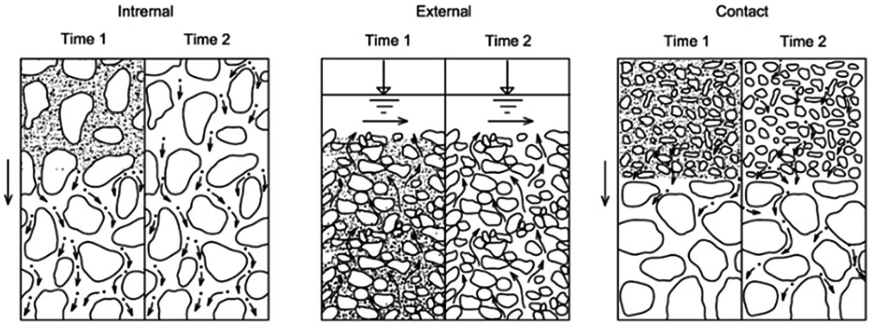

Fig. 2. Types of suffosion/suffusion (Busch and Luckner 1973)

In general, there are three types of suffosion/suffusion - internal, external and contact (Fig. 2).

2.2.4 Discussion

In the definition by Vukovic and Pusic (1992) the last sentence does not correspond with the definition used by Fannin and Moffat (2006), Richards and Reddy (2007) and others.

Terms suffosion and suffusion seem to be often misused and confused. In general, eastern literature uses term suffosion (apart from Kovacs 1981) while western literature uses most frequently term suffusion. Problems occur for criteria definition. Some consultation with other specialists will be required to solve this problem.

From the available literature and research done by Fannin it appears that suffusion is a special case of suffosion. Differences between suffosion and suffusion are better observed when the soil is compressed and subject to seepage. When the soil is suffosive critical gradient required to start the migration of fines is higher than when the soil is suffusive. That is given by fact that in suffosive soil some part of the load is transferred by fines while in suffusive soil the load is supported only by soil skeleton. That means that fines in suffusive soil are not bound within the soil structure, which leads to easier migration. As a result, consequences of suffusion might not be so alarming in terms of stress and deformation. On contrary, suffosion might lead to higher deformations as well as stress redistribution.

The authors suggest using term **suffosion** for any fine particle migration within soil and term **suffusion** only as a special case of suffosion (as described above) and some different term should be specified later based on the discussion.

2.2.5 Suggestions

Term: Suffosion, suffusion (as a special case of suffosion)

Definition: SUFFOSION is a process of selective removal of fine grains from the soil due to seepage. It typically occurs in non-uniform soils when the hydraulic gradient exceeds critical value. In special case if the coarse grains forming the skeleton of the porous medium remain in place the term SUFFUSION may be used. As a result of this process a change of porosity and hydraulic conductivity occurs and clogging may occur as well. In the following text the term **SUFFOSION** will be used only.

2.3 Internal Suffosion

2.3.1 Definitions

Kovacs (1981): Redistribution of fine grains within the layer when only the local permeability is altered.

Vukovic and Pusic (1992): See Sect. 2.2.2. Process within the porous medium is called internal.

Chugaev (1974) distinguishes three types of internal suffosion:

(a) Uniform suffosion comprising entire body of uniform soil.
(b) Internal suffosion at the contact of fine and coarse grains (here we call it contact suffosion).
(c) Casual suffosion occurs locally at the places with random unfavourable conditions like localities with poorly compacted soil, uneven settlement of foundation, defects (e.g. cracks) in the structures. This kind of suffosion may be more rapid than two cases mentioned above.

2.3.2 Discussion

Internal suffosion occurs only in cases where further transport of particles is possible, e.g. starting from geometrically instable soil contact or with external suffosion. The process occurs in non-uniform soil and may be accompanied by internal clogging in certain soil parts where fine particles can no longer pass through pores.

2.3.3 Suggestions

Term: Internal suffosion
Definition: Redistribution of fine grains **within** the layer (Fig. 3).

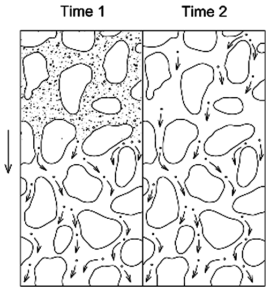

Fig. 3. Scheme of internal suffosion (Busch and Luckner 1973)

2.4 External Suffosion (Fig. 4)

See Fig. 4.

2.4.1 Definitions

Kovacs (1981): Scouring of fine grains when the volume of the solid matrix is reduced, accompanied by an increase in permeability, but the stability of the skeleton composed of the coarse grains is unaffected.

Vukovic and Pusic (1992): Form of defect caused by removal of fine grains from the soil due to seepage. It typically occurs in a porous medium of non-uniform grain-size

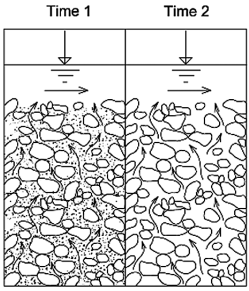

Fig. 4. Scheme of external suffosion (Busch and Luckner 1973)

composition, and only when the hydraulic gradient exceeds a certain critical value. Process along the interface between the porous medium and the free atmosphere or surface water is called external suffosion.

2.4.2 Discussion

In this section, suffosion is considered only under the influence of a pressure gradient. External suffosion may initiate internal suffosion (Busch and Luckner 1973).

2.4.3 Suggestions

Term: External suffosion

Definition: Process **along the interface** between the porous medium and the free atmosphere or surface water while the removal of fine grains occurs. The mass of the matrix is reduced followed by a permeability increase. The average grain size increases and the soil becomes more uniform. This change can lead to the end of the suffusion process (and may transfer to heave).

2.5 Contact Suffosion

2.5.1 Definition

Busch and Luckner (1973): Process when particles of the fine soil migrate into the pores of the coarser one, where the process generally continues as an internal suffosion (or as a clogging). According to the flow direction and the position of fine soil in relation to the coarse soil there are several possible scenarios (Figs. 5 and 6).

	fine / coarse	coarse / fine	fine / coarse
↓	Type 1/1		Type 1/3
↑		Type 2/2	Type 2/3
→	Type 3/1	Type 3/2	Type 3/3

Fig. 5. Possible contact suffosion/erosion scenarios (Busch and Luckner 1973)

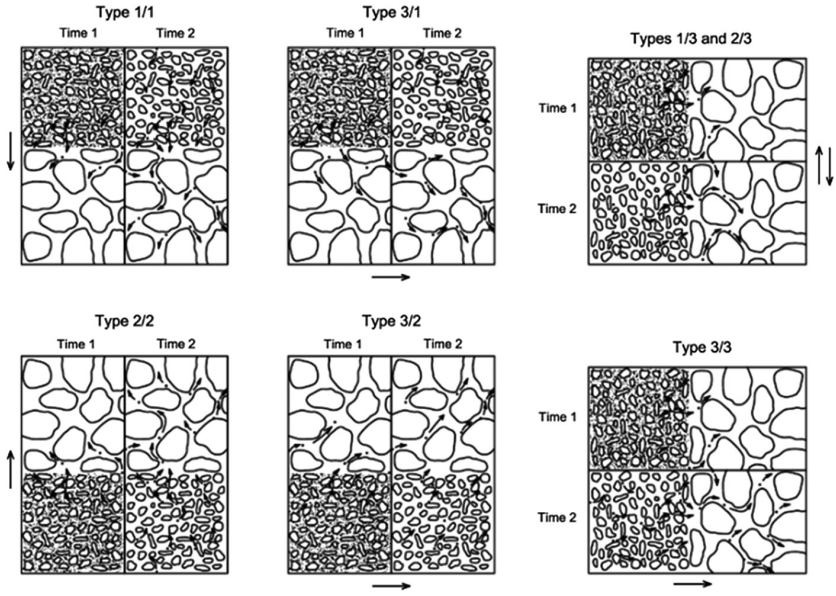

Fig. 6. Detailed schemes of contact suffosion scenarios (Busch and Luckner 1973)

2.5.2 Discussion

Type 1/1, 1/3 and 3/1 – gravity facilitates suffosion/erosion.
Type 2/2, 2/3 and 3/2 – gravity impedes suffosion/erosion.
Type 3/2 – hydraulic load has to be larger than friction (if cohesion is not considered).

2.5.3 Suggestions

Term: Contact suffosion
Definition: Process when fine soil particles migrate into the pores of the coarser one, where the process generally continues as an internal suffosion.

2.6 Erosion

There are various definitions of the term “erosion”. Most of the authors relate erosion to the action of surface processes, i.e. to the surface of the eroded soil.

2.6.1 Definitions

Busch and Luckner (1973): Erosion refers to the rearrangement and transport of almost all fractions of a soil. There are four basic types of erosion - internal, external, contact, piping (Fig. 7).

Vukovic and Pusic (1992): Deformation of the porous medium resulting from removal of grains along the preferential path of water flow. The flushed material may be brought to the surface, into the stream, or into fissures and voids (karst channels, boreholes, etc.) within the ground.

Bazant and Halek (1969): The process driven by a seepage. It typically creates flow path which is of a flat nature. Soil surrounding the flow path remains stable.

BAW MMB (2013): Detachment and migration of all soil fractions. The skeleton carrying the load is affected. Erosion process can threaten the stability of a soil or concrete structure.

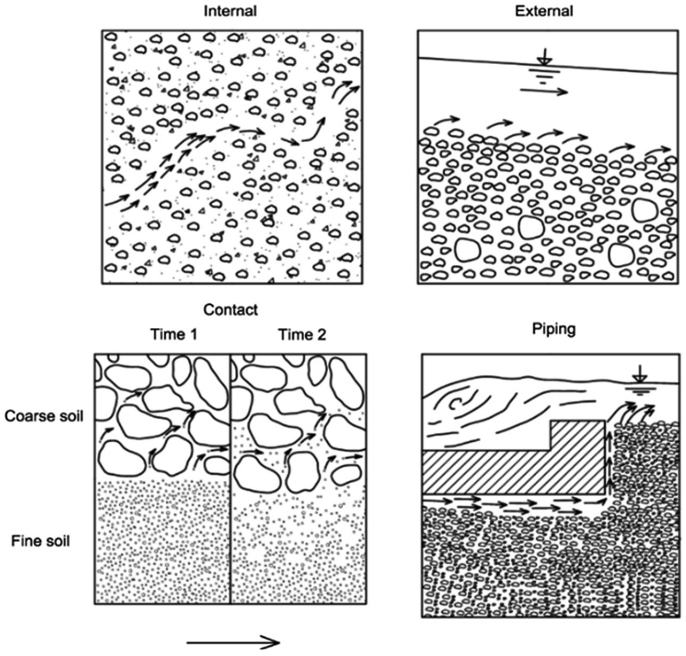

Fig. 7. Examples of erosion (Busch and Luckner 1973)

2.6.2 Discussion

The notion of the term "erosion" is not unified. The western school uses the term erosion as an umbrella for all discussed processes (Bulletin 164, 2015), eastern school considers erosion as the surface action of water on the soil. In general the erosion may concern both loose (uniform) and cohesive soils (exfoliation). During erosion all particles from given layer migrate and are flushed out.

2.6.3 Suggestions

Term: Erosion

Definition: Erosion refers to the detachment and transport of some fractions at the soil surface by the action of water. This refers namely to the concentrated leakage, backward piping and piping and also to the effect of surface erosion in the stream combined with external suffusion or heave.

2.7 Internal Erosion

Some authors and documents (Bulletin 164, 2015) consider the term "internal erosion" as an umbrella for all phenomena discussed.

2.7.1 Definitions

Busch et al. (1993): Internal erosion takes place in larger, mostly tubular cavities within the soil body often originated by plant roots or burrowing animals which continues by enlargement of the "canal" (Fig. 8). The surface erosion of the pipe sides is governed by the drag force. Vulnerability to erosion is difficult to be assessed by deterministic procedures, probabilistic approach is appropriate.

Benaissa et al. (2011): Progressive degradation of soil which is induced by the action of a flowing fluid (water) through the porous medium.

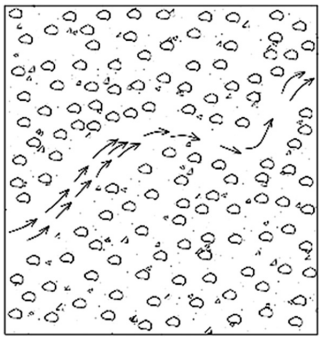

Fig. 8. Scheme of internal erosion (Busch and Luckner 1973)

EUROCODE 7 (2004): Failure by internal erosion is produced by the transport of soil particles within a soil stratum, at the interface of soil strata, or at the interface between the soil and a structure. This may finally result in regressive erosion, leading to collapse of the soil structure.

2.7.2 Discussion

According to Busch et al. (1993) the enlargement of pipes requires external or contact erosion so that internal erosion can continue. Internal erosion can be avoided by placing filter layers that stop particles´ detachment. The authors do not recommend using the EUROCODE 7 (2004) definition as it defines almost all deformations due to seepage.

2.7.3 Suggestions

Term: Internal erosion

Definition: Internal erosion takes place in larger, mostly tubular cavities within the soil body which are originated by plant or animal impacts or enlargement of pore canal by backward erosion.

2.8 External Erosion

2.8.1 Definition

Busch and Luckner (1973): External erosion occurs when exceeding the critical shear stress of the flowing surface water. The size of the eroded particles depends on the drag force (Fig. 9).

Other Used Terms: Scouring (Wieczysty 1970), scour, surface erosion.

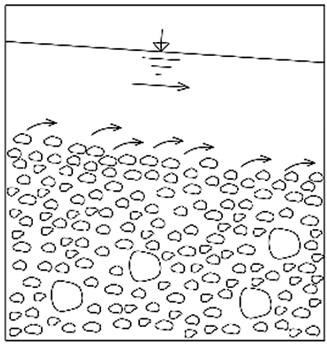

Fig. 9. Scheme of external erosion (Busch and Luckner 1973)

2.8.2 Discussion

The mentioned definition more likely describes the process of surface erosion. If particle detaches soil strata due to seepage the process is referred to external suffusion (at non-uniform soils) or heave. A combination of the upward seepage and surface flow may also occur. This situation leads to easier migration of particles.

2.8.3 Suggestions

Term: Surface erosion
Definition: The process starts by exceeding the critical shear stress on the surface.

2.9 Contact Erosion

2.9.1 Definitions

Bonelli (2012): Form of erosion that is internal to the hydraulic structure and takes place at the interface between two layers of different soil types. Contact erosion appears frequently at the interface of a layer of fine deposits whose silty particles are carried away by the flow that traverses the adjoining coarse grained layers. At contact erosion water flows through permeable soil thus fine soil is eroded at the interface (Fig. 10).

BULLETIN 164 (2015): Contact erosion occurs where a coarse soil such as a gravel is in contact with a fine soil, and flow parallel to the contact in the coarse soil erodes the fine soil. For example, flow through gravel alluvium in the foundations of dam or dike may erode the base of an overlying silt layer, or erosion of the finer layers of soil in a core may occur into a coarse gravelly layer formed by segregation during construction.

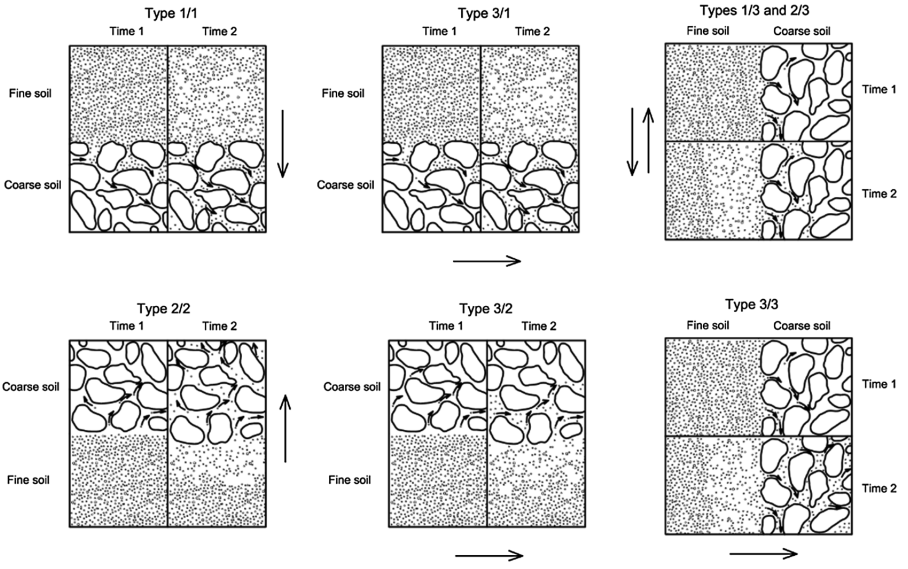

Fig. 10. Detailed schemes of contact erosion (Bonelli 2012)

2.9.2 Discussion

The phenomenon is similar to contact suffosion which occurs in case of non-uniform soils. In case of contact erosion all uniform soil is entering voids of following coarse material. The influence of gravity is the same as in case of suffosion.

2.9.3 Suggestions

Term: Contact erosion

Definition: Form of erosion that is internal to the hydraulic structure and takes place at the interface between two layers of different types of soil, namely at the interface between fine deposits whose particles of silt are carried away by the water flow that traverses the adjoining coarse grained layers. At the contact erosion water flows through a very permeable soil, thus fine soil is eroded at the interface.

2.10 Backward Erosion Piping

2.10.1 Definitions

Kollis (1966): The phenomenon of formation of a continuous passage in a soil which is filled with water or submerged soil with a disturbed structure (in the final phase - a suspension) and connecting places with higher and lower water pressure, e.g. caverns, upstream and downstream side. It is shown on the surface in the form of a source (crater) with a "boiling" ground suspension. In case of cohesionless soil underlying cohesive soil, it starts from uplifting the cohesive soil.

Busch et al. (1993): Backward erosion piping occurs along concrete structures. The mechanics is similar as for the internal erosion.

Fell and Fry (2005): The process in which erosion initiates at the exit point of seepage and progressive backward erosion results in the formation of a continuous passage or pipe.

BAW MMB (2013): Backward erosion develops at a joint between a concrete structure and a soil or between a non-cohesive soil and a cohesive soil above.

Ke and Takahashi (2014): The erosion of soil grains at the exit of a seepage path, such as the downstream face of a homogeneous embankment, where the erosion resistance of the soil is highly dependent on the hydraulic gradient and the soil stress state.

Van Beek (2015): Internal erosion mechanism in which hollow spaces (pipes) are formed in or underneath water-retaining structures as a result of the removal of soil by the action of water. Seepage causes sand grains to be transported to the downstream side of the structure, leading to the development of shallow pipes that form in an upstream direction, while depositing eroded material on the downstream side of the structure (Fig. 11).

BULLETIN 164 (2015): Backward erosion piping commences with the detachment of particles at the exit (downstream end) of leakage paths through or under embankments.

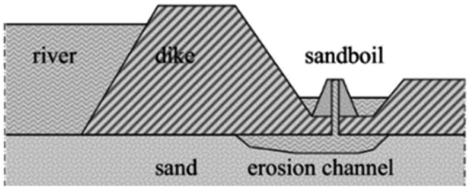

Fig. 11. Scheme of backward erosion piping (Sellmeijer 2006)

2.10.2 Suggestions

Term: Backward erosion piping

Definition: The process in which erosion initiates at the exit point of seepage. The progressive backward erosion results in the formation of a continuous passage, pipe or hollow spaces formed inside or underneath water-retaining structures. Seepage causes grains to be transported to the exit point, depositing them (Fig. 11) or flushing away by the stream at the downstream side of the water retaining structure. The condition of the process is presence of a "roof" for the eroding pipe (Bonelli 2012).

2.11 Piping (Fig. 12)

See Fig. 12.

2.11.1 Definitions

Moffat et al. (2011): The progressive development of internal erosion by seepage, appearing downstream as a hole through which water is discharged.

ICOLD Technical Dictionary (1978): The progressive development of internal erosion by seepage, appearing downstream as a hole through which water is discharged.

Wan and Fell (2002): Incidents involving the formation of a continuous tunnel (pipe) between the upstream and downstream side of an embankment dam. Piping may be initiated by backward erosion (Sect. 2.10) at locations where the exit gradient is high enough to cause detachment of soil particles. Piping may form along a concentrated leak through the embankment. The concentrated leak may be a crack through the dam core or a continuous permeable zone containing coarse and/or poorly compacted materials.

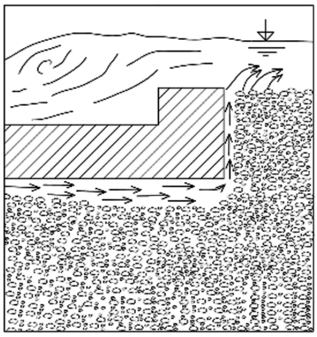

Fig. 12. Scheme of piping (Busch and Luckner 1973)

Ke and Takahashi (2014): The phenomenon that underground water flows along continuous openings such as cracks, and the soil on the wall of the tubular "pipe" is progressively washed away with the seepage flow, forming several large and instable soil channels which results in a significant loss of soil integrity.

EUROCODE 7 (2004): A piping is a particular form of failure, for example of a reservoir, by internal erosion, where erosion begins at the surface, then regresses until a pipe-shaped discharge tunnel is formed in the soil mass or between the soil and a foundation or at the interface between cohesive and non-cohesive soil strata. Failure occurs as soon as the upstream end of the eroded tunnel reaches the bottom of the reservoir. It is classified as a failure caused by hydraulic gradients (HYD).

Other Used Term: Concentrated leak erosion (Bonelli 2012)

2.11.2 Discussion

The term piping is equivalent to the concentrated leak erosion. The process of piping is governed by the surface erosion of the pipe walls. The piping may occur through the cracks, openings or is the last phase of backward erosion piping (Sect. 2.10).

2.11.3 Suggestions

Term: Piping

Definition: Incidents involving the formation and sustenance of a continuous pipe between the upstream and downstream side of an embankment dam. Piping may occur at cracks, may be initiated by backward erosion, by rotten plant roots or by activity of burrowing animals. Piping is accompanied by concentrated leak.

2.12 Heave

2.12.1 Definitions

Terzaghi and Peck (1948): Rise of a large body of soil adjoining the downstream toe of the structure. A failure of this kind occurs only if the seepage of the water that percolates upward becomes greater than the effective weight of the soil. The process greatly increases the permeability and finally the sand starts to boil (Fig. 13).

Bazant and Halek (1969): State of soil in which the non-cohesive soil starts to lose shear strength due to external forces. The loss of original physical properties leads to decrease of resistance of soil in terms of seepage.

EUROCODE 7 (2004): Failure by heave (HYD) occurs when upward seepage forces act against the weight of the soil, reducing the vertical effective stress to zero. Soil particles are lifted away by the vertical water flow and failure occurs (boiling).

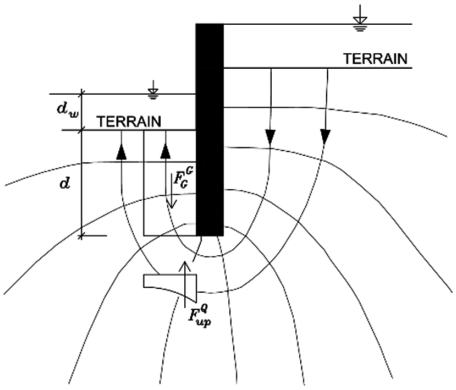

Fig. 13. Scheme of heave and uplift

2.12.2 Discussion

This process may occur even when the downstream toe is submerged. During the heave soil is losing shear strength and some grains are subject to fluidisation (effective stress equals to zero) and boiling. The process may continue with transport of fluidised particles by water flow.

2.12.3 Suggestions

Term: Heave

Definition: Heave occurs when upwards seepage forces act against the weight of the soil, reducing the vertical effective stress to zero. Soil particles are then lifted away by the vertical water flow (boiling) (EN B.1997.1, 2004).

2.13 Uplift

2.13.1 Definitions

Bazant and Halek (1969): The movement of the entire soil volume. The composition of the soil remains unaffected. Only conditions on the soil faces change. The soil movement is restricted by these conditions (Fig. 13).

Cistin (1967): The deformation of soil due to pressure induced by seepage flow which results in upward movement of the whole soil body.

EUROCODE 7 (2004): Uplift (UPL) occurs if pore water pressure under a structure or an impermeable soil layer exceeds the weight of the structure or the soil above.

2.13.2 Discussion

Uplift may occur both at cohesive and non-cohesive soils (e.g. less permeable sands covering highly permeable gravels – in case when water pressure increases rapidly in more permeable soil, the phenomena take place at the interface). In this case UPL failure precedes heave as the seepage is not fully developed in topsoil layer.

2.13.3 Suggestions

Term: Uplift
Definition: Uplift occurs if pore water pressure under a concrete structure or less permeable soil layer exceeds the weight of the structure or the soil above.

2.14 Clogging

Clogging is referred to be a deformation of the soil structure which involves filling of voids with fine particles. This process leads to a higher volume weight of the soil, i.e. smaller voids, and hence to lower seepage rates in the zone of clogging (Vukovic and Pusic 1992). As a result of clogging a change in permeability may occur which then leads to increase of the hydraulic gradient which may cause hydraulic fracturing. Similarly to previous types of deformation an external, internal and contact clogging may be recognised which can be characterised as backward for its progress in the upstream direction. Clogging is not further discussed in this text.

3 Dictionary

In Tables 1 and 2 dictionary of terms is presented. As can be seen some differences in terminology are present especially when comparing the eastern and western terms.

Table 1. Dictionary of terms (western)

Section number	English	German	French
2.2	Suffosion	Suffosion	Suffosion
2.2	Suffusion	Suffusion	Suffusion
2.3	Internal suffosion	Innere Suffosion	Suffosion interne
2.4	External suffosion	Äußere Suffosion	Suffosion externe
2.5	Contact suffosion	Kontaktsuffosion	Suffosion de contact
2.6	Erosion	Erosion	Erosion
2.7	Internal erosion	Innere Erosion	Erosion interne
2.8	Surface erosion	Kolk bzw. Oberflächen-erosion	Erosion externe
2.9	Contact erosion	Kontakterosion	Erosion de contact
2.10	Backward erosion piping	Fugenerosion	Erosion régressive de conduit
2.11	Piping, concentrated leak erosion	No special term	Renard, érosion de trou
2.12	Heave	Hydraulischer Grundbruch	Boulance
2.13	Uplift	Aufschwimmen	Soulèvement
2.14	Clogging	Kolmation	Colmatage

Table 2. Dictionary of terms (eastern)

Section number	Czech	Polish	Russian
2.2	Sufoze	Sufozja	Suffoziya
2.2	No special term	Sufozja	Vnutrennaya suffoziya
2.3	Vnitřní sufoze	Sufozja wewnętrzna	Vnutrennaya suffoziya
2.4	Vnější sufoze	Sufozja zewnętrzna	Vneshnaya suffoziya
2.5	Kontaktní sufoze	Sufozja kontaktowa	Vnutrennaya kontaktnaya suffoziya
2.6	Eroze	Erozja	Eroziya, suffoziya
2.7	Vnitřní eroze	Erozja wewnętrzna	Vnutrennaya suffoziya
2.8	Povrchová eroze	Erozja powierzchniowa	Razmyiv, razmyivanie
2.9	Kontaktní eroze	Erozja kontaktowa	Suffoziya, kontaktnyj razmyv
2.10	Zpětná eroze průsakové cesty	Erozja wsteczna, przebicie hydrauliczne	Grifon, filtratsionnyiy kanal
2.11	Piping, vývoj průsakové cesty	Przebicie hydrauliczne	skvoznoy filtratsionnyiy kanal
2.12	Ztekucení	Kurzawka, upłynnienie	Vzveshivanie, razzhizhenie
2.13	Prolomení	Wyparcie	Puchenie, nabuhanie
2.14	Kolmatace	Kolmatacja	Kolmataž, zailenie

4 Discussion and Conclusions

In this paper a summary of currently used terminology on the soil deformation due to seepage along with relevant definitions is presented together with the dictionary of the terms (Tables 1 and 2). Considering the differences in terminology used some suggestions of definitions are specified here together with short discussion. The presented explanations and proposal are not fixed yet and are rather subject for further debate.

The analysis shows two major differences. The most important one relates to the overall term for soil instability due to filtration. While "western" school including ICOLD documents uses term *Internal erosion* (Bulletin 164, 2015), the "eastern" school uses *Soil deformation due to seepage* (for example VNIIG (1989)). Here *internal erosion* is referred to only one of the modes of instability. The second difference consists in the distinguishing between the *suffosion* and *suffusion* by some "western" authors. This is not distinguished by Russian, Polish, Czech and also German authors. These facts were found when consulting co-authors.

The authors believe that the clarification of terminology may contribute to more rigorous selection and usage of appropriate criteria for the assessment of soil stability. Furthermore, authors suggest to harmonise another related terms (for ex. chemical and biological clogging) and to create an official glossary of all terms along with explanations and figures along with possible laboratory evaluation of described processes. Also an implementation in textbooks is recommended.

Acknowledgments. This paper was created with the support of the projects: FAST-J-18-5104 "Research on conditions of initiation and progression of privileged seepage paths", and FAST-J-18-5424 "Experimental testing of erosion of sealing geo-composites".

References

BAW MMB (2013) Materialtransport im Boden (MMB). Merkblatt, Bundesanstalt für Wasserbau (BAW). (in German)

Bazant Z, Halek V (1969) Příčiny porušování podloží ochranných hrází a nástin principu aktivní ochrany. Sborník Vysokého učení technického v Brně 1969(5):207–222 (in Czech)

Benaissa K, Larbi EB, Angel PVM, Kaoutar A (2011) Modeling approach of the water/soil interface in the hole erosion test (HET). Aust J Basic Appl Sci 5(7):1213–1220

Bonelli S (2012) Erosion of geomaterials. ISTE Ltd., London

Bonelli S, Marot D (2011) Micromechanical modelling of internal erosion. Eur J Environ Civ Eng 15(8):1207–1224

Bulletin 164 (2015) Internal erosion of existing dams, levees and dikes, and their foundations. Volume 1: internal erosion process and engineering assessment, France

Busch KF, Luckner L (1973) Geohydraulik. VEB Deutscher für Grundstoffindustrie, Leipzig (in German)

Busch KF, Luckner L, Tiemer K (1993) Geohydraulik, 3rd edn. Gebrüder Borntraeger, Berlin (in German)

Chugaev RR (1974) Hydraulic Terms. Vysshaya Shkola, Moscow (in Russian)

Cistin J (1967) Vnitřní sufoze nesoudržné zeminy při svislém vzestupném proudění. Sborník Vysokého učení technického v Brně 1967(1–2):181–185 (in Czech)

EN B. 1997. 1 (2004) Eurocode 7: geotechnical design-part 1: general rules. British Standards, London
Fannin RJ, Moffat R (2006) Observation on internal stability of cohesionless soils. Géotechnique 56(7):497–500
Fell R, Fry JJ (2005) Internal erosion of dams and their foundations. Taylor & Francis, New York
ICOLD Technical Dictionary (1978) ICOLD CIGB. http://www.icoldcigb.net/GB/dictionary/dictionary.asp. Accessed 05 Mar 2018
Ke L, Takahashi A (2014) Experimental investigations on suffusion characteristics and its mechanical consequences on saturated cohesionless soil. Soils Found 24(4):713–730
Kenney TC, Lau D (1985) Internal stability of granular filters. Can Geotech J 22:215–225
Kollis W (1966) Gruntoznawstwo techniczne. Wydawnictwo Arkady, Warszawa (in Polish)
Kovacs G (1981) Seepage hydraulics. Akadémiai Kiadó, Budapest
Moffat R, Fannin RJ, Garner SJ (2011) Spatial and temporal progression of internal erosion in cohesionless soil. Can Geotech J 48(3):399–412
Richards KS, Reddy KR (2007) Critical appraisal of piping phenomena in earth dams. Bull Eng Geol Env 66(4):381–402
Sellmeijer JB (2006). Numerical computation of seepage erosion below dams (piping). In: Proceedings of third international conference on scour and erosion, ISCE 3, 1.–3.11.2006, Netherland, Amsterdam, pp 596–601
Terzaghi K, Peck RB (1948) Soil mechanics in engineering. Wiley, New York
Van Beek V (2015) Backward erosion piping: initiation and progression. Dissertation. Technical University of Delft, Netherland
VNIIG (1989) Rekomendacii po proyektirovaniyu perekhodykh zon kamenno-zemlyanykh plotin. Vedeneev VNIIG, Leningrad (in Russian)
VNIIG (1991) Rekomendacii po metodike laboratorních ispytanij gruntov na vodopronicajemost i suffozionnuju ustojčivost. Vedeneev VNIIG, Saint Petersburg (in Russian)
Vukovic M, Pusic M (1992) Soil stability and deformation due to seepage. Water research publication, Colorado
Wan CF, Fell R (2002) Investigation of internal erosion and piping of soils in embankment dams by the slot erosion test and the Hole Erosion test—interpretative report. Sydney, Australia
Wieczysty A (1970) Hydrogeologia inżynierska. PWN, Warszawa (in Polish)

Correction to: Simplified Estimation of Some Main Characteristics of Pores and Constrictions in Granular Materials

Feda Seblany, Eric Vincens, and Christophe Picault

Correction to:
Chapter "Simplified Estimation of Some Main Characteristics of Pores and Constrictions in Granular Materials"
in: S. Bonelli et al. (Eds.): *Internal Erosion in Earthdams, Dikes and Levees*, LNCE 17,
https://doi.org/10.1007/978-3-319-99423-9_18

The original version of the chapter was inadvertently published, missing out some of the figure corrections provided by author in Chapter "Simplified Estimation of Some Main Characteristics of Pores and Constrictions in Granular Materials", which have been now incorporated.

The updated online version of this chapter can be found at
https://doi.org/10.1007/978-3-319-99423-9_18

S. Bonelli et al. (Eds.): EWG-IE 2018, LNCE 17, p. E1, 2019.
https://doi.org/10.1007/978-3-319-99423-9_32

Author Index

S. Bonelli et al. (Eds.): EWG-IE 2018, LNCE 17, pp. 367–368, 2019.
https://doi.org/10.1007/978-3-319-99423-9